MASSIVE STAR FORMATION ACROSS EVOLUTION AND ENVIRONMENT

Mengyao Liu
Harbin, Heilongjiang, China

B.S. Astronomy, Nanjing University, 2015

M.S. Astronomy, University of Florida, 2017

A Dissertation Presented to the Graduate
Faculty of the University of Virginia
in Candidacy for the Degree of
Doctor of Philosophy

Department of Astronomy

University of Virginia
December 2020

Committee Members:

Jonathan C. Tan
Crystal Brogan
Zhi-Yun Li
Kent Yagi

Abstract

Massive stars, i.e., those with more than 8 solar masses, play a key role in the regulation of galactic environments via their radiative, mechanical and chemical feedback. However, there is little consensus on the basic formation mechanism of these stars. Theories range from Core Accretion, e.g., the Turbulent Core Model (TCM), which is a scaled-up version of low-mass star formation from relatively ordered self-gravitating gas cores, to Competitive Accretion in which massive stars form more chaotically along with a cluster of lower-mass stars, and perhaps even involving Protostellar Collisions in the densest regions.

This thesis involves obtaining and analyzing multi-wavelength data of massive star-forming regions, especially early-stage Infrared Dark Clouds (IRDCs) and more evolved examples of high-mass and intermediate-mass protostars. The science goals include testing the Core Accretion paradigm by measuring properties of dense cores and early-stage protostars in IRDCs and the later-stage massive protostars. Thus a broad range of the evolutionary sequence of massive star formation is studied. The influence of environmental conditions on the star formation process is also investigated.

First, results studying star formation in IRDC environments are presented. The Atacama Large Mm/sub-mm Array (ALMA) was used to study 1.3 mm continuum emission tracing dusty, dense cores in 32 IRDC clumps. More than 100 cores were

identified and a global core mass function (CMF) measured that has a high-end power law distribution of the form $dN/d\log M \propto M^{-\alpha}$ with $\alpha \simeq 0.86 \pm 0.11$ for $M \geq 0.79\,M_{\odot}$, which is a significantly more top-heavy distribution than the Salpeter stellar initial mass function (IMF) that has an equivalent index of 1.35. Next the protostellar properties of these cores were investigated, including their outflow activity traced by SiO line emission, the presence of cm continuum radio jets (as observed by the VLA) and their mid-infrared (MIR) to far-infrared (FIR) spectral energy distributions (SEDs) (via archival Spitzer and Herschel telescope data). This study enables an estimate of the conditions needed for the onset of SiO emission (when $L \gtrsim 100\,L_{\odot}$) and cm continuum emission (at somewhat later stages) as diagnostic tracers of protostars. SiO outflows, like those previously studied via CO, tend to be collimated as expected in Core Accretion models, although one prominent example of more complex morphology is found, either indicating the presence of multiple sources and/or a more disordered outflow geometry.

The second part of the thesis concerns a study of a sample of about 40 high- and intermediate-mass protostars that make up the bulk of the SOFIA Massive (SOMA) Star Formation Survey observed with the FORCAST instrument from ~ 10 to 40 μm. These are selected to be MIR-bright sources, but are still expected to cover a range of evolutionary states and environments, i.e., from relatively early phase protostars in IRDCs to later phase ultracompact ionized regions, and from sources that are relatively isolated to those that are highly clustered. Multi-wavelength images of the protostars are presented. Core Accretion models predict that MIR morphologies are elongated along the direction of lower density outflow cavities, especially on the near-facing, blueshifted side. This signature is seen clearly in most of the largest, well-resolved sources, but is harder to detect in smaller, generally intermediate-mass,

protostars. The source SEDs are fit with radiative transfer (RT) models, especially those developed for the TCM that have only a few key physical parameters of initial core mass (M_c), environmental clump mass surface density ($\Sigma_{\rm cl}$) and current protostellar mass (m_*), along with viewing angle to outflow axis and amount of foreground extinction. Almost all the protostellar SEDs can be well fit with these models, although extensive degeneracies can be present in the allowed parameters. The only exception is a source of extreme luminosity and distance, which is not well fit by the models and is likely to be a cluster of several (proto)stars. Overall, based on averages of best fitting models, the SOMA sources span luminosities from $\sim 10^2 - 10^6\ L_\odot$, current protostellar masses from $\sim 0.5 - 44\, M_\odot$ and ambient clump mass surface densities, $\Sigma_{\rm cl}$ from $0.1 - 3\ {\rm g\,cm^{-2}}$. We find no evidence that a threshold value of clump mass surface density is needed to form protostars up to $\sim 25\, M_\odot$. However, there is tentative evidence that $\Sigma_{\rm cl}$ needs to be $\gtrsim 1\ {\rm g\,cm^{-2}}$ to form more massive protostars. We argue that this result is best explained by the effect of $\Sigma_{\rm cl}$ on the efficiency of star formation of the core that is set by outflow and radiative feedback, as predicted by the TCM. The SOMA protostars are being used for further tests of the Core Accretion theory, especially utilizing further multiwavelength follow-up observations that are now underway.

Acknowledgments

I sincerely want to thank my advisor, Jonathan C. Tan, for his guidance and support throughout the five and a half years. With his encouragement, I have been able to present my research to and learn from so many excellent scientists and peer students, to attend so many fruitful conferences and courses in so many beautiful places all over the world, and to have unforgettable research experiences in both University of Virginia and University of Florida. His passion and energy for work will always set a shining example to me and I will benefit from the discussions with him in both science and life. I would also like to thank Crystal Brogan, one of my committee members with whom I have worked on a side project. The inspiring discussions and the knowledges she shared on both specific problem-solving and general scientific questions are still refreshing to me. The empathy and understanding she showed to me as a woman scientist eased my anxiety. I thank Zhi-Yun Li, also one of my committee members as well as the Director of Graduate Program, for his helpful comments on my research, genuine advice on my career, and generous help when I was in trouble. I am thankful for Kent Yagi for serving on my committee and his kind words when learning about my experiences earlier this year. I acknowledge the SOFIA Thesis Enabling Program and the Jefferson Scholar Foundation for supporting my research.

I am grateful for my academic brothers, Yu Cheng, Shuo Kong, Wanggi Lim, Xiao Hu, Ben Wu, Juan Farias, as well as postdocs Kei Tanaka, Viviana Rosero, Yao-Lun

Yang, Jon Ramsey, Duncan Christie, Thomas Bisbas, Jan Staff for the general or detailed discussions on science, for helping answer my questions and confusions, for the fun we had together during conferences or at Jonathan's place. I also want to thank my collaborators Yichen Zhang, James De Buizer, Josh Marvil for their expertise and the knowledges they generously passed on to me. You are not only colleagues, but also friends to me.

I thank my UVa Astro fellows Xiaoshan Huang, Yiqing Song, Meng Sun, Chris Hayes, David Bordenave, Matt Pryal, Molly Finn, Robby Wilson, Xinlun Cheng, Haifeng Yang, Bruce Wu, Pallavi Patil, Allison Towner and many others for their support when I got stressful and the fun time at parties and restaurants. The summer weekend nights some of us watched Games of Thrones Season 7 together with melons and beer are among the most memorable moments I have had in Charlottesville. I also thank my UF Astro fellows Qi Li, Chenxing Dong, Bo Ma, Han Zhang, Chen Chen, Jingzha Ma, Yinan Zhao, Wenli Mo, Emily Moravic, Nolan Grieves for the happy times we spent. I am grateful for the support and help from faculties and staff at UVa Astronomy, NRAO and UF Astronomy.

I want to thank all the rest of my new and old friends whom I may meet in Mexico, in the UF Chinese Culture Club, in undergrad, in high school or on other occasions. I want to thank a few scientists that I met in conferences, whose words have in one way or another inspired, encouraged, and influenced me on my path in Astronomy. Last but not least, I thank two of my dearest friends, Guanying Zhu and Peiqi Zhang, for being there in my life, and my family, for their unconditional love and support.

Table of contents

List of Figures

List of Tables

Chapter 1

Introduction

1.1 Overview

High-mass stars, i.e., those with masses $> 8M_{\odot}$, have luminosities $\gtrsim 10^3 L_{\odot}$, main sequence spectral types of B3 or earlier (e.g., Martins et al. 2008). Given their powerful radiative, mechanical and chemical feedback to their environment, massive stars impact a vast range of scales and processes, from the evolution of galaxies to the formation of planets around low-mass stars in the same cluster or association. Despite their importance, there is no consensus on the basic formation mechanism of massive stars. This is partly due to the difficulty in observations, because massive protostars are rare, tend to be located at far distances ($\gtrsim$ a few kpc), embedded in clustered regions, and have high extinction at optical and NIR wavelengths (see, e.g., Tan et al. 2014, Rosen et al. 2020 for a review). Investigating massive star and cluster formation thus requires high angular resolution imaging at far-IR to (sub)millimeter wavelengths. The convergence of large far-IR-to-millimeter imaging surveys of the Galactic plane, and high-spatial resolution follow-up observations has recently opened a new window on massive star formation. The most complete and

sensitive surveys include Spitzer/GLIMPSE (Benjamin et al. 2003, Churchwell et al. 2006) and Spitzer/MIPSGAL (Carey et al. 2009) from 3.5 to 24 μm, Herschel/Hi-GAL from 70 to 500 μm (Molinari et al. 2016), APEX/ATLASGAL at 870 μm (Schuller et al. 2009), and the CSO/BGPS at 1.1 mm (Aguirre et al. 2011, Ginsburg et al. 2013).

1.2 Massive Star Formation Theories

The basic theoretical formation mechanism of massive stars remains uncertain. Theories include Turbulent Core Accretion, Competitive Accretion and Protostellar Collisions. Turbulent Core Accretion (e.g., McKee & Tan 2003) is one example of a class of models in which a massive star forms via an approximately monolithic collapse of a massive, self-gravitating core. In this model, cores are partially supported by turbulence and magnetic fields, with the fiducial reference case being that of global virial equilibrium. The cores are approximated as singular polytropic spheres with outer boundary pressure truncated by the ambient pressure of the surrounding, self-gravitating clump medium, parameterized by its mass surface density. In this model, cores can have masses much larger than the thermal Jeans mass. The Turbulent Core Accretion model predicts the existence of a core envelope-fed central accretion disk and relatively ordered and collimated bipolar outflows powered by accretion around a massive protostar.

Alternatively, Competitive Accretion (e.g., Bonnell et al. 2001; Wang et al. 2010) involves fragmentation of massive gas clumps into protostellar seeds with initial masses only of order the thermal Jeans mass, typically much less than a solar mass under these high pressure conditions. There are no massive, monolithic starless cores in this model. The formation of a massive star involves most of the mass reservoir

joining later, fed from the contracting protocluster clump. In many of the simulations of competitive accretion the star-forming clump undergoes global, typically free-fall collapse. Massive stars form hand in hand with the formation of a star cluster of mostly low-mass stars. If the collapse of the clump is regulated by outflow feedback, as in the model of Wang et al. (2010), then the rate of accretion to the massive star is also much reduced, including compared to the Turbulent Core Accretion model that has the mass reservoir starting in a dense core. Also, the geometry of accretion is expected to be much less ordered in Competitive Accretion compared to Core Accretion models (although Turbulent Cores will have some degree of asymmetries and disorder). An extension of the Competitive Accretion model is the Global Hierarchical Collapse model proposed by Vázquez-Semadeni et al. (2009, 2017), where accretion through inflowing gas streams driven by gravity replaces the Bondi-Hoyle accretion (Smith et al. 2009).

Protostellar Collision models (Bonnell et al. 1998) were motivated by the perceived difficulty of accreting dusty gas onto massive protostars. However, to be generally relevant this model requires cluster environments of extreme stellar densities, which have not yet been observed. Another difficulty is that this model predicts runaway growth of one or two extreme objects rather than generation of a more continuous stellar initial mass function (IMF).

Many questions remain to be answered. For the Turbulent Core Accretion scenario, which is basically a scaled-up version of low-mass star formation, do the predicted high mass prestellar cores exist? Are accretion disks ubiquitous around forming single and binary massive stars? For the Competitive Accretion, do massive stars always form at the center of a cluster in which the stellar mass is dominated by low-mass stars? Is the accretion rate to the star fast or slow, e.g., compared to formation of a

surrounding cluster? What is the effect of feedback in massive star formation?

1.3 Evolutionary Sequence of Massive Star Formation

For isolated low-mass star formation, the core accretion model has been summarized by Shu et al. (1987). As shown in Figure 1.1, four stages are involved – first, cores form within molecular clouds as magnetic support is lost through ambipolar diffusion; second, a protostar with a surrounding disk forms at the center of a cloud core collapsing from the inside-out; third, a protostellar outflow breaks out along the rotational axis of the system, creating a bipolar outflow; fourth, the infall terminates, revealing a newly formed star with a circumstellar disk.

Unlike the case for low-mass stars (e.g., Shu et al. 1987, André et al. 2000), the observational evolutionary sequence of massive star formation is not firmly established. One of the main differences between high-mass and low-mass stars is that the radiative feedback (i.e., thermal heating, dissociation/ionization of hydrogen, radiation pressure on dust) of a massive star plays a much more important role in its formation. The same is true for mechanical feedback from stellar winds (i.e., those from the stellar surface) and protostellar outflows (magneto-centrifugally-driven flows powered by accretion).

Despite the lack of a complete and detailed picture, in the context of core accretion, the general evolutionary progression of a massive star is believed to follow the path as shown in Figure 1.2. Massive stars are believed to start forming in cold clumpy molecular clouds. Then the cold, dense, preassembled core undergoes gravitational collapse and feeds the central protostar(s) in formation. The protostar

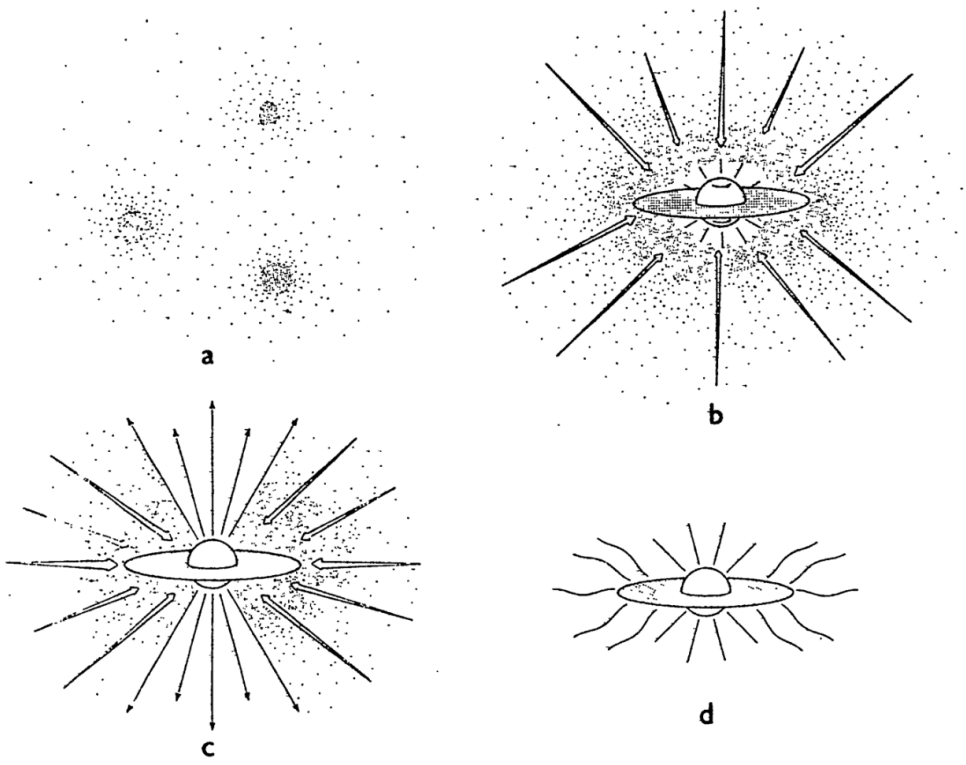

Fig. 1.1.— The four stages of low-mass star formation. Figure 7 in Shu et al. (1987).

accretes from the surrounding environment, generates jets/outflows and heats up the envelope releasing molecules into the surrounding environment through winds and shocks, entering the hot molecular core (HMC) phase. As the protostar evolves, contraction towards the main sequence structure leads to a rise in surface temperatures and causes production of Lyman continuum radiation. This begins to ionizes the gas of its surrounding outflow, then envelope and creates a hyper-compact HII (HC HII) region ($\lesssim$ 0.01 pc, Hoare et al. 2007), followed by an ultra-compact HII (UC HII) region ($\lesssim$ 0.1 pc), and finally a classical HII region (Churchwell 2002).

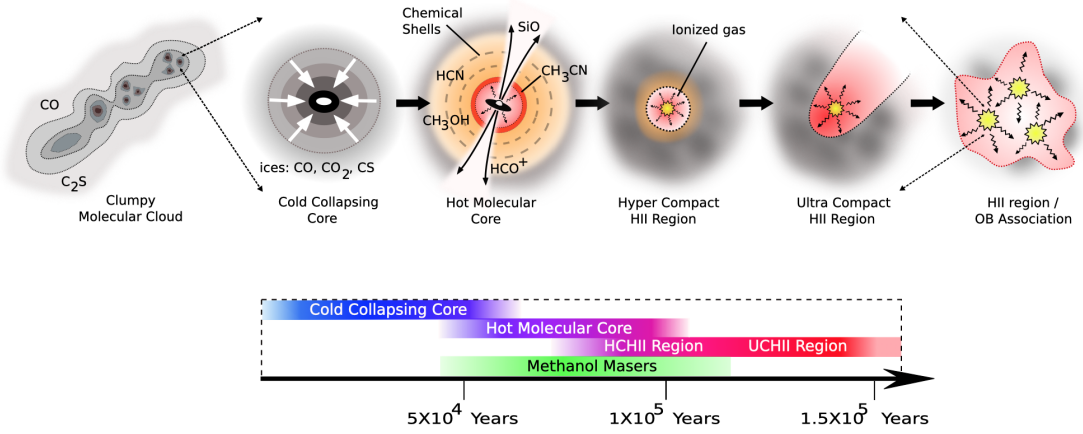

Fig. 1.2.— A cartoon of one example of an evolutionary sequence of massive star formation via core accretion (C. Purcell).

Some open questions include – is massive star formation triggered by external forces or spontaneous gravitational instability? Are the initial conditions close to equilibrium? Is the accretion process regulated or chaotic? Does an accretion disk exist in massive star formation as in the low-mass regime? When does accretion end? When do massive protostars go from having a radio morphology that is only a faint jet to appearing as a HC HII or UC HII region that is powered by photoionization? What is the time scale for each phase? What is the relation between the core mass

function (CMF) and the stellar IMF?

1.4 Environments of Massive Star Formation

Massive stars are observed to mostly form in Giant molecular clouds (GMCs) with $\Sigma \sim 0.02$g cm^{-2}. The basic physical properties of the regions hosting massive stars are shown in Figure 1.3, plotting mass surface density, $\Sigma = M/(\pi R)^2$, of the structure versus their mass, M. Star formation is seen to be localized within gas clumps in GMCs, which typically have $\Sigma_{\rm cl} \sim 0.1 - 1$g cm^{-2} (Tan et al. 2014).

Krumholz & Mckee (2008) suggested a minimum clump surface density $\Sigma_{\rm cl} \gtrsim$ 1g cm^{-2} for clumps to form massive stars. In a high pressure clump, the radiative feedback from surrounding lower-mass protostars with high accretion luminosities will prevent fragmentation of massive cores in the core accretion models. López-Sepulcre et al. (2010) found the outflow detection rate increase from 56% to 100% if they only include clumps with $\Sigma_{\rm cl} > 0.3$g cm^{-2}. Kauffmann et al. (2010) proposed a criterion for massive star formation equivalent to $\Sigma_{\rm cl} \geq 0.054(M_{\rm cl}/1000\ M_\odot)^{-1/2}$ g cm^{-2} from an observational analysis of three clouds that are forming massive stars compared to several others that are not, which is relatively low compared to the thresholds discussed above. Recently, Retes-Romero et al. (2020) studied 128 IRDCs and found that among the IRDCs satisfying the Kauffmann et al. criterion, only one third of them currently contain massive YSOs. This may indicate that a higher, more localized value of $\Sigma_{\rm cl}$ is needed to form a massive star. More work is needed to better establish if there are minimum threshold conditions for massive star formation. This is difficult since once a massive star is forming, it will alter its environment. Thus it may be more fruitful to study the formation requirements of massive prestellar cores, though there are currently very few examples (e.g., Kong et al. 2017).

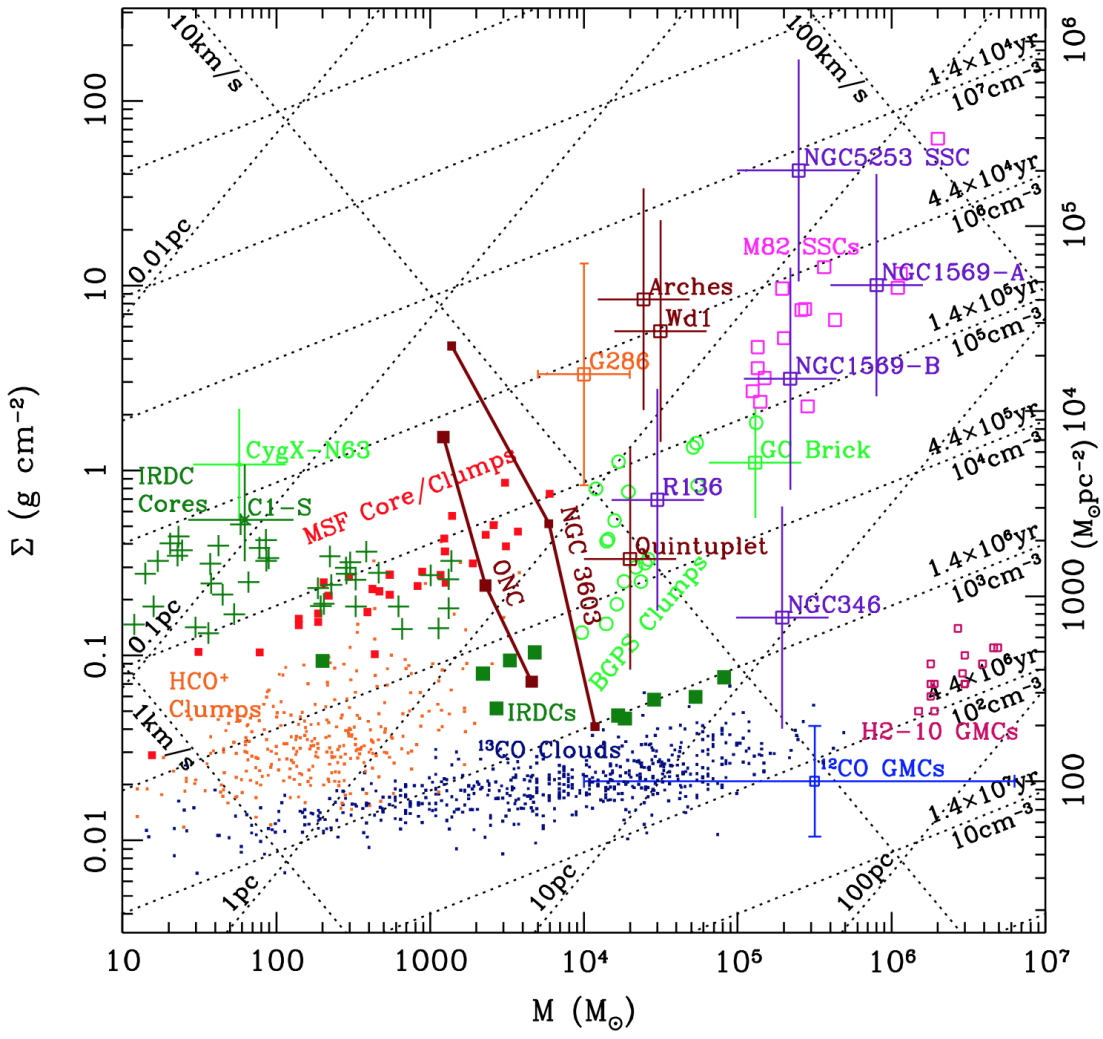

Fig. 1.3.— The environments of massive star formation. Figure 1 in Tan et al. (2014).

There is little or no variation of the shape of the high-mass IMF in the Galaxy from NGC 346 to the Arches or Westerlund 1 (Tan et al. 2014). This suggests that the process of massive star formation has a very weak dependence on density, which varies by two to three orders of magnitude between these clusters (see Figure 1.3).

Massive stars have also been observed to be likely to form in the center of clusters (e.g., Hillenbrand 1995; Qiu et al. 2008; Kirk & Myers 2012; Pang et al. 2013; Lim et al. 2013) and form in binary or multiples compared with lower-mass stars (Zinnecker & Yorke 2007). A common definition of a stellar cluster is a group of 35 or more physically related stars whose stellar mass density exceeds 1.0 $M_{\odot}$ pc^{-3} (Lada & Lada 2003). de Wit et al. (2005) found that only a low fraction ($4 \pm 2\%$) of Galactic field O stars are born in isolation.

Some open questions include – do massive stars tend to form earlier, later or contemporaneously with lower-mass stars? Do massive stars always form in clusters? If formed in a cluster, are massive stars always located in the center? How does massive star formation in isolated cases compare with crowded environments? Do clumps that form massive stars require a threshold Σ or other special properties? How does the core mass function (CMF) change in different environments?

1.5 Motivations and Outline of this Thesis

A detailed multi-wavelength comparison between theoretical models and observations of massive protostars is required to disentangle different massive star formation theories. Molecular outflows, thermal emission from circumstellar dust surrounding a protostellar core, radio jets can all serve to characterize evolutionary stages. In my thesis, I present observations of a series of high and intermediate-mass protostellar candidates that are expected to span a wide range of the evolutionary sequence and

that are forming in different environments.

To characterize starless and early-stage phases, many observations are being made of Infrared dark clouds (IRDCs, e.g., Rathborne et al. 2011, Sanhueza et al. 2013, Kong et al. 2017, Sanhueza et al. 2019, Li et al. 2019, 2020). These are cold (T $<$ 20 K), dense ($n \gtrsim 10^4$ cm^{-3}) regions of giant molecular clouds that are opaque at wavelengths $\sim$10 μm or more and thus appear dark against the diffuse Galactic background emission. They are usually thought to harbor the earliest stages of star formation. Therefore we target IRDCs and look for the onset of massive star formation through the mm/sub mm continuum and line emission.

Radiative transfer models (Zhang et al. 2014; Zhang & Tan 2018) based on Core Accretion predict distinct morphological signatures of massive protostars as one observes from $\sim$ 10 to 40 μm. At shorter wavelengths, where dust extinction is larger, light mostly escapes via outflow cavities and the appearance of the source can be highly asymmetric, being brighter along the near-facing outflow cavity. At longer wavelengths, the degree of asymmetry is reduced and the far-facing outflow cavity can become visible. Therefore we initiated the SOFIA Massive (SOMA) Star Formation Survey (De Buizer, Liu et al. 2017, Liu et al. 2019, Liu et al. 2020a, Liu et al. in prep.). The overall aim of this project is to obtain $\sim$ 10 to 40 μm images of a sample of $\gtrsim$ 50 high- and intermediate-mass protostars over a range of evolutionary stages and environments, and then compare observed spectral energy distributions (SEDs) and image intensity profiles with theoretical models. We have defined 4 protostellar types: Type I: "mid-infrared (MIR) sources in IRDCs" - relatively isolated sources in Infrared Dark Clouds, some without detected radio emission; Type II: "Hypercompact" - often jet-like, radio sources, where the MIR emission extends beyond the observed radio emission; Type III: "Ultra-compact" - radio sources where the radio

emission is more extended than the MIR emission; Type IV: "Clustered sources" - a MIR source exhibiting radio emission is surrounded by several other MIR sources within $\sim 60''$. Source selection mainly utilized the CORNISH survey (Hoare et al. 2012), complemented by radio-quiet MIR sources in IRDCs studied by Butler & Tan (2012). We included some non-Galactic plane sources and attempted, where possible, to have a relatively spread-out distribution on the sky for ease of observation with SOFIA. Our goal is to have ~ 10 sources per type so Poisson sampling uncertainties are $\lesssim 30\%$, plus ~ 10 examples of intermediate-mass sources. This thesis presents the results of observations and analysis of ~ 40 high- and intermediate-mass protostars from the SOMA survey. While division of sources into Types I-IV is quite approximate, we expect a rough evolutionary sequence from Type I to II to III as a massive protostar grows and increases its ionizing luminosity. The sample includes both relatively isolated sources, e.g., Types I and III, and more crowded environment Type IV sources. It is important to see if symmetric models can still be applied to these latter systems and whether or not they show any systematic differences compared to more isolated protostars. The SOFIA observations, combined with the RT models that follow full evolution of massive protostars (Zhang et al. 2014; Zhang & Tan 2018) allow us to derive protostellar properties, such as core mass, surrounding clump mass surface density, observed and true bolometric luminosities, outflow cavity orientation and opening angles (see, also the study of Towner et al. 2019 on 12 extended green objects (EGOs)). We will then be able to quantitively address important questions about massive star formation across evolution and environment.

The outline of my thesis is as below. I investigate early-stage massive star formation in §2 and §3 with observations towards 32 massive clumps in IRDCs. In §2[1] I present ALMA observations of 1.3 mm continuum emission of protostar candidates

[1]This chapter is a reproduction of Liu et al. (2018) published in ApJ.

and study the CMF. In §3[2] I present ALMA observations of SiO(5-4) emission and VLA observations of 6 cm continuum emission and study protostellar outflows and ionized jets as tracers of massive star formation. Then I investigate later-stage massive star formation in §4, §5, and §6, presenting results of the SOMA survey. In §4[3] I present overview of the SOMA survey and results of the first eight protostars. In §5[4] I characterize the protostellar sources with the highest luminosity as massive protostar candidates. In §6[5] I characterize intermediate-mass protostar candidates. In §7 I summarize the conclusions of my thesis.

[2]This chapter is a reproduction of Liu et al. (2020b) submitted to ApJ.

[3]This chapter is a reproduction of De Buizer, Liu et al. (2017) published in ApJ, used in this thesis with the permission of the first author.

[4]This chapter is a reproduction of Liu et al. (2019) published in ApJ.

[5]This chapter is a reproduction of Liu et al. (2020a) published in ApJ.

Chapter 2

The Core Mass Function in Infrared Dark Cloud Clumps

2.1 Introduction

The origin of the stellar initial mass function (IMF) remains one of the most important unsolved problems in astrophysics. In general, the IMF can be described as having a broad peak just below 1 $M_{\odot}$, similar in shape to a log normal, but then extending with a power law form at high masses (see, e.g., Bastian et al. 2010), i.e.,

$$\frac{\mathrm{d}N}{\mathrm{dlog}M} \propto M^{-\alpha}. \tag{2.1}$$

Salpeter (1955) derived $\alpha \simeq 1.35$ between 0.4 and 10 $M_{\odot}$ and this value has remained valid as the standard description of the $\gtrsim 1\ M_{\odot}$ IMF from more recent studies.

Observations of dense cores show that the core mass function (CMF) may be similar in shape to the IMF (e.g., Alves et al. 2007; André et al. 2010; Offner et al. 2014; Könyves et al. 2015; Ohashi et al. 2016; Cheng et al. 2018). Such a similarity is

taken as evidence that the stellar IMF is in large part determined by the fragmentation process in molecular clouds, after also allowing for a core to star formation efficiency. However, to most accurately test such a scenario, then observationally one should ideally measure the pre-stellar core (PSC) mass function, with PSCs being cores at an evolutionary stage just before the onset of star formation. This method has been carried out using FIR *Herschel* imaging of nearby regions, such as Aquila (d =260 pc), by, e.g., Könyves et al. (2015), who find a pre-stellar core mass function (PSCMF) that is similar in shape to the stellar IMF.

Unfortunately identifying PSCs in more distant star-forming regions is a non-trivial task. Using mm continuum emission to identify cores, i.e., the thermal emission from dust, is the typical method adopted (and will be the one used in this paper). This then allows a measure of the mass of the sources, assuming given dust emissivities, dust-to-gas mass ratio and dust temperature. At this point the sample likely contains a mixture of prestellar cores and protostellar cores, and with the latter tending to be more easily detected given their internal heating. Attempts can then be made to remove obvious protostellar sources, e.g., those cores associated with infrared or x-ray emission or with outflow tracers. Such an approach was adopted by Ohashi et al. (2016), who first identified 48 cores in IRDC G14.225-0.506 from 3 mm continuum emission and then proposed 28 of these to be PSCs, based on a lack of IR or x-ray emission. However, in high column density regions such as IRDCs, lack of detected IR emission, e.g., from *Spitzer* MIPSGAL 24 μm images (Carey et al. 2009), is no guarantee a core is pre-stellar, as found by, e.g., Tan et al. (2016), who find that the presence of protostellar outflows, e.g., as traced by CO, can be a more powerful probe of protostellar activity depending on the extinction in the region. Furthermore, even if a core is identified as being pre-stellar from the above methods, it is not clear at

which evolutionary stage it is at, i.e., whether it will grow much more in mass before forming a star.

An alternative approach is to try and select PSCs that are on the verge of forming stars via certain chemical species, especially deuterated species, such as N_2D^+ (see, e.g., Caselli & Ceccarelli 2012; Tan et al. 2013; Kong et al. 2017). However, this requires very sensitive observations, and then the question of measuring the masses of the PSCs still needs to be addressed, e.g., via associated mm continuum emission or dynamically via line widths from some measured size scale.

Given the above challenges, a first step for distant regions is to characterize the combined pre-stellar and protostellar CMF, by simply treating all the detected sources as cores of interest. This approach has been adopted by, e.g., Beuther & Schilke (2004), Zhang et al. (2015), Cheng et al. (2018) and Motte et al. (2018). Such an approach, which is the one we will also adopt in this paper, is really a measurement of the mm luminosity function of "cores" with potentially a mixture of PSCs and protostellar cores being included in the sample, although, it is the latter, being warmer, that will tend to be identified in a given protocluster.

Since there are large potential systematic uncertainties associated with both core identification and core mass measurement, it is important to attempt to provide uniform and consistent observational metrics of core populations in different star-forming regions and environments to allow comparison of relative properties. With this goal in mind, we derive the mm-continuum-based CMF from observations of dense regions of Infrared Dark Clouds (IRDCs), thought to be representative of early stages of massive star and star cluster formation (see, e.g., Tan et al. 2014). Most importantly, we use the same methods as our previous study of the more evolved protocluster G286.21+0.17 (hereafter G286) (Cheng et al. 2018, hereafter Paper I).

There have been several previous studies of clump and core mass functions in IRDCs. Rathborne et al. (2006) measured an IRDC clump ($\sim$0.3 pc-scale) mass function, with high-end power law slope $\alpha \simeq 1.1 \pm 0.4$ above a mass of 100 $M_\odot$ via 1.2 mm continuum emission. Ragan et al. (2009) identified structures on $\sim$0.1pc scales and found $\alpha \simeq 0.76 \pm 0.05$ from 30 to 3000 $M_\odot$ through dust extinction. Zhang et al. (2015) measured the masses of 38 dense cores (with $\sim$0.01 pc scales) in the massive IRDC G28.34+0.06, clump P1 (also known as C2 in the sample of Butler & Tan 2009, 2012) via 1.3 mm continuum emission and found a lack of cores in the range 1 to 2 $M_\odot$ compared with that expected from an extrapolation of the observed higher-mass population with a Salpeter power law mass function. Finally, as mentioned above, Ohashi et al. (2016) studied IRDC G14.225-0.506 and identified 28 starless cores on scales $\sim$0.03 pc and derived $\alpha \simeq 1.6 \pm 0.7$ from with masses ranging from 2.4 to 14 $M_\odot$ via 3 mm dust continuum emission.

We have conducted a 1.3 mm continuum and line survey of 32 IRDC clumps with *ALMA* in Cycle 2. These regions are of high mass surface density, being selected from mid-infrared (*Spitzer*-IRAC 8 μm) extinction (MIREX) maps of 10 IRDCs (A-J) (Butler & Tan 2012). The distances to the sources, based on near kinematic distance estimates, range from 2.4 kpc to 5.7 kpc. The first goal of this survey was to identify PSCs via $N_2D^+(3-2)$ emission, with about 100 such core candidates detected (Kong et al. 2017). Here we report on the analysis of the 1.3 mm continuum cores and derivation of the CMF in these 32 IRDC clumps. In §2.2 we describe the observations and analysis methods. In §2.3 we present our results on the construction of the CMF, including with completeness corrections, and the comparison to G286. We discuss the implications of our results and conclude in §2.4.

2.2 Observations and Analysis Methods

2.2.1 Observational Data

We use data from ALMA Cycle 2 project 2013.1.00806.S (PI: Tan), which observed 32 IRDC clumps on 04-Jan-2015, 10-Apr-2015 and 23-Apr-2015, using 29 12 m antennas in the array. The total observation time including calibration is 2.4 hr. The actual on-source time is ∼2-3 min for each pointing (30 pointings in total).

The spectral set-up included a continuum band centered at 231.55 GHz (LSRK frame) with width 1.875 GHz from 230.615 GHz to 232.490 GHz. At 1.3 mm, the primary beam of the ALMA 12 m antennas is 27″ (FWHM) and the largest recoverable scale for the array is $\sim 11''$ (~ 0.3 pc at a typical distance of 5 kpc). No ACA observations were performed. The sample of 32 targets was divided into two tracks, each containing 15 pointings. Track 1, with reference velocity of +58 kms^{-1}, includes A1, A2, A3, B1, B2, C2, C3, C4, C5, C6, C7, C8, C9, E1, E2 (following the nomenclature of Butler & Tan 2012). Track 2, with reference velocity of +66 kms^{-1}, includes D1, D2 (also contains D4), D3, D5 (also contains D7), D6, D8, D9, F3, F4, H1, H2, H3, H4, H5, H6. The continuum image reaches a 1σ rms noise of ∼0.2 mJy in a synthesized beam of $\sim 1.36'' \times 0.82''$. Other basebands were tuned to observe N_2D^+(3-2), SiO(5-4), $C^{18}O$(2-1), DCN(3-2), DCO^+(3-2) and CH_3OH $(5(1,4) - 4(2,2))$. These data have mostly been presented by Kong et al. (2017), with the SiO(5-4) data to be presented by Liu et al. (in prep.).

To investigate the flux recovery of our 12m data, we use the archival data from the Bolocam Galactic Plane Survey (BGPS) (Aguirre et al. 2011; Ginsburg et al. 2013), which are the closest in frequency single-dish millimeter data available. We measure the flux density in both ALMA and BGPS images of each clump (the aperture is 27″

across, i.e., one ALMA primary beam size) and then convert the BGPS flux density measurements at 267.8 GHz to the mean ALMA frequency of 231.6 GHz via $S_\nu \propto \nu^{\alpha_\nu}$ assuming $\alpha_\nu = 3.5 \pm 0.5$. For the ALMA data we measure the total flux above a 3σ noise level threshold. Finally we derive a median flux recovery fraction of 0.19 ± 0.02. As expected, these 12m array only ALMA observations filter out most of the total continuum flux from the clumps.

2.2.2 Core Identification

Our main objective is to identify cores using standard, reproducable methods. In particular, we aim to follow the methods used in our Paper I study of the G286 protocluster as closely as possible so that a direct comparison of the CMFs can be made. Thus for our fiducial core finding algorithm we will adopt the dendrogram (Rosolowsky et al. 2008) method as implemented in the astrodendro[1] python package. We set the minimum threshold intensity required to identify a parent tree structure (*trunk*) to be 4σ, where σ is the rms noise level in the continuum image prior to primary beam correction, with typical value $\sigma \sim 0.2$ mJy beam^{-1}, except for C9 where $\sigma = 0.6$ mJy beam^{-1} due to its large dynamic range.

For identification of nested substructures (*branches* and *leaves*), we require an additional 1σ increase in intensity. Finally, we set a minimum area of half the synthesized beam size for a leaf structure to be identified. These "leaves" are the identified "cores". The parameters associated with these three choices are the same as the fiducial choices of Paper I. We note that Paper I carried out an extensive exploration of the effects of these parameter choices on the derived CMF, which we do not carry out here, rather focusing on the comparison of fiducial-method CMFs between the

[1] `http://www.dendrograms.org/`

IRDC clump and G286 protocluster environments.

While the dendrogram algorithm is our preferred fiducial method of core identification, following Paper I, we will also consider the effects of using the clumpfind algorithm (Williams et al. 1994). The main differences of clumpfind are that it is non-hierarchical, so that all the detected signal is apportioned between the "cores", leading, in general, to more massive cores and thus a more top-heavy CMF (see Paper I).

We note that one difference between our methodology compared to that of Paper I is that our core identification is done in images before primary beam correction. This is because our observational data set consists of multiple individual pointings, whereas that of Paper I is a mosaic of a single region, i.e., with a more uniform noise level. The result of this difference is that our threshold levels that define cores vary depending on position in the image. Our method of implementing completeness corrections, described below, attempts to correct for this effect. Note, we restrict core identification to the area within the FWHM primary beam in each image.

2.2.3 Core Mass Estimation

We estimate core masses by assuming optically thin thermal emission from dust, following the same assumptions adopted in Paper I. The total mass surface density corresponding to a given specific intensity of mm continuum emission is

$$\begin{aligned} \Sigma_{\rm mm} &= 0.369 \frac{F_\nu}{\rm mJy} \frac{(1'')^2}{\Omega} \frac{\lambda_{1.3}^3}{\kappa_{\nu,0.00638}} \\ &\quad \times \left[\exp\left(0.553 T_{d,20}^{-1} \lambda_{1.3}^{-1}\right) - 1\right] \ {\rm g\ cm^{-2}} \\ &\rightarrow 0.272 \frac{F_\nu}{\rm mJy} \frac{(1'')^2}{\Omega} \ {\rm g\ cm^{-2}}, \end{aligned} \tag{2.2}$$

where F_ν is the total integrated flux over solid angle Ω, $\kappa_{\nu,0.00638} \equiv \kappa_\nu/(6.38 \times 10^{-3}\,\mathrm{cm^2\,g^{-1}})$ is the dust absorption coefficient, $\lambda_{1.3} = \lambda/1.30$ mm and $T_{d,20} = T_d/20$ K with T_d being the dust temperature. To obtain the above fiducial normalization of κ_ν, we assume an opacity per unit dust mass $\kappa_{1.3\mathrm{mm,d}} = 0.899\,\mathrm{cm^2 g^{-1}}$ (moderately coagulated thin ice mantle model of Ossenkopf & Henning 1994), which then gives $\kappa_{1.3\mathrm{mm}} = 6.38 \times 10^{-3}\,\mathrm{cm^2\,g^{-1}}$ using a gas-to-refractory-component-dust ratio of 141 (Draine 2011). The numerical factor following the $\rightarrow$ in the final line shows the fiducial case where $\lambda_{1.3} = 1$ and $T_{d,20} = 1$.

We note that even though temperatures in IRDCs are often measured to be cooler than $20\,K$, e.g., ~ 15 K from studies using inversion transitions of NH_3 (e.g., Pillai et al. 2006; Sokolov et al. 2017) or from multiwavelength sub-mm continuum emission maps (e.g., Lim et al. 2016), we expect that most of the cores identified in our images are protostellar cores that are internally heated to somewhat higher temperatures. If temperatures of 15 K or 30 K were to be adopted, then the mass estimates would differ by factors of 1.48 and 0.604, respectively.

2.2.4 Core Flux Recovery and Completeness Corrections

Following Paper I, we estimate two correction factors needed to estimate a "true" CMF from a "raw" observed CMF. The first factor is the flux recovery fraction, f_{flux}; the second factor is the number recovery fraction, f_{num}.

To evaluate these factors, artificial cores of a given mass (i.e., after primary beam correction) are inserted into each of the IRDC images, with three sources being inserted at a given time at random locations within the primary beam and this exercise repeated 50 times. This enables 150 experiments for each core mass. We note that the choice of random placement within the primary beam is different from that adopted

in Paper I, which used the ACA-only image of the mosaic region as a weighting factor for core placement. We also note that our method means that cores of a given mass that are placed near the edge of the primary beam have smaller fluxes in the image and thus are harder to detect. We explore a range of masses from 10^{-1} to $10^{1.2}$ $M_\odot$ with even spacing of 0.2 in log M. We assume the flux of the artificial cores has a gaussian distribution with the shape of the synthesized beam. This is an approximation that is most accurate in the limit of small, unresolved cores, which is where the correction factors become most important. The dendrogram algorithm is run to determine if the cores are recovered and then the recovered flux is compared to the true flux.

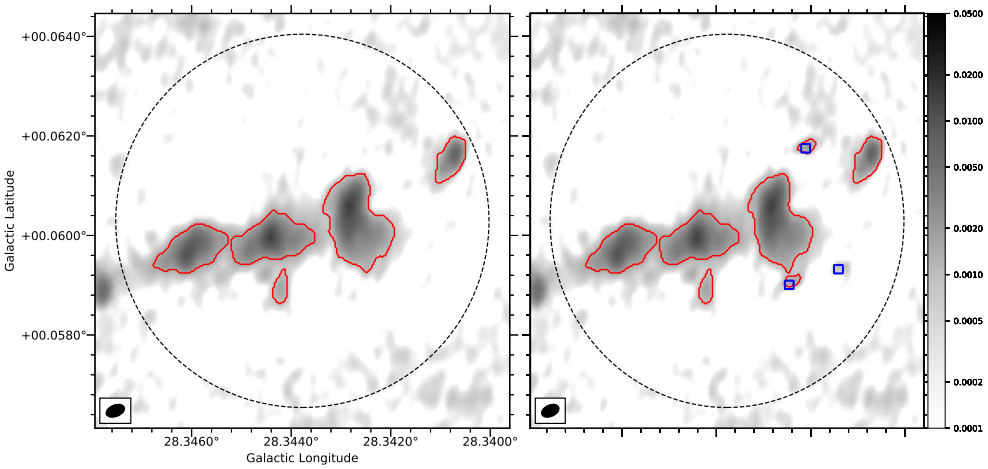

Fig. 2.1.— An example of artificial core insertion and recovery to evaluate completeness corrections for the C2 clump. *(a) Left:* Original 1.3 mm continuum image of the region (intensity scale in Jy beam^{-1}; dashed circle shows FWHM of primary beam; synthesized beam shown in bottom left), with boundaries of the identified cores shown in red. *(b) Right:* Same as (a) but now after inserting three artificial cores of 1.6 $M_\odot$ at random locations, with their centers marked by blue squares. Cores identified by the dendrogram algorithm are again marked with red contours: two out of three of the artificial cores are found.

An example of this procedure is shown in Figure 2.1. We can tell from the figure

that whether a core of $\sim 1.6\,M_{\odot}$, which has a peak flux of $\sim 10\,\sigma$ at 5.0 kpc, can be detected depends on its location within the filed of view, i.e., being harder to detect near the edge of the primary beam, and also on the local background. The local background can have two main effects. First, if a faint core happens to be placed on an already identified stronger core, then the artificial core is likely to be undetected due to confusion. Second, if a faint core is placed on a region of emission in the original image that was too faint to be detected as a core, this increases the chances that the core will now be recovered by the core finding algorithm. In this case its recovered flux will have been artificially boosted by the presence of this background emission, though the total recovered flux may still be less than that inserted, e.g., due to the threshold criteria of core finding algorithm.

The median value of the ratio of recovered to true flux defines $f_{\rm flux}$, with this quantity being measured both as a function of true flux (mass) and of recovered flux (mass). The ratio of the actual number of cores recovered to the number inserted defines $f_{\rm num}$. The derived values of $f_{\rm flux}$ and $f_{\rm num}$ are presented below in §2.3.

2.3 Results

2.3.1 Continuum Images

The continuum images of the 30 positions in the IRDCs, covering 32 clumps, are shown in Figure 2.2, together with the identified cores (i.e., leaves from the dendrogram algorithm). The size of the FWHM of the primary beam is shown with a dashed circle in each image.

Overall we have identified 107 cores in these images. Note that we only identify cores that are within the primary beam. Although there may be true cores that show

strong emission outside the primary beam, as in B2 and C2, in most cases the noise outside is relatively high and thus it is harder to identify cores of a given mass. We also note that we identify cores in all the regions apart from C3 and D2. Cores are named as, e.g., A1c1, A1c2, etc, in the region A1, with the numbering order from higher to lower Galactic latitude.

The properties of the identified cores (after primary beam correction) are listed in Table 2.1. The masses range from $0.261 M_\odot$ to 178 $M_\odot$ (0.150 $M_\odot$ to 178 $M_\odot$ without flux correction), given our fiducial methods of mass estimation. The median radius of the cores is $R_c \sim 0.02$ pc, with the radii evaluated as $R_c = \sqrt{A/\pi}$, where A is the projected area of the core. We then evaluate the mean mass surface density of the cores, $\Sigma_c \equiv M/A$, which have values $\gtrsim 0.3\,\mathrm{g\,cm^{-2}}$. This is consistent with expectations of the Turbulent Core Model of McKee & Tan (2003) given that the mass surface densities of the IRDC clump environments are at about this level of $\sim 0.3\,\mathrm{g\,cm^{-2}}$ (Butler & Tan 2012). We also evaluate the mean H nuclei number density in the cores, $n_{\mathrm{H},c} \equiv M_c/(\mu_{\mathrm{H}} V)$, where $\mu_{\mathrm{H}} = 1.4 m_{\mathrm{H}}$ is the mean mass per H assuming $n_{\mathrm{He}} = 0.1 n_{\mathrm{H}}$ and $V = 4\pi R_c^3/3$. The mean value of $\log_{10}(n_{\mathrm{H},c}/\mathrm{cm^{-3}})$ is 6.58, with a dispersion of 0.34.

From an inspection of the molecular line data of these regions, as presented by Kong et al. (2017), we note that more than half of the cores are associated with molecular line emission, e.g., N_2D^+(3-2), DCN(3-2), DCO^+(3-2), $C^{18}O$(2-1) and, occasionally, SiO(5-4). However, only the latter of these transitions is known to be a good tracer of outflows, especially from more massive protostars. Analysis of the SiO emission will be presented in a companion paper (Liu et al., in prep.).

Table 2.1. Estimated physical parameters for 1.3 mm continuum cores

Source	l (°)	b (°)	d (kpc)	$I_{\rm peak}$ (mJy beam^{-1})	S_ν (mJy)	$M_{\rm c,raw}$ ($M_\odot$)	M_c ($M_\odot$)	R_c (0.01 pc)	Σ_c (g cm^{-2})	$n_{\rm H,c}$ (10^6 cm^{-3})
A1c1	18.78746	-0.28505	4.8	1.11	0.714	0.501	0.949	1.29	0.380	3.05
A1c2	18.78864	-0.28598	4.8	9.92	32.8	23.0	23.0	5.25	0.559	1.11
A2c1	18.79969	-0.29520	4.8	2.14	3.76	2.64	3.49	2.47	0.382	1.60
A2c2	18.80070	-0.29687	4.8	3.46	4.97	3.49	4.36	2.57	0.442	1.79
A3c1	18.80637	-0.30411	4.8	7.17	9.21	6.47	7.40	2.81	0.625	2.30
A3c2	18.80596	-0.30428	4.8	1.24	0.843	0.592	1.12	1.32	0.428	3.36
A3c3	18.80509	-0.30452	4.8	14.24	23.4	16.5	16.5	3.33	0.992	3.09
A3c4	18.80703	-0.30487	4.8	2.51	2.64	1.86	2.69	1.68	0.635	3.92
A3c5	18.80738	-0.30536	4.8	2.31	1.38	0.971	1.73	1.25	0.741	6.15
B1c1	19.28735	0.08413	2.4	2.24	1.57	0.277	0.474	0.710	0.637	9.36
B1c2	19.28614	0.08382	2.4	17.10	23.8	4.18	4.47	1.27	1.85	15.1
B1c3	19.28565	0.08316	2.4	11.08	12.5	2.20	2.46	1.04	1.51	15.0
B1c4	19.28742	0.08028	2.4	1.69	7.20	1.26	1.52	1.87	0.291	1.62
B2c1	19.30985	0.06706	2.4	3.37	7.22	1.27	1.52	1.47	0.472	3.34
B2c2	19.30582	0.06671	2.4	1.54	1.67	0.293	0.493	0.840	0.466	5.75
B2c3	19.30440	0.06633	2.4	8.84	12.3	2.16	2.42	1.43	0.791	5.75
B2c4	19.30614	0.06615	2.4	1.98	4.44	0.780	1.00	1.32	0.387	3.05
B2c5	19.30770	0.06612	2.4	2.20	3.19	0.561	0.781	1.15	0.398	3.60
B2c6	19.30694	0.06584	2.4	1.35	4.66	0.818	1.04	1.56	0.287	1.91
B2c7	19.30648	0.06515	2.4	1.15	1.76	0.309	0.512	0.990	0.349	3.65
B2c8	19.30634	0.06414	2.4	2.69	2.50	0.440	0.660	0.890	0.560	6.54
C2c1	28.34072	0.06161	5.0	12.07	16.9	12.9	14.0	3.12	0.962	3.19
C2c2	28.34284	0.06061	5.0	14.05	63.6	48.5	48.5	6.57	0.750	1.18
C2c3	28.34440	0.05998	5.0	13.19	41.8	31.9	31.9	5.31	0.755	1.47
C2c4	28.34610	0.05963	5.0	12.74	43.4	33.1	33.1	4.80	0.960	2.07
C2c5	28.34423	0.05894	5.0	1.77	2.02	1.54	2.39	1.98	0.408	2.14
C4c1	28.35446	0.07388	5.0	6.73	22.1	16.8	16.8	4.01	0.700	1.81
C4c2	28.35596	0.07326	5.0	12.77	12.7	9.65	10.7	2.50	1.15	4.76
C4c3	28.35384	0.07194	5.0	2.31	3.07	2.34	3.23	2.13	0.477	2.32
C4c4	28.35276	0.07166	5.0	3.31	9.02	6.87	7.93	3.49	0.436	1.30
C4c5	28.35481	0.07128	5.0	5.68	7.23	5.51	6.55	2.67	0.614	2.39
C4c6	28.35599	0.07114	5.0	1.31	0.667	0.509	0.941	1.21	0.431	3.70
C4c7	28.35394	0.07086	5.0	4.58	4.52	3.45	4.39	2.16	0.627	3.01
C4c8	28.35356	0.06867	5.0	2.96	4.07	3.10	4.02	2.55	0.413	1.68
C5c1	28.35757	0.05759	5.0	2.02	2.20	1.68	2.55	1.99	0.428	2.23
C5c2	28.35705	0.05718	5.0	1.67	1.48	1.13	1.91	1.73	0.424	2.53
C5c3	28.35570	0.05621	5.0	1.99	1.75	1.33	2.15	1.83	0.431	2.45
C5c4	28.35622	0.05544	5.0	2.87	3.77	2.88	3.79	2.41	0.438	1.89
C5c5	28.35712	0.05489	5.0	1.87	1.04	0.794	1.47	1.36	0.533	4.08
C5c6	28.35660	0.05409	5.0	1.52	0.871	0.664	1.23	1.28	0.502	4.07
C6c1	28.36310	0.05336	5.0	11.38	12.2	9.30	10.4	2.27	1.35	6.18

Table 2.1—Continued

Source	l (°)	b (°)	d (kpc)	$I_{\rm peak}$ (mJy beam^{-1})	S_ν (mJy)	$M_{\rm c,raw}$ ($M_\odot$)	M_c ($M_\odot$)	R_c (0.01 pc)	Σ_c (g cm^{-2})	$n_{\rm H,c}$ (10^6 cm^{-3})
C6c2	28.36258	0.05322	5.0	4.38	3.95	3.01	3.93	1.66	0.956	5.98
C6c3	28.36456	0.05273	5.0	1.64	0.852	0.649	1.20	1.27	0.500	4.09
C6c4	28.35998	0.05273	5.0	2.38	1.76	1.34	2.15	1.58	0.579	3.81
C6c5	28.36085	0.05246	5.0	7.80	11.5	8.77	9.86	3.32	0.597	1.86
C6c6	28.36199	0.05221	5.0	9.28	15.5	11.8	13.0	3.96	0.553	1.45
C6c7	28.36557	0.05211	5.0	5.19	9.54	7.28	8.34	3.12	0.573	1.91
C6c8	28.36255	0.05169	5.0	1.11	0.774	0.590	1.09	1.44	0.352	2.53
C7c1	28.36448	0.12119	5.0	4.91	6.34	4.83	5.85	2.69	0.539	2.08
C8c1	28.38725	0.03586	5.0	5.85	5.09	3.88	4.84	2.11	0.724	3.55
C9c1	28.40073	0.08438	5.0	4.25	1.88	1.43	2.26	1.11	1.23	11.5
C9c2	28.40052	0.08209	5.0	4.09	1.77	1.35	2.17	1.16	1.08	9.64
C9c3	28.39941	0.08195	5.0	3.65	3.23	2.46	3.36	1.63	0.845	5.37
C9c4	28.39878	0.08139	5.0	8.38	8.36	6.37	7.42	2.07	1.16	5.78
C9c5	28.39701	0.08045	5.0	196.87	233	178	178	2.22	24.0	112
C9c6	28.40118	0.08028	5.0	11.94	18.2	13.9	15.0	2.74	1.34	5.05
C9c7	28.39806	0.08011	5.0	28.96	33.5	25.6	25.6	2.08	3.95	19.7
C9c8	28.39726	0.07993	5.0	85.31	51.3	39.1	39.1	1.28	16.0	130
D1c1	28.52798	-0.24990	5.7	1.30	1.92	1.90	2.89	2.24	0.385	1.78
D1c2	28.52670	-0.25007	5.7	1.25	0.603	0.598	1.02	1.28	0.416	3.38
D1c3	28.52771	-0.25108	5.7	1.29	0.890	0.882	1.50	1.52	0.433	2.95
D1c4	28.52666	-0.25146	5.7	2.47	5.39	5.34	6.37	3.34	0.383	1.19
D1c5	28.52569	-0.25191	5.7	1.66	1.77	1.75	2.74	2.02	0.451	2.32
D3c1	28.54259	-0.23477	5.7	1.27	0.597	0.591	1.01	1.26	0.422	3.46
D3c2	28.54416	-0.23529	5.7	2.17	2.17	2.15	3.15	1.93	0.565	3.04
D3c3	28.53926	-0.23668	5.7	2.37	4.2	4.16	5.18	2.74	0.463	1.75
D3c4	28.54037	-0.23710	5.7	1.59	1.02	1.01	1.71	1.47	0.528	3.72
D5c1	28.56724	-0.22810	5.7	2.43	2.64	2.61	3.61	1.93	0.649	3.49
D5c2	28.56276	-0.22987	5.7	1.35	0.988	0.979	1.66	1.53	0.471	3.18
D5c3	28.56693	-0.23105	5.7	5.69	7.96	7.89	8.96	3.13	0.612	2.03
D5c4	28.56324	-0.23129	5.7	1.32	0.799	0.792	1.35	1.42	0.448	3.27
D5c5	28.56470	-0.23313	5.7	1.69	1.77	1.76	2.74	1.95	0.483	2.57
D5c6	28.56463	-0.23445	5.7	4.89	8.90	8.82	9.91	3.09	0.695	2.33
D6c1	28.55565	-0.23721	5.7	5.47	8.73	8.65	9.74	3.22	0.628	2.02
D6c2	28.55507	-0.23721	5.7	1.46	0.658	0.652	1.11	1.23	0.488	4.11
D6c3	28.55527	-0.23794	5.7	1.18	0.645	0.639	1.09	1.34	0.407	3.16
D6c4	28.55899	-0.23936	5.7	10.89	19.8	19.6	19.6	3.99	0.823	2.14
D8c1	28.56923	-0.23289	5.7	3.59	3.70	3.67	4.68	2.03	0.763	3.91
D8c2	28.57080	-0.23321	5.7	1.41	0.851	0.843	1.43	1.39	0.495	3.69
D9c1	28.58939	-0.22855	5.7	3.94	2.40	2.38	3.38	1.46	1.06	7.55
D9c2	28.58877	-0.22855	5.7	22.55	28.5	28.3	28.3	3.13	1.93	6.39
E1c1	28.64497	0.13715	5.1	1.63	2.69	2.14	2.98	2.37	0.356	1.56

Table 2.1—Continued

Source	l (°)	b (°)	d (kpc)	$I_{\rm peak}$ (mJy beam^{-1})	S_ν (mJy)	$M_{\rm c,raw}$ ($M_\odot$)	M_c ($M_\odot$)	R_c (0.01 pc)	Σ_c (g cm^{-2})	$n_{{\rm H},c}$ (10^6 cm^{-3})
E2c1	28.64876	0.12534	5.1	1.22	0.511	0.405	0.704	1.16	0.352	3.15
E2c2	28.64883	0.12454	5.1	2.85	4.69	3.72	4.59	2.89	0.368	1.32
F3c1	34.44489	0.25046	3.7	1.95	0.979	0.409	0.661	0.870	0.588	7.03
F3c2	34.44461	0.25022	3.7	2.36	1.44	0.602	0.973	1.01	0.635	6.51
F4c1	34.45975	0.25920	3.7	4.91	7.55	3.15	3.60	1.85	0.706	3.97
F4c2	34.45840	0.25639	3.7	1.88	4.08	1.71	2.16	2.05	0.344	1.74
F4c3	34.45812	0.25597	3.7	2.23	3.19	1.33	1.78	1.74	0.391	2.32
H1c1	35.48076	-0.31016	2.9	1.74	0.783	0.201	0.348	0.630	0.592	9.80
H2c1	35.48347	-0.28791	2.9	4.90	6.58	1.69	1.97	1.49	0.595	4.15
H3c1	35.48853	-0.29211	2.9	2.21	1.29	0.330	0.540	0.800	0.565	7.33
H3c2	35.48856	-0.29451	2.9	1.39	0.586	0.150	0.261	0.620	0.455	7.62
H3c3	35.48693	-0.29513	2.9	20.70	22.8	5.86	6.17	1.68	1.46	8.98
H4c1	35.48512	-0.28377	2.9	2.33	1.46	0.374	0.603	0.760	0.707	9.71
H5c1	35.49632	-0.28640	2.9	4.93	5.34	1.37	1.65	1.42	0.543	3.96
H5c2	35.49570	-0.28688	2.9	1.36	0.732	0.188	0.326	0.700	0.443	6.55
H5c3	35.49611	-0.28813	2.9	6.12	24.9	6.39	6.70	2.74	0.599	2.27
H6c1	35.52338	-0.26935	2.9	8.98	10.7	2.74	3.03	1.46	0.955	6.80
H6c2	35.52529	-0.27115	2.9	1.79	0.867	0.222	0.386	0.640	0.625	10.1
H6c3	35.52251	-0.27205	2.9	7.24	9.03	2.31	2.60	1.64	0.645	4.08
H6c4	35.52029	-0.27226	2.9	3.54	6.03	1.55	1.82	1.52	0.530	3.63
H6c5	35.52425	-0.27247	2.9	1.33	1.26	0.322	0.529	0.910	0.423	4.81
H6c6	35.52397	-0.27296	2.9	1.51	0.921	0.236	0.407	0.760	0.478	6.56
H6c7	35.51908	-0.27330	2.9	2.33	1.41	0.363	0.587	0.740	0.726	10.2
H6c8	35.52352	-0.27337	2.9	7.96	9.86	2.53	2.82	1.31	1.10	8.74
H6c9	35.52314	-0.27365	2.9	3.05	2.46	0.631	0.892	0.850	0.820	9.98

Note. — M_c is the mass estimate after flux correction, which equals the raw, uncorrected mass estimate ($M_{c,\rm raw}$) multiplied by the value of $f_{\rm flux}^{-1}$ appropriate for M_c. This corrected mass is then used for the estimates of Σ_c and $n_{{\rm H},c}$.

2.3.2 Core Mass Function

As described in §2.2.4, we have estimated flux correction, $f_{\rm flux}$, functions for all the observed regions and these are shown in Figure 2.3a for the seven IRDCs. Here the values shown are the median of the results for each IRDC in each mass bin (excluding values $f_{\rm flux} > 1$, which we attribute to false assignments; and extrapolating with constant values at the low-mass end once an effective minimum is reached in the distribution: at even smaller values of M, the median $f_{\rm flux}$ is seen to rise, which we attribute to false assignment to weak image feature, including noise fluctuations). Similar to the results of Paper I for G286, our estimated values of $f_{\rm flux}$ rise from ~ 0.5 to 0.6 for $M \lesssim 1\ M_\odot$ towards close to unity for $M \gtrsim$ several $M_\odot$. The curves are shifted to lower masses for the most nearby IRDCs. Figure 2.3a also shows for each IRDC the masses corresponding to a core that has a flux level of 4σ at the position of half the beam size, which represents one of the detection threshold criteria (in this case the most stringent), assuming its flux distribution is shaped as the beam. These mass detection limits range from about $0.4\ M_\odot$ to $2\ M_\odot$, depending on the distance to the cloud. However, we note that these are only approximate limits, since, e.g., the core shape may not be exactly the same as the beam. In particular, less centrally peaked cores will be able to satisfy the area threshold condition at a lower mass.

As also described in §2.2.4, we then derive the number recovery fraction, $f_{\rm num}$, for the observed regions, again averaging for each IRDC (Fig. 2.3b). These rise steeply from near zero to near unity as M increases from ~ 0.2 to $1\ M_\odot$, depending on the distance to the IRDC.

Recall that overall we have identified 107 cores in the seven IRDCs. Cloud C contains the most (37), followed by cloud D (23) and cloud H (18). We will first derive the CMFs for each IRDC separately and then combine them.

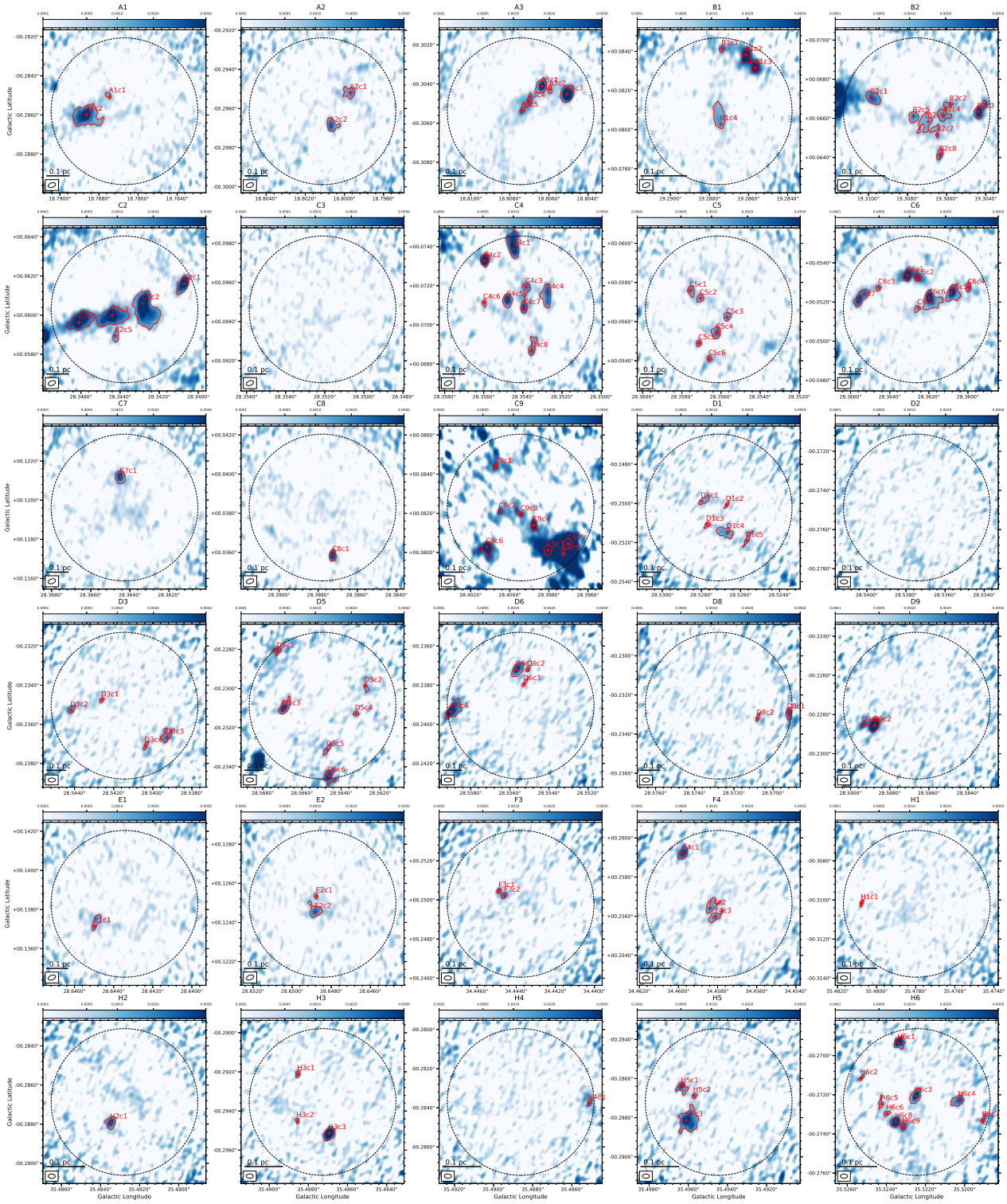

Fig. 2.2.— 1.3 mm continuum images of 30 pointings toward IRDC dense clumps (colorbar in Jy beam^{-1}). The dotted circle in each panel denotes the primary beam. The synthesized beam is shown in the bottom left corner of each panel. The cores identified by the fiducial dendrogram algorithm are marked on the images, with red contours showing "leaf" structures.

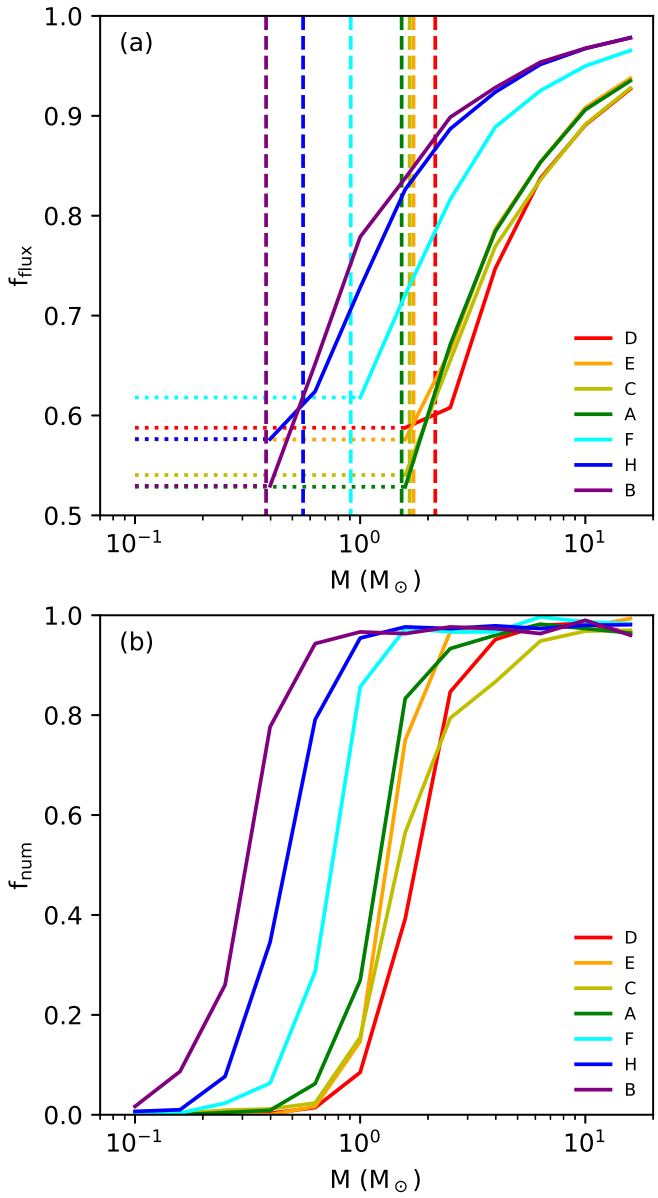

Fig. 2.3.— *(a) Top:* Average (median) flux recovery fractions, $f_{\rm flux}$, versus core mass, M, for the dendrogram core finding method as applied to each of the seven IRDCs (solid lines; see legend). Note that our method assumes a constant value of $f_{\rm flux}$ (dotted portion of lines) once an effective minimum is reached as M is reduced (see text). Vertical dashed lines show the mass corresponding to a core that has a flux level of 4σ at the position of half the beam size, which represents one of the detection threshold criteria, assuming its flux distribution is shaped as the beam. Note that the legend is ordered by cloud distance: IRDC B is the nearest; IRDC D is the most distant. *(b) Bottom:* Mean value of the number recovery fraction, $f_{\rm num}$, versus core mass, M, for the dendrogram core finding method as applied to each of the seven IRDCs (solid lines; see legend).

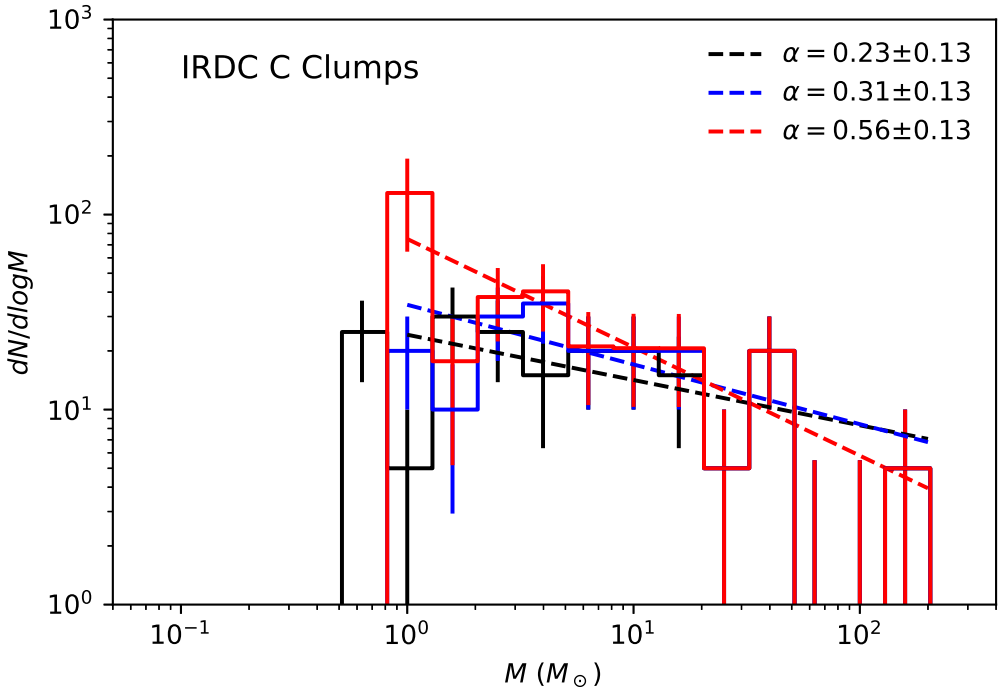

Fig. 2.4.— The dendrogram-derived combined CMF of the seven clumps observed in IRDC C. The black histogram shows the original, "raw" CMF. The blue histogram shows the CMF after flux correction and the red histogram shows the final, "true" CMF after then applying number recovery fraction correction. The error bars show Poisson counting errors. The black, blue and red dashed lines show the best power law fit results for the high-mass end ($M \geq 0.79\,M_{\odot}$) of these CMFs, respectively.

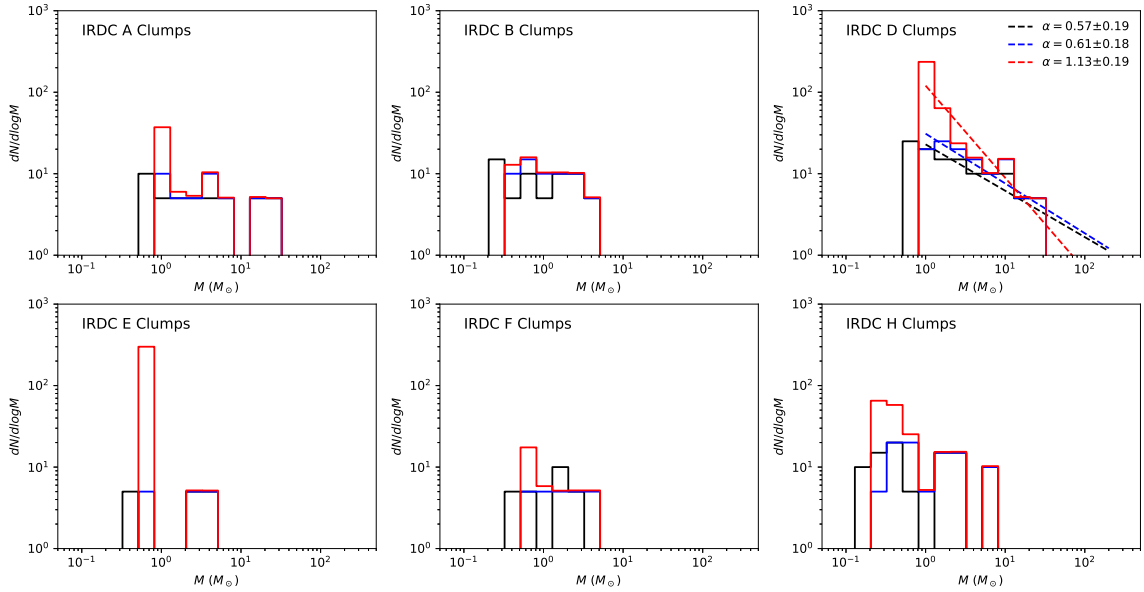

Fig. 2.5.— Similar to Figure 2.4 for IRDC C, the raw (black), flux-corrected (blue) and true (red) CMFs are shown here for IRDCs A, B, D, E, F and H. The black, blue and red dashed lines show the best power law fit results for the high-mass end ($M \geq 0.79 M_{\odot}$) of the CMF in IRDC D. Other IRDCs are not fit, given their relatively small number of cores.

The raw (uncorrected) CMF of IRDC C is shown by the black histogram in Figure 2.4. The mass binning has been chosen to match that used in Paper I, i.e., five bins per dex, with a bin centered on $1\,M_\odot$ (and thus also on $10\,M_\odot$ and $100\,M_\odot$, etc). The error bars on each bin indicate $N^{1/2}$ Poisson counting uncertainties. The CMF after flux correction is shown by the blue histogram: note that cores in the lowest mass bin of the raw CMF are all shifted to higher mass bins. Finally, the number correction is applied to the flux-corrected CMF to derive the final, "true" CMF, shown by the red histogram. Note, its error bars are assumed to be the same fractional size as those found for the blue histogram, i.e., the Poisson errors from this distribution, with no allowance for any additional systematic uncertainty in $f_{\rm num}$. Thus these uncertainties should be treated with caution, i.e., they likely underestimate the true uncertainties.

Following Paper I, we first carry out "simple" power law fitting to CMFs starting from the $1\,M_\odot$ bin, i.e., for $M \gtrsim 0.79\,M_\odot$. This fitting minimizes differences in the log of $dN/d{\rm log}M$, normalized using the asymmetric Poisson errors. For empty bins, to treat these as effective upper limits, we assume the point is 1 dex lower than the level if the bin had 1 data point and set the upper error bar such that it reaches up to the level if there were 1 data point. For bins that have 1 data point, the lower error bar extends down by 1 dex rather than to minus infinity. As with Paper I, we have verified that the global results are insensitive to the details of how empty bins are treated.

We also apply a maximum likelihood estimation (MLE) method to estimate the power law index (Newman et al. 2005). Let $p(x)dx$ be the fraction of cores with mass between x and $x + dx$. Then $p(x) = Cx^{-(\alpha+1)}$ and α is estimated as

$$\alpha = n \left[\sum_{i=1}^{n} {\rm ln} \frac{x_i}{x_{\rm min}} \right]^{-1} \tag{2.3}$$

with an uncertainty (confidence interval)

$$\sigma = \frac{\alpha}{\sqrt{n}}. \tag{2.4}$$

Here $x_{\rm min}$ is the starting mass of the power law, x_i is the mass of each core with mass above $x_{\rm min}$ and n is the number of such cores. We note that this estimate is valid assuming the upper limit (if any) of the distribution is much larger than $x_{\rm min}$. Note also, our fiducial results involve CMFs that have been corrected in logarithmic bins for flux and number incompleteness, so these are used to generate synthetic populations of cores, to which the MLE analysis method is then applied. We generate the corresponding number of random masses uniformly distributed in each mass bin and apply the MLE method. We repeat this for 50 times and then derive the median α and confidence interval σ.

For IRDC C, with simple power law fitting we derive a value of $\alpha = 0.56 \pm 0.13$ for the true CMF. The raw and flux-corrected CMFs had power law indices of 0.23 and 0.31, respectively, so we see the effects of these corrections has been to steepen the upper end slope of the CMF, as expected. For the MLE method we find $\alpha = 0.48 \pm 0.08$, 0.49 ± 0.08 and 0.75 ± 0.09 for the raw, flux-corrected and "true" CMF. The slopes derived from the MLE method are slightly steeper than those derived from the linear fitting method within 1.5 combined σ.

In Figure 2.5 we show the equivalent CMFs for the six other IRDCs, most of which are very sparsely sampled. We also carry out power-law fitting for IRDC D (23 cores). From simple power law fitting we derive a value of $\alpha = 1.13 \pm 0.19$ for the true CMF. This is significantly steeper than the result for IRDC C, however, it driven mostly by the lowest mass bin, i.e., $\sim 1\,M_{\odot}$, for which the completeness correction is about a factor of 10. Due to potential uncertainties associated with this correction,

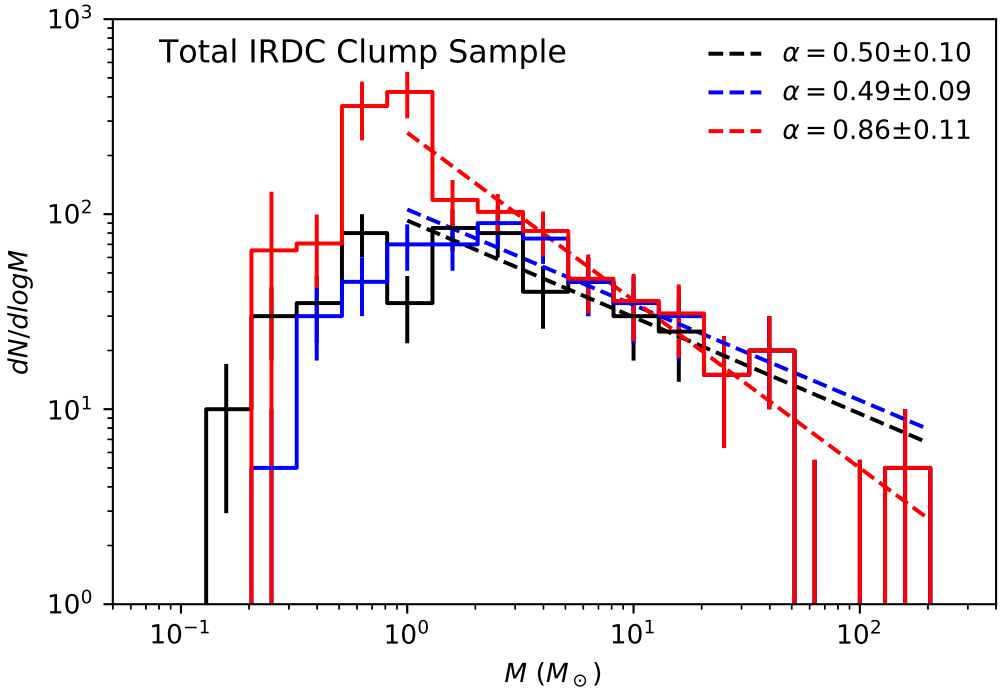

Fig. 2.6.— Combined dendrogram-derived CMF from observations of 30 positions covering dense clumps within seven IRDCs. The black histogram shows the original, "raw" CMF. The blue histogram shows the CMF after flux correction and the red histogram shows the final, "true" CMF after then applying number recovery fraction correction. The error bars show Poisson counting errors. The black, blue and red dashed lines show the best power law fit results for the high-mass end ($M \geq 0.79\,M_{\odot}$) of these CMFs, respectively.

as we discuss below, we will consider CMFs down to two mass thresholds, i.e., cases of including and excluding this mass bin.

Next, in Figure 2.6, we show the combined CMFs for the entire sample of seven IRDCs. The raw, flux-corrected and "true" CMFs (black, blue and red histograms, respectively) are obtained by simple addition of the equivalent CMFs for each individual IRDC. Note that the Poisson errors are now reduced. Note also, however, there are still two empty bins near 100 $M_{\odot}$ and only one core more massive that this. At the low-mass end, the CMFs of the seven individual IRDCs all have detections down to or below the bin centered on $M = 1\ M_{\odot}$, which is approximately the detection threshold of Cloud D, the farthest cloud.

For the raw, flux-corrected and "true" CMFs, with simple fitting we then derive power law indices for $M > 0.79\ M_{\odot}$ of $\alpha = 0.50 \pm 0.10$, 0.49 ± 0.09 and 0.86 ± 0.11, respectively. For MLE, we derive $\alpha = 0.61 \pm 0.07$, 0.63 ± 0.07 and 1.02 ± 0.08 for these three cases, respectively. Again, the slopes derived from the MLE method are slightly steeper than those derived from the linear fitting method within 1.5 combined σ. If we only fit to the true CMF starting from the next bin above 1 $M_{\odot}$ (i.e., allowing for the possibility that IRDC D is artificially distorting the low-end CMF), then we derive $\alpha = 0.70 \pm 0.13$ for the true CMF. The MLE analysis yields $\alpha = 0.83 \pm 0.09$.

While we prefer the dendrogram algorithm as our fiducial method of identifying cores, since it is a hierarchical method that we consider better at separating cores from a surrounding background clump environment (see §2.2.2 and Paper I), for completeness we also evaluate the CMF as derived from the clumpfind algorithm. With the fiducial parameters (i.e., a 4σ noise threshold, 3σ step size, minimum area of 0.5 beams; see Paper I), we find 120 cores with masses from 0.150 to 286 $M_{\odot}$. After flux and number recovery corrections on each IRDC, for the combined "true" CMF we

derive a high-mass end ($M > 0.79\,M_{\odot}$) power law index of $\alpha = 0.86 \pm 0.11$ with simple fitting and 1.02 ± 0.08 with MLE fitting. The first of these values is coincidentally the same (within the first two significant figures) as that derived from the dendrogram analysis. These results indicate that for our *ALMA* observations of IRDC clumps, the resulting core properties are not that sensitive to whether dendrogram or clumpfind is used as the identification algorithm. This contrasts with the results of Paper I for G286 (for the case of 1.5″resolution), which found a value of $\alpha = 1.12 \pm 0.18$ for dendrogram and $\alpha = 0.49 \pm 0.12$ for clumpfind. We expect that this difference is due, at least in part, to the observation of G286 utilizing both the 12-m and 7-m arrays, so that a larger range of scales are recovered. Thus more emission from the surrounding protocluster clump material is detected in G286, readily apparent from Figures 1 & 2 of Paper I, in comparison to our images of the IRDC clumps (Fig. 2.2). Since most of the larger-scale emission is resolved out in our IRDC observations (an approximate comparison with BGPS data of the clumps assuming a dust spectra index of 3.5 finds typical flux recovery of $\sim 20\%$ [see §2.2.1]), one then expects clumpfind results to be closer to those derived from dendrogram.

We examine whether the CMF we measure in IRDC environments is consistent with a Sapleter distribution ($\alpha = 1.35$). We can already infer from our measurements of $\alpha = 0.70 \pm 0.13$ (or with MLE $\alpha = 0.83 \pm 0.09$) for the true CMF at $M > 1.26\,M_{\odot}$, that the result differs from Salpeter by about 5.0σ (or 5.8σ for MLE). However, it is not known if the uncertainties in these parameters, especially given systematic uncertainties, will follow a simple gaussian distribution. More generally we compare the IRDC core population (including allowance for completeness corrections) with an idealized large (e.g., $1,000$, but result is independent of this size for large enough numbers) population of cores that follow the Salpeter distribution over

the same mass range. We carry out a Kolmogorov-Smirnov (KS) test with synthetic populations of cores by generating the corresponding number of random masses uniformly distributed in each mass bin and repeat for 50 times. We find that the median p value, which indicates the probability that these distributions are consistent with the same parent distribution, is $\lesssim 10^{-4}$. Thus we conclude that our estimated CMF in IRDC environments is top heavy compared to Salpeter. Such a conclusion has also recently been reported in the more evolved "mini-starburst" W43 region by Motte et al. (2018).

2.3.3 Comparison to G286

Here we present a detailed comparison of our fiducial dendrogram-derived CMF in IRDC clumps with that measured in the more evolved G286 protocluster in Paper I. We have already noted and summarize again that there are some unavoidable differences in our observational data and analysis methods compared to Paper I. In addition to the primary beam effect mentioned in §2.2.2, our observations do not include the 7m array and so lack sensitivity to larger-scale structures. Also, we compile a CMF from observations of multiple clouds that are at a range of distances, whereas Paper I studied a single protocluster, G286, at a single distance of 2.5 kpc. We will compare to the results of the 1.5″resolution analysis of Paper I, since, as discussed below, this is a better match to our observations of typically more distance IRDCs at ∼1″resolution.

Figure 2.7a shows shows the dendrogram-derived flux and number-corrected, i.e., "true" CMFs from the IRDC clumps and G286 together. Figure 2.7b shows these same CMFs, but now normalized by the number of cores they contain in the 1 $M_\odot$ mass bin and greater, i.e., $M \geq 0.79\ M_\odot$. Figure 2.7c shows the CMFs normalized

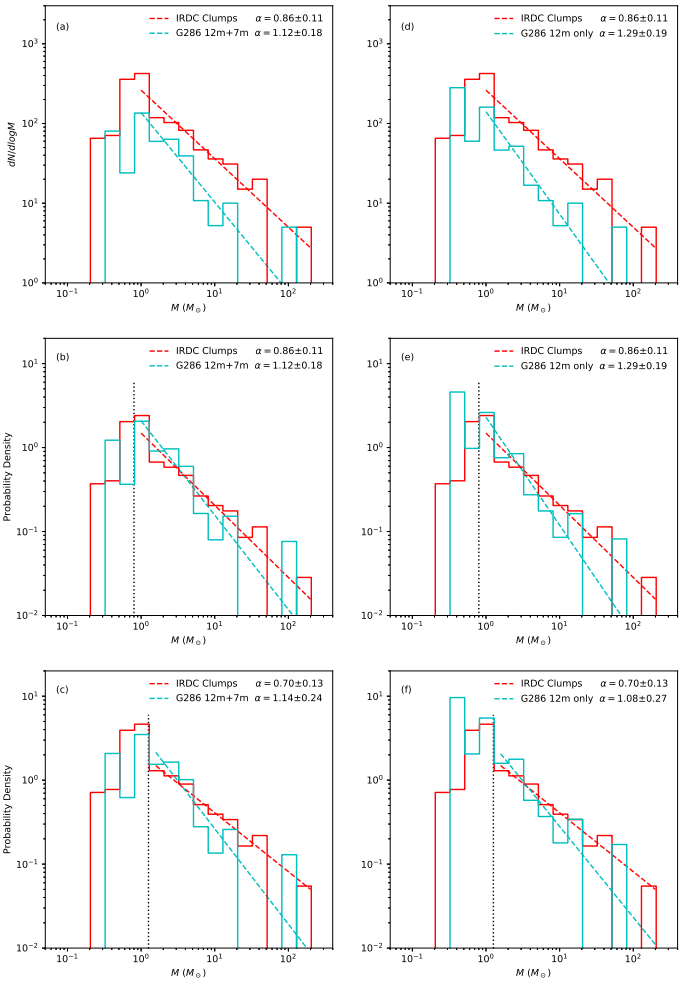

Fig. 2.7.— *(a) Top:* Flux and number-corrected "true" dendrogram-derived CMF of IRDC clumps (red histogram) compared with the same CMF derived from G286 in Paper I (cyan histogram). The simple power law fits to $M \geq 0.79\,M_{\odot}$ are also indicated. *(b) Middle:* As (a), but now showing CMFs normalized by the number of cores estimated, after completeness corrections, to have $M \geq 0.79\,M_{\odot}$, i.e., 176 cores in the IRDC Clumps and 66 cores in G286 after completeness corrections. This mass threshold is indicated by the vertical black dotted line. *(c) Bottom:* As (a), but now showing CMFs normalized by the number of cores with $M \geq 1.26\,M_{\odot}$, i.e., 91 cores in the IRDC Clumps and 39 cores in G286 after completeness corrections. This mass threshold is indicated by the vertical black dotted line. Simple power law fits for this mass range are also shown. *(d) Top:* As (a), but comparing to results from G286 12m-only data. *(e) Middle:* As (b), but comparing to results from G286 12m-only data (61 cores in G286 after completeness corrections are used for the normalization). *(f) Bottom:* As (c), but comparing to results from G286 12m-only data (29 cores in G286 after completeness corrections are used for the normalization).

by the number of cores they have with $M \geq 1.26\,M_{\odot}$, i.e., in case the $1\,M_{\odot}$ mass bin is adversely affected by systematic errors, especially from IRDC D. This panel also displays the power law indices that result from simple fitting over this slightly higher mass range.

The potential systematic difference resulting from the lack of 7-m array data for the IRDC clumps needs to be considered. Paper I found that the CMF derived without 7-m array data in G286 is steeper by about 0.1. Accounting for this effect thus may accentuate the difference between the IRDC clump and G286 CMFs. We proceed to re-analyze the G286 data but now excluding the 7m-array data, which gives the fairest comparison with our IRDC clump observations. These results are shown in Figure 2.7 d, e and f.

We carry out a KS test of the high-mass end CMFs to see if the distributions identified in IRDC clumps and in G286 (with 12m only data) are consistent with being drawn from the same parent distribution. For the case of CMFs in the range $M \geq 0.79\,M_{\odot}$, the resulting p value is 0.42. For the distributions in the range $M \geq 1.26 M_{\odot}$, the KS test yields $p = 0.23$. Thus these results indicate that the distributions are possibly consistent with one another, in spite of the apparent differences in their power law indices. If we were to boost the number of cores by a factor of 5 and keeping the same distributions, then the p values would become smaller to the point that they would be inconsistent with one another. This test indicates that such an increase in sample size is needed to be able to distinguish between CMFs that have a difference in α of about 0.4.

One potential systematic effect resulting from differences between the observations is that G286 is at a single distance of $d = 2.5\,\mathrm{kpc}$ and was observed with a resolution of about $1.5''$and with a noise level of 0.5 mJy beam^{-1}, while the IRDCs, are observed

with a resolution of $\sim 1''$ and noise level of ~ 0.2 mJy beam^{-1}. Paper I also presented results for 1.0″resolution and with a noise level of 0.45 mJy beam^{-1}, which yields $\alpha = 1.24 \pm 0.17$ for $M \geq 0.79\, M_{\odot}$, however, we have decided to focus on the lower resolution resolution results, given that the IRDCs span a range of distances from 2.4 to 5.7 kpc, but with IRDC C at 5 kpc and IRDC D at 5.7 kpc contributing a large fraction of the sample so that the average distance of the IRDC cores is 4.4 kpc. Thus in the end the effective linear resolutions are similar (within about 15%) for the average IRDC core and that achieved in G286. Overall the mass sensitivities are also quite similar between the two observations and the completeness correction factors are relatively modest, at least for $M \geq 1.26\, M_{\odot}$.

2.4 Discussion and Conclusions

We have measured the CMF in a sample of about 30 IRDC clumps, including accounting for flux and number recovery incompleteness factors. With simple fitting, we derived high-end power law indices of $\alpha \simeq 0.86 \pm 0.11$ for $M \geq 0.79\, M_{\odot}$ and $\alpha \simeq 0.70 \pm 0.13$ for $M \geq 1.26\, M_{\odot}$. An MLE analysis yielded similar values. These results indicate a CMF that is top heavy compared the standard Salpeter distribution with $\alpha = 1.35$.

To reduce the potential effects of systematic uncertainties, we have compared the above results to the CMF derived with similar methods in the more evolved protocluster G286 (Paper I). From the considerations of §2.3, we expect that the most reliable comparison is for the higher mass range of the CMF, $M \geq 1.26\, M_{\odot}$, for which we have found $\alpha = 1.08 \pm 0.27$ for G286 when only the 12m-array data are analyzed. These results thus indicate only a hint of a potential variation in the high-mass end of the CMF between the Galactic environments of IRDC clumps (i.e., early stage,

high pressure centers of protoclusters) and G286, i.e., a more evolved protocluster that is sampled more globally, i.e., both central and outer regions. One of the main factors limiting our ability to distinguish the distributions is the relatively small number of cores in each of the samples used in this direct comparison. Increasing the sample by about a factor of 5 is expected to enable these distributions to be reliably distinguished, if they maintain their currently observed forms.

Overall, the values of power law index of the CMF derived in G286 is similar to that of the Salpeter stellar IMF, i.e., $\alpha = 1.35$, while that in the IRDC clumps is shallower, indicating relatively more massive cores are present. This may indicate that massive stars are more likely to form in high mass surface density, high pressure regions of IRDCs. Such a difference in the CMF and resulting IMF could potentially be caused by a number of different physical properties of the gas that vary systematically between the regions. On the one hand, the higher density, higher pressure regions of IRDC clumps is expected to lead to a smaller Bonnor-Ebert mass, which would also take a value $\ll 1\ M_\odot$ (see, e.g., McKee & Tan 2003). The fact that we see evidence for a more top-heavy CMF indicates that thermal pressure is not the main factor resisting gravity in setting core masses in these environments, which would then indicate that some combination of increased turbulence and/or magnetic field support is present in IRDC clumps.

Note that IRDC clumps are cold regions, so that extra thermal heating of the ambient environment from radiative feedback from surrounding lower-mass stars, as proposed in the model of Krumholz & McKee (2008), is not expected to be greater here compared to more evolved stages as represented by G286. However, localized heating of the core from the protostar itself is expected to be higher in higher mass surface density environments, if powered mostly by accretion (Zhang & Tan 2015).

At the moment we do not have any direct indication if the localized temperatures of cores are higher in the IRDC clumps compared to G286. Note, if localized IRDC core temperatures were systematically higher than in G286, then we would have overestimated their masses. If this effect is greater for the more luminous mm cores and is systematically greater in the IRDC sample compared to G286, then this would make their intrinsic CMFs more similar. Such considerations highlight additional potential systematic effects due to temperature or dust opacity variations that need to be treated as caveats to our results, and indeed all results of CMFs derived from mm dust emission when individual core temperature and opacity data are not available.

Comparing with previous studies in IRDCs, our relatively flat high-mass end power law index is consistent with the results of Ragan et al. (2009), although they probed a different mass range of 30 to 3,000 $M_\odot$ and used different methods, i.e., MIR extinction, which is subject to a variety of systematic uncertainties (Butler & Tan 2012), including foreground corrections that effect lower column density regions and "saturation" effects at high optical depths causing the mass in high column density regions to be underestimated. Zhang et al. (2015) also found a relative lack of lower-mass cores compared to the Salpeter (1955) distribution, but their sample size was relatively small (only 38 cores selected in a single small, ~ 0.5 pc region) and they did not carry out completeness corrections. Still, their results do illustrate the effects of using higher angular resolution (by about a factor of two, i.e., $\sim 0.8''$), better sensitivity (by about a factor of three, i.e., 1σ rms of 75 μJy), but with more limited sensitivity to larger scale structures (given a more extended configuration of *ALMA* was employed) compared to our current study. The 5 cores we identify in the C2 clump are further decomposed into 34 cores by Zhang et al. (2015), i.e., the bulk of their sample, in their analysis of core identification, which is based on the den-

drogram method, but also supplemented by dendrogram-guided Gaussian fitting of additional structures. On the other hand, Ohashi et al. (2016) found a steeper power law index for the pre-stellar CMF derived in their study (28 cores in IRDC G14.225-0.506 found by 3 mm continuum emission), although the uncertainty in their result is large ($\alpha \simeq 1.6 \pm 0.7$) and, again, their methods differ from ours, especially the lack of completeness corrections for flux and number. Motte et al. (2018) have recently studied the 1.3 mm dust continuum derived CMF in the W43-MM1 "mini-starburst region", finding $\alpha = 0.90 \pm 0.06$ for $M > 1.6\,M_{\odot}$, based on a sample of 105 cores. We note they used different methods of core identification, i.e., the *getsources* algorithm (Men'shchikov et al. 2012), but also carried out a visual inspection step of removing cores that were "too extended, or whose ellipticity is too large to correspond to cores, or that are not centrally-peaked", so a direct comparison with our results is not as meaningful as our comparison to the G286 protocluster.

In summary, we see that quantitative direct comparison of our results with these previous studies is not particularly useful given the differences in the data and methods used to identify cores and estimate CMFs. We thus emphasize that, in addition to finding a more top heavy CMF compared to the Salpeter distribution, our main result for a hint of a potential variation in the CMF in different environments is based on the comparison with our Paper I study of G286, which used more similar data and methods.

Future progress in this field can take several directions. First, as discussed above, much larger samples of cores in these types of environments are needed. Second, a wider range of Galactic environments need to be probed. Third, the CMF should be probed to lower masses to better determine the location of any peak. This will require higher sensitivity and higher angular resolution observations. Such observations will

also likely change the shape of the high-mass end of the CMF by sometimes breaking up more massive "cores" into smaller units. Fourth, better constraints on potential systematic effects related to mass determination from mm continuum flux are needed, especially by individual temperature measurements of the cores. Fifth, the evolutionary stage of the cores should be determined, i.e., protostellar mass to core envelope mass, including determining if cores are pre-stellar, i.e., via astrochemical indicators or via an absence of outflow indicators or concentrated continuum emission. Such information is needed to better determine how the CMF and IMF are actually established in protocluster environments, as discussed by Offner et al. (2014).

Chapter 3

SiO Outflows as Tracers of Massive Star Formation in Infrared Dark Clouds

3.1 Introduction

Massive stars play a key role in the regulation of galactic environments and galaxy evolution yet there is no consensus on even the basics of their formation mechanism. Theories range from models based on Core Accretion, i.e., formation from massive self-gravitating cores (e.g., McKee & Tan 2003), to Competitive Accretion, i.e., chaotic clump-fed accretion concurrent with star cluster formation (e.g., Bonnell et al. 2001; Wang et al. 2010), to Protostellar Collisions (e.g., Bonnell et al. 1998; Bally & Zinnecker 2005).

Magneto-centrifugally driven protostellar outflows are thought to be an ubiquitous feature of ongoing formation of all masses of stars (e.g., Arce et al. 2007; Beltrán & de Wit 2016) and are likely to be essential or at least important for removing angu-

lar momentum from the accreting gas. Such outflows involving large scale magnetic fields threading the disk (i.e., "disk winds"; e.g., Königl & Pudritz 2000) and/or stellar magnetic fields (i.e., "x-winds"; e.g., Shu et al. 2000) lead to collimated bipolar outflows that can be the most obvious signpost of early star formation activity. Thus studies of the morphologies and kinematics of such outflows can help us understand protostellar activities from inner disk to core envelope scales and beyond. Whether protostellar outflow properties scale smoothly with the mass of the driving protostar will also shed light on how massive star formation differs from low-mass star formation. As one example, radio surveys have found an association of "radio jets", i.e., collimated radio emission, and molecular outflows that appears to be a common phenomenon in both low-mass (Anglada 1996) and high-mass protostars (Purser et al. 2016; Rosero et al. 2016, 2019b).

With the development of high-resolution, high-sensitivity facilities like ALMA and the J-VLA, more and more observations have been carried out towards massive star-forming regions. While most mm and radio surveys are towards more evolved massive protostars, the earlier stages remain relatively unexplored. To study such early stages, we focus on protostars in Infrared Dark Clouds (IRDCs). IRDCs are cold (T <20 K), dense ($n_{\rm H} \gtrsim 10^4\,{\rm cm}^{-3}$) regions of molecular clouds that are opaque at wavelengths $\sim$10 μm or more and thus appear dark against the diffuse Galactic background emission. They are likely to harbor the earliest stages of star formation (see, e.g., Tan et al. 2014).

We have conducted a survey of 32 IRDC clumps with ALMA (see Table 1 in Kong et al. 2017). This high mass surface density sample was selected from 10 IRDCs (A-J) by the mid-infrared (*Spitzer*-IRAC 8 μm) extinction (MIREX) mapping methods of Butler & Tan (2009, 2012). The distances range from 2.4 kpc to 5.7 kpc. The

first goal of this study was to find massive pre-stellar cores. About 100 such core candidates have been detected via their $N_2D^+(3-2)$ emission (Kong et al. 2017).

Next, we identified 1.3 mm continuum cores in the 32 clumps (Liu et al. 2018). In total, 107 cores were found with a dendrogram algorithm with a mass range from 0.150 to 178 $M_\odot$ assuming a temperature of 20 K Seven of the cores (C2c2, C2c3, C2c4, C9c5, C9c7, C9c8, D9c2) are high-mass protostellar candidates, i.e., with masses $> 25 M_\odot$, assuming a core-to-star efficiency of about 30%. Twelve others (A1c2, A3c3, C2c1, C4c1, C4c2, C6c1, C6c5, C6c6, C9c6, D5c6, D6c1, D6c4) are intermediate-mass protostellar candidates, i.e., with masses in the range 9 to 24 $M_\odot$.

The ALMA observations are also sensitive to SiO(5-4) emission. SiO is believed to form through sputtering of dust grains (e.g., Schilke et al. 1997). Unlike CO, SiO emission does not suffer from confusion with easily excited ambient material. While SiO emission with a narrow velocity range may come from large-scale colliding gas flows (e.g., Jiménez-Serra et al. 2010; Cosentino et al. 2018, 2020), SiO emission with a broad velocity range is considered to be an effective tracer of fast shocks from protostellar outflows. Here we use such SiO emission as a tracer of outflows, which then are signposts to help identify and characterize the protostars.

We have also carried out VLA follow-up observations towards our protostar sample to determine the onset of the appearance of radio continuum emission and thus diagnose when the protostars transition from a "radio quiet" to a "radio loud" phase.

The structure of the paper is as follows. In §2 we summarize the ALMA and VLA observations. We present the results of SiO outflows in §3 and 6 cm radio emission in §4. We discuss the implications of the results in §5. We summarize the conclusions in §6.

3.2 Observations

3.2.1 ALMA data

We use data from ALMA Cycle 2 project 2013.1.00806.S (PI: Tan), which observed 30 positions in IRDCs on 04-Jan-2015, 10-Apr-2015 and 23-Apr-2015, using 29 12 m antennas in the array. Track 1 with central $v_{\rm LSR}$ = 58 km/s includes clumps A1, A2, A3 ($v_{\rm LSR}$ ∼66 km/s), B1, B2 ($v_{\rm LSR}$ ∼26 km/s), C2, C3, C4, C5, C6, C7, C8, C9 ($v_{\rm LSR}$ ∼79 km/s), E1, E2 ($v_{\rm LSR}$ ∼80 km/s) with notations following Butler & Tan (2012) (see Table 1 in Kong et al. 2017 for a list of targets). Track 2 with central $v_{\rm LSR}$ = 66 km/s includes D1, D2 (also contains D4), D3, D5 (also contains D7), D6, D8, D9 ($v_{\rm LSR}$ ∼87 km/s), F3, F4 ($v_{\rm LSR}$ ∼58 km/s), H1, H2, H3, H4, H5, H6 ($v_{\rm LSR}$ ∼44 km/s). In Track 1, J1924-2914 was used as the bandpass calibrator, J1832-1035 was used as the gain calibrator, and Neptune was the flux calibrator. In Track 2, J1751+0939 was used as the bandpass calibrator, J1851+0035 was used as the gain calibrator, and Titan was the flux calibrator. The total observing time including calibration was 2.4 hr. The actual on-source time was ∼2-3 min for each pointing.

The spectral set-up included a continuum band centered at 231.55 GHz (LSRK frame) with width 1.875 GHz from 230.615 GHz to 232.490 GHz. At 1.3 mm, the primary beam of ALMA 12m antennas is $\sim 27''$ (FWHM) and the largest recoverable scale for the array is $\sim 7''$. The data were processed using NRAO's Common Astronomy Software Applications (CASA) package (McMullin et al. 2007). For reduction of the data, we used "Briggs" cleaning and set `robust = 0.5`. The continuum image reaches a 1σ rms noise of 0.2 mJy in a synthesized beam of $1.2'' \times 0.8''$. The spectral line sensitivity per 0.2 km s^{-1} channel is ∼0.02 Jy beam^{-1} for Track 1 and ∼0.03 Jy beam^{-1} for Track 2. Other basebands were tuned to observe N_2D^+(3-2), SiO(5-4),

$C^{18}O$ (2-1), DCN(3-2), DCO^+(3-2) and $CH_3OH(5(1,4) - 4(2,2))$.

3.2.2 VLA data

The 6 cm (C-band) observations were made towards some of the clumps with strongest SiO in both C configuration and A configuration. The C configuration data taken in 2017 are from project code 17A-371 (PI: Liu) and include A1, A2, A3 in Cloud A (gain calibrator: J1832-1035, positional accuracy 0.01 - 0.15″), B1, B2 in Cloud B (gain calibrator: J1832-1035), C1 (RA: 18:42:46.498, DEC: -4:04:15.964), C2, C4, C5, C6, C9 in Cloud C (gain calibrator: J1832-1035), D1, D8 in Cloud D (gain calibrator: J1832-1035) and H5, H6 in Cloud H (gain calibrator: J1824+1044, positional accuracy $< 0.002''$). The A configuration data taken in 2018 are from project code 18A-405 (PI: Liu) and include A1, A2, A3 in Cloud A (gain calibrator: J1832-1035), C1, C2, C4, C5, C6, C9 in Cloud C (gain calibrator: J1804+0101, positional accuracy $< 0.002''$) and H5, H6 in Cloud H (gain calibrator: J1824+1044). 3C286 was used as flux density and bandpass calibrator for all the regions with both configurations. Both sets of data consist of two 2 GHz wide basebands (3 bit samplers) centered at 5.03 and 6.98 GHz, where the first baseband was divided into 16 spectral windows (SPWs), each with a bandwidth of 128 MHz and the second baseband was divided into 15 SPWs with 14 SPWs 128 MHz wide each and 1 SPW 2 MHz wide for the 6.7 GHz methanol maser. The data were recorded in 31 unique SPWs, 30 comprised of 64 channels with each channel being 2 MHz wide and 1 comprised of 512 channels with each channel being 3.906 kHz wide, resulting in a total bandwidth of 3842 MHz (before "flagging"). For sources in Cloud A and C the observations were made alternating on a target source for 9.5 minutes and a phase calibrator for 1 minute, for a total on-source time of 47.5 minutes. For sources in Cloud B, D and H the observations were made alternating

on a target source for 8.5 minutes and a phase calibrator for 1 minute, for a total on-source time of 42.5 minutes.

The data were processed using NRAO's CASA package (McMullin et al. 2007). We used the VLA pipeline CASA v5.1 for the A configuration and pipeline CASA v4.7.2 for the C configuration for calibration. We ran one additional pass of CASA's `flagdata` task using the `rflag` algorithm on each target field to flag low-level interference. For Cloud A, C and H, for which we have data observed with both configurations, we used CASA's `concat` task to combine the A configuration and C configuration data giving a factor of 3 times more weight to the A configuration data, allowing us to obtain a more Gaussian-like PSF at a similar resolution as the A-configuration data. We made mosaic images combining all the fields in the same cloud since there was substantial overlap in their primary beams to improve sensitivity and UV coverage. For Cloud C we used "mosaic" gridder in CASA's `tclean` task to jointly deconvolve all 6 fields. The continuum images were made using 29 of the 30 wide-band spectral windows, since one SPW was excluded due to possible contamination by maser emission. All images were deconvolved using the `mtmfs` mode of CASA's `tclean` task and used `nterms=2` to model the sources' frequency dependencies. For Cloud A, B, D, H, we tried different approaches and concluded that the CASA `linearmosaic` tool gave us the optimal results. Note that mosaics of B and D clouds only include C configuration data. A list of the beam sizes and rms noise levels are shown in Table 3.1.

Table 3.1. VLA 6 cm Observations

Source	Configuration	Beam Size	Continuum Detection	Continuum 3σ rms (μJy beam^{-1})
A1	A, C	$0.659'' \times 0.364''$	Y	9.9
A2	A, C	$0.659'' \times 0.364''$	N	15.0
A3	A, C	$0.659'' \times 0.364''$	N	17.4
B1	C	$4.685'' \times 2.576''$	N	18.6
B2	C	$4.685'' \times 2.576''$	N	20.4
C1	A, C	$0.481'' \times 0.396''$	N	15.0
C2	A, C	$0.481'' \times 0.396''$	Y	9.0
C4	A, C	$0.481'' \times 0.396''$	Y	8.1
C5	A, C	$0.481'' \times 0.396''$	N	8.7
C6	A, C	$0.481'' \times 0.396''$	N	12.6
C9	A, C	$0.481'' \times 0.396''$	Y	13.8
D1	C	$3.332'' \times 2.701''$	N	20.7
D8	C	$3.332'' \times 2.701''$	N	25.2
H5	A, C	$0.407'' \times 0.326''$	N	9.3
H6	A, C	$0.407'' \times 0.326''$	N	9.0

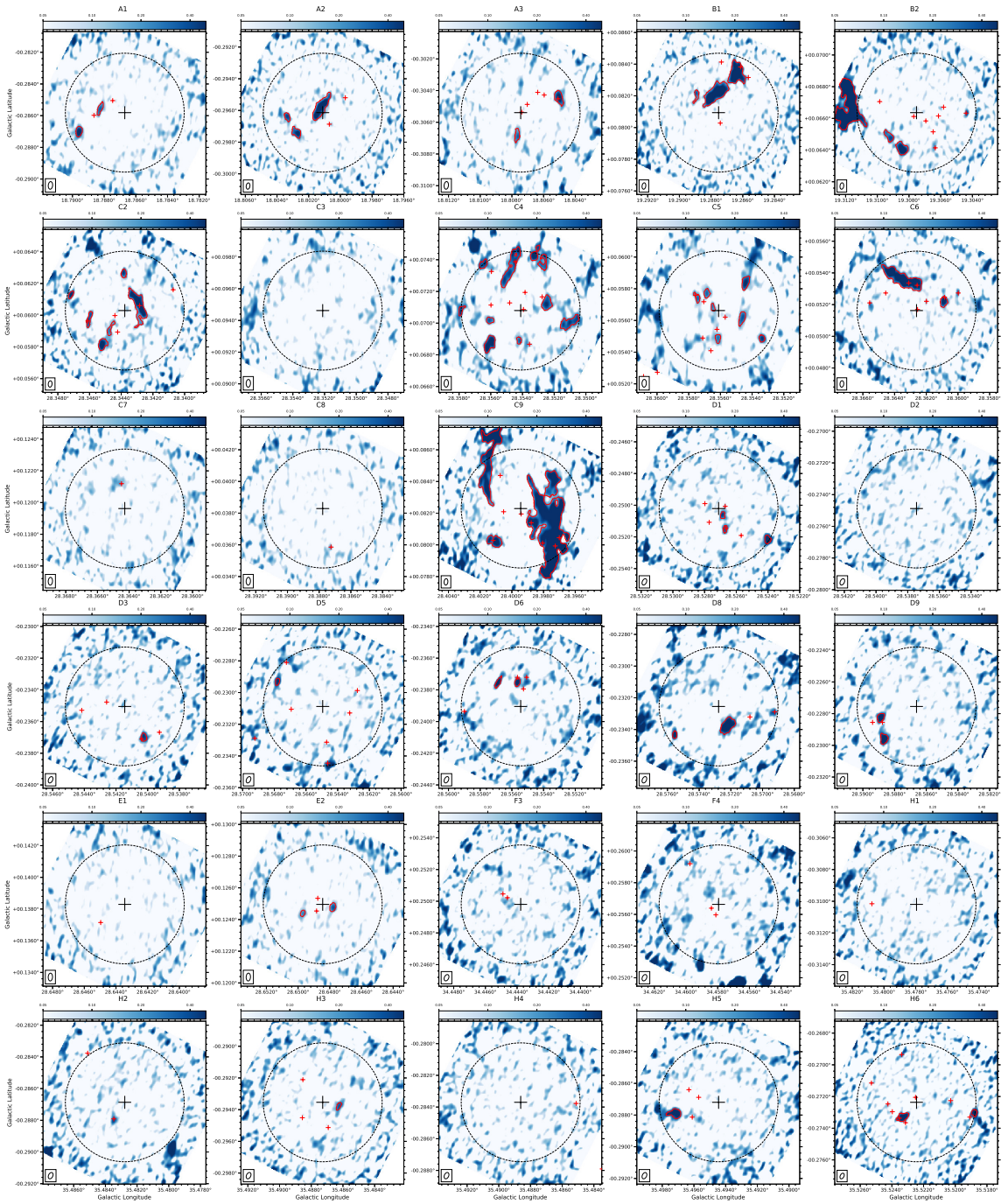

Fig. 3.1.— SiO(5-4) integrated intensity maps within ± 15 km s^{-1} relative to the cloud velocity of the 30 IRDC positions. The red contours show the *trunk* structures characterized by the dendrogram algorithm. The minimum threshold intensity required to identify a *trunk* structure is 3 σ. In the images prior to primary beam correction $\sigma \sim 50\,\mathrm{mJy\,km\,s^{-1}\,beam^{-1}}$ for Clouds A, C, E; $\sigma \sim 40\,\mathrm{mJy\,km\,s^{-1}\,beam^{-1}}$ for Cloud B; and $\sigma \sim 74\,\mathrm{mJy\,km\,s^{-1}\,beam^{-1}}$ for Clouds D, F and H. The minimum area is one synthesized beam size. The black plus sign denotes the center of the field. The red plus signs denote the 1.3 mm continuum cores detected in Liu et al. (2018). The dotted circle in each panel denotes the primary beam. The synthesized beam is shown in the bottom left corner of each panel.

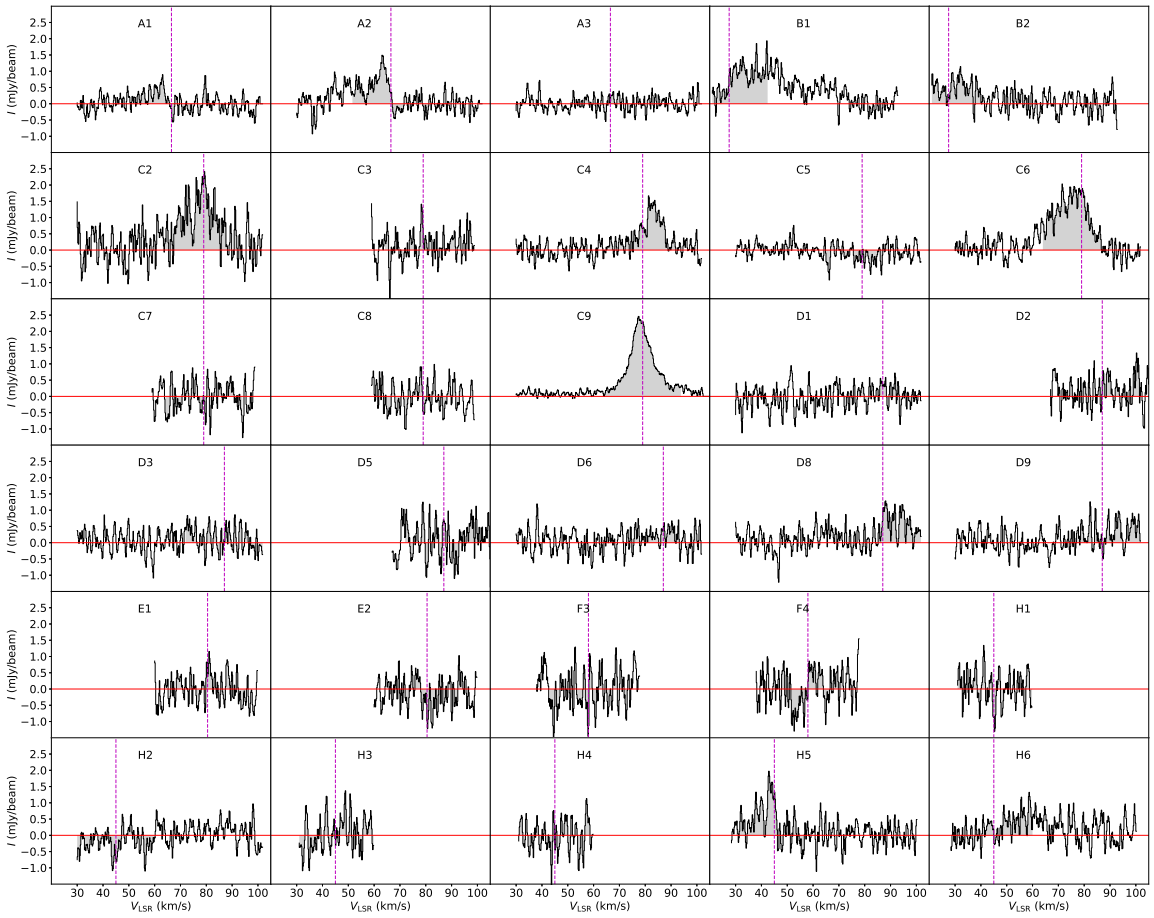

Fig. 3.2.— Spectra of SiO(5-4) emission of the 30 IRDC positions averaged within the primary beam. The flux of C9 has been reduced by a scale factor of 0.25 for ease of viewing. The dashed lines denote the estimates of the cloud LSR velocities. The grey area denotes emission within ± 15 km s^{-1} relative to the cloud velocity, which is used for identifying structures above 3 σ in the integrated intensity maps of SiO(5-4).

3.3 SiO outflows

3.3.1 SiO detection

Out of the 32 clumps observed, we have detected SiO(5-4) emission in 20 sources: A1, A2, A3, B1, B2, C2, C4, C5, C6, C9, D1, D3, D5, D6, D8, D9, E2, H3, H5, H6. We define a detection of SiO(5-4) emission with two methods. Method 1 is if there are at least 3 consecutive pixels with the peak emission greater than 3σ noise level in their spectra and the projected area of such pixels is larger than one beam size. Method 2 is if the integrated intensity of SiO(5-4) within ± 15 km s^{-1} relative to the cloud velocity is higher than the 3σ noise level and the area of such pixels is larger than one beam size (see Figure 3.1). We only consider emission inside the primary beam (except B2, see §3.3.2). When applying Method 2, the emission features were identified by the dendrogram algorithm (Rosolowsky et al. 2008), which is a code for identifying hierarchical structures. We set the minimum threshold intensity required to identify a parent tree structure (*trunk*) to be 3σ and a minimum area of the synthesized beam size. We use the images prior to primary beam correction to identify cores. We use astrodendro[1], a python package to compute dendrogram statistics. Only A2, B1, B2, C2, C4, C5, C6, C9 are reported detection with Method 1. More detections are made with Method 2. The spectra of the 30 IRDC positions averaged within the primary beam are shown in Figure 3.2. These figures also show the estimated systemic velocity of each cloud, adopted from Kong et al. (2017).

To identify the protostellar sources that are responsible for the generation of the SiO(5-4) emission, we search for 1.3 mm emission peaks that are in the vicinity. Although there is at least one continuum peak in every clump with SiO detection, it is ambiguous in many cases to tell the association of SiO and continuum peaks based

[1] `http://www.dendrograms.org/`

only on their spatial distributions.

We are more confident about the protostellar nature of the continuum peak if it is associated with a dense gas tracer. For each 1.3 mm continuum source identified in Liu et al. (2018), we define a $3'' \times 3''$ region centered at the continuum peak as the "core region" and derive the spectrum of each dense gas tracer within the core region. If there are more than 3 channels with signal above 2σ noise level, and the peak channel as well as its neighboring channels have signal above a 2σ noise level, then we consider there is detection of that line associated with the continuum core. We record the peak velocity of each line and take the mean value as the systemic velocity of the core. Generally $C^{18}O$(2-1) is the most common tracer. DCN(3-2) and DCO^+(3-2) can be relatively weak. The SiO detections and the association with dense gas tracers are summarized in Table 3.2.

Table 3.2. Integrated Flux Densities

	d	$L_{\rm SiO,total}$	SiO Detection					Plausible Driving Protostar										Photometry and SED Fitting			
Source	(kpc)	(Jy km s^{-1} pc^2)	No.	l (°)	b (°)	S_ν (Jy km s^{-1})		mm Peak	l (°)	b (°)	$M_{c,\rm raw}$ ($M_\odot$)	DCN	DCO$^+$	C^{18}O	CH$_3$OH	N$_2$D$^+$	velocity (km s−1)	$l_{\rm ap}$ (°)	$b_{\rm ap}$ (°)	$R_{\rm ap}$ ($''$)	$L_{\rm bol}$ $L_\odot$
A1	4.8	2.733e+08	1	18.78830	-0.28567	0.328		A1c2	18.78864	-0.28598	23.0	N	N	Y	N	Y	64.2	18.78897	-0.28477	16	5.771e+02
			2	18.78963	-0.28711	0.616		A1c2	18.78864	-0.28598	23.0	N	N	Y	N	Y	64.2				
A2	4.8	1.504e+09	1	18.80129	-0.29592	3.826		A2c2	18.80070	-0.29687	3.49	Y	Y	Y	N	N	55.2	18.80177	-0.29591	16	4.132e+02
			2	18.80340	-0.29650	0.444															
			3	18.80281	-0.29750	0.926															
A3	4.8	3.706e+08	1	18.80510	-0.30455	0.938		A3c3	18.80509	-0.30452	16.5	N	Y	Y	N	N	66.0	18.80612	-0.30392	16	4.194e+02
			2	18.80772	-0.30693	0.342		A3c5	18.80738	-0.30536	0.971	N	Y	Y	N	Y	65.3				
B1	2.4	9.686e+08	1	19.28645	0.08332	5.959		B1c2	19.28614	0.08382	4.18	Y	Y	Y	N	N	26.8	19.28618	0.08371	11	8.106e+01
			2	19.28777	0.08203	7.061		B1c2	19.28614	0.08382	4.18	Y	Y	Y	N	N	26.8				
			3	19.28898	0.08192	0.361		B1c2	19.28614	0.08382	4.18	Y	Y	Y	N	N	26.8				
B2	2.4	1.050e+10	1	19.31186	0.06678	35.549		B2c9	19.31166	0.06737	14.4	Y	N	Y	Y	N	26.0	19.31172	0.06726	15	2.976e+02
								B2c10	19.31149	0.06633	2.31	Y	N	Y	Y	N	26.4				
			2	19.30930	0.06477	0.700															
			3	19.30850	0.06399	2.048															
C2	5.0	2.350e+09	1	28.34389	0.06251	0.457												28.34574	0.06053	16	9.451e+02
			2	28.34721	0.06116	0.439															
			3	28.34298	0.06052	4.407		C2c2	28.34284	0.06061	48.5	Y	Y	Y	N	N	79.2				
			4	28.34607	0.05962	0.624		C2c4	28.34610	0.05963	33.1	Y	Y	Y	Y	N	83.7				
			5	28.34473	0.05901	0.372															
			6	28.34523	0.05804	1.181															
C4	5.0	2.899e+09	1	28.35328	0.07419	0.923												28.35456	0.07170	13	2.103e+02
			2	28.35274	0.07370	0.593															
			3	28.35651	0.07358	0.523		C4c2	28.35596	0.07326	9.65	Y	N	N	Y	N	94.8				
			4	28.35475	0.07349	2.566		C4c1	28.35446	0.07388	16.8	N	N	Y	Y	N	83.1				
			5	28.35254	0.07112	0.952		C4c4	28.35276	0.07166	6.87	N	N	Y	Y	N	81.3				
			6	28.35791	0.07067	0.336															
			7	28.35610	0.07006	0.284		C4c6	28.35599	0.07114	0.509										
			8	28.35110	0.06992	1.303															
			9	28.35427	0.06879	0.196		C4c8	28.35356	0.06867	3.10										
			10	28.35612	0.06858	1.552															
C5	5.0	7.864e+08	1	28.35447	0.05825	0.768												28.35620	0.05782	15	2.618e+02
			2	28.35690	0.05758	0.276		C5c2	28.35705	0.05718	1.13										
			3	28.35751	0.05732	0.247		C5c1	28.35757	0.05759	1.68										
			4	28.35653	0.05670	0.150															
			5	28.35470	0.05602	0.492															

Table 3.2—Continued

	d	$L_{\rm SiO,total}$	SiO Detection					Plausible Driving Protostar											Photometry and SED Fitting			
Source	(kpc)	(Jy km s^{-1} pc^2)	No.	l (°)	b (°)	S_ν (Jy km s^{-1})	mm Peak	l (°)	b (°)	$M_{c,\rm raw}$ ($M_\odot$)	DCN	DCO$^+$	C^{18}O	CH$_3$OH	N$_2$D$^+$	velocity (km s−1)	$l_{\rm ap}$ (°)	$b_{\rm ap}$ (°)	$R_{\rm ap}$ ($''$)	$L_{\rm bol}$ $L_\odot$
			6	28.35621	0.05475	0.247														
			7	28.35344	0.05475	0.323	C5c4	28.35622	0.05544	2.88										
C6	5.0	3.511e+09	1	28.36350	0.05346	10.276	C6c1	28.36310	0.05336	9.30	N	N	Y	Y	Y	80.0	28.36315	0.05323	15	4.484e+02
			2	28.36096	0.05206	0.901	C6c5	28.36085	0.05246	8.77	N	N	Y	N	N	79.4				
C9	5.0	1.981e+10	1	28.40145	0.08545	13.221											28.39708	0.08034	10	6.284e+03
			2	28.39759	0.08080	63.052	C9c5	28.39701	0.08045	178	Y	Y	Y	Y	N	77.0				
							C9c7	28.39806	0.08011	25.6	Y	Y	Y	Y	N	78.5				
							C9c8	28.39726	0.07993	39.1	Y	Y	Y	Y	N	80.0				
			3	28.40113	0.08011	1.883	C9c6	28.40118	0.08028	13.9	N	N	N	N	N					
D1	5.7	5.574e+08	1	28.52691	-0.25075	0.324											28.52727	-0.25093	15	2.957e+02
			2	28.52675	-0.25162	0.288	D1c4	28.52666	-0.25146	5.34	N	Y	Y	N	Y	86.6				
			3	28.52409	-0.25228	0.754														
D3	5.7	2.144e+08	1	28.54031	-0.23711	0.525	D3c4	28.54037	-0.23710	1.01	Y	Y	N	Y	N	88.1	28.54167	-0.23443	15	4.533e+02
D5	5.7	1.531e+08	1	28.56784	-0.22944	0.375	D5c1	28.56724	-0.22810	2.61	N	N	Y	N	N	87.4	28.56469	-0.23413	11	3.726e+02
D6	5.7	4.713e+08	1	28.55691	-0.23766	0.632											28.55816	-0.23847	15	2.758e+02
			2	28.55571	-0.23766	0.522	D6c1	28.55565	-0.23721	8.65	Y	Y	Y	N	N	83.0				
D8	5.7	1.413e+09	1	28.57227	-0.23388	2.960	D8c2	28.57080	-0.23321	0.843	N	N	Y	N	N	88.9	28.56960	-0.23314	11	2.330e+02
			2	28.57559	-0.23445	0.500														
D9	5.7	8.494e+08	1	28.58892	-0.22837	0.894	D9c2	28.58877	-0.22855	28.3	N	Y	Y	N	N	86.3	28.58980	-0.22818	12	1.653e+02
			2	28.58871	-0.22972	1.187	D9c2	28.58877	-0.22855	28.3	N	Y	Y	N	N	86.3				
E1	5.1		0	-	-	-	-	-	-	-	-	-	-	-	-	-	28.64497	0.13900	15	1.743e+02
E2	5.1	1.487e+08	1	28.64787	0.12465	0.312	E2c2	28.64883	0.12454	3.72	N	N	Y	Y	N	78.7	28.64893	0.12560	15	2.083e+02
			2	28.64975	0.12427	0.143	E2c2	28.64883	0.12454	3.72	N	N	Y	Y	N	78.7				
F3	3.7		0	-	-	-	-	-	-	-	-	-	-	-	-	-	34.44478	0.25019	6	2.398e+01
F4	3.7		0	-	-	-	-	-	-	-	-	-	-	-	-	-	34.45981	0.25909	15	8.865e+01
H1	2.9		0	-	-	-	-	-	-	-	-	-	-	-	-	-	35.48076	-0.31016	15	8.717e+01
H2	2.9		0	-	-	-	-	-	-	-	-	-	-	-	-	-	35.48380	-0.28637	10	3.910e+01
H3	2.9	3.077e+07	1	35.48633	-0.29391	0.291	H3c3	35.48693	-0.29513	5.86	N	Y	N	N	N	43.6	35.48765	-0.29326	11	3.370e+01
H4	2.9		0	-	-	-	-	-	-	-	-	-	-	-	-	-	35.48504	-0.28344	10	6.373e+01
H5	2.9	1.584e+08	1	35.49724	-0.28803	1.499	H5c3	35.49611	-0.28813	6.39	N	N	Y	N	N	44.7	35.49653	-0.28683	11	5.030e+01
H6	2.9	1.864e+08	1	35.51886	-0.27317	0.647	H6c7	35.51908	-0.27330	0.363	N	Y	Y	N	N	47.5	35.52357	-0.27351	12	8.366e+01
			2	35.52338	-0.27343	1.764	H6c8	35.52352	-0.27337	2.53	N	Y	Y	N	Y	45.2				

3.3.2 Strong SiO Sources

There are 6 clumps (B1, B2, C2, C6, C9, H6) in which the peak of the SiO integrated intensity is stronger than 10σ, as well as being associated with identified continuum sources. They are likely protostars driving SiO outflows. In this section we present the outflow morphologies, outflow kinematics and SED fitting results of the 6 protostar candidates which show strongest SiO outflow emission. As in the previous sub-section, the radial velocity of the protostar is estimated from the dense gas tracers $C^{18}O$(2-1), DCN(3-2) and DCO^+(3-2). First we find the 1.3 mm continuum emission peak associated with the SiO emission. Then we locate the peak emission of these dense gas tracers respectively within a $3'' \times 3''$ region centered at the continuum peak, i.e., the "core region." We select the tracers near the continuum peak and adopt the average of their velocities of peak emission as the systematic velocity of the protostellar core. Note that we only consider emission above 2σ as valid signals. Once the source velocity is defined, the velocity range of the SiO(5-4) emission for the source is determined by looking at the SiO spectra pixel by pixel in the outflow area.

Morphology and Kinematics

We show the continuum maps, integrated intensity maps of SiO(5-4) and velocity maps of SiO(5-4) of these sources in Figure 3.3. The names of the continuum cores are the same with those in Liu et al. (2018)[2]. We consider the emission of ± 3 km s^{-1} from the protostar to be "ambient" gas. The averaged spectra of SiO(5-4), extracted from the defined rectangular apertures around each source, are shown in Figure 3.4. The velocity span of the SiO emission from these sources is $\sim$30 km s^{-1}. The averaged

[2]We add two more continuum cores in B2 which are outside the primary beam, but associated with the strong SiO emission

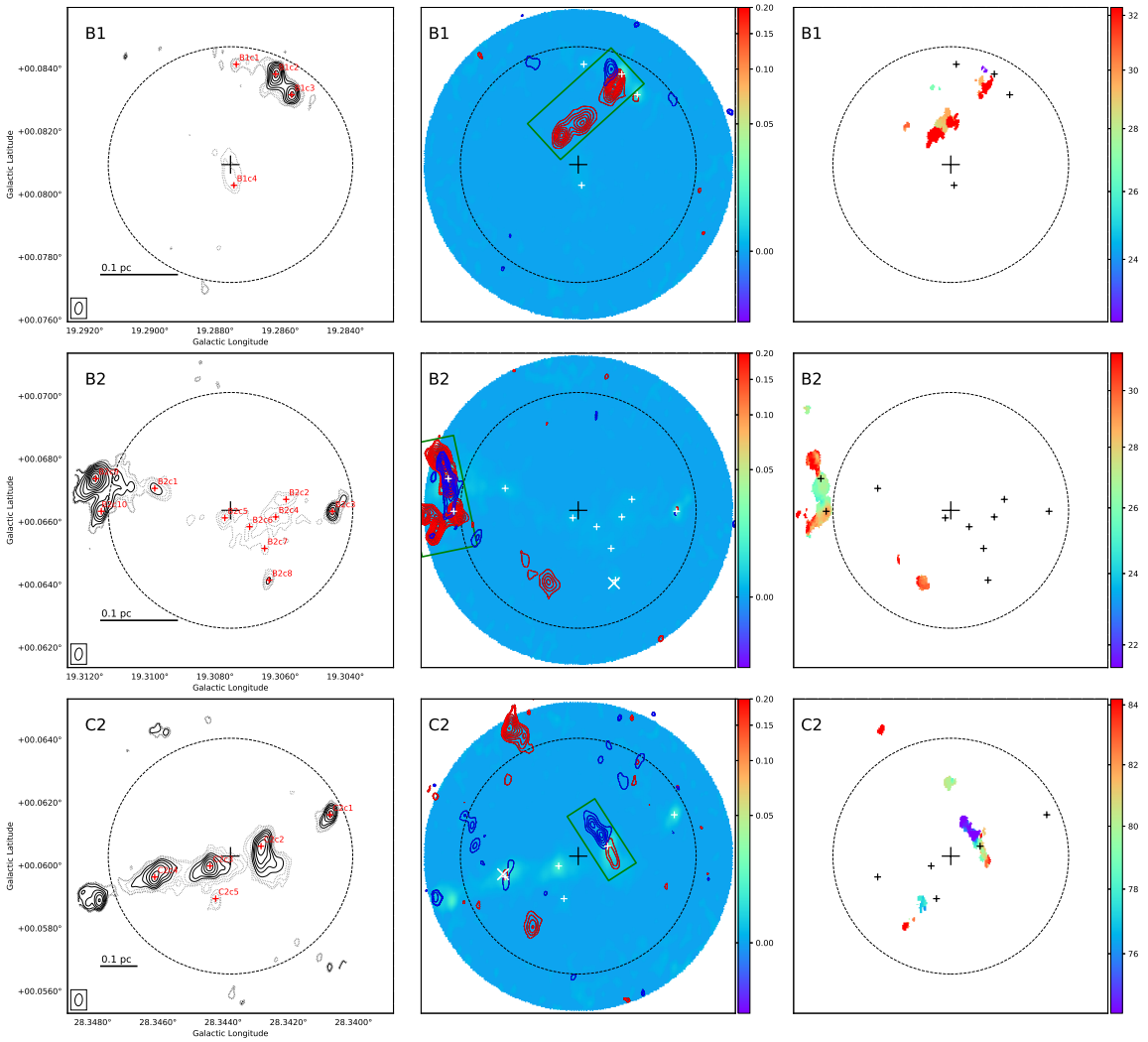

Fig. 3.3.— *Left Column*: 1.3 mm continuum maps. Contour levels are evenly spaced logarithmically, corresponding to 0.800, 1.15, 1.65, 2.36, 3.39, 4.86, 6.98, 10.0, 14.4, 20.6, 29.6, 42.5, 60.9, 87.4, 125, 180 mJy beam^{-1}. The rms noise level in each image is $\sim$ 0.2 mJy beam^{-1}, except for C9 that is dynamic range dominated and has an rms noise level of $\sim$ 0.6 mJy beam^{-1}. The contours below 2 mJy beam^{-1} are dotted. Note, here we only show emission above the 3 *sigma* noise level. The small red plus signs denote the peaks of the dendrogram-identified continuum cores (Liu et al. 2018). The large black plus sign denotes the center of the observation. The dashed circle shows the FWHM of the primary beam. A scale bar and beam size are shown in the lower left corner. *Middle Column*: Integrated intensity maps of SiO(5-4) emission (contours) over 1.3 mm continuum emission (color scale in Jy beam^{-1}). Contour levels start at 5σ in steps of 4σ noise level of the integrated intensity (see Section 3.3.2 for the blue-shifted and red-shifted velocity range and noise level). The green rectangles denote the apertures for deriving the averaged spectra and averaged PV diagrams. The small white plus signs denote the peaks of the dendrogram-identified continuum cores (Liu et al. 2018). White X signs denote water masers detected by Wang et al. (2016). The large black plus sign denotes the center of the observation. The dashed circle shows the primary beam. *Right Column*: Average velocity (first moment) maps of SiO(5-4) emission (color scale in km s^{-1}). Note we only use pixels with emission stronger than 3σ noise level for H6 and 4σ noise level for the other sources. The small

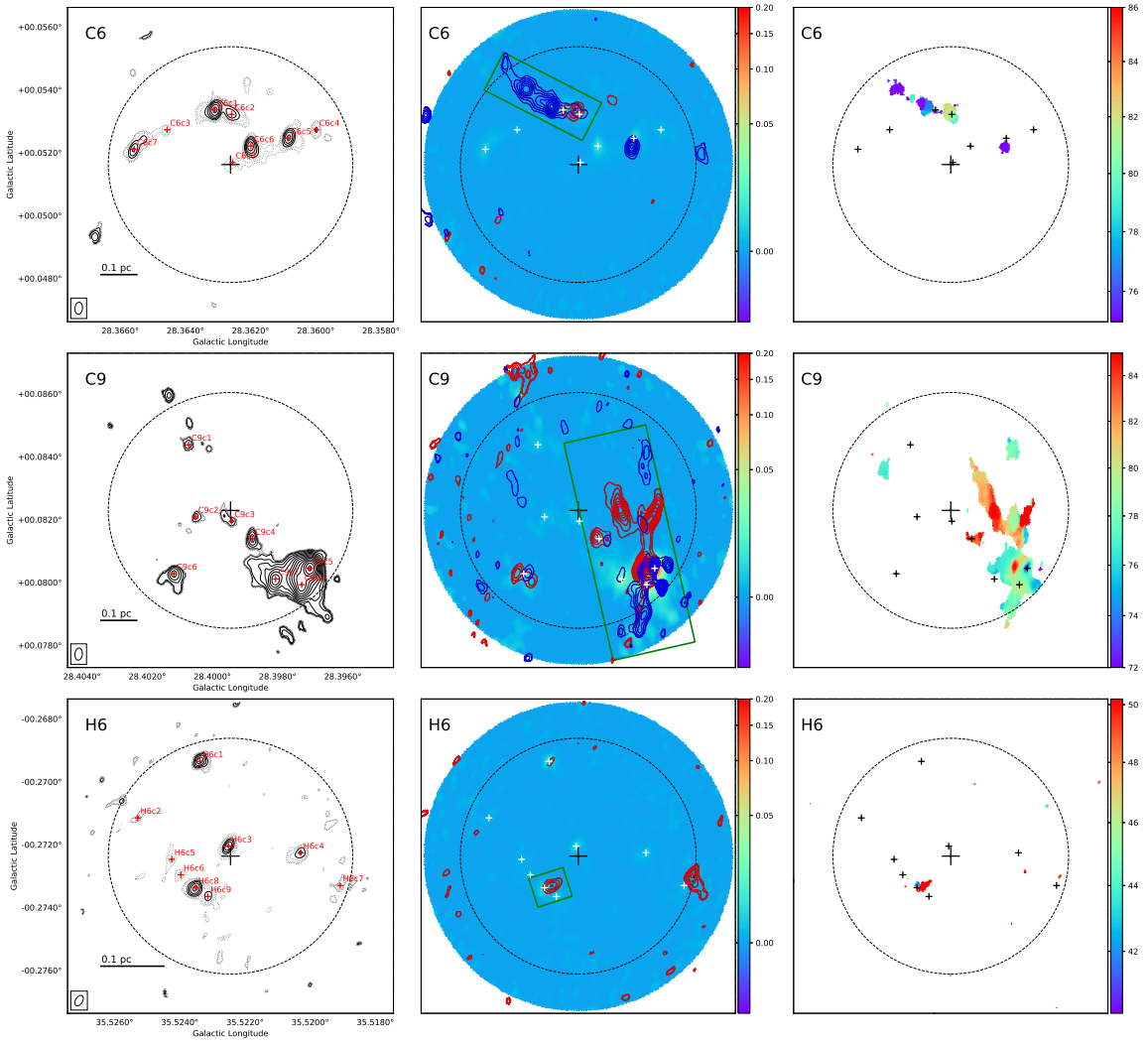

Fig. 3.3.— (cont.)

position-velocity (PV) diagrams in the rectangular apertures along the outflow axes are shown in Figure 3.5. We can see there is large velocity dispersion at a certain position in all the sources.

Overall, some outflows appear quite collimated, like C2 and C6, while others are less ordered, like C9. The morphologies and kinematics of the six sources are discussed individually below.

Source B1: The systemic velocity of the continuum source B1c2 is 26.8 km s^{-1}

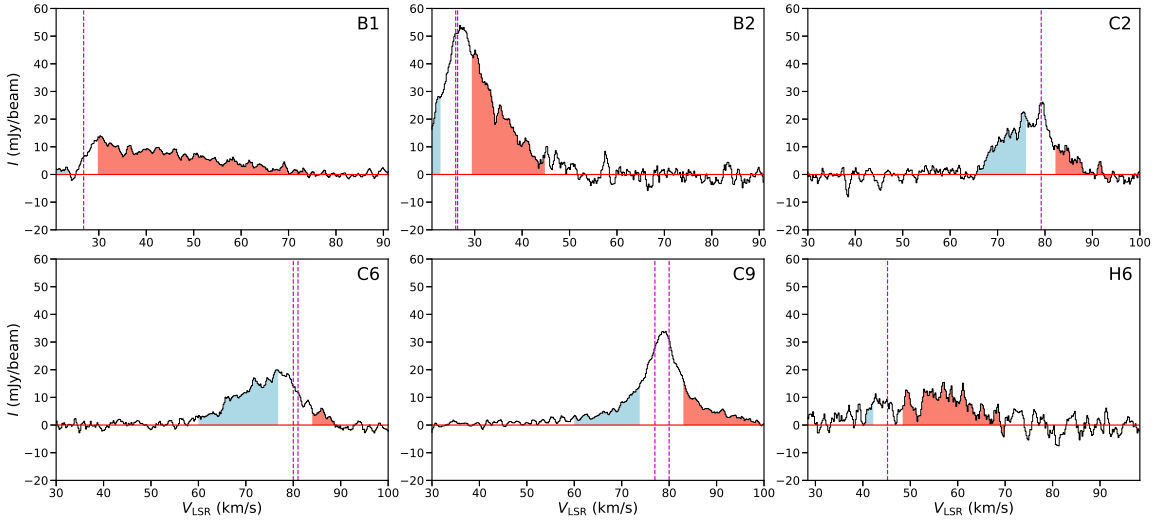

Fig. 3.4.— Averaged SiO(5-4) spectra extracted from the defined rectangular aperture of each source (see Figure 3.3). The dashed line denotes the systematic velocity of the 1.3 mm continuum sources. The blue and red areas denote the velocity range used to derive the blue- and red-shifted outflows respectively.

derived from DCN, DCO^+ and $C^{18}O$. Since the spectral set-up only starts at 21 km s^{-1}, we may miss some emission from blue-shifted velocities. The velocity range of SiO emission is $\sim$ 50 km s^{-1}. The velocity range for the blue-shifted component is 21.0 km s^{-1} - 23.8 km s^{-1} and for the red-shifted component 29.8 km s^{-1} - 80.0 km s^{-1}, as shown in Figure 3.3. The 1σ noise levels of the blue-shifted and red-shifted integrated intensities are 16 mJy $beam^{-1}$ km s^{-1} and 63 mJy $beam^{-1}$ km s^{-1}, respectively. The red-shifted component consists of three peaks. We do not see any more emission beyond the current displayed area. However, there may be more blue-shifted emission emerging to the west of the view and in that case the outflow axis would be oriented NW-SE. Otherwise, if the outflow axis is oriented N-S, then the origin of the two red-shifted SiO peaks in the east becomes less clear.

Source B2: There is very strong SiO emission located at the eastern edge of the primary beam. We used the same method in Liu et al. (2018) to identify continuum

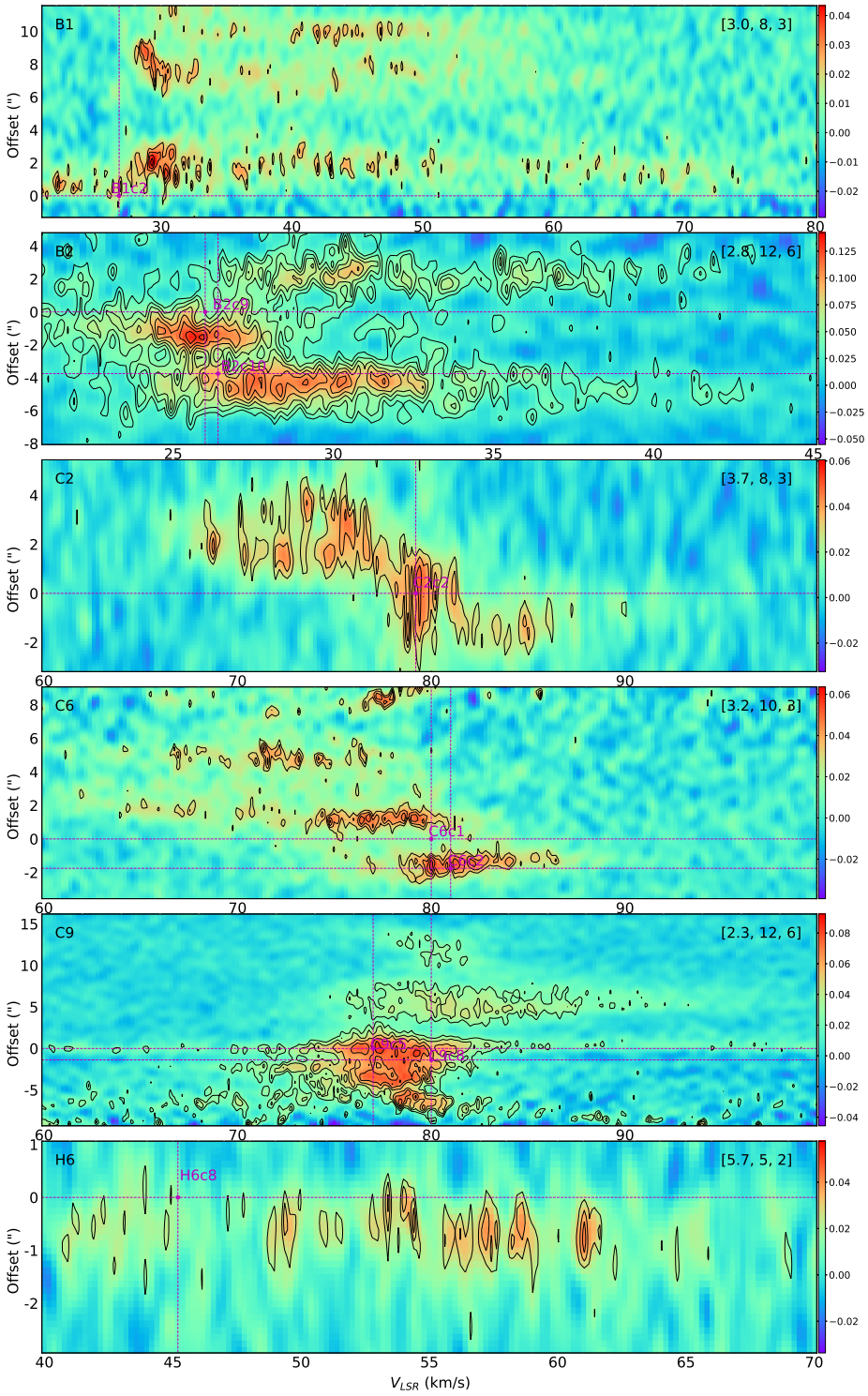

Fig. 3.5.— Averaged position-velocity diagram of SiO(5-4) emission along the long axis of the rectangles shown in Figure 3.3, i.e., the outflow axes. The offset from top to bottom corresponds to the offset from the reference position along the axis from east to west. The reference position is where the continuum peak is located. Other continuum peaks in the rectangle are also shown if any. Color scale is in Jy beam^{-1}. Contour level information is given in upper right: 1 σ noise level in mJy beam^{-1}; lowest contour level in number of σ; then step size between each contour in number of σ.

cores in the outflow region outside of the primary beam. Even though the noise is higher than inside the primary beam, we were still able to identify two cores B2c9 (l = 19.31166°, b = 0.06737°) and B2c10 (l = 19.31149°, b = 0.06633°). B2c9 has a mass of 14.4 $M_{\odot}$ and a mass surface density of 3.14 g cm^{-2} (assuming 20 K dust temperature). Similarly, B2c10 has a mass of 2.31 $M_{\odot}$ and a mass surface density of 1.32 g cm^{-2}. The systemic velocity of B2c9 is 26.0 km s^{-1} and that of B2c10 is 26.4 km s^{-1} derived from DCN and C^{18}O. The velocity range of SiO emission is ∼24 km s^{-1}. The velocity range for the blue-shifted component is 21.0 km s^{-1} - 23.0 km s^{-1} and for the red-shifted component 29.4 km s^{-1} - 45.0km s^{-1}, as shown in Figure 3.3. The 1σ noise levels of the blue-shifted and red-shifted integrated intensities are 14 mJy beam^{-1} km s^{-1} and 36 mJy beam^{-1} km s^{-1}, respectively. Like B1, given the spectral setting we may only see part of the blue-shifted component. The outflow does not reveal a clear bipolar structure and the blue lobes and red lobes overlap. There is also some red-shifted emission within the primary beam which may be connected to the eastern source(s).

Source C2: The 1.3 mm continuum image reveals five peaks. The systemic velocity of the continuum source C2c2 is 79.2 km s^{-1} derived from DCN, DCO^{+} and C^{18}O. The velocity range of the SiO emission is ∼30 km s^{-1}. The velocity range for the blue-shifted component is 65.0 km s^{-1} - 76.2 km s^{-1} and for the red-shifted component 82.2 km s^{-1} - 95.0 km s^{-1}, as shown in Figure 3.3. The 1σ noise levels of the blue-shifted and red-shifted integrated intensities are 30 mJy beam^{-1} km s^{-1} and 32 mJy beam^{-1} km s^{-1}, respectively. The outflow is highly symmetric and highly collimated with a half-opening angle of about 23°. Zhang et al. (2015) also observed this clump (G28.34 P1) via 1.3 mm continuum and multiple molecular lines including CO(2-1) and SiO(5-4) with a higher sensitivity, which shows similar results. They determined

sub-fragmentation in the 1.3 mm continuum cores with 2D Gaussian fitting. From Figure 3.5 we can see C2 shows a "Hubble-law" velocity structure (e.g., Lada & Fich, 1996) and similar to the expectation of a single bow shock (Lee et al. 2000), in which the highest velocity appears at the tip followed by a low-velocity "wake" or "bow wing" and the velocity dispersion decreases significantly in the post shocked region closer to the protostar. Arc-like PV structures, similar to those seen in Fig. 3.5, have been seen in pulsed jet simulations (e.g., Stone & Norman 1993; Lee & Sahai 2004), indicating that this mechanism may be operating here.

Source C6: The systemic velocity of the continuum source C6c1 is 80.0 km s^{-1} and that of C6c2 is 81.0 km s^{-1}, as derived from $C^{18}O$. The velocity range of the SiO emission is about 30 km s^{-1}. The velocity range for the blue-shifted component is 60.0 km s^{-1} - 77.0 km s^{-1} and for the red-shifted component is 84.0 km s^{-1} - 90.0 km s^{-1}, as shown in Figure 3.3. The 1σ noise levels of the blue-shifted and red-shifted integrated intensities are 37 mJy $beam^{-1}$ km s^{-1} and 22 mJy $beam^{-1}$ km s^{-1}, respectively. The two lobes are very asymmetric with the blue lobe extending much further and exhibiting higher velocities (see Figure 3.5). Similar asymmetry is also revealed in the CO(2-1) outflow, where there is strong blue-shifted emission but little red-shifted emission (Kong et al. 2019). It may be due to an inhomogeneous ambient cloud environment, which is denser in the south, or due to intrinsically variable jets. The blue-shifted outflow is highly collimated, consists of a chain of knots and also has a small wiggle, which resembles the SiO jets revealed in the HH 212 low-mass protostellar system (Lee et al. 2015) and the V380 Ori NE region (Choi et al. 2017), and the CO outflow in Serpens South (Plunkett et al. 2015). The knotty feature suggests an episodic ejection mechanism (e.g., Qiu & Zhang 2009; Plunkett et al. 2015; Chen et al. 2016) or alternatively oblique shocks (Reipurth 1992; Guilloteau

et al. 1992). The wiggle may be caused by jet precession (e.g., Choi et al. 2017) or instability in a magnetized jet (e.g., Lee et al. 2015). Since we do not see symmetric features in the red-shifted outflow, the orbiting source jet model of a protobinary (e.g., Lee et al. 2010) is not favored, though it is still possible if there is very dense ambient gas located where the red-shifted outflow should be. The PV diagram (see Figure 3.5) is similar to the SiO jet in H212 (Codella et al. 2007, see their Figure 2 Left). They suggested that the SiO lobes include a narrower and faster jet-like component distinct from the swept-up cavity and the high-velocity SiO is probably tracing the base of the large-scale molecular jet. The velocity structures look like "Hubble wedges" (Arce & Goodman 2001). Recent theoretical models of episodic protostellar outflows (e.g., Federrath et al. 2014; Offner & Arce 2014; Offner & Chaban 2017; Rohde et al. 2019) have been built to reproduce such features. A separate blue-shifted emission feature seems to be driven by the continuum core C6c5, which is associated with a CO(2-1) outflow (Kong et al. 2019). However, the systemic velocity of C6c5 cannot be determined accurately due to the weak emission of its dense gas tracers.

Source C9: The 1.3 mm continuum emission reveals 3 cores in the main outflow area. The brightest core, C9c5, has a peak intensity as high as 197 mJy beam^{-1}, while the second brightest core, C9c8, to its south has a peak intensity of 85.3 mJy beam^{-1}. The systemic velocity of C9c5 is $\sim$77 km s^{-1} and that of C9c8 is $\sim$80 km s^{-1}, as derived from DCN, DCO$^+$ and C^{18}O. At the position of continuum core C9c7, the peak velocity of DCN is $\sim$80.0 km s^{-1} and the peak velocity of DCO$^+$ is $\sim$79.6 km s^{-1}, while that of C^{18}O is $\sim$75.9 km s^{-1}. The systemic velocity of C9c4 and C9c6 cannot be determined accurately due to their weak emission in dense gas tracers. The velocity range of the SiO emission is about 40 km s^{-1}. The velocity range for the blue-shifted component is 60.0 km s^{-1} - 74.0 km s^{-1} and for the red-shifted component 83.0

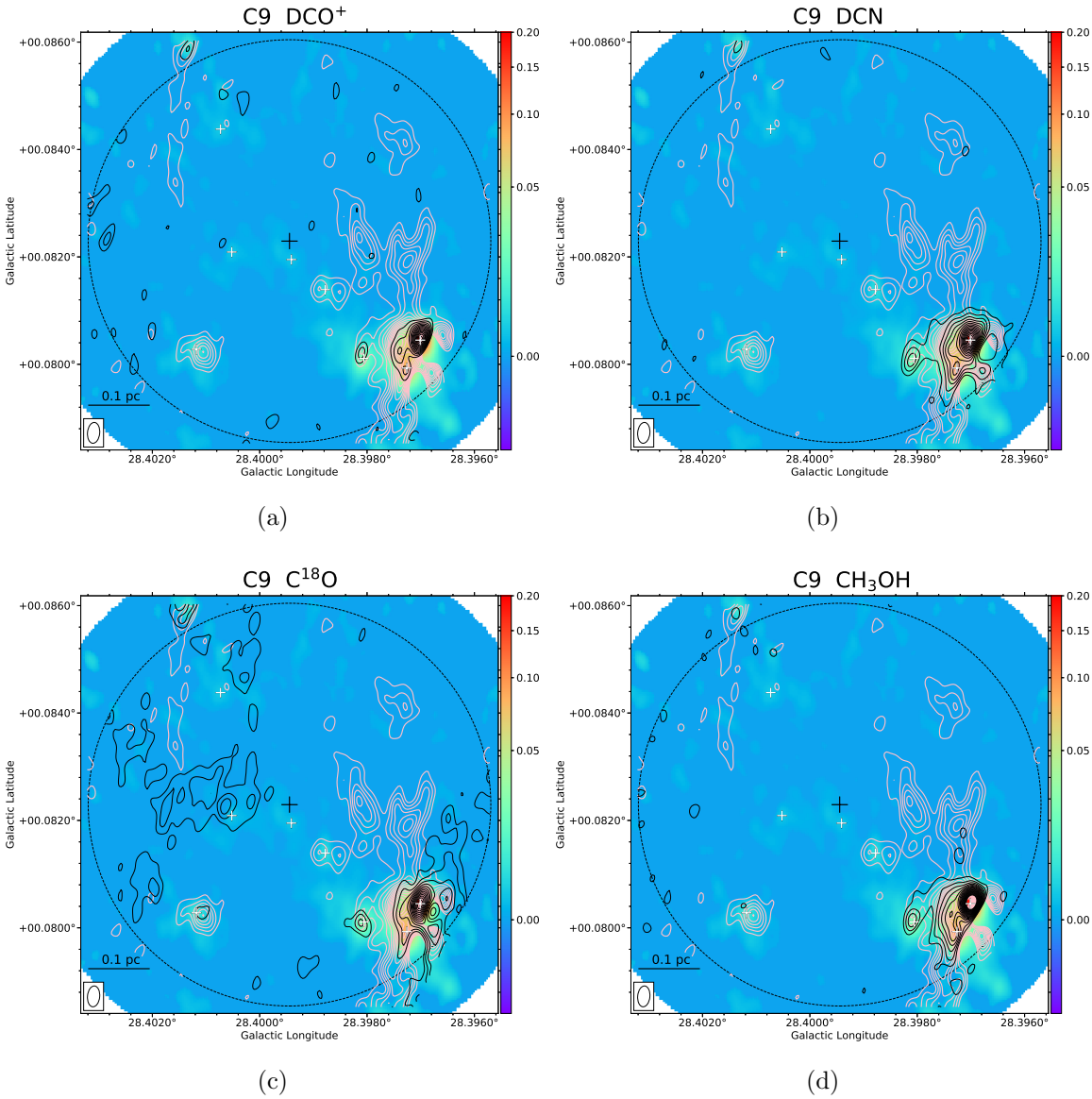

Fig. 3.6.— Integrated intensity map in C9 of: (a) DCO^+(3-2), σ = 19.8 mJy beam^{-1} km s^{-1}; (b) DCN(3-2), σ = 19.8 mJy beam^{-1} km s^{-1}; (c) $C^{18}O$(2-1), σ = 35.3 mJy beam^{-1} km s^{-1}; (d) CH_3OH, σ = 19.8 mJy beam^{-1} km s^{-1}. All of these are integrated within $\pm$ 5 km s^{-1} respect to the cloud velocity. Contour levels start at 5σ in steps of 4σ. The pink contours denote the SiO(5-4) emission of all the 360 velocity channels from 30 km s^{-1} to 102 km s^{-1}, starting at 380 mJy beam^{-1} km s^{-1} in steps of 304 mJy beam^{-1} km s^{-1}. The small white plus signs denote the positions of the continuum peaks. The large black plus sign denotes the center of view. The dashed circle shows the primary beam. A scale bar and beam size are shown in the lower left corner.

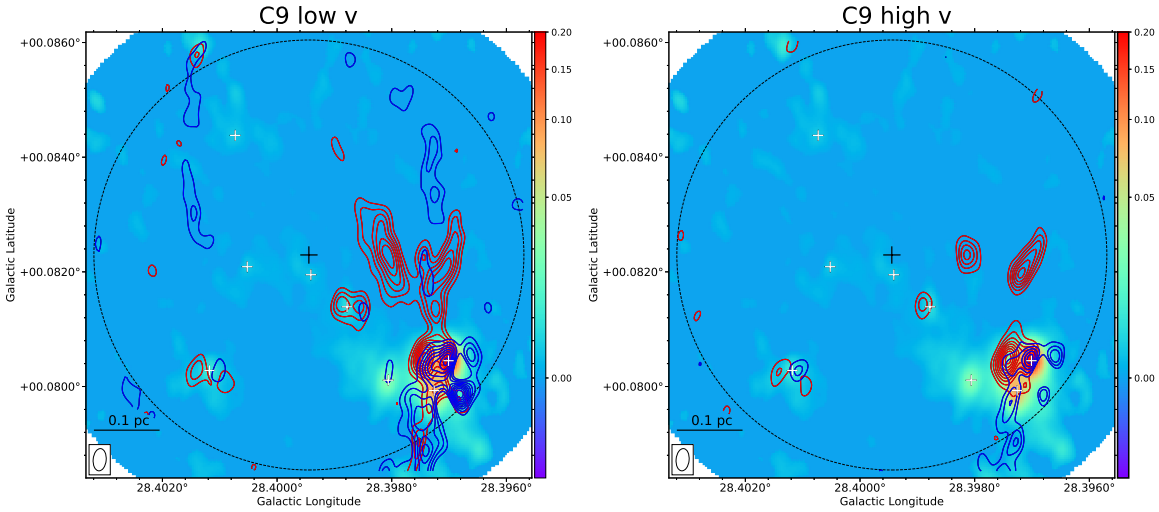

(a) (b)

Fig. 3.7.— C9 SiO velocity components. (a) Integrated intensity maps of SiO(5-4) emission with low velocity components over continuum emission. Blue contours show emission from 67.0 km s^{-1} to 74.0 km s^{-1}. Red contours show emission from 83.0 km s^{-1} to 90.0 km s^{-1}. Contour levels start at 5σ in steps of 4σ with σ = 24.0 mJy beam^{-1} km s^{-1} for both red- and blue-shifted components. The small white plus signs denote the positions of the continuum peaks. The large black plus sign denotes the center of view. The dashed circle shows the primary beam. A scale bar and beam size are shown in the lower left corner. (b) The same as (a), but with high velocity components. Blue contours show emission from 60.0 km s^{-1} to 67.0 km s^{-1}. Red contours show emission from 90.0 km s^{-1} to 100 km s^{-1}. Contour levels start at 5σ in steps of 4σ with σ = 28.6 mJy beam^{-1} km s^{-1} for the red-shifted component and σ = 24.0 mJy beam^{-1} km s^{-1} for the blue-shifted component.

km s^{-1} - 100.0 km s^{-1}, as shown in Figure 3.3. The 1σ noise levels of the blue-shifted and red-shifted integrated intensities are 34 mJy $beam^{-1}$ km s^{-1} and 37 mJy $beam^{-1}$ km s^{-1}, respectively. Figure 3.6 shows the emission from the dense gas tracers DCO^+, DCN, $C^{18}O$ and the hot gas tracer CH_3OH. Their peaks essentially overlap with the continuum peaks. DCN and CH_3OH also show extended structures associated with the SiO outflows, while $C^{18}O$ shows additional emission elsewhere. The disordered and asymmetric morphology of the SiO outflows is probably due to the crowded nature of the core region. Several velocity components are revealed from the PV diagram in Figure 3.5, with a hint of "Hubble wedge". The most extended red-shifted emission lies mostly in the north and the most extended blue-shifted emission in the south. The morphology could be a result of a combination of the extended outflows from both C9c5 and C9c8. We further display the outflows in low-velocity (< 10 km s^{-1} with respect to the systemic velocity) channels and high-velocity (> 10 km s^{-1} with respect to the systemic velocity) channels in Figure 3.7. Together with further investigation in the channel map (not shown here), it is more likely that the two farthest high-velocity red-shifted components revealed in Figure 3.7(b) come from two distinctive outflows rather than consisting of one outflow cavity wall. In addition to the most extended north-south outflows, there seem to be three other smaller scale outflows from Figure 3.7(b). One has its blue- and red-shifted components overlapping at C9c5 and is probably driven by this source. The second one has its blue-shifted component to the west of C9c5 and red-shifted components to the east of C9c5, and these features are likely also driven by C9c5. The third one has its blue-shifted component to the southwest of C9c5. From the spacial distribution, this outflow could be driven by either C9c5 or C9c8, and its red-shifted component either lies also to the east of C9c5 or extends further. It is possible that there are more unresolved protostars other than

C9c5 and C9c8 in the region that drive the multiple outflows, which would indicate a protobinary or multiple system within our resolution limit of 5000 AU and that they each drive an outflow of a different direction. Another possibility is that the outflow orientation may change over time as reported in other protostars (e.g., Cunningham et al. 2009; Plambeck et al. 2009; Principe et al. 2018; Goddi et al. 2018; Brogan et al. 2018). Nevertheless, the outflows associated with C9c6 and C9c4 are quite clear and relatively separate.

Source H6: The blue-shifted emission is quite weak in this source. This may be partly due to missing blue-shifted channels in our spectral setup. The systemic velocity of the continuum source H6c8 is 45.2km s^{-1}, as derived from DCO^+ and $C^{18}O$. The velocity range is about 30 km s^{-1}. The velocity range for the blue-shifted component is 40.0 km s^{-1} - 42.2 km s^{-1} and for the red-shifted component is 48.2 km s^{-1} - 70.0 km s^{-1}, as shown in Figure 3.3. The 1σ noise levels of the blue-shifted and red-shifted integrated intensities are 21 mJy $beam^{-1}$ km s^{-1} and 63 mJy $beam^{-1}$ km s^{-1}, respectively.

Outflow Mass and Energetics

Following the method of Goldsmith & Langer (1999) with an assumption of optically thin thermal SiO(5-4) emission in local thermodynamic equilibrium (LTE), we calculate the mass of the SiO(5-4) outflows using

$$N_u = \frac{4\pi}{hcA_{\rm ul}} \int (S_\nu/\Omega) dv, \tag{3.1}$$

$$N_{\rm tot} = N_u \frac{U(T_{\rm ex})}{g_u} e^{\frac{E_u}{kT_{\rm ex}}}, \tag{3.2}$$

$$M_{\rm out} = N_{\rm tot} \left[\frac{\rm H_2}{\rm SiO}\right] \mu_g m_{\rm H_2} D^2, \tag{3.3}$$

where S_ν/Ω is the SiO intensity at frequency ν, D is the source distance, $\mu_g = 1.36$ is the mean atomic weight and $m_{\rm H_2}$ is the mass of hydrogen molecule. We adopt an excitation temperature of 18 K and a ratio [H2]/[SiO] of 10^9, which are the typical values of IRDC protostellar sources in the survey of Sanhueza et al. (2012). The momentum and energy of the outflow are then derived following

$$P_{\rm out} = \sum M_{\rm out}(\Delta v)\Delta v \tag{3.4}$$

and

$$E_{\rm out} = \frac{1}{2}\sum M_{\rm out}(\Delta v)\Delta v^2, \tag{3.5}$$

where Δv denotes the outflow velocity relative to $v_{\rm cloud}$. To avoid contamination from the ambient molecular gas, we assume the ambient molecular gas has a velocity of $v_{\rm cloud} \pm 3$km s^{-1} and use channels $\geqslant 3$ km s^{-1} from the cloud velocity in the blue- and red-shifted outflows.

The dynamical timescale of the outflow is derived via $t_{\rm dyn} = L_{\rm flow}/v_{\rm max}$, where $L_{\rm flow}$ is the length of the flow extension and $v_{\rm max}$ is the maximum flow velocity relative to $v_{\rm cloud}$. In addition, we estimate the mass flow rate, $\dot{M}_{\rm out} = M_{\rm out}/t_{\rm dyn}$, and the momentum flow rate, $\dot{P}_{\rm out} = P_{\rm out}/\bar{t}_{\rm dyn}$. These results are listed in Table 3.3. Note we only count those pixels with integrated intensity higher than the $3\,\sigma$ noise level. No correction for inclination, which is uncertain, is applied here.

The derived total outflow masses range from 0.02 to about 2 $M_\odot$. The outflow crossing timescales range up to about 20,000 yr. Most of the mass outflow rates are no higher than 10^{-4} $M_\odot$ yr^{-1} and the momentum flow rates are $\sim 10^{-4}$ $M_\odot$ km s^{-1} yr^{-1}.

For comparison, low-mass protostars typically have momentum flow rates of 10^{-5} $M_\odot$ km s^{-1} yr^{-1} and molecular outflow mass fluxes as high as 10^{-6} $M_\odot$ yr^{-1}, while

mid- to early-B type protostars have mass outflow rates 10^{-5} to a few $\times$ 10^{-3} $M_{\odot}$ yr^{-1} and momentum flow rates 10^{-4} to 10^{-2} $M_{\odot}$ km s^{-1} yr^{-1} (e.g., Arce et al. 2007). Our sources are at the typical lower limit of mid- to early-B type protostar outflows. Based on the 1.3 mm continuum core mass, the C2 and C9 cores are likely to be high-mass protostellar objects. Compared with the massive molecular outflows traced by CO(2-1) in Beuther et al. (2002) and the massive outflows traced by SiO(5-4) in Gibb et al. (2007) and Sánchez-Monge (2013b), the outflow mass ($M_{\rm out}$), mass outflow rate ($\dot{M}_{\rm out}$) and the mechanical force ($\dot{P}_{\rm out}$) of C9 are comparable to those in their sample with a similar outflow length. There are several possibilities causing the relatively low outflow parameters of the high-/intermediate-mass protostars in our sample. First, the high-mass protostars may be still at an early stage when the outflows have not formed completely. However, there are protostars in Sánchez-Monge et al. (2013b) and Csengeri et al. (2016) that are also very young (indicated by L/M) but having strong SiO outflow emission (see furrther discussion in §3.5.3). Second, SiO as observed here may not be tracing the full extent of the outflows. This may explain the low SiO-derived outflow masses compared with CO outflows in Beuther et al. (2002).

Table 3.3. Estimated physical parameters for SiO outflows

Source	$M_{\rm out}^{\rm blue}$ ($M_{\odot}$)	$L_{\rm flow}^{\rm blue}$ (pc)	$t_{\rm dyn}^{\rm blue}$ (10^3 yr)	$M_{\rm out}^{\rm red}$ ($M_{\odot}$)	$L_{\rm flow}^{\rm red}$ (pc)	$t_{\rm dyn}^{\rm red}$ (10^3 yr)	$M_{\rm out}$ ($M_{\odot}$)	$P_{\rm out}$ ($M_{\odot}$ km s^{-1})	$E_{\rm out}$ (10^{43} erg)	$\dot{M}_{\rm out}$ (10^{-4} $M_{\odot}$ yr^{-1})	$\dot{P}_{\rm out}$ (10^{-4} $M_{\odot}$ km s^{-1}yr^{-1})
B1	0.006	0.03	5.59	0.174	0.13	2.40	0.18	2.32	53.34	0.74	5.80
B2	0.041	0.08	15.36	0.259	0.15	7.72	0.30	1.07	5.35	0.36	0.93
C2	0.154	0.12	8.31	0.079	0.08	5.04	0.23	1.86	17.41	0.34	2.79
C6	0.442	0.21	10.37	0.068	0.08	7.70	0.51	5.37	69.69	0.52	5.94
C9	0.883	0.20	11.70	1.044	0.39	16.67	1.93	18.50	219.61	1.38	13.04
H6	0.001	0.00	0.03	0.023	0.04	1.52	0.02	0.13	1.04	0.71	1.65

SED Modeling

We investigate the IR counterparts of the protostars that drive the six strongest SiO outflows with *Spitzer* and *Herschel* archival data, as shown in Figure 3.8. Note the dynamic range of Figure 3.8 is set in such a way that faint sources can still show strong contrast. However, the SNR can be very low as in B1, C2, C6 at all wavelengths, B2 at 8 μm, and H6 at 70 μm and 160 μm. The C2, C6, C9 and H6 cores appear dark against the Galactic background at 8 μm, which indicates they are at an early evolutionary stage. We build spectral energy distributions (SEDs) of the six sources from 3.6 μm up to 500 μm. Given the relatively large beam size of *Herschel*, we cannot resolve the individual cores revealed with ALMA and the SEDs represent emission from a larger scale region. The circular apertures are determined to include most of the source flux based on their 70 μm and 160 μm emission. For B1, C6, C9 and H6, we try to make the apertures centered at the protostar driving the main outflow. The typical aperture size is comparable to the primary beam size of our ALMA 1.3 mm observations.

We fit the fixed aperture, background-subtracted SEDs with the radiative transfer (RT) model developed by Zhang & Tan (2018), which describes the evolution of massive (and intermediate-mass) protostars based on the Turbulent Core model (MT03). The model is described by five physical parameters: the initial core mass (M_c), the mean mass surface density of the surrounding clump ($\Sigma_{\rm cl}$), the current protostellar mass (m_*), the foreground extinction (A_V), and the inclination angle of the outflow axis to the line of sight ($\theta_{\rm view}$). The models describe collapsing cores with bolometric luminosities ranging from 10 $L_\odot$ to 10^7 $L_\odot$ and envelope temperatures from 10 K to 100 K. The evolutionary timescales range from 10^3 yr to 10^6 yr. In the grid of models, M_c is sampled at 10, 20, 30, 40, 50, 60, 80, 100, 120, 160, 200, 240, 320, 400, 480 $M_\odot$

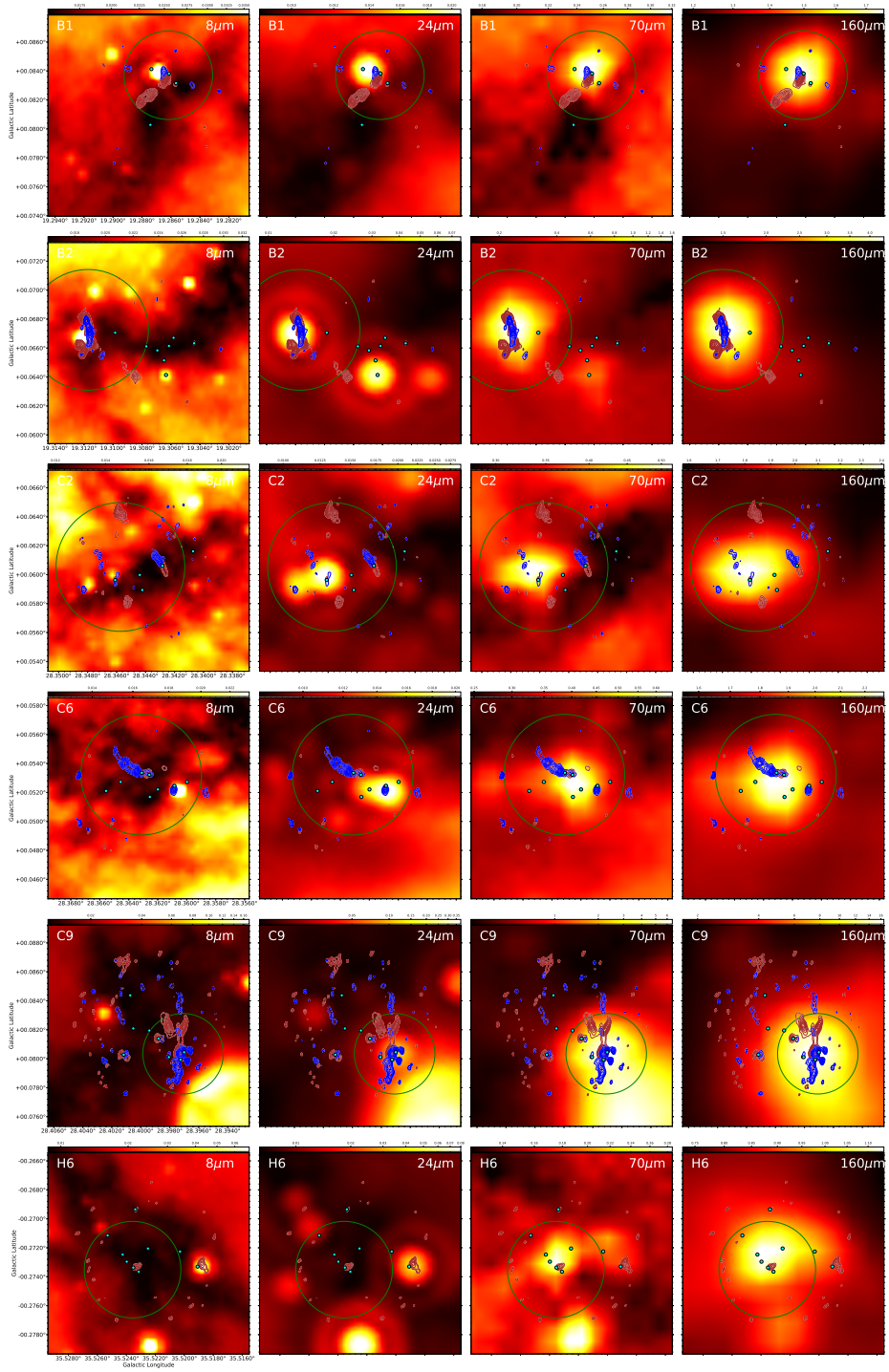

Fig. 3.8.— 8 μm, 24 μm, 70 μm and 160 μm emission of the detected protostars. The color scale is mJy pixel^{-1}. The blue and red contours denote the blue lobe and the red lobe of SiO outflows, contour levels the same as those in Figure 3.3. The green circle denotes the aperture size used for building SEDs. The aperture radius is 11″for B1, 15″ for B2, 16″ for C2, 15″ for C6, 10″ for C9 and 12″ for H6. The cyan dots denotes the positions of the 1.3 mm cores.

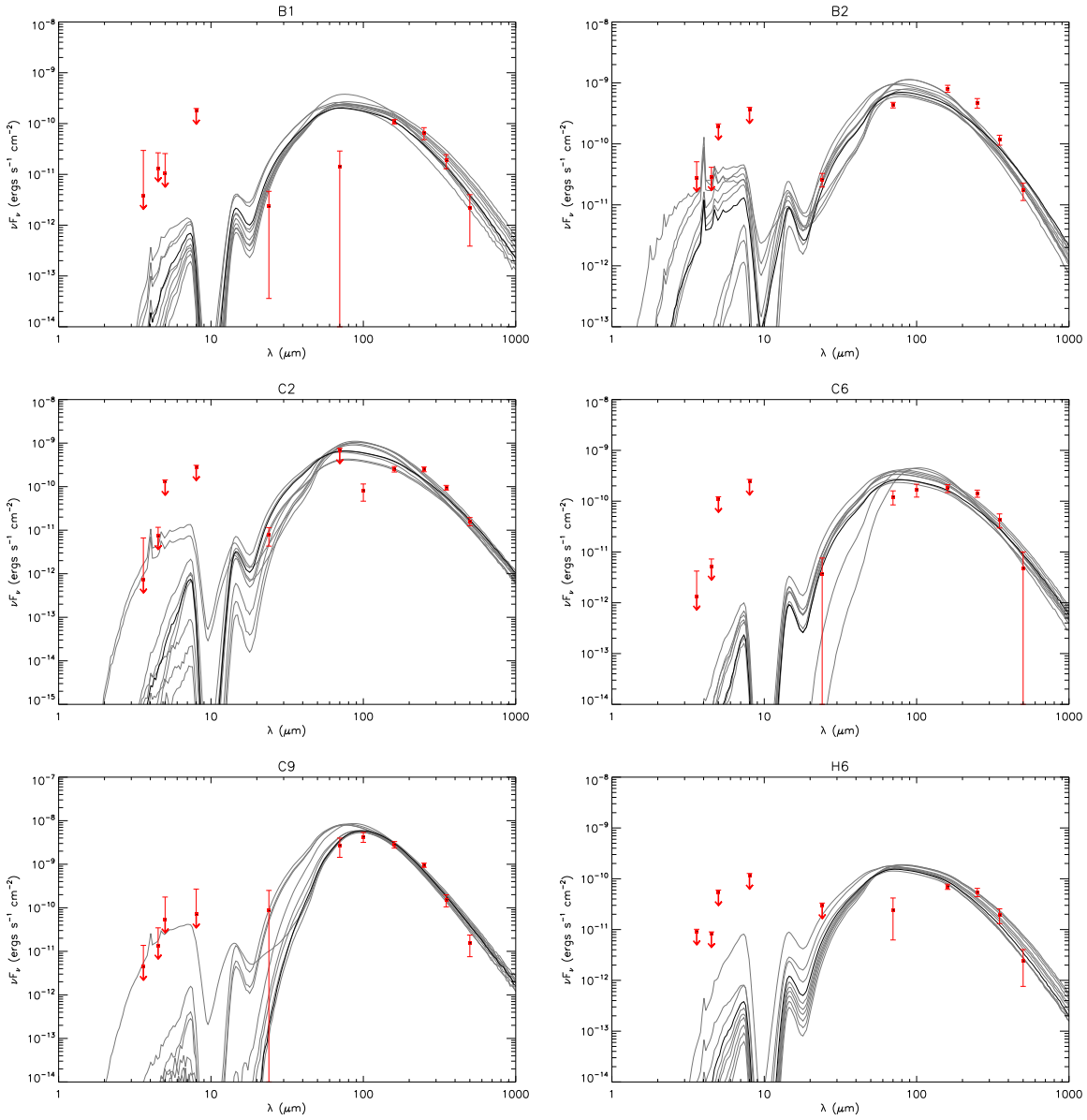

Fig. 3.9.— Protostar model fitting to the fixed aperture, background-subtracted SED data using the ZT model grid. For each source, the best fit model is shown with a solid black line and the next nine best models are shown with solid gray lines. Note that the data at $\lesssim 8\,\mu$m are treated as upper limits. If a background subtracted flux density is negative, the flux density without background subtraction is used as upper limits with a negligible error bar (see text). The model parameter results are listed in Table 3.4.

and $\Sigma_{\rm cl}$ is sampled at 0.10, 0.32, 1, 3.2 g cm^{-2}, for a total of 60 evolutionary tracks. Then along each track, m_* is sampled at 0.5, 1, 2, 4, 8, 12, 16, 24, 32, 48, 64, 96, 128, 160 $M_\odot$ (but on each track, the sampling is limited by the final achieved stellar mass, with star formation efficiencies from the core typically being ~ 0.5). There are then, in total, 432 physical models defined by different sets of (M_c, $\Sigma_{\rm cl}$, m_*).

We used PHOTUTILS, a PYTHON package to measure the flux density of the entire sample. Note that clumps with neither 1.3 mm continuum nor SiO emission are not taken into consideration. The circular aperture is determined based on the 70 μm and 160 μm 2D profile to cover most of the clumpy infrared emission. Sometimes when the boundary of the core and the background is unclear, we adopt an aperture radius of 15″, so that the aperture diameter is close to the beam size of *Herschel* 500 μm images. The aperture radii for most sources are around 15″. After measuring the flux inside the aperture, we carry out background subtraction using the median flux density in an annular region extending from 1 to 2 aperture radii to remove general background and foreground contamination and the effect of a cooler, more massive clump surrounding the core at long wavelengths (see also De Buizer et al. 2017; Liu et al. 2019, 2020; Moser et al. 2020). Note that if the annular region overlaps with the apertures of other sources, we exclude the overlapping part for background estimation. The error of the flux is estimated to be the quadratic sum of the 10% of the background subtracted flux as calibration uncertainty and the background fluctuation. The background fluctuation is derived in the following way: first we divide the annular region extending from 1 to 2 aperture radii evenly into six sectors and measure the standard deviation of the mean values in the six sectors; then we rotate every sector by 10°and measure the standard deviation in the same way again; we repeat the rotation for another four times and obtain six measured standard

deviations in total; finally we derive the mean value of the six standard deviation as the estimation of the background fluctuation. Source distances were adopted from the Butler & Tan (2012).

We use data at wavelengths < 8 μm as upper limits due to PAH emission and thermal emission from very small grains. Additionally, if the background is stronger than the flux density inside the aperture, then the flux density without background subtraction is given and treated as an upper limit. These upper limits can be distinguished by a negligible error bar. The fitting procedure involves convolving model SEDs with the filter response functions for the various telescope bands.

We note that different aperture sizes can make a significant difference in the flux derived especially for faint sources whose boundaries are not clear. Since we do not know the real distribution of the measurement error, the absolute value of the χ^2 is currently dominated by the size of measurement error and does not indicate the goodness of the model well. However, for the same source under the theoretical model we can tell which set of parameters describes the status of the protostar better by comparing their relative values of χ^2. For convenience we show the 10 best models. Amongst the best 10 models there can be a significant variation in model parameters, even though the shape of the model SED does not change much, which illustrates degeneracies that exist in trying to constrain protostellar properties from only their MIR to FIR SEDs (see also De Buizer et al. 2017; Rosero et al. 2019a; Liu et al. 2019, 2020). Based on experience, when the best model returns a χ^2 smaller than 1 it indicates there are too few valid data points constraining the fitting, so we would consider all the models with $\chi^2 < 2$ among the 10 best models as valid. When the best model returns a χ^2 higher than 1, we would consider all the models with χ^2 smaller than twice the χ^2 of the best model among the 10 best models as valid. For more

detailed discussion of the sensitivity of the model to choices in SED cconstruction for faint sources in IRDCs, see Moser et al. (2020). We show the 10 best models for each source in Figure 3.9. The physical parameters derived are listed in Table 3.4. Note that these are distinct physical models with differing values of M_c, $\Sigma_{\rm cl}$ and m_*, i.e., we do not display simple variations of $\theta_{\rm view}$ or A_V for each of these different physical models.

By fitting the SEDs with the models, we assume there is one source dominating the infrared luminosity in an aperture. Overall the fitting is reasonable except that the SEDs of B1 and C2 are not clearly characterized due to their bright infrared background. The peaks of the model SEDs seem to locate at a shorter wavelength than the observed SED, which may result in a more evolved stage. In general, the 10 best fit models have protostellar masses $m_* \sim 0.5 - 8\,M_\odot$ accreting at rates of $\sim 10^{-5} - 5\times10^{-4}\,M_\odot\,{\rm yr}^{-1}$ inside cores of initial masses $M_c \sim 10 - 500\,M_\odot$ embedded in clumps with mass surface densities $\Sigma_{\rm cl} \sim 0.1 - 3\,{\rm g\,cm}^{-2}$ (the full range of M_c and $\Sigma_{\rm cl}$ covered by the model grid). The disk accretion rates are close to the SiO outflow mass loss rates. The isotropic bolometric luminosity $L_{\rm bol,iso}$ of C9, the most luminous source, is no larger than $10^4\,L_\odot$. For the other sources $L_{\rm bol,iso} \sim 10^2 - 10^3\,L_\odot$. The half opening angle returned by the best ten models is comparable to the measured half opening angle of the SiO outflow from the ALMA observations for B1. For the other sources generally the half opening angles returned by the models are smaller than what may be inferred from SiO morphologies, if these are to be explained with a single protostellar source.

Table 3.4. Parameters of the Ten Best Fitted Models for Strong SiO Sources

Source	χ^2/N	$M_{\rm c}$ ($M_\odot$)	$\Sigma_{\rm cl}$ (g cm^{-2})	R_{core} (pc) ($''$)	m_* ($M_\odot$)	$\theta_{\rm view}$ (deg)	A_V (mag)	$M_{\rm env}$ ($M_\odot$)	$\theta_{w,\rm esc}$ (deg)	$\dot{M}_{\rm disk}$ ($M_\odot$/yr)	$L_{\rm bol,iso}$ ($L_\odot$)	$L_{\rm bol}$ ($L_\odot$)
B1	2.23	20	0.1	0.10 (9)	0.5	89	100.0	19	13	9.6e-06	7.0e+01	9.0e+01
d = 2.4 kpc	2.36	30	0.1	0.13 (11)	0.5	89	100.0	29	10	1.1e-05	7.6e+01	9.0e+01
R_{ap} = 11 $''$	2.65	40	0.1	0.15 (13)	0.5	89	100.0	39	8	1.1e-05	7.8e+01	8.8e+01
= 0.13 pc	2.89	20	0.1	0.10 (9)	2.0	89	100.0	15	30	1.7e-05	8.7e+01	1.9e+02
	2.94	50	0.1	0.16 (14)	0.5	89	100.0	49	7	1.2e-05	7.9e+01	8.7e+01
	3.04	20	0.1	0.10 (9)	1.0	89	100.0	17	20	1.3e-05	9.4e+01	1.5e+02
	3.28	60	0.1	0.18 (15)	0.5	89	100.0	59	6	1.3e-05	8.0e+01	8.7e+01
	3.49	10	0.3	0.04 (4)	2.0	65	100.0	5	43	3.0e-05	6.4e+01	2.8e+02
	3.96	10	0.3	0.04 (4)	1.0	86	100.0	8	28	2.5e-05	1.1e+02	2.6e+02
	4.45	80	0.1	0.21 (18)	0.5	89	100.0	79	5	1.4e-05	8.6e+01	9.2e+01
B2	6.80	320	0.1	0.42 (36)	1.0	13	80.8	315	3	2.8e-05	2.5e+02	2.0e+02
d = 2.4 kpc	6.87	240	0.1	0.36 (31)	1.0	13	100.0	240	4	2.6e-05	3.2e+02	2.4e+02
R_{ap} = 15 $''$	7.99	200	0.1	0.33 (28)	1.0	13	100.0	197	4	2.5e-05	2.7e+02	1.8e+02
= 0.17 pc	8.22	200	0.1	0.33 (28)	2.0	89	100.0	194	7	3.5e-05	3.2e+02	3.5e+02
	8.26	160	0.1	0.29 (25)	1.0	13	100.0	156	5	2.3e-05	3.3e+02	2.0e+02
	8.71	120	0.1	0.25 (22)	1.0	22	100.0	120	6	2.2e-05	2.2e+02	2.2e+02
	8.91	60	0.3	0.10 (9)	0.5	13	62.6	60	5	3.0e-05	3.0e+02	1.8e+02
	9.09	100	0.3	0.13 (11)	0.5	13	33.3	99	4	3.5e-05	3.1e+02	2.4e+02
	9.31	80	0.3	0.12 (10)	0.5	13	63.6	79	5	3.3e-05	3.7e+02	2.6e+02
	9.75	100	0.1	0.23 (20)	2.0	89	100.0	97	11	2.9e-05	3.2e+02	3.8e+02
C2	6.52	480	0.1	0.51 (21)	4.0	80	100.0	474	6	6.1e-05	9.3e+02	1.0e+03
d = 5.0 kpc	7.18	400	0.1	0.47 (19)	4.0	86	100.0	390	7	5.8e-05	9.4e+02	1.0e+03
R_{ap} = 16 $''$	8.58	480	0.1	0.51 (21)	2.0	29	100.0	477	4	4.3e-05	5.8e+02	5.7e+02
= 0.39 pc	9.47	320	0.3	0.23 (10)	2.0	13	100.0	314	4	9.2e-05	1.4e+03	1.1e+03
	9.54	400	0.3	0.26 (11)	2.0	13	100.0	401	4	9.8e-05	1.3e+03	1.1e+03
	10.05	400	0.1	0.47 (19)	2.0	22	100.0	391	4	4.1e-05	5.6e+02	5.5e+02
	10.33	240	0.1	0.36 (15)	4.0	71	100.0	229	9	5.1e-05	9.1e+02	1.0e+03
	10.77	160	0.3	0.17 (7)	2.0	22	100.0	157	7	7.7e-05	9.7e+02	1.0e+03
	10.84	160	0.3	0.17 (7)	4.0	39	100.0	153	11	1.1e-04	1.1e+03	1.2e+03
	10.99	240	0.3	0.20 (8)	2.0	22	100.0	235	5	8.6e-05	1.2e+03	1.2e+03
C6	2.57	320	0.1	0.42 (17)	2.0	68	100.0	315	5	3.9e-05	3.6e+02	3.8e+02
d = 5.0 kpc	2.80	320	0.1	0.42 (17)	4.0	89	100.0	308	7	5.5e-05	4.9e+02	5.4e+02
R_{ap} = 15 $''$	3.16	240	0.1	0.36 (15)	2.0	83	100.0	233	6	3.6e-05	4.8e+02	5.2e+02
= 0.36 pc	3.21	400	0.1	0.47 (19)	2.0	89	100.0	391	4	4.1e-05	5.3e+02	5.5e+02
	3.48	480	0.1	0.51 (21)	2.0	89	100.0	477	4	4.3e-05	5.5e+02	5.7e+02
	3.57	200	0.1	0.33 (14)	2.0	51	100.0	194	7	3.5e-05	3.4e+02	3.5e+02
	3.64	60	1.0	0.06 (2)	0.5	71	100.0	59	5	7.2e-05	3.9e+02	4.0e+02
	3.71	160	0.1	0.29 (12)	2.0	74	100.0	156	8	3.3e-05	3.9e+02	4.3e+02
	3.73	160	0.3	0.17 (7)	1.0	80	100.0	156	5	5.5e-05	4.5e+02	4.7e+02
	3.75	200	0.1	0.33 (14)	4.0	89	100.0	194	10	4.8e-05	5.7e+02	6.7e+02
C9	1.30	160	3.2	0.05 (2)	2.0	58	100.0	158	5	4.4e-04	5.0e+03	5.2e+03
d = 5.0 kpc	1.44	400	1.0	0.15 (6)	4.0	86	100.0	394	5	3.3e-04	4.6e+03	4.7e+03
R_{ap} = 10 $''$	1.56	480	1.0	0.16 (7)	4.0	13	100.0	478	5	3.4e-04	6.6e+03	5.0e+03
= 0.24 pc	1.59	320	1.0	0.13 (5)	4.0	58	100.0	315	6	3.1e-04	4.7e+03	4.9e+03
	2.08	240	1.0	0.11 (5)	4.0	44	100.0	235	8	2.9e-04	5.0e+03	5.3e+03
	2.18	100	3.2	0.04 (2)	2.0	48	100.0	96	8	3.9e-04	5.2e+03	5.6e+03
	2.30	400	0.3	0.26 (11)	8.0	83	100.0	383	8	1.9e-04	8.5e+03	9.2e+03
	2.38	480	0.3	0.29 (12)	8.0	86	100.0	462	8	2.0e-04	8.9e+03	9.4e+03
	2.44	100	3.2	0.04 (2)	4.0	86	100.0	92	12	5.4e-04	7.8e+03	1.0e+04
	2.60	320	0.3	0.23 (10)	8.0	39	100.0	306	10	1.8e-04	8.8e+03	9.7e+03
H6	2.16	30	0.1	0.13 (9)	0.5	86	100.0	29	10	1.1e-05	7.6e+01	9.0e+01
d = 2.9 kpc	2.28	40	0.1	0.15 (10)	0.5	89	100.0	39	8	1.1e-05	7.8e+01	8.8e+01
R_{ap} = 12 $''$	2.35	20	0.1	0.10 (7)	0.5	62	100.0	19	13	9.6e-06	7.3e+01	9.0e+01

Table 3.4—Continued

Source	χ^2/N	$M_{\rm c}$ ($M_\odot$)	$\Sigma_{\rm cl}$ (g cm^{-2})	R_{core} (pc) ($''$)	m_* ($M_\odot$)	$\theta_{\rm view}$ (deg)	A_V (mag)	$M_{\rm env}$ ($M_\odot$)	$\theta_{w,{\rm esc}}$ (deg)	$\dot{M}_{\rm disk}$ ($M_\odot$/yr)	$L_{\rm bol,iso}$ ($L_\odot$)	$L_{\rm bol}$ ($L_\odot$)
= 0.17 pc	2.45	50	0.1	0.16 (12)	0.5	89	100.0	49	7	1.2e-05	7.9e+01	8.7e+01
	2.66	20	0.1	0.10 (7)	1.0	86	100.0	17	20	1.3e-05	9.4e+01	1.5e+02
	2.69	60	0.1	0.18 (13)	0.5	89	100.0	59	6	1.3e-05	8.0e+01	8.7e+01
	2.71	20	0.1	0.10 (7)	2.0	51	100.0	15	30	1.7e-05	1.0e+02	1.9e+02
	3.61	80	0.1	0.21 (15)	0.5	89	100.0	79	5	1.4e-05	8.6e+01	9.2e+01
	4.09	100	0.1	0.23 (17)	0.5	89	100.0	99	4	1.5e-05	8.7e+01	9.1e+01
	4.14	120	0.1	0.25 (18)	0.5	89	100.0	118	4	1.5e-05	8.4e+01	8.8e+01

3.3.3 Weak SiO Sources

As shown in Figure 3.1, in A1, D9, and E2 there is a continuum source located right in the middle of two patches of SiO emission. In A1, A2 and C4 the main SiO emission is relatively elongated. In D8 and H5 the emission is more rounded. In other cases the shape of SiO is hardly resolved. We then investigate the kinematics of the SiO(5-4) emission via the channel maps of each source and try to find the driving source if the SiO emission appears to be an outflow.

For the sources that show relatively strong SiO emission (see Figure 3.2), like A1, A2, C4, D8, H5, from their channel maps the velocity range of the SiO emission above 3σ noise level exceeds 6 km s^{-1}. Duarte-Cabral et al. (2014) suggested that narrow line SiO emission ($\sigma_v < 1.5$ km s^{-1}, i.e., line width < 3.5 km s^{-1}) appears unrelated to outflows, but rather traces large scale collapse of material onto massive dense cores (see also Cossentino et al. 2018, 2020). Thus, in this context, in these five sources it is more likely that SiO traces shocks from outflows. In A1 there are two components revealed in Figure 3.1, while the northern component appears to be red-shifted and the southern component appears to be blue-shifted (see also §3.4). In A2 the large extended emission in the center of the field (see Figure 3.1) shows a hint of bipolar structure with the blue-shifted emission to the east of the field center and the red-shifted emission to the west. In C4, D8 and H5, no clear bipolar structure is seen.

In other sources the signal to noise ratio of SiO emission is low and most of the time the emission above the 3σ noise level in the channel maps appears as an unresolved peak and the velocity range does not exceed 4 km s^{-1}. In D9 the northern component appears blue-shifted and the southern component red-shifted. In E2 there is a hint that the eastern component is blue-shifted relative to the source velocity and

the western component red-shifted, though the emission is not stronger than the 2σ noise level. There is hardly any bipolar outflow structure revealed in the other sources. Thus for these sources we are not sure whether the SiO emission comes from protostellar outflows.

Overall, in A1, A2, D9, and E2 there is a hint of bipolar structures revealed in the channel maps. For A1, D9, and E2, the continuum source located in the middle of the two patches of SiO emission is likely responsible for driving the elongated SiO outflows. In sources like A2, the driving source of SiO is ambiguous. The emission of the dense gas tracers at the continuum peaks and the SiO peaks are all very weak. D8 is another example of an ambiguous SiO driving source. The velocity range of the central SiO emission is as wide as 30 km s^{-1} thus the SiO is not likely from large-scale cloud collision (Duarte-Cabral et al. 2014). The integrated intensity of the central SiO is even higher than H6. In D1, D3 and D8 the 1.3 mm continuum cores are not associated with any detectable dense gas tracers.

We show the SED fitting of these sources in Figure 3.10. The model parameters are listed in Table 3.5. Most of the SEDs are not well defined, likely because most sources are very young and even appear dark against the background at 70 μm. The stellar masses of the valid models range from 0.5 $M_{\odot}$ to 4 $M_{\odot}$. The isotropic luminosities ranges from 10^2 $L_{\odot}$ to 10^3 $L_{\odot}$.

Table 3.5. Parameters of the Ten Best Fitted Models for Weak SiO Sources

Source	χ^2/N	M_c ($M_\odot$)	Σ_{cl} (g cm^{-2})	R_{core} (pc) ($''$)	m_* ($M_\odot$)	θ_{view} (deg)	A_V (mag)	M_{env} ($M_\odot$)	$\theta_{w,esc}$ (deg)	$\dot{M}_{disk}$ ($M_\odot$/yr)	$L_{bol,iso}$ ($L_\odot$)	L_{bol} ($L_\odot$)
A1	0.28	320	0.1	0.42 (18)	4.0	39	100.0	308	7	5.5e-05	5.3e+02	5.4e+02
d = 4.8 kpc	0.29	400	0.1	0.47 (20)	2.0	83	100.0	391	4	4.1e-05	5.3e+02	5.5e+02
R_{ap} = 16 $''$	0.31	480	0.1	0.51 (22)	2.0	89	100.0	477	4	4.3e-05	5.5e+02	5.7e+02
= 0.37 pc	0.37	240	0.1	0.36 (15)	2.0	29	100.0	233	6	3.6e-05	5.2e+02	5.2e+02
	0.38	200	0.1	0.33 (14)	4.0	34	100.0	194	10	4.8e-05	6.4e+02	6.7e+02
	0.38	320	0.1	0.42 (18)	2.0	13	92.9	315	5	3.9e-05	5.9e+02	3.8e+02
	0.48	160	0.1	0.29 (13)	4.0	83	100.0	151	12	4.5e-05	7.5e+02	9.1e+02
	0.49	160	0.3	0.17 (7)	1.0	39	100.0	156	5	5.5e-05	4.6e+02	4.7e+02
	0.50	200	0.3	0.19 (8)	1.0	80	100.0	196	4	5.8e-05	5.1e+02	5.2e+02
	0.57	120	0.1	0.25 (11)	4.0	65	100.0	111	14	4.2e-05	7.7e+02	9.4e+02
A2	0.60	200	0.1	0.33 (14)	2.0	86	100.0	194	7	3.5e-05	3.2e+02	3.5e+02
d = 4.8 kpc	0.60	160	0.1	0.29 (13)	2.0	86	100.0	156	8	3.3e-05	3.9e+02	4.3e+02
R_{ap} = 16 $''$	0.60	120	0.1	0.25 (11)	2.0	22	100.0	117	9	3.0e-05	4.3e+02	4.3e+02
= 0.37 pc	0.62	240	0.1	0.36 (15)	1.0	48	100.0	240	4	2.6e-05	2.4e+02	2.4e+02
	0.64	320	0.1	0.42 (18)	1.0	44	100.0	315	3	2.8e-05	2.0e+02	2.0e+02
	0.64	100	0.1	0.23 (10)	4.0	83	100.0	91	15	4.0e-05	6.6e+02	8.8e+02
	0.65	80	0.1	0.21 (9)	4.0	22	100.0	71	18	3.7e-05	9.0e+02	8.5e+02
	0.66	100	0.3	0.13 (6)	0.5	44	100.0	99	4	3.5e-05	2.4e+02	2.4e+02
	0.66	80	0.3	0.12 (5)	1.0	34	100.0	79	7	4.6e-05	3.3e+02	3.5e+02
	0.69	100	0.1	0.23 (10)	2.0	13	88.9	97	11	2.9e-05	1.2e+03	3.8e+02
A3	1.58	320	0.1	0.42 (18)	2.0	89	100.0	315	5	3.9e-05	3.6e+02	3.8e+02
d = 4.8 kpc	1.82	200	0.1	0.33 (14)	2.0	34	100.0	194	7	3.5e-05	3.5e+02	3.5e+02
R_{ap} = 16 $''$	2.02	160	0.1	0.29 (13)	2.0	34	100.0	156	8	3.3e-05	4.2e+02	4.3e+02
= 0.37 pc	2.12	240	0.1	0.36 (15)	2.0	89	100.0	233	6	3.6e-05	4.8e+02	5.2e+02
	2.16	240	0.1	0.36 (15)	1.0	13	51.5	240	4	2.6e-05	3.2e+02	2.4e+02
	2.18	320	0.1	0.42 (18)	1.0	13	0.0	315	3	2.8e-05	2.5e+02	2.0e+02
	2.22	320	0.1	0.42 (18)	4.0	89	100.0	308	7	5.5e-05	4.9e+02	5.4e+02
	2.40	200	0.1	0.33 (14)	4.0	89	100.0	194	10	4.8e-05	5.7e+02	6.7e+02
	2.40	120	0.1	0.25 (11)	2.0	22	100.0	117	9	3.0e-05	4.3e+02	4.3e+02
	2.79	100	0.1	0.23 (10)	4.0	48	100.0	91	15	4.0e-05	7.3e+02	8.8e+02
C4	1.36	200	0.1	0.33 (14)	1.0	83	100.0	197	4	2.5e-05	1.7e+02	1.8e+02
d = 5.0 kpc	1.39	320	0.1	0.42 (17)	1.0	89	100.0	315	3	2.8e-05	1.9e+02	2.0e+02
R_{ap} = 13 $''$	1.44	160	0.1	0.29 (12)	1.0	65	100.0	156	5	2.3e-05	1.9e+02	2.0e+02
= 0.32 pc	1.54	120	0.1	0.25 (11)	1.0	51	100.0	120	6	2.2e-05	2.1e+02	2.2e+02
	1.54	240	0.1	0.36 (15)	1.0	89	100.0	240	4	2.6e-05	2.3e+02	2.4e+02
	1.57	200	0.1	0.33 (14)	0.5	13	100.0	200	3	1.7e-05	1.5e+02	1.3e+02
	1.64	100	0.1	0.23 (10)	1.0	22	100.0	98	7	2.0e-05	2.0e+02	2.0e+02
	1.81	80	0.1	0.21 (9)	2.0	68	100.0	75	12	2.7e-05	2.9e+02	3.5e+02
	1.86	80	0.1	0.21 (9)	1.0	34	100.0	77	8	1.9e-05	1.8e+02	1.9e+02
	1.89	100	0.1	0.23 (10)	2.0	89	100.0	97	11	2.9e-05	3.2e+02	3.8e+02
C5	0.02	240	0.1	0.36 (15)	1.0	83	100.0	240	4	2.6e-05	2.3e+02	2.4e+02
d = 5.0 kpc	0.02	320	0.1	0.42 (17)	1.0	89	100.0	315	3	2.8e-05	1.9e+02	2.0e+02
R_{ap} = 15 $''$	0.03	120	0.1	0.25 (11)	2.0	83	100.0	117	9	3.0e-05	3.7e+02	4.3e+02
= 0.36 pc	0.03	100	0.1	0.23 (10)	2.0	22	61.6	97	11	2.9e-05	3.8e+02	3.8e+02
	0.03	100	0.3	0.13 (5)	0.5	44	100.0	99	4	3.5e-05	2.4e+02	2.4e+02
	0.03	200	0.1	0.33 (14)	1.0	22	0.0	197	4	2.5e-05	1.9e+02	1.8e+02
	0.04	80	0.3	0.12 (5)	0.5	29	100.0	79	5	3.3e-05	2.5e+02	2.6e+02
	0.04	160	0.1	0.29 (12)	1.0	22	0.0	156	5	2.3e-05	2.1e+02	2.0e+02
	0.04	200	0.1	0.33 (14)	2.0	89	100.0	194	7	3.5e-05	3.2e+02	3.5e+02
	0.04	80	0.3	0.12 (5)	1.0	89	100.0	79	7	4.6e-05	3.2e+02	3.5e+02
C7	0.11	200	0.1	0.33 (14)	0.5	86	100.0	200	3	1.7e-05	1.3e+02	1.3e+02
d = 5.0 kpc	0.15	100	0.1	0.23 (10)	1.0	39	100.0	98	7	2.0e-05	2.0e+02	2.0e+02
R_{ap} = 15 $''$	0.16	120	0.1	0.25 (11)	1.0	86	100.0	120	6	2.2e-05	2.0e+02	2.2e+02

Table 3.5—Continued

Source	χ^2/N	M_c ($M_\odot$)	Σ_{cl} (g cm^{-2})	R_{core} (pc) ($''$)	m_* ($M_\odot$)	θ_{view} (deg)	A_V (mag)	M_{env} ($M_\odot$)	$\theta_{w,esc}$ (deg)	$\dot{M}_{disk}$ ($M_\odot$/yr)	$L_{bol,iso}$ ($L_\odot$)	L_{bol} ($L_\odot$)
= 0.36 pc	0.17	160	0.1	0.29 (12)	0.5	13	0.0	158	3	1.6e-05	1.2e+02	9.8e+01
	0.18	160	0.1	0.29 (12)	1.0	89	100.0	156	5	2.3e-05	1.9e+02	2.0e+02
	0.19	80	0.1	0.21 (9)	1.0	34	100.0	77	8	1.9e-05	1.8e+02	1.9e+02
	0.19	200	0.1	0.33 (14)	1.0	86	100.0	197	4	2.5e-05	1.7e+02	1.8e+02
	0.20	80	0.1	0.21 (9)	2.0	89	100.0	75	12	2.7e-05	2.8e+02	3.5e+02
	0.21	60	0.1	0.18 (7)	2.0	22	100.0	55	15	2.5e-05	3.5e+02	3.5e+02
	0.23	60	0.3	0.10 (4)	0.5	22	100.0	60	5	3.0e-05	1.8e+02	1.8e+02
C8	0.18	80	0.1	0.21 (9)	1.0	83	0.0	77	8	1.9e-05	1.7e+02	1.9e+02
d = 5.0 kpc	0.18	60	0.1	0.18 (7)	2.0	86	100.0	55	15	2.5e-05	2.6e+02	3.5e+02
R_{ap} = 15 $''$	0.18	50	0.3	0.09 (4)	0.5	80	100.0	48	6	2.9e-05	1.8e+02	1.9e+02
= 0.36 pc	0.19	40	0.1	0.15 (6)	4.0	44	100.0	30	27	3.0e-05	5.1e+02	7.5e+02
	0.19	50	0.1	0.16 (7)	2.0	22	26.3	46	16	2.4e-05	3.1e+02	3.1e+02
	0.19	30	0.3	0.07 (3)	1.0	86	100.0	28	13	3.5e-05	3.3e+02	4.3e+02
	0.19	30	0.3	0.07 (3)	2.0	86	100.0	26	21	4.8e-05	3.7e+02	6.2e+02
	0.19	40	0.3	0.08 (3)	0.5	51	0.0	39	7	2.7e-05	1.8e+02	1.9e+02
	0.20	60	0.1	0.18 (7)	1.0	39	0.0	57	10	1.8e-05	1.9e+02	2.0e+02
	0.20	30	0.3	0.07 (3)	4.0	58	100.0	21	29	6.4e-05	5.7e+02	1.2e+03
D1	0.34	320	0.1	0.42 (15)	1.0	44	100.0	315	3	2.8e-05	2.0e+02	2.0e+02
d = 5.7 kpc	0.36	240	0.1	0.36 (13)	1.0	48	100.0	240	4	2.6e-05	2.4e+02	2.4e+02
R_{ap} = 15 $''$	0.38	200	0.1	0.33 (12)	2.0	74	100.0	194	7	3.5e-05	3.2e+02	3.5e+02
= 0.41 pc	0.41	160	0.1	0.29 (11)	2.0	80	100.0	156	8	3.3e-05	3.9e+02	4.3e+02
	0.41	200	0.1	0.33 (12)	1.0	22	100.0	197	4	2.5e-05	1.9e+02	1.8e+02
	0.43	120	0.1	0.25 (9)	2.0	22	100.0	117	9	3.0e-05	4.3e+02	4.3e+02
	0.44	160	0.1	0.29 (11)	1.0	13	100.0	156	5	2.3e-05	3.3e+02	2.0e+02
	0.45	320	0.1	0.42 (15)	2.0	89	100.0	315	5	3.9e-05	3.6e+02	3.8e+02
	0.46	100	0.1	0.23 (8)	2.0	22	100.0	97	11	2.9e-05	3.8e+02	3.8e+02
	0.47	100	0.3	0.13 (5)	0.5	44	100.0	99	4	3.5e-05	2.4e+02	2.4e+02
D3	0.92	320	0.1	0.42 (15)	2.0	39	100.0	315	5	3.9e-05	3.8e+02	3.8e+02
d = 5.7 kpc	0.98	320	0.1	0.42 (15)	4.0	86	100.0	308	7	5.5e-05	4.9e+02	5.4e+02
R_{ap} = 15 $''$	1.07	240	0.1	0.36 (13)	2.0	77	100.0	233	6	3.6e-05	4.8e+02	5.2e+02
= 0.41 pc	1.08	400	0.1	0.47 (17)	2.0	86	100.0	391	4	4.1e-05	5.3e+02	5.5e+02
	1.16	480	0.1	0.51 (18)	2.0	89	100.0	477	4	4.3e-05	5.5e+02	5.7e+02
	1.16	200	0.1	0.33 (12)	4.0	74	100.0	194	10	4.8e-05	5.8e+02	6.7e+02
	1.17	200	0.1	0.33 (12)	2.0	13	100.0	194	7	3.5e-05	7.3e+02	3.5e+02
	1.23	160	0.1	0.29 (11)	2.0	22	100.0	156	8	3.3e-05	4.3e+02	4.3e+02
	1.37	240	0.1	0.36 (13)	1.0	13	26.3	240	4	2.6e-05	3.2e+02	2.4e+02
	1.38	320	0.1	0.42 (15)	1.0	13	0.0	315	3	2.8e-05	2.5e+02	2.0e+02
D5	0.51	320	0.1	0.42 (15)	2.0	29	100.0	315	5	3.9e-05	3.9e+02	3.8e+02
d = 5.7 kpc	0.89	200	0.1	0.33 (12)	2.0	22	46.5	194	7	3.5e-05	3.6e+02	3.5e+02
R_{ap} = 11 $''$	0.92	320	0.1	0.42 (15)	4.0	89	100.0	308	7	5.5e-05	4.9e+02	5.4e+02
= 0.30 pc	0.94	160	0.1	0.29 (11)	2.0	34	100.0	156	8	3.3e-05	4.2e+02	4.3e+02
	1.06	240	0.1	0.36 (13)	2.0	89	100.0	233	6	3.6e-05	4.8e+02	5.2e+02
	1.18	60	1.0	0.06 (2)	0.5	29	100.0	59	5	7.2e-05	3.9e+02	4.0e+02
	1.23	320	0.1	0.42 (15)	1.0	22	0.0	315	3	2.8e-05	2.1e+02	2.0e+02
	1.24	240	0.1	0.36 (13)	1.0	22	0.0	240	4	2.6e-05	2.4e+02	2.4e+02
	1.27	160	0.3	0.17 (6)	1.0	83	100.0	156	5	5.5e-05	4.5e+02	4.7e+02
	1.29	120	0.1	0.25 (9)	2.0	22	100.0	117	9	3.0e-05	4.3e+02	4.3e+02
D6	0.04	240	0.1	0.36 (13)	1.0	80	100.0	240	4	2.6e-05	2.3e+02	2.4e+02
d = 5.7 kpc	0.04	100	0.3	0.13 (5)	0.5	13	42.4	99	4	3.5e-05	3.1e+02	2.4e+02
R_{ap} = 15 $''$	0.04	320	0.1	0.42 (15)	1.0	22	94.9	315	3	2.8e-05	2.1e+02	2.0e+02
= 0.41 pc	0.04	80	0.3	0.12 (4)	0.5	13	78.8	79	5	3.3e-05	3.7e+02	2.6e+02
	0.06	80	0.3	0.12 (4)	1.0	29	51.5	79	7	4.6e-05	3.3e+02	3.5e+02
	0.06	200	0.1	0.33 (12)	1.0	51	100.0	197	4	2.5e-05	1.8e+02	1.8e+02

Table 3.5—Continued

Source	χ^2/N	M_c ($M_\odot$)	Σ_{cl} (g cm^{-2})	R_{core} (pc) ($''$)	m_* ($M_\odot$)	θ_{view} (deg)	A_V (mag)	M_{env} ($M_\odot$)	$\theta_{w,esc}$ (deg)	$\dot{M}_{disk}$ ($M_\odot$/yr)	$L_{bol,iso}$ ($L_\odot$)	L_{bol} ($L_\odot$)
	0.06	40	0.3	0.08 (3)	1.0	48	100.0	38	11	3.8e-05	3.8e+02	4.5e+02
	0.06	160	0.1	0.29 (11)	1.0	86	100.0	156	5	2.3e-05	1.9e+02	2.0e+02
	0.06	320	0.1	0.42 (15)	2.0	89	100.0	315	5	3.9e-05	3.6e+02	3.8e+02
	0.07	60	0.3	0.10 (4)	0.5	13	86.9	60	5	3.0e-05	3.0e+02	1.8e+02
D8	0.62	100	0.3	0.13 (5)	0.5	77	100.0	99	4	3.5e-05	2.4e+02	2.4e+02
$d = 5.7$ kpc	0.66	60	0.3	0.10 (4)	0.5	62	100.0	60	5	3.0e-05	1.8e+02	1.8e+02
$R_{ap} = 11\ ''$	0.68	80	0.3	0.12 (4)	0.5	86	100.0	79	5	3.3e-05	2.5e+02	2.6e+02
$= 0.30$ pc	0.69	240	0.1	0.36 (13)	1.0	74	100.0	240	4	2.6e-05	2.3e+02	2.4e+02
	0.70	320	0.1	0.42 (15)	1.0	48	100.0	315	3	2.8e-05	2.0e+02	2.0e+02
	0.73	50	0.3	0.09 (3)	0.5	58	100.0	48	6	2.9e-05	1.8e+02	1.9e+02
	0.76	200	0.1	0.33 (12)	2.0	89	100.0	194	7	3.5e-05	3.2e+02	3.5e+02
	0.80	100	0.1	0.23 (8)	2.0	80	100.0	97	11	2.9e-05	3.2e+02	3.8e+02
	0.82	40	0.3	0.08 (3)	0.5	48	100.0	39	7	2.7e-05	1.8e+02	1.9e+02
	0.84	80	0.1	0.21 (8)	2.0	58	100.0	75	12	2.7e-05	3.0e+02	3.5e+02
D9	0.25	200	0.1	0.33 (12)	0.5	86	100.0	200	3	1.7e-05	1.3e+02	1.3e+02
$d = 5.7$ kpc	0.44	80	0.1	0.21 (8)	1.0	89	100.0	77	8	1.9e-05	1.7e+02	1.9e+02
$R_{ap} = 12\ ''$	0.49	100	0.1	0.23 (8)	1.0	89	100.0	98	7	2.0e-05	1.8e+02	2.0e+02
$= 0.33$ pc	0.52	200	0.1	0.33 (12)	1.0	89	100.0	197	4	2.5e-05	1.7e+02	1.8e+02
	0.53	160	0.1	0.29 (11)	0.5	22	75.8	158	3	1.6e-05	1.0e+02	9.8e+01
	0.55	60	0.1	0.18 (7)	1.0	83	100.0	57	10	1.8e-05	1.8e+02	2.0e+02
	0.63	160	0.1	0.29 (11)	1.0	89	100.0	156	5	2.3e-05	1.9e+02	2.0e+02
	0.70	120	0.1	0.25 (9)	1.0	89	100.0	120	6	2.2e-05	2.0e+02	2.2e+02
	0.71	50	0.1	0.16 (6)	1.0	65	100.0	48	11	1.7e-05	1.5e+02	1.7e+02
	0.76	50	0.1	0.16 (6)	2.0	89	100.0	46	16	2.4e-05	2.2e+02	3.1e+02
E1	0.22	30	0.1	0.13 (5)	2.0	86	100.0	25	23	2.0e-05	1.4e+02	2.4e+02
$d = 5.1$ kpc	0.22	30	0.1	0.13 (5)	1.0	86	100.0	27	15	1.5e-05	1.3e+02	1.7e+02
$R_{ap} = 15\ ''$	0.23	40	0.1	0.15 (6)	0.5	58	0.0	39	8	1.1e-05	8.1e+01	8.8e+01
$= 0.37$ pc	0.23	60	0.1	0.18 (7)	16.0	83	100.0	7	76	2.0e-05	6.5e+02	2.5e+04
	0.23	50	0.1	0.16 (7)	0.5	77	100.0	49	7	1.2e-05	7.9e+01	8.7e+01
	0.24	30	0.1	0.13 (5)	0.5	22	0.0	29	10	1.1e-05	8.8e+01	9.0e+01
	0.25	60	0.1	0.18 (7)	0.5	83	100.0	59	6	1.3e-05	8.0e+01	8.7e+01
	0.26	10	1.0	0.02 (1)	2.0	39	91.9	5	39	7.5e-05	1.0e+03	7.6e+02
	0.27	10	0.3	0.04 (2)	0.5	29	0.0	9	18	1.9e-05	1.4e+02	1.9e+02
	0.27	20	0.1	0.10 (4)	4.0	48	42.4	10	43	2.1e-05	3.4e+02	6.8e+02
E2	0.16	50	0.1	0.16 (7)	2.0	77	100.0	46	16	2.4e-05	2.2e+02	3.1e+02
$d = 5.1$ kpc	0.16	40	0.3	0.08 (3)	0.5	74	100.0	39	7	2.7e-05	1.8e+02	1.9e+02
$R_{ap} = 15\ ''$	0.16	40	0.1	0.15 (6)	4.0	89	100.0	30	27	3.0e-05	4.0e+02	7.5e+02
$= 0.37$ pc	0.17	60	0.1	0.18 (7)	1.0	86	100.0	57	10	1.8e-05	1.8e+02	2.0e+02
	0.18	30	0.3	0.07 (3)	0.5	34	100.0	29	9	2.5e-05	1.8e+02	2.0e+02
	0.20	80	0.1	0.21 (8)	1.0	89	100.0	77	8	1.9e-05	1.7e+02	1.9e+02
	0.20	50	0.3	0.09 (4)	0.5	80	100.0	48	6	2.9e-05	1.8e+02	1.9e+02
	0.21	50	0.1	0.16 (7)	1.0	22	0.0	48	11	1.7e-05	1.7e+02	1.7e+02
	0.21	40	0.1	0.15 (6)	2.0	29	9.1	36	19	2.2e-05	2.3e+02	2.7e+02
	0.21	60	0.1	0.18 (7)	2.0	86	100.0	55	15	2.5e-05	2.6e+02	3.5e+02
F3	0.55	10	0.1	0.07 (4)	2.0	89	100.0	4	50	1.1e-05	2.0e+01	1.3e+02
$d = 3.7$ kpc	1.84	10	0.3	0.04 (2)	4.0	89	100.0	1	68	2.4e-05	2.9e+01	6.7e+02
$R_{ap} = 6\ ''$	2.93	10	0.1	0.07 (4)	1.0	89	100.0	7	31	1.0e-05	4.4e+01	1.1e+02
$= 0.11$ pc	3.40	40	0.1	0.15 (8)	12.0	89	100.0	2	82	9.5e-06	5.7e+01	1.1e+04
	3.48	10	0.1	0.07 (4)	0.5	89	100.0	9	20	7.8e-06	4.6e+01	7.5e+01
	4.34	30	0.3	0.07 (4)	12.0	89	100.0	1	81	2.2e-05	7.0e+01	1.2e+04
	7.21	10	0.3	0.04 (2)	2.0	89	100.0	5	43	3.0e-05	5.8e+01	2.8e+02
	10.19	20	0.1	0.10 (6)	0.5	89	100.0	19	13	9.6e-06	7.0e+01	9.0e+01
	12.52	30	0.1	0.13 (7)	0.5	89	100.0	29	10	1.1e-05	7.6e+01	9.0e+01

Table 3.5—Continued

Source	χ^2/N	$M_{\rm c}$ ($M_\odot$)	$\Sigma_{\rm cl}$ (g cm^{-2})	R_{core} (pc) ($''$)	m_* ($M_\odot$)	$\theta_{\rm view}$ (deg)	A_V (mag)	$M_{\rm env}$ ($M_\odot$)	$\theta_{w,{\rm esc}}$ (deg)	$\dot{M}_{\rm disk}$ ($M_\odot$/yr)	$L_{\rm bol,iso}$ ($L_\odot$)	$L_{\rm bol}$ ($L_\odot$)
	13.42	40	0.1	0.15 (8)	0.5	89	100.0	39	8	1.1e-05	7.8e+01	8.8e+01
F4	0.01	40	0.1	0.15 (8)	0.5	86	100.0	39	8	1.1e-05	7.8e+01	8.8e+01
d = 3.7 kpc	0.01	50	0.1	0.16 (9)	0.5	89	100.0	49	7	1.2e-05	7.9e+01	8.7e+01
R_{ap} = 15 $''$	0.02	60	0.1	0.18 (10)	0.5	89	100.0	59	6	1.3e-05	8.0e+01	8.7e+01
= 0.27 pc	0.02	30	0.1	0.13 (7)	0.5	80	100.0	29	10	1.1e-05	7.7e+01	9.0e+01
	0.02	20	0.1	0.10 (6)	0.5	34	100.0	19	13	9.6e-06	8.0e+01	9.0e+01
	0.02	80	0.1	0.21 (12)	0.5	89	100.0	79	5	1.4e-05	8.6e+01	9.2e+01
	0.02	20	0.1	0.10 (6)	2.0	34	100.0	15	30	1.7e-05	1.4e+02	1.9e+02
	0.02	20	0.1	0.10 (6)	1.0	39	100.0	17	20	1.3e-05	1.1e+02	1.5e+02
	0.02	100	0.1	0.23 (13)	0.5	89	100.0	99	4	1.5e-05	8.7e+01	9.1e+01
	0.02	120	0.1	0.25 (14)	0.5	89	100.0	118	4	1.5e-05	8.4e+01	8.8e+01
H1	0.05	10	0.1	0.07 (5)	0.5	22	76.8	9	20	7.8e-06	1.5e+02	7.5e+01
d = 2.9 kpc	0.06	10	0.3	0.04 (3)	2.0	48	32.3	5	43	3.0e-05	9.0e+01	2.8e+02
R_{ap} = 15 $''$	0.06	20	0.1	0.10 (7)	2.0	86	100.0	15	30	1.7e-05	8.7e+01	1.9e+02
= 0.21 pc	0.07	10	0.1	0.07 (5)	1.0	34	48.5	7	31	1.0e-05	8.1e+01	1.1e+02
	0.07	20	0.1	0.10 (7)	0.5	89	100.0	19	13	9.6e-06	7.0e+01	9.0e+01
	0.10	20	0.1	0.10 (7)	1.0	89	100.0	17	20	1.3e-05	9.4e+01	1.5e+02
	0.13	30	0.1	0.13 (9)	0.5	89	100.0	29	10	1.1e-05	7.6e+01	9.0e+01
	0.15	40	0.1	0.15 (10)	12.0	86	71.7	2	82	9.5e-06	8.6e+01	1.1e+04
	0.16	10	0.1	0.07 (5)	2.0	51	82.8	4	50	1.1e-05	8.1e+01	1.3e+02
	0.18	40	0.1	0.15 (10)	0.5	89	100.0	39	8	1.1e-05	7.8e+01	8.8e+01
H2	1.71	10	0.1	0.07 (5)	2.0	71	100.0	4	50	1.1e-05	2.4e+01	1.3e+02
d = 2.9 kpc	2.49	10	0.1	0.07 (5)	1.0	89	100.0	7	31	1.0e-05	4.4e+01	1.1e+02
R_{ap} = 10 $''$	2.65	10	0.1	0.07 (5)	0.5	89	100.0	9	20	7.8e-06	4.6e+01	7.5e+01
= 0.14 pc	2.81	40	0.1	0.15 (10)	12.0	89	100.0	2	82	9.5e-06	5.7e+01	1.1e+04
	3.40	10	0.3	0.04 (3)	4.0	83	100.0	1	68	2.4e-05	3.4e+01	6.7e+02
	3.64	10	0.3	0.04 (3)	2.0	89	100.0	5	43	3.0e-05	5.8e+01	2.8e+02
	4.26	30	0.3	0.07 (5)	12.0	89	100.0	1	81	2.2e-05	7.0e+01	1.2e+04
	4.79	20	0.1	0.10 (7)	0.5	89	100.0	19	13	9.6e-06	7.0e+01	9.0e+01
	5.66	30	0.1	0.13 (9)	0.5	89	100.0	29	10	1.1e-05	7.6e+01	9.0e+01
	5.73	20	0.1	0.10 (7)	2.0	89	100.0	15	30	1.7e-05	8.7e+01	1.9e+02
H3	1.27	10	0.1	0.07 (5)	2.0	71	100.0	4	50	1.1e-05	2.4e+01	1.3e+02
d = 2.9 kpc	1.81	10	0.3	0.04 (3)	4.0	89	100.0	1	68	2.4e-05	2.9e+01	6.7e+02
R_{ap} = 11 $''$	2.45	40	0.1	0.15 (10)	12.0	89	100.0	2	82	9.5e-06	5.7e+01	1.1e+04
= 0.15 pc	3.03	10	0.1	0.07 (5)	1.0	89	100.0	7	31	1.0e-05	4.4e+01	1.1e+02
	3.34	10	0.1	0.07 (5)	0.5	89	100.0	9	20	7.8e-06	4.6e+01	7.5e+01
	3.65	30	0.3	0.07 (5)	12.0	89	100.0	1	81	2.2e-05	7.0e+01	1.2e+04
	5.03	10	0.3	0.04 (3)	2.0	89	100.0	5	43	3.0e-05	5.8e+01	2.8e+02
	5.76	20	0.1	0.10 (7)	0.5	89	100.0	19	13	9.6e-06	7.0e+01	9.0e+01
	6.50	30	0.1	0.13 (9)	0.5	89	100.0	29	10	1.1e-05	7.6e+01	9.0e+01
	6.84	40	0.1	0.15 (10)	0.5	89	100.0	39	8	1.1e-05	7.8e+01	8.8e+01
H4	0.34	10	0.1	0.07 (5)	1.0	89	100.0	7	31	1.0e-05	4.4e+01	1.1e+02
d = 2.9 kpc	0.39	40	0.1	0.15 (10)	12.0	86	96.0	2	82	9.5e-06	8.6e+01	1.1e+04
R_{ap} = 10 $''$	0.48	10	0.1	0.07 (5)	0.5	89	100.0	9	20	7.8e-06	4.6e+01	7.5e+01
= 0.14 pc	0.54	10	0.1	0.07 (5)	2.0	51	98.0	4	50	1.1e-05	8.1e+01	1.3e+02
	1.05	10	0.3	0.04 (3)	4.0	74	87.9	1	68	2.4e-05	6.8e+01	6.7e+02
	1.31	30	0.3	0.07 (5)	12.0	89	86.9	1	81	2.2e-05	7.0e+01	1.2e+04
	2.23	10	0.3	0.04 (3)	2.0	89	100.0	5	43	3.0e-05	5.8e+01	2.8e+02
	7.10	20	0.1	0.10 (7)	0.5	89	100.0	19	13	9.6e-06	7.0e+01	9.0e+01
	34.00	30	0.1	0.13 (9)	0.5	86	100.0	29	10	1.1e-05	7.6e+01	9.0e+01
	47.52	40	0.1	0.15 (10)	0.5	89	100.0	39	8	1.1e-05	7.8e+01	8.8e+01
H5	1.50	10	0.1	0.07 (5)	0.5	74	100.0	9	20	7.8e-06	4.7e+01	7.5e+01
d = 2.9 kpc	1.66	10	0.1	0.07 (5)	1.0	65	100.0	7	31	1.0e-05	4.6e+01	1.1e+02

Table 3.5—Continued

Source	χ^2/N	$M_{\rm c}$ ($M_\odot$)	$\Sigma_{\rm cl}$ (g cm^{-2})	R_{core} (pc) ($''$)	m_* ($M_\odot$)	$\theta_{\rm view}$ (deg)	A_V (mag)	$M_{\rm env}$ ($M_\odot$)	$\theta_{w,{\rm esc}}$ (deg)	$\dot{M}_{\rm disk}$ ($M_\odot$/yr)	$L_{\rm bol,iso}$ ($L_\odot$)	$L_{\rm bol}$ ($L_\odot$)
$R_{ap} = 11\ ''$	2.50	10	0.3	0.04 (3)	2.0	89	76.8	5	43	3.0e-05	5.8e+01	2.8e+02
= 0.15 pc	3.28	20	0.1	0.10 (7)	0.5	89	100.0	19	13	9.6e-06	7.0e+01	9.0e+01
	3.97	20	0.1	0.10 (7)	2.0	89	100.0	15	30	1.7e-05	8.7e+01	1.9e+02
	4.54	10	1.0	0.02 (2)	4.0	89	100.0	1	59	7.7e-05	1.1e+02	1.1e+03
	4.55	10	0.1	0.07 (5)	2.0	51	100.0	4	50	1.1e-05	8.1e+01	1.3e+02
	4.69	30	0.1	0.13 (9)	0.5	89	100.0	29	10	1.1e-05	7.6e+01	9.0e+01
	4.90	40	0.1	0.15 (10)	12.0	86	100.0	2	82	9.5e-06	8.6e+01	1.1e+04
	5.21	20	0.1	0.10 (7)	1.0	89	100.0	17	20	1.3e-05	9.4e+01	1.5e+02

3.4 6 cm Radio Emission

We searched for 6 cm radio emission in the ALMA field of view ($\sim 27''$in diameter) of each clump. Out of the 15 clumps observed with VLA, we only detected radio emission above the $3\,\sigma$ noise level in four sources A1, C2, C4, C9. The peak positions and flux measurements of the 6 cm radio continuum are reported in Table 3.6. The radio continuum emission is shown in Figure 3.11. The emission in A1, C2 and C4 is hardly resolved, while the emission in C9 is resolved into two peaks. The negative artifacts are not significant with no stronger than -2 σ level in C2 and C9 and no stronger than -3 σ level in A1 and C4. We note that the low detection rate of 6 cm radio emission may be partly due to limited sensitivities. The sensitivities of the 6 cm images vary by a factor of almost 3, and the detections in A1, C2, and C4 come from relatively more sensitive images, while in the B and D cloud, where no 6 cm emission is detected, the sensitivity is much worse.

We attempt to derive the in-band spectra index, α, of the two sources in C9, i.e., assuming $F_\nu \propto \nu^\alpha$, by dividing the continuum data into two centered at 5.03 GHz and 6.98 GHz respectively. In A1, C2 and C4 the sources detected in the combined continuum data do not have enough signal to noise for such an estimate. We derive an α of -0.52 for C9r1 and -2.36 for C9r2. However, as discussed in Rosero et al. (2016), the in-band spectral index derived from only two data points can be highly uncertain and more measurements at other wavelengths are required for confirmation of these results.

There are offsets between the radio continuum peak and the 1.3mm continuum peak in all the sources, typically about 500 mas, i.e., about 1 VLA synthesized beam width and corresponding to $\sim$ 2500 AU. Such offsets likely indicate that the radio emission comes from jet lobes and/or that the offset is due to a gradient in the optical

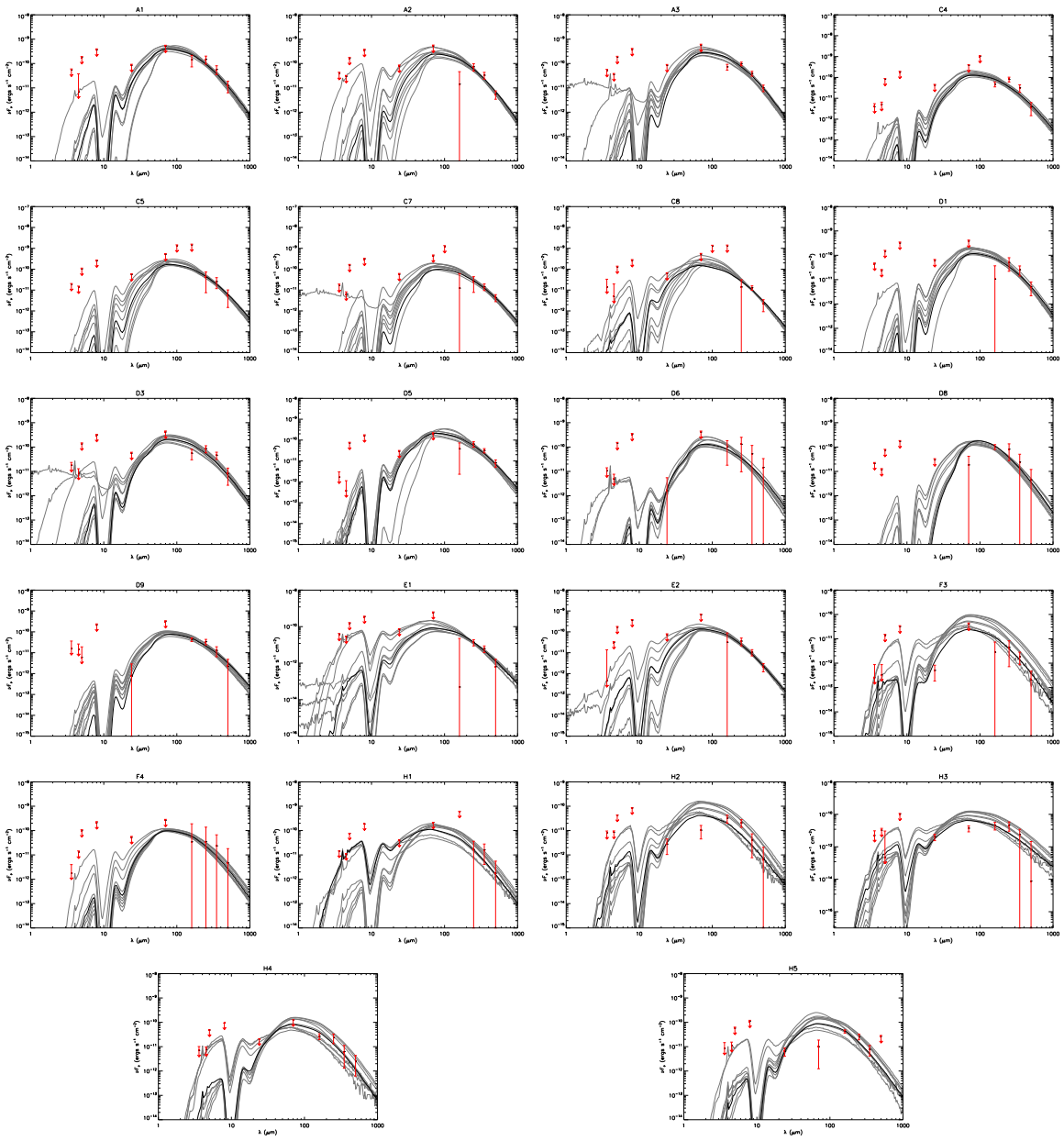

Fig. 3.10.— The same with Figure 3.9 but for weak SiO sources. The model parameter results are listed in Table 3.5.

depth. Another possibility is that the offset is due to astrometric uncertainties in the VLA data, but this would require an uncertainty several times larger than we have estimated ($\lesssim$ 170 mas). This error takes into account the accuracy of the phase calibrator and VLA antenna positions, the transfer of solutions from the phase calibrator to the target, and the statistical error in measuring the source's peak position. The unresolved emission in A1, C2 and C4 basically follows the direction and shape of the VLA beam and it is hard to compare with the direction of the outflows. The extension of the emission in C9 is not along the direction of the large scale north-south outflow. However, it could be related to the small scale outflows in the region.

3.5 Discussion

3.5.1 SiO Detection Rate

We have detected SiO(5-4) emission in 20 out of 32 IRDC clumps, a detection rate of 62%. Our sample has a distance range of 2.4-5.7 kpc. The cloud with the lowest detection rate, Cloud F, is located at a moderate distance of 3.7 kpc. The cloud with

Table 3.6. Parameters of 6 cm Radio Continuum

Source	R.A. (J2000)	Decl. (J2000)	$I_{\rm peak}$ (μJy beam^{-1})	$S_{\rm 6GHz}$ (μJy)
A1	18:26:15.442	-12:41:37.505	14.44	24.14
C2r1	18:42:50.228	-4:03:21.022	31.37	24.80
C2r2	18:42:50.762	-4:03:11.534	21.79	68.65
C4	18:42:48.724	-4:02:21.433	13.16	5.85
C9r1	18:42:51.979	-3:59:54.534	40.05	47.70
C9r2	18:42:51.979	-3:59:53.734	35.87	46.97

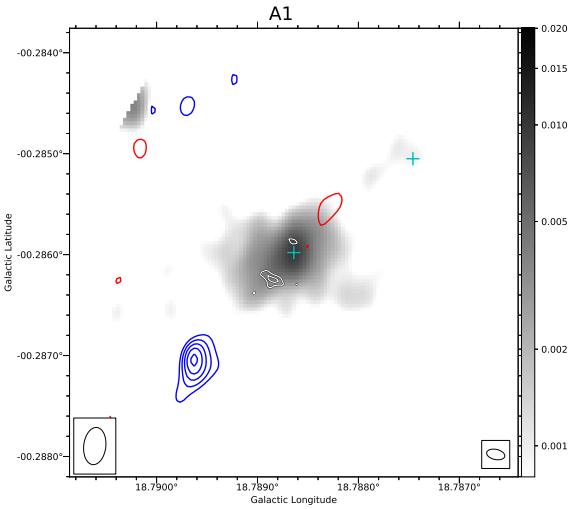

White contours: starting level: 3σ, step: 1σ, σ value: $3.3\,\mu$Jy beam^{-1}.
Blue contours: starting level: 4σ, step: 2σ, σ value: 39 mJy beam^{-1} km s^{-1}, velocity range: 45-63.5 km s^{-1}.
Red contours: starting level: 4σ, step: 2σ, σ value: 36 mJy beam^{-1} km s^{-1}, velocity range: 69.5-85 km s^{-1}.

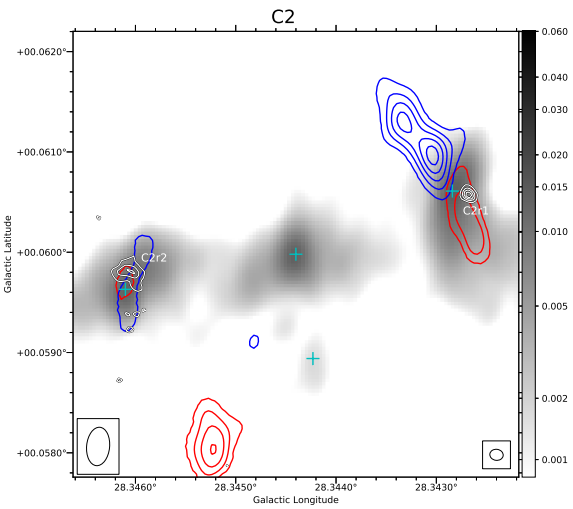

White contours: starting level: 3σ, step: 2σ, σ value: $3.0\,\mu$Jy beam^{-1}.
Blue contours: starting level: 5σ, step: 4σ, σ value: 30 mJy beam^{-1} km s^{-1}, velocity range: 65-76.2 km s^{-1}.
Red contours: starting level: 5σ, step: 4σ, σ value: 32 mJy beam^{-1} km s^{-1}, velocity range: 82.2-95 km s^{-1}.

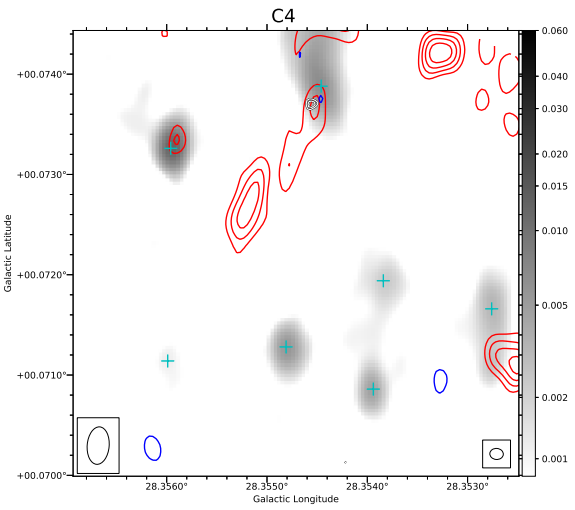

White contours: starting level: 3σ, step: 1σ, σ value: $2.7\,\mu$Jy beam^{-1}.
Blue contours: starting level: 5σ, step: 3σ, σ value: 36 mJy beam^{-1} km s^{-1}, velocity range: 60-76 km s^{-1}.
Red contours: starting level: 5σ, step: 3σ, σ value: 38 mJy beam^{-1} km s^{-1}, velocity range: 82-100 km s^{-1}.

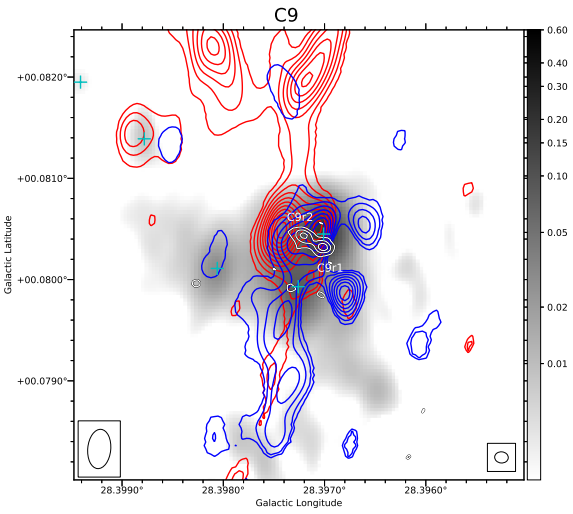

White contours: starting level: 3σ, step: 2σ, σ value: $4.6\,\mu$Jy beam^{-1}.
Blue contours: starting level: 5σ, step: 5σ, σ value: 34 mJy beam^{-1} km s^{-1}, velocity range: 60-74 km s^{-1}.
Red contours: starting level: 5σ, step: 5σ, σ value: 37 mJy beam^{-1} km s^{-1}, velocity range: 83-100 km s^{-1}.

Fig. 3.11.— 6 cm radio emission and SiO outflow emission over 1.3 mm continuum. White contours are the 6 cm radio continuum. Blue and red contours are the blue- and red-shifted SiO integrated intensity. Grayscale is the 1.3mm continuum. Plus signs denote the 1.3mm continuum peaks. The beam size of the ALMA 1.3 mm continuum observations is shown in the lower left corner. The beam size of the VLA

the highest detection rate, cloud D, happens to be located at the largest distance. Thus the detection rate does not appear to have a strong dependence on distance. López-Sepulcre et al. (2011) derived an SiO detection rate of 88% towards 20 high-mass ($M_{\rm clump} \gtrsim 100\,M_\odot$) IR-dark clumps (not detected at 8 μm with the *Midcourse Space eXperient* (MSX)) with SiO(2-1) and SiO(3-2). Csengeri et al. (2016) derived an SiO detection rate of 61% towards 217 IR-quiet clumps (a threshold of 289 Jy at 22 μm at 1 kpc) with SiO(2-1). In particular, the SiO detection rate is 94% for a subsample of clumps with $M_{\rm clump} > 650\,M_\odot$ and 1 kpc $< d <$ 7 kpc. With a more evolved sample, Harju et al. (1998) derived an SiO detection rate of 38% for protostars above $10^3\,L_\odot$ with SiO(2-1) and SiO(3-2). Gibb et al. (2007) detected SiO emission in five out of 12 (42%) massive protostars with SiO(5-4). Li et al. (2019) detected SiO(5-4) emission in 25 out of 44 IRDCs with a detection rate of 57%, and 32 out of 86 protostars in massive clumps (a subsample defined to be at the intermediate evolutionary stage between IRDCs and HII regions) with a detection rate of 37%.

Our result is similar to that of the full sample of Csengeri et al. (2016) and the IRDC sample of Li et al. (2019). The clumps in our sample are not as massive as those of López-Sepulcre et al. (2011). The non-detection of SiO tends to be in clumps with weak or non-detected 1.3 mm continuum emission ($M_{\rm core} < 5\,M_\odot$, Liu et al. 2018), and dark against background up to 100 μm (except H2). This indicates in IRDCs, representative of the earliest evolutionary phases, shocked gas is more common in the higher mass regime. The non-detections may reflect the more diffuse clumps without star formation as suggested in Csengeri et al. (2016). However, as discussed in §3.3.1, there is possible large scale SiO emission in those regions, which is resolved out with our observations. On the other hand, we do see SiO emission in clumps with only low-mass 1.3 mm cores detected and low luminosity. Overall,

compared with more evolved IR bright protostars in Harju et al. (1998) and Gibb et al. (2007), the detection rate of SiO in our sample, most of which have a luminosity $< 10^3\,L_\odot$ and still appear dark against background at 70 μm, and other early stage IR-quiet protostars (López-Sepulcre et al. 2011, Csengeri et al. 2016, Li et al. 2019), is higher.

Compared with Kong et al. (2019), who mapped CO(2-1) outflows in Cloud C and covered our C2, C4, C5 and C6 regions, we see that CO outflows are generally more common than SiO outflows. We find 2 overlapping identified continuum sources (those with $< 1''$difference in core coordinates) in C2, 4 in C4, 4 in C5 and 3 in C6 that are found to drive CO outflows as seen by Kong et al. (2019) and drive SiO outflows as seen in our work.

3.5.2 Characteristics of the Protostellar Sources

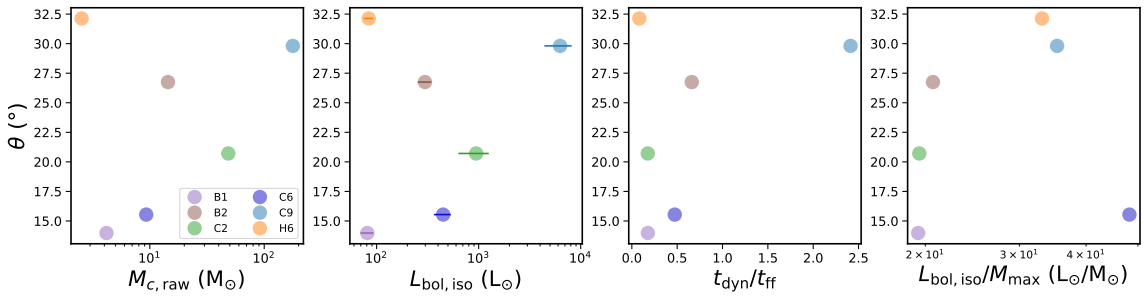

Fig. 3.12.— Outflow half opening angle θ versus the mm core mass $M_{c,\mathrm{raw}}$, isotropic bolometric luminosity $L_{\mathrm{bol,iso}}$, the ratio of outflow dynamical time scale over free-fall time scale $t_{\mathrm{dyn}}/t_{\mathrm{ff}}$, and luminosity to mass ratio $L_{\mathrm{bol,iso}}/M_{\mathrm{max}}$.

We investigate the potential correlations between outflow collimation and core mass, luminosity, time scale, luminosity-to-mass ratio, etc., as shown in Figure 3.12. Note the outflow half opening angle and the dynamical time adopt the values of the representative flow of each source, i.e., red flow for B1, B2, H6 and blue flow for

C2, C6 and C9. The free-fall time is derived from $t_{\rm ff} = \sqrt{\frac{3\pi}{32G\rho}}$. ρ is derived from the 1.3mm dust continuum core mass from Liu et al. (2018). Here for $L_{\rm bol,iso}/M_{\rm max}$ in each source, we use the mass of the one main core driving the outflows (B1c2, B2c9, C2c2, C6c1, C9c5, H6c8) from Liu et al. (2018), which happens to be the most massive core in each field, and assumes the bolometric luminosity derived from the SED fitting mainly comes from this core. The collimation of the outflow lobes that are not very extended, like H6, may be influenced if they were to be corrected for inclination. Overall, if assuming the same inclination for every source, i.e., with no relative effects of inclination, we do not see apparent correlations between outflow opening angles and other source properties. This indicates that, at least for these six protostellar sources with strong SiO emisssion, that the collimation of outflows does not depend strongly on core mass, luminosity and evolutionary stage.

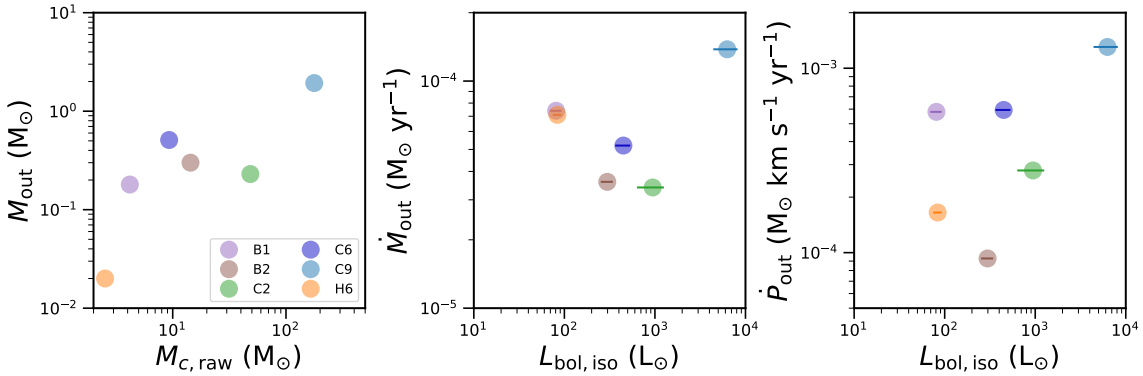

Fig. 3.13.— From left to right: outflow mass $M_{\rm out}$ versus the mm core mass $M_{c,\rm raw}$, outflow mass rate $\dot{M}_{\rm out}$ versus isotropic bolometric luminosity $L_{\rm bol,iso}$, outflow momentum rate $\dot{P}_{\rm out}$ versus isotropic bolometric luminosity $L_{\rm bol,iso}$.

We also investigate the mass entrainment of the strong SiO outflows as shown in Figure 3.13. The outflow mass seems to increase with the core mass, which is consistent with the results of Beuther et al. (2002). Previous outflow studies have also found correlation between the bolometric luminosity and the mechanical force

and momentum, which holds over six orders of magnitude of $L_{\rm bol}$ (e.g., Figure 4 in Beuther et al. 2002, Figure 7 in Maud et al. 2015), and is interpreted as evidence for a single outflow mechanism that scales with the stellar luminosity, and the outflows motion being momentum driven. From the six sources presented here, the potential correlation of the mechanical force and mass entrainment rate with luminosity has significant scatter.

Since we can only resolve the protostellar cores down to a typical scale of 5000 AU, we are unable to further distinguish the outflow launching mechanism (e.g., the X-wind model (Shu et al. 2000) and the disk-wind model (Königl & Pudritz 2000)).

H_2O maser emission traces shocked gas propagating in dense regions ($n_{H_2} > 10^6$ cm^{-3}) at velocities between 10 and 200 km s^{-1} (e.g., Hollenbach et al. 2013) and is considered to be a signpost of protostellar outflows within a few 1000 AU of the driving source. Surveys have found H_2O masers associated with young stellar objects with luminosities of 1-10^5 $L_\odot$ (Wouterloot & Walmsley 1986; Churchwell et al. 1990; Palla et al. 1993; Claussen et al. 1996). Wang et al. (2006) observed H_2O maser emission toward a sample of 140 compact, cold IRDC cores with the VLA. All the 32 regions except for C9 are covered by their observation. Only at B2c8 (0.66 $M_\odot$), C2c4 (33 $M_\odot$), C4c1 (17 $M_\odot$), D5c1 (3.6 $M_\odot$) are water masers detected with emission higher than the detection limit of 1 Jy (see Figure 3.3). Our VLA observations are sensitive to CH_3OH masers, which trace high-mass star formation. The CH_3OH maser results will be presented in a later paper (Rosero et al. in prep.). From an initial inspection, it appears that there is only detection in the B2 and C9 clump (associated with the C9r1 core).

Compared with the SED fitting results of more evolved massive YSOs (De Buizer et al. 2017; Liu et al. 2019, 2020), the accretion rates derived in our IRDC sample

are about one order of magnitude lower even for the high-/intermediate-mass sources, though the photometry scale may be smaller by a factor of 2. Further comparison of protostellar properties of the sources studied here and those of the SOMA survey sample has been presented by Liu et al. (2020).

3.5.3 Strength of SiO Emission

We measured the bolometric luminosity of the sources defined by their MIR emission (geometric mean $L_{\rm bol,iso}$ of the valid models in the ten best models of each source) and the SiO line luminosity inside the aperture to explore how SiO acts as an outflow tracer across the luminosity regime. The flux inside the contours denoting *trunk* structures in Figure 3.1 is used to calculate the SiO line luminosity. Note here we adopt a universal velocity range of $\pm 15\,{\rm km\ s^{-1}}$ relative to the systemic velocity for all the sources, given that the SNRs for more than half of the 32 sources are too low to determine a distinct velocity range. For most sources this velocity range represents the SiO emission well, though in B1 the SiO line luminosity is underestimated. We sum up flux from all the *trunks* inside the ALMA field of view for each source. Note in B2, C9 and H6 we only include part of the SiO which is inside the apertures shown in Figure 3.8. For all the other sources almost all the detected SiO emission falls inside the aperture used for photometry.

The results are shown in Figure 3.14. Where there is SiO, we can always find 1.3 mm continuum emission and some infrared emission nearby, but not vice versa. Those clumps with no detectable SiO emission are denoted with $3\,\sigma$ SiO detection thresholds in Figure 3.14. In C3 and D2 there is neither SiO or 1.3 mm continuum cores detected, so we think there are no protostars in these two clumps and do not measure the luminosities there. We also include measurement of SiO(5-4) from the

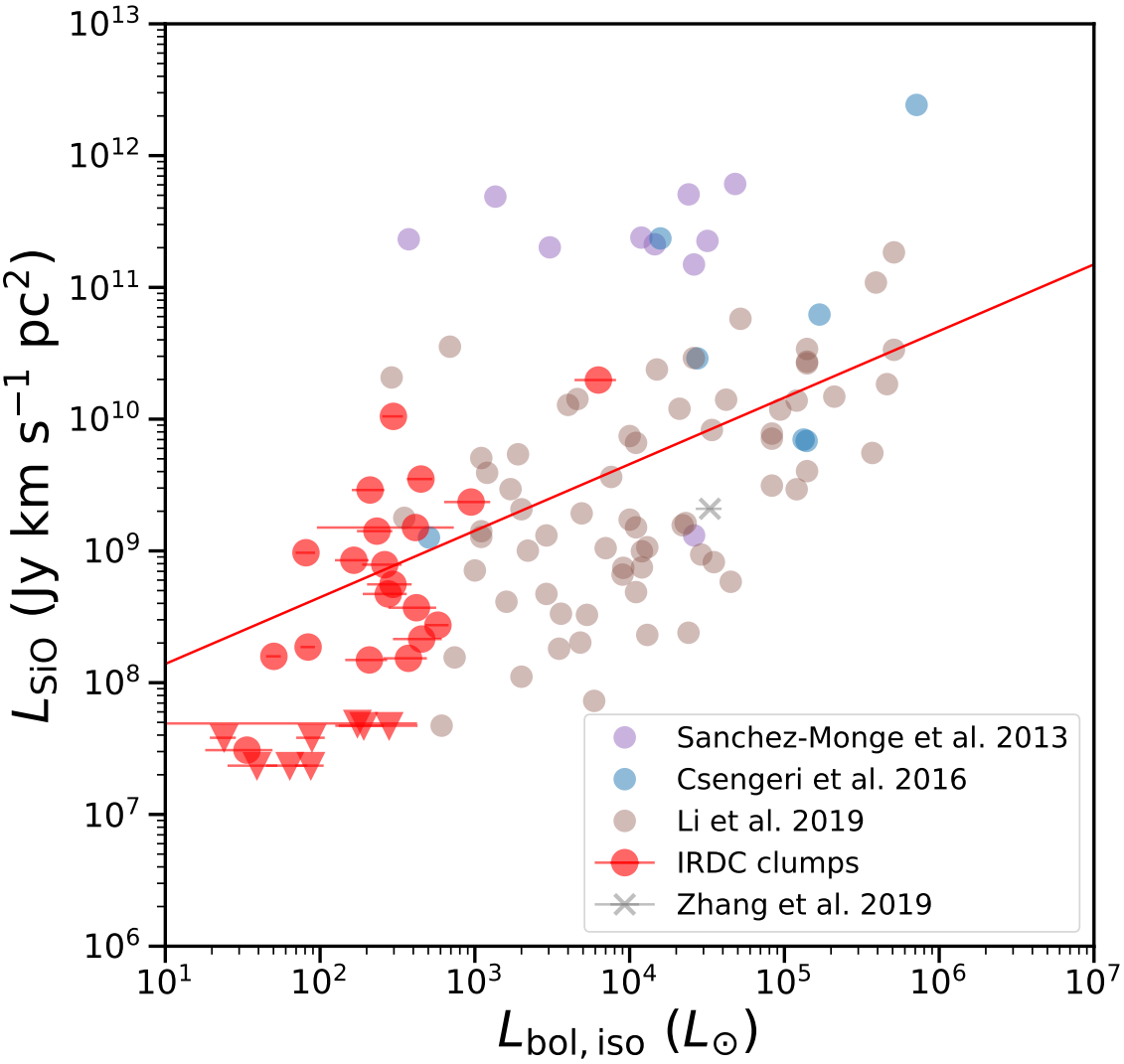

Fig. 3.14.— SiO(5-4) line luminosity $L_{\rm SiO}$ as a function of protostar bolometric luminosity $L_{\rm bol,iso}$. The red dots denote our SiO(5-4) data, while the red empty triangles indicate upper limits for SiO line luminosity. The error bar is derived from the geometric standard deviation of $L_{\rm bol,iso}$ among the valid models. The purple dots denote SiO(5-4) data from Sánchez-Monge et al. (2013b). The blue dots denote SiO(5-4) data from Csengeri et al. (2016). The brown dots denote SiO(5-4) data from Li et al. (2019). The gray cross denotes SiO(5-4) data from Zhang et al. (2019). The red line shows a linear fit $f(x) = 0.50x + 7.64$.

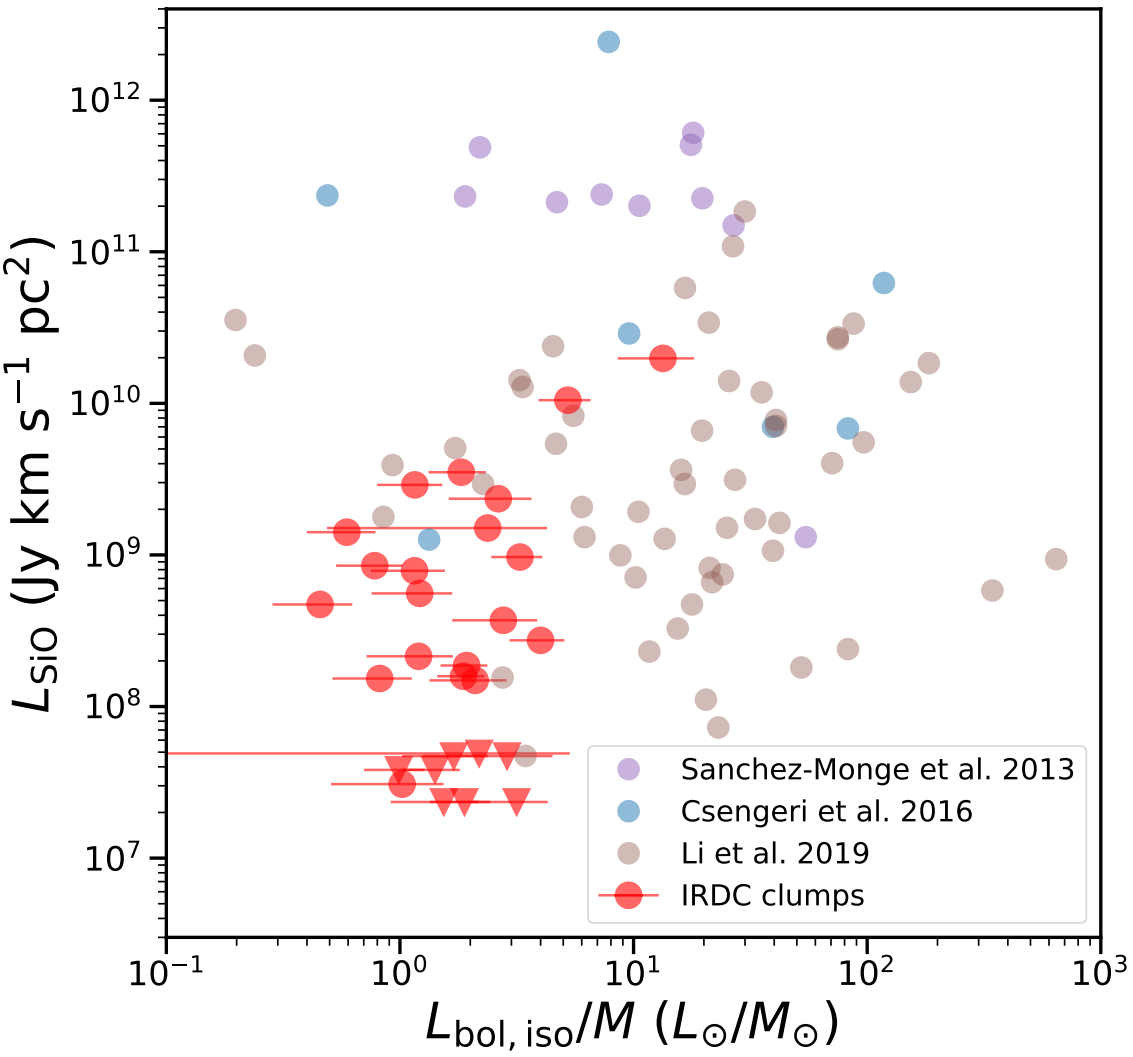

Fig. 3.15.— SiO(5-4) line luminosity $L_{\rm SiO}$ as a function of the bolometric luminosity-mass ratio $L_{\rm bol,iso}/M$. The markers are the same as in Figure 3.14. The error bar is derived from a combination of the geometric standard deviation of $L_{\rm bol,iso}$ among the valid models and 20% flux uncertainty of the BGPS data in the measurement of M.

literature. We notice there may be biases to combine the data due to differences in instrument and method. Nevertheless, we see a slight increasing trend of SiO line luminosity with the bolometric luminosity. We obtain a linear fit of $f(x) = (0.50 \pm 0.08)x + (7.64 \pm 0.33)$ and the Pearson correlation coefficient is ~ 0.51. Our result is consistent with the results of Codella et al. (1999). They studied SiO emission towards both low- and high-mass YSOs and found a trend of brighter SiO emission from higher luminosity sources, suggesting more powerful shocks in the vicinity of more massive YSOs.

On the other hand, Motte et al. (2007) found that the SiO integrated intensities of the infrared-quiet cores are higher than those of the luminous infrared sources. Sakai et al. (2010) also found the SiO integrated intensities of some MSX sources are much lower than those of the MSX dark sources. They suggested that the SiO emission from the MSX sources traces relatively older shocks, whereas it mainly traces newly-formed shocks in the MSX dark sources, which results in the observed decrease in the SiO abundance and SiO line width in the late stage MSX sources. Sánchez-Monge et al. (2013b) argued that SiO is largely enhanced in the first evolutionary stages, probably owing to strong shocks produced by the protostellar jet. They suggested that as the object evolves, the power of the jet decreases and so does the SiO abundance.

To help break the degeneracy between mass and evolution, we also plot the SiO luminosity versus $L_{\rm bol,iso}/M$, as shown in Figure 3.15, together with data from literature. The $L_{\rm bol}/M$ ratio is commonly used as a tracer of evolutionary stage (e.g., Molinari et al. 2008; Ma et al. 2013; Urquhart et al. 2014; Leurini et al. 2014; Csengeri et al. 2016) with a higher value corresponding to a later stage. Here, M is derived from the flux measurement of the archival 1.1mm BGPS data in the same

aperture used for constructing SEDs according to

$$M_{\rm dust} = \frac{F_\nu D^2}{B_\nu(T_{\rm dust})\kappa_\nu}, \tag{3.6}$$

where $M_{\rm dust}$ is the dust mass, F_ν is the continuum flux at frequency ν, D is the source distance, and $B_\nu(T_{\rm dust})$ is the Planck function at dust temperature $T_{\rm dust}$ = 20 K. A common choice of κ_ν is predicted by the moderately coagulated thin ice mantle dust model of Ossenkopf & Henning (1994), with opacity per unit dust mass of $\kappa_{1.2{\rm mm,\ d}} = 0.899$ cm^{2}g^{-1}. A gas-to-refractory-component-dust-mass ratio of 141 is estimated by Draine (2011) so $\kappa_{1.2{\rm mm}} = 6.376 \times 10^{-3}$ cm^{2}g^{-1}. Note in Sánchez-Monge et al. (2013b) and Csengeri et al. (2016), M also represent the same scale with their $L_{\rm bol}$. Overall, we do not see clear relation between the SiO luminosity and the evolutionary stage.

A number of studies have found a decrease in SiO abundance with increasing L/M in massive star-forming regions (e.g., Sánchez-Monge et al. 2013b; Leurini et al. 2014; Csengeri et al. 2016). However, in Sánchez-Monge et al. (2013b), SiO(2-1) and SiO(5-4) outflow energetics seem to remain constant with time (i.e., an increasing L/M). In Csengeri et al. (2016), SiO column density estimated from the LTE assumption and the (2-1) transition also seems to remain constant with time. In López-Sepulcre et al. (2011) there seems to be no apparent correlation between the SiO(2-1) line luminosity and L/M, though they claimed a dearth of points at low L/M and low SiO luminosity. Li et al. (2019) also find the SiO luminosities and the SiO abundance do not show apparent differences among various evolutionary stages in their sample from IRDCs to young H II regions.

The protostars in our sample mostly occupy a luminosity range of $10^2 - 10^3$ $L_{\rm bol}$. Given the fact that most of them have SiO detection, it seems that as long as a

protostar approaches a luminosity of $\sim 10^2\ L_{\rm bol}$, the shocks in the outflow are strong enough to form SiO emission.

3.5.4 Nature of the Radio Sources

In Sanna et al. (2018), the detection rate of 22 GHz continuum emission towards 25 H_2O maser sites is 100% and they suggested H_2O masers are preferred signposts of bright radio thermal jets ($\gg$ 1mJy). Here we see coincidence of 6 GHz radio continuum emission and H_2O masers at C2c4 and C4c1.

We have a radio detection rate of $\sim$ 27% out of the 15 IRDC clumps with both SiO outflows and 1.3 mm continuum emission. In Rosero et al. (2016) detection rates of radio sources associated with the millimeter dust clumps within IRDCs with and without IR sources (CMC–IRs and CMCs, respectively), and hot molecular cores (HMCs) are 53%, 6%, and 100%, respectively. The majority of our 15 sources should belong to their CMC category. The low detection rate in our sample is consistent with increasing high-mass star formation activity from CMCs to HMCs. The offsets between the 1.3 mm continuum peak and the 6 cm continuum peak are typically $\sim$ 2500 AU, smaller than that of 4000 au and 10000 au for CMC–IRs and HMCs, respectively, in Rosero et al. (2016).

The mm cores associated with detected radio emission are not always the cores that drive the strongest SiO outflows or that have the highest bolometric luminosity as implied in Anglada et al. (2018). However, they are among the most massive ones in all the 32 clumps in our ALMA survey. Furthermore, although the emission is hardly resolved, we still see a hint that the structures are not simply bipolar and the extension is not always aligned with the SiO outflows.

As photoionization cannot account for the observed radio continuum emission of

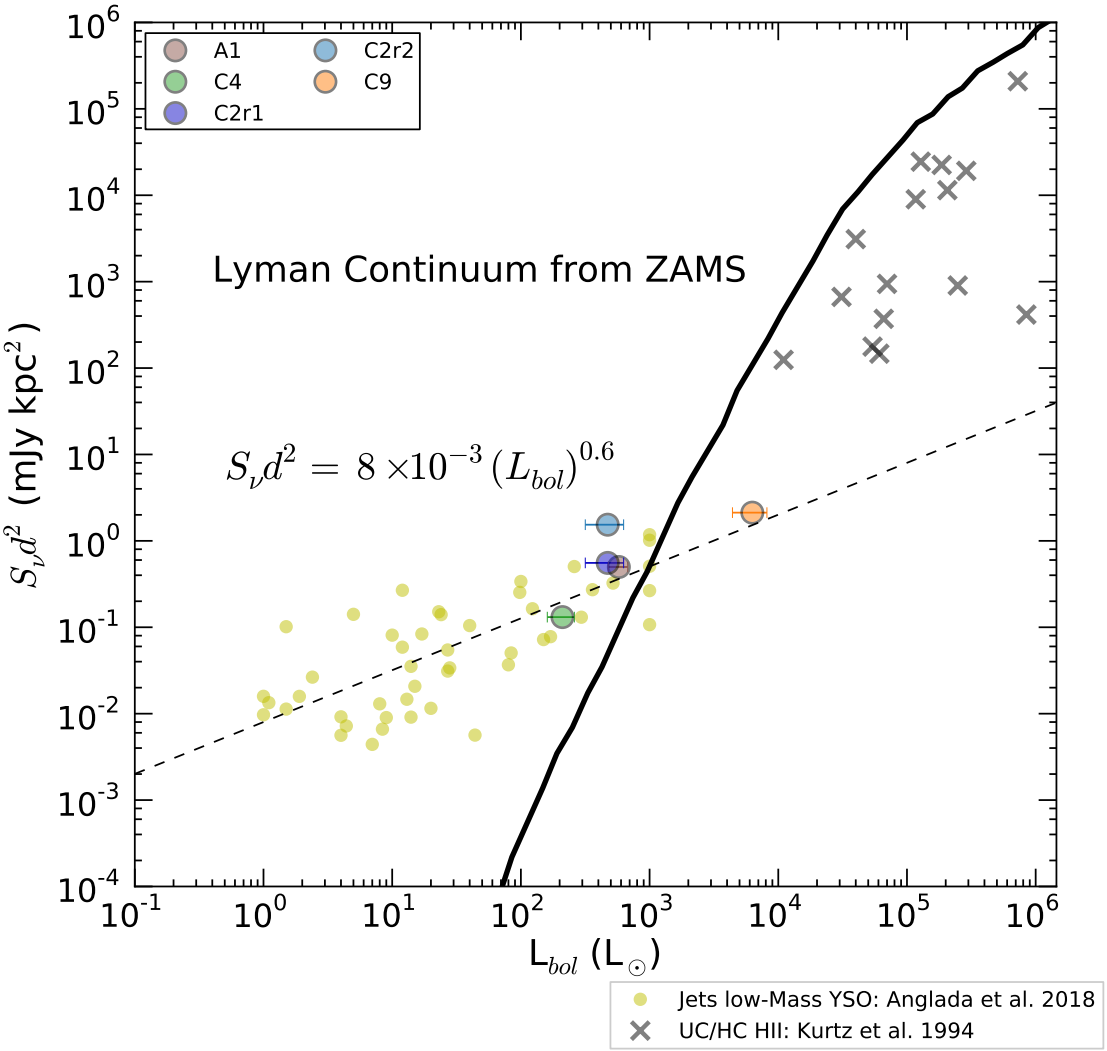

Fig. 3.16.— Radio luminosity scaled to 5 GHz (assuming a spectral index $\alpha = 0.6$) versus the bolometric luminosity. Note for the two radio sources in C2 we adopt a luminosity value of $L_{\rm bol}$ of C2 divided by 2. The bolometric luminosity is given by the geometric mean value of the isotropic luminosity returned by the valid models for each source. The yellow circles represent ionized jets toward low-mass stars from Anglada (2018). The dashed line shows a power law relation for these sources, given by Anglada et al. (2015): $\left(\frac{S_\nu d^2}{\rm mJy\ kpc^2}\right) = 8 \times 10^{-3} \left(\frac{L_{\rm bol}}{L_\odot}\right)^{0.6}$. The $\times$ symbols are UC and HC HII regions from Kurtz et al. (1994). The continuous black line is the expected Lyman continuum photon rate from a single zero-age main-sequence (ZAMS) star at a given luminosity (Sánchez-Monge et al. 2013a).

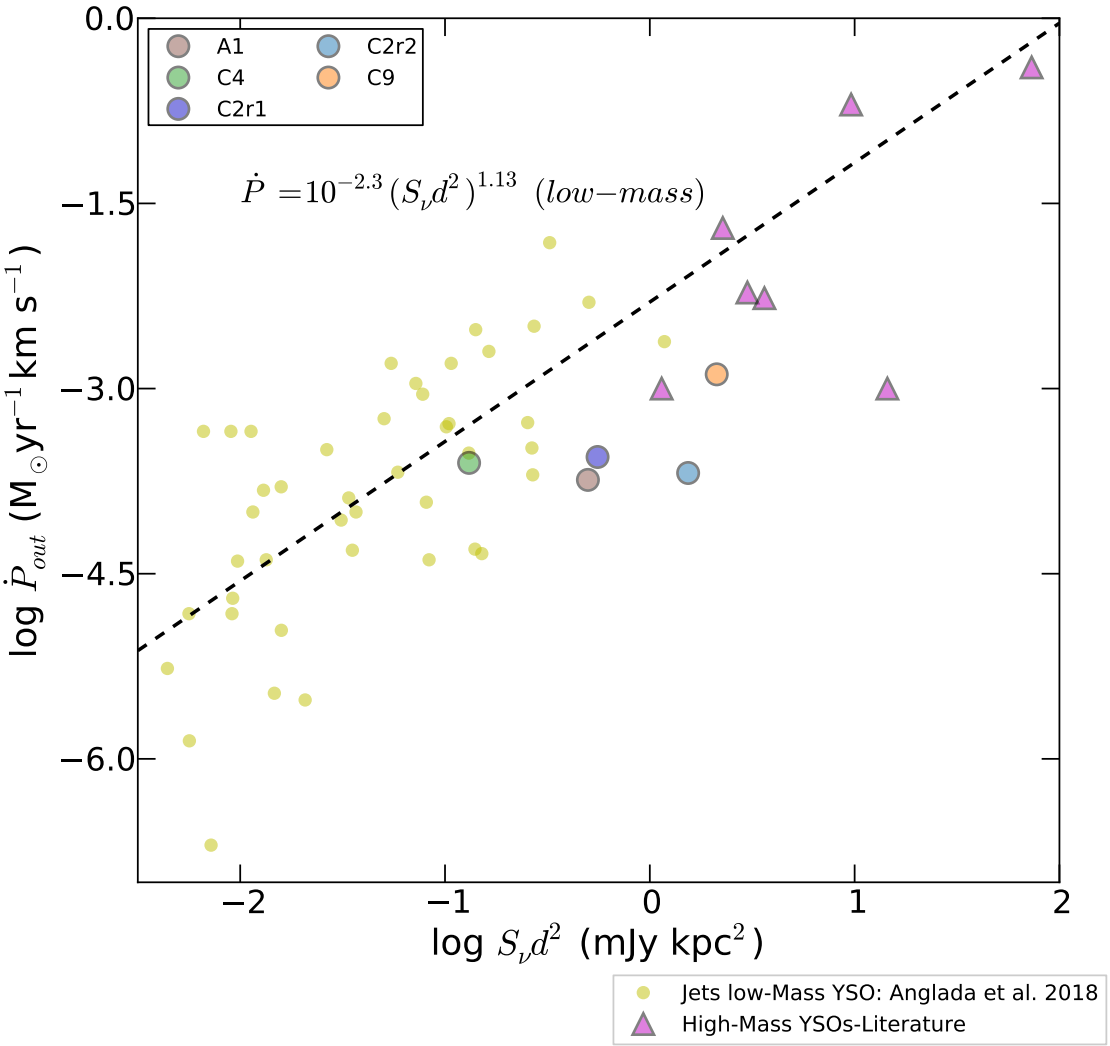

Fig. 3.17.— Momentum rate of the molecular outflow as a function of the radio luminosity at 5 GHz. The momentum rate values of the molecular outflow for our sources are measured from our SiO data; for the rest of the data the values are collected from the literature. The yellow circles represent ionized jets associated with low-mass protostars from Anglada et al. (2018). The purple triangles represent ionized jets associated with high-mass stars (Rodríguez et al. (2008); Moscadelli et al. (2016)). The dashed line relation shows the correlation found by Anglada (1995) derived for jets from low-mass stars.

low luminosity objects, shock ionization has been proposed as a viable alternative mechanism (Curiel et al. 1987; González & Cantó 2002) and the correlation of the bolometric and radio luminosities is interpreted as a consequence of the accretion and outflow relationship (Anglada et al. 2018). From Figure 3.16 it seems the radio emission in A1, C2, C4 and C9 is more likely to be from shock ionized thermal radio jets than a HC HII region, i.e., from the radio/bolometric luminosity comparison. Note for the two radio sources in C2 we adopt a luminosity value of $L_{\rm bol}$ of C2 divided by 2. More information is needed to confirm their nature, such as a robust spectral index derived from multi bands and resolved morphology. If they are shock ionized jets, they are likely to be detected because the cores are massive enough to drive strong shocks. There is no clear relation between the detection and the evolutionary stage (indicated by L/M and $t_{\rm dyn}/t_{\rm ff}$). It is likely that our sample is overall at an early stage and photoionization has not become significant enough yet to form a HC HII region, even for the high-mass cores C2 and C9, which would eventually evolve to HII regions based on their current core mass. However, we are not sure why other intermediate-mass cores with strong SiO outflows do not have radio detections like the cores in C6. The hint of the different orientation of the jet and the outflow may indicate that they are launched at different time and/or that there is precession.

It has also been found previously that the outflow momentum rate is correlated with the radio luminosity, which can be explained by the shock ionization mechanism working in radio jets (Anglada et al. 2018). However, with our radio sources such a correlation does not appear to be strong.

Also, it has been found previously that the outflow momentum rate is correlated with the radio luminosity, which can be explained by the shock ionization mechanism working in radio jets (Anglada et al. 2018). In particular, the shocked-induced

ionization model implies $\left(\frac{S_\nu d^2}{\mathrm{mJy\,kpc^2}}\right) = 10^{3.5}\eta\left(\frac{\dot{P}}{M_\odot\,\mathrm{yr^{-1}\,km\,s^{-1}}}\right)$ at $\nu = 5$ GHz where η is the ionization fraction. In Figure 3.17 we show the momentum rate ($\dot{P}$) of our SiO molecular outflows that are associated with centimeter emission as a function of the radio luminosity ($S_\nu d^2$) of the ionized jet estimated from our flux values at 5 GHz. The purple triangles represent ionized jets associated with high-mass stars as collected from the literature (Rodríguez et al. (2008); Moscadelli et al. (2016)) and the yellow circles represent ionized jets associated with low-mass protostars from Anglada et al. (2018). The molecular outflow data from the literature are from observations using different spectral lines and telescopes, thus the scatter in the data. The dashed line relation in Figure 3.17 shows the observational correlation found by Anglada (1995) derived for jets associated with low-mass stars with an ionization fraction of $\sim 10\%$. Despite the scatter in the data in Figure 3.17, our observations appear to suggest that the ionization fraction or the fraction of material that gets ionized by shocks may be higher than $\sim 10\%$ for high-mass protostars than for the low-mass counterpart (see Rosero et al. 2019b for a further discussion). However, a larger and homogeneous sample is required for drawing any conclusions.

3.6 Conclusions

In this work, we have present the results of ALMA observations of SiO(5-4) and VLA 6 cm radio observations made towards 32 IRDC clumps potentially harboring prestellar/protostellar sources. Our goal is to characterize a large number of protostars from low-mass to high-mass at the earliest phases with their outflow emission, and investigate the onset of SiO emission as shock tracers and the onset of ionization, to understand massive star formation. In summary, our main results and conclusions are as follows.

1. We have detected SiO(5-4) emission in 20 out of 32 IRDC clumps with a detection rate of 62%. From the non-detection in our sample and comparison with the SiO detection rate in other IR-dark clumps, it seems at early evolutionary stages, shocked gas is more common in the higher mass regime. Compared with more evolved IR-bright protostars, the SiO detection rate is overall higher in early-stage protostars.

2. In the 20 sources with detected SiO, 11 sources with relatively strong SiO emission seem to host SiO outflows from their wide line widths. Most SiO outflows show bipolar structures though they can be highly asymmetric. Some SiO outflows are collimated while others are less ordered. There is evidence for successive ejection events as well as multiple outflows originating from $\lesssim$ 0.1pc, which can be due to outflow changing orientation over time. For the six protostellar sources with strongest SiO outflow emission, we do not see clear dependence of the collimation of the outflows on core mass, luminosity and evolutionary stage.

3. For the six protostars with strongest SiO emission, we locate the protostellar sources driving the outflows, which appear as nearby mm continuum peaks, in position-velocity space utilizing dense gas tracers DCN(3-2), DCO^+(3-2) and $C^{18}O$(2-1). They have relatively low outflow masses, mass outflow rates and momentum flow rates, in spite of the fact that some of them are high-mass protostellar candidates based on their mm core masses. The accretion rates returned by SED models are also lower than more evolved protostars. The outflow masses appear to increase with the core mass. The dependence of the mechanical force and mass entrainment rate on the bolometric luminosity is not strong.

4. Where there is SiO(5-4) emission seen, we can always find 1.3 mm continuum emission and some infrared emission nearby, but not vice versa. The low luminosity and stellar mass returned by SED fitting suggest the sources in our sample are at an

early stage. With the entire sample and data from literature, we see a slight increasing trend of SiO line luminosity with the bolometric luminosity, which suggests more powerful shocks in the vicinity of more massive YSOs. We do not see clear relation between the SiO luminosity and the evolutionary stage indicated by L/M. Given the fact that most of our sample have SiO detection, it seems that as long as a protostar approaches a luminosity of $\sim\ 10^2\ L_{\odot}$, the shocks in the outflow are strong enough to form SiO emission.

5. We detect 6 cm radio continuum emission in 4 out of 15 sources, which show stronger SiO emission than the rest. The radio emission is likely due to shock-ionized jets associated with most massive protostellar cores. It is likely that our sample is overall at an early stage and photoionization has not become significant enough yet to form HC HII regions, even for the high-mass cores. Considering only the 6 cm detections, there is no clear relation between the radio detection and the SiO strength, bolometric luminosity and evolutionary stage. There is an offset between the 6 cm radio continuum peak and the 1.3 mm continuum peak in all the four sources. The hint of the different orientation of the jet and the outflow may indicate that they are launched predominantly from different recent times and/or that there is precession of the outflow.

Chapter 4

The SOFIA Massive (SOMA) Star Formation Survey. I. Overview and First Results

4.1 Introduction

The enormous radiative and mechanical luminosities of massive stars impact a vast range of scales and processes, from reionization of the universe, to galaxy evolution, to regulation of the interstellar medium, to formation of star clusters, and even to formation of planets around stars in such clusters. There is evidence our own solar system was influenced in this way (Adams 2010). Furthermore, synthesis and dispersal of heavy elements by massive stars play key roles in the chemical evolution of the cosmos. In spite of this importance, there is still no consensus on the basic formation mechanism of massive stars. Theories range from Core Accretion models, i.e., scaled-up versions of low-mass star formation (e.g., McKee & Tan 2003 [MT03]), to Competitive Accretion models at the crowded centers of forming star clusters (Bon-

nell et al. 2001; Wang et al. 2010), to Stellar Collisions (Bonnell et al. 1998; Bally & Zinnecker 2005). This confusion is due in part to the typically large distances and extinctions to massive protostars. See, e.g., Tan et al. (2014) for a review.

Massive stars form in dense gas clumps with mass surface densities of $\Sigma \sim 1 \mathrm{g\,cm^{-2}}$ (i.e., $A_V \sim 200$ mag; $A_{8\mu\mathrm{m}} \sim 8$ mag; $A_{37\mu\mathrm{m}} \sim 3$ mag; Ossenkopf & Henning 1994). If forming from massive cores in approximate pressure and virial equilibrium with this clump (MT03), then such a core with mass M_c has radius $R_c = 0.057(\Sigma/\mathrm{g\,cm^{-2}})^{-1/2}(M_c/60\,M_\odot)^{1/2}$ pc. If the degree of rotational support is similar to low-mass cores, then the disk size should be ~ 100–10^3 AU in radius. The accretion rate is expected to be a few $\times 10^{-4}\,M_\odot\,\mathrm{yr^{-1}}$. Collimated bipolar outflows are observed from massive protostars (e.g., Beuther et al. 2002) and massive early-stage cores (Tan et al. 2016). These are expected to limit the star formation efficiency from a core to ~ 0.5 (Matzner & McKee 1999; Zhang, Tan & Hosokawa 2014, hereafter ZTH14), since they expel core material from polar directions. Creation of low-density outflow cavities has a profound effect on the MIR appearance of massive protostars (De Buizer 2006).

Radiative transfer (RT) calculations of the MT03 Core Accretion model of massive protostars have confirmed the importance of outflow cavities on the MIR to FIR images and spectral energy distributions (SEDs) (Zhang & Tan 2011; Zhang, Tan & McKee 2013; ZTH14). Shorter wavelength light tends to emerge along the outflow cavity that is directed towards our line of sight. At NIR wavelengths the scattered light is most important. Moving to MIR wavelengths $\gtrsim 10\,\mu$m, thermal emission from warm dust in the outflow and outflow cavity walls makes the dominant contribution. The far-facing outflow cavity appears much fainter because of absorption by the dense, colder dusty material in the core envelope. However, as one observes at longer

wavelengths (e.g., $\gtrsim 70\mu$m), the optical depth is reduced, the far-facing outflow cavity becomes more visible and the appearance of the protostar (i.e., the intensity profile along its outflow axis) becomes more symmetric.

The *Stratospheric Observatory For Infrared Astronomy* (*SOFIA*) FORCAST instrument has the ability to observe from MIR wavelengths up to $\sim$40 μm with $\lesssim 3''$ angular resolution. It is thus able to test the above key predictions of Core Accretion models of massive star formation, i.e., their MIR morphologies should be aligned with outflow cavities and that at longer wavelengths the far-facing cavity should become visible as the overall appearance becomes more symmetric.

We used *SOFIA*-FORCAST Early Science observations of the massive protostar G35.20-0.74 for such a test of the models (Zhang et al. 2013b). The observations at 37 μm were able to achieve a high dynamic range in flux brightness sensitivity of a factor of $\sim 10^4$ and clearly detected the fainter far-facing outflow cavity at both 31 and 37 μm. Detailed modeling of the multi-wavelength intensity profiles along the outflow axis, together with the SED, provided the following constraints on the properties of a massive protostar: a current stellar mass of $m_* \sim 20 - 34\,M_\odot$, embedded in a core with $M_c = 240\,M_\odot$, in a clump with $\Sigma_{\rm cl} \simeq 0.4 - 1$ g cm^{-2}.

This work has motivated observations of a larger sample of protostars, i.e., the *SOFIA* Massive (SOMA) Star Formation Survey (PI: Tan). The goal is to observe at least $\sim$50 protostars spanning a range of environments, evolutionary stages and core masses. We have defined four types of sources: Type I: "MIR sources in IRDCs" - relatively isolated sources in Infrared Dark Clouds, some without detected radio emission; Type II: "Hyper-compact" - often jet-like, radio sources, where the MIR emission extends beyond the observed radio emission (e.g., G35.20-0.74); Type III: "Ultra-compact" - radio sources where the radio emission is more extended than

the MIR emission; Type IV: "Clustered sources" - a MIR source exhibiting radio emission is surrounded by several other MIR sources within $\sim 60''$. Such classification is somewhat arbitrary, but an evolutionary sequence is expected to hold from Types I to III.

Source selection mainly utilized the CORNISH survey (Hoare et al. 2012), complemented by radio-quiet MIR sources in IRDCs studied by Butler & Tan (2012) and protostars studied at 24 μm by de Wit et al. (2009). We included some non-Galactic plane sources and attempted, where possible, to have a relatively spread-out distribution on the sky, which aids scheduling of *SOFIA* observations.

In this first paper of the SOMA survey we present the results of the first eight sources (including G35.20-0.74), which were observed up to the end of 2014. These are all Type II sources. Our goal here is to present the survey data, including public release of the calibrated images, of these eight sources. We will use these sources to further test the hypothesis that the appearance of the MIR morphologies of massive young stellar objects may be influenced by outflows. We will also measure the SEDs of the sources and compare fitting solutions from RT models. Future papers will carry out more detailed analyses of images, including outflow axis intensity profiles, as well as presenting data for additional sources.

4.2 Observations

4.2.1 *SOFIA* data

All eight targets were observed by *SOFIA*[1] (Young et al. 2012) with the FORCAST instrument (Herter et al. 2013) (see Table 4.1). FORCAST is a facility imager and spectrograph that employs a Si:As 256×256 blocked-impurity band (BIB) detector array to cover a wavelength range of 5 to 25 μm and a Si:Sb 256× 256 BIB array to cover the range from 25 to 40 μm. FORCAST has a dichroic that allows simultaneous imaging with both arrays, if desired. In imaging mode the arrays cover a 3.4'×3.2' instantaneous field-of-view with 0.768"[2] pixels (after distortion correction).

Data were taken on multiple flights spanning the Early Science period, Cycle 1, and Cycle 2 *SOFIA* observing cycles, though typically a single target was observed to completion on a single flight. All observations were taken at an altitude between 39000 and 43000 ft, which typically yields precipitable water vapor overburdens of less than 25 μm. All data were taken by employing the standard chop-nod observing technique used in the thermal infrared, with chop and nod throws sufficiently large

[1] *SOFIA* is jointly operated by the Universities Space Research Association, Inc. (USRA), under NASA contract NAS2-97001, and the Deutsches SOFIA Institut (DSI) under DLR contract 50 OK 0901 to the University of Stuttgart.

Table 4.1. *SOFIA* FORCAST Observations:
Obs. Dates & Exposure Times (s)

Source	Obs. Date	7.7 μm	11.1 μm	19.7 μm	25.3 μm	31.5 μm	37.1 μm
AFGL 4029	2014-03-29	112	...	158	...	282	678
AFGL 437	2014-06-11	217	...	2075	...	2000	884
IRAS 07299	2015-02-06	280	...	697	...	449	1197
G35.20-0.74	2011-05-25	...	...	...	...	...	...
G45.47+0.05	2013-06-26	...	309	...	588	316	585
IRAS 20126	2013-09-13	...	484	...	1276	487	1317
Cep A	2014-03-25	242	...	214	...	214	1321
NGC 7538	2014-06-06	215	...	653	...	491	923

to sample clear off-source sky.

SOFIA data are calibrated by the *SOFIA* pipeline with a system of stellar calibrators taken across all flights in a flight series and applied to all targets within that flight series (see also the FORCAST calibration paper by Herter et al. 2013). Corrections are made for airmass of the science targets as well. The main source of uncertainty in the *SOFIA* calibrations is the variability observed in the standard stars' observed flux throughout the flight and from flight to flight due to changing atmospheric conditions. The standard deviation of these measurements will be used as our 1-sigma error on the quoted flux density measurements, and these are: 2.9% at 7 μm, 1.0% at 11 μm, 3.1% at 19 μm, 5.1% and 25 μm, 3.6% at 31 μm, and 4.6% at 37 μm.

4.2.2 *Spitzer* and *Herschel* archival data

For all objects, data were retrieved from the *Spitzer* Heritage Archive from all four IRAC (Fazio et al. 2004) channels (3.6, 4.5, 5.8, and 8.0 μm). In many cases, the sources in this sample were so bright that they are saturated in the IRAC images and could not be used to derive accurate fluxes. Additionally, we incorporated publicly-available imaging observations performed with the *Herschel Space Observatory*[2] (Pilbratt et al. 2010) and its PACS (Poglitsch et al. 2010) and SPIRE (Griffin et al. 2010) instruments at 70, 160, 250, 350 and 500 μm. The exception is IRAS 07229-6151, for which no *Herschel* data exist.

In addition to using these data for deriving multi-wavelength flux densities of our

[2] *Herschel* is an ESA space observatory with science instruments provided by European-led Principal Investigator consortia and with important participation from NASA. The *Herschel* data used in this paper are taken from the Level 2 (flux-calibrated) images provided by the *Herschel* Science Center via the NASA/IPAC Infrared Science Archive (IRSA), which is operated by the Jet Propulsion Laboratory, California Institute of Technology, under contract with NASA.

sources, the *Spitzer* 8 μm and *Herschel* 70 μm images are presented for comparison with our *SOFIA* images in §4.4.1.

The *Herschel* images, particularly at 70 μm, suffer from relatively poor image quality due to observations being taken in fast scanning mode. Point-sources are often not circularly symmetric, and can be severely triangular or square. To enable comparative morphology as a function of wavelength, the *Hershel* 70 μm were deconvolved to remove most of this asymmetry and to improve the resolution to be more comparable to the resolution of *SOFIA* at 37 μm.

4.2.3 Data resolutions and deconvolutions

The resolution of *SOFIA* through the FORCAST wavelength range is only slightly dependent upon effective filter central wavelength. This is because the image quality is dominated by in-flight telescope pointing stability, at least at shorter wavelengths of FORCAST. Therefore the typical resolutions that were achieved for the observations was about 3″, for filters with effective central wavelengths less than 25 μm. However, at wavelengths greater than 20 μm, it appears that we are observing near the diffraction limit. Resolutions presented in Figures 1-8 are very similar for all figures with typical resolutions of 2.0″ for the *Spitzer* 8 μm images, 2.7″ at *SOFIA* 7 μm, 2.9″ at *SOFIA* 11 μm, 3.3″ at *SOFIA* 19 and 25 μm, 3.4″ at 31 μm, and 3.5″ at 37 μm.

As discussed in the previous section, the *Herschel* 70 μm images presented in Figures 1f-8f have been deconvolved to remove image abnormalities and improve resolution. Deconvolution techniques employ an iterative approach, where the greater the number of iterations, the better the effective resolution. However, iterating too much can create artifacts and false structure in the final deconvolved images. We employed a maximum likelihood approach, using the script written by F. Varosi and available

in the public IDL astronomy program database (http://idlastro.gsfc.nasa.gov). We mildly deconvolved the images (employing no more than 30 iterations), which tends to correct image PSF abnormalities and create images with effective resolutions a factor of 1.5-2.0 better than the native image resolution. Proper deconvolutions require an accurate representation of the image PSF. Therefore, for each source in our survey, the rest of the *Herschel* image field was scoured for point sources and a median combination of all these point-sources (after normalization) was created and used in the deconvolution. The resultant images have resolutions of 5.0-5.2″, which is ∼1.6 times better resolution than the measured 8.1″ native resolution of *Herschel* at 70 μm.

4.2.4 Astrometry

SOFIA observations were performed in such a way using the simultaneous observations with the dichroic that the relative astrometry between the four *SOFIA* images has been determined to be better than a FORCAST pixel (∼0.77″). The absolute astrometry of the *SOFIA* data comes from matching the morphology at the shortest *SOFIA* wavelength (either 7 or 11 μm) with the *Spitzer* 8 μm image (or shorter IRAC wavelength, if saturated at 8 μm). The *Herschel* 70 μm data were found to be off in their absolute astrometry by up to 5″. For all targets in this survey, we were able to find multiple sources in common between the 70 μm *Herschel* image and sources found in the *SOFIA* or *Spitzer* field of view that allowed us to correct the *Herschel* 70 μm absolute astrometry, which is then assumed to have errors of less than 1″.

4.2.5 Other ground-based IR data

Published and unpublished data from other facilities were also available for a few sources in our survey and were incorporated into the SEDs and model fitting (see

Table 2). For G35.20-0.74 the *SOFIA* data presented here have already been presented in Zhang et al. (2013b) and the 11.7 μm (*Si-5*) and 18.3 μm (*Qa*) data from the T-ReCS instrument (De Buizer & Fisher 2004) on *Gemini Observatory* were first published in De Buizer (2006). For IRAS 20126+4104, T-ReCS/*Gemini* 12.5 μm (*Si-6*) and 18.3 μm data were also previously published in De Buizer (2007). There are also previously unpublished T-ReCS/*Gemini* 11.7 μm and 18.3 μm data for IRAS 07299-1651 presented here. For G45.47+0.05, we have on hand previously unpublished imaging data from the *NASA/Infrared Telescope Facility* (*IRTF*) at K and L from the NSFCam instrument (Shure et al. 1994), as well as previously published (De Buizer et al. 2005) 11.7 μm (*N4*) and 20.8 μm (*Q3*) data from the mid-infrared camera MIRLIN (Ressler et al. 1994).

4.3 Analysis Methods

4.3.1 Derivation of Spectral Energy Distributions

We build spectral energy distributions (SEDs) of the eight sources from 3.6 μm up to 500 μm with photometric data of *Spitzer*, *IRTF*, *Gemini*, *SOFIA* and *Herschel*. The uncertainty mainly comes from calibration which is about 10%. We used PHOTUTILS, a PYTHON package to measure the flux photometry.

The position of the protostellar source is generally fixed from published literature results, e.g., radio continuum emission (see §4.4.1). Then circular apertures of radius $R_{\rm ap}$ are chosen to cover most of the emission. We try two methods: (1) Fixed Aperture Radius—the radius is set by considering the morphology of the *Herschel* 70 μm image[3] so as to include most of the source flux, while minimizing contamination from

[3]For IRAS 07299 we adopt the aperture size based on *SOFIA* 37 μm data since no *Herschel* data are available.

neighboring sources; (2) Variable Aperture Radius—the radii at wavelengths $< 70\,\mu$m are varied based on the morphology at each wavelength, again aiming to minimize contamination from neighboring sources.

The emission at the longer *Herschel* wavelengths ($\geq 160\,\mu$m) is typically more extended, which is both a real effect of the presence of a cooler, massive clump surrounding the protostars, and also a result of the lower resolution of these data. This is the main motivation for us to then carry out background subtraction of the fluxes, based on the median flux density in an annular region extending from 1 to 2 aperture radii.

4.3.2 SED Models and Fitting

Zhang & Tan (ZT) Models

In a series of papers, Zhang & Tan (2011), Zhang, Tan & McKee (2013), ZTH14, and Zhang & Tan (in prep.) have developed a model for the evolution of massive (and intermediate-mass) protostars based on the Turbulent Core model (MT03). The initial conditions are pressurized dense massive cores embedded in high mass surface density "clump" environments, which are parameterized by their initial masses (M_c) and the mean mass surface densities of their surrounding clumps ($\Sigma_{\rm cl}$). The latter affects the surface pressure on the cores and therefore, together with M_c, determines their sizes and densities. Cores undergoe inside-out collapse (Shu 1977; McLaughlin & Pudritz 1996; McLaughlin & Pudritz 1997) with the effect of rotation described with the solution by Ulrich (1976).

Massive disks are expected to form around massive protostars due to the high accretion rates. We assume the mass ratio between the disk and the protostar is a constant $f_d = m_d/m_* = 1/3$, considering the rise in effective viscosity due to disk self-

gravity at about this value of f_d (Kratter et al. 2008). The disk size is calculated from the rotating collapse of the core (ZTH14), with the rotational-to-gravitational energy ratio of the initial core β_c set to be 0.02, which is a typical value from observations of low and high-mass prestellar cores (e.g., Goodman et al. 1993; Li et al. 2012; Palau et al. 2013). The disk structure is described with an "α-disk" solution (Shakura & Sunyaev 1973), with an improved treatment to include the effects of the outflow and the accretion infall to the disk (Zhang et al. 2013).

Half of the accretion energy is released when the accretion flow reaches the stellar surface (the boundary layer luminosity $L_{\rm acc} = Gm_*\dot{m}_*/(2r_*)$), but we assume this part of luminosity is radiated along with the stellar luminosity isotropically as a single black-body ($L_{*,\rm acc} = L_* + L_{\rm acc}$). The other half of the accretion energy is partly radiated from the disk and partly converted to the kinetic energy of the disk wind.

The density distribution of the disk wind is described by a semi-analytic solution which is approximately a Blandford & Payne (1982) wind (see Appendix B of Zhang et al. 2013), and the mass loading rate of the wind relative to the stellar accretion rate is assumed to be $f_w = \dot{m}_w/\dot{m}_* = 0.1$ which is a typical value for disk winds (Königl & Pudritz 2000). Such a disk wind carves out cavities from the core which gradually open up as the protostar evolves. The opening angle of the outflow cavity is estimated following the method of Matzner & McKee (2000) by comparing the wind momentum and that needed to accelerate the core material to its escape speed (ZTH14). The accretion rate to the protostar is regulated by this outflow feedback.

The evolution of the protostar is solved using the model by Hosokawa & Omukai (2009) and Hosokawa et al. (2010) from the calculated accretion history. A photospheric boundary condition, which is usually associated with the situation of disk

accretion, is used in the protostellar evolution calculation.

In the above modeling, the evolution of the protostar and its surrounding structures are all calculated self-consistently from the two initial conditions of the core: the initial mass of the core M_c and the mean surface density of the ambient clump $\Sigma_{\rm cl}$. A third parameter, the protostellar mass m_*, is used to specify a particular stage on these evolutionary tracks. In our current model grid (Zhang & Tan, in prep.), M_c is sampled at 10, 20, 30, 40, 50, 60, 120, 240, 480 $M_\odot$, $\Sigma_{\rm cl}$ is sampled at 0.1, 0.3, 1, 3 $\rm g\,cm^{-2}$, forming 36 evolutionary tracks. m_* is sampled at 0.5, 1, 2, 4, 8, 12, 16, 24, 32, 48, 64, 96 $M_\odot$ (for each track, it is limited by the final stellar mass). There are then, in total, 226 physical models defined by different sets of ($M_c,\ \Sigma_{\rm cl},\ m_*$).

Monte-Carlo continuum radiation transfer simulations were performed for these models using the latest version of the HOCHUNK3d code by Whitney et al. (2003; 2013). The code was updated to include gas opacities, adiabatic cooling/heating and advection (Zhang, Tan & McKee 2013). For each model, 20 inclinations are sampled evenly in cosine space to produce the SEDs. To compare with the observations, an additional foreground extinction A_V is applied to the model SEDs and the model SEDs are also convolved with the transmission profiles of instrument filters to produce flux densities of various observational bands.

We use χ^2 minimization to find the best models to fit a given set of observations. The reduced χ^2 is defined as

$$\chi^2 = \frac{1}{N}\left\{\sum_{i=1}^{N}\left[\frac{\log_{10} F_{\nu,\rm obs}(\lambda_i) - \log_{10} F_{\nu,\rm mod}(\lambda_i)}{\sigma(\log_{10} F_{\nu,\rm obs}(\lambda_i))}\right]^2 + P_{\rm up} + P_{\rm lo}\right\}, \tag{4.1}$$

where $F_{\nu,\rm obs}$ and $F_{\nu,\rm mod}$ are the observed and model predicted flux densities at wavelengths λ_i, σ is the observational uncertainty in $\log_{10}\rm F_{\nu,obs}$, and $P_{\rm up}$ and $P_{\rm lo}$ are the penalties brought by the constraint of upper limits $F_{\nu,\rm up}(\lambda_j)$ and $F_{\nu,\rm lo}(\lambda_j)$. They are

defined as

$$P_{\rm up} = \sum_{F_{\nu,\rm up}<F_{\nu,\rm mod}} \left[\frac{\log_{10} F_{\nu,\rm up}(\lambda_j) - \log_{10} F_{\nu,\rm mod}(\lambda_j)}{\sigma(\log_{10} F_{\nu,\rm up}(\lambda_j))}\right]^2 \tag{4.2}$$

and

$$P_{\rm lo} = \sum_{F_{\nu,\rm lo}>F_{\nu,\rm mod}} \left[\frac{\log_{10} F_{\nu,\rm lo}(\lambda_j) - \log_{10} F_{\nu,\rm mod}(\lambda_j)}{\sigma(\log_{10} F_{\nu,\rm lo}(\lambda_j))}\right]^2. \tag{4.3}$$

For each set of (M_c, $\Sigma_{\rm cl}$, m_*), we search for a minimum χ^2 by varying the inclination $\theta_{\rm view}$ and the foreground extinction A_V. The foreground extinction A_V is constrained within a range corresponding to 0.1 $\Sigma_{\rm cl}$ to 10 $\Sigma_{\rm cl}$, i.e., we assume that the foreground extinction is somewhat related to that expected of the ambient clump surrounding the core.

We then compare the minimum χ^2 of different (M_c, $\Sigma_{\rm cl}$, m_*) to find the best models. In this paper we set the distance to be a given value, based on literature estimates. Therefore our SED model grid has only five free parameters: M_c, $\Sigma_{\rm cl}$, m_*, $\theta_{\rm view}$ and A_V. With such models, our intention is to explore to what extent the observed SEDs can be explained by the different evolutionary stages of a relatively limited set of initial conditions of massive star formation from the Turbulent Core Model. We will show the results of the best five models for each source.

Robitaille et al. Models

We also fit the SEDs with the models of Robitaille et al. (2007) for comparison with the results of the ZT models. To do this we use the SED fitting PYTHON package *sedfitter*[4] developed by Robitaille et al. (2007). Note that in their fitting code they adjust the value of the data point to the middle of the error bar. This influence can be significant when the error bar is large and asymmetric.

We note that the Robitaille et al. models were developed mostly with the in-

[4]http://sedfitter.readthedocs.io/en/stable/

tention of fitting lower-mass protostars that are typically observed in lower pressure environments and with lower accretion rates than the massive protostars of the ZT models. There are ∼30 output parameters in Robitaille et al. models. The key parameters include stellar mass, stellar radius, stellar temperature, envelope accretion rate, envelope outer radius, envelope inner radius, envelope cavity opening angle, viewing angle, bolometric luminosity, disk mass, disk outer radius, disk inner radius, disk accretion rate, extinction inside the model down to the stellar surface, centrifugal radius, envelope cavity density, ambient density around the envelope, among others. We will show the results for some of these parameters—those directly comparable with the ZT models—for the best five Robitaille et al. models.

General SED Fitting Considerations

We fit the fiducial SEDs (with fixed aperture size and with background subtracted) with the ZT models and Robitaille et al. (2007) models. The error bars are set to be the larger of either 10% of the background subtracted flux density or the value of the estimated background flux density. The fitting procedure involves convolving model SEDs with the filter response functions for the various telescope bands. Source distances were adopted from the literature. For each source we present the five best fitting models.

Note that short wavelength fluxes, i.e., at $\lesssim 8\ \mu$m, may be affected by PAH emission and thermal emission from very small grains that are transiently heated by single photons. Neither of these effects are included in the ZT radiative transfer models. Therefore we treat the data at these wavelengths as upper limit constraints on the models.

4.4 Results

The *SOFIA* images for each source are shown below in §4.4.1. Also, the type of multiwavelength data available for each source, the flux densities derived and the aperture sizes adopted are listed in Table 4.2. $F_{\lambda,\mathrm{fix}}$ is the flux density derived with a fixed aperture size and $F_{\lambda,\mathrm{var}}$ is the flux density derived with a variable aperture size. The value of flux density listed in the upper row is derived with background subtraction. The flux density derived without background subtraction is also listed in the brackets in the lower row.

Table 4.2. Integrated Flux Densities

Facility	λ (μm)	$F_{\lambda,fix}$ (Jy)	[a]$F_{\lambda,var}$ (Jy)	[b]R_{ap} ($''$)	[c] $F_{\lambda,fix}$ (Jy)	$F_{\lambda,var}$ (Jy)	R_{ap} ($''$)	$F_{\lambda,fix}$ (Jy)	$F_{\lambda,var}$ (Jy)	R_{ap} ($''$)	$F_{\lambda,fix}$ (Jy)	$F_{\lambda,var}$ (Jy)	R_{ap} ($''$)	$F_{\lambda,fix}$ (Jy)	$F_{\lambda,var}$ (Jy)	R_{ap} ($''$)	$F_{\lambda,fix}$ (Jy)	$F_{\lambda,var}$ (Jy)	R_{ap} ($''$)	$F_{\lambda,fix}$ (Jy)	$F_{\lambda,var}$ (Jy)	R_{ap} ($''$)	$F_{\lambda,fix}$ (Jy)	$F_{\lambda,var}$ (Jy)	R_{ap} ($''$)
		AFGL 4029			AFGL 437			IRAS 07299			G35.20-0.74			G45.47+0.05			IRAS 20126			Cep A			NGC 7538		
IRTF/NSFCam	2.1	-	-	-	-	-	-	-	-	-	-	-	-	0.02 (0.08)	0.02 (0.03)	7.7	-	-	-	-	-	-	-	-	-
Spitzer/IRAC	3.6	2.60 (2.71)	2.14 (2.23)	4.8	2.26 (2.39)	1.36 (1.49)	12.0	1.34 (1.42)	1.19 (1.28)	6.0	0.50 (0.60)	0.30 (0.34)	14.0	-	-	-	0.68 (0.73)	0.24 (0.28)	4.8	15.87 (16.51)	6.72 (7.09)	15.0	2.80 (2.99)	2.15 (2.24)	6.0
IRTF/NSFCam	3.8	-	-	-	-	-	-	-	-	-	-	-	-	0.12 (0.08)	0.08 (0.08)	7.7	-	-	-	-	-	-	-	-	-
Spitzer/IRAC	4.5	3.62 (3.75)	2.82 (2.96)	3.6	2.77 (2.87)	1.89 (2.00)	12.0	2.41 (2.54)	2.18 (2.33)	6.0	1.24 (1.24)	0.90 (0.95)	14.0	0.25 (0.35)	0.18 (0.22)	7.7	-	-	-	27.90 (28.67)	13.89 (14.65)	15.0	7.89 (8.15)	5.69 (5.99)	6.0
Spitzer/IRAC	5.8	7.13 (7.63)	6.54 (6.86)	7.2	10.27 (11.05)	5.52 (6.19)	12.0	2.96 (3.15)	2.53 (2.71)	6.0	1.84 (2.64)	1.43 (1.65)	14.0	-	-	-	1.90 (2.24)	0.76 (0.92)	4.8	27.61 (30.11)	13.51 (14.78)	15.0	39.55 (41.17)	31.41 (32.14)	6.0
SOFIA/FORCAST	7.7	12.88 (12.72)	12.22 (12.28)	7.7	29.60 (28.96)	17.04 (18.58)	11.5	3.48 (3.31)	3.48 (3.31)	7.7	-	-	-	-	-	-	-	-	-	21.25 (19.00)	11.08 (12.02)	15.0	64.24 (62.75)	59.12 (59.89)	6.1
Spitzer/IRAC	8.0	10.34 (11.08)	8.86 (9.43)	7.2	24.98 (27.03)	13.38 (15.01)	12.0	2.30 (2.51)	2.12 (2.29)	6.0	3.22 (4.90)	2.85 (3.22)	14.0	0.15 (0.13)	0.14 (0.14)	7.7	1.36 (2.04)	0.44 (0.64)	4.5	13.80 (17.40)	6.52 (7.38)	15.0	41.64 (44.25)	27.49 (29.06)	6.0
IRTF/OSCIR	10.5	-	-	-	-	-	-	-	-	-	-	-	-	2.37 (0.38)	0.07 (0.24)	7.7	-	-	-	-	-	-	-	-	-
SOFIA/FORCAST	11.1	-	-	-	-	-	-	-	-	-	-	-	-	0.36 (0.21)	0.02 (0.05)	7.7	0.41 (0.42)	0.21 (0.26)	3.2	-	-	-	-	-	-
Gemini/T-ReCS	11.7	-	-	-	-	-	-	1.56 (1.71)	1.62 (1.66)	1.8	nan (3.82)	2.14 (2.31)	5.0	0.32 (0.14)	0.36 (0.36)	5.0	-	-	-	-	-	-	-	-	-
Gemini/T-ReCS	12.5	-	-	-	-	-	-	-	-	-	-	-	-	-	-	-	1.87 (1.87)	1.67 (1.69)	6.4	-	-	-	-	-	-
Gemini/T-ReCS	18.3	-	-	-	-	-	-	-	-	-	nan (63.03)	44.96 (48.00)	7.0	2.29 (2.56)	4.92 (4.85)	5.0	23.84 (23.84)	24.12 (24.12)	6.4	-	-	-	-	-	-
SOFIA/FORCAST	19.7	57.25 (59.43)	54.59 (56.22)	7.7	271 (269)	217 (2219)	11.5	73.82 (74.04)	73.82 (74.04)	7.7	68.18 (55.91)	64.87 (63.46)	14.0	-	-	-	-	-	-	138 (132)	179 (167)	24.0	172 (168)	152 (154)	6.1
IRTF/MIRLIN	20.8	-	-	-	-	-	-	-	-	-	-	-	-	5.14 (6.57)	8.78 (8.79)	7.7	-	-	-	-	-	-	-	-	-
SOFIA/FORCAST	25.3	-	-	-	-	-	-	-	-	-	-	-	-	45.98 (33.75)	45.89 (42.18)	7.7	188 (190)	159 (163)	6.4	-	-	-	-	-	-
SOFIA/FORCAST	31.5	187 (194)	171 (178)	7.7	732 (726)	656 (665)	15.4	446 (458)	446 (458)	7.7	553 (551)	502 (512)	14.0	144 (138)	135 (134)	7.7	438 (440)	352 (365)	6.4	2771 (2726)	2453 (2466)	24.0	616 (620)	520 (534)	7.7
SOFIA/FORCAST	37.1	405 (419)	352 (371)	7.7	878 (878)	769 (783)	15.4	681 (705)	681 (705)	7.7	1193 (1120)	1061 (1071)	14.0	214 (202)	189 (189)	7.7	729 (739)	528 (561)	6.4	6262 (6275)	5362 (5451)	24.0	843 (837)	679 (699)	7.7
Herschel/PACS	70.0	350 (394)	350 (394)	11.2	1132 (1181)	1132 (1181)	32.0	-	-	-	2628 (2733)	2628 (2733)	32.0	938 (1093)	938 (1093)	14.4	1398 (1519)	1398 (1519)	12.8	14637 (15298)	14637 (15298)	48.0	1568 (1681)	1568 (1681)	25.6

Table 4.2—Continued

Facility	λ (μm)	$F_{\lambda,fix}$ (Jy)	[a]$F_{\lambda,var}$ (Jy)	[b]R_{ap} ($''$)	[c] $F_{\lambda,fix}$ (Jy)	$F_{\lambda,var}$ (Jy)	R_{ap} ($''$)	$F_{\lambda,fix}$ (Jy)	$F_{\lambda,var}$ (Jy)	R_{ap} ($''$)	$F_{\lambda,fix}$ (Jy)	$F_{\lambda,var}$ (Jy)	R_{ap} ($''$)	$F_{\lambda,fix}$ (Jy)	$F_{\lambda,var}$ (Jy)	R_{ap} ($''$)	$F_{\lambda,fix}$ (Jy)	$F_{\lambda,var}$ (Jy)	R_{ap} ($''$)	$F_{\lambda,fix}$ (Jy)	$F_{\lambda,var}$ (Jy)	R_{ap} ($''$)	$F_{\lambda,fix}$ (Jy)	$F_{\lambda,var}$ (Jy)	R_{ap} ($''$)
Herschel/PACS	160.0	180 (264)	180 (264)	11.2	677 (825)	677 (825)	32.0	-	-	-	2386 (2807)	2386 (2807)	32.0	622 (886)	622 (886)	14.4	655 (783)	655 (783)	12.8	10877 (12006)	10877 (12006)	48.0	1019 (1296)	1019 (1296)	25.6
Herschel/SPIRE	250.0	41 (104)	41 (104)	11.2	243 (342)	243 (342)	32.0	-	-	-	-	-	-	245 (388)	245 (388)	14.4	143 (210)	143 (210)	12.8	-	-	-	344 (525)	344 (525)	25.6
Herschel/SPIRE	350.0	10.17 (31.72)	10.17 (31.72)	11.2	75 (120)	75 (120)	32.0	-	-	-	429 (594)	429 (594)	32.0	61 (113)	61 (113)	14.4	25.39 (51.61)	25.39 (51.61)	12.8	1054 (1292)	1054 (1292)	48.0	91 (177)	91 (177)	25.6
Herschel/SPIRE	500.0	1.16 (8.16)	1.16 (8.16)	11.2	20.02 (36.77)	20.02 (36.77)	32.0	-	-	-	127 (196)	127 (196)	32.0	8.67 (27.61)	8.67 (27.61)	14.4	2.93 (11.07)	2.93 (11.07)	12.8	318 (411)	318 (411)	48.0	13.62 (52.04)	13.62 (52.04)	25.6

[a]Flux density derived with a fixed aperture size of the 70 μm data.

[b]Flux density derived with various aperture sizes.

[c]Aperture radius.

Note. — The value of flux density in the upper row is derived with background subtraction. The value in the bracket in the lower line is flux density derived without background subtraction.

4.4.1 Description of Individual Sources

Here we describe details about each source as well as presenting their *SOFIA* and ancillary imaging data.

AFGL 4029

The giant H II radio region W5 is divided into two subregions, W5-E and W5-W. W5-E is coincident with the molecular cloud IC 1848A, and on its eastern border lies the bright infrared region AFGL 4029. Beichman (1979) showed that AFGL 4029 is actually composed of two mid-IR sources, IRS1 and IRS2, which are separated by 22″. IRS2 appears to be a more evolved H II region containing a small stellar cluster dominated by a B1V star (Deharveng et al. 1997, Zapata et al. 2001). IRS1 is a luminous ($\sim 10^4\ L_\odot$) and highly reddened ($A_V \sim 30$) massive young stellar object (Deharveng et al. 1997), and has a radio component that has been given the designation G138.295+1.555 (Kurtz et al. 1994). Later observations by Zapata et al. (2001) show IRS1 itself to be a binary radio source with a separation of 0.5″ (or 1000 AU given the distance to the region of 2 kpc from Deharveng et al. 2012). Deharveng et al. (1997) detect H_2 emission in the NIR emanating from IRS1 at a position angle of ∼265°, which is coincident with the high velocity optical jet seen in [S II] (Ray et al. 1990). There also appears to be a smaller (∼1″) radio jet at a similar angle (∼270°) to the optical jet (Zapata et al. 2001), as well as a larger, high energy CO outflow (Ginsburg et al. 2011).

Though IRS1 is the source of interest to this work, both IRS1 and IRS2 are prominently detected in all four wavelengths of *SOFIA* (Figure 1). The diffuse and extended nature of IRS2 can be best seen in the 7 μm *SOFIA* data, consistent with flocculent morphology seen in the radio continuum maps (Zapata et al. 2001) and

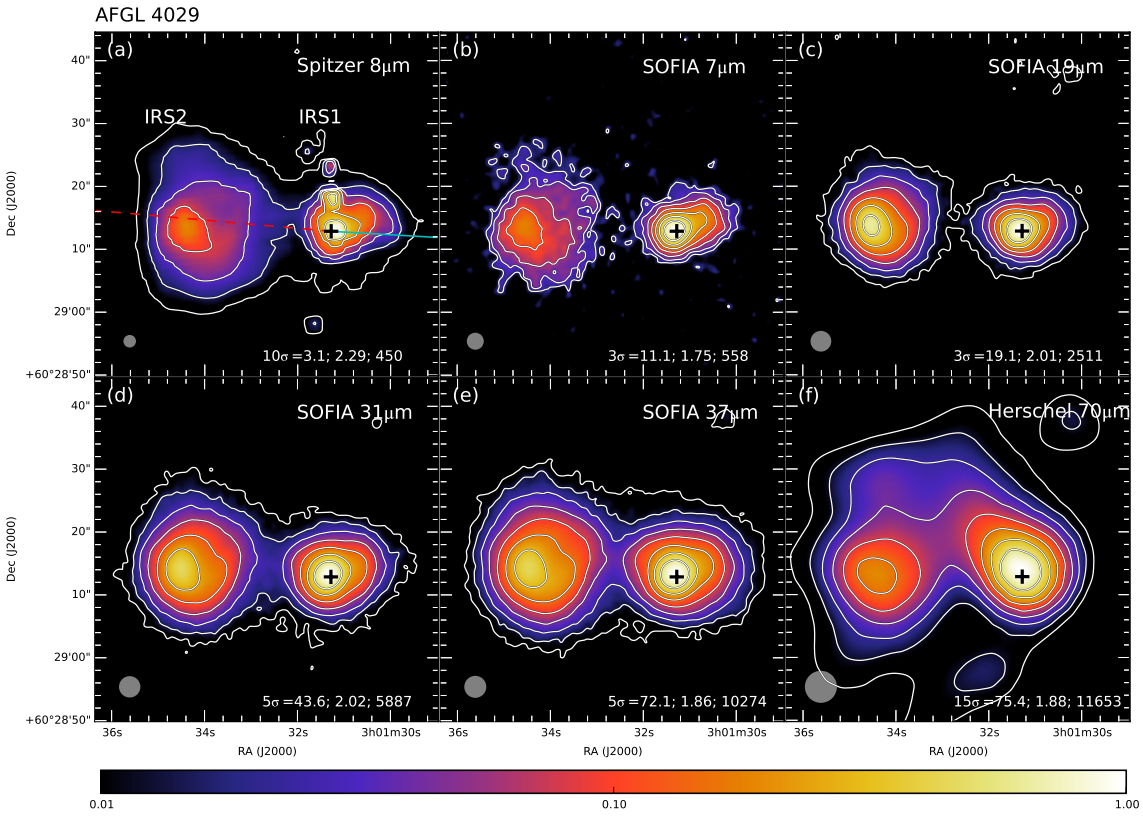

Fig. 4.1.— Multiwavelength images of AFGL 4029, with facility and wavelength given in upper right of each panel. Contour level information is given in lower right: lowest contour level in number of σ above the background noise and corresponding value in mJy per square arcsec; then log step size between each contour. In the lower left, the filled, gray circle shows the resolution of the image. Sources IRS1 (target of interest of this paper) and IRS2 are labeled in panel (a). The white cross in all panels denotes the position of radio source G138.295+1.555(S) from Zapata et al. (2001) at R.A.(J2000) = $03^h01^m31\overset{s}{.}28$, Decl.(J2000) = $+60°29'12\overset{''}{.}87$. The line in panel (a) shows the outflow axis angle, with the solid span tracing the blue-shifted direction and dotted span the red-shifted direction. In this case, the outflow axis angle is from the H_2 and optical jet emission of Deharveng et al. (1997), and the blue-shifted outflow direction is given by the CO observations of Ginsburg et al. (2011). In panel (a), the point sources to the north of the G138.295+1.555(S) position are ghosts in the *Spitzer* image and should not be interpreted as real structure.

H and K' images (Deharveng et al. 1997). IRS1 appears to have a bright peak with a "tongue" of emission extending to the northwest at all SOFIA wavelengths. IRS1 has been observed at sub-arcsecond resolution in the mid-infrared by Zavagno et al. (1999; 8–11 μm) and de Wit et al. (2009; 24.5 μm) and it appears that this "tongue" is an arc-shaped dust condensation, possibly related to the outflow cavity.

AFGL 437 (a.k.a. GL 437, G139.909+0.197, IRAS 03035+5819)

AFGL 437 is a compact infrared cluster (Wynn-Williams et al. 1981; Weintraub & Kastner 1996) that is dominated by four bright sources named AFGL 437 N, S, E and W. Based on a combination of kinematic and spectroscopic distance measurements, Arquilla & Goldsmith (1984) estimated the distance of this region to be 2.0 kpc, and the total luminosity of the cluster is estimated to be $\sim 3 \times 10^4\ L_\odot$. Radio cm continuum emission was first detected from two of the sources, with most of the emission coming from source W (determined to be an H II region), with some weak emission coming from source S (Torrelles et al. 1992). In the infrared, Weintraub & Kastner (1996) found that source N could be resolved into two components, with the south-eastern source of the two, dubbed WK 34, found to be the most embedded source in the cluster, and also associated with weak radio continuum emission.

This cluster of infrared sources is at the center of a CO molecular outflow (Gómez et al. 1992; Qin et al. 2008) that is roughly oriented north-south and poorly collimated, making it difficult to accurately determine which source(s) might be driving the outflow. Weintraub & Kastner (1996) found the cluster to be surrounded by an infrared reflection nebula that has a polarization pattern centro-symmetric with respect to source WK 34, which they believe traces an outflow cavity from that source. Kumar Dewangan & Anandarao (2010) resolve a finger-shaped "green fuzzy" emission

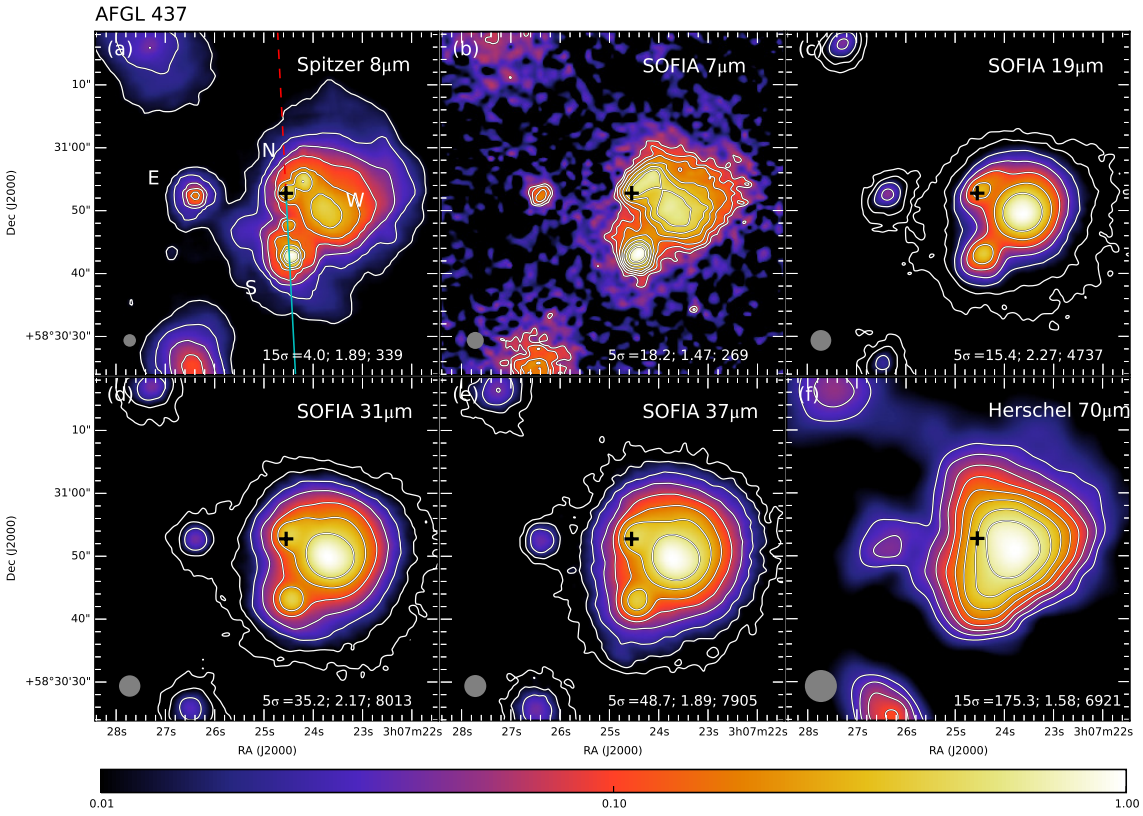

Fig. 4.2.— Multiwavelength images of AFGL 437, following format of Fig. 4.1. The location of the radio continuum source WK34 (Weintraub & Kastner 1996) is shown as a cross in all panels at R.A.(J2000) = $03^h07^m24\overset{s}{.}55$, Decl.(J2000) = $+58°30'52\overset{''}{.}76$. The outflow axis angle is from the NIR bipolar emission angle from Meakin et al. (2005), and the blue-shifted outflow direction is given by the CO observations of Gómez et al. (1992).

region extending north from WK 34 in *Spitzer* IRAC images, which they speculate is tracing H_2 emission from an outflow lobe (though such emission is not a dependable outflow tracer; see De Buizer & Vacca 2010 and Lee et al. 2013). Perhaps the most convincing evidence of an outflow from WK 34 comes from the *Hubble* NICMOS polarimetric imaging of this source (Meakin et al. 2005), which resolves a well-collimated bipolar reflection nebula that is oriented north-south and consistent with the outflow observations described above. If this is the main source of outflow, previous SED modeling of WK 34 yields an estimated source mass and luminosity to be $\sim 7\,M_{\odot}$ and $\sim 1 \times 10^3\,L_{\odot}$, respectively (Kumar Dewangan & Anandarao 2010), which is more consistent with an intermediate-mass object than a true MYSO. We will see below that the most favored ZT radiative transfer model is one with $m_* = 8\,M_{\odot}$, although higher mass cases are still allowed.

In the *SOFIA* data, we barely resolve source AFGL 437 N at $7\,\mu$m into WK 34 and its companion, but they are resolved in the *Spitzer* $8\,\mu$m data (Figure 2). We see no evidence of infrared emission to the north of WK 34 in the *SOFIA* data, which is where the green fuzzy emission has been seen. However, if the larger-scale CO outflow is being driven by WK 34, observations by Gómez et al. (1992) and Qin et al. (2008) show that the blue-shifted outflow lobe should be to the south. The expectation would be that we should see the blue-shifted outflow cavity more readily due to decreased extinction. Unfortunately, any southern outflow cavity from WK 34 cannot be discerned from the *SOFIA* data due to the resolution of the observations and the close proximity of source S to the south. However, the sub-arcsecond resolution $24.5\,\mu$m images from de Wit et al. (2009) conclusively show that there is no extended emission south of WK 34 at that wavelength (at least to within their detection limit).

Interestingly, the source with the peak infrared brightness is AFGL 437 S at the

shorter mid-infrared wavelengths, but at wavelengths longer than 19 μm the UC H II region AFGL 437 W is where the brightness peaks (see also de Wit et al. 2009), perhaps further indicating that WK 34 is not a MYSO.

IRAS 07299-1651 (a.k.a. AFGL 5234, S302, DG 121, RCW 7, G232.62+01.00)

Figure 4.3 presents our standard multiwavelength data for IRAS 07299-1651. The NIR emission from this source was shown to have a compact center with diffuse emission extended at a position angle of 305° (Walsh et al. 1999). Follow-up observations in the MIR in the N-band ($\sim$10 μm) by Walsh et al. (2001) with the ESO Max Planck-Institute 2.2-m telescope show a compact, perhaps slightly elongated source at this location. Our *Gemini* South 8-m observations at 11.7 μm at higher resolution and sensitivity show an elongated appearance resembling the NIR morphology, with a compact core and extended diffuse emission (see Figure 4.4). However, the MIR emission is not coincident with the NIR emission, and neither is coincident with the radio continuum peak of Walsh et al. (1998). The peak in emission in the *Spitzer* 8 μm image (Figure 4.3a) is coincident with the peak in the 11.7 μm *Gemini* image to within the accuracies of our astrometry ($\lesssim$0.5″)[5]. As one looks to shorter wavelengths in the *Spitzer* IRAC data, the peak moves closer and closer to the 2 μm peak location, suggesting that extinction might be playing a role. At the resolution of SOFIA, the object looks rather point-like, with a possible extension of emission to the north west seen at 31 and 37 μm (Figure 4.3d & e).

Given the extended nature of the NIR/MIR emission of this target at high angular resolution, it was deemed a good candidate for being morphologically influenced by an outflow. The hypothesis is that the radio continuum source also drives an outflow,

[5]This is different than the location of the peak seen in the N-band image of Walsh et al. 2001, which is likely in error.

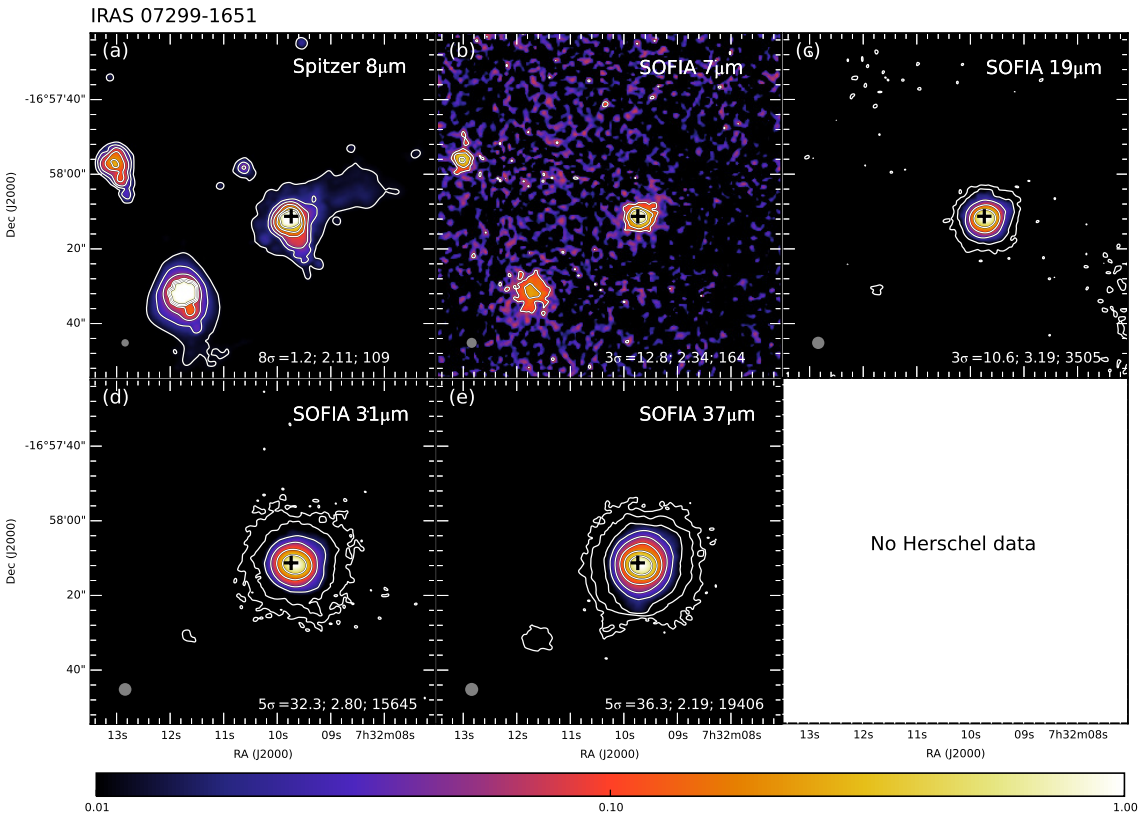

Fig. 4.3.— Multiwavelength images of IRAS 07299-1651, following format of Fig. 4.1. The black areas in panel (a) are where the sources have saturated in the IRAC image. Also in panel (a) there are extensions to the southwest of the three brightest sources, which are ghosts that should not be interpreted as real structure. The location of the radio continuum source of Walsh et al. (1998) is shown as a cross in all panels at R.A.(J2000) = $07^h32^m09\overset{s}{.}74$, Decl.(J2000) = $-16°58'11\overset{''}{.}28$. There are no outflow maps from which to discern an outflow angle or direction for this source.

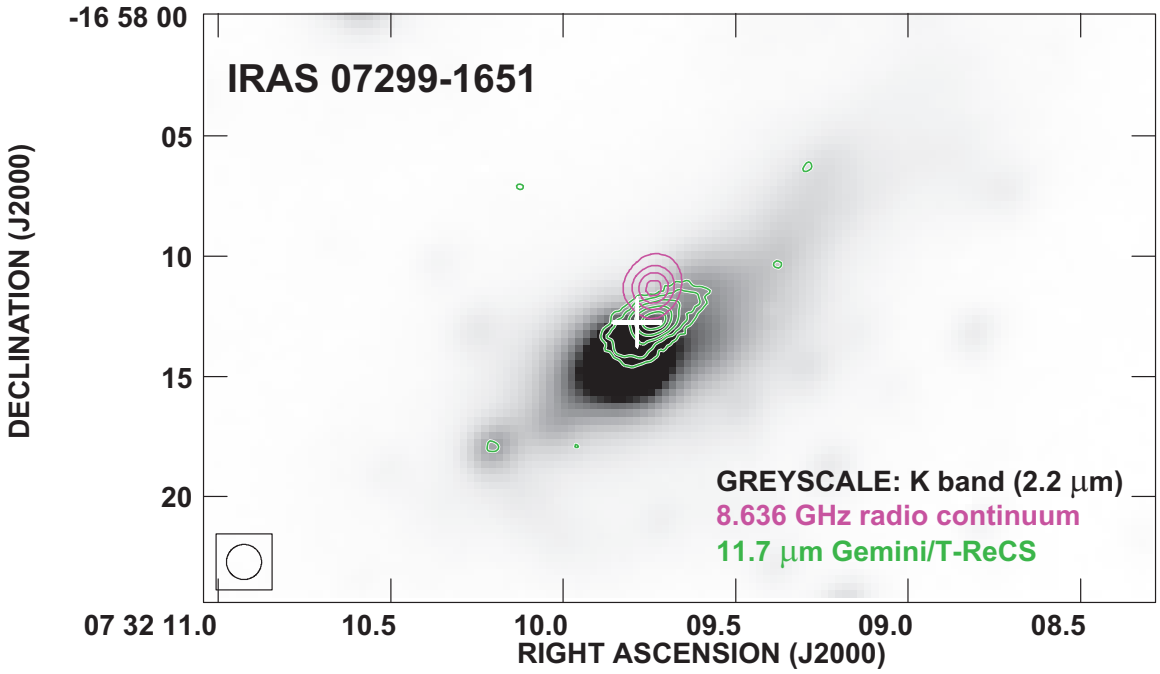

Fig. 4.4.— This image of IRAS 07299-1651 compares the 11.7um Gemini/T-ReCS image (green contours) with the near-infrared (greyscale) and radio continuum (red contours) emission, as well as methanol maser location (white cross) from Walsh et al. (1999).

and the extended MIR and NIR emission are coming from the blue-shifted outflow cavity. To date, however, there are no maps of outflows indicators of this source from which we may derive an outflow axis. Evidence of an outflow from this region does exist, including spectra that show that the ^{12}CO gas is considered to be in a "high-velocity" state (Shepherd & Churchwell 1996). Liu et al. (2010) mapped the integrated ^{13}CO emission at $\sim$1$'$ resolution, and found it to be extended parallel and perpendicular to the NIR/MIR extension on the scale of $\sim$4$'$ in each direction. No velocity maps are presented in that work, and they claim that the emission is tracing a molecular core (not outflow), from which they estimate a gas mass of 1.2×10^3 $M_\odot$.

De Buizer (2003) claims that in some cases the groupings of 6.7 GHz methanol maser spots may lie in elongated distribution that are parallel to the outflow axis for some massive young stellar objects. Fujisawa et al. (2014) show that the 6.7 GHz methanol maser spots are distributed over two groupings separated by about 60 mas with total distributed area of about 20 mas $\times$ 70 mas (or 40 AU $\times$ 120 AU, given the distance of 1.68 kpc estimated from the trigonometric parallax measurements of the 12 GHz methanol masers present in this source by Reid et al. 2009). Though there are two groups of masers, they have a velocity gradients along their shared axis of elongation and are distributed at a position angle of 340°.

G35.20-0.74 (a.k.a. IRAS 18566+0136)

The G35.20-0.74 star forming region, lying at a distance of 2.19 kpc (Zhang et al. 2009; Wu et al. 2014), was first identified as a star-forming molecular cloud through ammonia observations by Brown et al. (1982). Dent et al. (1985a) were the first to resolve the emission in this region into a molecular ridge running northwest to southeast seen in CS(2-1), with a nearly perpendicular outflow seen in CO (1-0). Dent

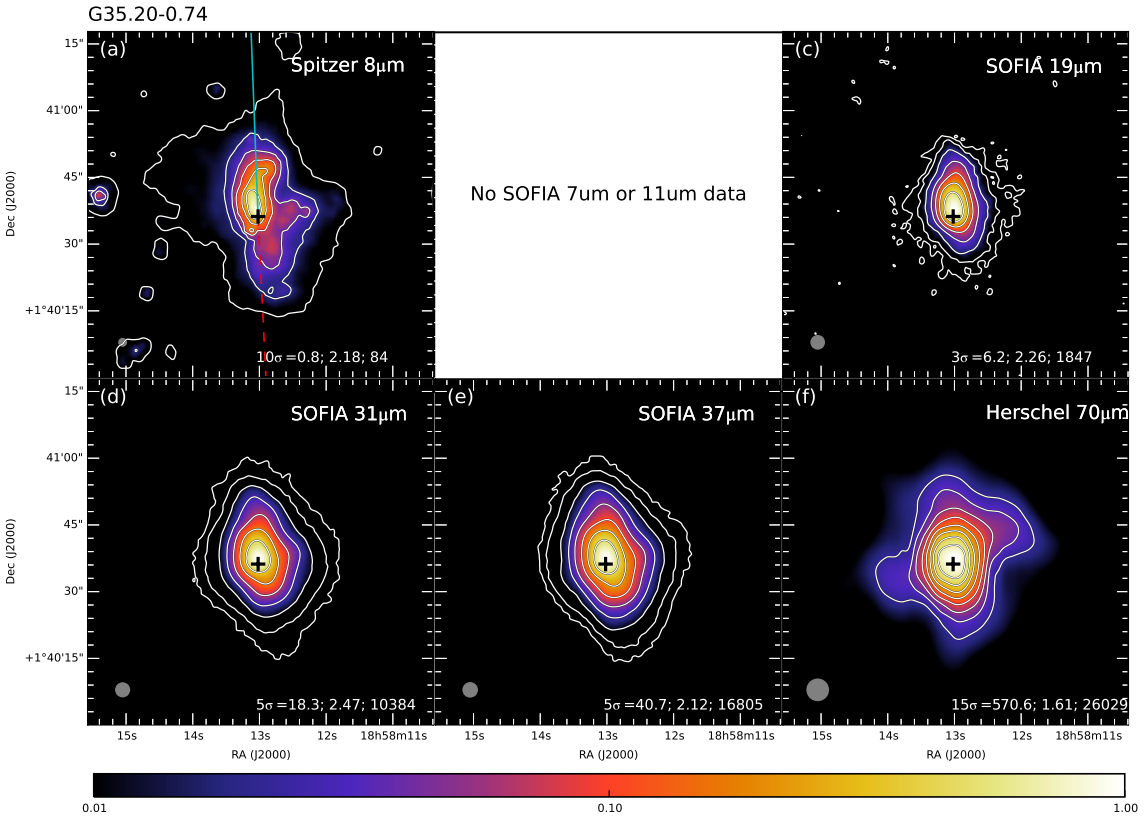

Fig. 4.5.— Multiwavelength images of G35.20-0.74, following format of Fig. 4.1. The location of radio continuum source 7 from Gibb et al. (2003) is shown as a cross in all panels at R.A.(J2000) = $18^h58^m13\overset{s}{.}02$, Decl.(J2000) = $+01°40'36\overset{''}{.}2$. In panel (a) the axis of the radio jet is shown (Gibb et al. 2003); blue-shifted direction is derived from CO observations of Birks et al. (2006).

et al. (1985b) found the NIR emission to be coming from an elongated north-south distribution. Heaton & Little (1988) observed this region in cm radio continuum and were able to resolve three compact sources arranged north-south, and concluded that the central source was likely an UC H II region while the north and south sources had spectral indices consistent with free-free emission from a collimated, ionized, bipolar jet. The orientation of this jet (p.a.$\sim$2°) is appears to be different from that of the CO outflow (p.a.$\sim$58°), which has been interpreted either as evidence for precession of the ionized jet (Heaton & Little 1988; Little et al. 1998; Sánchez-Monge et al. 2014; Beltrán et al. 2016), or multiple outflows from multiple sources (Gibb et al. 2003; Birks et al. 2006).

G35.20-0.74 was the first source observed among those in the SOMA survey sample, and were presented by Zhang et al. (2013b). These data helped define the infrared SED of the source, which implied an isotropic luminosity of $3.3 \times 10^4\ L_\odot$. However, modeling the emission (with early versions of the ZT radiative transfer models that had fixed outflow cavity opening angles, ZTM13), including 10 to 40 μm intensity profiles, as being due to a single protostar driving an outflow along the N-S axis, Zhang et al. (2013b) derived a true bolometric luminosity in the range $\sim (0.7 - 2.2) \times 10^5\ L_\odot$, i.e., after correcting for foreground extinction and anisotropic beaming. Note, these estimates were based on a limited, ad hoc exploration of model parameter space. They correspond to protostellar masses in the range $m_* \simeq 20$ to $34 M_\odot$ accreting at rates $\dot{m}_* \sim 10^{-4} M_\odot \mathrm{yr}^{-1}$ from cores with initial mass $M_c = 240 M_\odot$ in clump environments with $\Sigma_{\rm cl} = 0.4$ to $1.0\ \mathrm{g\ cm^{-2}}$ and with foreground extinctions from $A_V = 0$ to 15 mag.

Such an interpretation of outflow orientation is broadly consistent with the subarcsecond *VLA* observations of this field by Gibb et al. (2003) at cm wavelengths,

which show that the three concentrations of radio continuum emission from Heaton & Little (1988) break up into eleven individual knots all lying along a north-south position angle. The central source itself is resolved into two sources separated by 0.8″. The northern of the two central sources (source 7) has a spectral index typical of a UC H II region and was claimed by Gibb et al. to be the most likely driving source of the radio jet. Beltrán et al. (2016) have also identified this source, a component of a binary system they refer to as 8a, as the likely driving source. To be able to ionize the UC H II region, Beltrán et al. (2016) estimate that it have the H-ionizing luminosity of at least that of a spectral type B1 zero age main sequence (ZAMS) star. This radio source is coincident with Core B of Sánchez-Monge et al. (2014) seen at 870 μm with *ALMA* (which is the same as source MM1b from the 880 μm *SMA* observations of Qiu et al. 2013), who estimate the core mass in this vicinity to be 18 $M_{\odot}$. We will return to a discussion of the nature of the driving source of G35.20-0.74, below, following the results of our new SED model fitting.

The scenario of north-south directed protostellar outflows is also supported by MIR imaging. High-resolution MIR images of this region by De Buizer (2006) showed that the emission is peaked to the north of radio source 7 and elongated in a north-south orientation, very similar to what was seen in the NIR for the first time by Dent et al. (1985b). A weak extended area of emission was seen to the south, and can be seen in the much more sensitive *Spitzer* 8 μm data (Figure 4.5a). The outflow/jet is blue-shifted to the north (e.g., Wu et al. 2005; Gibb et al. 2003) and is likely to be the reason why we see emission predominantly from that side of source 7 at shorter MIR wavelengths. However, as discussed by Zhang et al. (2013b), the longer wavelength *SOFIA* images (Figure 4.5) are able to detect emission also from the southern, far-facing outflow cavity.

Finally, we note that for G35.20-0.74 we could not derive an accurate background subtracted flux density for the Gemini data with the fixed aperture size due to the small size of the images. Thus in this case we estimate a background subtracted flux density derived from a smaller aperture size.

G45.47+0.05

G45.47+0.05 was first detected as an UC H II region in the radio continuum at 6 cm (Wood & Churchwell 1989) and lies at a distance of 8.4 kpc, based upon the trigonometric parallax measurements of masers in nearby G45.45+0.05 (Wu et al. 2014). G45.47+0.05 has a relatively high luminosity ($\sim 10^6\ L_\odot$) (Hernandez-Hernandez et al. 2014) testifying to its nature as a MYSO. The UC H II region is also coincident with other MYSO tracers like hydroxyl and water masers (Forster and Caswell 1989).

There is some debate as to the nature of the outflow and driving source in this region. *Spitzer* IRAC images show a source that is a bright "green fuzzy," and consequently was categorized as being a "likely MYSO outflow candidate" in the work of Cyganowski et al. (2008). However, Lee et al. (2013) find no H_2 emission component to the green fuzzy, and classify the NIR emission as a reflection nebula (possibly from an outflow cavity). This region was mapped in HCO^+(1-0), an potential outflow indicator, by Wilner et al. (1996), who showed that the emission is oriented roughly north-south (p.a.$\sim$3°) and centered on the location of the UC H II region, with blue-shifted emission to the north. They also mapped the area in another outflow indicator, SiO(2-1), and find emission at the location of the UC H II region with a single blue shifted component lying $\sim$14″ to the northwest at a position angle of about -25° (see Figure 4.6). However, Ortega et al. (2012) mapped the area in ^{12}CO(3-2) and found the red and blue-shifted peaks to be oriented at an angle of $\sim$15°, but with an axis

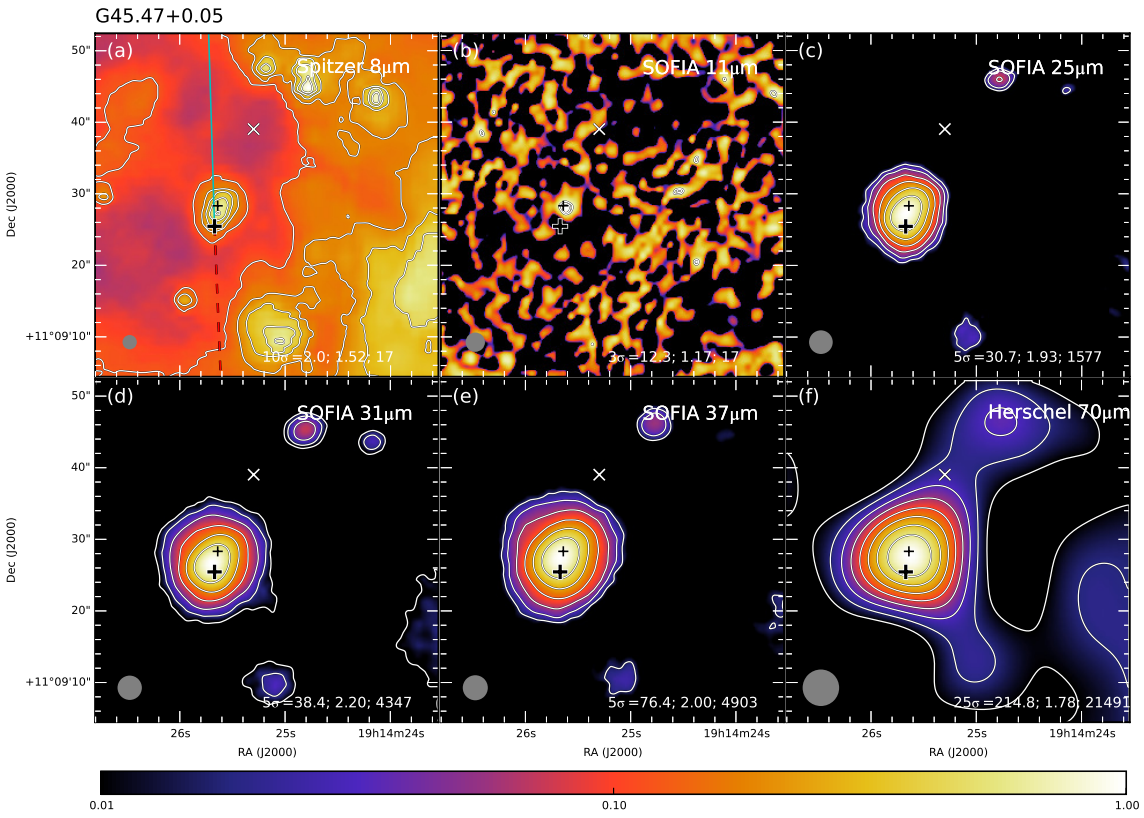

Fig. 4.6.— Multiwavelength images of G45.47+0.05, following format of Fig. 4.1. The location of the 6 cm radio continuum peak of the UC H II region of White et al. (2005) is shown as a large cross in all panels at R.A.(J2000) = $19^h14^m25\overset{s}{.}67$, Decl.(J2000) = $+11°09'25\overset{''}{.}45$. The location of the 2MASS source J19142564+1109283 is shown by the small cross. The location of the peak of the blue-shifted SiO(2-1) emission of Wilner et al. (1996) is shown as an X. The outflow axis angle and the blue-shifted outflow direction are given by the HCO^+ observations of Wilner et al. (1996).

offset $\sim$10″ southeast of the UC H II region.

The observations of De Buizer et al. (2005) first showed that the MIR emission in this region is offset $\sim$2.5″ northwest of the radio continuum peak. *Spitzer* IRAC and *2MASS* data confirm this offset of the peak of the NIR/MIR emission, and show a similar extended morphology, with the axis of elongation oriented at a position angle of about -30° and pointing radially away from the radio continuum peak. The *SOFIA* data (Figure 4.6) show this same morphology at wavelengths greater than 19 μm (the 11 μm *SOFIA* observation is a shallow integration that only barely detects the peak emission from the source). We also present high angular resolution *Gemini* T-ReCS imaging at 11.7 and 18.3 μm in Figure 4.7, which also shows this offset and elongation. We note that the elongated morphology persists out to even longer wavelengths, as seen in both the *Herschel* 70 μm data, as well as *JCMT* SCUBA images at 850 μm (Hernandez-Hernandez et al. 2014).

There are two main scenarios to describe the outflow and driving source in this region. The first is that the massive star(s) powering the UC H II region is(are) also driving a roughly north-south outflow, with the CS, HCO^+, and SiO emission tracing different parts of the wide-angled outflow. The NIR and MIR emission are emerging from the blue-shifted outflow cavity. The slight offset between the UC H II region peak and the NIR/MIR emission would be due to the high extinction towards the UC H II region itself. The high spatial resolution adaptive optics imaging in the NIR of this source (Paron et al. 2013) show it to be a triangular-shaped emission region, with its southern apex pointing directly back at the UC H II region location. The opening angle of this outflow cone is $\sim$50°, with its axis of symmetry pointing towards the blue-shifted SiO emission, hinting that this might be a cone-shaped outflow cavity/reflection nebula emanating from the UC H II region. Furthermore, while the

SOFIA 11 μm emission is peaked close to the MIR and NIR peaks seen by *Spitzer* and *2MASS*, the peak of the longer wavelength MIR emission does peak closer to the UC H II region peak, as would be expected in this scenario. It is not clear that we are detecting any additional emission from the red-shifted outflow cavity, even at the longest *SOFIA* wavelengths.

The second scenario is that the outflow is coming from a NIR star at the western apex of the triangular-shaped NIR emitting region seen in the adaptive optics images of Paron et al. (2013). They dub this source 2MASS J19142564+1109283 (see Figure 4.6a), which is actually the name of the entire NIR emitting region (*2MASS* did not have the resolution to separate this stellar source from the rest of the extended emission). In this scenario, the outflow cone from 2MASS J19142564+1109283 would have a much wider opening angle of about $\sim$90° and have an axis of symmetry that points towards the blue-shifted ^{12}CO(3-2) peak seen by Ortega et al. (2012). This scenario is not favored here because it does not explain the location of the southern red-shifted ^{12}CO outflow peak which would be at an angle $\sim$80° from the outflow axis, nor does it explain the roughly north-south outflow emission seen in HCO^+(1-0) and SiO(2-1).

Whether the driving source is a stellar object at the center of the UC H II region or 2MASS J19142564+1109283, it appears that the MIR emission observed in the region is coming from a blue-shifted outflow cavity.

IRAS 20126+4104 (a.k.a. G078.12+03.64)

At a distance of 1.64 kpc (Moscadelli et al. 2011) in the Cygnus-X star-forming region, IRAS 20116+4104, along with G35.20-0.74, could be considered a prototypical example of a MYSO with an outflow, and consequently, there have been numerous

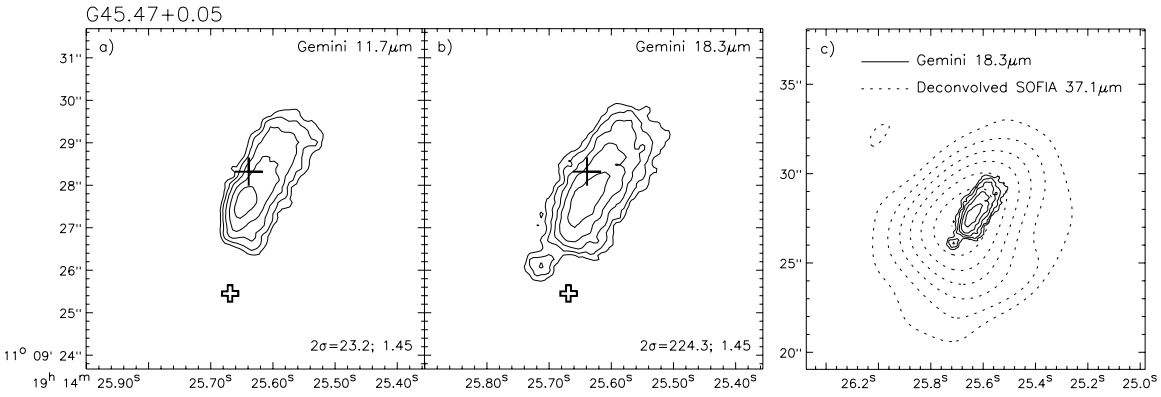

Fig. 4.7.— Sub-arcsecond resolution MIR images of G45.47+0.05 from *Gemini* T-ReCS. Symbols and annotation are the same as in Figure 4.6.

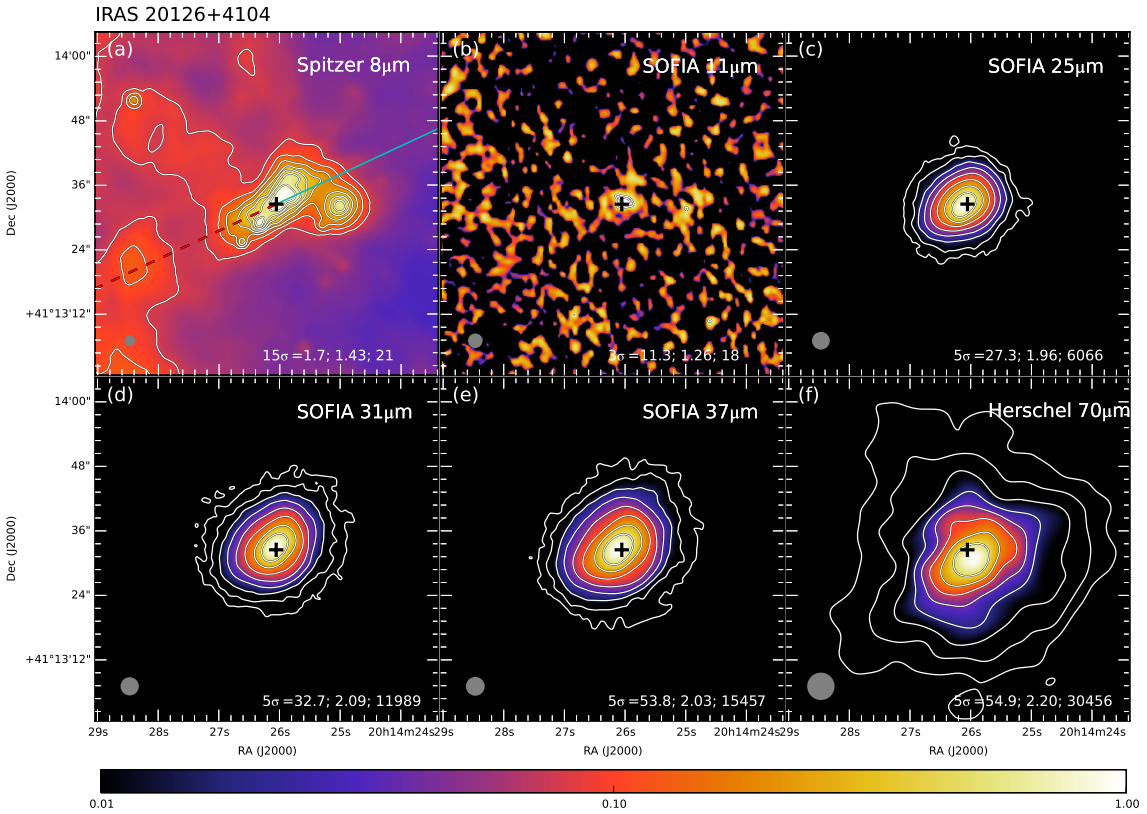

Fig. 4.8.— Multiwavelength images of IRAS 20126+4104, following format of Fig. 4.1. The nominal location of protostar, derived from the model fit to the proper motions of the water masers from Moscadelli et al. (2011), is shown as a large cross in all panels at R.A.(J2000) = $20^h14^m26\overset{s}{.}05$, Decl.(J2000) = $+41°13'32\overset{''}{.}48$. The outflow axis angle and the blue-shifted outflow direction are given by the HCO^+ observations of Cesaroni et al. (1999).

studies directed toward this object. Observations suggest a luminosity of $1.3 \times 10^4\,L_\odot$ with a central protostar having an estimated mass of 7 to 12 $M_\odot$ (Cesaroni et al. 1997; Keto & Zhang 2010; Johnston et al. 2011). This source is surrounded by a resolved accretion disk, believed to be undergoing Keplerian rotation (Cesaroni et al. 1997; 1999; 2005) at a position angle of $\sim$53°. Though this source appears to be a MYSO, it might be too embedded or young to have produced an UC H II region; radio continuum emission observations at cm wavelengths show that the emission components near the center of the outflow are consistent with free-free emission from ionized gas in an outflow. The location of the driving source of the outflow was determined through proper motion studies of water masers, which seem to be moving away from a common location (Moscadelli et al. 2011). This location is coincident with the center of the accretion disk as delineated by CH_3CN(12-11) emission from Cesaroni et al. (1999).

IRAS 20126+4104 has a well-collimated bipolar molecular outflow oriented at an angle roughly perpendicular to the disk (p.a.$\sim$115°) with an inclination angle of the outflow axis to the plane of the sky of only $\sim$10° (Zhang et al. 1999; Su et al. 2007; Hofner et al. 2007; Moscadelli et el. 2011). De Buizer (2007) made the first suggestion that the extended MIR emission observed toward this source might be related to the outflow.

At wavelengths greater than 19 μm, *SOFIA* data (Figure 4.8) show an elongated morphology at an angle (p.a.$\sim$125°) similar to that of the outflow (the 11 μm *SOFIA* observation is a shallow integration that only barely detects the peak emission from the source). Even the *Herschel* 70 μm data show an elongation along this outflow axis direction. The location of the driving source from Moscadelli et al. (2011) is coincident with the MIR/FIR peak (to within the astrometric accuracy), and the

amount of extended emission seen to the NW of this peak is comparable to that seen to the southeast. This might not be that surprising since the outflow is oriented almost in the plane of the sky, and consequently there should be little bias of emission from just the blue-shifted lobe.

Cepheus A

Cep A contains a massive bipolar molecular outflow primarily aligned east-west that was initially identified by Rodriguez et al. (1980), however at higher spatial resolutions the outflow morphology is quite complex. The central $\sim 2'$ of the outflow appears to be dominated by components aligned NE-SW (Bally & Lane 1990; Torrelles et al. 1993; Narayanan & Walker 1996; Gómez et al. 1999; Zapata et al. 2013). This central region contains a compact, extremely high-velocity CO outflow (Narayanan & Walker 1996) with an axis at a position angle of $\sim 50^{\circ}$ that is believed to trace a younger component than the rest of the outflow (Cunningham et al. 2009). This central outflow component appears to have an axis close to the plane of the sky but with blue-shifted emission to the NE (Gómez et al. 1999; Zapata et al. 2013). At NIR wavelengths the region displays an extremely bright reflection nebula (Cunningham et al. 2009), almost wholly contained within this blue-shifted outflow cavity.

At the center of this outflow is a cluster of radio sources, and there is confusion as to which source(s) might be driving the outflow(s) (Zapata et al. 2013). One of the main candidates for driving the outflow, and the brightest radio continuum source in the region, is HW 2 (Hughes & Wouterloot 1984). It has a luminosity of about $10^4\ L_{\odot}$ (Garay et al. 1996), suggesting it is a B0.5 star approaching 20 $M_{\odot}$, given a distance to the source of 700 pc based on parallax measurements of 12 GHz methanol masers in the region (Moscadelli et al. 2009) and of radio source HW 9 (Dzib et al.

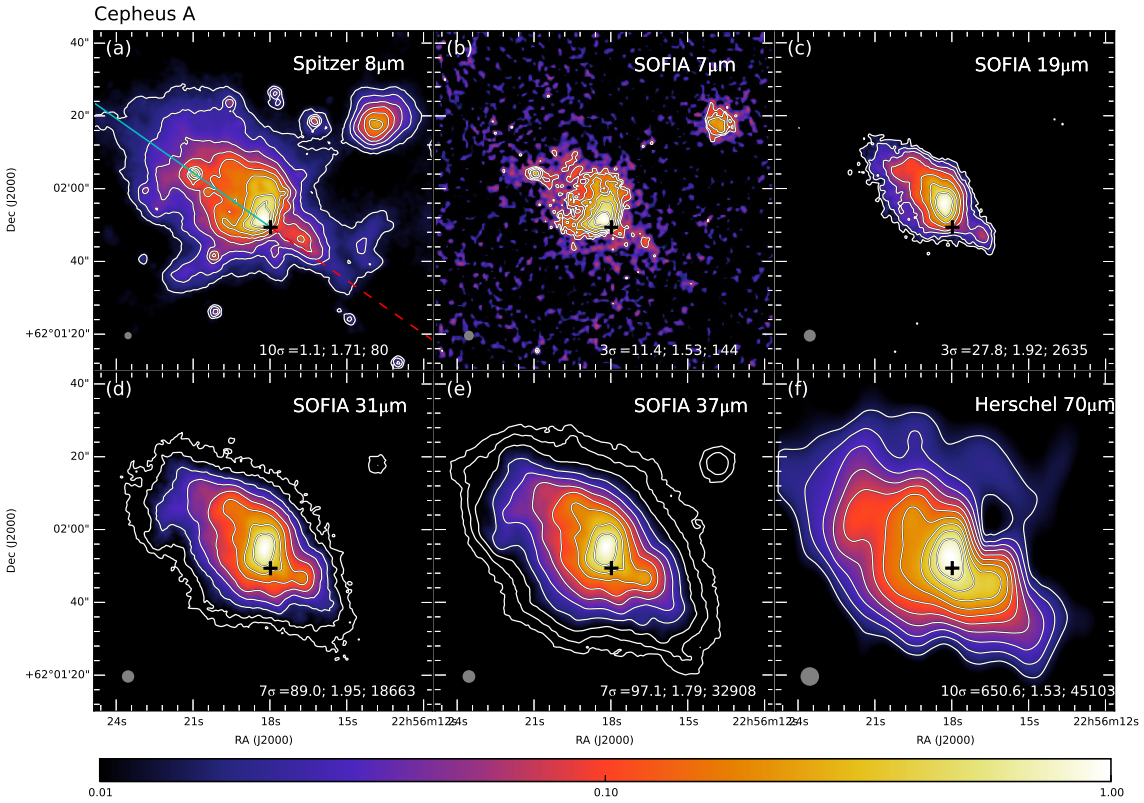

Fig. 4.9.— Multiwavelength images of Cepheus A, following format of Fig. 4.1. The white cross in each panel shows the location of radio continuum source HW 2 at R.A.(J2000) = $22^h56^m17^s.98$, Decl.(J2000) = $+62°01'49''.39$. The outflow axis angle and the blue-shifted outflow direction are given by the HCO^+ observations of Gómez et al. (1999).

2011). HW 2 has not been detected at NIR wavelengths (Casement & McLean 1996; Cunningham et al. 2009; Jones et al. 2014), nor in the MIR (De Buizer et al. 2005; de Wit et al. 2009; also Cunningham et al. 2009, however the absolute astrometry of their MIR images, and hence placement of radio sources with respect to the MIR sources, appear to be off by over 6″.)

The estimated extinction to the region around HW 2 is A_V ∼300–1000 magnitudes (Goetz et al. 1998; Cunningham et al. 2009), and therefore it is not surprising it is not directly detected in the NIR, MIR, or in our *SOFIA* data (Figure 4.9). However, it does appear that the contour peak shifts towards this location in the 70 μm *Herschel* data (Figure 4.9f).

At 7 μm the emission seen by *SOFIA* corresponds well to the NIR reflection nebula and blue-shifted outflow cavity. As one goes to longer *SOFIA* wavelengths, we begin to see increasingly brighter emission to the SW, which corresponds to the direction of the red-shifted outflow. We suggest that we are beginning to penetrate the higher extinction towards this region and the emission we are seeing at wavelengths >30 μm is coming from the red-shifted outflow/outflow cavity.

NGC 7538 IRS 9

NGC 7538 is an optically visible H II region (Fich & Blitz 1984) located at a distance of 2.65 kpc, as determined from trigonometric parallax measurements (Moscadelli et al. 2009). Infrared observations of this region by Wynn-Williams et al. (1974) and Werner et al. (1979) led to the identification of multiple discrete sources in the vicinity of the optical nebula, which were named IRS 1 through 11. The source IRS 9 lies ∼2′ to the SE of the prominent and well-studied IRS 1 region. It powers its own reflection nebula, and has a total luminosity of about 3.5×10^4 $L_\odot$ (Sandell et al.

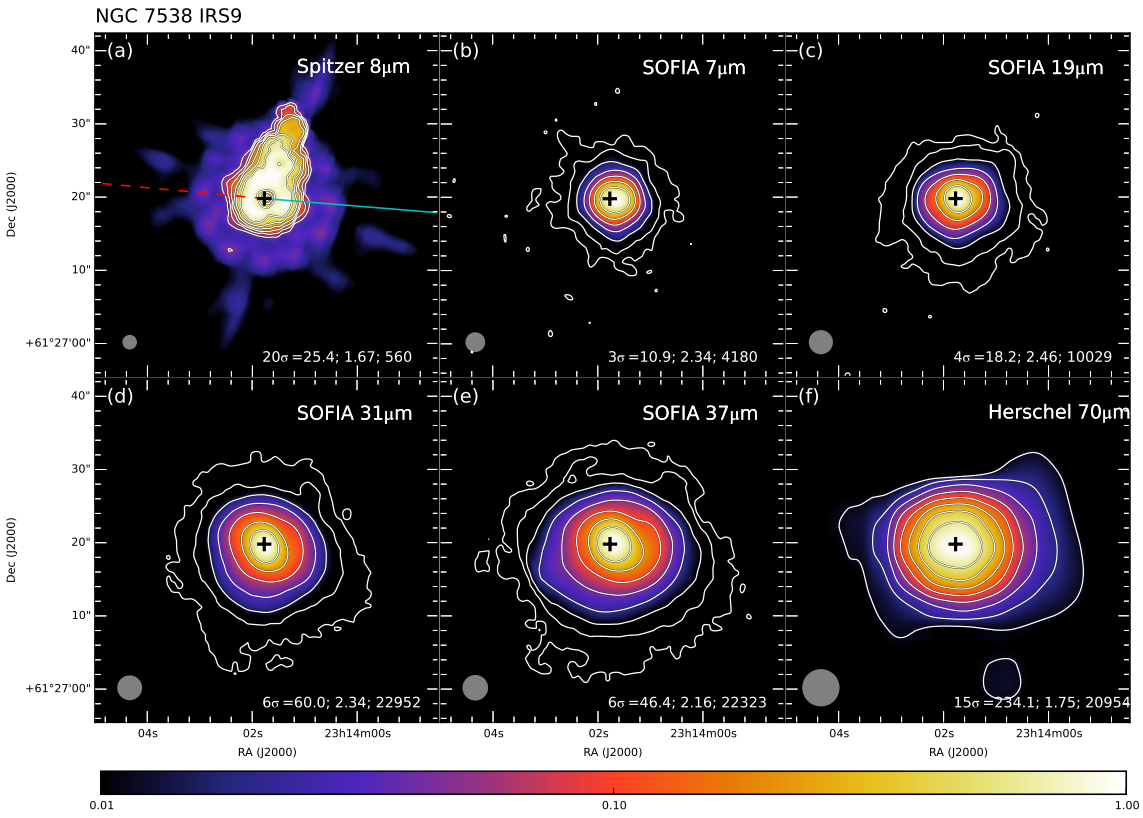

Fig. 4.10.— Multiwavelength images of NGC 7538 IRS9, following format of Fig. 4.1. The black areas in panel (a) are where the source has saturated in the IRAC image. The extension to the northwest in panel (a) is a ghost, and not a real structure. The location of the 3.6 cm radio continuum peak from Sandell et al. (2005) is shown as a large cross in all panels at R.A.(J2000) = $23^h14^m01\overset{s}{.}77$, Decl.(J2000) = $+61°27'19\overset{''}{.}8$. The outflow axis angle and the blue-shifted outflow direction are given by the HCO^+ observations of Sandell et al. (2005).

2005, corrected to the distance from Moscadelli et al. 2009), which is the equivalent of a B0.5 ZAMS star.

Though IRS 9 has the luminosity of a typical MYSO, it has very weak radio continuum emission. Sandell et al. (2005) found that the object has a flat radio spectrum consistent with free-free emission from a collimated, ionized jet. They also disentangled the rather complex structures seen in various outflow tracers into distinct outflows from three different sources, suggesting a cluster associated with IRS 9. The outflow associated most closely with the position of IRS 9 itself was measured to have a very high-velocity (Mitchell & Hasegawa 1991), leading to the suggestion that we might be observing the system nearly face-on (Barentine & Lacy 2012). The high spatial resolution ($\sim$6″) HCO^+ maps of Sandell et al. (2005) show that IRS 9 indeed drives a bipolar, extremely high-velocity outflow approximately oriented E-W (p.a.$\sim$85°) that is inclined by only $\sim$20° to the line of sight. Given this orientation, the outflow lobes seen in HCO^+ do not extend very far from IRS 9 in projection ($\sim$14″), but the blue shifted outflow lobe is clearly to the west of IRS 9, and the red-shifted outflow lobe to the east (Figure 4.10a).

Our *SOFIA* data for this source look rather point-like at 7 μm, however beginning at 19 μm the source begins to show signs of being elongated in an E-W orientation, similar to the outflow axis (Figure 4.10). The *Herschel* 70 μm data also show a more prominent east-west elongation with the a larger extension to the west in the direction of the blue-shifted outflow cavity.

4.4.2 General Results from the SOFIA Imaging

G35.20-0.74 was the first source observed for this survey, and it has been the subject of its own paper (Zhang et al. 2013b) describing how the outflow from this massive

young stellar object is likely to directly influence the morphology we see at infrared wavelengths. The hypothesis is that massive stars form in dense cores surrounded by dense accretion disks, creating extinctions (A_V) in the range of 100s to 1000s of magnitudes along the line of sight to the central accreting star. Outflows are a consequence of accretion and can effectively clear out material surrounding the core along the outflow axis direction, significantly decreasing extinction in those areas of the core. As a consequence, radiation will readily leave the system through outflow cavities, and if the orientation of the outflow to our line of sight is favorable, we can detect infrared emission from these systems via such cavities. Of course, because of extinction, the blue-shifted outflow cavities should be easiest to see. However as one observes these systems at longer wavelengths, it should be possible to begin to pick up emission from the red-shifted outflow cavities (though this may depend on the inclination angles of the outflow axis to the line of sight and amount of overall extinction present toward the region). The previous subsection discussed the observational evidence that indicates that each of the regions in our sample contains a high-mass or intermediate-mass young stellar object that is likely to be driving an outflow. How wide-spread is the evidence in our sample that MYSOs are morphologically influenced at MIR wavelengths by the presence of outflow cavities?

Of the eight sources in our sample, only AFGL 437 (which is likely the only intermediate mass object in the survey and in a crowded region of emission) does not show clear signs of extended MIR/FIR emission. Of the remaining seven sources, all are extended in their MIR/FIR emission at a position angle comparable to the orientation of their outflow axes with the exception of IRAS 07299-1651, which can be considered inconclusive because no outflow maps exist for this source. However, since this source displays similar behavior in morphology as a function of wavelength as the rest of the

sources in the sample, we predict that the outflow in this region is at a position angle of $\sim$300°, with a blue-shifted lobe to the SE of the radio continuum source (assuming it is the driving source). For two of the sources in the sample it appears that their MIR emission is extended to one side of the central stellar source: AFGL 4029 and G45.47+0.05. In both cases, this extended MIR/FIR emission is on the blue-shifted side of the source driving the outflow. Three sources have the appearance of being extended to one side of the source driving the outflow at shorter wavelengths and more symmetric at longer wavelengths: G35.20-0.74, IRAS 20126+4104, and Cepheus A. In all three cases, the emission at shorter wavelengths comes predominantly from the blue-shifted side of the outflow. At longer wavelength it appears we begin to detect emission from the expected locations of the red-shifted outflow cavities/lobes. The remaining source is NGC 7538 IRS 9, which, perhaps because of an almost pole-on outflow orientation, we only see modest amounts of extended MIR/FIR emission. However, the little MIR/FIR extension that is seen is at the angle of the projected outflow axis. Somewhat surprising, however, is that the elongated morpholgies seen at 7–40 μm are also present in most cases in the *Herschel* 70 μm images, showing that outflows can impact the morphology of MYSOs even out to such FIR wavelengths.

Thus the first eight sources of the SOMA Star Formation survey convincingly show that the MIR morphology of MYSOs appear to be shaped by their outflow cavities. The generally bipolar nature of these outflows is a generic prediction of Core Accretion models. MIR to FIR morphologies can thus give important clues about the orientation of outflows from deeply embedded intermediate and high-mass protostars.

4.4.3 Results of SED Model Fitting

For G35.20-0.74, Zhang et al. (2013b) modeled both the SED and multiwavelength flux profiles along the outflow cavity axis to derive more precise constraints on protostellar properties. We intend to carry out such an analysis for our eight source sample in a future paper. However, below we first focus on simple SED model fits to the sample. We also compare the results derived from the ZT model grid with those from the Robitaille et al. grid.

Figure 4.11 shows the SEDs of the eight sources that have been discussed in this paper. The figure illustrates the effects of using fixed or variable apertures, as well as the effect of background subtraction. Our fiducial method is that with fixed aperture and with background subtraction carried out. This tends to have moderately larger fluxes at shorter wavelengths than the variable aperture SED. However, the $\leq 8\,\mu$m flux is in any case treated as an upper limit in the SED model fitting, given concerns of PAH and transiently-heated small grain effects that are not well-treated in the models. Apart from IRAS 07299, which lacks *Herchel* data, all the SEDs are well characterized: in particular the peaks are well covered by the combination of *SOFIA* FORCAST and *Herschel* PACS & SPIRE data.

We note that in the case of G35.20-0.74, our derived fiducial SED differs modestly ($\lesssim 20\%$) from that estimated by Zhang et al. (2013b). These differences are due to our use of a fixed aperture size and geometry. Also our SED now replaces *IRAS* fluxes with those measured by *Herschel*.

Figure 4.12 shows the results of fitting the ZT protostellar radiative transfer models to the fixed aperture, background-subtracted SEDs. Note that the data at $\lesssim 8\,\mu$m are treated as upper limits given that PAH emission and transiently-heated small grain emission are not well treated in the models.

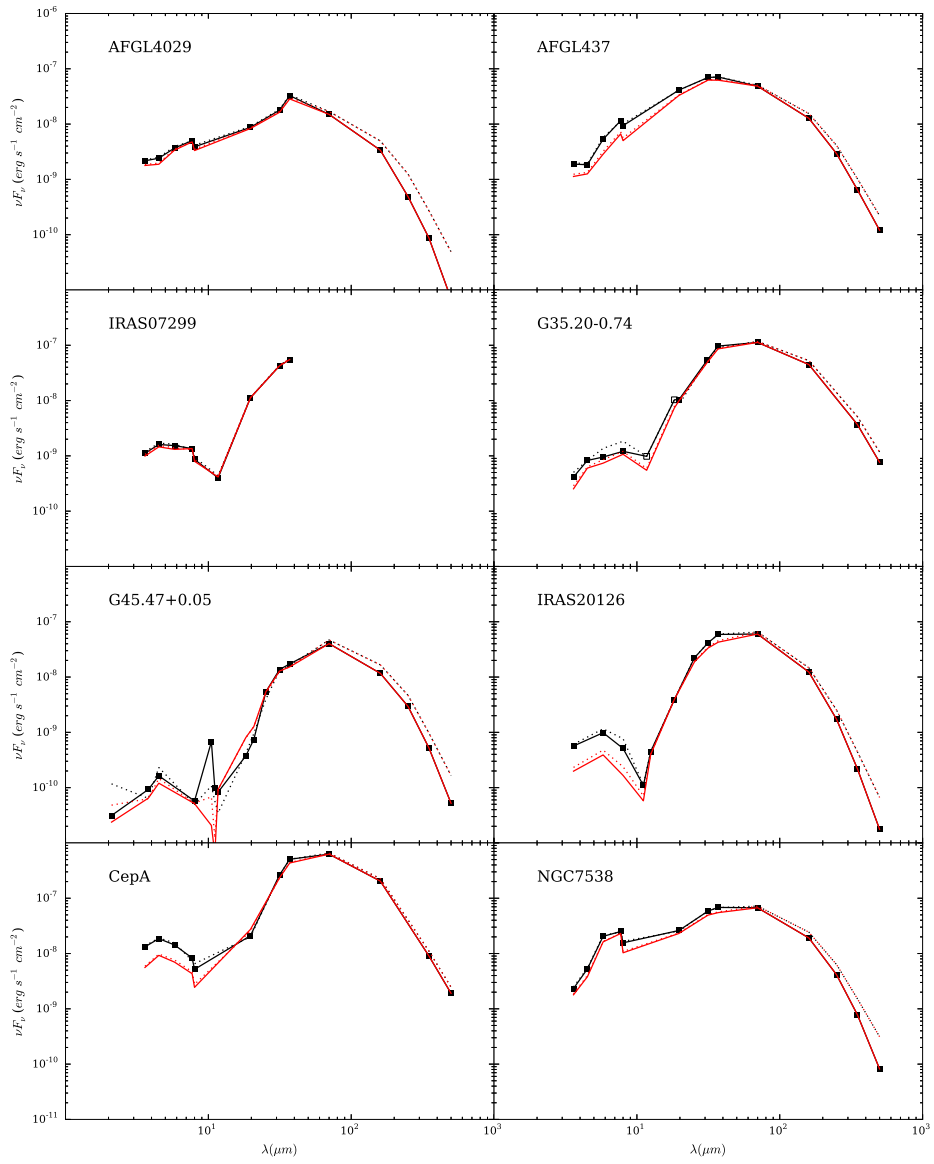

Fig. 4.11.— SEDs of the first eight sources of the SOMA Survey. Total fluxes with no background subtraction applied are shown by dotted lines. The fixed aperture case is black dotted; the variable aperture (at $< 70\,\mu$m) case is red dotted. The background subtracted SEDs are shown by solid lines: black for fixed aperture (the fiducial case); red for variable aperture. Black solid squares indicate the actual measured values that sample the fiducial SED. Note the open squares in the *Gemini* data of G35.20-0.74 are values where no background subtraction could be done given the limited field of view of the observations.

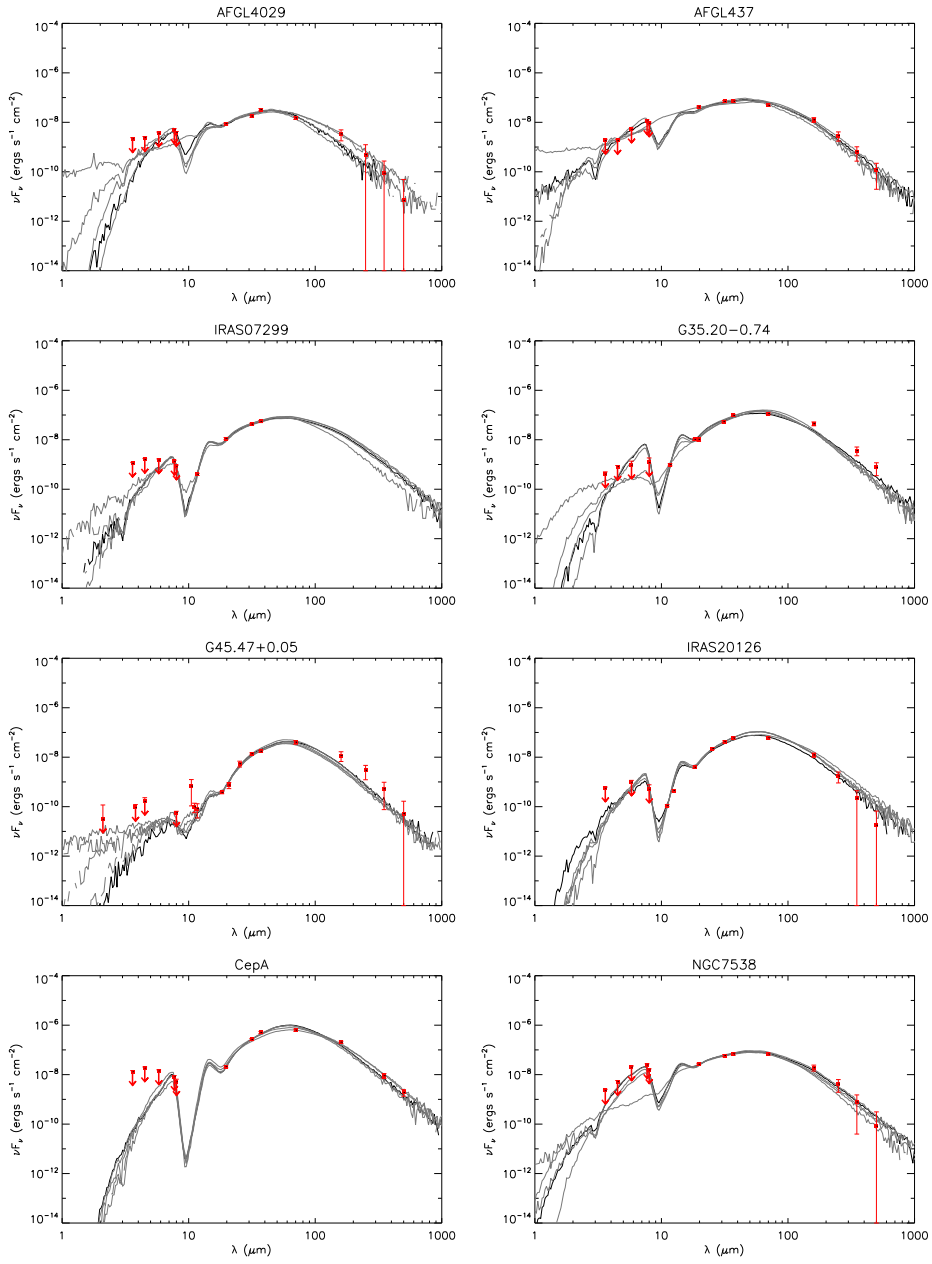

Fig. 4.12.— Protostar model fitting to the fixed aperture, background-subtracted SED data using the ZT model grid. For each source, the best fit model is shown with a solid black line and the next four best models are shown with solid gray lines. Flux values are those from Table 4.2. Note that the data at $\lesssim 8\,\mu$m are treated as upper limits (see text). The resulting model parameter results are listed in Table 4.3.

Table 4.3. Parameters of the Five Best Fitted Models of Zhang & Tan and Robitaille

Source	Zhang & Tan models										Robitaille et al. models							
	χ^2/N	M_c ($M_\odot$)	Σ_{cl} (g cm^{-2})	m_* ($M_\odot$)	θ_{view} (deg)	A_V (mag)	M_{env} ($M_\odot$)	$\theta_{w,esc}$ (deg)	$\dot{M}_{disk}$ ($M_\odot$/yr)	L_{bol} ($L_\odot$)	χ^2/N	m_* ($M_\odot$)	θ_{view} (deg)	A_V (mag)	$\theta_{w,esc}$ (deg)	$\dot{M}_{env}$ ($M_\odot$/yr)	$\dot{M}_{disk}$ ($M_\odot$/yr)	L_{bol} ($L_\odot$)
AFGL4029	3.4	30	1.0	12	62	0.1	6	53	1.9×10^{-4}	4.2×10^{4}	1.8	13	18	55.2	42	1.7×10^{-4}	4.4×10^{-7}	1.2×10^{4}
	3.4	30	3.2	16	65	93.3	1	56	5.1×10^{-4}	1.1×10^{5}	1.8	13	32	53.8	42	1.7×10^{-4}	4.4×10^{-7}	1.2×10^{4}
	4.1	120	0.1	24	89	43.3	42	57	6.3×10^{-5}	7.5×10^{4}	1.8	12	18	55.7	41	2.9×10^{-4}	2.3×10^{-6}	1.2×10^{4}
	4.2	50	0.3	12	51	2.0	22	46	1.0×10^{-4}	2.5×10^{4}	1.8	13	41	64.9	45	1.7×10^{-4}	1.5×10^{-6}	1.4×10^{4}
	4.8	40	0.3	8	39	9.3	22	36	9.2×10^{-5}	1.2×10^{4}	1.8	13	18	66.6	45	1.7×10^{-4}	1.5×10^{-6}	1.4×10^{4}
AFGL437	2.6	50	3.2	8	29	0.1	35	25	6.0×10^{-4}	1.7×10^{4}	0.8	15	87	15.7	35	2.9×10^{-4}	9.7×10^{-6}	2.3×10^{4}
	3.9	40	3.2	12	39	46.4	18	35	6.5×10^{-4}	5.1×10^{4}	0.8	15	81	16.3	35	2.9×10^{-4}	9.7×10^{-6}	2.3×10^{4}
	4.8	120	0.3	24	55	5.0	57	47	1.8×10^{-4}	9.5×10^{4}	1.0	16	76	12.9	17	1.8×10^{-4}	2.9×10^{-4}	2.0×10^{4}
	4.8	50	1.0	12	39	23.1	26	36	2.8×10^{-4}	4.7×10^{4}	1.1	14	81	10.0	30	2.9×10^{-4}	3.0×10^{-7}	1.9×10^{4}
	5.2	240	0.1	12	39	0.1	211	19	8.5×10^{-5}	2.1×10^{4}	1.1	16	87	10.0	24	3.1×10^{-4}	1.8×10^{-7}	2.3×10^{4}
IRAS07299	1.4	60	0.3	12	77	9.3	32	40	1.2×10^{-4}	2.8×10^{4}	1.1	18	76	13.2	10	4.3×10^{-4}	...	8.3×10^{3}
	3.0	60	0.3	8	44	3.3	43	28	1.1×10^{-4}	1.2×10^{4}	1.1	17	76	10.0	6	4.0×10^{-4}	...	6.6×10^{3}
	3.6	240	0.1	8	86	30.5	226	13	7.1×10^{-5}	1.1×10^{4}	1.1	17	81	10.0	6	4.0×10^{-4}	...	6.6×10^{3}
	4.8	60	3.2	8	34	24.8	45	22	6.4×10^{-4}	1.8×10^{4}	1.2	18	81	12.5	10	4.3×10^{-4}	...	8.3×10^{3}
	5.4	50	0.3	8	51	0.1	32	31	1.0×10^{-4}	1.2×10^{4}	1.2	17	87	10.0	6	4.0×10^{-4}	...	6.6×10^{3}
G35.20-0.74	4.3	120	3.2	12	29	37.6	99	18	9.6×10^{-4}	5.4×10^{4}	2.3	20	87	20.7	34	1.6×10^{-3}	2.8×10^{-7}	4.7×10^{4}
	8.0	120	1.0	24	48	57.2	68	37	4.9×10^{-4}	1.5×10^{5}	2.4	20	81	24.1	34	1.6×10^{-3}	2.8×10^{-7}	4.7×10^{4}
	8.0	120	1.0	12	29	3.5	96	20	4.0×10^{-4}	5.0×10^{4}	2.5	20	76	33.0	34	1.6×10^{-3}	2.8×10^{-7}	4.7×10^{4}
	9.8	60	3.2	16	48	81.1	31	32	8.4×10^{-4}	1.2×10^{5}	2.5	19	70	16.4	27	1.5×10^{-3}	2.6×10^{-7}	4.3×10^{4}
	10.8	60	3.2	12	48	7.1	38	27	7.6×10^{-4}	5.2×10^{4}	2.7	18	76	16.8	29	1.2×10^{-3}	3.9×10^{-6}	3.6×10^{4}
G45.47+0.05	3.5	240	1.0	32	86	15.2	170	30	7.2×10^{-4}	2.7×10^{5}	3.4	31	57	16.8	20	4.1×10^{-3}	...	1.4×10^{5}
	5.1	120	3.2	24	86	40.4	75	28	1.3×10^{-3}	3.0×10^{5}	3.8	31	63	10.0	20	4.1×10^{-3}	...	1.4×10^{5}
	5.6	240	1.0	24	39	40.4	192	23	6.6×10^{-4}	1.8×10^{5}	3.9	31	70	44.1	22	2.4×10^{-3}	3.9×10^{-9}	1.3×10^{5}
	5.7	240	3.2	48	83	100.0	138	33	2.1×10^{-3}	7.9×10^{5}	4.0	27	49	10.0	14	3.0×10^{-3}	1.9×10^{-5}	1.0×10^{5}
	6.4	240	3.2	32	89	75.6	175	23	1.9×10^{-3}	5.2×10^{5}	4.0	29	63	10.0	13	2.8×10^{-3}	8.2×10^{-9}	1.2×10^{5}
IRAS20126	2.3	120	0.3	24	86	61.4	57	47	1.8×10^{-4}	9.5×10^{4}	1.1	18	87	87.1	17	4.4×10^{-4}	5.7×10^{-7}	2.3×10^{4}
	7.2	50	1.0	12	44	100.0	26	36	2.8×10^{-4}	4.7×10^{4}	1.1	18	76	89.6	17	4.4×10^{-4}	5.7×10^{-7}	2.3×10^{4}
	7.7	60	1.0	12	44	70.5	36	31	3.1×10^{-4}	4.9×10^{4}	1.1	18	81	88.1	17	4.4×10^{-4}	5.7×10^{-7}	2.3×10^{4}
	8.4	50	3.2	12	44	100.0	28	30	7.1×10^{-4}	5.2×10^{4}	1.2	18	70	93.9	17	4.4×10^{-4}	5.7×10^{-7}	2.3×10^{4}
	9.0	120	0.3	16	58	46.4	82	32	1.8×10^{-4}	4.8×10^{4}	1.2	17	63	67.7	11	4.8×10^{-4}	3.4×10^{-5}	1.9×10^{4}
CepA	4.9	480	0.1	12	83	81.1	458	12	1.0×10^{-4}	2.4×10^{4}	1.5	15	49	64.3	15	1.3×10^{-3}	8.1×10^{-6}	2.9×10^{4}
	5.0	480	0.1	16	89	100.0	441	15	1.2×10^{-4}	3.9×10^{4}	1.5	19	70	35.5	17	1.4×10^{-3}	5.9×10^{-5}	2.8×10^{4}
	6.9	120	0.3	12	62	61.4	93	24	1.6×10^{-4}	3.7×10^{4}	1.5	17	63	21.9	15	1.5×10^{-3}	4.2×10^{-6}	2.6×10^{4}
	7.0	60	3.2	16	68	87.0	31	32	8.4×10^{-4}	1.2×10^{5}	1.5	19	57	52.5	17	1.4×10^{-3}	5.9×10^{-5}	2.8×10^{4}
	7.4	120	1.0	24	55	100.0	68	37	4.9×10^{-4}	1.5×10^{5}	1.5	19	63	42.5	17	1.4×10^{-3}	5.9×10^{-5}	2.8×10^{4}

Table 4.3—Continued

Source	Zhang & Tan models										Robitaille et al. models							
	χ^2/N	M_c ($M_\odot$)	Σ_{cl} (g cm^{-2})	m_* ($M_\odot$)	θ_{view} (deg)	A_V (mag)	M_{env} ($M_\odot$)	$\theta_{w,esc}$ (deg)	$\dot{M}_{disk}$ ($M_\odot$/yr)	L_{bol} ($L_\odot$)	χ^2/N	m_* ($M_\odot$)	θ_{view} (deg)	A_V (mag)	$\theta_{w,esc}$ (deg)	$\dot{M}_{env}$ ($M_\odot$/yr)	$\dot{M}_{disk}$ ($M_\odot$/yr)	L_{bol} ($L_\odot$)
NGC7538	0.6	480	0.1	16	22	9.3	441	15	1.2×10^{-4}	3.9×10^{4}	0.3	17	18	44.9	15	1.5×10^{-3}	4.2×10^{-6}	2.6×10^{4}
	1.2	240	0.1	24	44	37.6	171	33	1.1×10^{-4}	8.3×10^{4}	0.4	15	18	39.0	16	1.7×10^{-3}	1.9×10^{-5}	2.3×10^{4}
	1.4	240	0.1	32	48	65.8	140	42	1.1×10^{-4}	1.5×10^{5}	0.4	16	18	42.8	11	1.1×10^{-3}	2.5×10^{-7}	2.6×10^{4}
	1.7	60	3.2	12	34	14.2	38	27	7.6×10^{-4}	5.2×10^{4}	0.4	17	32	24.1	20	1.1×10^{-3}	6.8×10^{-6}	3.0×10^{4}
	2.3	60	3.2	16	39	61.4	31	32	8.4×10^{-4}	1.2×10^{5}	0.4	16	18	46.0	25	1.3×10^{-3}	2.8×10^{-8}	2.9×10^{4}

The parameters of the best five ZT models for each source are listed in Table 4.3: for each source they are listed from best to worst as measured by χ^2/N. Recall that these models are based on the Turbulent Core Accretion scenario (MT03), which links protostellar accretion rate to core mass, clump mass surface density and evolutionary stage (i.e., the mass of the protostar, m_*). The accretion disk is always assumed to have a mass that is 1/3 of m_*. In general the best model fits yield protostellar masses $m_* \sim 10$–$30\,M_\odot$ accreting at rates of $\sim 1\times10^{-4}$–$1\times10^{-3}\,M_\odot\,\mathrm{yr}^{-1}$ inside cores of initial masses $M_c \sim 30$–$500\,M_\odot$ embedded in clumps with mass surface densities $\Sigma_{\rm cl} \sim 0.1$–$3\,\mathrm{g\,cm^{-2}}$.

We note that there is usually quite a large range in the values of χ^2/N amongst the best five models, which indicates that there is a significant preference for the best model over the worst. Amongst the best five models there can also be a significant variation in all model parameters.

Again considering in particular the case of G35.20-0.74, our new best fit model has $m_* = 12\,M_\odot$ accreting at a rate of $9.6\times10^{-4}\,M_\odot\,\mathrm{yr}^{-1}$ inside a core of initial masses $M_c = 120\,M_\odot$ embedded in a clump environment with mass surface density $\Sigma_{\rm cl} = 3.2\,\mathrm{g\,cm^{-2}}$. This implies the original core had a radius of 0.045 pc. The foreground extinction has $A_V = 37.6$ mag and the angle between the line of sight and the outflow axis is 29°. In this model the protostar is at a relatively early stage of formation, so the lateral opening angle of its outflow cavity is quite narrow, i.e., 18°. This is quite similar to the morphology shown by the high resolution 11 and 18 μm images of the source presented by De Buizer (2006; see also Zhang et al. 2013b). Inspecting the model fit in Figure 4.12, we notice it underpredicts at long wavelengths, but that the data here are quite uncertain because of background subtraction. The peak of the model SED is close to 70 μm, but rises about a factor

of 1.7 above the observed *Herschel* flux at this wavelength. Improved model fits are likely to be possible, by running a finer grid of models, and also by using image profile information (e.g., see Zhang et al. 2013b), and we will investigate such improvements in a future paper.

In Figure 4.13 we show the results of fitting the Robitaille et al. (2007) models to the SOMA Survey SEDs. The parameters of the best five models are also shown in Table 4.3. The values of χ^2/N for the Robitaille et al. models tend to be smaller than those for the ZT models, however, this is probably because of the larger number of models being sampled in the Robitaille et al. grid. Fitting these models we generally find slightly higher protostellar masses, but with much lower accretion rates: typically $\sim 100\times$ smaller. In some cases, the models do not require any disk component (indicated by "..." in the tabulated accretion rates). The envelope infall rate is usually much larger than the disk accretion rate, so the models are not physically self-consistent, at least in the context of a steadily accreting system. The outer core envelope radii can also be quite large. For the distant source G45.47+0.05 this is (10^5 AU), which is only marginally smaller than the fixed aperture size (1.15×10^5 AU). However, for the other sources the envelope outer radius is larger than the fixed aperture size (the outer radius is 10^5 AU for all except IRAS07299 and NGC 7538 that have a size between $\sim 10^4$ and 10^5 AU). Thus these models are not internally self-consistent with the observations.

Considering the particular case of G35.20-0.74 is again instructive. Like the case of ZT models, the best fit Robitaille et al. models underpredict at long wavelengths and (slightly) overpredict near the peak of the SED. A protostellar mass of $m_* = 20\,M_\odot$ is estimated, but with an accretion rate of only $2.8\times10^{-7}\,M_\odot\,\mathrm{yr}^{-1}$ (so accretion power is negligible). The viewing angle is found to be 87°, so that the outflow axis would

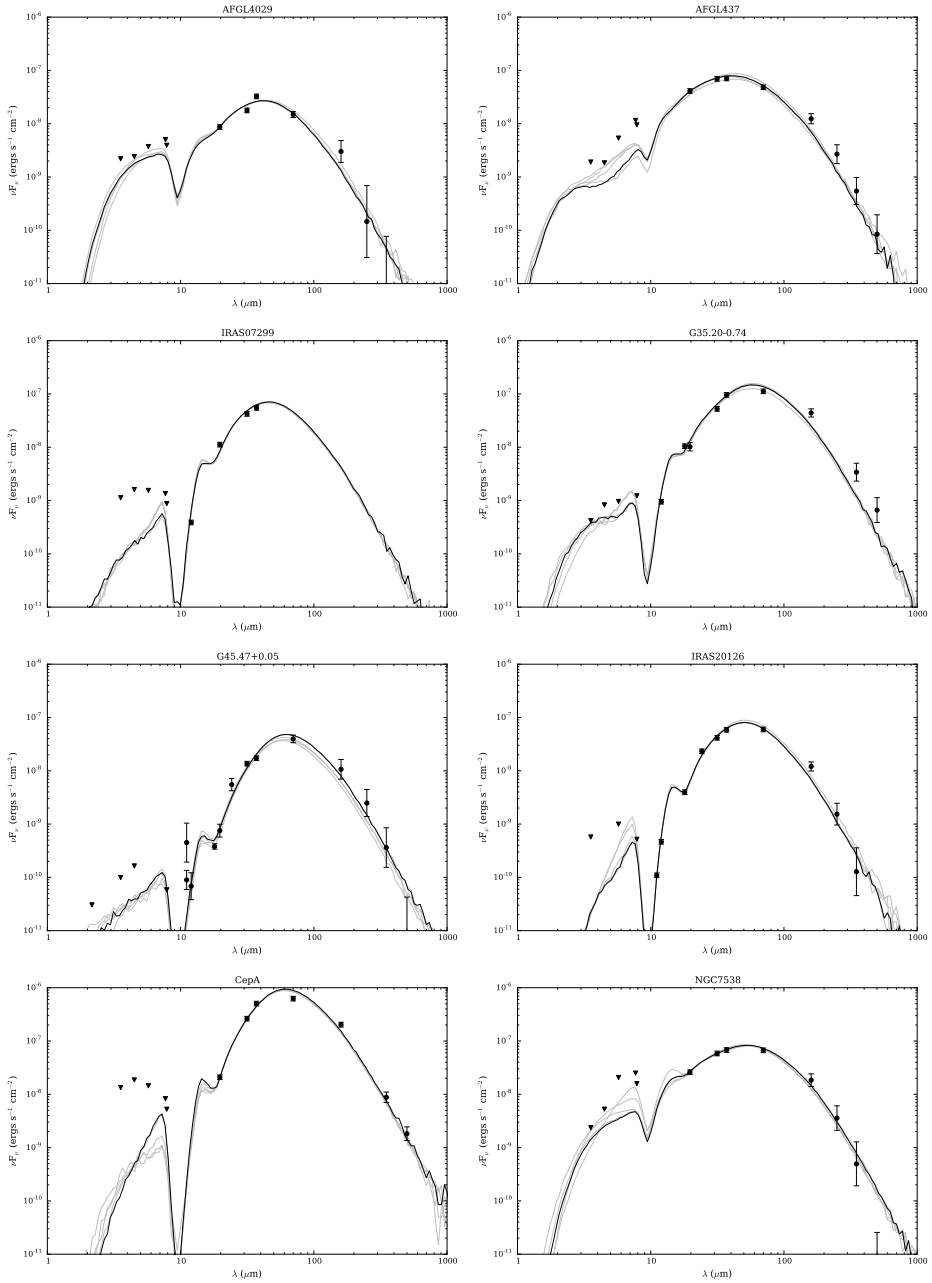

Fig. 4.13.— Protostar model fitting to the fixed aperture, background-subtracted SED data using the Robitaille et al. (2007) model grid. For each source, the best fit model is shown with a solid black line and the next four best models are shown with solid gray lines. Flux values are those from Table 4.2. Note that the data at $\lesssim 8\,\mu$m are treated as upper limits (see text). Also, the fitting method sets the data point to be at the middle of the errorbar range. The resulting model parameter results are listed in Table 4.3.

be close to the plane of the sky, which is very different from the result of the best ZT model. Such a geometry would not be expected to lead to strong asymmetries in the MIR/FIR morphologies of the blue and redshifted outflow cavities.

These considerations illustrate some of the difficulties and uncertainties of determining protostellar properties from simple SED fitting methods. We consider the results of the ZT model fitting to be more reliable since the models are designed with the typical expected properties of massive protostars in mind and they yield results that are internally self-consistent both physically (i.e., accretion rates through the disk are directly related to infall rates in the core envelopes; such high disk accretion rates are likely to be needed to drive powerful outflows) and observationally (i.e., the cores are more compact and are generally a better match to the aperture sizes used to define the SEDs).

Finally in Figure 4.14 we show the bolometric luminosity spectral energy distributions of the eight protostars, i.e., the νF_ν SEDs have been scaled by $4\pi d^2$, so that the height of the curves gives an indication of the luminosity of the sources, assuming isotropic emission. This figure allows one to visualize the range in luminosities present in the sample, along with any potential trends in SED shape. However, on inspecting the distributions, we do not perceive any obvious trends in SED shape with luminosity, although a larger sample is probably needed to reveal such trends given the expected variation that can result from, e.g., viewing angle and varying levels of foreground extinction.

We can compare the ordering of the vertical height of these distributions with the rank ordering of the predicted true luminosity of the protostars from the best fit ZT models (the legend in Fig. 4.14 lists the sources in order of decreasing ZT model luminosity). There is some, but not perfect, correspondence with the flux ordering

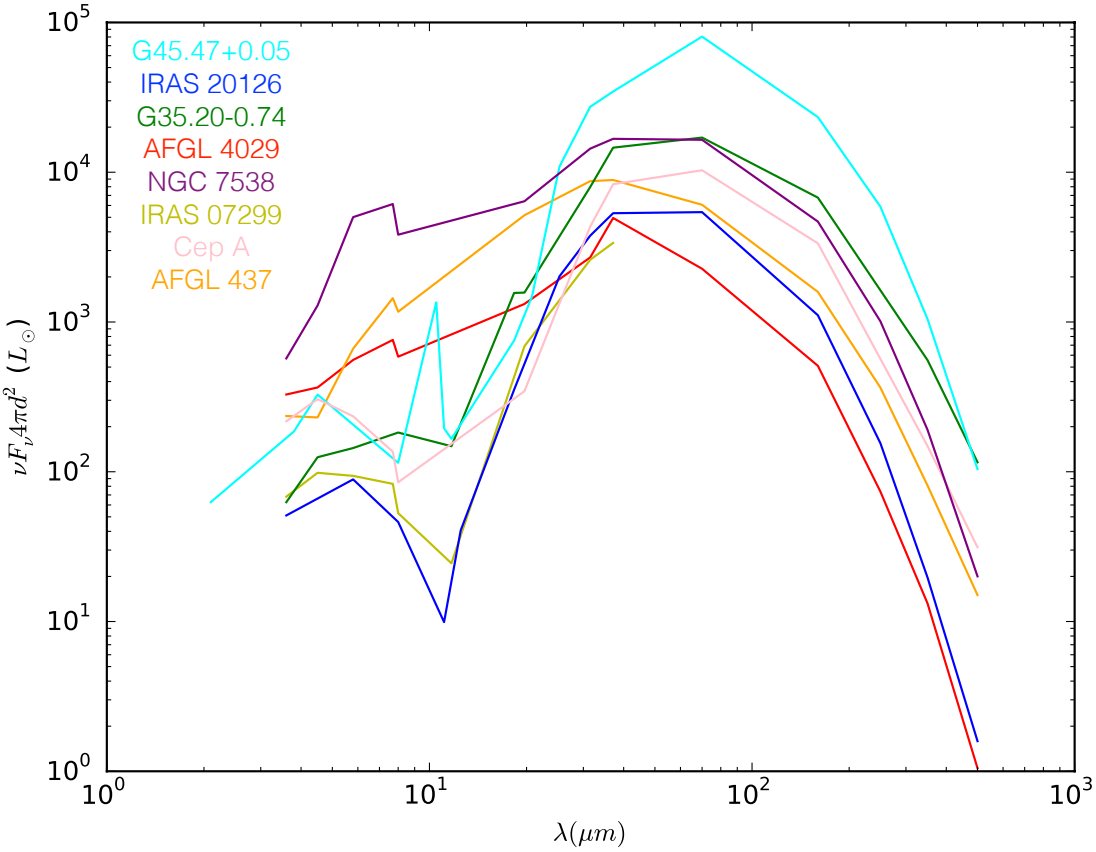

Fig. 4.14.— Bolometric luminosity weighted SEDs of the eight SOMA protostars analyzed in this paper. The ordering of the legend is from high to low ZT best fit model luminosity (top to bottom).

seen in the figure. Differences may be due to different levels of foreground extinction and anisotropic beaming (i.e., the "flashlight effect").

4.5 Conclusions

We have presented an overview and first results of the SOMA Star Formation Survey. The survey's scientific rationale is to test predictions of Core Accretion models of massive star formation, specifically the MIR to FIR thermal emission, including the influence of outflow cavities. We have presented results for the first eight sources observed in the survey. These tend to show extended MIR emission that aligns with known outflows, and being brighter on the near-facing, blue-shifted side, which are predictions of Core Accretion models.

Global SEDs have been constructed and effects of choices of aperture definition and background subtraction investigated. Our fiducial method is an SED derived from a fixed aperture and including an estimate of background subtraction, i.e., the emission from the surrounding clump environment.

These SEDs have been used to constrain theoretical radiative transfer models of massive star formation via the Turbulent Core Accretion model. These yield protostellar masses $m_* \sim 10$–$30\ M_\odot$ accreting at rates of $\sim 1 \times 10^{-4}$–$1 \times 10^{-3}\ M_\odot\ \mathrm{yr}^{-1}$ inside cores of initial masses $M_c \sim 30$–$500\ M_\odot$ embedded in clumps with mass surface densities $\Sigma_{\mathrm{cl}} \sim 0.1$–$3\ \mathrm{g\,cm}^{-2}$. We note that these are results from a relatively coarse sampling of initial core masses and clump envelope mass surface densities, yet quite reasonable fits are found. The derived accretion rates are comparable to the values estimated by other means, e.g., via observed infall rates in core envelopes (e.g., Wyrowski et al. 2016) and via mass outflow rates (e.g., Beltrán & de Wit 2016).

Comparison with the widely-used Robitaille et al. (2007) model grid finds large

differences, especially in the derived disk accretion rates. We suspect that these differences are due, at least in part, to there being a wider choice of free parameters in the Robitaille et al. grid, that can lead to models that we consider less physically realistic, i.e., high mass infall rates in the core envelope, but small disk accretion rates.

Finally, we emphasize the importance that *SOFIA* FORCAST observations in the wavelength range $\sim$ 10 to 40 μm have for constraining the theoretical models. In combination with *Herschel* 70 to 500 μm data, they allow definition of the thermal emission that defines the peak of the SED and probes the bulk of the bolometric flux. We consider this thermal emission simpler to model than that at shorter wavelengths, $\lesssim 8\mu$m, which is more affected by PAH emission and emission from transiently heated small dust grains.

Future papers in this series will present additional sources, especially probing a wider range of environmental conditions, evolutionary stages and protostellar core masses. Additional analysis that examines and models flux profiles along outflow cavity axes will be carried out, following methods developed by Zhang et al. (2013b). Ancillary observations that trace the outflowing gas will also be presented.

Chapter 5

The SOFIA Massive (SOMA) Star Formation Survey. II. High Luminosity Protostars

5.1 Introduction

Massive stars play a key role in the regulation of galaxy environments and their overall evolution, yet there is no consensus on their formation mechanism. Theories range from Core Accretion (e.g., McLaughlin & Pudritz 1996; McKee & Tan 2003 [MT03]) in which massive stars form via a monolithic collapse of a massive core, to Competitive Accretion (e.g., Bonnell et al. 2001; Wang et al. 2010) in which massive stars have most of the mass reservoir joining later and form hand in hand with the formation of a cluster of mostly low-mass stars, to Protostellar Collisions (Bonnell et al. 1998). The confusion remains partly due to the difficulty of observations towards massive star formation given the typically large distances and high extinction of the regions.

Outflows appear to be a ubiquitous phenomenon in the formation of stars of all masses. They may limit the formation efficiency from a core since they expel material along polar directions. The resulting outflow cavities have been proposed to affect the appearance of massive sources in the mid-IR (MIR) up to $\sim$40 μm (De Buizer 2006; Zhang et al. 2013a) and this is seen in radiative transfer (RT) calculations of the Turbulent Core Model of MT03 (e.g., Zhang et al. 2013b, Zhang et al. 2014; Zhang & Tan 2018).

Motivated by the need of observations of a larger sample of massive protostars to test theoretical models of massive star formation, we are carrying out the *SOFIA* Massive (SOMA) Star Formation Survey (PI: Tan). The overall goal is to obtain $\sim$ 10 to 40 μm images with the *SOFIA*-FORCAST instrument of a sample of $\gtrsim$ 50 high- and intermediate-mass protostars over a range of evolutionary stages and environments, and then compare the observed spectral energy distributions (SEDs) and image intensity profiles with theoretical models. The results and SED analysis of the first 8 sources of the survey have been published by De Buizer et al. (2017) (hereafter Paper I).

In this paper, we now present the next seven most luminous protostars from the sample of completed observations, which are expected to be the highest-mass protostars. In this work we still focus on the SED analysis. Comparison with the image intensity profiles will be presented in a future paper. The observations and data used are described in §5.2. The analysis methods are described in §5.3. We present the MIR imaging and SED fitting results in §5.4 and discuss these results and their implications in §5.5. A summary is given in §5.6.

5.2 Observations

5.2.1 SOFIA Data

The following seven sources, listed in order of decreasing isotropic bolometric luminosity, were observed by *SOFIA*[1] (Young et al. 2012) with the FORCAST instrument (Herter et al. 2013) (see Table 5.1): G45.12+0.13; G309.92+0.48; G35.58-0.03; IRAS 16562-3959; G305.20+0.21; G49.27-0.34; G339.88-1.26.

SOFIA data were calibrated by the *SOFIA* pipeline with a system of stellar calibrators taken across all flights in a flight series and applied to all targets within that flight series (see also the FORCAST calibration paper by Herter et al. 2013). Corrections were also made for the airmass of the sources. The main uncertainty in the *SOFIA* calibrations is caused by the apparent variability in the flux of the standard stars throughout the flight and from flight to flight due to changing atmospheric conditions. The calibration error is estimated to be in the range $\sim$ 3% - 7%.

5.2.2 Other IR Data

For all objects, data were retrieved from the *Spitzer* Heritage Archive from all four IRAC (Fazio et al. 2004) channels (3.6, 4.5, 5.8 and 8.0 μm). In some cases, the sources are so bright that they are saturated in the IRAC images and so these could not be used to derive accurate fluxes. For IRAS 16562, we used unsaturated *WISE* archival data (3.4 μm and 4.6 μm) as a substitute.

We also incorporated publicly-available imaging observations performed with the *Herschel Space Observatory*[2] (Pilbratt et al. 2010) and its PACS (Poglitsch et al.

[1] *SOFIA* is jointly operated by the Universities Space Research Association, Inc. (USRA), under NASA contract NAS2-97001, and the Deutsches SOFIA Institute (DSI) under DLR contract 50 OK 0901 to the University of Stuttgart.

[2] *Herschel* is an ESA space observatory with science instruments provided by European-led Prin-

2010) and SPIRE (Griffin et al. 2010) instruments at 70, 160, 250, 350 and 500 μm.

In addition to using these data for deriving multi-wavelength flux densities of our sources, the *Spitzer* 8 μm and *Herschel* 70 μm images are presented for comparison with our *SOFIA* images in §5.4.1. We note that the data being analyzed here were typically collected within a time frame of about 10 years (i.e., for the *Spitzer*, *Herschel*, and *SOFIA* observations).

We also present previously unpublished *Gemini* 8-m data taken with the instrument T-ReCS (De Buizer & Fisher 2004) for sources G309.92, G35.58, and G305.20. For both G309.92 and G35.58, only 11.7 μm data were taken, with on-source exposures times of 304s and 360s, respectively. For G305.20, we have images through ten T-ReCS filters from 3.8 μm (L-band) to 24.5 μm, all with an exposure time of 130s. Most T-ReCS filters have modest flux calibration errors (for MIR observations) with standard deviations between 2 and 10%. For instance, the 11.7 μm filter has a 1-sigma flux calibration error of 3%. Flux calibration through certain filters, however, is more difficult due to the presence of various atmospheric absorption lines contaminating the filter bandpass, some of which can be highly variable. Those filters most affected are the 7.7 μm (21%), 12.3 m (19%), 18.3 m (15%), and 24.6 m (23%) filters (De Buizer et al. 2005).

NIR images from the VISTA/VVV3 (Minniti et al. 2010) and the WFCAM/UKIDSS (Lawrence et al. 2007) surveys are also used to investigate the environments of the protostellar sources and look for association with the MIR counterparts.

---

cipal Investigator consortia and with important participation from NASA. The *Herschel* data used in this paper are taken from the Level 2 (flux-calibrated) images provided by the *Herschel* Science Center via the NASA/IPAC Infrared Science Archive (IRSA), which is operated by the Jet Propulsion Laboratory, California Institute of Technology, under contract with NASA.

5.2.3 Astrometry

The absolute astrometry of the *SOFIA* data comes from matching the centroids of point sources in the *SOFIA* 7 μm image with the *Spitzer* 8 μm image (or shorter IRAC wavelength, if saturated at 8 μm). The relative astrometry between the four *SOFIA* images is reduced to be better than 0.4″, which is around half a FORCAST pixel. Thus the astrometry precision is about 0.1″for the *SOFIA* 7 μm image and 0.4″for longer wavelength *SOFIA* images. The *Herschel* data can also be off in their absolute astrometry by up to 5″. For all targets in this survey, we were able to find point sources in common between the *Herschel* image and sources found in the *SOFIA* or *Spitzer* field of view that allowed us to correct the *Herschel* absolute astrometry. The astrometry is then assumed to have errors of less than 1″.

The *Gemini* images are calibrated using the *Spitzer* data and the astrometry precision is better than $\sim$ 0.2″. The archival WISE data and NIR data from the VVV survey and the UKIDSS survey were calibrated using 2MASS point source catalog and should have a positional accuracy $<$ 0.1″.

5.3 Methods

5.3.1 SED Construction

We follow the methods in Paper I and use PHOTUTILS, a Python package, to measure the flux photometry. When building the SEDs, we try two different methods. One is using fixed aperture size for all wavelengths, which is our fiducial case. The aperture size is mainly based on the *Herschel* 70 μm image, which is typically close to the peak of the SED, in order to capture the most flux from the source, while minimizing contamination from other sources. We assume this is the “core” scale

from which the protostar forms as described in the Turbulent Core Model (MT03). If there is no *Herschel* data available, we use the *SOFIA* 37 μm image to determine the aperture size. Sometimes we see multiple IR peaks in the aperture at shorter wavelengths, but without corresponding resolved structures at longer wavelengths, as in G45.12, G309.92, G35.58, and G49.27. This is a combined effect of larger beam sizes at the longer wavelengths and the fact that the emission from the secondary sources appears to be weaker at longer wavelengths. Note that due to the limited size of the field of view of the Gemini images, even for the fixed aperture method, we adopt an aperture radius of $9''$, $9''$, and $10''$ for the photometry of the Gemini images of G309.92, G35.58 and G305.20, respectively, which are the largest aperture sizes possible to allow for background subtraction in each image.

The alternate method is to use variable aperture sizes for each wavelength $< 70\mu$m. In this case, we typically use smaller apertures at shorter wavelength to exclude secondary sources that appear resolved from the main massive protostar in the fiducial aperture in the *Spitzer* and *SOFIA* images and compare the effects on the SEDs. The aperture is always centered at the radio continuum source (or the location of the methanol maser if there is no radio emission as in G305.20), where we assume the protostar is located.

After measuring the flux inside the aperture, we carry out background subtraction using the median flux density in an annular region extending from 1 to 2 aperture radii, as in Paper I, to remove general background and foreground contamination and the effect of a cooler, more massive clump surrounding the core at long wavelengths. The aperture radii are typically several times larger than the beam sizes for wavelengths ≤ 70 μm (and by greater factors for the fixed aperture method that uses the 70 μm aperture radii across all bands). At wavelengths > 70 μm, the fixed aperture

radius set at 70 μm is always used, and the aperture diameter is still usually larger than the image resolution (except for G305.20 whose fixed aperture diameter becomes similar to the resolution at the longest wavelength 500 μm).

5.3.2 Zhang & Tan Radiative Transfer Models

We use Zhang & Tan (2018, [ZT18]) radiative transfer (RT) models (hereafter ZT models) to fit the SEDs and derive key physical parameters of the protostars. In a series of papers, Zhang & Tan (2011), Zhang et al. (2013b), Zhang et al. (2014) and ZT18 have developed models for the evolution of high- and intermediate-mass protostars based on the Turbulent Core Model (MT03). In this model, massive stars are formed from pre-assembled massive pre-stellar cores, supported by internal pressure that is provided by a combination of turbulence and magnetic fields. With various analytic or semi-analytic solutions, they calculate the properties of a protostellar core with different components, including the protostar, disk, infall envelope, outflow, and their evolutions, self-consistently from given initial conditions. The main free parameters in this model grid are: the initial mass of the core M_c; the mass surface density of the clump that the core is embedded in $\Sigma_{\rm cl}$; and the protostellar mass, m_*, which indicates the evolutionary stage. In addition, there are secondary parameters of inclination angle of line of sight to the outflow axis, $\theta_{\rm view}$, and the level of foreground extinction, A_V.

The evolutionary history of a protostar from a given set of initial conditions (M_c and $\Sigma_{\rm cl}$) is referred to as an evolutionary track, and a particular moment on such a track is a specified m_*. Therefore the model grid is of three dimensions (M_c-$\Sigma_{\rm cl}$-m_*), including the entire set of tracks. Currently, M_c is sampled at 10, 20, 30, 40, 50, 60, 80, 100, 120, 160, 200, 240, 320, 400, 480 $M_\odot$, $\Sigma_{\rm cl}$ is sampled at 0.1, 0.32, 1,

3.2 g cm^{-2}, forming 60 evolutionary tracks. Then m_* is sampled at 0.5, 1, 2, 4, 8, 12, 16, 24, 32, 48, 64, 96, 128, 160 $M_\odot$. Note that not all of these m_* are sampled for each track. In particular, the maximum protostellar mass is limited by the final stellar mass achieved in a given evolutionary track. As a result, there are 432 different physical models defined by different sets of M_c, $\Sigma_{\rm cl}$ and m_*.

There are several things to note about the models. First, the models describe one protostar forming through monolithic collapse from the parent core. The formation of binary and multiple systems is not included in the models. Second, compared with the Robitaille et al. (2007) RT models that mostly focus on lower-mass protostars, the ZT18 model grid has broader parameter space relevant to high pressure, high density and thus high accretion rate conditions of massive star formation, while keeping the number of free parameters low. Third, the models do not explicitly include the clump component, which contributes to foreground extinction at short wavelengths and additional emission at long wavelengths. The former effect is compensated for by the free parameter A_V. The latter effect requires the model grid fitting to be done on clump-envelope-background-subtracted SEDs. Fourth, the aperture scale for the measured SED is not considered in the fitting process. The predicted SEDs in the model grid are total SEDs, which include modest contributions from parts of the outflow that extend beyond the core. We assume with the aperture adopted we also measure the total emission from the protostar and ideally the models that describe that observed SED best would predict a similar scale (this can be checked after the fitting results are returned). Fifth, PAH emission and thermal emission from transiently (single-photon) heated very small grains at $\lesssim 8$ μm is not modeled, and so our method is to use the SEDs at these wavelengths as upper limits. Lastly, while the general trends of the features of the SEDs are determined by the initial/environmental

conditions and evolution, some detailed features, such as the peak wavelength and long-wavelength spectral index, may be affected by the particular dust models used in the radiative transfer simulations.

5.3.3 SED Fitting

When fitting the SEDs to the models, we use our fiducial case, i.e., using fixed aperture size for all wavelengths, and set data points at wavelengths ≤ 8 μm as upper limits since the effects of PAH emission and thermal emission from very small grains are not included in the ZT RT models. For G309, the Spitzer 4.5 μm, 5.8 μm and 8 μm data have a ghosting problem. For G45.12 and IRAS 16562 all Spitzer data have ghosting problems. Thus we do not use these data for the SED fitting. The error bars are set to be the larger of either 10% of the clump background-subtracted flux density to account for calibration error, or the value of the estimated clump background flux density (see §5.3.1), which is used for background subtraction, given that order unity fluctuations in the surrounding background flux are often seen.

The fitting procedure involves convolving model SEDs with the filter response functions for the various telescope bands. Source distances are adopted from the literature. For each source, we present the five best-fitting models. Again we note that the SED model fitting performed here assumes that there is a single dominant source of luminosity, i.e., effects of multiple sources, including unresolved binaries, are not accounted for. This is a general limitation and caveat associated with this method as discussed in Paper I.

5.4 Results

The types of multi-wavelength data available for each source, the flux densities derived, and the aperture sizes adopted are listed in Table 5.2. $F_{\lambda,\mathrm{fix}}$ is the flux density derived with a fixed aperture size and $F_{\lambda,\mathrm{var}}$ is the flux density derived with a variable aperture size. The value of flux density listed in the upper row of each source is derived with background subtraction, while that derived without background subtraction is listed in brackets in the lower row. The *SOFIA* images for each source are presented in §5.4.1. General results of the *SOFIA* imaging are summarized in §5.4.2. The SEDs and fitting results are presented in §5.4.3.

Table 5.1. *SOFIA* FORCAST Observations:
Observation Dates & Exposure Times (seconds)

Source	R.A.(J2000)	Decl.(J2000)	d (kpc)	Obs. Date	7.7 μm	19.7 μm	31.5 μm	37.1 μm
G45.12+0.13	$19^h13^m27\overset{s}{.}859$	$+10°53'36\overset{''}{.}645$	7.4	2016 Sep 17	2443	882	623	1387
G309.92+0.48	$13^h50^m41\overset{s}{.}847$	$-61°35'10\overset{''}{.}40$	5.5	2016 Jul 14	291	828	532	1691
G35.58-0.03	$18^h56^m22\overset{s}{.}563$	$+02°20'27\overset{''}{.}660$	10.2	2016 Sep 20	335	878	557	1484
IRAS 16562-3959	$16^h59^m41\overset{s}{.}63$	$-40°03'43\overset{''}{.}61$	1.7	2016 Jul 17	1461	772	502	1243
G305.20+0.21	$13^h11^m10\overset{s}{.}49$	$-62°34'38\overset{''}{.}8$	4.1	2016 Jul 18	1671	763	539	1028
G49.27-0.34	$19^h23^m06\overset{s}{.}61$	$+14°20'12\overset{''}{.}0$	5.55	2016 Sep 20	290	716	664	1307
G339.88-1.26	$16^h52^m04\overset{s}{.}67$	$-46°08'34\overset{''}{.}16$	2.1	2016 Jul 20	1668	830	527	1383

Note. — The source positions listed here are the same as the positions of the black crosses denoting the radio continuum peak (methanol maser in G305.20) in each source in Figures 5.1, 5.2, 5.4, 5.6, 5.7, 5.9, 5.10. The ordering of the sources is based on their isotropic luminosity estimate from high to low (top to bottom). Source distances are from the literature, discussed below.

Table 5.2. Integrated Flux Densities

Facility	λ (μm)	$F_{\lambda,fix}$ (Jy)	[a]$F_{\lambda,var}$ (Jy)	[b]R_{ap} ($''$)	[c] $F_{\lambda,fix}$ (Jy)	$F_{\lambda,var}$ (Jy)	R_{ap} ($''$)	$F_{\lambda,fix}$ (Jy)	$F_{\lambda,var}$ (Jy)	R_{ap} ($''$)	$F_{\lambda,fix}$ (Jy)	$F_{\lambda,var}$ (Jy)	R_{ap} ($''$)	$F_{\lambda,fix}$ (Jy)	$F_{\lambda,var}$ (Jy)	R_{ap} ($''$)	$F_{\lambda,fix}$ (Jy)	$F_{\lambda,var}$ (Jy)	R_{ap} ($''$)	$F_{\lambda,fix}$ (Jy)	$F_{\lambda,var}$ (Jy)	R_{ap} ($''$)
		G45.12+0.13			G309.92+0.48			G35.58-0.03			IRAS 16562			G305.20+0.21			G49.27-0.34			G339.88-1.26		
WISE	3.4	...	...	...	...	...	...	...	...	...	1.62 (2.53)	0.62 (0.89)	12.0	...	...	...	...	...	...	...	...	...
Spitzer/IRAC	3.6	5.04 (5.64)	2.83 (3.04)	12.0	2.68 (2.93)	1.56 (1.65)	6.0	0.51 (0.76)	0.05 (0.09)	6.0	...	...	...	1.15 (1.44)	0.62 (0.69)	4.6	0.10 (0.32)	0.05 (0.07)	7.7	1.10 (1.65)	0.39 (0.56)	12.0
Gemini/T-ReCS	3.8	...	...	...	...	...	...	...	...	...	...	...	...	0.82 (1.10)	0.83 (0.87)	2.0	...	...	...	...	...	...
Spitzer/IRAC	4.5	7.30 (7.87)	4.79 (5.08)	12.0	4.75 (4.98)	2.92 (3.12)	6.0	0.52 (0.73)	0.12 (0.17)	6.0	...	...	...	2.89 (3.18)	2.00 (2.11)	4.6	0.77 (0.99)	0.55 (0.59)	7.7	2.90 (3.67)	1.75 (2.01)	12.0
WISE	4.6	...	...	...	...	...	...	...	...	...	4.20 (5.42)	0.73 (1.56)	12.0	...	...	...	...	...	...	...	...	...
Gemini/T-ReCS	4.7	...	...	...	...	...	...	...	...	...	...	...	...	2.95 (3.35)	2.77 (2.85)	2.0	...	...	...	...	...	...
Spitzer/IRAC	5.8	41.05 (45.17)	22.97 (24.95)	12.0	18.39 (19.66)	15.11 (16.18)	14.5	2.22 (3.91)	0.30 (0.60)	6.0	...	...	...	6.95 (9.24)	4.14 (4.56)	4.6	2.07 (3.75)	1.55 (1.73)	7.7	...	...	...
SOFIA/FORCAST	7.7	103.95 (92.89)	57.19 (60.84)	12.0	48.04 (47.17)	35.46 (37.55)	14.5	8.95 (5.83)	0.92 (1.62)	6.0	77.53 (81.72)	58.03 (60.63)	12.0	24.90 (26.31)	13.70 (14.95)	4.6	4.10 (4.20)	2.77 (3.02)	7.7	11.11 (17.69)	1.09 (1.67)	6.0
Gemini/T-ReCS	7.9	...	...	...	...	...	...	...	...	...	...	...	...	9.39 (12.88)	12.05 (12.28)	2.0	...	...	...	...	...	...
Spitzer/IRAC	8.0	72.80 (84.64)	25.68 (30.73)	12.0	28.21 (33.57)	20.29 (22.56)	14.5	5.15 (9.58)	0.73 (1.46)	6.0	...	...	...	17.92 (23.82)	8.62 (9.75)	4.6	2.34 (7.00)	1.78 (2.18)	7.7	...	...	...
Gemini/T-ReCS	8.8	...	...	...	...	...	...	...	...	...	...	...	...	12.81 (15.58)	14.85 (15.01)	2.0	...	...	...	...	...	...
Gemini/T-ReCS	9.7	...	...	...	...	...	...	...	...	...	...	...	...	17.14 (17.65)	17.24 (17.41)	2.0	...	...	...	...	...	...
Gemini/T-ReCS	10.4	...	...	...	...	...	...	...	...	...	...	...	...	25.66 (26.33)	25.19 (25.41)	2.0	...	...	...	...	...	...
Gemini/T-ReCS	11.7	...	...	...	79.11 (80.37)	78.60 (79.26)	6.0	2.19 (2.25)	2.15 (2.21)	6.0	...	...	...	40.91 (47.11)	44.94 (45.33)	2.0	...	...	...	...	...	...
Gemini/T-ReCS	12.3	...	...	...	...	...	...	...	...	...	...	...	...	54.23 (59.14)	56.18 (56.68)	2.0	...	...	...	...	...	...
Gemini/T-ReCS	18.3	...	...	...	...	...	...	...	...	...	...	...	...	137 (174)	161 (164)	2.0	...	...	...	...	...	...
SOFIA/FORCAST	19.7	1128 (1087)	976 (988)	12.0	380 (376)	345 (350)	10.0	21.78 (25.61)	18.40 (19.32)	7.0	254 (241)	212 (214)	12.0	282 (280)	194 (201)	4.6	2.97 (2.84)	2.12 (2.25)	11.0	26.94 (19.63)	24.87 (25.66)	6.0
Gemini/T-ReCS	24.5	...	...	...	...	...	...	...	...	...	...	...	...	311 (428)	375 (385)	2.0	...	...	...	...	...	...

Table 5.2—Continued

Facility	λ (μm)	$F_{\lambda,fix}$ (Jy)	[a]$F_{\lambda,var}$ (Jy)	[b]R_{ap} ($''$)	[c]$F_{\lambda,fix}$ (Jy)	$F_{\lambda,var}$ (Jy)	R_{ap} ($''$)	$F_{\lambda,fix}$ (Jy)	$F_{\lambda,var}$ (Jy)	R_{ap} ($''$)	$F_{\lambda,fix}$ (Jy)	$F_{\lambda,var}$ (Jy)	R_{ap} ($''$)	$F_{\lambda,fix}$ (Jy)	$F_{\lambda,var}$ (Jy)	R_{ap} ($''$)	$F_{\lambda,fix}$ (Jy)	$F_{\lambda,var}$ (Jy)	R_{ap} ($''$)	$F_{\lambda,fix}$ (Jy)	$F_{\lambda,var}$ (Jy)	R_{ap} ($''$)
SOFIA/FORCAST	31.5	3077 (3048)	2345 (2423)	12.0	1896 (1899)	1700 (1735)	12.0	276 (275)	210 (221)	7.7	2078 (2073)	1758 (1797)	16.0	687 (710)	521 (546)	7.7	63.37 (69.24)	41.77 (45.96)	11.0	720 (714)	541 (566)	7.7
SOFIA/FORCAST	37.1	4126 (4112)	2952 (3082)	12.0	2601 (2607)	2298 (2352)	12.0	525 (531)	365 (394)	7.7	3015 (3032)	2444 (2531)	16.0	892 (925)	654 (694)	7.7	89.39 (86.18)	58.83 (62.34)	11.0	1202 (1210)	815 (870)	7.7
Herschel/PACS	70.0	5848 (6205)	5848 (6205)	48.0	3403 (3536)	3403 (3536)	32.0	1538 (1647)	1538 (1647)	25.6	...	...	...	1250 (1617)	1250 (1617)	16.0	449 (593)	449 (593)	28.8	3610 (3846)	3610 (3846)	32.0
Herschel/PACS	160.0	3517 (4045)	3517 (4045)	48.0	2088 (2454)	2088 (2454)	32.0	968 (1193)	968 (1193)	25.6	...	...	...	644 (1032)	644 (1032)	16.0	864 (1198)	864 (1198)	28.8	2723 (3046)	2723 (3046)	32.0
Herschel/SPIRE	250.0	1506 (1796)	1506 (1796)	48.0	...	...	...	404 (545)	404 (545)	25.6	...	...	...	234 (433)	234 (433)	16.0	517 (736)	517 (736)	28.8	...	...	...
Herschel/SPIRE	350.0	469 (591)	469 (591)	48.0	289 (395)	289 (395)	32.0	129 (191)	129 (191)	25.6	...	...	...	60 (143)	60 (143)	16.0	193 (292)	193 (292)	28.8	...	...	...
Herschel/SPIRE	500.0	136 (187)	136 (187)	48.0	80 (122)	80 (122)	32.0	30.87 (56.16)	30.87 (56.16)	25.6	267 (374)	267 (374)	32.0	20.61 (59.45)	20.61 (59.45)	16.0	54.19 (94.92)	54.19 (94.92)	28.8	...	...	...

[a]Flux density derived with a fixed aperture size of the 70 μm data.

[b]Flux density derived with various aperture sizes.

[c]Aperture radius.

Note. — The value of flux density in the upper row is derived with background subtraction. The value in the bracket in the lower line is flux density derived without background subtraction.
$F_{\lambda,fix}$ of the Gemini images of G309.92, G35.58 and G305.20 are derived with an aperture radius of 9$''$, 9$''$, and 10$''$, respectively. See more detail in §5.3.1.

5.4.1 Description of Individual Sources

In this section we describe the MIR morphology of each source and also try to identify the nature of the structures revealed by our *SOFIA* or *Gemini* imaging, together with archival NIR data and other data from the literature.

G45.12+0.13

This UC HII region, also known as IRAS 19111+1048, has a measured far kinematic distance of 7.4 kpc (Ginsburg et al. 2011). The radio morphology of this region shows a highly inhomogeneous ionized medium (Vig et al. 2006), which is consistent with the extended MIR morphology revealed here in Figure 5.1. Vig et al. (2006) proposed the source is an embedded cluster of Zero Age Main Sequence (ZAMS) stars with twenty compact sources, including one non-thermal source, identified by their radio emission. The central UC HII source S14 is deduced to be of spectral type O6 from the integrated radio emission. They also found there are two NIR objects, IR4 and IR5, within the S14 region, while IR4 is at the peak of the radio emission and matches the OH maser position obtained by Argon et al. (2000). We see that most sources revealed at 8μm and 37μm in the central region have counterparts in NIR bands (see Figure 5.12), which also indicates that this site is probably a protocluster.

An extended bipolar outflow is revealed in CO(2–1), CO(3–2), CO(6–5), ^{13}CO(2–1) and C^{18}O(2–1) by Hunter et al. (1997). Higher resolution ^{13}CO(1–0) observations resolve the system into at least two outflows. The highest velocity outflow appears centered on the UC HII region S14. The additional bipolar outflow was identified with a dynamical center lying offset (-8″, -3″) from S14, named "G45.12+0.13 west" by Hunter et al. (1997). Hunter et al. (1997) argued that G45.12+0.13 west most likely represents dust emission from a younger or lower-mass protostar that formed

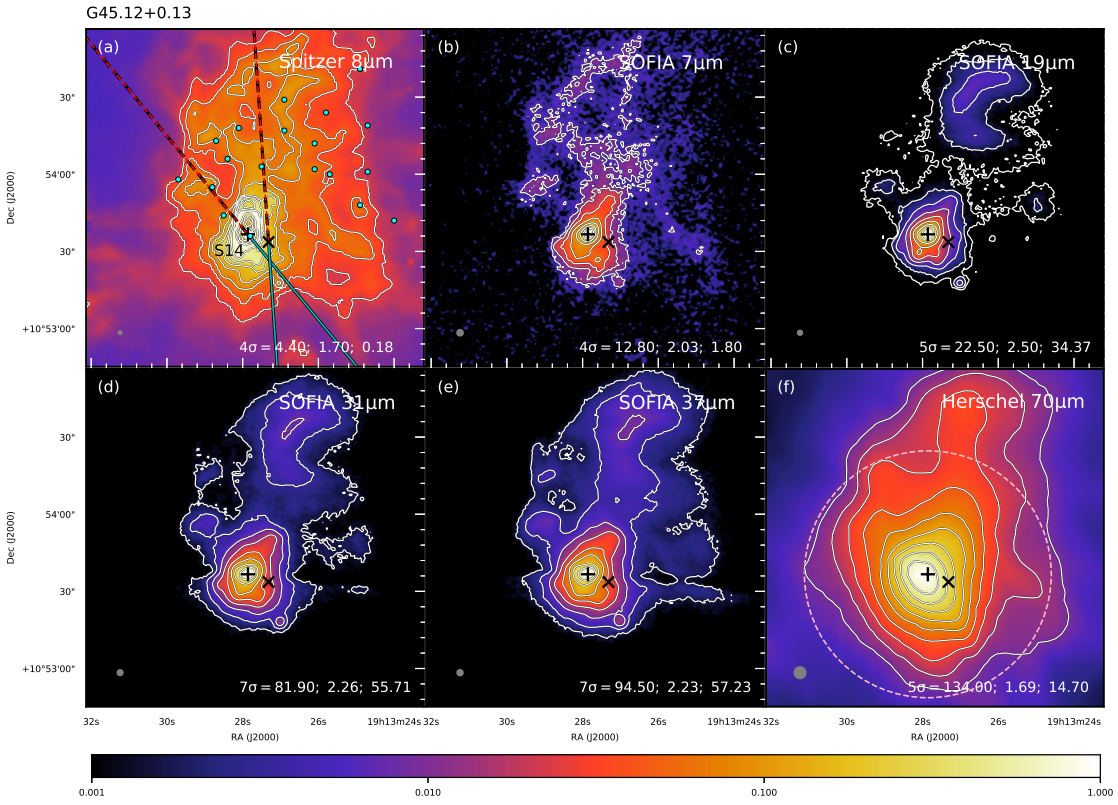

Fig. 5.1.— Multi-wavelength images of G45.12+0.13 with facility and wavelength given in upper right of each panel. Contour level information is given in lower right: lowest contour level in number of σ above the background noise and corresponding value in mJy per square arcsec; then step size between each contour in $\log_{10}$ mJy per square arcsec, then peak flux in Jy per square arcsec. The color map indicates the relative flux intensity compared to that of the peak flux in each image panel. The pink dashed circle shown in (f) denotes the aperture used for the fiducial photometry. Gray circles in the lower left show the resolution of each image. The black cross in all panels denotes the peak position of the 6 cm continuum at R.A.(J2000) = $19^h13^m27\overset{s}{.}859$, Decl.(J2000) = $+10°53'36\overset{''}{.}645$ from Wood & Churchwell (1989). The $\times$ sign marks the suspected origin, G45.12+0.13 west, of one of the ^{13}CO(1-0) outflows described in Hunter et al. (1997). The lines in panel (a) show the orientation of outflow axes, with the solid spans tracing blue-shifted directions and dashed spans red-shifted directions. In this case, the outflow axis angles are estimated from the ^{13}CO(1-0) emission described in Hunter et al. (1997). The cyan dots in panel (a) mark the 1.28 GHz radio continuum sources extracted in Vig et al. 2006.

Figure 5.1

during the same epoch as the ionizing star of S14. They also argued the absence of H_2O masers in the G45.12+0.13 cloud core suggests that both of the outflow sources have evolved beyond the H_2O maser phase.

In our SOFIA images we see MIR to FIR emission peaking at the S14 position. We do not see a distinct source at the position of G45.12+0.13 west, though the MIR extension to the southwest of S14 could be due to the two blue-shifted outflows, which are also revealed in NIR (see Figure 5.12). There is a MIR peak $\sim 7.7''$to the SE of S14, which is best revealed at 19 μm and further down $\sim 22''$to the SW of S14 there is another MIR peak. The closer one is seen in all J, H, K bands while the further one is seen in H and K bands as shown in Figure 5.12. They could be more evolved low-mass protostars.

G309.92+0.48

This region is located at a distance of 5.5 kpc (Murphy et al. 2010). The MIR emission in this area was resolved into 3 sources with the CTIO 4-m at 10.8 μm and 18.2 μm, labeled 1 through 3 (see Figure 2 in De Buizer et al. 2000). In addition to these sources, our *Gemini* 11.7 μm data also shows three additional fainter point-sources, as shown in Figure 5.3, which we label 4 through 6. Note that all the sources that appear in the *Gemini* field in Figure 5.3 are located within the northern patch revealed by *SOFIA* 7.7 μm in Figure 5.2.

Source 1 is the brightest source in the MIR and is coincident with a cm radio continuum source believed to be a HC HII region (Phillips et al. 1998; Murphy et al. 2010). Our *Gemini* 11.7 μm image resolves Source 1 into two components as shown in Figure 5.3, which we name 1N and 1S. Since both sources are elongated at the same position angle, it may be that the dark lane between them is an area of higher

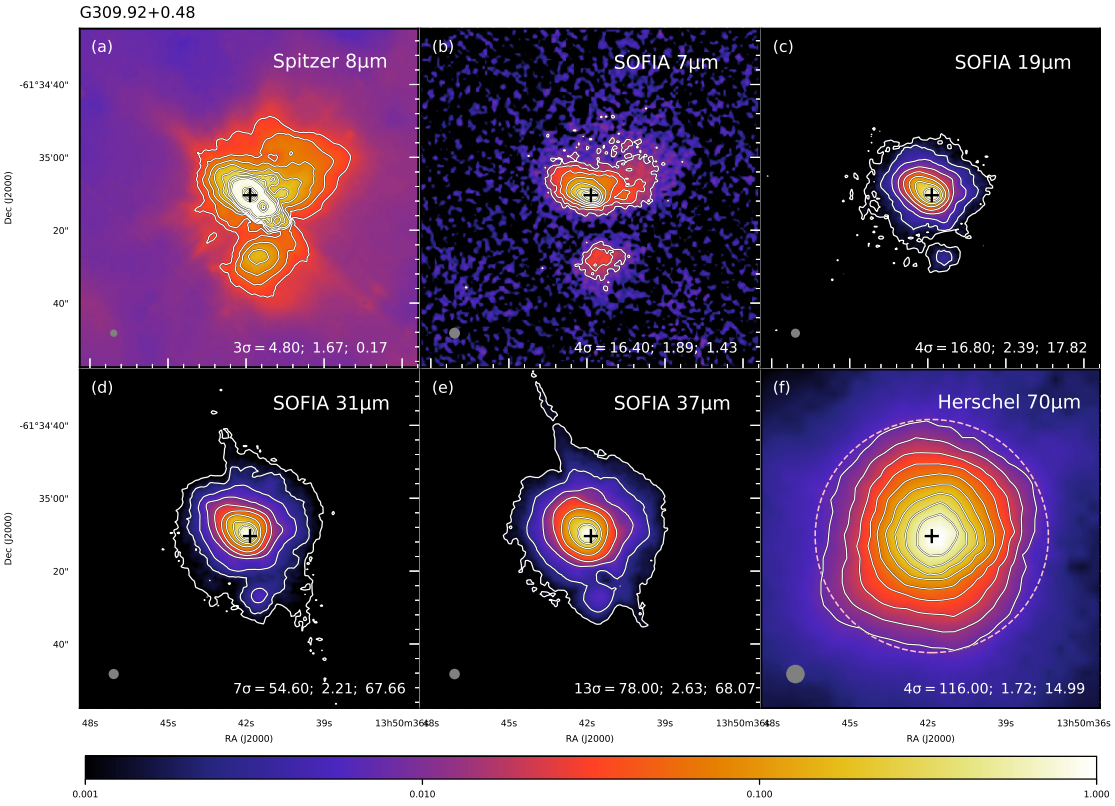

Fig. 5.2.— Multi-wavelength images of G309.92+0.48, following the format of Figure 5.1. The black cross in all panels denotes the peak position of the 8.6 GHz radio continuum estimated from Figure 5 in Philips et al. (1998) at R.A.(J2000) = $13^h50^m41^s.847$ ($\pm 0^s.015$), Decl.(J2000) = $-61°35'10''.40$ ($\pm 0''.12$). Note that the extension of the central source to the southwest in panel (a) is a ghosting effect, and not a real structure. The stripes in panel (d) and (e) are also artifact features caused by very bright point sources on the array.

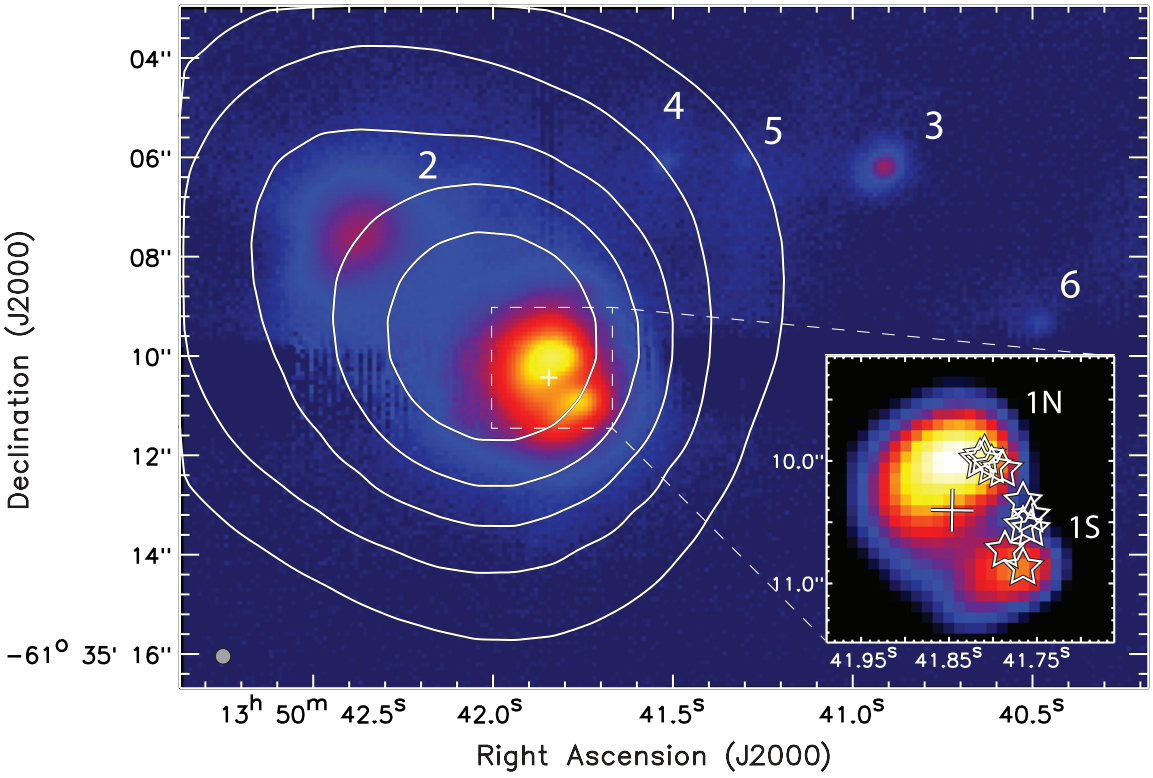

Fig. 5.3.— G309.92-0.48: color image is the *Gemini* 11.7 μm image, with IR source names labeled. The white contours are the SOFIA 37 μm data. The cross shows the peak location of the 8.6 GHz radio continuum source of Phillips et al. (1998). The resolution of the Gemini data is given by the gray circle in the lower left. The inset shows a close-up of Source 1 at 11.7 μm, which is resolved into two components labeled 1N and 1S. The radio continuum peak is again shown as the cross, and the stars represent the locations of the 6.7 GHz methanol masers which form an arc-shaped distribution. Astrometry between the radio masers (and continuum peak) and the 11.7 μm image is better than 0.2″. Note that all the sources that appear in the *Gemini* field here are located within the northern patch revealed by *SOFIA* 7.7 μm in Figure 5.2.

obscuration. In fact, the radio continuum emission at 8.6 GHz (Walsh et al. 1998, Philips et al. 1998) and 19 GHz (Murphy et al. 2010) towards Source 1 shows a peak nearly in between mid-infrared Source 1N and 1S, possibly tracing the location of the highly embedded protostar. Both of the radio observations of Philips et al. (1998) and Murphy et al. (2010) show elongation in the same direction as the MIR-dark lane. However, in both cases the beam profile is also elongated in the same direction. The 8.6 GHz observations of Walsh et al. (1998) have similar resolution and a nearly circular beam, and do not show any elongation.

OH and Class II methanol masers are found to be distributed along an arc centered near the primary radio continuum peak (see inset in Figure 5.3) with increasingly negative line-of-sight velocities from north to south (Caswell 1997). Norris et al. (1993) considered this site to have a well-defined methanol maser velocity gradient and forwarded the idea that they are tracing a near-edge-on circumstellar disk. The MIR morphology seen in the Gemini data do not appear to support this idea. If the dark lane between elongated Sources 1N and 1S is indeed the location of the protostar as the radio peak suggests, then the morphology at 11.7 μm would be best explained as the emission from the walls of outflow cavities or flared disk surfaces, with the dark lane representing a nearly edge-on, optically-thick (in the IR), circumstellar disk. This disk plane would be perpendicular to the methanol maser distribution. Thus the Class II methanol masers may be coming from a region which experiences both strong shocks, but also a strong radiation field, which enables radiative pumping of the masers. To help infer the outflow orientation, De Buizer (2003) observed the field for signs of H_2 emission, however, none was detected (note, however, that this H_2 survey was relatively shallow). We could not find any additional outflow information about this region. Note that the extension of the central source in the *Spitzer* 8 μm

image and the stripes in the *SOFIA* 31 μm and 37 μm images in Figure 5.2 are artifact features caused by very bright sources on the array.

With the NIR VVV data, we find there is little to no NIR emission from 1N, which suggests that it is the most obscured source seen in the MIR. In the J-band there is a compact emission source $\sim$2$''$ NE of the peak of Source 1N in the direction of Source 2, but no emission directly coming from Source 1N or 1S. The H-band image shows a source in this same location, but with the addition of an extended source with a peak coincident with 1S, and a "tail" to the SE. At Ks, there is only an extended source with a peak at 1S, and extended emission in the same direction as the tail seen in H-band, with emission also extending NE towards 1N. Source 2 lies to the northeast of Source 1 at a position angle of 53°. Both Source 1 and 2 are seen at 8.6 GHz by Phillips et al. (1998) and in the NIR by Walsh et al. (1999). With the NIR VVV data, we find that Sources 2 and 3 are also seen at J, H and Ks. Source 6 is also seen at J, H, and Ks, Source 4 is seen at H and Ks, but Source 5 is not detected in the NIR. In our 7.7 μm *SOFIA* data we see fingers of emission reaching the area around Sources 3 and 5, as well as Source 6, though these are not detected at longer wavelengths in the *SOFIA* data.

In the larger field of view of the *SOFIA* data, we detect another extended (r$\sim$5$''$) emission region $\sim$18$''$ south of Source 1 at all *SOFIA* wavelengths. The nature of this region is unknown, however.

G35.58-0.03

The star-forming region G35.58-0.03 is located at the far kinematic distance of 10.2 kpc (Fish et al. 2003; Watson et al. 2003). Kurtz et al. 1994 resolved the 2 cm and 3.6 cm continuum emission here into two UC HII regions $\sim$2$''$ apart, with the western

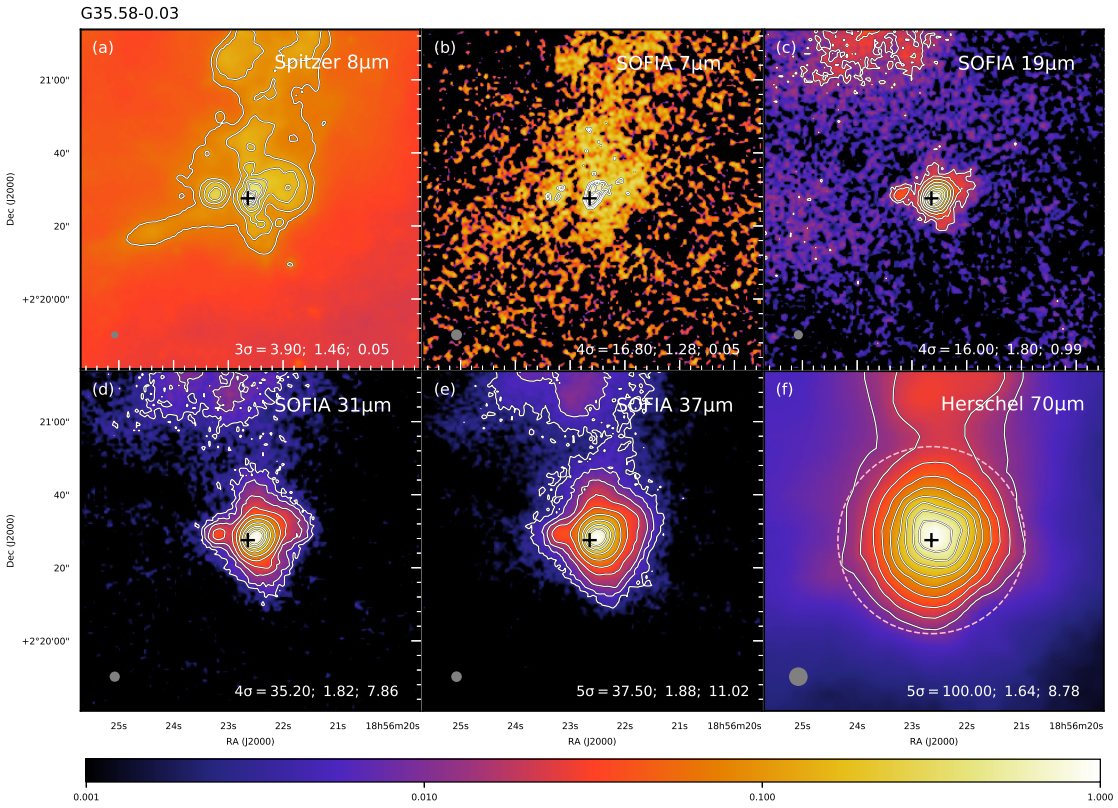

Fig. 5.4.— Multi-wavelength images of G35.58-0.03, following the format of Figure 5.1. The black cross in all panels denotes the peak position of the UC HII region G35.578-0.031 from Kurtz et al. (1994) 2 cm radio continuum emission at R.A.(J2000) = $18^h56^m22\overset{s}{.}644$, Decl.(J2000) = $+02°20'27\overset{''}{.}559$.

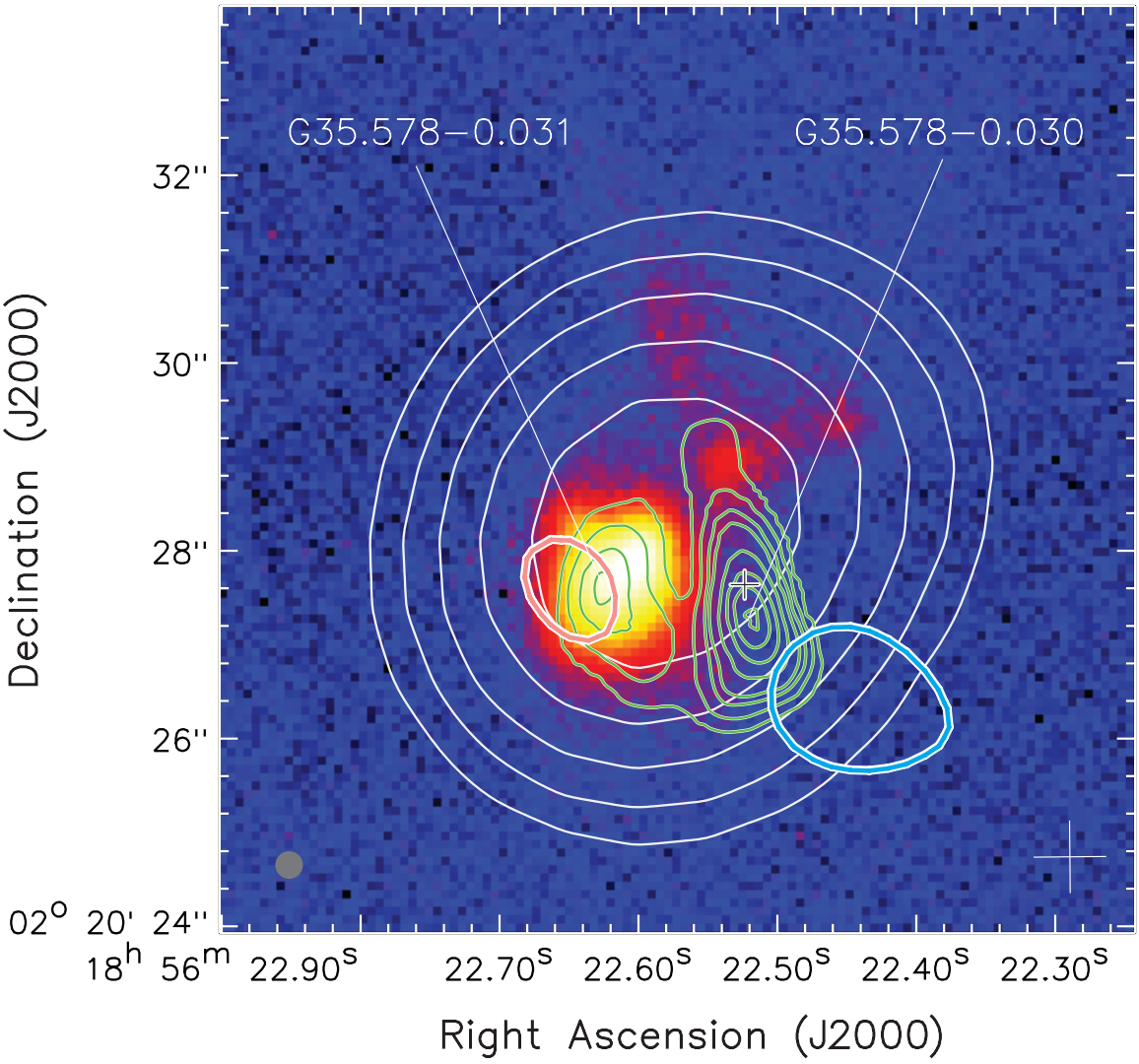

Fig. 5.5.— G35.58-0.03. The color image is the *Gemini* 11.7 μm data. The white contours are the *SOFIA* 37 μm data. The green contours are the 2 cm radio continuum emission as seen by Kurtz et al. (1994), and the names of the two radio sources are labeled. The black cross shows the peak location of the ammonia and 1.3 cm radio continuum source of Zhang et al. (2014). The size of this cross also denotes the astrometric error between the between all of the radio data and the 11.7 μm image (0.3″). The red and blue contours are the brightest red- and blue-shifted CO(2–1) outflow contours from Zhang et al. (2014). The resolution of the *Gemini* data is given by the gray circle in the lower left corner. The astrometry uncertainty between the *SOFIA* 37 μm contours and the radio data are given by the white cross in the lower right corner.

source named G35.578-0.030 and the eastern source named G35.578-0.031. G35.578-0.030 contains water and OH masers, but no methanol masers (Caswell et al. 1995). Zhang et al. (2014) found that there is an ammonia clump peaked co-spatially with their observed 1.3 cm radio continuum peak, which is $\sim$0.4″ north of the 2 cm peak of G35.578-0.030 (Kurtz et al. 1994; 1999). H30α shows evidence of an ionized outflow connecting to a molecular outflow seemingly centered on the radio continuum peak of G35.578-0.030. Only faint 1.3 cm continuum emission was found from the eastern source, G35.578-0.031, and no signs of outflow or ammonia emission.

De Buizer et al. (2005) presented $\sim$0.6″ resolution MIR images of this region at 10 and 20 μm, which showed a single source with some extension to the northwest. Due to poor astrometry of the data, it was unclear which UC HII region the mid-infrared emission was associated with. They argued that, due to the fact that the western source, G35.578-0.030, appears to have a similar extension to the northwest at 3.6 cm as seen by Kurtz et al. (1999), that the MIR emission is likely to be associated with that source.

Our data obtained at 11.7 μm from *Gemini* with $\sim$0.3″ resolution further resolve the MIR emission into a main bright peak with two fingers of extended diffuse emission to the north and northwest. Using *Spitzer* 8 μm images to confirm our astrometry, it is revealed that the MIR peak is not associated with the western UC HII region, but instead the eastern UC HII region, G35.578-0.031 (see Figure 5.5). The relative astrometric error between the *Gemini* 11.7 μm image and the radio data is better than 0.3″. No MIR emission is detected at the location of G35.578-0.030 out to 37 μm. The MIR peak is, however, close to the location of the redshifted outflow cavity of G35.578-0.030 seen in CO(2–1) by Zhang et al. (2014). However, if high extinction was causing the general lack of MIR emission from G35.578-0.030, it seems unlikely

that the MIR emission we are seeing would come from the even more extinguished red-shifted outflow cavity of G35.578-0.030. It is more plausible that the MIR emission is coming solely from the eastern UC HII region, G35.578-0.031.

Our *SOFIA* images of this region (Figure 5.4) show a bright source peaked at the location of G35.578-0.031 and extended slightly to the northwest, as is seen in the higher spatial resolution *Gemini* 11.7 μm image Figure 5.5. The nature of this extension is unclear, since the outflow seen by Zhang et al. (2014) has an axis oriented east-west. A second compact source is detected in our *SOFIA* data (and in the *Spitzer*-IRAC data) located $\sim$10$''$ to the east of G35.578-0.031. There is also a hint of MIR extension to the west, which may be due to the outflow.

The eastern MIR source seen in the *SOFIA* data has a counterpart at K-band as can be seen from Figure 5.12. Thus it may be a more evolved protostar, closer to the end of its accretion. From the NIR image (see Figure 5.12) there are at least two K-band sources within the highest contour of the 37 μm emission. The southern K-band source is associated with the peak at 8 μm and the main bright peak at 11.7 μm, while the northern K-band source has some overlap with the northern finger in *Gemini* 11.7 μm image (not shown here). There could be one or two lower luminosity companion sources in that region together with the southern main massive protostar, but they are not well resolved in the MIR and FIR.

IRAS 16562-3959

This source (also known as G345.49+1.47) is located at a distance of 1.7 kpc (Guzmán et al. 2010). It is believed that the massive core hosts a high-mass star in an early stage of evolution, including ejection of a powerful collimated outflow (Guzmán et al. 2010). Guzmán et al. (2010) carried out ATCA observations to reveal five 6 cm radio

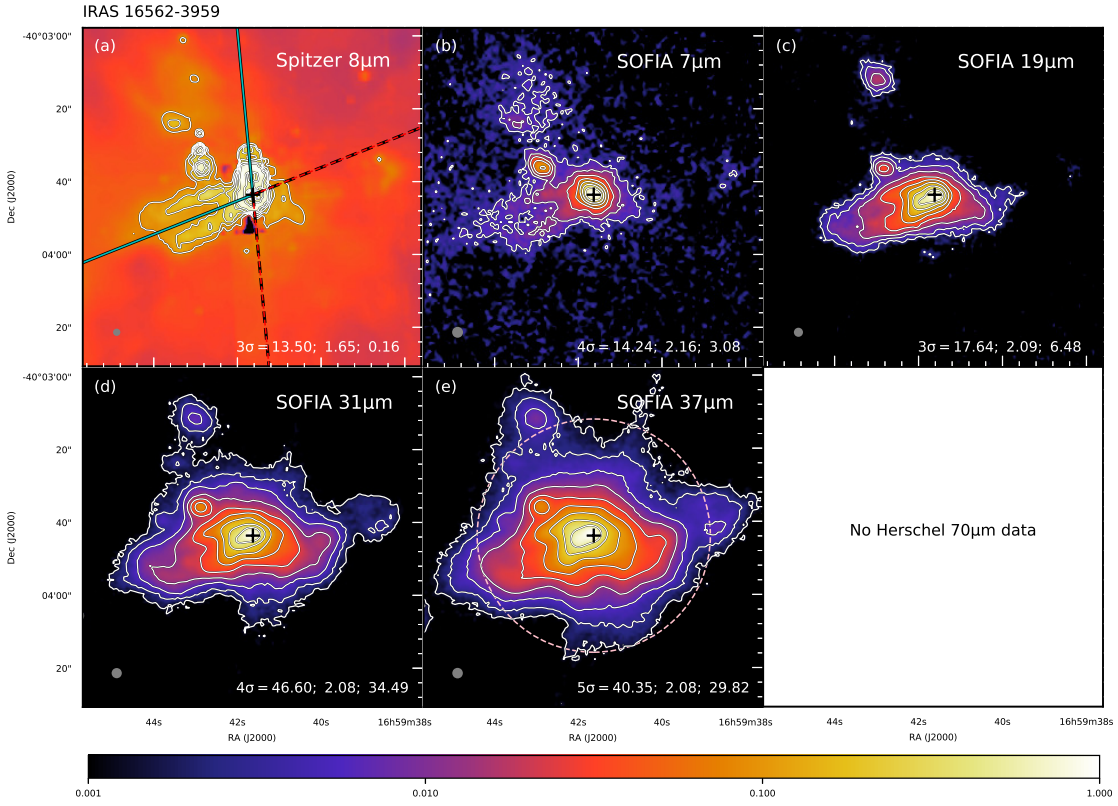

Fig. 5.6.— Multi-wavelength images of IRAS 16562, following the format of Figure 5.1. The black cross in all panels denotes the position of the central 8.6 GHz radio source (C) from Guzman et al. (2010) at R.A.(J2000) = $16^h59^m41\overset{s}{.}63$, Decl.(J2000) = $-40°03'43\overset{''}{.}61$. The lines in panel (a) show the outflow axis angles, with the solid spans tracing the blue-shifted directions and dashed spans the red-shifted directions. The outflow axis angles are from the CO(6-5) emission of Guzman et al. (2011). Note the extension and the dark appearance at the center in panel (a) are ghosting effects.

sources: a compact bright central (C) component, two inner lobes that are separated by about 7″ and symmetrically offset from the central source, and two outer lobes that are separated by about 45″ (see Figure 4 in Guzman et al. 2010). The central radio source has a 3 mm counterpart, source 10 in Guzmán et al. (2014), and an X-ray counterpart, source 161 in Montes et al. (2018), and is associated with OH maser emission (Caswell 1998, 2004). It is interpreted as a HC HII region based on hydrogen recombination line (HRL) observations (Guzmán et al. 2014). The continuum at 218 GHz and CH_3CN(12–11) (methylcyanide) observations by Cesaroni et al. (2017) revealed that the central source 10 actually consists of two peaks. The four other symmetrically displaced sources are interpreted as shock-ionized lobes (Guzmán et al. 2010) and are observed to move away from the central source at high speed (Guzmán et al. 2014).

On the other hand, the molecular observations of CO(6–5) and CO(7–6) show the presence of high-velocity gas exhibiting a quadrupolar morphology (Guzmán et al. 2011), most likely produced by the presence of two collimated outflows, one major outflow lying with a southeast-northwest (SE-NW) orientation, and the other with a N-S orientation, which may come from the unresolved mm source 13 in Guzmán et al. (2014) to the east of the central source. The SE-NW molecular outflow is aligned with the string of radio continuum sources. Extended Ks-band emission probably tracing excited H_2-2.12 μm is also associated with the SE-NW flow.

In Guzmán et al. (2014), the molecular core in which the outflow is embedded presents evidence of being in gravitational contraction as shown by the blue asymmetric peak seen in HCO^+(4–3). The emission in the SO_2, ^{34}SO, and SO lines exhibits velocity gradients interpreted as arising from a rotating compact ($\sim$ 3000 AU) molecular core with angular momentum aligned with the jet axis. López-Calderón et al.

(2016) reported ^{13}CO(3–2) APEX observations of this region and showed that the high-mass protostellar candidate is located at the column density maximum. Montes et al. (2018) decomposed the wider region into 11 subclusters with results from *Chandra* X-ray observations together with VISTA/VVV and *Spitzer*-GLIMPSE catalogs and the subcluster containing the high-mass protostar was found to be the densest and the youngest in the region with the high-mass protostar located near its center.

In our MIR images, the extended IR emission is likely tracing the illuminated inner outflow cavity containing the jet. There are two knots to the northeast of the central source revealed by *SOFIA*. The closer knot located ∼15″ NE of the central source is associated with the 92.3 GHz peak 18 in Guzmán et al. (2014), as well as a K-band source (see Figure 5.12). It may correspond to the X-ray source 178 in Montes et al. (2018). There is OH maser emission (Caswell 1998, 2004), but no radio continuum emission detected. Thus it may be a low-mass protostar. The farther knot, located ∼36″ northeast of the central source, has counterparts in all of the J, H, K bands. We did not find any associated X-ray source for this knot in the Montes et al. (2018) sample.

G305.20+0.21

G305.20+0.21 is a massive star-forming region located at a distance of $4.1^{+1.2}_{-0.7}$ kpc from parallax of 6.7 GHz methanol masers (Krishnan 2017). Class II methanol (CH_3OH) masers were reported in two positions by Norris et al. (1993): G305.21+0.21 and G305.20+0.21 separated by approximately 22″. Walsh & Burton (2006) refer to these maser sites as G305A and G305B, respectively, and we will adopt that nomenclature here.

The brightest MIR source appears to be associated with the methanol masers

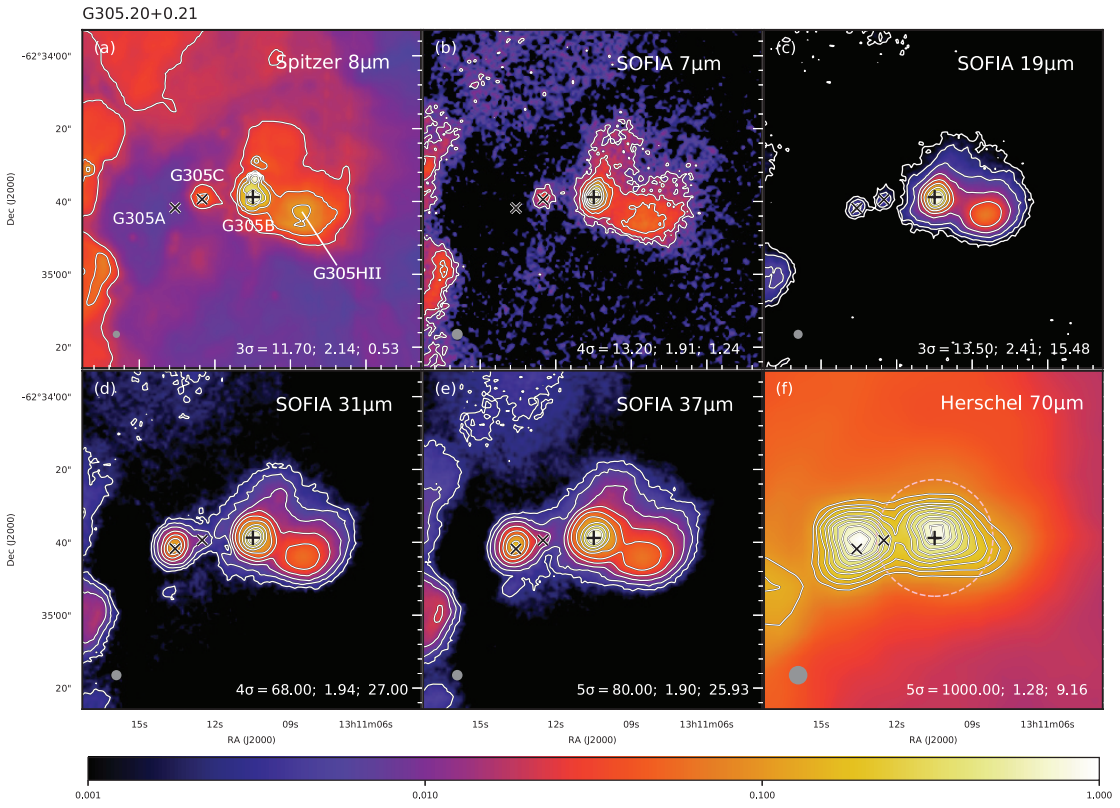

Fig. 5.7.— Multi-wavelength images of G305.20+0.21, following the format of Figure 5.1. The black cross in all panels denotes the peak position of the 6.7 GHz methanol maser from Caswell, Vaile & Forster (1995b) at R.A.(J2000) = $13^h11^m10^s.49$, Decl.(J2000) = $-62°34'38''.8$. The × signs denote the MIR peak positions of G305A and G305C determined from the *SOFIA* 19 μm image.

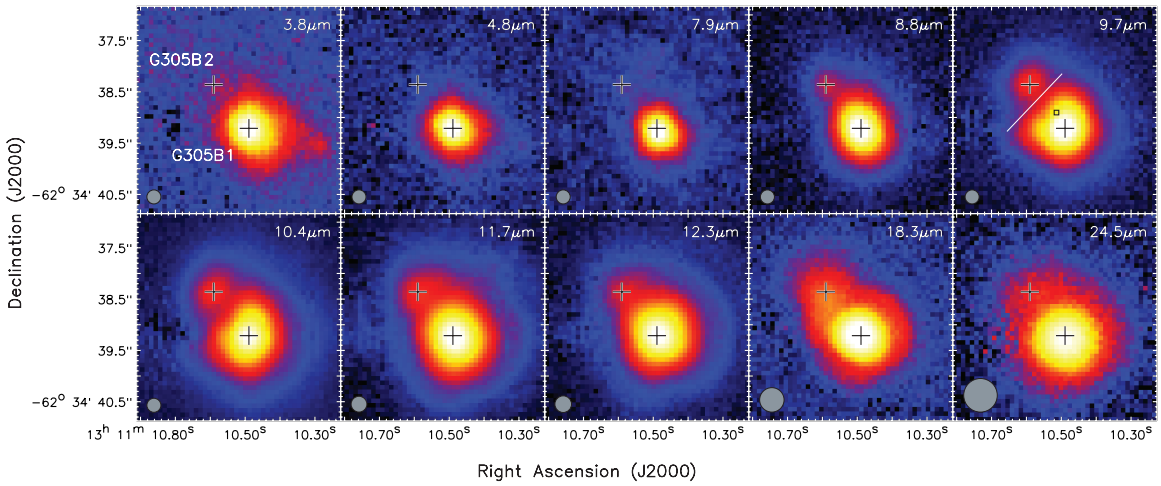

Fig. 5.8.— G305.20+0.21. We present *Gemini* images at 10 different MIR wavelengths from 3.8 to 24.5 *mu*m. The wavelength of the image is given in the upper right corner of each panel and the resolution is given by the gray circle in the lower left corner of each panel. Infrared source names are labeled in the top left panel, and their peak locations (as determined from the 9.7 μm image) are given in each panel by the crosses. The square in the upper right panel represents the location of the 6.7 GHz methanol maser reference feature of Phillips et al. (1998). Astrometry between the maser location and the *Gemini* data is better than 0.2″. The white line in the upper right panel is present to demonstrate the flatness of the northeast side of G305B1.

of G305B, but does not possess detectable radio continuum emission (below a 4σ detection limit of 0.9 mJy beam^{-1} (beam $\sim 1.5''$) at 8.6 GHz in Phillips et al. 1998, and a 3σ detection limit of 0.09 mJy at 18 GHz in Walsh et al. 2007). Walsh et al. (2007) found no HC_3N, NH_3, OCS, or water at the position of G305B and proposed that it has evolved enough to the point that it has already had time to clear out its surrounding molecular material. By contrast, Boley et al. (2013) proposed G305B is a massive protostar in a pre-UCHII-region stage. Our *SOFIA* images show that G305B is the brightest MIR source out to 37 μm. Our high-spatial-resolution *Gemini* data (Figure 5.8) show G305B is resolved into two emission components, with the fainter secondary source (which we name G305B2) lying $\sim 1''$ to the NE of the brighter source (G305B1). G305B2 is only visible at wavelengths greater than 8.8 μm. By contrast, G305B1 is seen to have emission in all *Gemini* images from 3.8 to 24.5 μm, and has a NIR counterpart as well (see Figure 5.12 and Walsh et al. 1999). Using four infrared sources seen in both the *Gemini* 3.8 μm image (but not shown in Figure 5.3) and the Spitzer 3.6μm image we were able to confirm the absolute astrometry of the *Gemini* data at all wavelengths to better than $0.2''$. This places the Class II methanol maser reference feature (i.e., the brightest maser spot) from Phillips et al. (1998) $\sim 0.5''$NE of the MIR peak (see the 9.7μm image in Figure 5.8). It is not clear what these masers are tracing.

What is the nature of the MIR double source associated with G305B? G305B2 could be a more embedded source, since it is not visible at shorter IR wavelengths. However, it appears to change shape considerably as a function of wavelength, flattening and becoming more diffuse at 18.3 and 24.5 μm. G305B1 also changes shape modestly with wavelength and its shape at 9.7 and 10.4 μm is peculiar. The northeast side of G305B1 is very flat, and almost completely straight at 9.7 and 10.4 μm

(see white line in the 9.7μm panel of Figure 5.8 as reference). As these filters are sampling the wavelength of peak dust extinction (Gao et al. 2009), it may be that the morphologies of both sources could be explained if the dark lane between them is a "silhouette" of a circumstellar disk or toroid that is optically thick in the MIR. The brighter MIR source G305B1 would be the side of the disk or outflow cavity facing towards us, and G305B2 the side facing away which we only see at longer wavelengths due to extinction from the disk along the line of sight. We could corroborate the outflow cavity hypothesis if we had evidence of an outflow and knew its angle. Walsh et al. (2006) did image the area in commonly used outflow tracers ^{13}CO and HCO$^+$, and presented the data as integrated emission maps. However, the emission appears to peak on G305A and extends at larger scales in a direction parallel to the dark lane orientation, tracing the location of the extended 1.2 mm continuum emission (rather than an outflow). However, if the hypothesis of Walsh et al. (2007) is correct, i.e., that due to low chemical abundance this source is more evolved and has cleared much of its surrounding molecular material, then the source may have passed the stage where it would exhibit an active outflow. Conversely, a Class I methanol maser was detected by Walsh et al. (2007) 3$''$ due east of G305B, and they are generally only found in outflows.

Walsh et al. (2001) observed the 6.7 GHz methanol maser site G305A in the MIR (10.5 μm and 20 μm) and found that G305A is not associated with any MIR source. G305A is out of the field of our *Gemini* images. However, we see strong emission from G305A in our *SOFIA* images at 19 μm and longer, and it becomes the dominant source in the FIR starting at *Herschel* 70 μm. G305A is also not associated with any 8.6 GHz continuum emission with a flux density limit of 0.55 mJy beam^{-1} (Phillips et al. 1998) or 18 GHz continuum emission with a detection limit of 0.15 mJy (Walsh et

al. 2007), but is rich in molecular tracers (Walsh et al. 2007) indicating it is a source that is likely much younger and more embedded than G305B and in a hot core phase, prior to the onset of a UC HII region.

About 15″ to the southwest of G305B is an extended HII region, G305HII, with a flux of 195 mJy at 8.6 GHz (Phillips et al. 1998). We detect this source in all of our *SOFIA* images. We also detect an infrared source between G305A and G305B, which we call G305C, located $\sim$ 14″east of G305B. It is present at all wavelengths in the *SOFIA* images, but becomes less pronounced at longer wavelengths. It also has NIR counterparts, as shown in Figure 5.12, which seem to be resolved into three peaks. The nature of the source is uncertain, but it may be a low mass YSO. Besides the G305HII region there is no other radio emission in the field shown in Figure 5.7 revealed by the 18 GHz continuum in Walsh et al. (2007).

G49.27-0.34

This source, classed as an "extended green object" (EGO) is in an IRDC with near kinematic distance of 5.55 $\pm$ 1.66 kpc (Cyganowski et al. 2009). The MIR peak (see Figure 5.9) is associated with the 3.6 cm radio source CM2 in Cyganowski et al. (2011a). Towner et al. (2017) did not detect a 1.3 cm counterpart to CM2 at the a 4σ detection limit of 0.28 mJy beam^{-1} (beam $\sim$ 1″). The MIR extension to the northeast is associated with a stronger radio source CM1 detected at 3.6 cm and 1.3 cm by Cyganowski et al. (2011a) and at 20 cm by Mehringer (1994).

We did not find any outflow information about this source. De Buizer & Vacca (2010) obtained *Gemini* L- and M-band spectra for this EGO, and detected only continuum emission (no H_2 or CO). However, Cyganowski et al. (2011a) suspected that an outflow, perhaps driven by CM2 or by a massive protostar undetected at cm

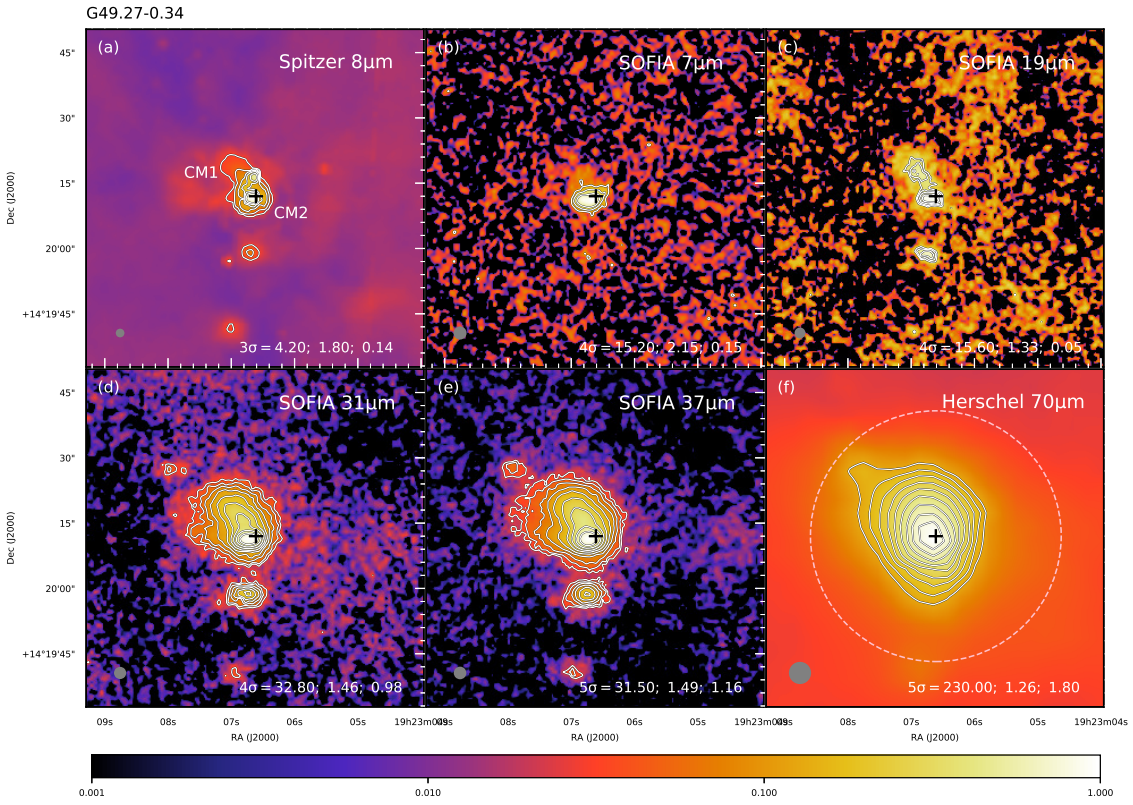

Fig. 5.9.— Multi-wavelength images of G49.27-0.34, following the format of Figure 5.1. The black cross in all panels denotes the peak position CM2 of the 3.6 cm continuum from Cyganowski et al. (2011a) at R.A.(J2000) = $19^h23^m06\overset{s}{.}61$, Decl.(J2000) = $+14°20'12\overset{''}{.}0$.

wavelengths, may exist, but is not detected, given the 44 GHz Class I CH_3OH masers and 4.5 μm emission in the south. SiO(5–4), HCO^+ and $H^{13}CO^+$ emission is detected toward this EGO with JCMT (Cyganowski et al. 2009). No 6.7 GHz CH_3OH emission is detected towards this EGO (Cyganowski et al. 2009). Neither thermal nor maser 25 GHz CH_3OH emission is detected (Towner et al. 2017).

There is a secondary component revealed by our *SOFIA* data to the south of the main MIR peak. It is neither seen at 3.6 cm (Cyganowski et al. 2011a) nor at 1.3 cm (Towner et al. 2017). The nature of this source is unknown. We do not see obvious counterparts in the NIR image (see Figure 5.12).

G339.88-1.26

This source, also named IRAS 16484-4603 is located at $2.1^{+0.4}_{-0.3}$ kpc, determined from trigonometric parallax measurements of the 6.7 GHz methanol masers using the Australian Long Baseline Array (Krishnan et al. 2015).

De Buizer et al. (2002) resolved the central MIR emission of G339.88 into three peaks (1A, 1B, and 1C) at 10 and 18 μm that all lie within an extended MIR region elongated at a position angle of $\sim$120° (Figure 5.11a). Interferometric radio continuum observations have revealed an elongated, ionized jet/outflow at a position angle of $\sim$45° with a scale of 15″, approximately perpendicular to the elongation of the infrared emission (Ellingsen et al. 1996; Purser et al. 2016). Recent ALMA ^{12}CO(2–1) observations by Zhang et al. (2019) also reveal a major molecular outflow with a E-W orientation and a tentative second outflow with a NE-SW orientation (at the same angle as the ionized outflow seen by Purser et al. 2016). Zhang et al. (2019) suggest that the 1.3 mm continuum peak, which is $\sim$ 0.5″ to the west of 1B, is the likely location of the origin of both outflows, which may indicate an unresolved

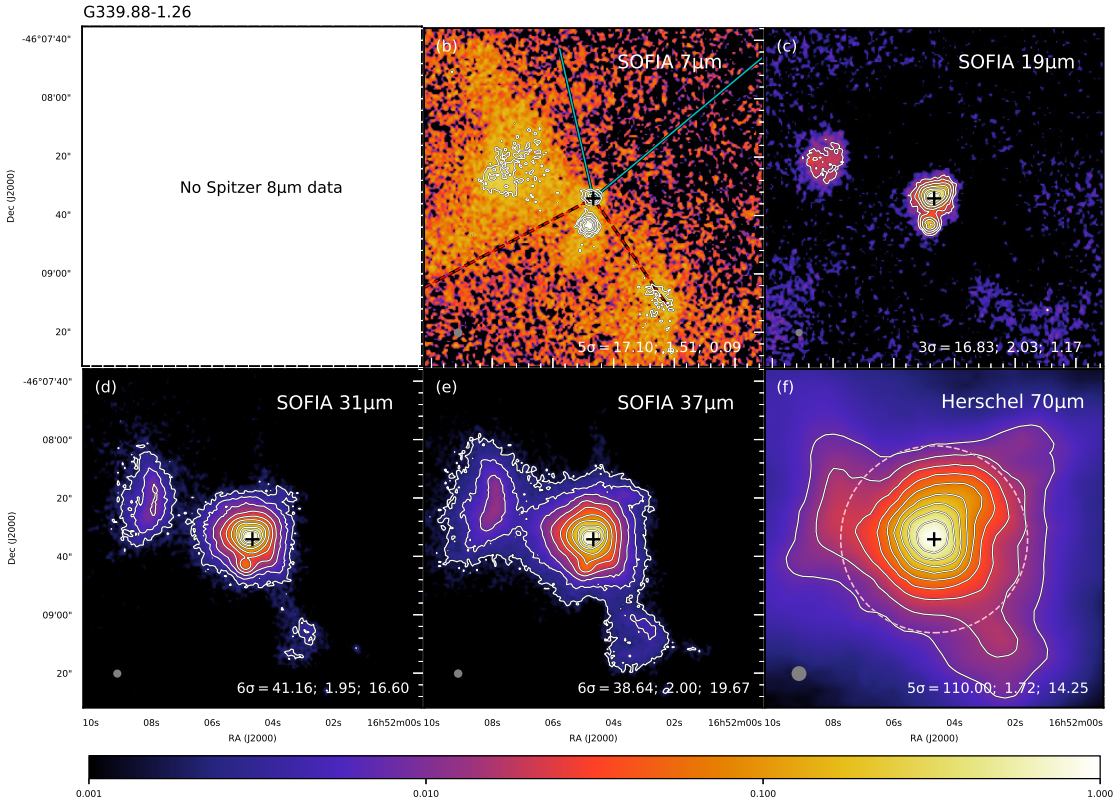

Fig. 5.10.— Multi-wavelength images of G339.88-1.26, following the format of Figure 5.1. The black cross in all panels denotes the 9 GHz radio peak position of the component C from Purser et al. (2016) at R.A.(J2000) = $16^h52^m04\overset{s}{.}67$, Decl.(J2000) = $-46°08'34\overset{''}{.}16$.

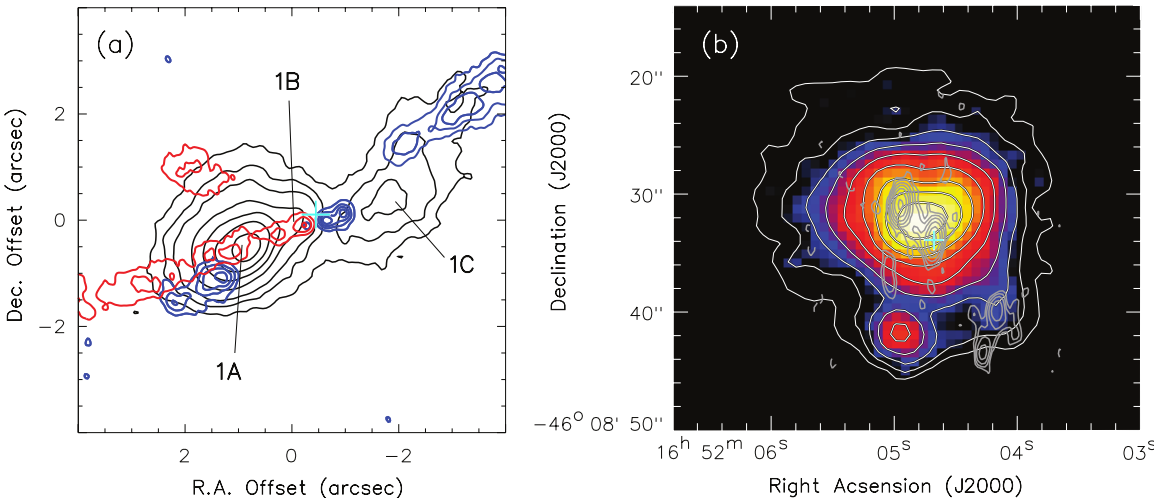

Fig. 5.11.— G339.88-1.26. (a) The black contours are the Keck 18 μm data, with the MIR peaks labeled. The red and blue contours show the blue- ($V_{\rm lsr}$ = −80 to −20 km s^{-1}) and red-shifted ($V_{\rm lsr}$ = −50 to +10 km s^{-1}) ALMA ^{12}CO(2–1) observations (systematic velocity $V_{\rm lsr}$ = −33 km s^{-1}) by Zhang et al. (2019). Note that emission from the secondary ^{12}CO(2–1) outflow is outside the field of view. The cyan plus sign shows the location of the 8.6 GHz radio continuum peak (Ellingsen et al. 1996). (b) The *SOFIA* 31 μm image in color and white contours with the 9 GHz radio continuum contours from Purser et al. (2016). The central radio source is identified as a radio jet and the two other sources as radio outflow lobes (Purser et al. 2016). The cyan plus sign shows the location of the 8.6 GHz radio continuum peak (Ellingsen et al. 1996).

proto-binary system. All of the 10 and 18 μm MIR emission seen by De Buizer et al. (2002) is therefore mainly tracing the outflow cavities of the molecular outflow seen at a position angle of $\sim$120° (Figure 5.11a). Our *SOFIA* data (see Figure 5.10) show an extension in this direction as well, seen best at 19.7 μm. At wavelengths longer than 20 μm, there is a faint pull of emission to the NE and another faint extension to the SW, both of which correspond to the radio lobes of the ionized outflow (Figure 5.11b). Therefore, both outflows are revealed in the IR, with the ionized outflow only showing up at longer wavelengths, which again may be due to extinction. Detection of red and blue-shifted emission on both sides suggests a near side-on view of the outflows.

There is a large half-moon feature to the east of the main MIR peak in our *SOFIA* data. It has radio continuum emission (see Ellingsen et al. 2005) and could be a cometary compact HII region. Closer to the main MIR peak, we also see a secondary source $\sim 10''$to the south. There is no CO outflow associated with this source. We see a counterpart of this source in H and K band as seen in Figure 5.12. It could be a more evolved low-mass protostar. The source that is further SW, which is getting stronger at wavelengths longer than 31 μm, might be related to the ionized radio jet (Purser et al. 2016), though there is no hint of ionized emission from it in the study of Ellingsen et al. (2005).

5.4.2 General Results from the SOFIA Imaging

Overall in the sample of sources we have studied here, we often see that the MIR morphologies appear to be influenced by the presence of outflow cavities, which create regions of low dust extinction, and the presence of relatively cool, dense gas structures (potentially including disks and infall envelopes), which have high dust extinction, even at relatively long wavelengths. The presence of such structures is a general fea-

ture of Core Accretion models. A number of sources also appear to have companions, including from being in regions where a star cluster is likely forming, which can also complicate the appearance in the MIR.

In addition to the monochromatic images presented above, we also construct three-color images of all the sources, presented together in Figure 5.13. Note, however, that these RGB images have different beam sizes for the different colors (especially blue), with the effect being to tend to give small sources an extended red halo. In spite of this effect, in G45.12, G309.92, G35.58, IRAS 16562 and G339.88, short wavelength emission seems to dominate the extended structure. In IRAS 16562, we can see the near-facing outflow cavity appears bluer while the more extincted, far-facing outflow cavity appears redder. For the other sources we do not see obvious color gradients across the sources.

We summarize the properties of the protostellar sources in Table 5.3. The ordering of the sources is from high to low for the luminosity estimate (top to bottom). For two out of the three sources with detected outflows, the MIR morphology is significantly influenced by outflow cavities. For those lacking outflow information, we consider that it is still likely that the MIR emission is tracing outflows or flared disks. Especially in G309.92 and G305.20, high-resolution *Gemini* data reveals a flat dark lane, which could be the optically thick disk.

We see that at wavelengths $\gtrsim 19\,\mu$m, there is an offset between the radio emission, if that is where the protostar is located, and the MIR peaks in G309.92, G35.58, G49.27, G339.88. In Paper I we found that the MIR peaks appear displaced away from the protostar towards the blue-shifted, near-facing side of the outflow due to the higher extinction of the far-facing side at short wavelength. Here G339.88 may reveal a hint of this trend of the displacement. For the other sources, due to the lack

of outflow information, the cause of the offset is not yet clear.

We have also found candidates of more evolved, probably lower-mass protostars in the company of the massive protostar in most regions, based on the common peaks seen in multi-wavelength MIR and NIR data and how their fluxes change with wavelength. With the caveat that our sample is likely incomplete, the projected separation between the massive protostar and the nearest lower-mass companion revealed by *SOFIA* is about 0.28 pc in G45.12, 0.49 pc in G35.58, 0.12 pc in IRAS16562, 0.28 pc in G305.20, and 0.10 pc in G339.88. Note that Core Accretion models, such as the Turbulent Core Model of McKee & Tan (2003), can be applied to conditions inside protoclusters, as well as to more isolated regions, while Competitive Accretion (Bonnell et al. 2001) and Protostellar Collision (Bonnell et al. 1998) models require the presence of a rich stellar cluster around the protostar. To the extent that some of the presented sources appear to be in relatively isolated environments is thus tentative evidence in support of Core Accretion models, but deeper observations to probe the low-mass stellar population are needed to confirm this.

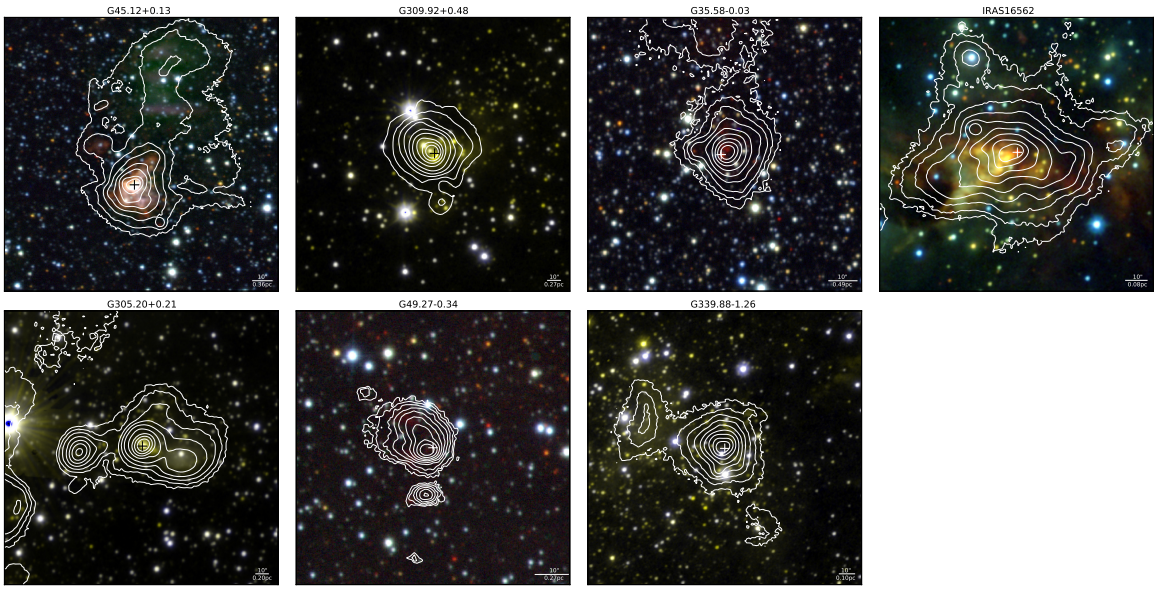

Fig. 5.12.— NIR RGB images of the seven protostellar sources, as labeled. The data of G45.12, G35.58, G49.27 and S235 come from the UKIDSS survey. The data of G309, IRAS16562, G305 and G339 come from the VVV survey. K band data is shown in red. H band data is shown in green. J band data is shown in blue. The white contours are SOFIA 37μm emission, with the same levels displayed in the previous individual figures for each source. The crosses in each panel are the same as the crosses in the previous individual figures, denoting the radio sources (methanol maser in G305). The scale bar is shown in the right corner of each panel.

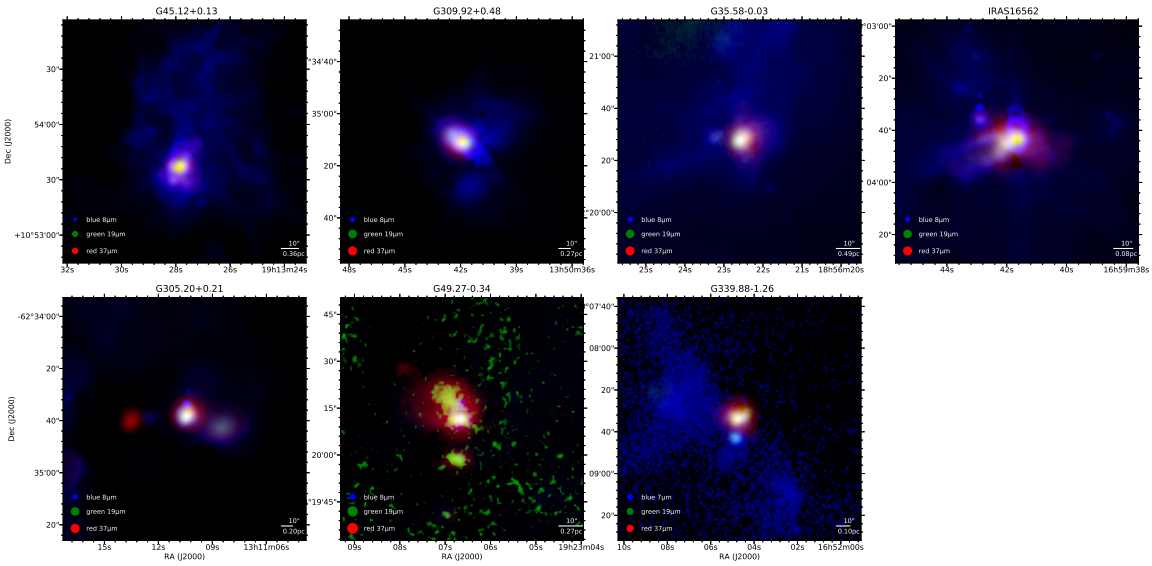

Fig. 5.13.— Gallery of RGB images of the seven protostellar sources, as labeled. The color intensity scales are stretched as arcsinh and show a dynamic range of 100 from the peak emission at each wavelength, except for the 19 μm image of G49.27, where only a dynamic range of 10 is shown due to its relatively low signal to noise ratio. The legend shows the wavelengths used and the beam sizes at these wavelengths. *SOFIA*-FORCAST 37 μm is shown in red. SOFIA-FORCAST 19 μm is shown in green. Blue usually shows *Spitzer* IRAC 8 μm, except for G339.88-1.26, where it displays *SOFIA*-FORCAST 7 μm.

Table 5.3. Summary of Properties of the Protostellar Sources

Source	Radio emission?	Outflow?	Multiple (proto)stars within 20″?	What regulates the MIR morphology?
G45.12+0.13	UC HII	Two	Cluster?[a]	Ionized medium
G309.92+0.48	HC HII	...	MIR companion. Resolved.	Outflow cavities or flared disk surface?
G35.58-0.03	UC HII	N	Nearby HII region with an outflow. Low-mass YSO?[b]	Outflows from nearby sources?
IRAS 16562-3959	HC HII with jet	Two	Cluster?[c]	Outflow cavities
G305.20+0.21	N	...	Nearby HII region. MIR companion. Resolved?[d] Low-mass YSO?[b]	Outflow cavities or flared disk surface?
G49.27-0.34	Y	...	Radio companion. MIR companion.	...
G339.88-1.26	Jet	Two	MIR companion. Resolved?[e] Binary?[f] Low-mass YSO?[b] Nearby HII region?	Outflow cavities and extinction

[a]Based on radio sources from Vig et al. 2006.

[b]Based on multi-wavelength MIR and NIR data.

[c]Based on X-ray sources from Montes et al. 2018.

[d]We suspect here the resolved structures are more likely to be emission separated by optically thick disk rather than two distinct protostars.

[e]We suspect here the resolved structures are emission tracing the outflow cavities rather than multiple distinct protostars. See also Zhang et al. 2019.

[f]Based on the fact of two outflows.

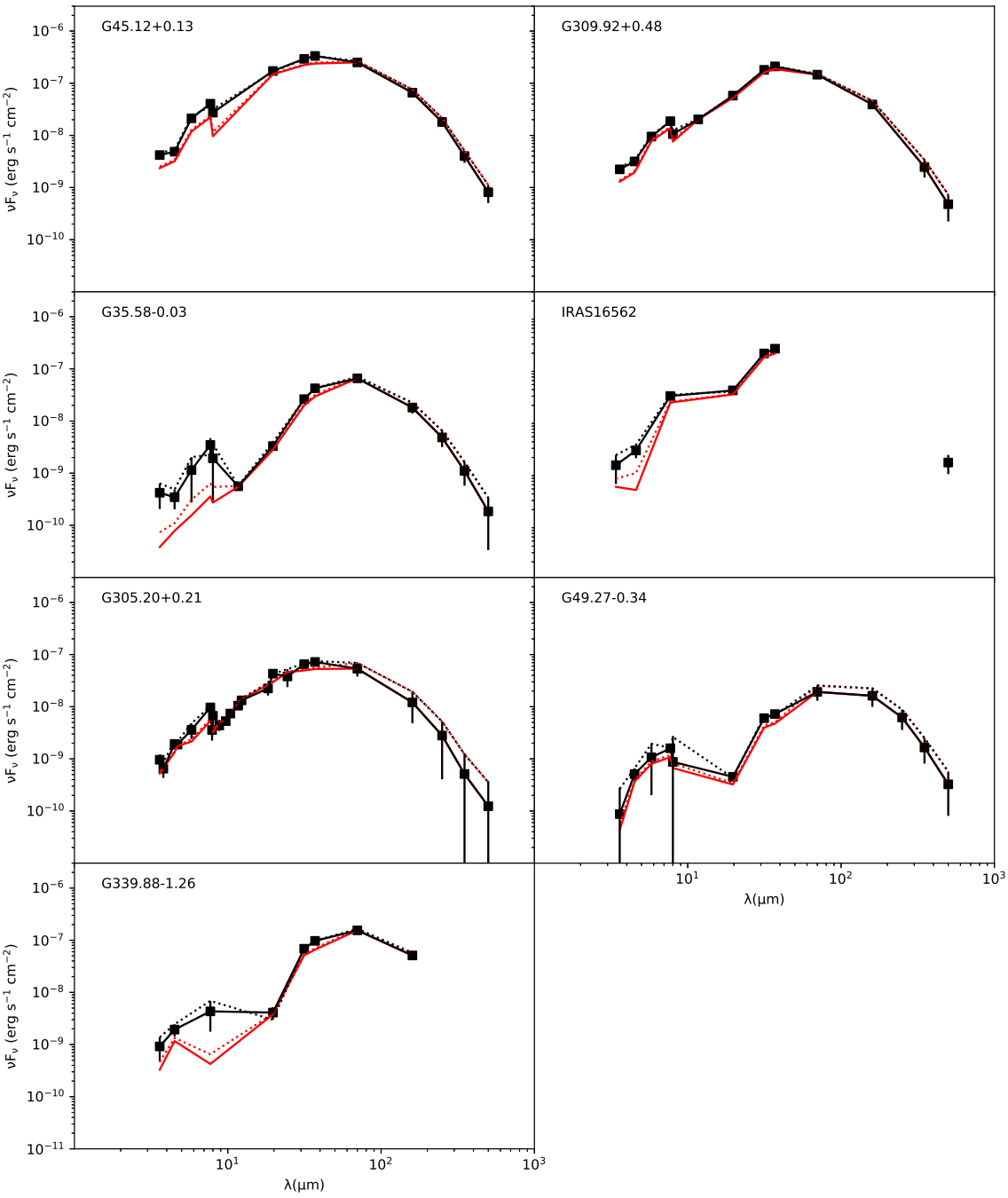

Fig. 5.14.— SEDs of the seven presented sources. Total fluxes with no background subtraction applied are shown by dotted lines. The fixed aperture case is black dotted; the variable aperture (at $< 70\ \mu$m) case is red dotted. The background subtracted SEDs are shown by solid lines: black for fixed aperture (the fiducial case); red for variable aperture. Black solid squares indicate the actual measured values that sample the fiducial SED. Note the Spitzer 4.5 μm, 5.8 μm and 8 μm data of G309 and all Spitzer data of G45.12 have ghosting problems and are not used for the SED fitting.

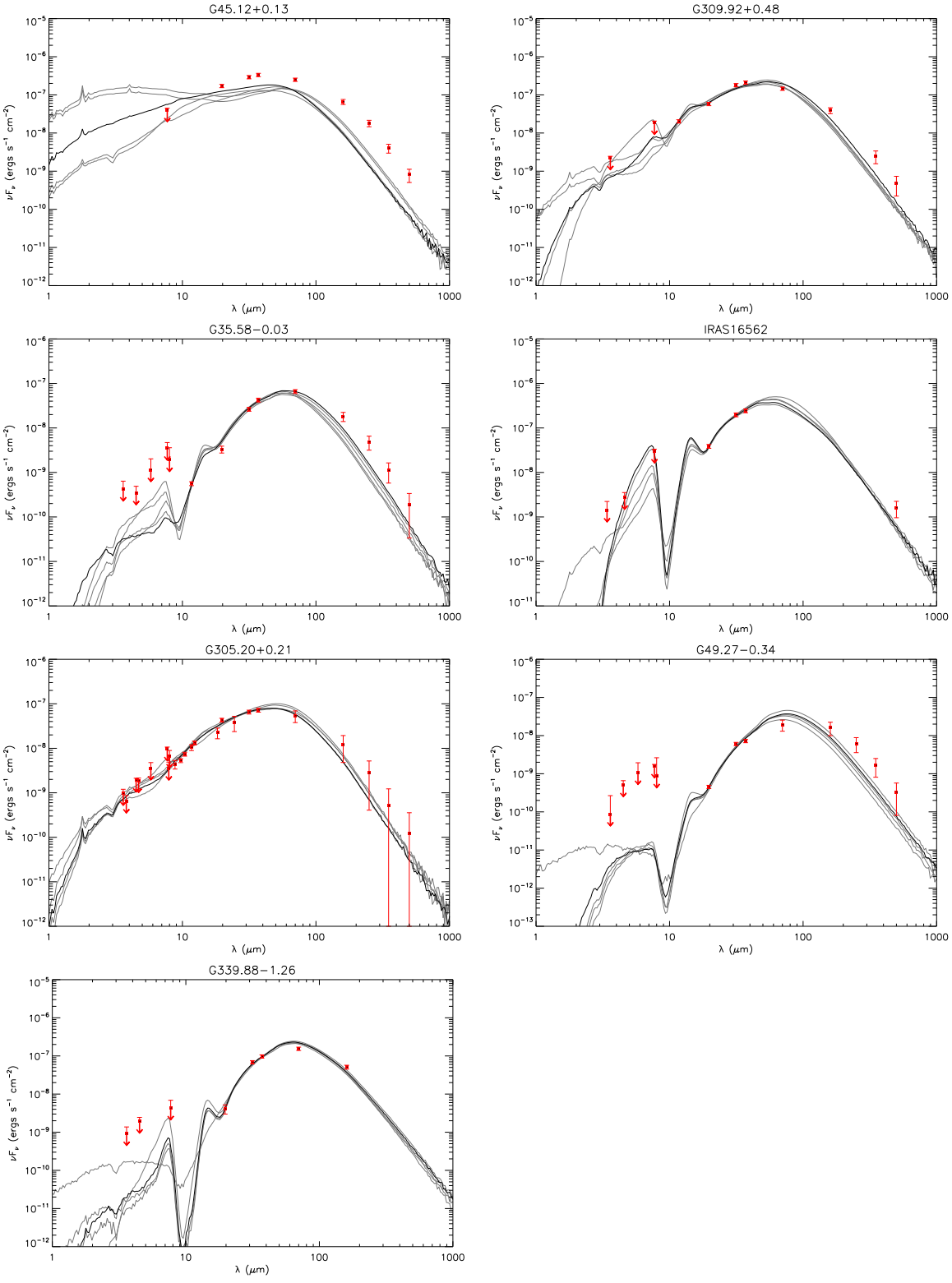

Fig. 5.15.— Protostar model fitting to the fixed aperture, background-subtracted SED data using the ZT model grid. For each source, the best fit model is shown with a solid black line and the next four best models are shown with solid gray lines. Flux values are those from Table 5.2. Note that the data at $\lesssim 8\,\mu$m are treated as upper limits (see text). The resulting model parameter results are listed in Table 5.4.

5.4.3 Results of SED Model Fitting

The SEDs

Figure 5.14 shows the SEDs of the seven sources that have been discussed in this paper. The figure illustrates the effects of using fixed or variable apertures, as well as the effect of background subtraction. Our fiducial method is that with fixed aperture and with background subtraction carried out. This tends to have moderately larger fluxes at shorter wavelengths than the variable aperture SED especially for G35.58, IRAS16562 and G339.88 where emission from secondary sources can be significant at wavelengths $\leq 8\,\mu$m. However, as in Paper I, the $\leq 8\,\mu$m flux is in any case treated as an upper limit in the SED model fitting, given the difficulties of modeling emission from PAHs and transiently heated small grains. The flux density derived from the two methods between $10\,\mu$m and $70\,\mu$m is generally close. For flux densities longer than $70\,\mu$m, the influence of secondary sources is not illustrated by the variable aperture method. However, we tried measuring the SEDs up to $37\,\mu$m of the MIR companions alone, which are resolved from the emission of the main protostar, and found that their flux density at each wavelength is $\leq 5\%$ of that of the main protostar (except that the $19\,\mu$m flux density of the southern patch in G49.27 is $\sim 20\%$ of that of the massive protostar). Moreover, all of them have a SED peak $\leq 31\,\mu$m except that the southern patch in G49.27 has a nearly flat rising slope between $31\,\mu$m and $37\,\mu$m. Thus the influence of secondary sources is generally not severe at long wavelengths that control the SED fitting.

Again, as mentioned in §5.3.1, for the cases where there seem to be multiple sources in the fiducial aperture, the model assumes one source dominates the luminosity and the key is to measure the flux from the same region across all wavelengths. If a source is isolated, then the fixed aperture at shorter wavelengths, which tends to be

Table 5.4. Parameters of the Best Five Fitted Models

Source	χ^2/N	$M_{\rm c}$ ($M_\odot$)	$\Sigma_{\rm cl}$ (g cm^{-2})	$R_{\rm core}$ (pc) ($''$)	m_* ($M_\odot$)	$\theta_{\rm view}$ ($^\circ$)	A_V (mag)	$M_{\rm env}$ ($M_\odot$)	$\theta_{w,{\rm esc}}$ (deg)	$\dot{M}_{\rm disk}$ ($M_\odot$/yr)	$L_{\rm bol,iso}$ ($L_\odot$)	$L_{\rm bol}$ ($L_\odot$)
G45.12+0.13	54.39	480	1.0	0.161 (4)	64.0	34	0.0	325	32	1.2×10^{-3}	6.5×10^5	8.4×10^5
d = 7.4 kpc	63.23	480	1.0	0.161 (4)	48.0	29	0.0	367	25	1.1×10^{-3}	4.5×10^5	5.4×10^5
R_{ap} = 48 $''$	65.40	480	3.2	0.091 (3)	24.0	13	0.0	441	12	2.0×10^{-3}	1.1×10^6	2.9×10^5
= 1.72 pc	66.41	400	3.2	0.083 (2)	24.0	13	0.0	362	13	1.9×10^{-3}	1.3×10^6	3.0×10^5
	69.30	240	3.2	0.064 (2)	32.0	29	0.0	175	23	1.9×10^{-3}	4.5×10^5	5.0×10^5
G309.92+0.48	2.82	320	3.2	0.074 (3)	24.0	22	12.1	277	15	1.8×10^{-3}	3.3×10^5	3.1×10^5
d = 5.5 kpc	3.90	480	1.0	0.161 (6)	48.0	29	39.4	367	25	1.1×10^{-3}	4.5×10^5	5.4×10^5
R_{ap} = 32 $''$	4.38	240	3.2	0.064 (2)	32.0	34	17.2	175	23	1.9×10^{-3}	3.2×10^5	5.0×10^5
= 0.85 pc	4.71	240	3.2	0.064 (2)	24.0	29	0.0	194	18	1.6×10^{-3}	2.6×10^5	3.1×10^5
	4.97	400	1.0	0.147 (6)	48.0	34	4.0	289	29	1.0×10^{-3}	3.0×10^5	5.3×10^5
G35.58-0.03	1.70	480	3.2	0.091 (2)	24.0	22	16.2	441	12	2.0×10^{-3}	2.9×10^5	2.9×10^5
d = 10.2 kpc	2.14	400	3.2	0.083 (2)	24.0	22	46.5	362	13	1.9×10^{-3}	3.0×10^5	3.0×10^5
R_{ap} = 26 $''$	3.41	320	3.2	0.074 (1)	24.0	29	35.4	277	15	1.8×10^{-3}	2.7×10^5	3.1×10^5
= 1.27 pc	4.28	480	1.0	0.161 (3)	48.0	34	39.4	367	25	1.1×10^{-3}	3.0×10^5	5.4×10^5
	4.49	480	1.0	0.161 (3)	64.0	39	72.7	325	32	1.2×10^{-3}	3.6×10^5	8.4×10^5
IRAS16562	0.53	400	0.1	0.465 (56)	32.0	44	100.0	304	29	1.5×10^{-4}	9.2×10^4	1.6×10^5
d = 1.7 kpc	0.64	480	0.1	0.510 (62)	24.0	71	55.6	418	21	1.4×10^{-4}	5.7×10^4	8.7×10^4
R_{ap} = 32 $''$	0.65	480	0.1	0.510 (62)	32.0	48	100.0	391	26	1.6×10^{-4}	9.8×10^4	1.6×10^5
= 0.26 pc	0.67	320	0.3	0.234 (28)	16.0	22	17.2	283	16	2.5×10^{-4}	5.3×10^4	6.1×10^4
	0.83	120	3.2	0.045 (6)	16.0	29	100.0	90	21	1.1×10^{-3}	1.0×10^5	1.2×10^5
G305.20+0.21	0.79	80	3.2	0.037 (2)	24.0	48	14.1	35	37	1.1×10^{-3}	7.5×10^4	2.6×10^5
d = 4.1 kpc	0.92	100	3.2	0.041 (2)	32.0	51	18.2	37	42	1.2×10^{-3}	7.9×10^4	3.5×10^5
R_{ap} = 16 $''$	0.97	160	1.0	0.093 (5)	32.0	44	13.1	88	39	5.9×10^{-4}	8.2×10^4	2.3×10^5
= 0.32 pc	1.04	80	3.2	0.037 (2)	16.0	34	8.1	50	27	9.5×10^{-4}	7.2×10^4	1.1×10^5
	1.11	160	3.2	0.052 (3)	48.0	58	16.2	59	45	1.6×10^{-3}	9.0×10^4	6.4×10^5
G49.27-0.34	1.87	240	3.2	0.064 (2)	12.0	22	54.5	219	12	1.2×10^{-3}	4.5×10^4	4.8×10^4
d = 5.55 kpc	1.96	200	3.2	0.059 (2)	12.0	22	92.9	179	13	1.1×10^{-3}	4.9×10^4	5.2×10^4
R_{ap} = 29 $''$	2.18	320	3.2	0.074 (3)	12.0	22	0.0	302	10	1.3×10^{-3}	4.7×10^4	4.9×10^4
= 0.77 pc	2.37	160	3.2	0.052 (2)	12.0	29	77.8	139	15	1.0×10^{-3}	4.4×10^4	5.3×10^4
	2.73	120	3.2	0.045 (2)	12.0	34	73.7	99	18	9.6×10^{-4}	3.6×10^4	5.2×10^4
G339.88-1.26	2.21	400	0.3	0.262 (26)	12.0	22	17.2	373	11	2.3×10^{-4}	3.7×10^4	4.0×10^4
d = 2.1 kpc	2.30	320	0.3	0.234 (23)	12.0	68	6.1	293	13	2.2×10^{-4}	3.3×10^4	4.0×10^4
R_{ap} = 32 $''$	2.48	480	0.3	0.287 (28)	12.0	22	7.1	459	10	2.5×10^{-4}	3.8×10^4	4.0×10^4
= 0.33 pc	2.62	320	0.3	0.234 (23)	16.0	22	90.9	283	16	2.5×10^{-4}	5.3×10^4	6.1×10^4
	2.84	120	3.2	0.045 (4)	12.0	44	0.0	99	18	9.6×10^{-4}	3.3×10^4	5.2×10^4

larger than the source appears, may include more noise and make the photometry less accurate than the variable aperture method. However, since we set the clump background emission as the magnitude of the uncertainty, this effect should be very minor.

The peaks of the SEDs are generally between 37 μm and 70 μm. In particular, the SED peaks of G45.12, G309.92, G305.20 appear to be closer to 37 μm, while the peaks of G35.58, G49.27 and G339.88 appear to be closer to 70 μm. This may be related to the evolutionary stage and/or viewing angle of the sources (see §5.4.3).

ZT Model Fitting Results

Figure 5.15 shows the results of fitting the ZT protostellar radiative transfer models to the fixed aperture, background-subtracted SEDs. Note that the data at ≤ 8 μm are considered to be upper limits given that PAH emission and transiently heated small grain emission are not well treated in the models. The parameters of the best-fit ZT models are listed in Table 5.4. From left to right the parameters are reduced χ^2 (i.e., normalized by the number of data points in the SED, N), the initial core mass (M_c), the mean mass surface density of the clump ($\Sigma_{\rm cl}$), the initial core radius ($R_{\rm core}$), the current protostellar mass (m_*), the viewing angle ($\theta_{\rm view}$), foreground extinction (A_V), current envelope mass ($M_{\rm env}$), half opening angle of the outflow cavity ($\theta_{w,{\rm esc}}$), accretion rate from the disk to the protostar ($\dot{m}_*$), the luminosity integrated from the unextincted model SEDs assuming isotropic radiation ($L_{\rm bol,iso}$), and the inclination corrected, true bolometric luminosity ($L_{\rm bol}$). For each source, the best five models are shown, ordered from best to worst as measured by χ^2. Note that these are distinct physical models with differing values of M_c, $\Sigma_{\rm cl}$, and/or m_*, i.e., we do not display simple variations of $\theta_{\rm view}$ or A_V for each of these different physical models.

The best-fit models imply the sources have protostellar masses $m_* \sim 12 - 64\,M_\odot$ accreting at rates of $\dot{m}_* \sim 10^{-4} - 10^{-3}\,M_\odot\,\mathrm{yr}^{-1}$ inside cores of initial masses $M_c \sim 100 - 500\,M_\odot$ embedded in clumps with mass surface densities $\Sigma_{\rm cl} \sim 0.1 - 3\,\mathrm{g\ cm}^{-2}$ and span a luminosity range of $10^4 - 10^6\,L_\odot$.

In most sources the best five models have similar values of χ^2, but there is still significant variations in the model parameters even for G305.20 which has the most SED data points. As stated in Paper I, this illustrates the degeneracy in trying to constrain the protostellar properties from only MIR to FIR SEDs, which would be improved by extended SEDs fitting including centimeter continuum flux densities (Rosero et al. 2019) and image intensity profile comparison. From the SED shape the most variation between models appears at shorter wavelengths. Here more data points can help better constrain the models, as in G305.20. Again we note that although sometimes the χ^2 may look high, as in G45.12+0.13, here we focus more on the relative comparison of χ^2 between the models available in the model grid, which still give us constraints on the protostellar properties. At wavelengths $>$ 70 μm the models tend to be lower than the data points in many sources. Note the values of $R_{\rm core}$ returned by the models are usually much smaller than the aperture radii. This would indicate that, even after a first attempt at clump background subtraction, the measured flux still has significant contribution from the cool surrounding clump. Recall that this component is not included in the ZT radiative transfer models and can thus lead to the offset at long wavelengths, i.e., with models under-predicting the observed fluxes.

We also tried fitting the SEDs with variable apertures across wavelength. Most sources have $R_{\rm core}$ similar to that derived in the fiducial case and still the models appear lower than the data points at long wavelengths for G309.92, G35.58, G305.20

and G49.27.

We note that m_* appears quite high for G45.12+0.13, G309.92+0.48, G35.58-0.03, IRAS 16562, G305.20+0.21. This is likely due to there being more than one protostar inside the aperture, even with the variable aperture case, like the source G35.20-0.74 in Paper I, where the stellar mass returned by the models is around the sum of the two binary protostars in the center (Beltrán et al. 2016, Zhang et al. 2018).

The location of the SED peak is thought to show a dependence on the evolutionary stage of the source. We compare the current age derived from the models and the corresponding total star formation time scale based on Eq. (44) in MT03 assuming a star formation efficiency of 0.5. G305.20 appears to be the most evolved followed by G309.92 and G45.12. G339.88 appears to be the least evolved followed by G49.27. G339.88 is still deep embedded with high dust extinction while G49.27 is an IRDC source. They are likely the youngest YSOs among the seven sources. The evolutionary stage revealed by the models is consistent with the picture that more evolved sources have a SED peak located at shorter wavelengths, as described in §5.4.3. However, orientation effects may also be playing a role, since the peak of the SED shifts to shorter wavelengths when viewing sources at angles closer to their outflow axis.

Next we describe the fitting results of each individual source and compare with previous literature results.

G45.12+0.13: This is our most luminous source (almost $10^6\ L_\odot$) and hits the boundary of the parameter space of the ZT model grid, which is partly why the models do not seem to fit the data points very well, as shown in Figure 5.15, since there are only a few models around $10^6\ L_\odot$ (Zhang & Tan 2018). As an experiment, we tried changing the distance from 7.4 kpc to 1 kpc and were able to obtain fitting results that have much smaller values of χ^2. On the other hand, this region is likely

to be a protocluster hosting many ZAMS stars. Thus the assumption of one source dominating the luminosity may not work well here. The current best models indicate high initial core mass $M_c \sim 500\ M_\odot$, high $\Sigma_{\rm cl} \gtrsim 1.0$ g cm^{-2} clump environment and high protostellar mass $m_* \geq 24\ M_\odot$ for the dominant source. The accretion rate is $\sim 10^{-3} M_\odot$ yr^{-1}. The current envelope mass is also typically as high as $\sim 400\ M_\odot$. The foreground extinction A_V is estimated to be very low, but this may be an artefact of other problems of the model fitting. The best five models all give a $\theta_{\rm view}$ close to $\theta_{w,{\rm esc}}$, which leads to high levels of short wavelength emission.

G309.92+0.48: The best models prefer a massive protostar of ~ 24 to 48 $M_\odot$ accreting at $\sim 10^{-3} M_\odot$ yr^{-1} in a massive core of ~ 240 to 480 $M_\odot$ in high $\Sigma_{\rm cl} \gtrsim 1.0$ g cm^{-2} clump environments. The protostar is slightly inclined $\sim 30°$. Walsh et al. (1997) concluded that if the region were powered by a single star, it would have to be an O5.5 star with a luminosity of $3.1 \times 10^5 L_\odot$, which agrees well with the isotropic luminosities returned by our models. The viewing angle is close to the outflow half opening angle, resulting in a relatively flat SED shape at shorter wavelengths.

G35.58-0.03: The best models prefer a massive protostar of ~ 24 to 64 $M_\odot$ accreting at $\sim 10^{-3} M_\odot$ yr^{-1} in a massive core of ~ 320 to 480 $M_\odot$ in high $\Sigma_{\rm cl} \gtrsim 1.0$ g cm^{-2} clump environments. We also tried fitting the SEDs with the flux measured in variable apertures without setting short wavelength data as upper limits, which exclude the flux from the secondary source to the east at short wavelengths. The best five models have almost the same range for M_c, $\Sigma_{\rm cl}$, m_*, $\dot{m}_*$ and $L_{\rm bol,iso}$ (there is one model having $m_* \sim 96\ M_\odot$) as our fiducial case. An early-type star equivalent to an O6.5 star is postulated to have formed within the HC HII region based on the derived Lyman continuum photon number in Zhang et al. (2014). The molecular envelope shows evidence of infall and outflow with an infall rate of 0.05 $M_\odot$ yr^{-1} and

a mass loss rate of $5.2 \times 10^{-3}\ M_\odot\ \mathrm{yr}^{-1}$, which is somewhat higher than our derived disk accretion rate, but may reflect infall on larger scales.

IRAS 16562-3959: There are only 4 fully valid data points constraining the fitting. Since we have 5 free parameters and the χ^2 is derived by dividing the number of total data points including those as upper limits, the small number of fully valid data points largely leads to the relatively small χ^2. The first four best models tend to give high core masses $\sim$ 320 to 480 $M_\odot$ and low $\Sigma_{\rm cl} \lesssim 0.3\,\mathrm{g\,cm^{-2}}$ clump environments, while the fifth best model gives a less massive initial core of 120 $M_\odot$ and a much denser $\Sigma_{\rm cl} \sim 3.2\,\mathrm{g\,cm^{-2}}$ clump. Note in the first three models the core radii are larger than the aperture radius. The bolometric luminosity of the source is reported to be $5 - 7 \times 10^4\ L_\odot$ by Lopez et al. (2011), which agrees well with most of the models. Guzman (2010) also fit this source with Robitaille et al. (2007) models. The stellar mass of their result 14.7 $M_\odot$ is close to our fourth and fifth best models. Their disk accretion rate $5.5 \times 10^{-4} M_\odot\ \mathrm{yr}^{-1}$ is closest to our fourth best model. Their envelope mass 1700 $M_\odot$ is much larger than our results. Guzmán et al. (2011) estimated the inclination angle of the SE-NW outflow to be 80°, which is similar to our second best model.

G305.20+0.21: We have the most data for this source to constrain the model fitting. The initial core mass returned is moderate, ranging from 80 to 160 $M_\odot$. Consistently, the envelope mass for this source is also much lower than previous sources. The stellar mass ranges from 16 to 48 $M_\odot$, accreting at a high rate $\sim 10^{-3} M_\odot \mathrm{yr}^{-1}$. Four models give $\Sigma_{\rm cl}$ as high as $3.2\mathrm{g\,cm^{-2}}$ and one gives $\Sigma_{\rm cl} \sim 1.0\mathrm{g\,cm^{-2}}$. The viewing angle is close to the outflow half opening angle, resulting in a flat SED shape at short wavelengths. The extrapolated IRAS luminosity is $\gtrsim 10^5\ L_\odot$ (Walsh et al. 2001), which is consistent with the $L_{\rm bol}$ derived here.

G49.27-0.34: The models at short wavelengths are much lower than the data points, perhaps indicating significant PAH emission or small dust grain emission from additional heating sources in the region. The best five models all return m_* of 12 $M_\odot$ and $\Sigma_{\rm cl}$ of 3.2 g cm^{-2}. The initial core mass ranges from 120 to 320 $M_\odot$. The accretion rates are $\sim 10^{-3}\ M_\odot\ {\rm yr}^{-1}$.

G339.88-1.26: The best four models prefer a protostar of $\sim 12\ M_\odot$ accreting at $\sim 2 \times 10^{-4}\ M_\odot\ {\rm yr}^{-1}$ in massive cores of 320 to 480 $M_\odot$ in clumps with low $\Sigma_{\rm cl} \sim 0.3\,{\rm g\,cm}^{-2}$. Alternatively, the fifth best model gives a less massive initial core mass of 120 $M_\odot$, but a much denser clump environment with $\Sigma_{\rm cl} \sim 3.2\ {\rm g\ cm}^{-2}$ and a higher accretion rate of $\sim 10^{-3}\ M_\odot\ {\rm yr}^{-1}$. The bolometric luminosity has been estimated to be $6.4{\times}10^4 L_\odot$ from the SED fitting to infrared fluxes with Robitaille et al. (2007) models in Mottram et al. (2010, 2011), which is similar to the luminosities in our five best models.

Recent ALMA observations (Zhang et al. 2019) reveal collimated CO outflows with a half opening angle of $\sim 10°$. In particular, they determine the outflow to be much edge-on so the second model here with $i \approx 20°$ is favored. They also estimate the dynamical mass from the gas kinematics as $\sim 11\ M_\odot$, which is also consistent with our results.

In summary, the massive protostellar sources investigated in this paper tend to have very massive initial cores, high protostellar masses and high accretion rates. The mass surface densities of the clump environments show significant variation. The high envelope masses indicate the protostars are still in an active stage of accretion. Viewing angles tend to be more face-on than edge-on. This allows shorter wavelength photons to more easily escape through the outflow cavities towards the observer, though still regulated partially by extinction of core infall envelope and foreground

clump material. Since SOMA survey sources have been selected based on their previously known MIR emission, it is not surprising that the sample may have such a bias towards having more face-on inclinations. Future studies examining inclinations constrained from MIR image intensity profiles and outflow kinematics will allow better measurement of source orientations and a more thorough examination of this effect.

5.5 Discussion

Compared with the first eight protostars in Paper I, we have extended the upper limit of the luminosity range by one order of magnitude as shown in Figure 5.16. The seven sources in this paper are more luminous, and thus likely to be more massive protostars embedded in higher mass cores. However, there is the caveat of there being multiple sources sometimes present.

Figure 5.17 shows the χ^2 distribution in $\Sigma_{\rm cl}$ - M_c space, m_* - M_c space and m_* - $\Sigma_{\rm cl}$ space for 6 of the sources, i.e., all except G45.12 due to its large χ^2. These diagrams illustrate the full constraints in the primary parameter space derived by fitting the SED data, and the possible degeneracies among these parameters. Thus these diagrams give a fuller picture of potential protostellar properties than just the best five models.

Similar to Paper I, M_c and m_* are relatively well constrained, while $\Sigma_{\rm cl}$ usually spans the full range (for G49.27 the best five models return a universal $\Sigma_{\rm cl}$ of 3.2 g cm^{-2} though). The best models ($\chi^2 - \chi^2_{\rm min} < 5$, within the red contours) tend to occupy a region with lower M_c at higher $\Sigma_{\rm cl}$ and higher M_c at lower $\Sigma_{\rm cl}$, similar to the sources in Paper I as discussed in ZT18. The black dashed line denotes a constant R_c with $R_c = R_{\rm ap}$ using $R_c = 0.057(\Sigma_{\rm cl}/{\rm g\ cm^{-2}})^{-1/2}\ (M_c/60M_\odot)^{1/2}$ pc (MT03). Parameter sets higher than this line mean they have a R_c smaller than $R_{\rm ap}$, which is more

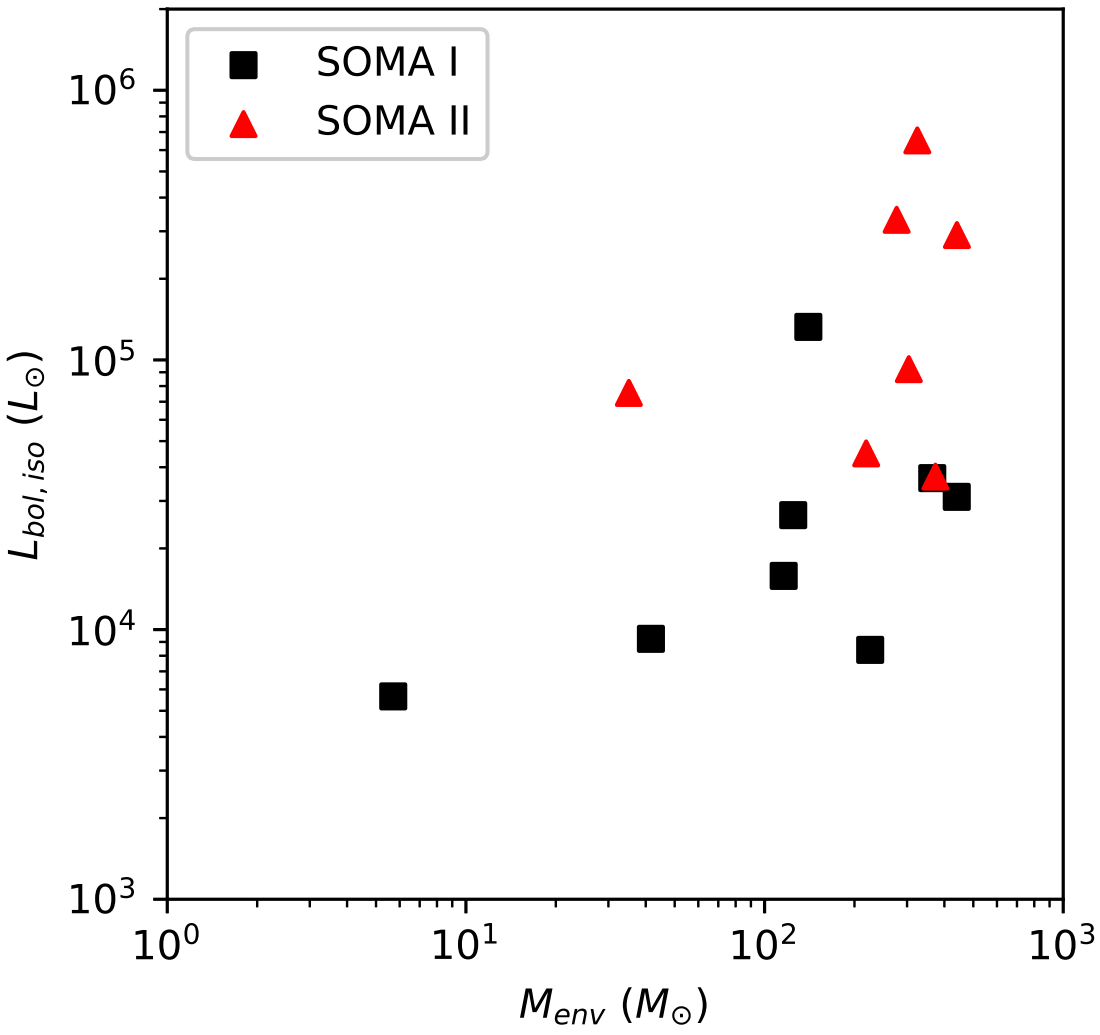

Fig. 5.16.— Diagram of isotropic luminosity versus the envelope mass returned by the ZT best model. Squares denote the sample in Paper I. Triangles denote the sample in this paper.

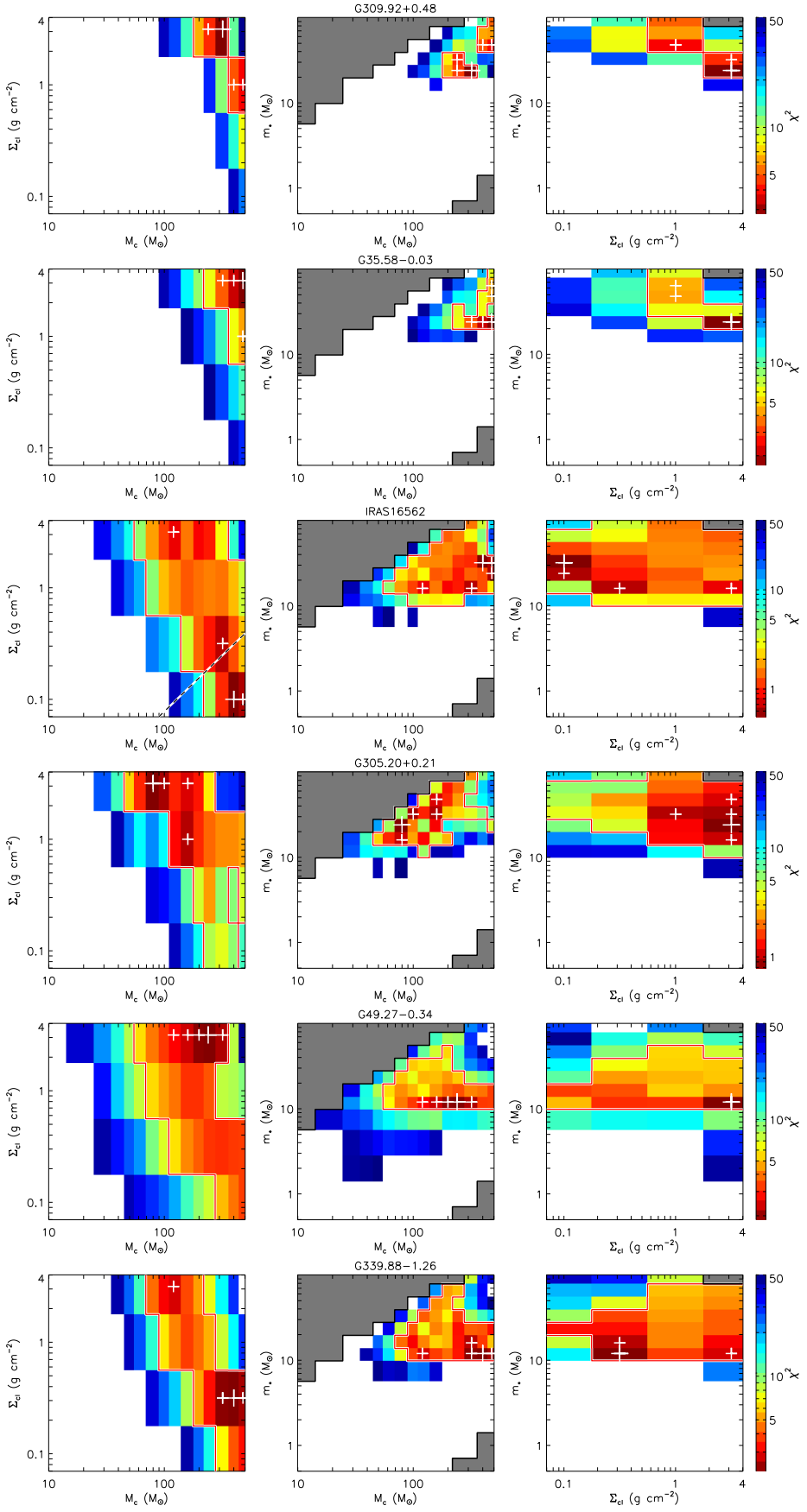

Fig. 5.17.— Diagrams of χ^2 distribution in $\Sigma_{\rm cl}$ - M_c space, m_* - $M_{\rm c}$ space and m_* - $\Sigma_{\rm cl}$ space. The white crosses mark the locations of the five best models, and the large

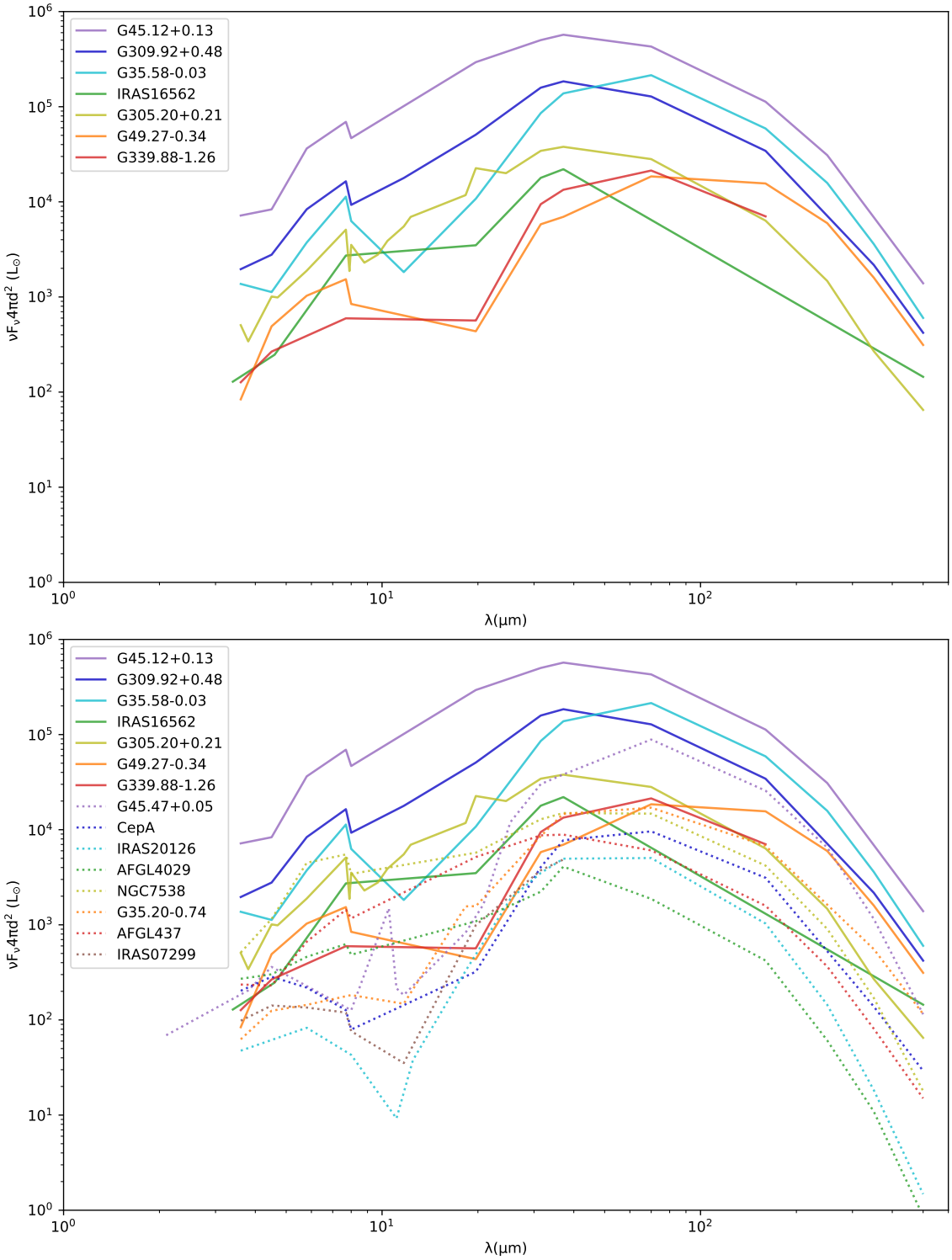

Fig. 5.18.— *Top panel:* Bolometric luminosity weighted SEDs of the eight SOMA protostars analyzed in this paper. The ordering of the legend is from high to low ZT best fit model isotropic luminosity (top to bottom). *Bottom panel:* Same as Top, but now with dotted lines denoting sample in Paper I.

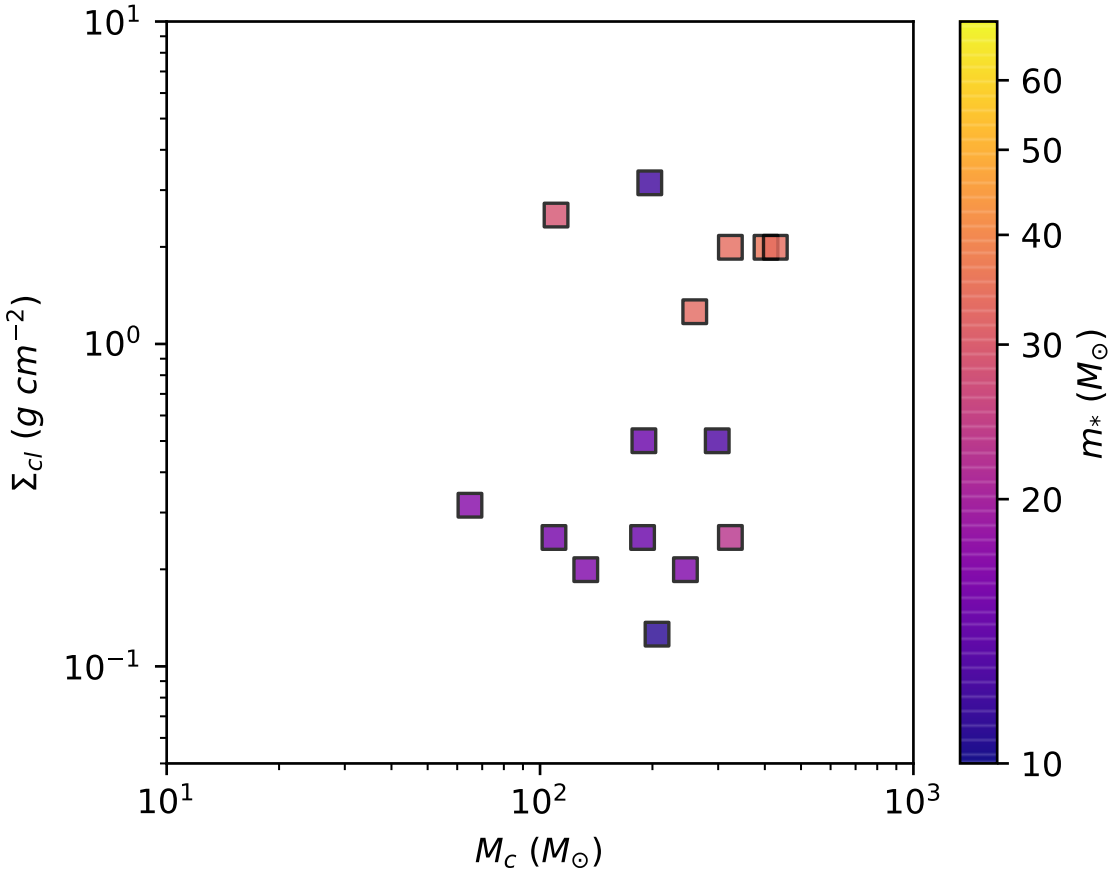

Fig. 5.19.— Diagram of the geometric mean clump surface density versus the geometric mean initial core mass of the five best ZT models for each source in Paper I and this work. The color indicates the geometric mean protostellar mass.

physical since we assume the aperture we choose covers the whole envelope. This line only appears in IRAS 16562 because in other sources the $R_{\rm ap}$ is so large that they all appear to the right of the available $\Sigma_{\rm cl}$ - M_c space. We can see for most sources at least the best models satisfy this criterion.

In Figure 5.18 we show the bolometric luminosity spectral energy distributions of the seven high luminosity protostars of this paper, together with the sample from Paper I. Here the νF_ν SEDs have been scaled by $4\pi d^2$ so that the height of the curves gives an indication of the luminosity of the sources assuming isotropic emission. The ordering of the vertical height of these distributions is largely consistent with the rank ordering of the predicted isotropic luminosity of the protostars from the best-fit ZT models (the legend in Figure 5.18 lists the sources in order of decreasing ZT best model isotropic luminosity). The curve of G305.20 appears higher than IRAS 16562. However, if we look at all the five best models the isotropic luminosity of G305.20 and IRAS 16562 are actually quite close. The foreground extinction of G305.20 is also generally lower than IRAS 16562, which leads to a higher $4\pi d^2 \nu F_\nu$. Similarly, the foreground extinction of G339.88 is on average lower than G49.27, so that G339.88 has a larger height of the bolometric luminosity SED.

We find no obvious systematic variation in SED shape with varying luminosity. This was investigated by plotting the slope between 19 μm and 37 μm versus the isotropic luminosity of the sources (not shown here). We also investigated the relation between $\Sigma_{\rm cl}$, M_c and m_* in Figure 5.19. To form high-mass stars naturally requires relatively massive cores (this assumption is built in to the models). However, $\Sigma_{\rm cl}$ does not have to be very high. However, the models with $\Sigma_{\rm cl} \sim 0.1$ g cm^{-2} have $R_{\rm core} > R_{\rm ap}$ most of the time, which is physically inconsistent with the analysis method. The models with $\Sigma_{\rm cl} \sim 0.3$ g cm^{-2} only have $R_{\rm core} > R_{\rm ap}$ occasionally, while

the other models with higher $\Sigma_{\rm cl}$ do not have such a problem. Thus it is massive protostellar core models with $\Sigma_{\rm cl} \gtrsim 0.3\,{\rm g\,cm^{-2}}$ surrounding clump environments that are currently consistent with the observed sources.

Overall the ZT models can fit the observed SEDs reasonably well assuming a single protostar forming through an axisymmetric monolithic collapse from a massive core. Only in G45.12, which has stronger evidence for their being multiple protostars that are part of a forming cluster, do the models fare badly and have relatively large values of χ^2 (although this may also be due to its extreme luminosity causing it to be near the edge of the ZT model grid). There are reported examples of quite ordered protostellar cores, i.e., with collimated, symmetric outflows: e.g., the case of the early-stage protostar C1-Sa (Tan et al. 2016) and G339.88-1.26 (Zhang et al. 2019, presenting follow-up ALMA observations of one of these SOMA sources). On the other hand, there are also cases that appear much more disordered in both their accretion flows (W51e2e, W51e8, and W51 north, Goddi et al. 2018) and outflows (Orion KL, Bally et al. 2017). The combination of MIR to FIR SED and image fitting with high resolution studies of infall and outflow morphologies for larger samples will allow us to better determine the limitations of simple axisymmetric protostellar core models for Galactic massive star formation studies.

5.6 Conclusions

We have presented the results of MIR and FIR observations made towards the next seven highest luminosity protostars in the SOMA survey, built their SEDs and fit them with RT models of massive star formation via the Turbulent Core Accretion model. Our goal has been to expand the observational massive protostar sample size to test the star formation models over a wider range of properties and environments

and investigate trends and conditions in their formation. Compared with the first eight protostars in Paper I, the seven YSOs in this paper are more luminous, and thus likely to be more massive protostars. Some of the new sources appear to be in more clustered environments and/or have lower-mass companions relatively nearby. In summary, our main results and conclusions are as follows.

1. The MIR emission of massive protostars is strongly influenced by outflow cavities, where extinction is relatively low. We see MIR extension along detected outflows in IRAS16562 and G339.88. Away from these cavities, extinction can be very high and block MIR emission. There is also a hint that the MIR emission may reveal the presence of the optically thick disk perpendicular to the outflow as in G309.92 and G305.20, though more evidence of the position of the protostar from mm or radio continuum observations will be needed to confirm the disk. The high extinction in the MIR tells us that large quantities of high column density material is present close to the protostar, as expected in the Turbulent Core model.

2. The sources span a luminosity range of $10^4 - 10^6\ L_\odot$. Fitting the SEDs with RT models yields protostellar masses $m_* \sim 12 - 64\ M_\odot$ accreting at rates of $\dot{m}_* \sim 10^{-4} - 10^{-3}\ M_\odot\ \mathrm{yr}^{-1}$ inside cores of initial masses $M_c \sim 100 - 500\ M_\odot$ embedded in clumps with mass surface densities $\Sigma_{\rm cl} \sim 0.1 - 3\ \mathrm{g\ cm}^{-2}$. The relatively high protostellar mass in several sources is possibly due to there being more than one protostar in the region and the m_* derived could be the sum of multiple sources.

3. The SED shape, especially the slope at short wavelengths, appears related to the viewing angle and the outflow opening angle. When the viewing angle is close to the outflow opening angle, a relatively flat slope at short wavelengths results. However, the SED shape, especially the location of the SED peak, is also likely to be related to the evolutionary stage of the protostar: more evolved protostars tend to

peak at relatively shorter wavelengths. So far we do not see obvious relations between SED shape and bolometric luminosity.

4. To form high-mass stars naturally requires high values of M_c, but not seem to require especially high values of $\Sigma_{\rm cl}$. We see high-mass protostars are able to at least form from $\Sigma_{\rm cl} \gtrsim 0.3$ g cm^{-2} environments.

5. Radiative transfer models based on the Turbulent Core Accretion scenario can reasonably well describe the observed SEDs of most relatively isolated massive protostars, but may not be valid for the most luminous regions in the sample, which may be better treated as protoclusters containing multiple sources. Whether or not core accretion models can apply on smaller physical scales within these regions requires higher angular resolution MIR to FIR observations.

Chapter 6

The SOFIA Massive (SOMA) Star Formation Survey. III. From Intermediate- to High-Mass Protostars

6.1 Introduction

Intermediate-mass (IM) protostars are important as representatives of the transition between the extremes of low- (i.e., $\lesssim 2\ M_{\odot}$) and high- (i.e., $\gtrsim 8\ M_{\odot}$) mass star formation. These objects are relatively rare compared to their low-mass counterparts and tend to be located at greater distances. They are precursors of Herbig Ae and Be stars. The immediate environments of IM protostars can appear quite complex, with extended emission often resolved into multiple sources when observed at high resolution (e.g., G173.58+2.45, Shepherd & Watson 2002). However, there are also examples with relatively simpler, more isolated morphologies (e.g., Cep E, Moro-

Martín et al. 2001). Observations of IM protostars indicate that they share some similar physical properties as low-mass protostars, such as circumstellar disks (e.g., Zapata et al. 2007; Sánchez-Monge et al. 2010; van Kempen et al. 2012; Takahashi et al. 2012) and collimated molecular outflows (e.g., Gueth et al. 2001; Beltrán et al. 2008, 2009; Palau et al. 2010; Velusamy et al. 2011), but with the latter being more powerful when driven from IM protostars. Furthermore, IM protostars also share many characteristics with their higher-mass counterparts, such as correlations between the outflow kinematics and the properties of their driving sources (e.g., Cabrit & Bertout 1992; Bontemps et al. 1996; Wu et al. 2004; Hatchell et al. 2007; Beltrán et al. 2008), and hot core chemistry (e.g., Fuente et al. 2005; Neri et al. 2007; Sánchez-Monge et al. 2010). Thus, the observational evidence suggests that intermediate-mass protostars form in a similar way as low-mass protostars, and that this formation mechanism is also shared with at least early B-type or late O-type protostars (Beltrán 2015).

In this paper, we study a sample of 14 IM protostars selected from the *SOFIA* Massive (SOMA) Star Formation Survey (PI: Tan), which aims to characterize a sample of $\gtrsim$ 50 high- and intermediate-mass protostars over a range of evolutionary stages and environments with their $\sim$ 10 to 40 μm images observed with the *SOFIA*-Faint Object infraRed CAmera for the *SOFIA* Telescope (FORCAST) instrument. In Paper I of the survey (De Buizer et al. 2017), the first eight sources were presented, which were mostly massive protostars. In Paper II (Liu et al. 2019), seven especially luminous sources were presented, corresponding to some of the most massive protostars in the survey. Thus the IM sample presented here, which consists of 7 new target regions from which 12 protostars have been studied plus 2 more protostars extracted as secondary sources from Papers I and II target regions, serves to extend

the luminosity and mass range of the survey sample down to lower values.

Our approach is to follow the same methods developed in Papers I and II to build the spectral energy distributions (SEDs) of the sources. As before, we then fit these SEDs with the Zhang & Tan (2018, hereafter ZT18) protostellar radiative transfer (RT) models to estimate intrinsic source properties. In this way, all the protostars are analyzed in an uniform way. Finally, we search for trends in source properties among the overall SOMA sample of 29 sources that have been so far analyzed in Papers I, II and III.

The observations and data used are described in §6.2. The analysis methods are described in §6.3. We present the MIR imaging and SED fitting results in §6.4 and discuss these results and their implications in §6.5. A summary is given in §6.6.

6.2 Observations

The following seven target regions were observed by *SOFIA*[1] (Young et al. 2012) with the FORCAST instrument (Herter et al. 2013) (see Table 6.1): S235, IRAS 22198+6336, NGC 2071, Cep E, L1206 (A and B), IRAS22172+5549 (MIR 1, MIR 2, and MIR 3), IRAS 21391+5802 (BIMA 2, BIMA 3, and MIR 48). The angular resolutions of the *SOFIA*-FORCAST images are 2.7″ at 7 μm, 2.9″ at 11 μm, 3.3″ at 19 μm, 3.4″ at 31 μm, and 3.5″ at 37 μm. We also fit the SEDs of two more sources G305.20+0.21 A (hereafter, G305 A) and IRAS 16562-3959 N (hereafter, IRAS 16562 N), which are secondary sources near primary targets of Paper II. Thus a total of 14 protostars will be analyzed here for the first time as SOMA Survey sources.

In addition to *SOFIA* observations, for all objects, we also retrieve publicly-

[1] *SOFIA* is jointly operated by the Universities Space Research Association, Inc. (USRA), under NASA contract NAS2-97001, and the Deutsches SOFIA Institute (DSI) under DLR contract 50 OK 0901 to the University of Stuttgart.

available images of *Spitzer*/IRAC (Fazio et al. 2004) at 3.6, 4.5, 5.8 and 8.0 μm from the *Spitzer* Heritage Archive, *Herschel*/PACS and SPIRE (Griffin et al. 2010) at 70, 160, 250, 350 and 500 μm from the *Herschel* Science Archive, and Higher Resolution IRAS Images (*HIRES*)[2] (Neugebauer et al. 1984) at 60, 100 μm from the NASA/IPAC Infrared Science Archive.

The calibration and astrometry methods are the same as those of Paper II, except that for Cep E and IRAS 21391 we use the *SOFIA* 19 μm image instead of 7 μm to calibrate the other *SOFIA* images and the *Herschel* images given the high noise level in their 7 μm images. For *SOFIA* observations the calibration error is estimated to be in the range $\sim$ 3% - 7%. The astrometric precision is about 0.1″ for the *SOFIA* 7 μm image, 0.4″ for longer wavelength *SOFIA* images, and 1″ for *Herschel* images. Note that we use HIRES results of the *IRAS* data to achieve a resolution $\sim$ 1′. The astrometric precision is about 20 - 30″. Fluxes measured from HIRES agree with those of the Point Source Catalog (PSC2) to within 20% and ringing (a ring of lower level flux may appear around a point source) can contribute up to another 10% uncertainty in the measurement of the background subtracted flux of the source. Thus the total uncertainty, summing in quadrature, is 23%. Near-Infrared (NIR) images from the Wide Field Camera (WFC)/ UKIRT InfraRed Deep Sky Survey (UKIDSS) (Lawrence et al. 2007) surveys and the Two Micron All Sky Survey (2MASS) Atlas images (Skrutskie et al. 2006) are also used to investigate the environments of the protostellar sources and look for association with the MIR counterparts.

[2]https://irsa.ipac.caltech.edu/applications/Hires/

6.3 Methods

We follow the methods described in Papers I and II to construct the SEDs (see §3 of Papers I and II for more detailed discussion). In summary, fixed circular aperture, background-subtracted photometry is estimated from MIR to FIR wavelengths for the sources. The aperture radius is chosen with reference to the 70 μm *Herschel*-PACS source morphology, when available (else the 37 μm *SOFIA*-FORCAST source morphology), with the goal of enclosing the majority of the flux, while avoiding contamination from surrounding sources.

We also follow the methods of Papers I and II to fit the SEDs with ZT18 protostellar radiative transfer models. For IRAS 22198, NGC 2071, Cep E, G305 A, IRAS 16562 N, which have *Herschel* data, we do not use *IRAS* data for the SED fitting. For L1206, our *SOFIA* images show that L1206 A is much brighter than L1206 B at long wavelengths: e.g., at 37 μm L1206 A contributes 96% of the total flux. Thus we assume L1206 A is the main source at wavelengths longer than 37 μm and use the IRAS flux densities at 60 μm and 100 μm as a normal data point for the SED fitting of L1206 A and upper limits for the SED fitting of L1206 B. For the other sources, IRAS data are used as upper limits given its resolution and aperture size.

There are a few special cases for the SED fitting. For G305 A, at wavelengths shorter than 8 μm there is hardly any emission and the local noise leads to a negative flux measurement at 7 μm. Thus we use the non-background subtracted fluxes as upper limits at 3.6, 4.5, 5.8 and 8.0 μm. In the IRAS 16562 region, the flux densities at wavelengths longer than 250 μm are dominated by the main source in Paper II, thus the background subtracted flux for IRAS 16562 N is negative at these wavelengths because of the contamination of the main source. Thus we use the non-background

subtracted fluxes as upper limits at 250, 350 and 500 μm.

6.4 Results

Table 6.2 lists the types of multi-wavelength data available for each source, the flux densities derived, and the aperture sizes adopted. $F_{\lambda,\mathrm{fix}}$ is the flux density derived with a fixed aperture size and $F_{\lambda,\mathrm{var}}$ is the flux density derived with a variable aperture size. The value of flux density listed in the upper row of each source is derived with background subtraction, while that derived without background subtraction is listed in parentheses in the lower row. The *SOFIA* images for each source are presented in §6.4.1. General results of the *SOFIA* imaging are summarized in §6.4.2. The SEDs and fitting results are presented in §6.4.3.

Table 6.1. *SOFIA* FORCAST Observations:
Observation Dates & Exposure Times (seconds)

Source	R.A.(J2000)	Decl.(J2000)	d (kpc)	Obs. Date	7.7 μm	19.7 μm	31.5 μm	37.1 μm
S235	$05^h40^m52\overset{s}{.}4$	$+35°41'30''$	1.8	2016 Sep 20	404	779	642	1504
IRAS 22198+6336	$22^h21^m26\overset{s}{.}68$	$+63°51'38\overset{''}{.}2$	0.764	2015 Jun 05	278	701	482	743
NGC 2071	$05^h47^m04\overset{s}{.}741$	$+00°21'42\overset{''}{.}96$	0.39	2018 Sep 08	492	1319	825	2020
Cepheus E	$23^h03^m12\overset{s}{.}8$	$+61°42'26''$	0.73	2015 Nov 04	281	899	818	281
L1206	$22^h28^m51\overset{s}{.}41$	$+64°13'41\overset{''}{.}1$	0.776	2015 Nov 20	116	308	162	630
IRAS 22172+5549	$22^h19^m09\overset{s}{.}478$	$+56°05'00\overset{''}{.}370$	2.4	2015 Jun 03	337	664	386	466
IRAS 21391+5802	$21^h40^m41\overset{s}{.}90$	$+58°16'12\overset{''}{.}3$	0.75	2015 Nov 06	334	806	488	1512

Note. — The source positions listed here are the same as the positions of the black crosses denoting the radio continuum peak (mm continuum peak in Cep E and L1206 A, and MIR peak in IRAS22172 MIR2) in each source in Figures 6.1-6.7. Source distances are from the literature, as discussed below.

Table 6.2. Integrated Flux Densities

Facility	λ (μm)	$F_{\lambda,fix}$ (Jy)	[a]$F_{\lambda,var}$ (Jy)	[b]R_{ap} ($''$)	[c] $F_{\lambda,fix}$ (Jy)	$F_{\lambda,var}$ (Jy)	R_{ap} ($''$)	$F_{\lambda,fix}$ (Jy)	$F_{\lambda,var}$ (Jy)	R_{ap} ($''$)	$F_{\lambda,fix}$ (Jy)	$F_{\lambda,var}$ (Jy)	R_{ap} ($''$)	$F_{\lambda,fix}$ (Jy)	$F_{\lambda,var}$ (Jy)	R_{ap} ($''$)	$F_{\lambda,fix}$ (Jy)	$F_{\lambda,var}$ (Jy)	R_{ap} ($''$)
		S235			IRAS 22198			NGC2071			Cep E			L1206 A			L1206 B		
Spitzer/IRAC	3.6	0.50 (0.54)	0.48 (0.51)	9.0	0.05 (0.08)	0.01 (0.01)	6.6	0.34 (0.38)	0.12 (0.14)	3.6	0.05 (0.06)	0.06 (0.08)	28.0	0.11 (0.12)	0.13 (0.15)	12.0	...	...	...
Spitzer/IRAC	4.5	0.46 (0.51)	0.44 (0.47)	9.0	0.13 (0.15)	0.03 (0.04)	4.8	1.24 (1.32)	0.54 (0.63)	3.6	0.17 (0.18)	0.24 (0.25)	28.0	0.25 (0.27)	0.30 (0.33)	12.0	...	...	...
Spitzer/IRAC	5.8	1.99 (2.24)	1.90 (2.06)	9.0	0.20 (0.43)	0.08 (0.10)	5.4	2.54 (2.78)	1.59 (1.71)	3.6	0.23 (0.31)	0.27 (0.38)	28.0	0.28 (0.33)	0.33 (0.41)	12.0	2.10 (2.19)	2.10 (2.19)	10.0
SOFIA/FORCAST	7.7	6.39 (6.24)	6.22 (6.13)	9.0	0.85 (1.41)	0.20 (0.29)	5.4	5.58 (5.53)	4.04 (4.32)	3.8	0.17 (0.19)	0.23 (0.20)	6.0	0.12 (0.19)	0.30 (0.27)	4.6	2.21 (2.04)	1.53 (1.65)	5.0
Spitzer/IRAC	8.0	6.12 (6.76)	5.83 (6.25)	9.0	0.23 (0.84)	0.15 (0.20)	6.6	6.08 (6.48)	4.09 (4.34)	3.8	0.31 (0.56)	0.34 (0.70)	28.0	0.21 (0.29)	0.24 (0.37)	12.0	3.45 (3.59)	3.45 (3.59)	10.0
SOFIA/FORCAST	19.7	33.66 (34.25)	32.64 (33.28)	9.0	10.35 (15.13)	5.40 (6.17)	7.0	86.65 (86.97)	63.79 (66.50)	3.8	1.41 (1.43)	1.69 (1.56)	6.0	2.11 (2.42)	1.82 (2.09)	6.2	4.70 (4.08)	4.32 (4.05)	8.0
SOFIA/FORCAST	31.5	70.87 (72.92)	70.87 (72.92)	12.0	91.08 (90.51)	77.83 (80.47)	9.2	310 (318)	169 (190)	3.8	20.50 (21.61)	16.73 (17.47)	7.7	65.17 (67.06)	63.01 (65.13)	7.7	5.50 (3.37)	5.50 (3.37)	10.0
SOFIA/FORCAST	37.1	84.95 (88.39)	84.95 (88.39)	12.0	132 (130)	111 (115)	9.2	375 (382)	176 (205)	3.8	25.89 (25.40)	23.56 (24.02)	7.7	116 (117)	116 (117)	9.0	7.20 (5.09)	7.20 (5.09)	10.0
IRAS	60.0	... ...	2281 (2386)	186.6	... ...	224 (235)	109.2	... ...	1146 (1213)	200.0	... ...	66.13 (63.58)	141.0	... ...	432 (445)	125.2	... ...	432 (445)	125.2
Herschel/PACS	70.0	...	...	...	449 (471)	449 (471)	25.6	694 (753)	694 (753)	9.6	99 (103)	99 (103)	23.0	...	...	...	...	...	...
IRAS	100.0	... ...	2897 (3255)	244.5	... ...	525 (666)	180.0	... ...	2559 (2879)	205.1	... ...	152 (137)	177.5	... ...	880 (947)	215.7	... ...	880 (947)	215.7
Herschel/PACS	160.0	...	...	...	360 (401)	360 (401)	25.6	421 (572)	421 (572)	9.6	127 (143)	127 (143)	23.0	...	...	...	...	...	...
Herschel/SPIRE	250.0	...	...	...	190 (217)	190 (217)	25.6	...	...	...	71.43 (87.60)	71.43 (87.60)	23.0	...	...	...	...	...	...
Herschel/SPIRE	350.0	...	...	...	93 (107)	93 (107)	25.6	...	...	...	29.35 (38.37)	29.35 (38.37)	23.0	...	...	...	...	...	...
Herschel/SPIRE	500.0	...	...	...	35.06 (40.65)	35.06 (40.65)	25.6	...	...	...	7.61 (12.45)	7.61 (12.45)	23.0	...	...	...	...	...	...

[a]Flux density derived with a fixed aperture size of the 70 μm data.

[b]Flux density derived with various aperture sizes.

[c]Aperture radius.

Note. — The value of flux density in the upper row is derived with background subtraction. The value in parentheses in the lower line is the flux density derived without background subtraction. The center of the aperture used for photometry of the IRAS images is not the same as those used at other wavelengths, but is determined based on the emission of the image alone. See more details in Papers I & II.

Table 6.2. Integrated Flux Densities (continued)

Facility	λ (μm)	$F_{\lambda,fix}$ (Jy)	$F_{\lambda,var}$ (Jy)	R_{ap} ($''$)	$F_{\lambda,fix}$ (Jy)	$F_{\lambda,var}$ (Jy)	R_{ap} ($''$)	$F_{\lambda,fix}$ (Jy)	$F_{\lambda,var}$ (Jy)	R_{ap} ($''$)	$F_{\lambda,fix}$ (Jy)	$F_{\lambda,var}$ (Jy)	R_{ap} ($''$)	$F_{\lambda,fix}$ (Jy)	$F_{\lambda,var}$ (Jy)	R_{ap} ($''$)	$F_{\lambda,fix}$ (Jy)	$F_{\lambda,var}$ (Jy)	R_{ap} ($''$)	$F_{\lambda,fix}$ (Jy)	$F_{\lambda,var}$ (Jy)	R_{ap} ($''$)	$F_{\lambda,fix}$ (Jy)	$F_{\lambda,var}$ (Jy)	R_{ap} ($''$)
		IRAS22172 MIR2			IRAS22172 MIR1			IRAS22172 MIR3			IRAS21391 BIMA2			IRAS21391 BIMA3			IRAS21391 MIR48			IRAS16562 N [d]			G305 A [e]		
Spitzer/IRAC	3.6	0.15 (0.17)	0.09 (0.11)	2.4	0.07 (0.09)	0.07 (0.08)	3.6	0.02 (0.03)	0.02 (0.03)	3.6	0.01 (0.02)	0.01 (0.01)	4.6	0.02 (0.03)	0.01 (0.02)	3.6	0.05 (0.05)	0.04 (0.04)	3.6	0.06 (0.13)	0.04 (0.09)	6.0	... (0.16)	... (0.16)	12.0
Spitzer/IRAC	4.5	0.43 (0.46)	0.29 (0.31)	2.4	0.07 (0.09)	0.05 (0.06)	2.4	0.02 (0.03)	0.01 (0.01)	2.4	0.07 (0.09)	0.05 (0.06)	4.6	0.06 (0.08)	0.05 (0.06)	4.5	0.09 (0.09)	0.08 (0.09)	4.5	0.08 (0.16)	0.06 (0.11)	6.0	... (0.19)	... (0.19)	12.0
Spitzer/IRAC	5.8	0.71 (0.77)	0.43 (0.50)	2.4	0.17 (0.25)	0.07 (0.12)	2.4	0.16 (0.20)	0.12 (0.15)	3.6	0.11 (0.17)	0.10 (0.12)	4.6	0.10 (0.15)	0.09 (0.11)	4.5	0.15 (0.18)	0.14 (0.16)	5.4	0.20 (0.75)	0.07 (0.30)	4.5	... (1.13)	... (1.13)	12.0
SOFIA/FORCAST	7.7	0.95 (1.10)	0.69 (0.85)	2.7	0.43 (0.71)	0.58 (0.88)	5.4	0.54 (0.70)	0.54 (0.70)	4.6	0.29 (0.39)	0.13 (0.22)	4.6	0.17 (0.37)	0.10 (0.24)	6.4	0.21 (0.27)	0.26 (0.27)	6.4	0.73 (1.80)	0.16 (0.73)	4.5	...	...	...
Spitzer/IRAC	8.0	1.03 (1.18)	0.66 (0.83)	2.7	0.38 (0.60)	0.40 (0.63)	4.8	0.40 (0.53)	0.42 (0.55)	4.8	0.12 (0.21)	0.11 (0.14)	4.6	0.10 (0.20)	0.11 (0.16)	6.4	0.21 (0.26)	0.21 (0.25)	7.2	0.52 (1.77)	0.27 (1.16)	6.0	... (2.71)	... (2.71)	12.0
SOFIA/FORCAST	19.7	3.64 (3.83)	3.49 (3.70)	3.6	0.64 (0.72)	0.26 (0.38)	2.3	0.85 (0.92)	0.49 (0.59)	2.3	0.45 (0.52)	0.46 (0.49)	5.4	0.28 (0.20)	0.49 (0.38)	5.4	0.93 (0.92)	0.92 (0.90)	7.6	3.83 (3.94)	3.83 (3.94)	7.7	1.60 (0.02)	1.58 (1.20)	4.6
SOFIA/FORCAST	31.5	4.99 (5.76)	4.99 (5.76)	3.8	1.96 (2.47)	1.63 (2.08)	3.8	3.30 (3.77)	3.30 (3.77)	4.6	6.81 (7.09)	6.26 (6.63)	6.2	8.30 (8.77)	8.26 (8.69)	8.1	3.32 (3.07)	3.34 (3.10)	7.6	11.06 (14.82)	11.06 (14.82)	7.7	91 (104)	87 (92)	7.7
SOFIA/FORCAST	37.1	6.15 (7.10)	6.15 (7.10)	3.8	3.18 (4.25)	3.18 (4.25)	4.6	4.22 (4.66)	4.22 (4.66)	4.6	11.27 (11.83)	11.27 (11.83)	7.7	12.94 (13.76)	12.94 (13.76)	8.5	4.66 (3.91)	4.66 (3.91)	8.0	13.68 (20.70)	13.68 (20.70)	7.7	153 (172)	149 (158)	9.2
IRAS	60.0	... ...	134 (220)	94.7	... ...	134 (220)	94.7	... ...	134 (220)	94.7	... ...	163 (178)	77.0	... ...	163 (178)	77.0	... ...	163 (178)	77.0	...	...	...	...	...	...
Herschel/PACS	70.0	...	...	...	...	...	...	...	...	...	...	...	...	...	...	...	...	...	...	...	...	...	968 (1287)	968 (1287)	12.0
IRAS	100.0	... ...	501 (937)	180.9	... ...	501 (937)	180.9	... ...	501 (937)	180.9	... ...	363 (430)	100.0	... ...	363 (430)	100.0	... ...	363 (430)	100.0	...	...	...	...	...	...
Herschel/PACS	160.0	...	...	...	...	...	...	...	...	...	...	...	...	...	...	...	...	...	...	...	...	...	668 (1160)	668 (1160)	12.0
Herschel/SPIRE	250.0	...	...	...	...	...	...	...	...	...	...	...	...	...	...	...	...	...	...	... (73.55)	... (73.55)	7.7	...	...	...
Herschel/SPIRE	350.0	...	...	...	...	...	...	...	...	...	...	...	...	...	...	...	...	...	...	... (29.09)	... (29.09)	7.7	74 (187)	74 (187)	12.0
Herschel/SPIRE	500.0	...	...	...	...	...	...	...	...	...	...	...	...	...	...	...	...	...	...	... (8.59)	... (8.59)	7.7	9.65 (44.62)	9.65 (44.62)	12.0

[d]Aperture is centered at the 37 μm peak at R.A. (J2000) = $16^h59^m43\overset{s}{.}010$, Decl.(J2000) = $-40°03'11\overset{''}{.}560$.

[e]Aperture is centered at the position of the 6.7 GHz methanol maser at R.A. (J2000) = $13^h11^m13\overset{s}{.}795$, Decl.(J2000) = $-62°34'41\overset{''}{.}741$ (Norris et al. 1993).

Note. — The background subtracted flux density of IRAS16562 N at 250, 350, 500 μm is negative due to contamination of the IRAS 16562 main source presented in Paper II. So we use the non-background subtracted flux density at these wavelengths as upper limits for the SED fitting of IRAS16562 N.
There is no emission at wavelengths shorter than 8 μm from G305 A. So we use the non-background subtracted flux density at these wavelengths as upper limits for the SED fitting of G305 A.

6.4.1 Description of Individual Sources

S235

Estimates of the distance to the S235 A-B region vary from 1.6 - 2.5 kpc (e.g., Israel & Felli 1978; Burns et al. 2015). We adopt 1.8 kpc, following Evans & Blair (1981), Dewangan et al. (2016) and Shimoikura et al. (2016). High-resolution mm line and continuum and radio continuum observations towards S235 A-B were reported by Felli et al. (2004, 2006). Shimoikura et al. (2016) carried out observations of $C^{18}O$ emission toward S235 A-B and revealed that the clump has an elliptical shape, with a mass of $\sim 1000\,M_{\odot}$ and an average radius of ~ 0.5 pc. Two compact HII regions, called S235 A and S235 B (e.g., Felli et al. 1997; Klein et al. 2005; Saito et al. 2007) are located in this clump, along with a mm continuum core with HCO^{+}(1-0) outflows in-between, which is thought to be an embedded, earlier-stage YSO (Felli et al. 2004). The mm core has a MIR counterpart S235 AB-MIR and several water masers and methanol masers nearby (Kurtz et al. 2004). From their estimate of a luminosity of $\sim 10^{3} L_{\odot}$ of the source, Felli et al. (2004) suggested that S235 AB-MIR is an intermediate-mass YSO driving the molecular outflows and supplying the energy for the -60 km s^{-1} water maser nearby. On the other hand, Dewangan & Anandarao (2011) concluded from SED fitting that S235 AB-MIR is the most massive protostar in the region with $m_{*} \sim 11\,M_{\odot}$ and still actively accreting and so not yet able to excite an HII region. However, they were cautious about the reliability of these results due to the limited number of data points (three in the MIR from IRAC bands and two in the sub-mm-continuum from Felli et al. 2004).

Another NIR K-band source with the largest infrared excess, M1, is reported to be associated with the radio source VLA-1 by Felli et al. (2006) and they suggested that it could be a B2-B3 star with an UCHII region, while Dewangan & Anandarao et

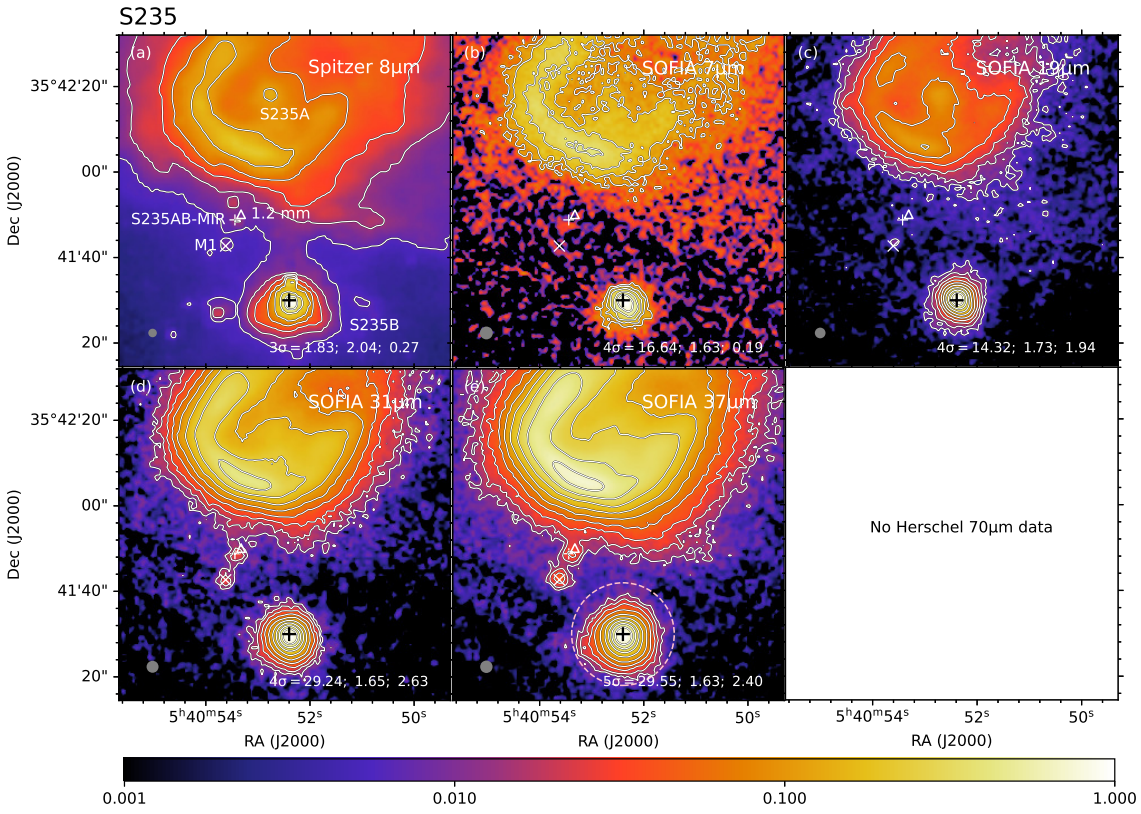

Fig. 6.1.— Multi-wavelength images of S235 with facility and wavelength given in the upper right corner of each panel. Contour level information is given in the lower right: lowest contour level in number of σ above the background noise and corresponding value in mJy per square arcsec; then step size between each contour in $\log_{10}$ mJy per square arcsec, then peak flux in Jy per square arcsec. The color map indicates the relative flux intensity compared to that of the peak flux in each image panel. The pink dashed circle shown in (e) denotes the aperture used for the fiducial photometry. Gray circles in the lower left show the resolution of each image. The black cross in all panels denotes the position of the radio source VLA-2 of Felli et al. (2006) at R.A.(J2000) = $05^h40^m52\overset{s}{.}40$, Decl.(J2000) = $+35°41'30''$. The triangle sign marks the position of the 1.2 mm core. The small white cross marks the positionFigure 6.1 of S235AB-MIR. The × sign marks the position of the NIR K-band source M1 as well as VLA-1.

al. (2011) suggested that it is a low-mass star, relatively young in its evolution. Both S235 AB-MIR (counterpart of the 1.2mm core) and M1 can be seen in our *SOFIA* images in Figure 6.1. However, due to their weak MIR emission, we do not focus on them in this paper.

Our analysis is focussed on the MIR source S235 B, which is associated with the radio source VLA-2 (Felli et al. 2006). S235 B is the brightest object in the S235 A-B cluster in all broad-bands from U to K, and thus may be a massive YSO (Boley et al. 2009). Krassner et al. (1982) detected hydrogen recombination lines and polycyclic aromatic hydrocarbon (PAH) emission features at 3.3, 8.7 and 11.3 μm. However, no 3.3 mm or 1.2 mm continuum or molecular lines are detected associated with S235 B (Felli et al. 2004). While there is large-scale ^{12}CO, ^{13}CO and C^{18}O emission in the whole S235 region (Shimoikura et al. 2016; Dewangan & Ojha 2017), smaller-scale outflows specifically associated with S235 B have not yet been reported. For example, even in the high-resolution HCO$^+$(1-0) map of Felli et al. (2004), whose field of view covers S235 B, there is no sign of HCO$^+$(1-0) outflows emerging from S235 B. Boley et al. (2009) classified the central star of S235 B as an early-type (B1V) Herbig Be star surrounded by an accretion disk based on its spectrum from 3800-7200 Å, its location in a region of active star formation, the presence of the nearby nebulosity, the Balmer emission lines in the stellar spectrum, and the large H-K excess. Furthermore, its spectrum shows that the S235 B nebulosity is reflective in nature, with the central YSO in S235 B as the illuminating source. Given the mass inferred from the spectral type ($> 10 M_\odot$), Boley et al. suggested S235 B is likely to already be on the main sequence.

In our *SOFIA* images as shown in Figure 6.1, S235 B is much brighter than S235 AB-MIR and M1. The weak second component to the north of the radio source in the

Spitzer 8 μm image is likely to be produced by a ghosting effect of the primary source, since it is not seen in the other IRAC images, the *SOFIA* images or the *UKIDSS* JHK band images.

IRAS 22198+6336

IRAS 22198+6336 was previously considered to be a massive YSO (Palla et al. 1991; Molinari et al. 1996; Sánchez-Monge et al. 2008) until an accurate distance of 764 $\pm$ 27 pc was derived from the parallax measurements of 22 GHz associated water masers (Hirota et al. 2008). These authors, after reanalyzing the protostellar SED, then proposed IRAS 22198+6336 is an intermediate-mass deeply embedded YSO with spectral type of late-B, equivalent to a Class 0 object in low-mass star formation. Sánchez-Monge et al. (2010) detected a compact source at 3.5, 2.7, and 1.3 mm coincident with the centimeter source reported by Sánchez-Monge et al. (2008) and surrounded by a faint structure extended toward the southwest. The high rotational temperature (100-150 K) derived from CH_3CN and CH_3OH, together with the chemically rich spectrum, is clear evidence that IRAS 22198 is an intermediate-mass hot core. The CO(1-0) emission in Sánchez-Monge et al. (2010) reveals an outflow with a quadrupolar morphology clearly centered on the position of the main dust condensation. Observations of the high-velocity emission of different outflow tracers HCO^+(1-0), HCN(1-0) and SiO(2-1) seem to favor the superposition of two bipolar outflows. Higher angular resolution observations at 1.3 mm by Palau et al. (2013) reveal a counterpart of the cm source (MM2 in their nomenclature) and a faint extension to its south (MM2-S). Palau et al. suggest that MM2 is likely driving the southwest-northeast outflow, while an unresolved close companion of MM2 or MM2-S, which is only detected at 3.6μm, could be the driving source of the northwest-southeast outflow. Periodic flares of the

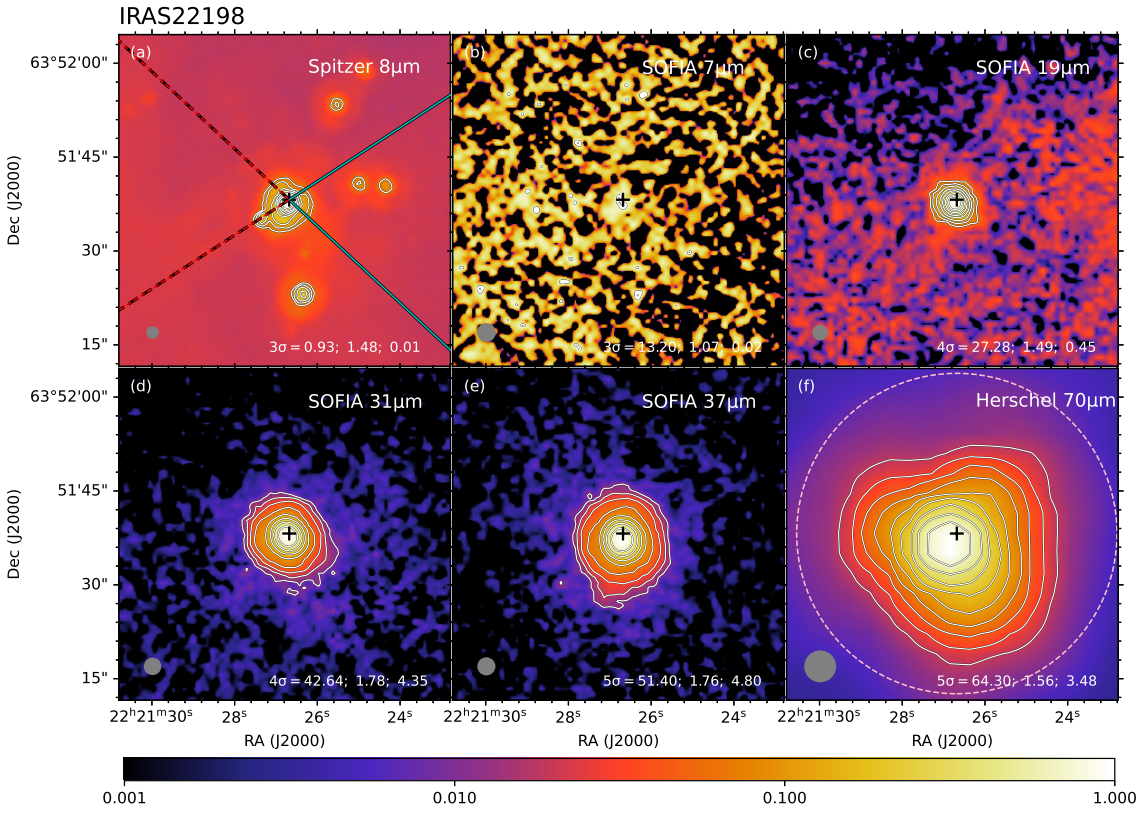

Fig. 6.2.— Multi-wavelength images of IRAS 22198+6336, following the format of Figure 6.1. The black cross in all panels denotes the position of the 3.6 cm source in Sánchez-Monge et al. (2008) at R.A.(J2000) = $22^h21^m26\overset{s}{.}68$, Decl.(J2000) = $+63°51'38\overset{''}{.}2$. The lines in panel (a) show the orientation of outflow axes, with the solid spans tracing blue-shifted direction and the dashed spans red-shifted direction. The outflow axis angles are from the CO(1-0) outflow emission of Sánchez-Monge et al. (2010).

6.7-GHz methanol maser have been detected in IRAS 22198 and their characteristics can be explained by a colliding-wind binary model (Fujisawa et al. 2014).

Our *SOFIA* images reveal the MIR counterpart of the centimeter/millimeter source. Extended emission is seen towards the blue-shifted outflow in the south-west at 19 and 31 μm. In contrast, the extended emission at μm directly points to the south. Faint extended emission is also seen along the axes of the two outflows at 70 μm.

NGC 2071

NGC 2071 is a reflection nebula located at a distance of 390 pc in the L1630 molecular cloud of Orion B (Anthony-Twarog 1982). The three brightest members of the infrared cluster at 10 μm, IRS1, IRS2 and IRS3, are each associated with compact radio sources at 5 GHz (Snell & Bally 1986). The radio continuum emission of IRS1 and IRS3 and the water masers associated with them suggest that both sources are associated with thermal jets (Smith & Beck 1994; Torrelles et al. 1998; Seth et al. 2002). Higher resolution VLA observations (Trinidad et al. 2009) break IRS1 into three continuum peaks (IRS1E, 1C and 1W), aligned in the east-west direction. Both the morphology and spectral index suggest that IRS1C is a thermal radio jet, while IRS1E and IRS1W could be condensations ejected by IRS1C. An energetic bipolar CO outflow has been observed toward NGC 2071, extending in the northeast-southwest direction and reaching ∼15' in length (Bally 1982). In addition, shock-excited molecular hydrogen emission at 2.12 μm has also been reported showing a spatial extent similar to that of the CO outflow and revealing several H_2 outflows in the field, including one (flow II) perpendicular to the main outflow (flow I) (Eislöffel 2000). Stojimirović et al. (2008) also detected CO(1-0) emission in the direction of flow II.

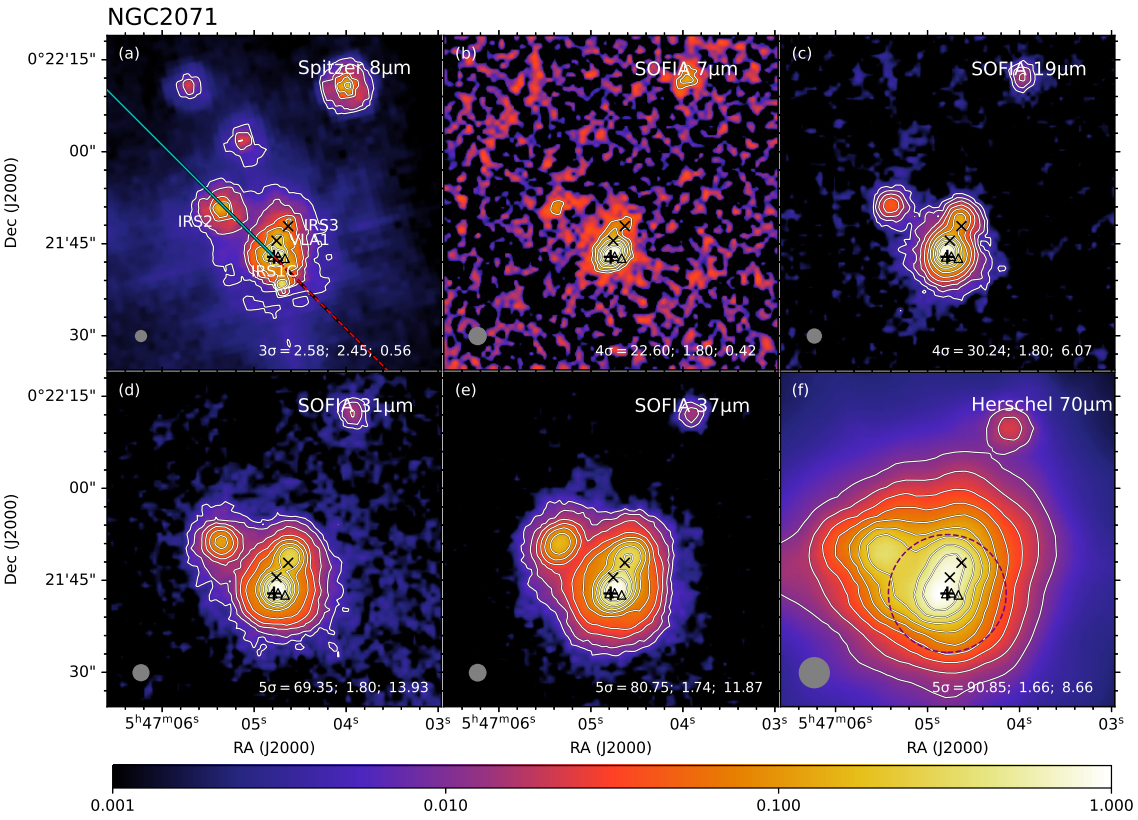

Fig. 6.3.— Multi-wavelength images of NGC 2071. The black cross in all panels denotes the position of the 1.3 cm source IRS 1C in Trinidad et al. (2009) at R.A.(J2000) = $05^h47^m04\overset{s}{.}741$, Decl.(J2000) = $+00°21'42\overset{''}{.}96$. The × signs from north to south mark the positions of the 1.3 cm sources IRS3 and VLA1, respectively. The triangle signs from east to west mark the positions of the 1.3 cm sources IRS1E, IRS1W, and IRS1Wb, respectively. The lines in panel (a) show the orientation of the outflow axis (flow I), with the solid span tracing the blue-shifted direction and the dashed span the red-shifted direction. The outflow axis angle is from the high-velocity CO(1-0) main outflow emission of Stojimirović et al. (2008). Note that the center of the outflow has an uncertainty of ∼5″ and is not necessarily at IRS1C.

Trinidad et al. (2009) tried to identify individual driving sources for each outflow based on the observations of Eislöffel (2000) and the elongation of the IRS3 jet. However, we note that higher resolution observations of the outflows are needed to better distinguish the driving sources in this region.

Based on radio continuum emission indicating presence of thermal jets and water masers that are tracing disk-YSO-outflow systems, it has been proposed that IRS1 and IRS3 are intermediate- and low-mass YSOs, respectively (Smith & Beck 1994; Torrelles et al. 1998; Seth et al. 2002, Trinidad et al. 2009). In our *SOFIA* images, the three sources IRS1, IRS2 and IRS3 are revealed at all wavelengths (see Fig. 6.3). Here, we will focus on the SED of the IRS1 source, but the aperture we adopt also includes IRS3.

Cepheus E

The Cepheus E (Cep E) molecular cloud is located at a distance of 730 pc (Sargent 1977). Since its early discovery by Wouterloot & Walmsley (1986) and Palla et al. (1993), subsequent studies have confirmed the central source Cep E-mm to be an isolated intermediate-mass protostar in the Class 0 stage (Lefloch et al. 1996; Moro-Martín et al. 2001). The source drives a very luminous molecular outflow and jet (Lefloch et al. 2011, 2015), terminated by the bright Herbig-Haro object HH377 in the south (Ayala et al. 2000). The 21″-long jet, the HH 377 terminal bow-shock, and the outflow cavity are clearly revealed in multiple CO transitions and the [OI] 63 μm line (Gusdorf et al. 2017). The observations are interpreted by means of time-dependent magneto-hydrodynamics (MHD) shock models by (Lefloch et al. 2015). Ospina-Zamudio et al. (2018) reveal Cep E-mm as a binary protostellar system with *NOEMA* observations. They identified two components from a two-component fit

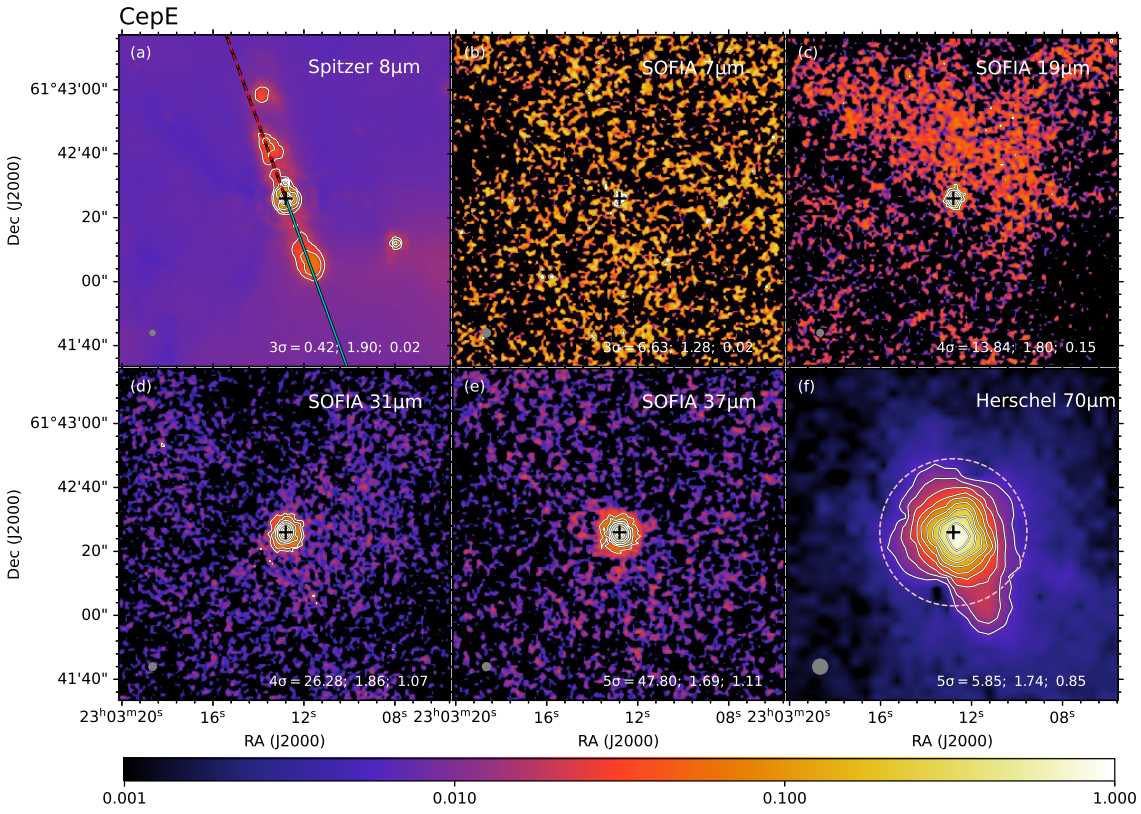

Fig. 6.4.— Multiwavelength images of Cep E. The black cross in all panels denotes the position of the 1.3 mm source CepE-A in Ospina-Zamudio et al. (2018) at R.A.(J2000) = $23^h03^m12\overset{s}{.}8$, Decl.(J2000) = $+61°42'26''$. The lines in panel (a) show the orientation of the outflow axis, with the solid span tracing the blue-shifted direction and the dashed span the red-shifted direction. The outflow axis angle is defined by the CO(2-1) outflow emission of Lefloch et al. (2015).

to the visibilities, Cep E-A and Cep E-B, which are separated by $\sim 1.7''$. Ospina-Zamudio et al. argued Cep E-A dominates the core continuum emission and powers the well-known, high-velocity jet associated with HH 377, while the lower flux source Cep E-B powers another high-velocity molecular jet revealed in SiO(5-4) propagating in a direction close to perpendicular with respect to the Cep E-A jet. The spectra of molecular lines observed by NOEMA show bright emission of O- and N-bearing complex organic molecules (COMs) around Cep E-A and no COM emission towards Cep E-B.

From our *SOFIA* images (Fig. 6.4), we are not able to resolve the potential binary system, so our modeling will be an approximation of the properties of Cep E-A, assuming it dominates the system. The IR emission along the main jet is clearly seen in the *Spitzer* 8 μm image and also in the *Herschel* 70 μm image, since these space-based observations are more sensitive to fainter emission features.

L1206

L1206, also known as IRAS 22272+6358, is located at a distance of 776 pc from the trigonometric parallaxes of 6.7 GHz methanol masers (Rygl et al. 2010). There are two MIR sources presented in our field of view. The western source IRAS 22272+6358 A (hereafter referred to as L1206 A) has no optical counterpart, and at near-infrared wavelengths, it has only been seen in scattered light (Ressler & Shure 1991). Given its extremely low 60/100 μm color temperature, L1206 A is believed to be very embedded, cold and young (Ressler & Shure 1991, Beltrán et al. 2006). It has been detected at 2.7 and 2 mm, but not at 2 or 6 cm (Wilking et al. 1989; McCutcheon et al. 1991; Sugitani et al. 2000; Beltrán et al. 2006). The 2.7 mm continuum observations by Beltrán et al. (2006) revealed four sources, OVRO 1, OVRO 2, OVRO 3, and

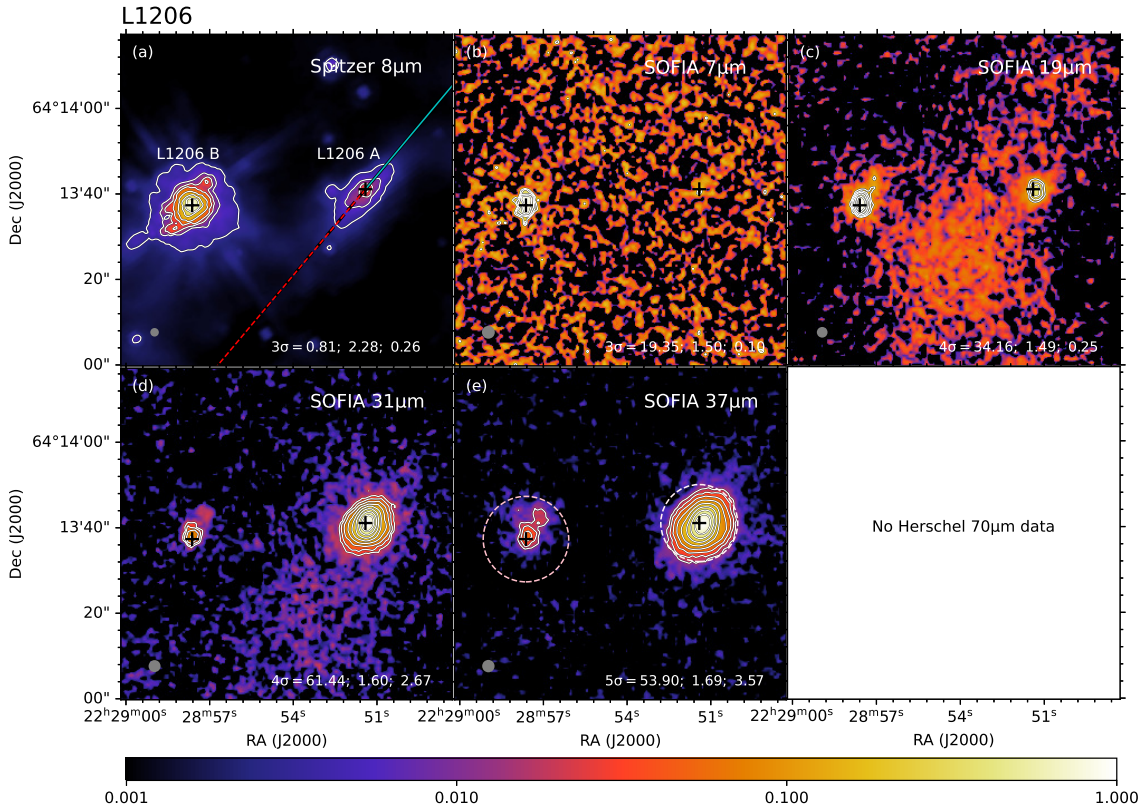

Fig. 6.5.— Multi-wavelength images of L1206. The black crosses in all panels from east to west denote the position of the 8μm peak of L1206 B at R.A.(J2000) = $22^h28^m57\overset{s}{.}626$, Decl.(J2000) = $+64°13'37\overset{''}{.}348$ and the position of L1206 A coincident with that of the 2.7 mm source OVRO 2 in Beltrán et al. (2006) at R.A.(J2000) = $22^h28^m51\overset{s}{.}41$, Decl.(J2000) = $+64°13'41\overset{''}{.}1$, respectively. The lines in panel (a) show the orientation of the outflow axis from L1206 A, with the solid span tracing blue-shifted direction and the dashed span red-shifted direction. The outflow axis angle is given by the CO(1-0) outflow emission of Beltrán et al. (2006).

OVRO 4, in a 12″ vicinity of L1206 A. The strongest millimeter source OVRO 2 is most likely the YSO associated with L1206 A, and is probably the driving source of the CO molecular outflow detected in the region. The dust emission morphology and properties of OVRO 2 suggest that this intermediate-mass protostar is probably in transition between Class 0 and I.

The K, L, L' and M filter images of L1206 A reveal clearly lobes in a bipolar system (Ressler & Shure 1991). There is a distinct 3-4″ gap between the two lobes at the K, L, L' bands. Since the proposed illuminating source lies within this gap, it is suggested by Ressler & Shure (1991) that this gap is produced by the extreme extinction of a thick, circumstellar disk. We also see such a gap in the 3.6, 4.5, and 5.8 μm images. The CO(1-0) observations of Beltrán et al. (2006) reveal a very collimated outflow driven by OVRO 2 with a very weak southeastern red lobe and a much stronger northwestern blue lobe. The relative brightness of the red lobe also decreases monotonically at K, L, L' bands (Ressler & Shure 1991). Beltrán et al. (2006) suggested a scenario in which photodissociation produced by the ionization front coming from the bright-rimmed diffuse H II region in the south could be responsible for the weakness of the redshifted lobe and its overall morphology.

The elongation along the outflow direction of L1206 A is clearly revealed at 8 mum. We see a slight extension along the outflow direction in our *SOFIA* images, especially at 31μm and 37 μm (see Fig. 6.5).

IRAS 22272 + 6358 B (hereafter referred to as L1206 B) is a bluer but less luminous object, which lies approximately 40″ to the east of L1206 A. Since L1206 B is directly visible at NIR and is likely to be a less obscured young stellar object, Ressler & Shure (1991) suggested that L1206 B is most likely a late Class I object or perhaps an early Class II object, whose photospheric spectrum is heavily extinguished

by the parent cloud and is also affected by emission from a circumstellar disk.

From our *SOFIA* images, it can be seen that the emission of L1206 B becomes weaker as one goes to longer wavelengths, which also indicates that L1206 B may be more evolved than L1206 A.

IRAS 22172+5549

IRAS 22172+5549 is located at a kinematic distance of 2.4 kpc (Molinari et al. 2002). As a luminous IRAS source in the survey of Molinari et al. (2002), IRAS 22172 shows the presence of a compact dusty core without centimeter continuum emission, with prominent wings in the HCO^+(1-0) line. Fontani et al. (2004) studied the 3 mm continuum and CO(1-0) emission in this region, finding a CO bipolar outflow centered at MIR2 (IRS1 in their nomenclature), which is offset by $\sim 7.5''$ from the 3.4 mm peak. They suggested that the dusty core might host a source in a very early evolutionary stage prior to the formation of an outflow. From the outflow parameters, they proposed that MIR2, as the driving source, must be relatively massive. Palau et al. (2013) carried out higher angular resolution 1.3 mm and CO(2-1) observations. They detected more mm sources, including one confirmed protostar with no infrared emission that is driving a small outflow (MM2), two protostellar candidates detected only in the millimeter range (MM3 and MM4), and one protostellar object detected in the mm and infrared, with no outflow (MM1). MIR2 is still detected only in the infrared and is driving the larger CO(1-0) outflow. No mm emission or molecular outflows are detected towards MIR1 or MIR3. It is clear that IRAS 22172 harbors a rich variety of YSOs at different evolutionary stages.

Our *SOFIA* images (see Fig. 6.6) reveal extended emission along the blue-shifted outflow from MIR2, which could come from the outflow cavity.

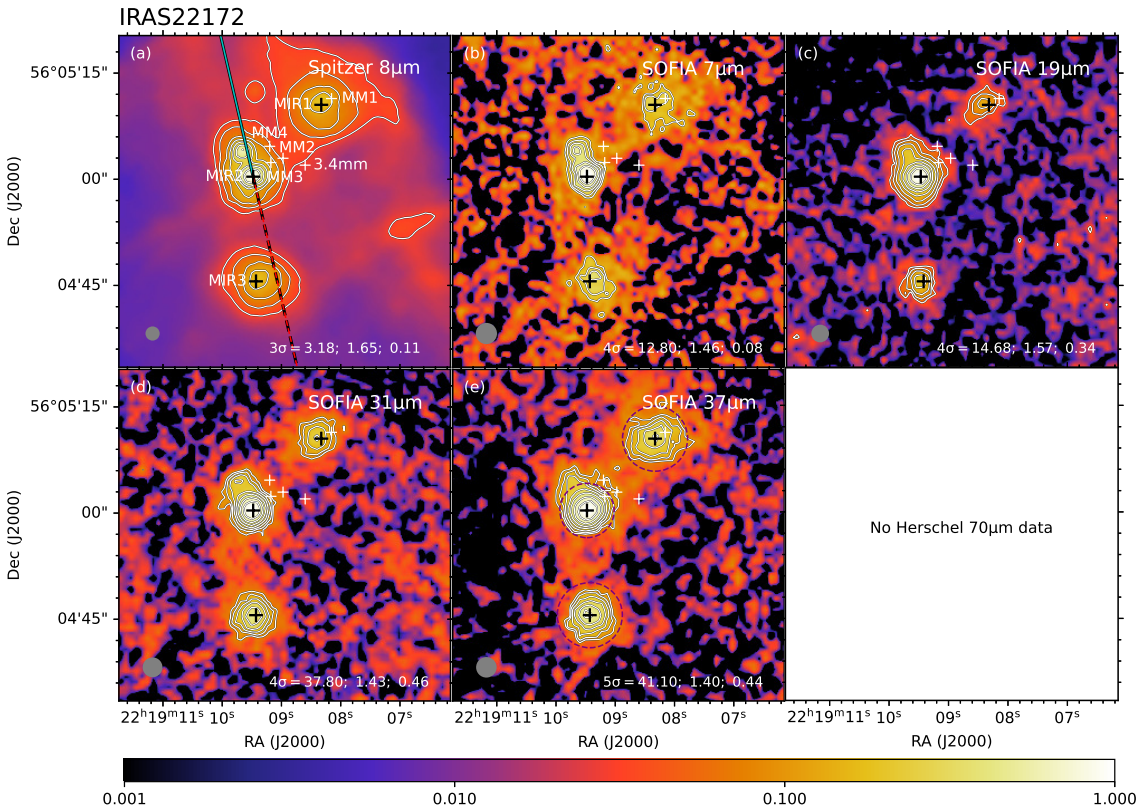

Fig. 6.6.— Multi-wavelength images of IRAS 22172. The black crosses in all panels from north to south denote the positions of the MIR peaks at 37μm MIR1 at R.A.(J2000) = $22^h19^m08\overset{s}{.}328$, Decl.(J2000) = $+56°05'10\overset{''}{.}522$, MIR2 at R.A.(J2000) = $22^h19^m09\overset{s}{.}478$, Decl.(J2000) = $+56°05'00\overset{''}{.}370$, and MIR3 at R.A.(J2000) = $22^h19^m09\overset{s}{.}430$, Decl.(J2000) = $+56°04'45\overset{''}{.}581$, respectively. The white crosses from north to south mark the positions of the 1.3 mm sources MM1, MM4, MM2, MM3 in Palau et al. (2013) and the 3.4 mm source in Molinari et al. (2002) (also the mm core I22172-C in Fontani et al. 2004), respectively. The lines in panel (a) show the orientation of the outflow axis from MIR2, with the solid span tracing blue-shifted direction and the dashed span red-shifted direction. The outflow axis angle is from the CO(1-0) outflow emission of Fontani et al. (2004).

IRAS 21391+5802

IRAS 21391+5802 is deeply embedded in the bright-rimmed globule IC 1396N located at a distance of 750 pc (Matthews 1979). This region exhibits all of the signposts of an extremely young object, such as strong sub-mm and mm dust continuum emission (Wilking et al. 1993; Sugitani et al. 2000; Codella et al. 2001), line emission from high-density gas tracers (Serabyn et al. 1993; Cesaroni et al. 1999; Codella et al. 2001), and water maser emission (Felli et al. 1992; Tofani et al. 1995; Patel et al. 2000; Valdettaro et al. 2005). Sugitani et al. (1989) discovered an extended CO bipolar outflow, which was also mapped later by Codella et al. (2001). NIR images of the region have revealed a collimated 2.12μm H_2 jet driven by IRAS 21391 (Nisini et al. 2001, Beltrán et al. 2009). Based on mm observations, Beltrán et al. (2002) resolved IRAS 21391 into an intermediate-mass source named BIMA 2, surrounded by two less massive and smaller objects, BIMA 1 and BIMA 3. Choudhury et al. (2010) identified MIR-50 and 54 as the mid-infrared counterparts of BIMA 2 and BIMA 3 and did not detect any source associated with BIMA 1. The source located $\sim 25''$ to the north of BIMA 2 was identified as MIR-48. BIMA 1, BIMA 2 and BIMA 3 are all associated with 3.6 cm continuum emission (Beltrán et al. 2002). Figure 6.7 shows the region as seen by *Spitzer* at 8 μm and by *SOFIA*-FORCAST. Our analysis focusses on the MIR-48, BIMA 2 and BIMA3 sources.

A strong CO(1-0) outflow along the east-west direction is centered at the position of BIMA 2, and another collimated, weaker, and smaller bipolar outflows elongated along the north-south direction are associated with BIMA 1, which is only detected at low velocities (see Figure 4 in Beltrán et al. 2002). At the position of MIR-48, we see weak, overlapping blue- and red-shifted CO(1-0) emission, which is also only detected at low velocities. There is no molecular emission detected towards BIMA

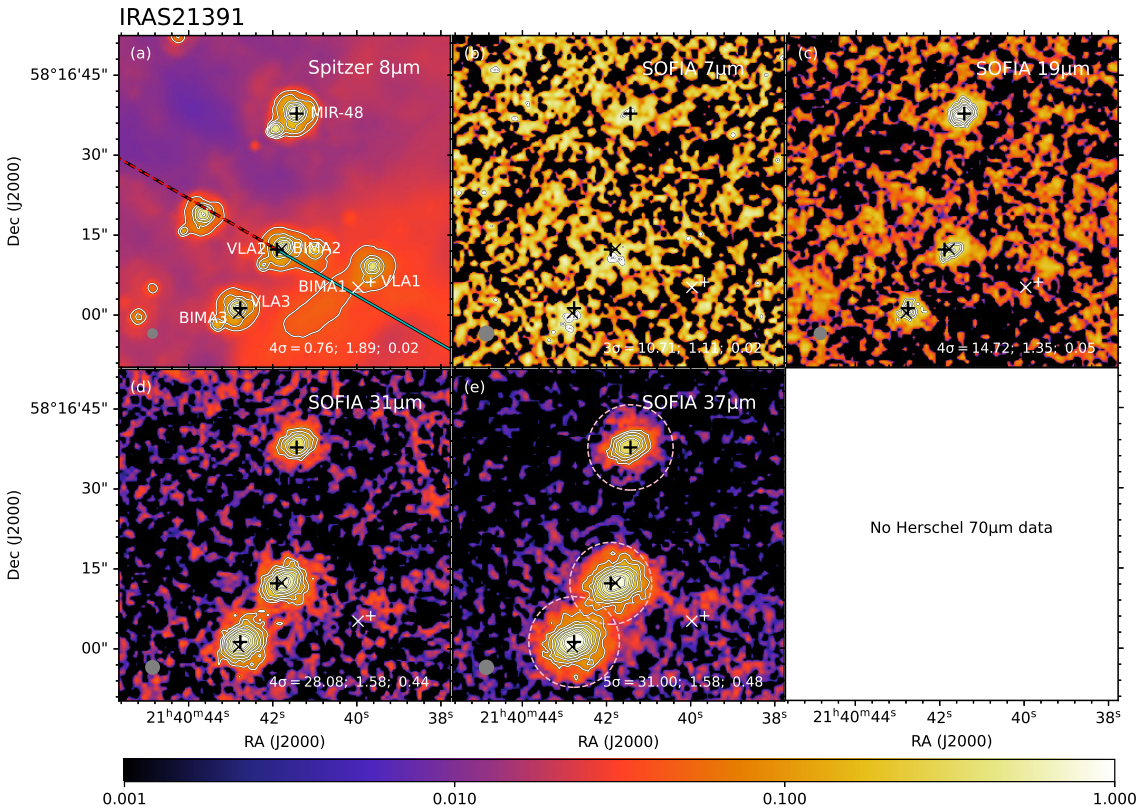

Fig. 6.7.— Multi-wavelength images of IRAS 21391. The black crosses in all panels from north to south denote the positions of the MIR source MIR-48 at R.A.(J2000) = $21^h40^m41\overset{s}{.}43$, Decl.(J2000) = $+58°16'37\overset{''}{.}8$ in Choudhury et al. (2010) and 3.6 cm sources VLA2 at R.A.(J2000) = $21^h40^m41\overset{s}{.}90$, Decl.(J2000) = $+58°16'12\overset{''}{.}3$ and VLA3 at R.A.(J2000) = $21^h40^m42\overset{s}{.}77$, Decl.(J2000) = $+58°16'01\overset{''}{.}3$ in Beltrán et al. (2002). The white cross sign marks the position of the 3.6 cm source VLA1. The × signs from east to west mark the positions of the 3.1 mm sources BIMA3, BIMA2 and BIMA1, respectively. The lines in panel (a) show the orientation of the outflow axis from VLA2/BIMA2, with the solid span tracing blue-shifted direction and the dashed span red-shifted direction. The outflow axis angle is given by the high-velocity CO(1-0) main outflow emission of Beltrán et al. (2002).

3. The east-west outflow driven by BIMA 2 is highly collimated, and the collimation remains even at low outflow velocities. Beltrán et al. (2002) interpreted the complex morphology of the outflows as being the result of the interaction of the high velocity gas with dense clumps surrounding the protostar. They also suggested that BIMA 2 fits very well correlations between source and outflow properties for low-mass Class 0 objects given by Bontemps et al. (1996).

Neri et al. (2007) used still higher angular resolution millimeter interferometric observations to reveal that BIMA 2 is a cluster of multiple compact sources with the primary source named IRAM 2A. The detection of warm CH_3CN in IRAM 2A implies that this is the most massive protostar and could be the driving source of this energetic outflow. This interpretation is also supported by the morphology of the 1.2 mm and 3.1 mm continuum emission, which are extended along the outflow axis tracing the warm walls of the biconical cavity (Fuente et al. 2009). The CH_3CN abundance towards IRAM 2A is similar to that found in low-mass hot corinos and lower than that expected towards IM and high mass hot cores. Based on the low CH_3CN abundance, Fuente et al. (2009) suggested that IRAM 2A is a low-mass or a Herbig Ae star instead of the precursor of a massive Be star, or alternatively, IRAM 2A is a Class 0/I transition object that has already formed a small photodissociation region (PDR).

For BIMA 1 and BIMA 3, Beltrán et al. (2002) suggested they are more evolved low-mass objects given their small dust emissivity index and the more compact appearance of their dust emission.

While extended morphologies of the three sources are revealed in our *SOFIA* images (see Fig. 6.7), the extension of BIMA 2 does not follow the northeast-southwest direction of the major outflow or the north-south direction of the weak, low-velocity

outflow.

6.4.2 General Results from the SOFIA Imaging

Most of the sources presented in this paper are associated with outflows. In a few cases, such as IRAS 22198, L1206 A and IRAS 22172 MIR2, the SOFIA 20 to 40 μm images show modest extensions in the directions of the outflow axes, which was a common feature of the high-mass protostars in Papers I and II. However, the appearance of most of the IM protostars in the *SOFIA* images is quite compact, i.e., only a few beams across, and relatively round. In some of these cases, such as IRAS 22198, Cep E and IRAS 21391 (BIMA 2) Spitzer 8 μm images, which are sensitive to lower levels of diffuse emission, do reveal outflow axis elongation, which the *SOFIA* images are not able to detect. One contributing factor here is likely to be that the IM protostars are intrinsically less luminous than high-mass protostars and so produce less extended MIR emission. Another factor may be that the mass surface densities of their clump environments are lower than those of high-mass protostars (this is revealed in the derived values of $\Sigma_{\rm cl}$ from the SED fitting; see Section 6.4.3) and thus their MIR to FIR emission can appear more compact and more apparently symmetric. Three-color images of all the sources are presented together in Figure 6.8.

We notice that three of our sources are resolved into at least two components by higher angular resolution mm observations (within $\sim$ 0.01pc) including IRAS 22198, Cep E, IRAS 21391 BIMA2. A few mm sources are detected close to the main MIR source in IRAS 22172 located 3$''$- 8$''$(0.03 - 0.09 pc) away and a few mm sources are detected close to L1206 A located $\sim$ 12$''$(0.04 pc) away. Several jet-like condensations are revealed by radio observations in NGC 2071 IRS1 (within $\sim$ 0.01pc). This indicates that at least some of the protostars in our sample may have

nearby companions.

From Figure 6.9, we see that three of the sources have high-resolution UKIDSS NIR imaging: S235, IRAS 22172 and IRAS 21391. These images show the presence of a number of NIR sources in the vicinities of the protostars, especially for S235 and IRAS 22172, which may be associated clusters of YSOs. On the other hand, IRAS 22198, NGC 2071, Cep E and L1206 appear more isolated in their NIR images, although is must be noted that these images have lower resolution and higher noise levels. We also note that S235 B is located (in projection) near the center of its cluster, while IRAS22172 MIR2 is closer to the eastern edge of its cluster.

6.4.3 Results of SED Model Fitting

The SEDs

Figure 6.10 shows the SEDs of the 14 sources presented in this paper. There are 10 sources that lack *Herschel* 70 and 160 μm observations, which makes it difficult to determine the location of the peak of their SEDs. For the remaining 4 sources, NGC 2071 has a SED that peaks between 37 and 70 μm, while IRAS 22198, Cep E and G305 A have their peaks around 70 μm. It is noticeable that L1206 B, IRAS22172 MIR2, IRAS22172 MIR1, IRAS21391 MIR48 and IRAS16562 N have very flat MIR SEDs, especially L1206 B even shows decreasing flux densities as the wavelength increases.

ZT Model Fitting Results

We now consider the results of fitting the ZT protostellar radiative transfer models to the SEDs. Note that a general comparison of differences in results when using the Robitaille et al. (2007) radiative transfer models was carried out in Paper I, with some

of the main results being that the Robitaille et al. models often give solutions with very low accretion rates, which are not allowed in the context of the ZT models. As discussed in Paper I, our preference is to use the ZT models for analysis of the SOMA sources, since these models have been developed specifically for massive star formation under a physically self-consistent scenario, including full protostellar evolution, and with relatively few free parameters. Figure 6.11 shows the results of fitting the ZT protostellar radiative transfer models to the fixed aperture, background-subtracted SEDs, which is the fiducial analysis method presented in Papers I and II. In general, reasonable fits can be found to the observed SEDs, i.e., with relatively low values of reduced χ^2.

A summary of fitted parameter results in the $\Sigma_{\rm cl}$ - M_c - m_* parameter space is shown for each source in Figure 6.12. Note that the clump environment mass surface density, $\Sigma_{\rm cl}$ (ranging from 0.1 to 3 g cm^{-2}), and initial core mass, M_c (ranging from 10 to 480 $M_\odot$), are the primary physical parameters of the initial conditions of the ZT models, while the current protostellar mass, m_* (ranging from 0.5 $M_\odot$ up to about 50% of M_c, with this efficiency set by disk wind driven outflow feedback), describes the evolutionary state of stars forming from such cores. The two other independent parameters of the models are the angle of the line of sight to the outflow axis, $\theta_{\rm view}$, and the amount of foreground extinction, A_V, with all other model parameters being completely specified by $\Sigma_{\rm cl}$, M_c, and m_*. Note that $L_{\rm bol,iso}$ represents the isotropic bolometric luminosity, i.e., without correction for the inclination, and $L_{\rm bol}$ represents the intrinsic bolometric luminosity. The best five model fits for each source are listed in Table 6.3. Note that χ^2 listed in this table is the reduced χ^2, i.e., already normalized by the number of data points used in the fitting. Note, also that Table 4 of Paper II listed, incorrectly, this as quantity as χ^2/N, rather than as χ^2 used here and in Paper

I.

The best-fit models indicate that S235 and G305 A are more likely to be high-mass protostars, with most of the models (except the best model for S235) returning protostellar masses $m_* \geq 12\,M_\odot$, accretion rates $\dot{m}_* \sim 10^{-5} -$ a few $\times 10^{-4}\,\mathrm{M_\odot\,yr^{-1}}$, initial core masses $M_c \sim 50 - 400\,M_\odot$, clump mass surface densities $\Sigma_{\rm cl} \sim 0.1 - 1$ g cm^{-2}, and isotropic luminosities $L_{\rm bol,iso} \sim 10^3 -$ a few $\times 10^4\,\mathrm{L_\odot}$.

We find that IRAS 22198, NGC 2071, L1206 A, L1206 B, IRAS22172 MIR2, IRAS22172 MIR3, IRAS21391 MIR48, and IRAS16562 N are likely to *currently* be intermediate-mass protostars, with most models returning protostellar masses $m_* \sim 2 - 8\,M_\odot$, accretion rates $\dot{m}_* \sim 10^{-5} - 10^{-4}\,M_\odot\,\mathrm{yr^{-1}}$, initial core masses M_c ranging from 10 to 480 $M_\odot$, clump mass surface densities $\Sigma_{\rm cl}$ ranging from 0.1 to 3.2 g cm^{-2}, and isotropic luminosities $L_{\rm bol,iso} \sim 10 -$ a few $\times 10^2\,\mathrm{L_\odot}$. However, given the estimated remaining envelope masses around these protostars, for many models the final outcome would be a massive star, since star formation efficiencies are typically $\sim 50\%$ in the models (see also Tanaka et al. 2017; Staff et al. 2019).

Considering the remaining sources, we see that Cep E, IRAS22172 MIR1, IRAS21391 BIMA2, IRAS21391 BIMA3 are likely to *currently* be low-mass protostars, with most models returning protostellar masses $m_* \sim 0.5 - 2\,M_\odot$, accretion rates $\dot{m}_* \sim 10^{-5} - 10^{-4}\,M_\odot\,\mathrm{yr^{-1}}$, initial core masses M_c ranging from 10 to 160 $M_\odot$, the clump mass surface densities $\Sigma_{\rm cl}$ ranging from 0.1 to 0.3 g cm^{-2}, and isotropic luminosities $L_{\rm bol,iso} \sim 10^2\,L_\odot$. Given that the models used for the fitting all have initial core masses of $10\,M_\odot$ or greater, then the outcome of the evolution would always be formation of at least intermediate-mass stars. However, within the degeneracies of the model fits, there are some solutions that would imply we are catching a massive star in the very earliest stages of its formation.

Below, we describe the fitting results of each individual source and compare then with previous estimates from the literature.

S235: From the best five model fits, this source has an estimated isotropic bolometric luminosity of ~ 1 to $2 \times 10^3\ L_\odot$. However, the intrinsic bolometric luminosity of these models spans a much wider range from 3×10^3 to $2 \times 10^5\ L_\odot$. We note that for this source there are effectively only three measurements of the SED, all from the *SOFIA* FORCAST data, with observations at other wavelengths being used as upper limits. The large intrinsic luminosities for this source are possible because of the "flashlight effect", i.e., most of the flux is not directed towards us due to high local extinction in the core. This range of intrinsic luminosities means that there is a wide range of protostellar properties that are consistent with the observed SED, i.e., there are significant degeneracies in the derived protostellar parameters (see Fig. 6.12). In particular, while the best fit model has a low initial core mass ($10\ M_\odot$) and current protostellar mass ($2\ M_\odot$) forming from a high $\Sigma_{\rm cl}$ environment ($3\ {\rm g\,cm^{-2}}$) that is viewed at a relatively small angle to the outflow axis, the next four best models are all with larger core and protostellar masses in lower density environments viewed at angles nearly orthogonal to the outflow axis, i.e., close to the equatorial plane where there would be the most line of sight extinction.

Among previous studies of S235, Felli et al. (2006) used JHK band images and MSX fluxes and derived a luminosity of $410 L_\odot$, which they claimed must be considered to be a lower limit because the FIR part of the spectrum is not taken into account in their calculation. Dewangan & Anandarao (2011) used JHK band images and 2MASS and IRAC fluxes to do SED fitting with models from Robitaille et al. (2006, 2007). They derived $m_* \sim 6.5 M_\odot$, $L_{\rm bol} \sim 575 L_\odot$ and $M_{\rm env} \sim 9 M_\odot$. The stellar source itself has been classified as a B1V star by Boley et al. (2009), with emission-line profiles

indicative of an accretion disk. Based on the intensity of the reflected component, it was concluded that the accretion disk must be viewed nearly edge-on, which agrees with four of our best models and explains the discrepancy between $L_{\rm bol,iso}$ and $L_{\rm bol}$. Boley et al. (2009) estimated a mass accretion rate of $2 - 6 \times 10^{-6} M_{\odot}{\rm yr}^{-1}$ for a B1V star with a mass of 13 $M_{\odot}$ using the Brγ luminosity, which is comparable with the mass-loss rate of $4 \times 10^{-6} M_{\odot}{\rm yr}^{-1}$ derived by Felli et al. (2006) from the radio flux density. However, our best models have disk accretion rates more than ten times higher. It should be noted that the accretion rate is not a free parameter in the ZT models and that the range of accretion rates is generally relatively high, being set by the properties of the initial cores and the mass surface density of their clump environments.

IRAS 22198: The best models are those with a protostar with current mass of 2 - 4 $M_{\odot}$, forming in a low mass surface density clump (0.1 - 0.3 g cm^{-2}). Our estimate of the isotropic luminosity is about 600 $L_{\odot}$, with the intrinsic luminosity being about 800 $L_{\odot}$. Sánchez-Monge et al. (2010) fit the SED of IRAS 22198 from NIR to centimeter wavelengths with a modified blackbody plus a thermal ionized wind and derived a bolometric luminosity of $\sim$370 $L_{\odot}$ and an envelope mass of $\sim$5 $M_{\odot}$, remarking that the SED of IRAS 22198 resembles that of Class 0 objects (Andre et al. 1993). Our derived isotropic luminosity is slightly higher, while our envelope mass is much higher, $\sim 50\, M_{\odot}$, than their results. However, their $M_{\rm env}$ was derived from interferometric flux measurements and thus should be treated as a lower limit. The single-dish measurement at mm wavelengths of the dense core mass is 17 $M_{\odot}$ within a radius of 2,650 au (3.5″) (Palau et al. 2013). Thus the reason for our larger mass estimate is likely due to our analysis applying to a much larger scale, i.e., within a radius of 0.089 pc (26″).

NGC 2071: The best models suggest a currently intermediate-mass protostar with a mass of 2 - 4 $M_\odot$ forming within a core with initial mass of 10 - 60 $M_\odot$. Trinidad et al. (2009) estimated a central mass of $\sim 5 \pm 3 M_\odot$ for IRS1 and $\sim 1.2 \pm 0.4 M_\odot$ for IRS3 based on the observed velocity gradient of the water masers, which is consistent with our estimate. The single-dish measurement at mm wavelength of the dense core mass is 39 $M_\odot$ within a radius of 4,700 AU (11″) (Palau et al. 2013), which is similar to the $M_{\rm env}$ returned by most of our best fit models inside 10″.

Cep E: The best 5 models all return a $\Sigma_{\rm cl}$ of 0.1 g cm^{-2} and most models have m_* as low as 1 - 2 $M_\odot$. Crimier et al. (2010) modeled the MIR to mm SED with the 1D radiative transfer code DUSTY and derived a luminosity of ∼100 $L_\odot$ and an envelope mass of 35 $M_\odot$, which are similar to our results.

L1206: The best models of L1206 A involve a protostar forming inside a relatively massive initial core (40 - 480 $M_\odot$) with low clump mass surface density (0.1 - 0.3 g cm^{-2}). All the best 5 models give a value of $m_* = 4\ M_\odot$. Ressler & Shure (1991) found a total luminosity of 1100 $L_\odot$ by fitting four IRAS fluxes plus the 2.7 mm data of Wilking et al. (1989) with a single-temperature dust spectrum at 1 kpc, which is similar to our result. Beltrán et al. (2006) estimated the core mass of OVRO 2 to be 14.2 $M_\odot$ from the 2.7 mm dust continuum emission at a distance of 910 pc. This core mass estimate is derived from interferometric observations that may be missing flux, and indeed three of our best-fit models give a much higher value of $M_{\rm env}$. Ressler & Shure (1991) suggested that L1206 A is seen only in scattered light because of heavy obscuration by an almost edge-on circumstellar disk. Four of the best five models return a nearly edge-on line of sight.

L1206 B has a very flat and slightly decreasing SED at short wavelengths. A circumstellar disk could explain the infrared excess, as suggested by Ressler & Shure

(1991), and the protostar may have already cleared a significant portion of its envelope, thus explaining the decreasing spectrum between 10 and 30 μm. The favored ZT models have a wide range of stellar mass $m_* \sim 0.5 - 12\ M_\odot$, but low initial core mass $M_{\rm c} \sim 10 - 40\ M_\odot$, low current envelope mass of 1 to 9 $M_\odot$ and low mass surface density $\Sigma_{\rm cl} \sim 0.1 - 0.3$ g cm^{-2} of the clump environment.

IRAS 22172: The models for the three MIR sources all involve protostars with masses $\sim$ 1 - 4 $M_\odot$ forming in relatively low-mass initial cores of 10 - 40 $M_\odot$. Fontani et al. (2004) divided the SED between the NIR cluster and the cold 3.4 mm core (their I22172-C) and performed two grey-body fits to the SED. The grey-body fit to the MSX and IRAS data with $\lambda \leqslant 25\mu$m, which represent the emission due to the cluster of stars surrounding the mm core I22172-C, yields a luminosity of $2.2 \times 10^2\, L_\odot$. Based on the beam size and the MSX 21μm emission, their photometry should cover the whole field, i.e., all the three MIR sources. However, in our analysis we derive a much higher combined luminosity from the region, with contributions from the three MIR sources analyzed. The single-dish measurement at mm wavelengths of the dense core mass of MIR2 is 150 $M_\odot$ (Palau et al. 2013), much higher than the $M_{\rm env}$ given by our models. However, their core radius, represented by the deconvolved FWHM/2, is about 10$''$, while our mass estimate is based on an aperture radius of 4$''$.

IRAS 21391: Previous SED fitting with low-resolution data estimated the bolometric luminosity of IRAS 21391 to range from 235 $L_\odot$ (Saraceno et al. 1996) to 440 $L_\odot$ (Sugitani et al. 2000). Our fitting results for the three sources BIMA 2, BIMA 3 and MIR 48[3] all return isotropic luminosities $\lesssim 100\ L_\odot$. By using the relationship between the momentum rate and the bolometric luminosity (Cabrit & Bertout 1992), Beltrán et al. (2002) inferred a bolometric luminosity of 150 $L_\odot$ for BIMA 2.

[3]Note that we follow the nomenclature in Beltrán et al. (2002), but the photometry centers of IRAS 21391 BIMA2 and IRAS 21391 BIMA3 are VLA2 and VLA3, respectively.

Choudhury et al. (2010) fit the 1 - 24 μm SED derived from optical BVRI, Spitzer IRAC and MIPS observations with Robitaille et al. (2007) models and derived a luminosity of 197 $L_{\odot}$ and a stellar mass of 6 $M_{\odot}$ for BIMA 2 (their MIR-50), which are both higher than our results. As indicated by Figure 6.17, ZT models with m_{*} higher than 5 $M_{\odot}$ have a very large χ^2. The envelope mass of Choudhury et al. (2010) of 41 $M_{\odot}$ is also slightly higher than the M_c and $M_{\rm env}$ in our first 3 best models. However, their disk accretion rate is about 1000 times lower than that in our best models, which is a known issue when comparing Robitaille et al. (2007) and ZT models (see discussion in De Buizer et al. 2017). Beltrán et al. (2002) estimated the circumstellar mass to be 5.1 $M_{\odot}$ based on BIMA 3.1 mm continuum observations, which should be treated as a lower limit of $M_{\rm env}$ given that it is an interferometric measurement subject to missing flux. Beltrán et al. (2002) suggested that the axis of the outflow should be close to the plane of the sky, given the morphology of the CO(1-0) outflows at low velocities with blue-shifted and redshifted gas in both lobes. However, in our best 5 models, only the third model has a more edge-on inclination.

Our best models for IRAS 21391 BIMA3 involve a protostar with a current stellar mass of 0.5 $M_{\odot}$ with a bolometric luminosity $\sim$ 100 $L_{\odot}$. The best-fit model in Choudhury et al. (2010) for BIMA 3 (their MIR-54) yields a luminosity of 33.4 $L_{\odot}$ and a stellar mass of 1.5 $M_{\odot}$. Beltrán et al. (2002) derived a circumstellar mass of 0.07 $M_{\odot}$ for BIMA 3, which is much lower than the predicted $M_{\rm env}$ by our best models.

Our best models for IRAS 21391 MIR48 involve a protostar with a mass ranging from 1 to 12 $M_{\odot}$. The best-fit model in Choudhury et al. (2010) for MIR-48 yields a luminosity of 280 $L_{\odot}$ and a stellar mass of 5 $M_{\odot}$, which is similar to the isotropic luminosity and the stellar mass in our best two models.

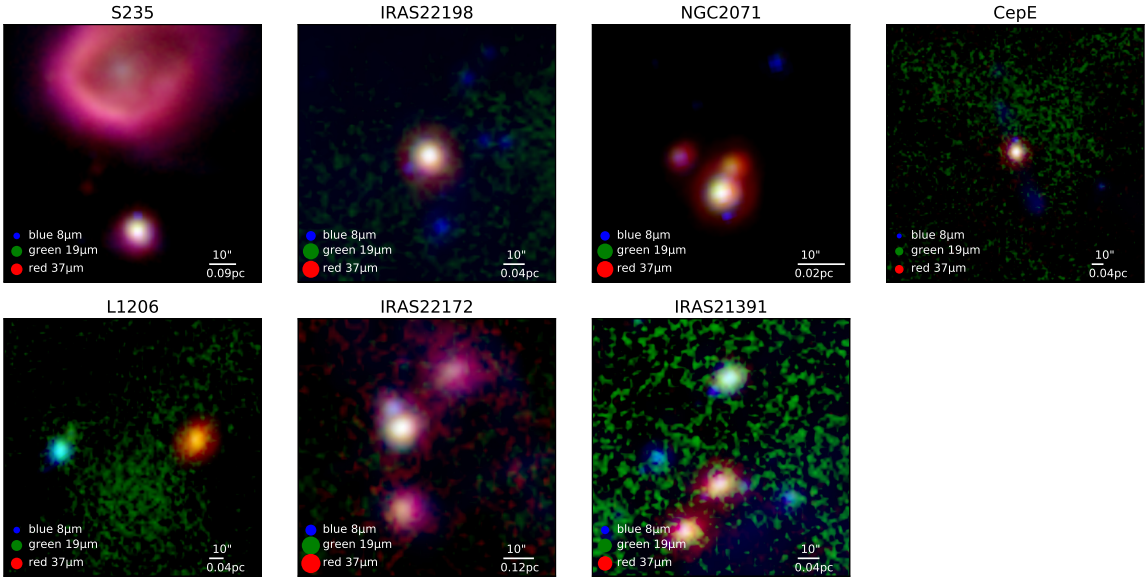

Fig. 6.8.— Gallery of RGB images of the seven new regions analyzed in this paper, as labeled. The color intensity scales are stretched as arcsinh and show a dynamic range of 100 from the peak emission at each wavelength. The legend shows the wavelengths used and the beam sizes at these wavelengths. *SOFIA*-FORCAST 37 μm is shown in red. *SOFIA*-FORCAST 19 μm is shown in green. *Spitzer* 8 μm is shown in blue.

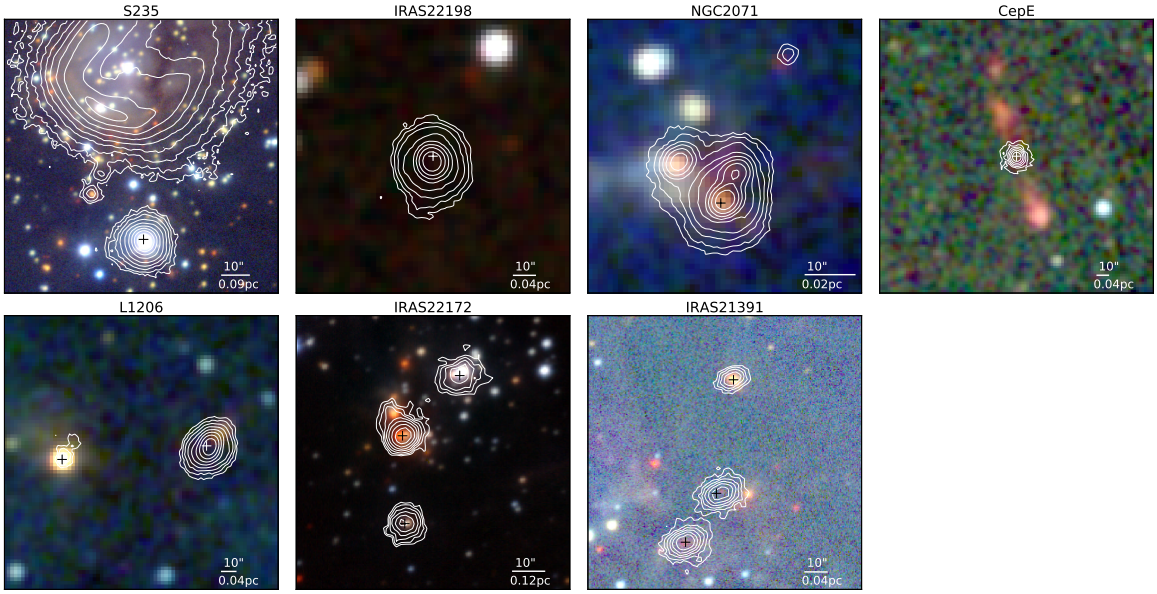

Fig. 6.9.— NIR RGB images of the seven new regions analyzed in this paper, as labeled. The data of S235, IRAS 22172 and IRAS 21391 are from the UKIDSS survey (Lawrence et al. 2007). The data of IRAS 22198, NGC 2071, Cep E and L1206 are from the 2MASS survey (Skrutskie et al. 2006). K band data are shown in red, H band data in green and J band data in blue. The white contours are the *SOFIA* 37μm emission, with the same levels as displayed in the previous individual figures for each source. The crosses in each panel are the same as those in the previous individual figures. The scale bar is shown in the right corner of each panel.

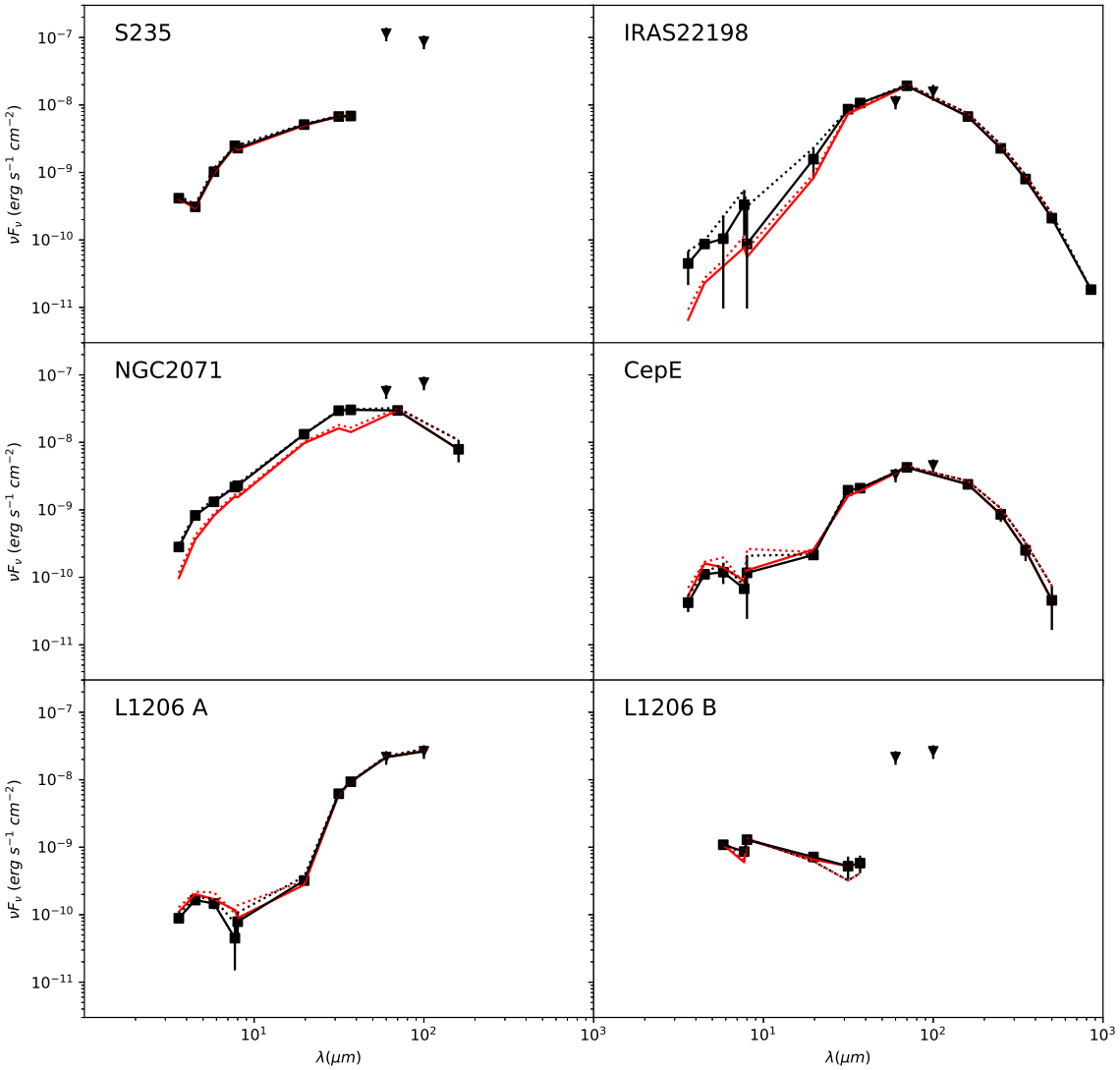

Fig. 6.10.— SEDs of the 14 presented sources. Total fluxes with no background subtraction applied are shown with dotted lines. The fixed aperture case is black dotted; the variable aperture (at $< 70\ \mu$m) case is red dotted. The background subtracted SEDs are shown with solid lines: black for fixed aperture (the fiducial case); red for variable aperture. Black solid squares indicate the actual measured values that sample the fiducial SED. Black triangles denote the flux densities measured with *IRAS*. The down arrows in G305 A and IRAS16562 N denote that those data points are fluxes with no background subtraction and are treated as upper limits.

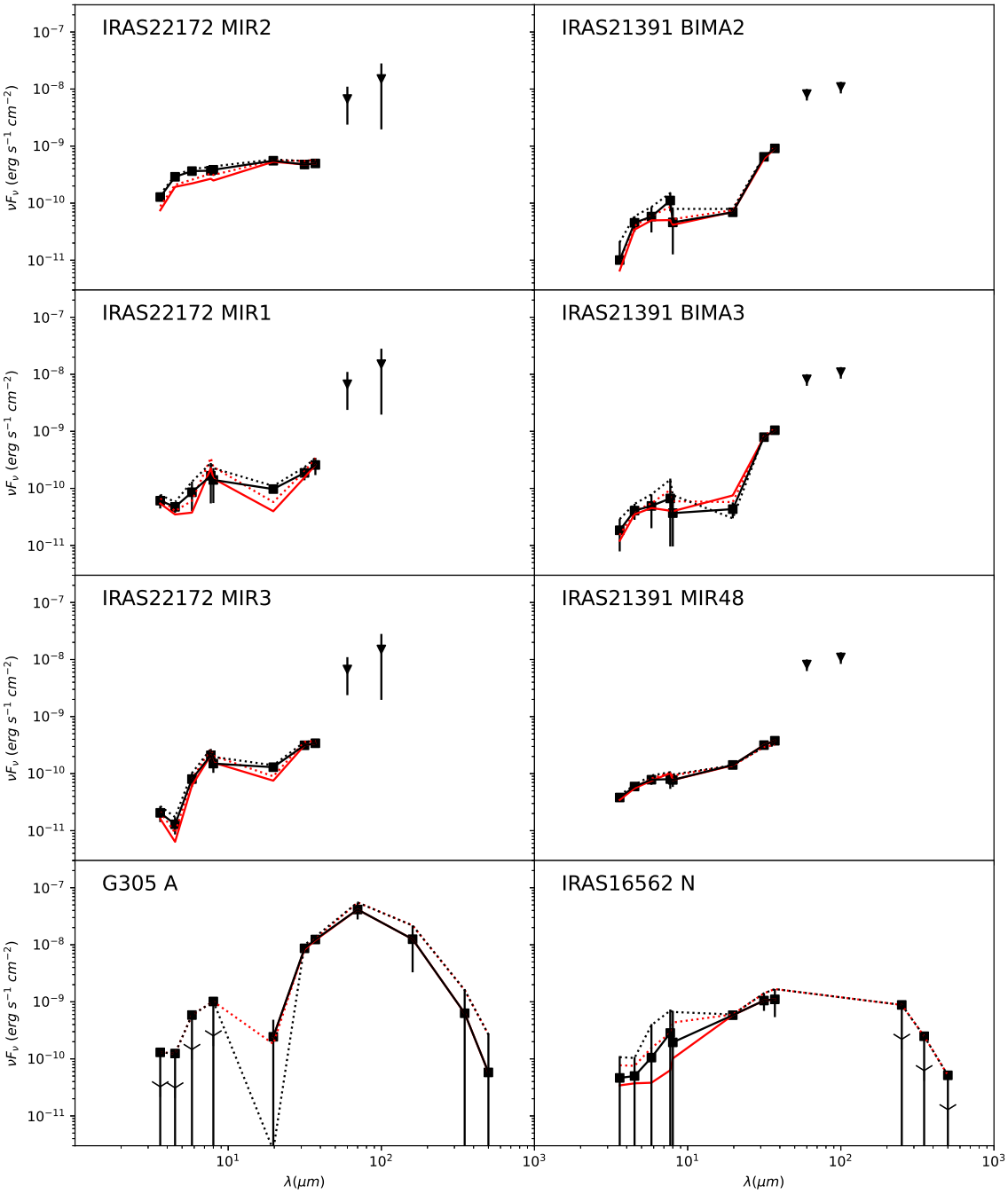
IRAS22172 MIR2
IRAS21391 BIMA2
IRAS22172 MIR1
IRAS21391 BIMA3
IRAS22172 MIR3
IRAS21391 MIR48
G305 A
IRAS16562 N
νF_ν (erg s^{-1} cm^{-2})
$\lambda(\mu m)$

Fig. 6.10.— (cont.)

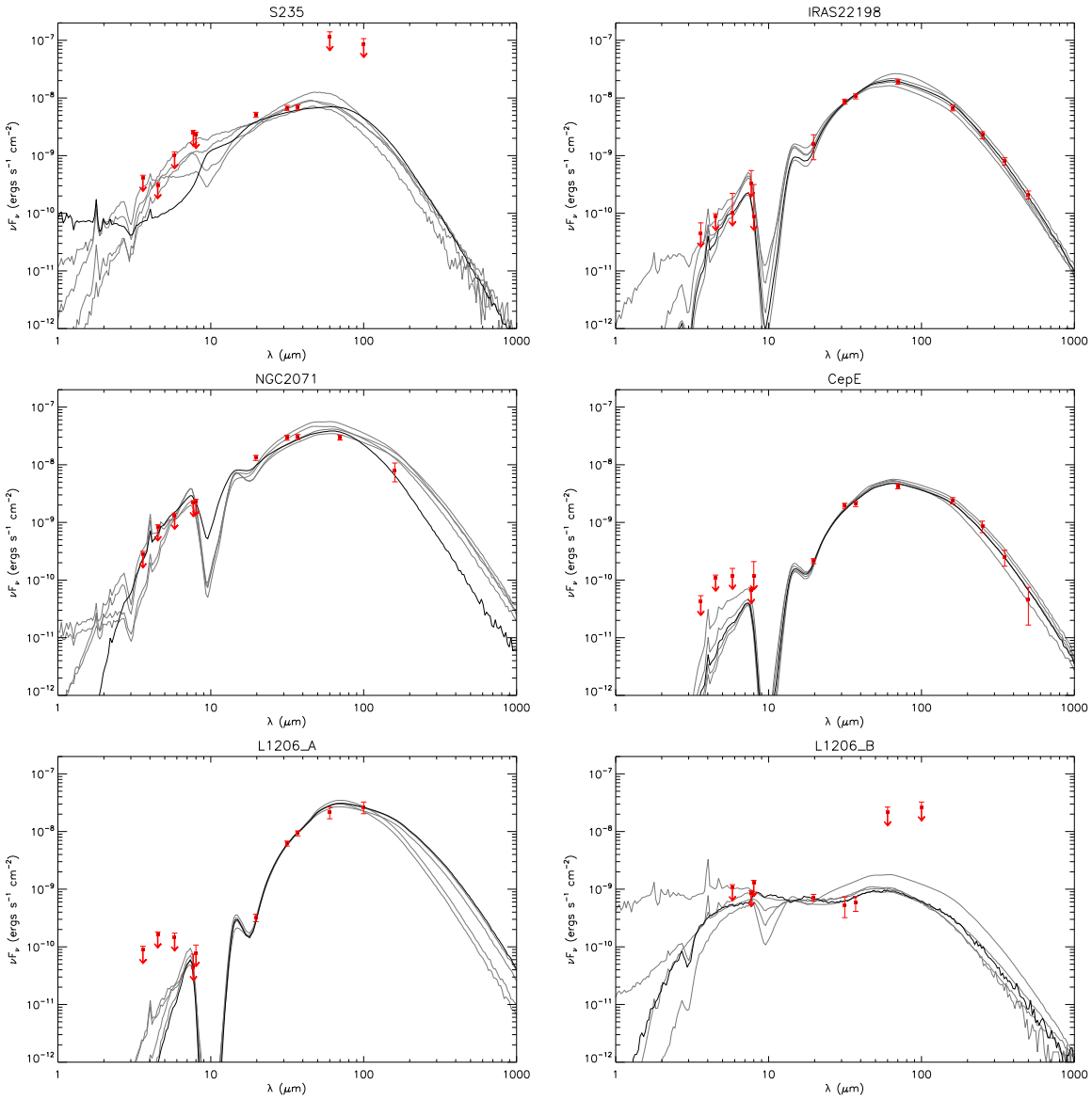

Fig. 6.11.— Protostar model fitting to the fixed aperture, background-subtracted SED data using the ZT model grid. For each source, the best fit model is shown with a solid black line and the next four best models are shown with solid gray lines. Flux values are those from Table 6.2. Note that the data at $\lesssim 8\,\mu$m are treated as upper limits (see text). The resulting model parameter results are listed in Table 6.3.

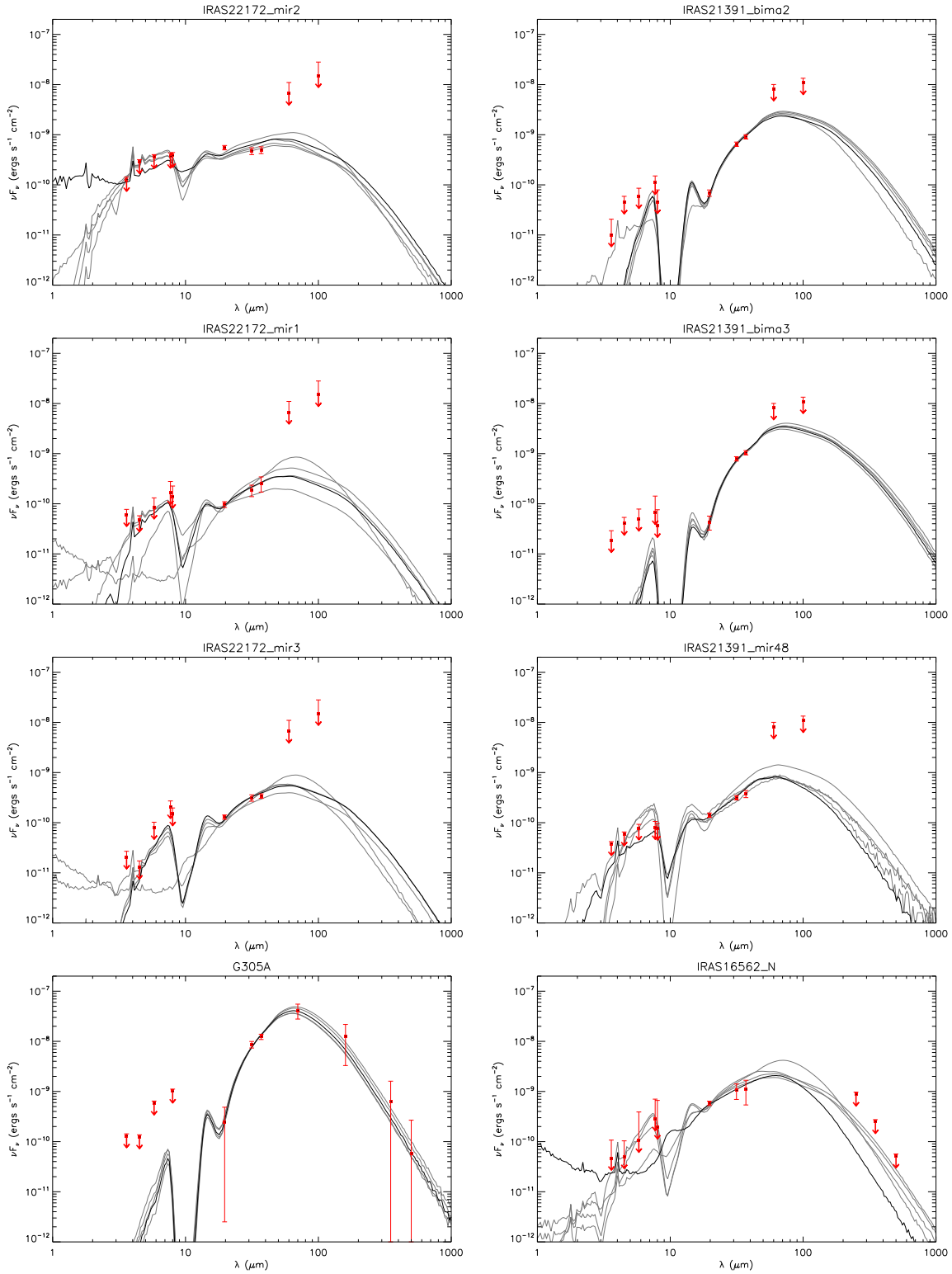
IRAS22172_mir2
IRAS21391_bima2
IRAS22172_mir1
IRAS21391_bima3
IRAS22172_mir3
IRAS21391_mir48
G305A
IRAS16562_N
λ (μm)
νF_ν (ergs s^-1 cm^-2)

Fig. 6.11.— (cont.)

Table 6.3. Parameters of the Best Five Fitted Models

Source	χ^2	$M_{\rm c}$ ($M_\odot$)	$\Sigma_{\rm cl}$ (g cm^{-2})	$R_{\rm core}$ (pc) ($''$)	m_* ($M_\odot$)	$\theta_{\rm view}$ (°)	A_V (mag)	$M_{\rm env}$ ($M_\odot$)	$\theta_{w,{\rm esc}}$ (deg)	$\dot{M}_{\rm disk}$ ($M_\odot$/yr)	$L_{\rm bol,iso}$ ($L_\odot$)	$L_{\rm bol}$ ($L_\odot$)
S235	1.26	10	3.2	0.013 (2)	2.0	39	0.0	6	35	1.8×10^{-4}	1.4×10^{3}	2.6×10^{3}
d = 1.8 kpc	2.55	60	1.0	0.057 (7)	24.0	89	11.1	5	71	1.9×10^{-4}	2.1×10^{3}	9.3×10^{4}
R_{ap} = 12 $''$	2.74	50	0.1	0.165 (19)	12.0	89	4.0	15	59	3.4×10^{-5}	1.4×10^{3}	1.4×10^{4}
= 0.10 pc	3.00	80	1.0	0.066 (8)	32.0	89	15.2	3	79	1.4×10^{-4}	1.6×10^{3}	1.6×10^{5}
	3.02	50	0.3	0.093 (11)	16.0	80	0.0	8	68	7.1×10^{-5}	1.4×10^{3}	3.1×10^{4}
IRAS22198	0.18	80	0.1	0.208 (56)	4.0	89	29.3	71	18	3.7×10^{-5}	6.0×10^{2}	8.5×10^{2}
d = 0.8 kpc	0.27	60	0.1	0.180 (49)	4.0	62	41.4	51	21	3.4×10^{-5}	6.1×10^{2}	8.9×10^{2}
R_{ap} = 26 $''$	1.08	100	0.1	0.233 (63)	4.0	89	35.4	91	15	4.0×10^{-5}	6.5×10^{2}	8.8×10^{2}
= 0.09 pc	1.47	40	0.3	0.083 (22)	2.0	22	9.1	35	17	5.3×10^{-5}	6.5×10^{2}	7.5×10^{2}
	1.78	50	0.1	0.165 (44)	4.0	62	25.3	41	24	3.2×10^{-5}	5.1×10^{2}	7.9×10^{2}
NGC2071	3.14	10	3.2	0.013 (7)	4.0	58	57.6	2	56	1.9×10^{-4}	5.0×10^{2}	1.9×10^{3}
d = 0.4 kpc	3.59	30	0.1	0.127 (67)	4.0	65	12.1	21	33	2.7×10^{-5}	3.6×10^{2}	7.7×10^{2}
R_{ap} = 10 $''$	5.79	40	0.1	0.147 (78)	4.0	62	11.1	30	27	3.0×10^{-5}	4.4×10^{2}	7.5×10^{2}
= 0.02 pc	7.06	60	0.1	0.180 (95)	2.0	29	0.0	55	15	2.5×10^{-5}	3.2×10^{2}	3.5×10^{2}
	7.57	50	0.1	0.165 (87)	2.0	29	0.0	46	16	2.4×10^{-5}	2.8×10^{2}	3.1×10^{2}
CepE	0.63	30	0.1	0.127 (36)	1.0	83	29.3	27	15	1.5×10^{-5}	1.3×10^{2}	1.7×10^{2}
d = 0.7 kpc	0.70	30	0.1	0.127 (36)	2.0	65	60.6	25	23	2.0×10^{-5}	1.5×10^{2}	2.4×10^{2}
R_{ap} = 23 $''$	0.80	40	0.1	0.147 (42)	1.0	89	21.2	38	12	1.6×10^{-5}	1.3×10^{2}	1.7×10^{2}
= 0.08 pc	1.40	50	0.1	0.165 (46)	1.0	89	19.2	48	11	1.7×10^{-5}	1.4×10^{2}	1.7×10^{2}
	1.67	20	0.1	0.104 (29)	4.0	71	100.0	10	43	2.1×10^{-5}	1.9×10^{2}	6.8×10^{2}
L1206 A	0.08	480	0.1	0.510 (136)	4.0	89	45.5	474	6	6.1×10^{-5}	9.2×10^{2}	1.0×10^{3}
d = 0.8 kpc	0.09	400	0.1	0.465 (124)	4.0	83	56.6	390	7	5.8×10^{-5}	9.4×10^{2}	1.0×10^{3}
R_{ap} = 9 $''$	0.17	50	0.3	0.093 (25)	4.0	55	41.4	41	22	7.7×10^{-5}	8.8×10^{2}	1.4×10^{3}
= 0.03 pc	0.21	40	0.3	0.083 (22)	4.0	89	28.3	31	25	7.2×10^{-5}	7.3×10^{2}	1.4×10^{3}
	0.23	240	0.1	0.360 (96)	4.0	89	74.7	229	9	5.1×10^{-5}	9.0×10^{2}	1.0×10^{3}
L1206 B	0.13	40	0.1	0.147 (39)	12.0	89	8.1	2	82	9.5×10^{-6}	5.7×10^{1}	1.1×10^{4}
d = 0.8 kpc	0.45	30	0.3	0.072 (19)	12.0	89	30.3	1	81	2.2×10^{-5}	7.0×10^{1}	1.2×10^{4}
R_{ap} = 10 $''$	0.55	10	0.3	0.041 (11)	4.0	77	0.0	1	68	2.4×10^{-5}	4.9×10^{1}	6.7×10^{2}
= 0.04 pc	0.71	10	0.1	0.074 (20)	2.0	51	0.0	4	50	1.1×10^{-5}	8.1×10^{1}	1.3×10^{2}
	2.26	10	0.1	0.074 (20)	0.5	22	34.3	9	20	7.8×10^{-6}	1.5×10^{2}	7.5×10^{1}
IRAS22172 MIR2	1.67	40	0.1	0.147 (13)	2.0	22	0.0	36	19	2.2×10^{-5}	3.9×10^{2}	2.7×10^{2}
d = 2.4 kpc	2.27	30	0.1	0.127 (11)	2.0	22	32.3	25	23	2.0×10^{-5}	8.0×10^{2}	2.4×10^{2}
R_{ap} = 4 $''$	2.39	20	0.1	0.104 (9)	4.0	48	6.1	10	43	2.1×10^{-5}	3.4×10^{2}	6.8×10^{2}
= 0.04 pc	2.51	30	0.1	0.127 (11)	1.0	13	37.4	27	15	1.5×10^{-5}	8.7×10^{2}	1.7×10^{2}
	2.81	10	1.0	0.023 (2)	2.0	39	50.5	5	39	7.5×10^{-5}	1.0×10^{3}	7.6×10^{2}
IRAS22172 MIR1	0.04	20	0.1	0.104 (9)	2.0	34	25.3	15	30	1.7×10^{-5}	1.4×10^{2}	1.9×10^{2}
d = 2.4 kpc	0.04	20	0.1	0.104 (9)	1.0	22	50.5	17	20	1.3×10^{-5}	2.7×10^{2}	1.5×10^{2}
R_{ap} = 5 $''$	0.20	10	3.2	0.013 (1)	4.0	71	0.0	2	56	1.9×10^{-4}	1.9×10^{2}	1.9×10^{3}
= 0.05 pc	0.23	10	0.1	0.074 (6)	1.0	34	1.0	7	31	1.0×10^{-5}	8.1×10^{1}	1.1×10^{2}
	0.40	30	0.1	0.127 (11)	1.0	22	16.2	27	15	1.5×10^{-5}	1.7×10^{2}	1.7×10^{2}
IRAS22172 MIR3	0.19	30	0.1	0.127 (11)	1.0	22	0.0	27	15	1.5×10^{-5}	1.7×10^{2}	1.7×10^{2}
d = 2.4 kpc	0.39	30	0.1	0.127 (11)	2.0	34	13.1	25	23	2.0×10^{-5}	1.9×10^{2}	2.4×10^{2}
R_{ap} = 5 $''$	0.45	10	3.2	0.013 (1)	4.0	68	0.0	2	56	1.9×10^{-4}	2.1×10^{2}	1.9×10^{3}
= 0.05 pc	0.61	10	1.0	0.023 (2)	4.0	68	0.0	1	59	7.7×10^{-5}	1.5×10^{2}	1.1×10^{3}
	0.97	20	0.1	0.104 (9)	1.0	29	0.0	17	20	1.3×10^{-5}	1.2×10^{2}	1.5×10^{2}
IRAS21391 BIMA2	0.04	20	0.1	0.104 (29)	0.5	34	74.7	19	13	9.6×10^{-6}	8.0×10^{1}	9.0×10^{1}
d = 0.8 kpc	0.07	30	0.1	0.127 (35)	0.5	22	74.7	29	10	1.1×10^{-5}	8.8×10^{1}	9.0×10^{1}
R_{ap} = 8 $''$	0.08	10	0.3	0.041 (11)	2.0	71	19.2	5	43	3.0×10^{-5}	6.2×10^{1}	2.8×10^{2}
= 0.03 pc	0.14	40	0.1	0.147 (40)	0.5	22	59.6	39	8	1.1×10^{-5}	8.7×10^{1}	8.8×10^{1}
	0.18	50	0.1	0.165 (45)	0.5	22	48.5	49	7	1.2×10^{-5}	8.7×10^{1}	8.7×10^{1}
IRAS21391 BIMA3	0.18	80	0.1	0.208 (57)	0.5	86	2.0	79	5	1.4×10^{-5}	8.6×10^{1}	9.2×10^{1}
d = 0.8 kpc	0.20	100	0.1	0.233 (64)	0.5	55	0.0	99	4	1.5×10^{-5}	8.9×10^{1}	9.1×10^{1}
R_{ap} = 8 $''$	0.23	60	0.1	0.180 (50)	0.5	83	9.1	59	6	1.3×10^{-5}	8.0×10^{1}	8.7×10^{1}

Table 6.3—Continued

Source	χ^2	$M_{\rm c}$ ($M_\odot$)	$\Sigma_{\rm cl}$ (g cm^{-2})	$R_{\rm core}$ (pc) ($''$)	m_* ($M_\odot$)	$\theta_{\rm view}$ (°)	A_V (mag)	$M_{\rm env}$ ($M_\odot$)	$\theta_{w,\rm esc}$ (deg)	$\dot{M}_{\rm disk}$ ($M_\odot$/yr)	$L_{\rm bol,iso}$ ($L_\odot$)	$L_{\rm bol}$ ($L_\odot$)
= 0.03 pc	0.24	120	0.1	0.255 (70)	0.5	22	0.0	118	4	1.5×10^{-5}	9.0×10^{1}	8.8×10^{1}
	0.26	160	0.1	0.294 (81)	0.5	22	0.0	158	3	1.6×10^{-5}	1.0×10^{2}	9.8×10^{1}
IRAS21391 MIR48	0.33	10	0.3	0.041 (11)	4.0	89	43.4	1	68	2.4×10^{-5}	2.9×10^{1}	6.7×10^{2}
d = 0.8 kpc	0.58	10	0.1	0.074 (20)	2.0	68	13.1	4	50	1.1×10^{-5}	2.5×10^{1}	1.3×10^{2}
R_{ap} = 8 $''$	2.70	40	0.1	0.147 (40)	12.0	89	98.0	2	82	9.5×10^{-6}	5.7×10^{1}	1.1×10^{4}
= 0.03 pc	3.75	30	0.3	0.072 (20)	12.0	89	100.0	1	81	2.2×10^{-5}	7.0×10^{1}	1.2×10^{4}
	5.51	10	0.1	0.074 (20)	1.0	39	92.9	7	31	1.0×10^{-5}	6.4×10^{1}	1.1×10^{2}
G305 A	0.16	240	0.3	0.203 (10)	12.0	83	85.9	216	15	2.0×10^{-4}	3.1×10^{4}	4.1×10^{4}
d = 4.1 kpc	0.17	320	0.3	0.234 (12)	12.0	71	79.8	293	13	2.2×10^{-4}	3.3×10^{4}	4.0×10^{4}
R_{ap} = 12 $''$	0.19	200	0.3	0.185 (9)	12.0	80	81.8	173	17	1.9×10^{-4}	2.8×10^{4}	4.0×10^{4}
= 0.24 pc	0.20	200	0.3	0.185 (9)	16.0	83	97.0	162	22	2.2×10^{-4}	3.0×10^{4}	5.3×10^{4}
	0.20	400	0.3	0.262 (13)	12.0	22	90.9	373	11	2.3×10^{-4}	3.7×10^{4}	4.0×10^{4}
IRAS16562 N	0.05	10	3.2	0.013 (2)	4.0	62	0.0	2	56	1.9×10^{-4}	2.9×10^{2}	1.9×10^{3}
d = 1.7 kpc	0.14	50	0.1	0.165 (20)	2.0	22	0.0	46	16	2.4×10^{-5}	3.1×10^{2}	3.1×10^{2}
R_{ap} = 8 $''$	0.28	10	1.0	0.023 (3)	1.0	29	17.2	8	25	6.0×10^{-5}	5.6×10^{2}	7.7×10^{2}
= 0.06 pc	0.37	60	0.1	0.180 (22)	2.0	22	0.0	55	15	2.5×10^{-5}	3.5×10^{2}	3.5×10^{2}
	0.38	30	0.1	0.127 (15)	4.0	62	7.1	21	33	2.7×10^{-5}	3.8×10^{2}	7.7×10^{2}

G305 A: The best models are those with a high-mass protostar with a current mass of 12 - 16 $M_{\odot}$ forming from a core with initial mass of 200 - 400 $M_{\odot}$ and initial clump mass surface density of 0.3 g cm^{-2}. In Paper II we mentioned G305A is likely to be much younger and more embedded than G305B and in a hot core phase, prior to the onset of an UC H II region.

IRAS16562 N: The best models involve a low-mass protostar with current mass of 1 - 4 $M_{\odot}$ forming from a core with initial mass of 10 - 60 $M_{\odot}$. $\Sigma_{\rm cl}$ is not well constrained, varying from 0.1 to 3.2 g cm^{-2}.

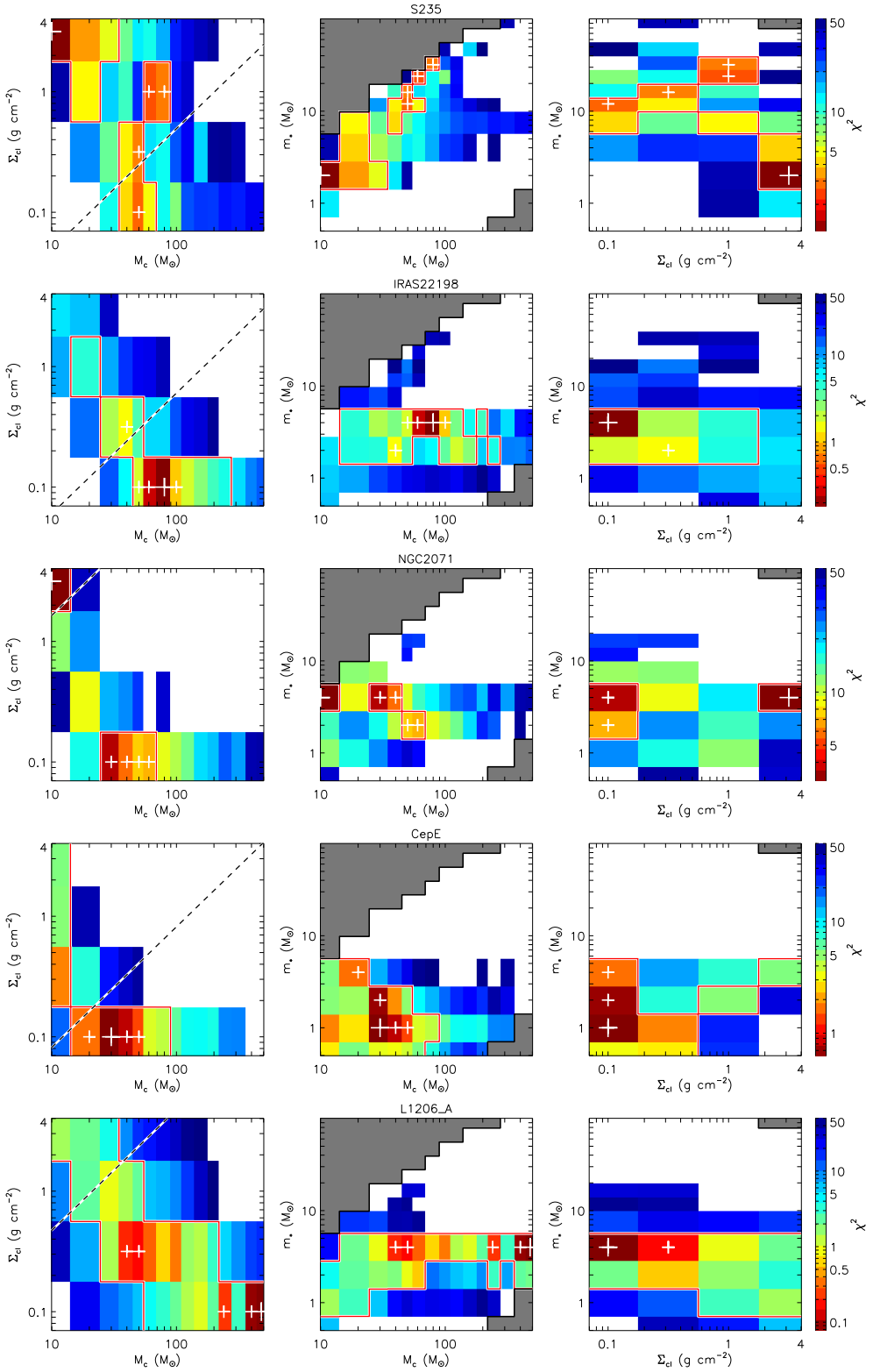

Fig. 6.12.— Diagrams of χ^2 distribution in $\Sigma_{\rm cl}$ - M_c space, m_* - $M_{\rm c}$ space and m_* - $\Sigma_{\rm cl}$ space. The white crosses mark the locations of the five best models, and the large cross is the best model. The grey regions are not covered by the model grid, and the white regions are where the χ^2 is larger than 50. The red contours are at the level of $\chi^2 = \chi^2_{min} + 5$. The dashed line denotes when $R_c = R_{\rm ap}$.

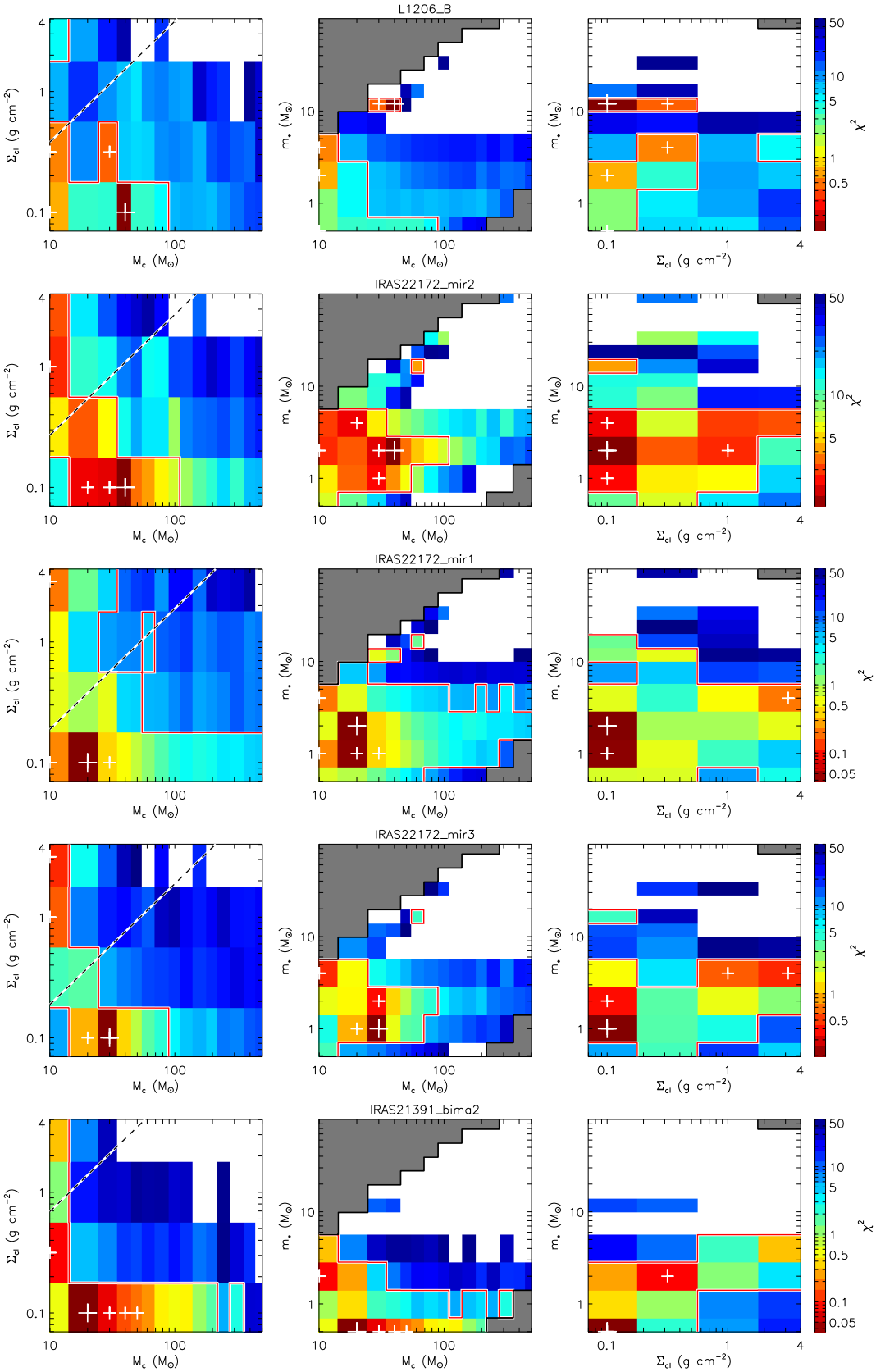
L1206_B
IRAS22172_mir2
IRAS22172_mir1
IRAS22172_mir3
IRAS21391_bima2
Σ_{cl} (g cm^{-2})
M_c ($M_\odot$)
$m_\star$ ($M_\odot$)
χ^2

Fig. 6.12.— (cont.)

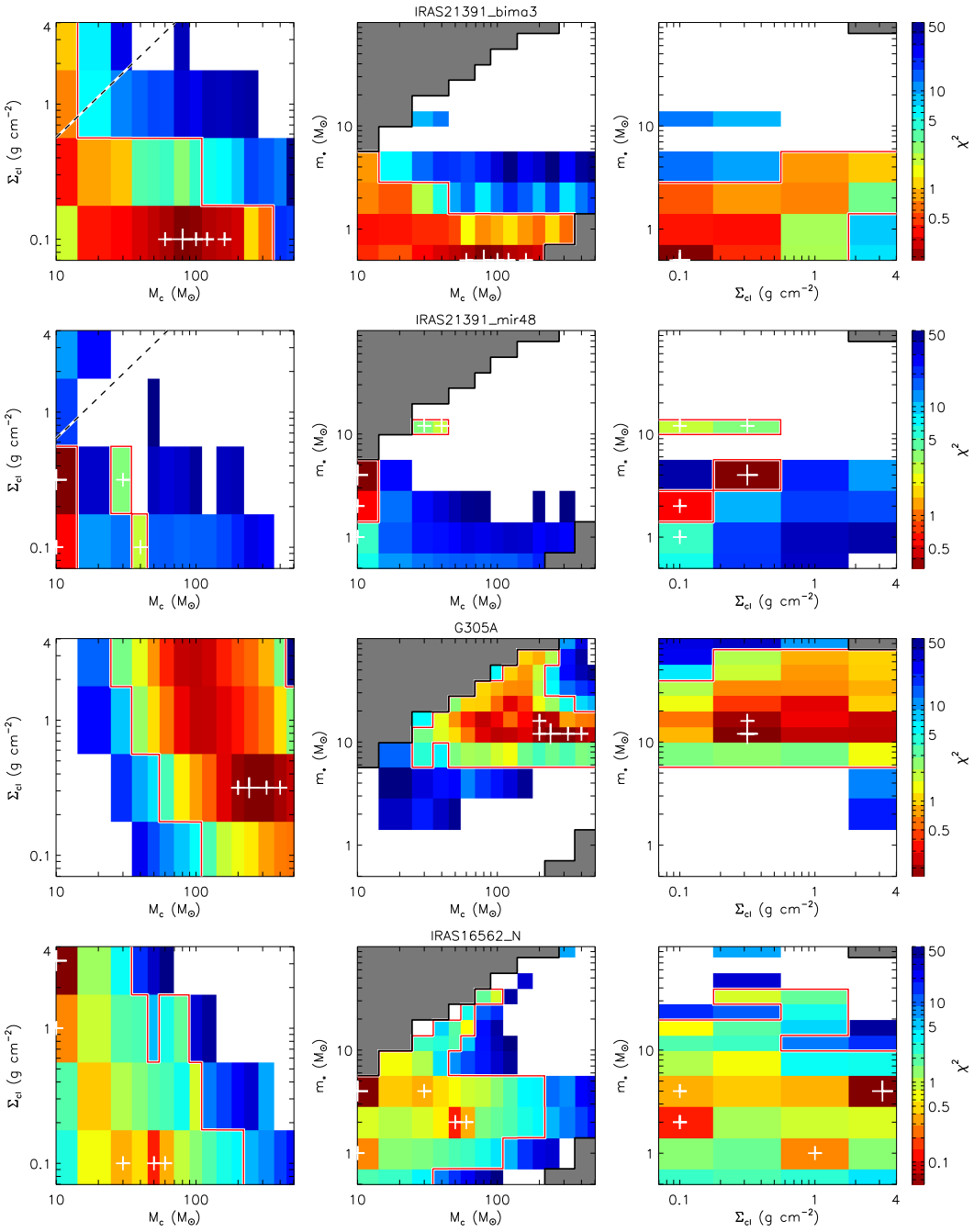
IRAS21391_bima3
IRAS21391_mir48
G305A
IRAS16562_N
Σ_{cl} (g cm^{-2})
M_c ($M_\odot$)
m_* ($M_\odot$)
χ^2

Fig. 6.12.— (cont.)

Figure 6.12 shows the χ^2 distribution in $\Sigma_{\rm cl}$ - M_c space, m_* - M_c space and m_* - $\Sigma_{\rm cl}$ space for the 14 sources. As also discussed in Paper II, these diagrams illustrate the full constraints in the primary parameter space derived by fitting the SED data, and the possible degeneracies. In general, all the three parameters span a larger range compared with the sources of Papers I and II.

Follow-up observations and analysis of SOMA sources can be helpful in breaking degeneracies that arise from simple SED fitting. One example of such follow-up work is that of Rosero et al. (2019), who examined cm radio continuum data of the SOMA sources presented in Paper I. Radio free-free emission from photoionized gas, first expected to be present in the outflow cavity, is particularly useful for contraining the mass of the protostar once it reaches $\gtrsim 10\ M_\odot$ and begins to contract to the zero age main sequence. However, at lower masses most of the ionization associated with the source is expected to be due to shock ionization, e.g., due to internal shocks in the outflow (see also Fedriani et al. 2019). Quantitative models for the amount of shock ionization and associated radio emission have not yet been developed for the ZT protostellar models. For the mainly intermediate-mass sources presented in this paper, we anticipate that cm radio emission will main be due to shock ionization, so such observations may be more challenging to interpret to help break SED fit degeneracies. On the other hand, measurements of protostellar outflow properties, including cavity opening angle and mass and momentum fluxes may provide more diagnostic power.

In contrast with the high-mass protostars in Papers I and II, the best models ($\chi^2 - \chi^2_{\rm min} < 5$, within the red contours shown in Figure 6.12) of the intermediate-mass protostars also occupy the region with lower M_c at lower $\Sigma_{\rm cl}$. Another striking feature is that most sources have best models with a core size larger than the aperture

size, i.e., they appear below the dashed line denoting when $R_c = R_{\rm ap}$ in Figure 6.12. To examine this matter further, we analyzed the image profiles of the best 5 models of the sources and found that the flux density at 37 μm usually decays to 10^{-3} of the peak flux density within 5″ from the center and the flux density at 70 μm usually decays to 10^{-3} of the peak flux density within 15″ from the center. The typical aperture radius is $\sim 10''$ (except for the three sources in IRAS 22172 where it is $\sim 5''$, but their best models have the flux density decaying to 10^{-3} of the peak within 2″ and 5″ at 37 and 70 μm, respectively). This indicates that when the models have a core size larger than the aperture used for measuring the SED, only a small amount of the total flux from the model is being missed (however, the proportion of missed flux would be larger at longer wavelengths). Nevertheless, to better illustrate the importance of this effect, in the following discussion we present two cases, i.e., with and without the constraint on the model core size needing to be within a factor of two of the aperture size.

6.5 Discussion

We now discuss results of the global sample of 29 protostars that have been derived from an uniform SED fitting analysis that always includes *SOFIA*-FORCAST data, as presented in Papers I, II and III.

In general, we select the best five or fewer models that satisfy $\chi^2 < \chi^2_{\rm min} + 5$, where $\chi^2_{\rm min}$ is the value of χ^2 of the best model, and then present averages of model properties. However, for G45.12+0.13, which was discussed in Paper II as not being especially well fit by the ZT models because of its high luminosity (it is likely to be multiple sources), there is only one model with $\chi^2 < \chi^2_{\rm min} + 5$. Thus for this source we average all the best 5 models. The model properties are averaged in log space, i.e.,

geometric averages, except for A_V, $\theta_{\rm view}$ and $\theta_{\rm w,esc}$, which are evaluated as arithmetic means.

Then, as explained at the end of the last section, we also consider two cases, i.e., without and with the constraint of "best-fit" models having core sizes that are within a factor of two of the aperture size. Without the core size constraint, the best five models of all sources automatically satisfy $\chi^2 < \chi^2_{\rm min} + 5$, except for G45.12+0.13. With the core size constraint (which we regard as our best, fiducial method), there can be cases, especially of intermediate-mass sources from Paper III (i.e., this work), where there are fewer than five models with $\chi^2 < \chi^2_{\rm min} + 5$. Still, G45.12+0.13 is kept as a special case, as above. Key average source properties are listed in Table 6.4.

6.5.1 The SOMA Sample Space

Figure 6.13a shows $L_{\rm bol,iso}$ versus $M_{\rm env}$ for the SOMA protostar sample from Papers I, II and this work, i.e., Paper III. Figure 6.13b shows $L_{\rm bol}$ versus $M_{\rm env}$ of the same sample. This is the more fundamental property of the protstar, since $L_{\rm bol,iso}$ is affected by the orientation of protostellar geometry to our line of sight and the flashlight effect. Compared with the sources presented in Papers I and II, which were exclusively high-mass protostars, $L_{\rm bol,iso}$, $L_{\rm bol}$ and $M_{\rm env}$ all extend down to lower values. When we apply the constraint on model core sizes, i.e., radii of the models need to be no larger than twice the radius of the aperture used to define the SED, then we see from Figures 6.13c and d that there is an apparent tightening of the correlations between $L_{\rm bol,iso}$ or $L_{\rm bol}$ with $M_{\rm env}$. Note that the highest-mass, highest-luminosity YSOs usually have best models with $R_c \lesssim R_{\rm ap}$ and are thus less influenced by this constraint.

Figures 6.13e and f show the sample distribution in the context of the whole ZT

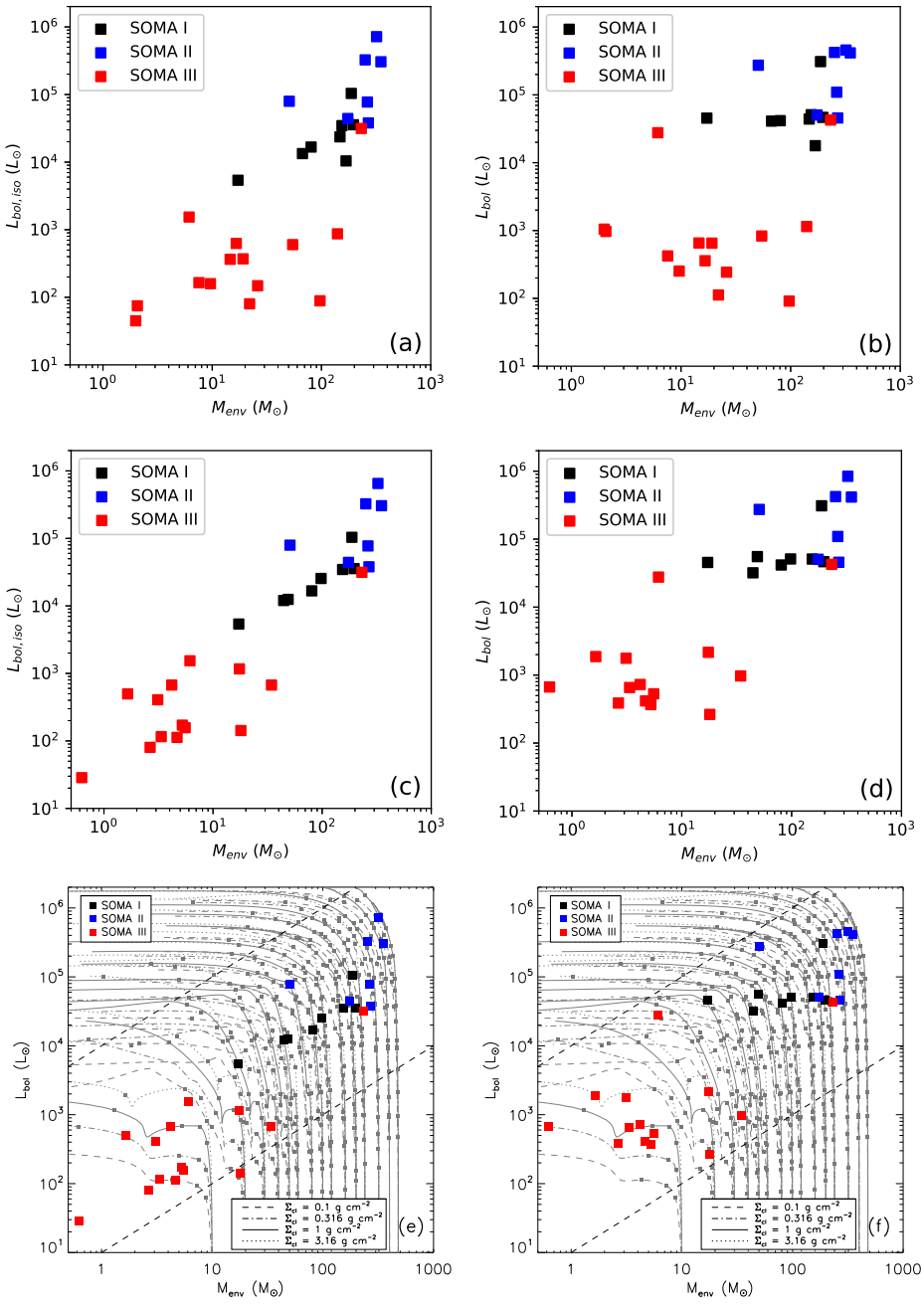

Fig. 6.13.— (a) Average (geometric mean) isotropic bolometric luminosity versus envelope mass returned by the best five (see text) ZT models for each SOMA source from Papers I, II and III (this work), as labelled. (b) Same as (a), but now with true bolometric luminosities plotted versus envelope mass. (c) Same as (a), but now using the average of the best five or fewer models with $R_c \lesssim 2R_{\rm ap}$ and $\chi^2 < \chi^2_{\rm min} + 5$. (d) Same as (c), but now with true bolometric luminosities plotted versus envelope mass. (e) Same as (c), but now also showing the ZT18 protostar models (grey squares), which are a collection of different evolutionary tracks (grey lines) for different initial core masses and clump mass surface densities (see legend). The two dashed black lines indicate $L_{\rm bol}/M_{\rm env} = 10$ and 10^4 $L_\odot/M_\odot$, respectively. (f) Same as (e), but now with true bolometric luminosities plotted versus envelope mass.

model grid, where lines indicate evolutionary tracks, i.e., from low luminosity and high envelope mass to high luminosity and low envelope mass, for different clump environment mass surface densities, $\Sigma_{\rm cl}$.

The SOMA sample spans a relatively broad range of evolutionary stages with $L_{\rm bol}/M_{\rm env}$ extending from $\sim 10\ L_\odot/M_\odot$ up to almost $10^4\ L_\odot/M_\odot$, indicated by the dashed lines in Figure 6.13f. As a result of this broad range and given the even wider range that is expected from the theoretical models, we do not fit the observed $L_{\rm bol}$ versus $M_{\rm env}$ distribution with a power law relation (c.f., Molinari et al. 2008; Urquart et al. 2018). Rather, we simply note that the sources that have so far been analyzed in the SOMA sample span this wide range of evolutionary stages, but the expected very late stages and very early stages are not especially well represented.

To further explore the evolutionary context of the SOMA protostars, in Figure 6.14 we show the SOMA sample in the luminosity versus envelope mass plane, together with protostellar sources identified in Infrared Dark Clouds (IRDCs), which are expected to be at earlier stages of evolution. Two samples of protostars selected from IRDC environments are shown, with the source SED construction and ZT model fitting following the same methods as have been used for the SOMA sample. The first, labelled "IRDCs A-H", is the sample of 28 sources from Liu et al. (2018) and Liu et al., in prep., based on *ALMA* observations of 32 clumps in IRDCs A to H from the sample of Butler & Tan (2009, 2012). The second, labelled "IRDC C", is a complete census of the protostellar sources in IRDC C carried out by Moser et al. (2020), based on sources identified in the region by *Herschel* 70 μm emission from the Hi-GAL point source catalog (Molinari et al. 2016). After allowing for a few poorly resolved sources that are treated as a single protostar in the SED modeling, a total of 35 protostars have been analyzed by Moser et al. (2020). The IRDC sources include

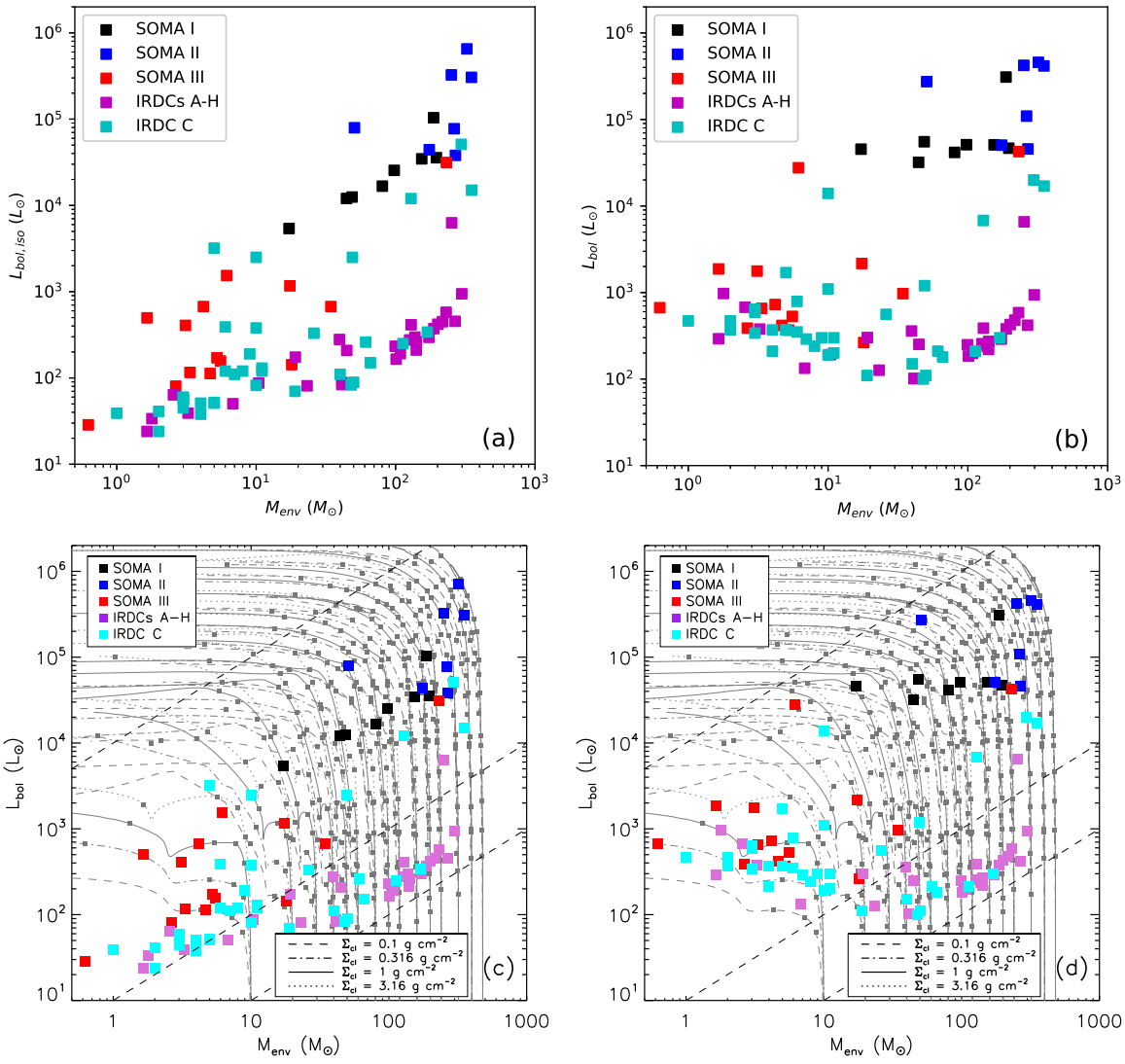

Fig. 6.14.— Protostellar evolutionary stages probed by the SOMA sample and IRDC protostar samples: "IRDC A-H" (Liu et al. 2018; Liu et al., in prep.); "IRDC C" (Moser et al. 2020). The format of the figures is otherwise the same as Figures 6.13c, d, e, f, respectively, but with the average (geometric mean) results of the valid models of IRDC sources added. The three dashed black lines in panels c and d indicate $L_{\rm bol}/M_{\rm env} = 1, 10$ and 10^4 $L_\odot/M_\odot$.

protostars with intrinsic bolometric luminosities down to about 100 $L_{\odot}$, including within relatively massive core envelopes, so that the sampled values of $L_{\rm bol}/M_{\rm env}$ now extend down to $\sim 1\ L_{\odot}/M_{\odot}$.

Various biases in the input catalog for the SOMA survey likely account for the lack of sources at the final evolutionary stages of high $L_{\rm bol}$ and low $M_{\rm env}$. For example, these sources will have relatively weak MIR to FIR emission, which was used as a consideration to target SOMA protostars. Such sources may also be embedded within ultracompact H II regions, which we have tended to avoid, so far for analysis, even if they are within our fields of view: here the challenge is to isolate emission from any remaining protostellar core from the thermal emission from hot dust in the large scale H II region. Finally, this later phase of evolution may be relatively short, so objects here may be intrinsically rare. Future studies will attempt to identify such sources.

Finally, we note that a future goal is to extend complete surveys of high- and intermediate-mass protostars across their full range of evolutionary stages and across larger regions so that the samples can be used for demographic analyses that will inform about topics such as the duration of formation timescales. Previous work in this area, e.g., Davies et al. (2011), which covered large regions of the Galactic plane, focused only on high-mass protostars and have been relatively restricted in their coverage of earlier evolutionary stages.

6.5.2 The Shapes of SEDs

In Figure 6.15 we show the bolometric luminosity spectral energy distributions of the 14 protostars of this paper, together with the sample of 15 generally higher luminosity sources from Papers I and II. Here the νF_{ν} SEDs have been scaled by $4\pi d^2$ so that the height of the curves gives an indication of the luminosity of the

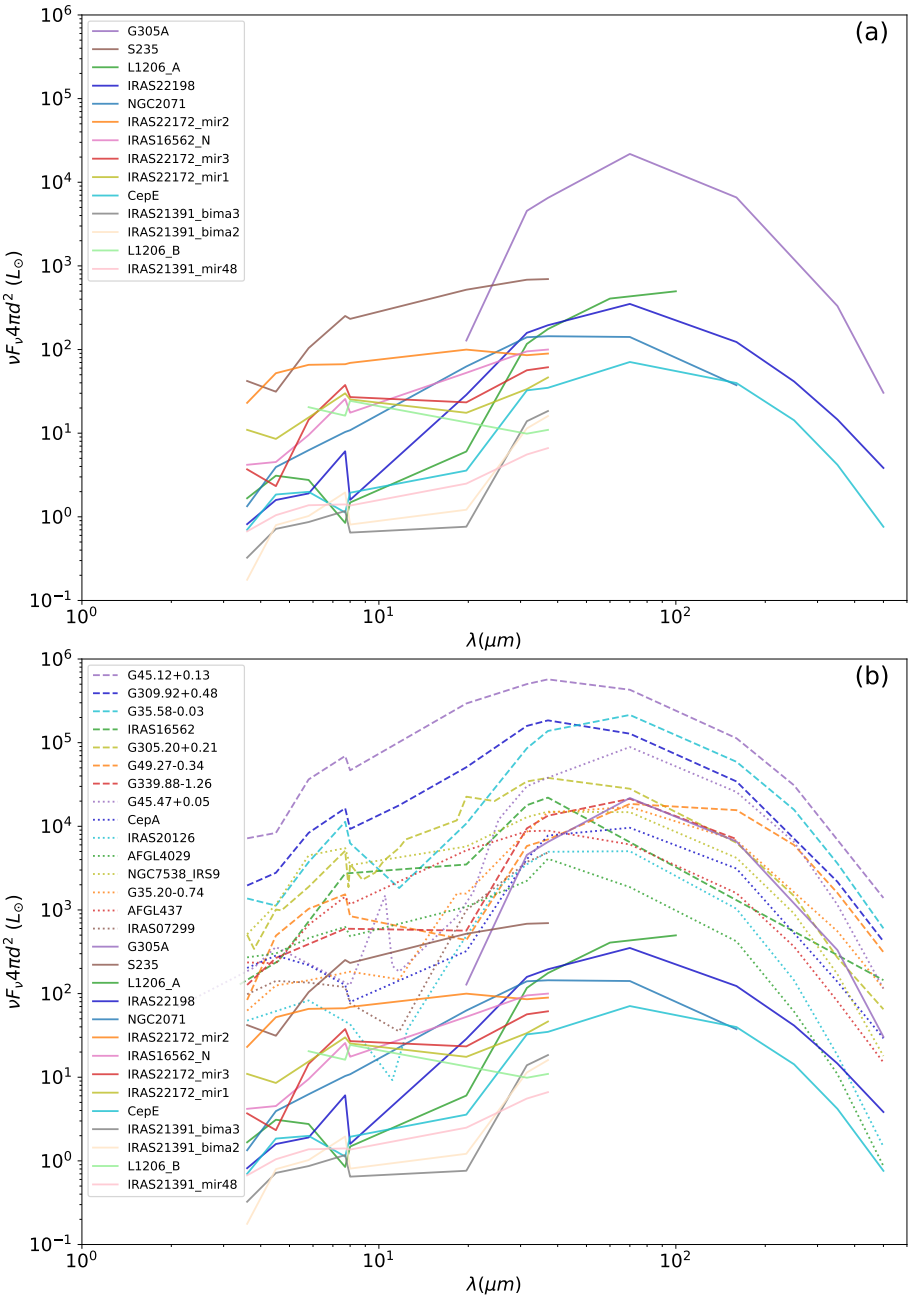

Fig. 6.15.— *a) Top panel:* Bolometric luminosity weighted SEDs of the 14 SOMA protostars analyzed in this paper. The ordering of the legend is from high to low ZT best fit model isotropic luminosity (top to bottom). *b) Bottom panel:* Same as (a), but now with addition of dashed lines denoting the sample of 15 sources from Papers I and II.

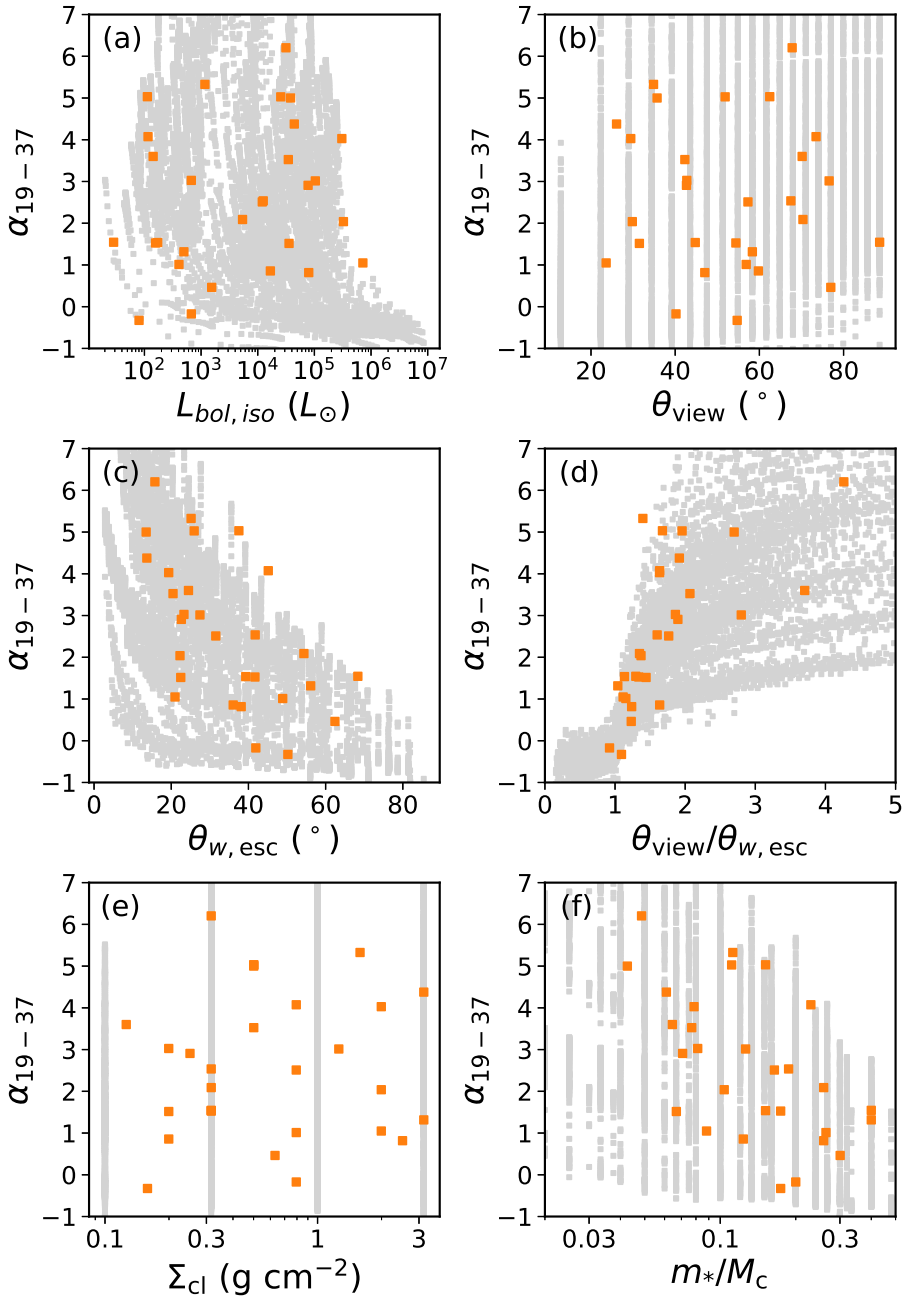

Fig. 6.16.— Spectral index, α_{19-37} between 19 μm and 37 μm (see text) versus: the geometric mean isotropic luminosity $L_{\rm bol,iso}$ (a: top left); the arithmetic mean inclination of viewing angle $\theta_{\rm view}$ (b: top right); the arithmetic mean opening angle $\theta_{w,\rm esc}$ (c: middle left); arithmetic mean $\theta_{\rm view}/\theta_{w,\rm esc}$ (d: middle right); the geometric mean clump surface density $\Sigma_{\rm cl}$ (e: bottom left); and geometric mean $m_*/M_{\rm c}$ (f: bottom right) returned by the best five or fewer models with $R_c \lesssim 2R_{\rm ap}$ and $\chi^2 < \chi^2_{\rm min} + 5$. The grey squares represents the ZT18 protostar models. Note that the spectral index of the models are calculated without foreground extinction and thus could be different from observations.

sources assuming isotropic emission. The ordering of the vertical height of these distributions is largely consistent with the rank ordering of the predicted isotropic luminosity of the protostars from the best-fit ZT models (the legend in Figure 6.15 lists the sources in order of decreasing ZT best model isotropic luminosity).

We define a 19–37 μm spectral index via

$$\alpha_{19-37} = \frac{\nu_{37\mu m} F_{\nu,37\mu m} - \nu_{19\mu m} F_{\nu,19\mu m}}{\lambda_{37\mu m} - \lambda_{19\mu m}}. \tag{6.1}$$

In general, we expect that this index may vary systematically with protostellar source properties. Figure 6.16 shows the dependence of α_{19-37} of the SEDs on luminosity, inclination of viewing angle, outflow cavity opening angle, ratio of inclination of viewing angle to outflow cavity opening angle, $\Sigma_{\rm cl}$, and m_*/M_c, respectively. In all these panels, the results have been averaged over those of the best 5 or fewer models with core radii smaller than twice the aperture radius and $\chi^2 < \chi^2_{\rm min} + 5$ (except for G45.12+0.13, see above). We see that the outflow cavity opening angle has a strong influence on the 19–37 μm index, following the expectation that a relatively greater flux of shorter wavelength photons are able to escape from the protostellar core if the outflow cavity opening angle is larger. Also a viewing angle inclination that is relatively small compared to the outflow cavity opening angle will result in a flatter shorter wavelength SED, as also discussed in Paper II.

In Figure 6.16, we also plot the ZT18 models as grey squares beneath the observations to illustrate the model coverage. Note that the range shown here serves to best show the observations and does not represent the full parameter space of the ZT18 models. We note that while the observed correlations are in general built in the ZT models, the results of Figure 6.16 show how tight (or loose) the correlations are in practice of the observed SED spectral index in the *SOFIA*-FORCAST bands

with best average protostellar parameters derived from the fitting the entire available MIR to FIR SED. This information gives an idea of how much information can be derived from only an observed value of α_{19-37}.

Finally, and along the same lines, another important feature that is revealed by α_{19-37} is the protostellar evolutionary stage, as measured by m_*/M_c (Figure 6.16f). Again, this general trend is expected in the context of the ZT models, since the outflow cavity systematically opens up during the course of the evolution and the envelope mass is depleted, resulting in lower overall extinction. There is also generally lower levels of extinction in protostellar cores in lower $\Sigma_{\rm cl}$ environments, but little correlation is seen here between α_{19-37} and $\Sigma_{\rm cl}$ (Figure 6.16e), indicating other factors have a more important influence.

6.5.3 Dependence of Massive Star Formation on Environment

Figure 6.17 shows the distribution of values of M_c (i.e., initial core mass), $\Sigma_{\rm cl}$ and m_* of the 29 sources of the SOMA sample to date. With no constraint on the model core size, there appears to be an absence of protostars with low M_c in high $\Sigma_{\rm cl}$ environments. However, this feature is not seen after applying the core size constraint, which we regard as the best method. Thus, the SOMA sample appears to contain protostars that have a range of initial core masses that can be present in the full range of protocluster clump mass surface density environments. However, note that these properties of M_c and $\Sigma_{\rm cl}$ are not measured directly, but are inferred from the SED fitting.

We next examine if current protostellar properties depend on protocluster clump environment mass surface density. Figure 6.18 shows m_* versus $\Sigma_{\rm cl}$. Figure 6.18a,

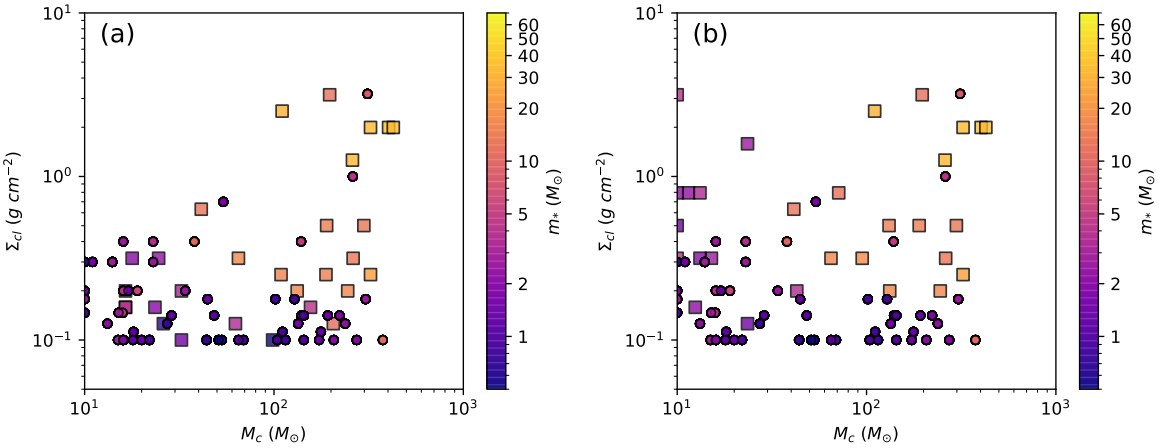

Fig. 6.17.— *a) Left:* Average clump mass surface density, $\Sigma_{\rm cl}$, versus average initial core mass, M_c, of the SOMA sources (squares) and IRDC sources (circles, Liu et al. 2018; Moser et al. 2020; Liu et al., in prep.), based on ZT model fits: the average is made for the best five selected models. *b) Right:* Same as (a), but with the average made for the best five or fewer models with $R_c \lesssim 2R_{\rm ap}$ and $\chi^2 < \chi^2_{\rm min} + 5$.

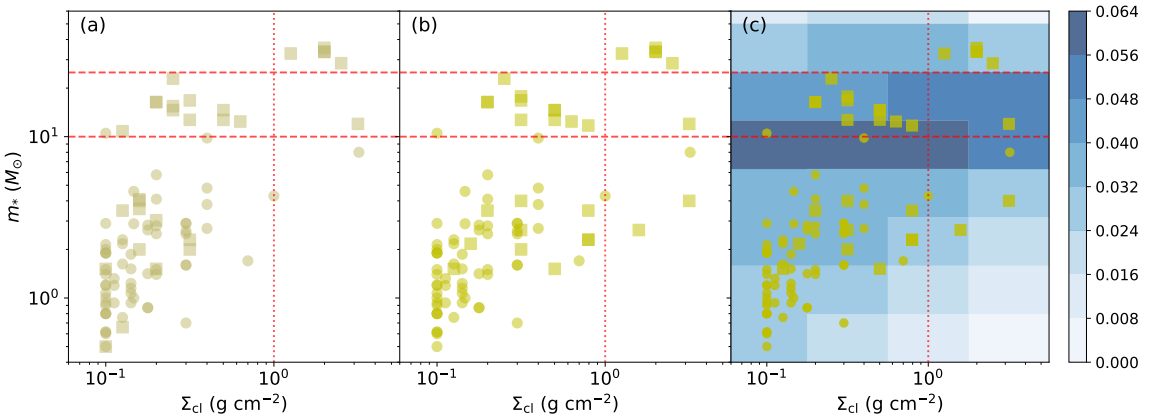

Fig. 6.18.— *a) Left:* Average protostellar mass, m_*, versus average clump mass surface density, $\Sigma_{\rm cl}$, of SOMA sources (squares) and IRDC sources (circles, Liu et al. 2018; Moser et al. 2020; Liu et al., in prep.), based on ZT model fits: the average is made for the best five selected models. The red dotted and dashed lines indicate fiducial threshold values of m_* (10 and 25 $M_\odot$) and $\Sigma_{\rm cl}$ (1 g cm^{-2}, see text). *b) Middle:* Same as (a), but with the average made for best five or fewer models with $R_c \lesssim 2R_{\rm ap}$ and $\chi^2 < \chi^2_{\rm min} + 5$. *c) Right:* Same as (b), but now also showing the distribution of models in the ZT model grid (shading indicates the density of models).

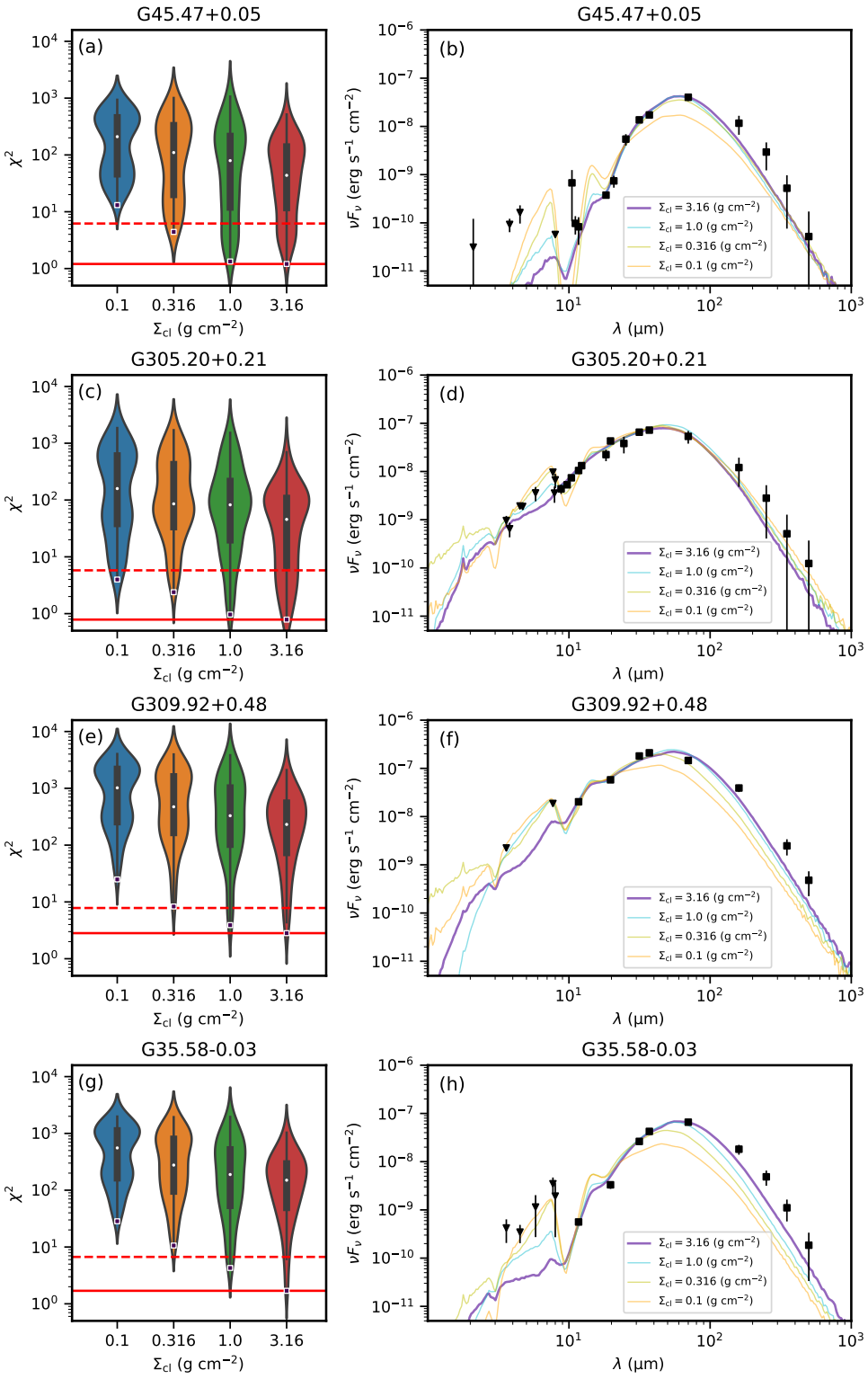

Fig. 6.19.— *Left column*: Violin plots of χ^2 versus Σ_{cl} of all the models for several of the most massive protostars: G45.47+0.05, G305.20+0.21, G309.92+0.48 and G35.58-0.03. For the violin of each Σ_{cl}, the white dot denotes the median χ^2. The black bar in the center of the violin denotes the interquartile range (IQR). The black lines stretched from the bar denote the lower/upper adjacent values – defined as the furthest observation within 1.5 IQR of the lower/upper end of the bar. The width of the violin represents the probability density of the data value smoothed by a kernel

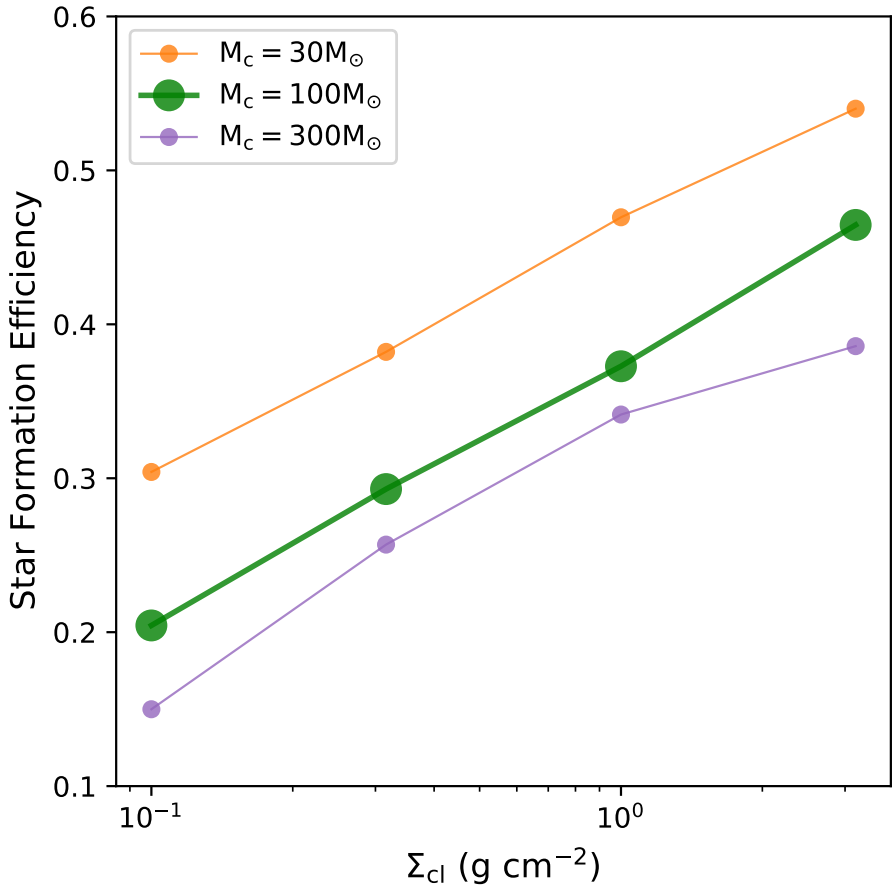

Fig. 6.20.— Star formation efficiency as a function of clump mass surface density, $\Sigma_{\rm cl}$, from model calculations of Tanaka et al. (2017). Models for initial core masses of $M_c = 30,\ 100$, and $300\,{\rm M}_\odot$ are shown, as labelled.

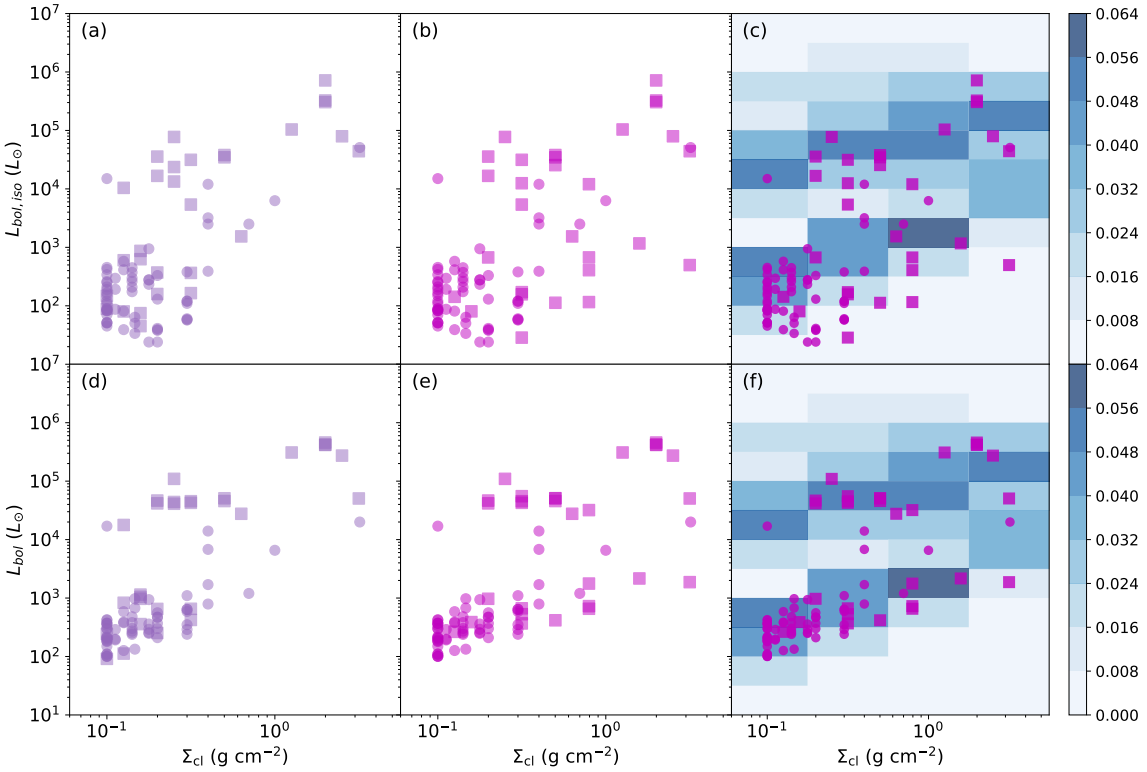

Fig. 6.21.— *a) Top Left:* Average protostellar isotropic bolometric luminosity, $L_{\rm bol,iso}$, versus average clump mass surface density, $\Sigma_{\rm cl}$, of SOMA sources (squares) and IRDC sources (circles, Liu et al. 2018; Moser et al. 2020; Liu et al., in prep.), based on ZT model fits: the average is made for the best five selected models. *b) Top Middle:* Same as (a), but with the average made for best five or fewer models with $R_c \lesssim 2R_{\rm ap}$ and $\chi^2 < \chi^2_{\rm min} + 5$. *c) Top Right:* Same as (b), but now also showing the distribution of models in the ZT model grid (shading indicates the density of models). *d) Bottom Left:* Same as (a), but now for intrinsic bolometric luminosity, $L_{\rm bol}$. *e) Bottom Middle:* Same as (b), but now for intrinsic bolometric luminosity, $L_{\rm bol}$. *f) Bottom Right:* Same as (c), but now for intrinsic bolometric luminosity, $L_{\rm bol}$.

similar to the results shown in Figure 6.17a, appears to show a lack of lower-mass sources in high-$\Sigma_{\rm cl}$ environments. However, this changes once the core size versus SED aperture constraint is applied (Fig. 6.18b), so we do not consider this to be a real effect. From the data shown in Fig. 6.18b, one potential trend that we notice is a lack of highest mass ($m_* \gtrsim 25\ M_\odot$) protostars in lower mass surface density environments ($\Sigma_{\rm cl} \lesssim 1\ {\rm g\,cm^{-2}}$). All of the five protostars with $m_* > 25\ M_\odot$ (G45.47+0.05, G45.12+0.13, G305.20+0.21, G309.92+0.48, G35.58-0.03) are inferred to be in $\Sigma_{\rm cl} > 1\ {\rm g\,cm^{-2}}$ environments. In Fig. 6.18c, we see that this trend is not a direct result of ZT model parameter space sampling, with density of models in the grid shown by the blue shading. High m_* protostars forming from cores in low $\Sigma_{\rm cl}$ environments are present among the ZT models. We note that these models include protostellar outflow feedback, which sets star formation efficiencies close to 50%, but do not include radiative feedback, which would reduce the efficiency (see below).

We further examine how low $\Sigma_{\rm cl}$ models fail for high m_* sources in Figure 6.19. Here we exclude G45.12+0.13 because none of the models fit particularly well for this source (see Paper II). We can see that the median χ^2 and the smallest χ^2 achieved generally decrease with $\Sigma_{\rm cl}$. Compared with high $\Sigma_{\rm cl}$ models, low $\Sigma_{\rm cl}$ models usually have higher fluxes at shorter wavelengths, i.e., $\lesssim 8\mu$m. These can be higher than the observational upper limits, which leads to a significant penalty in the fitting. Low $\Sigma_{\rm cl}$ models also tend to have lower fluxes at longer wavelength, i.e., $\gtrsim 20\mu$m. Therefore, they deviate away from the shape of the observed SEDs. We also tried manually adjusting A_V or $L_{\rm bol}$ of the low $\Sigma_{\rm cl}$ models (not shown here), but such changes do not lead to significant improvement in model SED shape in comparison to the data.

Thus, we conclude there is tentative evidence from the SOMA sample analyzed so far that the most massive protostars require their cores to be in $\Sigma_{\rm cl} > 1\ {\rm g\,cm^{-2}}$

environments, but larger further testing with a larger number of sources is clearly needed to confirm this.

Krumholz & McKee (2008) proposed that a minimum mass surface density of 1 g cm^{-2} is needed for massive star formation, based on protostellar heating suppression of fragmentation of massive cores by a population of surrounding lower-mass protostars (these protostars have higher accretion rates and thus luminosities in higher $\Sigma_{\rm cl}$ environments). While our result appears to confirm this prediction, we caution that the Krumholz & McKee model also predicts that 10 $M_\odot$ protostars would not be able to form in $\Sigma_{\rm cl} \lesssim 0.3$ g cm^{-2} environments, which is inconsistent with the SOMA data. As an alternative, magnetic suppression of fragmentation to allow the existence of massive, early-stage cores has been discussed by, e.g., Butler & Tan (2012), with evidence of strong, ~ 1 mG B-fields inferred several cores in the IRDC 18310-4 region (Beuther et al. 2018).

The assembly of the highest mass pre-stellar cores, e.g., via a bottom-up process of merging smaller pre-stellar cores together or by general accumulation of clump gas, is expected to be more efficient in denser regions and this could provide an explanation, in the context of core accretion models, of the trends seen in Figure 6.18.

Once cores initiate star formation, then their accretion rates would also be higher in high surface density environments and this is expected to allow higher protostellar masses to be formed. Tanaka et al. (2017) assessed the expected star formation efficiency from cores due to both radiative and mechamical (i.e., outflow) feedback as a function of $\Sigma_{\rm cl}$ and found it can decrease by more than a factor of two for a given initial core as $\Sigma_{\rm cl}$ decreases from 3.2 to 0.1 g cm^{-2} (see Figure 6.20). The decrease is greatest for more massive cores, since once they start forming stars with $m_* \gtrsim 20 M_\odot$, radiative feedback becomes powerful enough to truncate further accretion. For example, the

$\Sigma_{\rm cl} = 0.1\,{\rm g\,cm^{-2}}$ models shown in Figure 6.20 reach $m_* \simeq 10\,M_\odot$ starting from a $30\,M_\odot$ core, $m_* \simeq 20\,M_\odot$ starting from a $100\,M_\odot$ core, and $m_* \simeq 45\,M_\odot$ starting from a $300\,M_\odot$ core. However, the equivalent $\Sigma_{\rm cl} = 1\,{\rm g\,cm^{-2}}$ models reach values of $m_* \simeq 15, 40$, and $100\,M_\odot$, respectively. Thus, in the context of these models, it is much more difficult to produce, e.g., $30\,M_\odot$ protostars in low-$\Sigma_{\rm cl}$ environments due to feedback effects, especially since the pre-stellar core mass function is expected to decline rapidly with increasing mass.

For competitive accretion models (Bonnell et al. 2001; Wang et al. 2010), higher mass surface density environments are also expected to lead to higher accretion rates and thus will probably also allow formation of higher-mass stars. However, the equivalent calculations for the effect of feedback have not yet been carried out for these models.

From an observational analysis of three clouds that are forming massive stars compared to several others that are not, Kauffmann et al. (2010) proposed a criterion for massive star formation equivalent to $\Sigma_{\rm cl} \geq 0.054(M_{\rm cl}/1000\,M_\odot)^{-1/2}\,{\rm g\,cm^{-2}}$, which is relatively low compared to the thresholds discussed above. Also, this is a value smaller than the minimum of the range probed in the ZT18 protostellar model grid of $\Sigma_{\rm cl} = 0.1g\ cm^{-2}$. Recently, Retes-Romero et al. (2020) studied 128 IRDCs to investigate if the Kauffmann et al. criterion predicts which of these IRDCs contains massive stars. They found that among the IRDCs satisfying this criterion, only one third of them currently contain massive YSOs. This may indicate that a higher, more localised value of $\Sigma_{\rm cl}$ is needed to form a massive star. For further progress on the general question of massive star formation thresholds, more direct measures of $\Sigma_{\rm cl}$, e.g., from dust continuum emission (in contrast to our indirect methods based on model fitting), on scales immediately surrounding the massive protostars and

comparison to protostellar properties, e.g., as derived from SED fitting in the SOMA sample, are needed. However, such an analysis, which we defer to a future study, will inevitably be sensitive to how and where the protostellar core boundary is defined and such sensitivity will also need to be explored.

In summary, our results indicate, tentatively, that to form the most massive, $\gtrsim 25\ M_\odot$ protostars requires $\gtrsim 1\ \mathrm{g\,cm^{-2}}$ protocluster clump environments, although this is based on a relatively small number of (five) of protostellar sources that are in this mass range. We have a larger number (about 10) of protostars with $10\ M_\odot \lesssim m_* \lesssim 25\ M_\odot$ that are best fitted by models with $\Sigma_{\rm cl} \lesssim 0.3\ \mathrm{g\,cm^{-2}}$, so that there does not appear to be a particular mass surface density threshold, in this range, needed to form $10\,M_\odot$ protostars. These environmental dependencies on massive star formation need confirmation with larger numbers of sources. Such trends are consistent with several different theoretical expectations from core accretion models, including that due to decreasing star formation efficiency due to self-feedback for massive protostars in lower mass surface density environments.

Finally, we investigate the dependence of $L_{\rm bol,iso}$ and $L_{\rm bol}$ on $\Sigma_{\rm cl}$ in Figure 6.21. Once model core size to aperture constraints are applied (panels b and e), there is no strong correlation present in the overall distribution. The highest luminosity sources, which have the highest protostellar masses, are preferentially found in high mass surface density environments. This is not due to the sources having higher current accretion rates, since for these high m_* sources, the accretion luminosity is only a relatively minor component of the total luminosity. Thus this trend is simply a reflection of those seen in the mass distribution of the sources.

Table 6.4. Average Parameters of SOMA Protostars

Source	M_c ($M_\odot$)	Σ_{cl} (g cm^{-2})	m_* ($M_\odot$)	m_*/M_c	M_{env} ($M_\odot$)	$L_{bol,iso}$ ($L_\odot$)	L_{bol} ($L_\odot$)	θ_{view} (°)	$\theta_{w,esc}$ (°)	$\theta_{view}/\theta_{w,esc}$	α_{19-37}
G45.12+0.13	403	2.0	35.5	0.09	319	7.2e+05	4.6e+05	24	21	1.12	1.05
	403	2.0	35.5	0.09	319	7.2e+05	4.6e+05	24	21	1.12	1.05
G309.92+0.48	323	2.0	33.5	0.10	251	3.3e+05	4.2e+05	30	22	1.37	2.04
	323	2.0	33.5	0.10	251	3.3e+05	4.2e+05	30	22	1.37	2.04
G35.58-0.03	427	2.0	33.5	0.08	350	3.1e+05	4.2e+05	29	19	1.63	4.03
	427	2.0	33.5	0.08	350	3.1e+05	4.2e+05	29	19	1.63	4.03
IRAS16562	323	0.3	22.9	0.07	263	7.7e+04	1.1e+05	43	23	1.90	2.91
	323	0.3	22.9	0.07	263	7.7e+04	1.1e+05	43	23	1.90	2.91
G305.20+0.21	110	2.5	28.5	0.26	51	7.9e+04	2.7e+05	47	38	1.24	0.82
	110	2.5	28.5	0.26	51	7.9e+04	2.7e+05	47	38	1.24	0.82
G49.27-0.34	197	3.2	12.0	0.06	174	4.4e+04	5.1e+04	26	14	1.92	4.38
	197	3.2	12.0	0.06	174	4.4e+04	5.1e+04	26	14	1.92	4.38
G339.88-1.26	298	0.5	12.7	0.04	269	3.8e+04	4.6e+04	36	14	2.70	5.00
	298	0.5	12.7	0.04	269	3.8e+04	4.6e+04	36	14	2.70	5.00
G45.47+0.05	260	1.3	32.8	0.13	187	1.0e+05	3.1e+05	77	27	2.80	3.01
	260	1.3	32.8	0.13	187	1.0e+05	3.1e+05	77	27	2.80	3.01
CepA	188	0.3	14.6	0.08	148	2.4e+04	4.4e+04	62	24	3.05	5.03
	132	0.5	14.6	0.11	98	2.6e+04	5.1e+04	52	26	1.96	5.03
IRAS20126	109	0.3	15.5	0.14	67	1.3e+04	4.1e+04	67	35	2.14	2.54
	95	0.3	17.8	0.19	49	1.2e+04	5.5e+04	67	42	1.60	2.54
AFGL4029	65	0.3	16.8	0.26	17	5.4e+03	4.5e+04	70	54	1.35	2.09
	65	0.3	16.8	0.26	17	5.4e+03	4.5e+04	70	54	1.35	2.09
NGC7538_IRS9	245	0.2	16.4	0.07	196	3.6e+04	4.7e+04	31	22	1.44	1.52
	245	0.2	16.4	0.07	196	3.6e+04	4.7e+04	31	22	1.44	1.52
G35.20-0.74	190	0.5	14.6	0.08	154	3.5e+04	5.1e+04	42	20	2.07	3.53
	190	0.5	14.6	0.08	154	3.5e+04	5.1e+04	42	20	2.07	3.53
AFGL437	133	0.2	16.4	0.12	80	1.7e+04	4.2e+04	60	36	1.64	0.86
	133	0.2	16.4	0.12	80	1.7e+04	4.2e+04	60	36	1.64	0.86
IRAS07299	206	0.1	10.8	0.05	168	1.0e+04	1.8e+04	83	21	4.85	2.51
	71	0.8	11.7	0.16	44	1.2e+04	3.2e+04	57	32	1.77	2.51
S235	41	0.6	12.4	0.30	6	1.5e+03	2.8e+04	77	62	1.23	0.46
	41	0.6	12.4	0.30	6	1.5e+03	2.8e+04	77	62	1.23	0.46
IRAS22198	63	0.1	3.5	0.06	55	6.0e+02	8.3e+02	65	19	3.52	3.03
	43	0.2	3.5	0.08	34	6.7e+02	9.7e+02	43	23	1.86	3.03
NGC2071	32	0.2	3.0	0.09	19	3.7e+02	6.5e+02	49	29	1.80	1.32
	10	3.2	4.0	0.40	2	5.0e+02	1.9e+03	58	56	1.04	1.32
CepE	32	0.1	1.5	0.05	26	1.5e+02	2.4e+02	79	21	5.05	3.60
	24	0.1	1.5	0.06	18	1.4e+02	2.6e+02	70	24	3.70	3.60
L1206_A	156	0.2	4.0	0.03	140	8.7e+02	1.1e+03	81	14	8.64	5.33
	24	1.6	2.6	0.11	17	1.2e+03	2.2e+03	35	25	1.40	5.33
L1206_B	16	0.2	3.6	0.22	2	7.5e+01	9.7e+02	66	60	1.09	-0.33
	12	0.2	2.2	0.17	3	8.0e+01	3.9e+02	55	50	1.09	-0.33
IRAS22172_mir2	24	0.2	2.0	0.09	17	6.3e+02	3.6e+02	29	28	1.02	-0.17
	11	0.8	2.3	0.20	4	6.7e+02	7.3e+02	40	42	0.92	-0.17
IRAS22172_mir3	18	0.3	2.0	0.11	8	1.6e+02	4.2e+02	44	35	1.35	1.53
	15	0.3	2.6	0.17	6	1.6e+02	5.3e+02	54	42	1.34	1.53
IRAS22172_mir1	16	0.2	1.5	0.09	10	1.6e+02	2.5e+02	37	31	1.22	1.54
	13	0.3	2.0	0.15	5	1.7e+02	3.7e+02	45	39	1.13	1.54
IRAS21391_bima2	26	0.1	0.7	0.03	22	8.0e+01	1.1e+02	34	16	2.52	4.07
	10	0.8	2.3	0.23	3	1.2e+02	6.6e+02	73	45	1.64	4.07
IRAS21391_bima3	98	0.1	0.5	0.01	97	8.9e+01	9.1e+01	54	5	11.10	5.03
	10	0.5	1.5	0.15	5	1.1e+02	4.2e+02	62	38	1.68	5.03
IRAS21391_mir48	16	0.2	4.1	0.25	2	4.5e+01	1.0e+03	75	63	1.22	1.54

Table 6.4—Continued

Source	$M_{\rm c}$ ($M_\odot$)	$\Sigma_{\rm cl}$ (g cm^{-2})	m_* ($M_\odot$)	$m_*/M_{\rm c}$	$M_{\rm env}$ ($M_\odot$)	$L_{\rm bol,iso}$ ($L_\odot$)	$L_{\rm bol}$ ($L_\odot$)	$\theta_{\rm view}$ (°)	$\theta_{w,{\rm esc}}$ (°)	$\theta_{\rm view}/\theta_{w,{\rm esc}}$	α_{19-37}
	10	0.3	4.0	0.40	1	2.9e+01	6.7e+02	89	68	1.30	1.54
G305A	262	0.3	12.7	0.05	231	3.1e+04	4.3e+04	68	16	4.26	6.20
	262	0.3	12.7	0.05	231	3.1e+04	4.3e+04	68	16	4.26	6.20
IRAS16562_N	25	0.3	2.3	0.09	15	3.7e+02	6.5e+02	39	29	1.40	1.01
	13	0.8	3.5	0.26	3	4.1e+02	1.8e+03	57	49	1.15	1.01

Note. — The first line of each source shows the average (geometric mean, except for $\theta_{\rm view}$, $\theta_{\rm w,esc}$ and $\theta_{\rm view}/\theta_{w,{\rm esc}}$ for which arithmetic means are evaluated) of the values of the best five models without any core size versus aperture constraint applied. The second line shows the results of the best five or fewer models with $R_c \leq 2R_{\rm ap}$ and $\chi^2 \leq \chi^2_{\rm min} + 5$.

6.6 Conclusions

We have presented the results of MIR and FIR observations carried out towards 14 protostars in the SOMA survey, with most of them being intermediate-mass protostars. Following our standard methods developed in Papers I & II, we have built their SEDs with additional archival *Spitzer*, *Herschel* and *IRAS* data and fit them with Zhang & Tan (2018) RT models of massive star formation via the Turbulent Core Accretion paradigm. We have also supplemented the sample with protostars identified in Infrared Dark Clouds (IRDCs) and expected to be at very early stages in their evolution. By these methods we have extended the range of masses, luminosities and evolutionary stages of protostellar sources that have been analyzed in an uniform manner to test core accretion theory. Our main results and conclusions are:

1. The intermediate-mass protostars presented in this paper appear relatively compact at 20 – 40 μm, compared to the high-mass protostars in Papers I & II, whose 20 – 40 μm images more clearly show extension along their outflow axes. The protostars presented here are forming in a variety of protocluster environments, as revealed by NIR images. Higher resolution sub-mm images often reveal presence of secondary dense gas cores within 0.1 pc (in projection).

2. The SEDs of the 14 protostars of this paper are generally fit quite well by the ZT models, but there are significant degeneracies among acceptable models. These degeneracies in key model parameters, i.e., initial core mass, M_c, clump mass surface density, $\Sigma_{\rm cl}$, and current protostellar mass, m_*, are typically larger than for the higher mass protostars, but this is often a reflection of the more limited wavelength coverage of the intermediate-mass sources, which are often away from the Galactic plane and thus lacking, e.g., longer wavelength *Herschel* data. For the sources analyzed here, we find that well-fitting models can often have $R_{\rm c} > R_{\rm ap}$. Thus we have applied a

further constraint that model core radii should not exceed the aperture radius used to define the SED by more than a factor of two.

3. The SOMA sources analyzed in this paper and Papers I & II span a range of bolometric luminosities of $\sim 10^2\ L_\odot$ to $\sim 10^6\ L_\odot$. The isotropic luminosity can be quite different from the intrinsic luminosity, indicating a significant flashlight effect in the sources.

4. The presented SOMA sample spans a range of light to mass ratios of $L_{\rm bol}/M_{\rm env}$ from $\sim 10\ L_\odot/M_\odot$ to $\sim 10^4\ L_\odot/M_\odot$. The addition of IRDC protostars extends this range down to $\sim 1\ L_\odot/M_\odot$, which is expected to be near the very earliest phases of the star formation process. Relatively late stages of evolution are currently missing from the sample.

5. The SED shape, as measured by the spectral index from 19 to 37 microns, shows trends with outflow opening angle, ratio of viewing angle to outflow opening angle, and evolutionary stage, i.e., m_*/M_c. However, such trends are features that are inherent in the ZT18 models and independent confirmation, e.g., from high resolution continuum and line studies of outflows and outflow cavities, is needed.

6. Protostars from low masses up to $\sim 25\ M_\odot$ are inferred to be forming at all the clump mass surface densities probed by the models, i.e., from 0.1 to 3 g cm^{-2}. However, to form protostars with $> 25\ M_\odot$ appears to require $\Sigma_{\rm cl} \gtrsim 1$ g cm^{-2} clump environments. Larger numbers of sources in this mass range are needed to confirm this result. While this finding is consistent with several possible theoretical expectations, we favor one based on internal feedback in the protostellar core, which becomes less effective for the denser cores that are associated with higher $\Sigma_{\rm cl}$ environments (Tanaka et al. 2017).

Chapter 7

Summary

7.1 Early Stage Massive Star Formation in IRDCs

To study the early phases of massive star formation, we presented *Atacama Large Millimeter/submillimeter Array* (*ALMA*) observations of 1.3 mm continuum emission, SiO(5-4) emission and VLA observations of 6 cm continuum emission towards 32 Infrared Dark Cloud (IRDC) clumps at a resolution of $\sim 1''$.

We identified 107 cores with the dendrogram algorithm, with a median radius of about 0.02 pc. Their masses range from about 0.3 to 180 $M_\odot$. After applying completeness corrections, we fit the combined IRDC CMF with a power law of the form $dN/d\log M \propto M^{-\alpha}$ and derived an index of $\alpha \simeq 0.86 \pm 0.11$ for $M \geq 0.79\,M_\odot$ and $\alpha \simeq 0.70 \pm 0.13$ for $M \geq 1.26\,M_\odot$, which is a significantly more top-heavy distribution than the Salpeter stellar initial mass function (IMF) that has an equivalent index of 1.35. We also made a direct comparison of these IRDC clump CMF results to those measured in the more evolved protocluster G286 derived with similar methods, which have $\alpha \simeq 1.29 \pm 0.19$ and 1.08 ± 0.27 in these mass ranges, respectively. These results provide a hint that, especially for the $M \geq 1.26\,M_\odot$ range where completeness

corrections are modest, the CMF in high pressure, early-stage environments of IRDC clumps may be top-heavy compared to that in the more evolved, global environment of the G286 protoclusters. Such a difference in the CMF and resulting IMF could potentially be caused by a number of different physical properties of the gas that vary systematically between the regions, and may indicate that massive stars are more likely to form in high mass surface density, high pressure regions of IRDCs and thermal pressure is not the main factor resisting gravity in setting core masses in such environments. However, larger samples of cores, a wider range of Galactic environments, more accurate determination of the CMF peak via higher-sensitivity and higher-resolution observations probing the low-mass end, and better constraints on the mass determination and the evolutionary stages of the cores are needed to better establish the robustness of this potential CMF variation.

Out of the 32 IRDC clumps, we detected SiO emission in 20, and in 11 of them it is relatively strong and likely tracing protostellar outflows. Most of the SiO outflows show collimated, bipolar structures, although they can be highly asymmetric. There is one prominent example of a very disordered SiO outflow, which may reflect its intrinsic nature or may be due to the presence of multiple outflows from the same region on scales $\lesssim 0.1$ pc (in projection). There is some evidence for episodic ejection events. For the six strongest SiO outflows, we estimated basic outflow properties. We did not see a clear dependence of the degree of collimation of the outflows on core mass, luminosity and evolutionary stage. In our entire sample, where there is SiO emission, we always found 1.3 mm continuum emission and some infrared emission nearby, but not vice versa. We built the spectral energy distributions (SEDs) of all the cores with 1.3 mm continuum emission and fit them with radiative transfer (RT) models. The low luminosities and stellar masses returned by SED fitting

suggest these are early stage protostars. We saw a slight trend of increasing SiO line luminosity with bolometric luminosity, which suggests more powerful shocks in the vicinity of more massive YSOs. However, we did not see a clear relation between the SiO luminosity and the evolutionary stage indicated by L/M. We found that as a protostar approaches a bolometric luminosity of $\sim 10^2\,L_\odot$, the shocks in the outflow are generally strong enough to form SiO emission.

The VLA 6 cm observations toward the 15 clumps with the strongest SiO emission detected emission in four clumps, which is likely to be shock ionized jets associated with the more massive of these protostellar cores. We did not see a clear relation between the radio detections and the SiO line strength, bolometric luminosity and evolutionary stage. Some differences in orientation of the radio jet and the SiO outflow were found, perhaps implying different launching times and/or precession of the outflow.

7.2 Later Stage Massive Star Formation from MIR-Bright Protostars

To study the later phases of massive star formation, we presented $\sim 10 - 40\,\mu$m *SOFIA*-FORCAST images of about 40 high- to intermediate-mass protostars, making up the bulk of the *SOFIA* Massive (SOMA) Star Formation Survey, using the FORCAST instrument. These wavelengths trace thermal emission from warm dust that in Core Accretion models is heated in and around the inner regions of protostellar outflow cavities. Dust in the dense core envelope can also imprint characteristic extinction patterns at these wavelengths causing intensity peaks to shift along the outflow axis and profiles to become more symmetric at longer wavelengths.

Multi-wavelength images, including some ancillary ground-based MIR observations and archival *Spitzer*, *Herschel* and *IRAS* data, were analyzed and presented. We compiled SEDs and used these to derive protostellar properties by fitting theoretical radiative transfer models. Fitting the Zhang & Tan models, which are based on the Turbulent Core Model, SOMA protostars span luminosities from $\sim 10^2 - 10^6\ L_\odot$, current protostellar masses from $\sim 0.5 - 45\,M_\odot$ and ambient clump mass surface densities, $\Sigma_{\rm cl}$ from $0.1 - 3\,{\rm g\,cm^{-2}}$. For most sources the RT models provide reasonable fits to the SEDs, though the colder surrounding clump material often influences the long wavelength fitting. However, for highest luminosity sources in very clustered environments, the model SEDs are not a good description of the data, indicating potential limitations of the models for these regions. We also tried fitting the Robitaille et al. models to the first eight sources in the survey. The fitting results of Robitaille et al. models typically lead to slightly higher protostellar masses, but with accretion rates $\sim 100\times$ smaller, which we attribute to limitations in these models, i.e., they are not designed to follow a physically consistent evolutionary sequence of protostellar growth.

A wide range of evolutionary states of the individual protostars and of the protocluster environments are also probed. We have also considered the about 50 protostars identified in the IRDCs and expected to be at the earliest stages of their evolution. With this global sample, most of the evolutionary stages of high- and intermediate-mass protostars are probed. The most massive protostars are often in a clustered environment or have a companion protostar relatively nearby. From the best fitting models, there is no evidence of a threshold value of protocluster clump mass surface density being needed to form protostars up to $\sim 25\,M_\odot$. However, to form more massive protostars, there is tentative evidence that $\Sigma_{\rm cl}$ needs to be $\gtrsim 1\,{\rm g\,cm^{-2}}$.

This is consistent with expectations from core accretion models that include internal feedback from the forming massive star.

The SOMA protostars constitute an important sample of well characterized massive protostars, which can be used for further tests of theoretical models. Extensive follow-up observations are underway. For example, radio continuum observations probe ionized components of the outflows (Rosero et al. 2019), the properties of which can help break degeneracies present protostellar properties derived only from MIR to FIR SED fitting. NIR studies of the sources also constrain protostellar properties, such as outflow cavity geometries and other properties (e.g., Fedriani et al. 2019).

Appendix A The SOFIA Massive (SOMA) Star Formation Survey. IV. Isolated Protostars

Here I present preliminary results of another ten sources in the SOMA survey, which are mostly isolated. We find that previous conclusions in Paper I, II and III, specifically the dependence of massive star formation on $Sigma$, still hold with the addition of these sources. In the highest mass regime of protostar with $m_* \gtrsim 25\ M$, we now have 8 sources in total with 3 more massive protostars from this work.

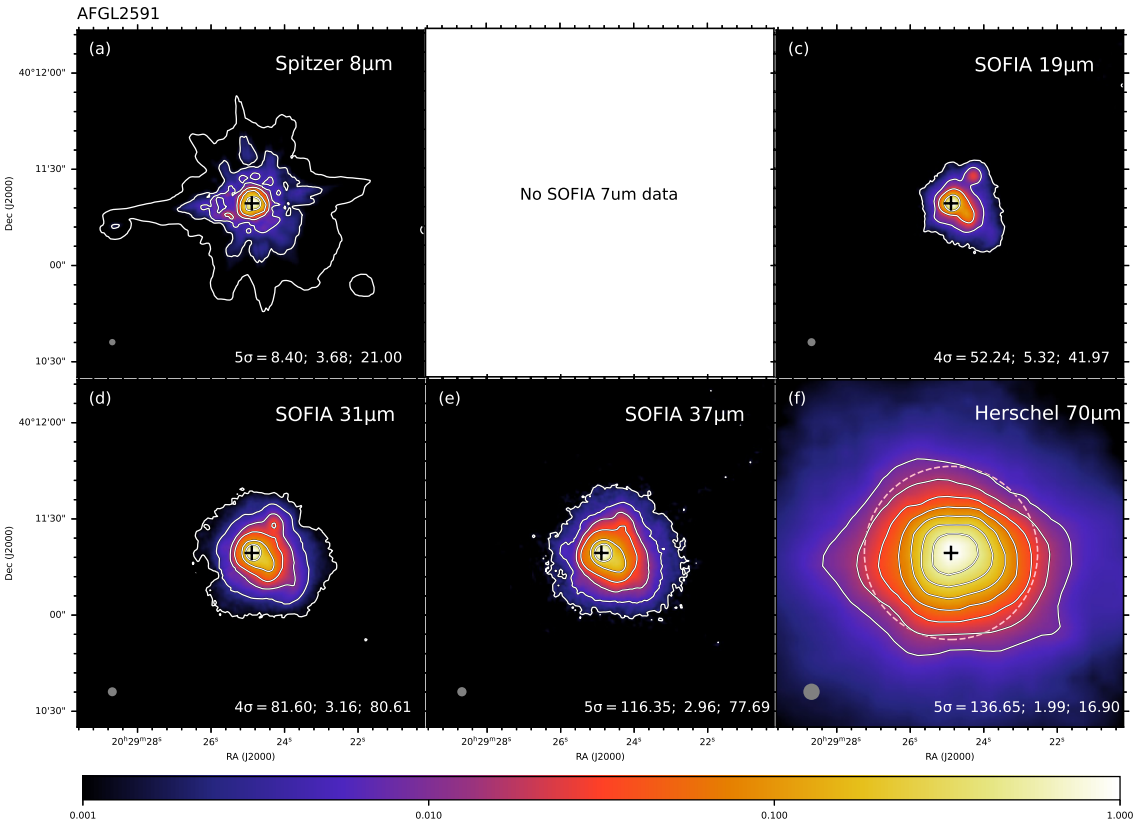

Fig. 7.1.— Multi-wavelength images of AFGL 2591 with facility and wavelength given in upper right of each panel. Contour level information is given in lower right: lowest contour level in number of σ above the background noise and corresponding value in mJy per square arcsec; then step size between each contour in $\log_{10}$ mJy per square arcsec, then peak flux in Jy per square arcsec. The color map indicates the relative flux intensity compared to that of the peak flux in each image panel. The pink dashed circle shown in (e) denotes the aperture used for the fiducial photometry. Gray circles in the lower left show the resolution of each image. The black cross in all panels denotes the position of the 3.6 cm radio source VLA3 in Trinidad et al. (2003) at R.A.(J2000) = $20^h29^m24\overset{s}{.}8916$, Decl.(J2000) = $+40°11'19\overset{''}{.}388$.

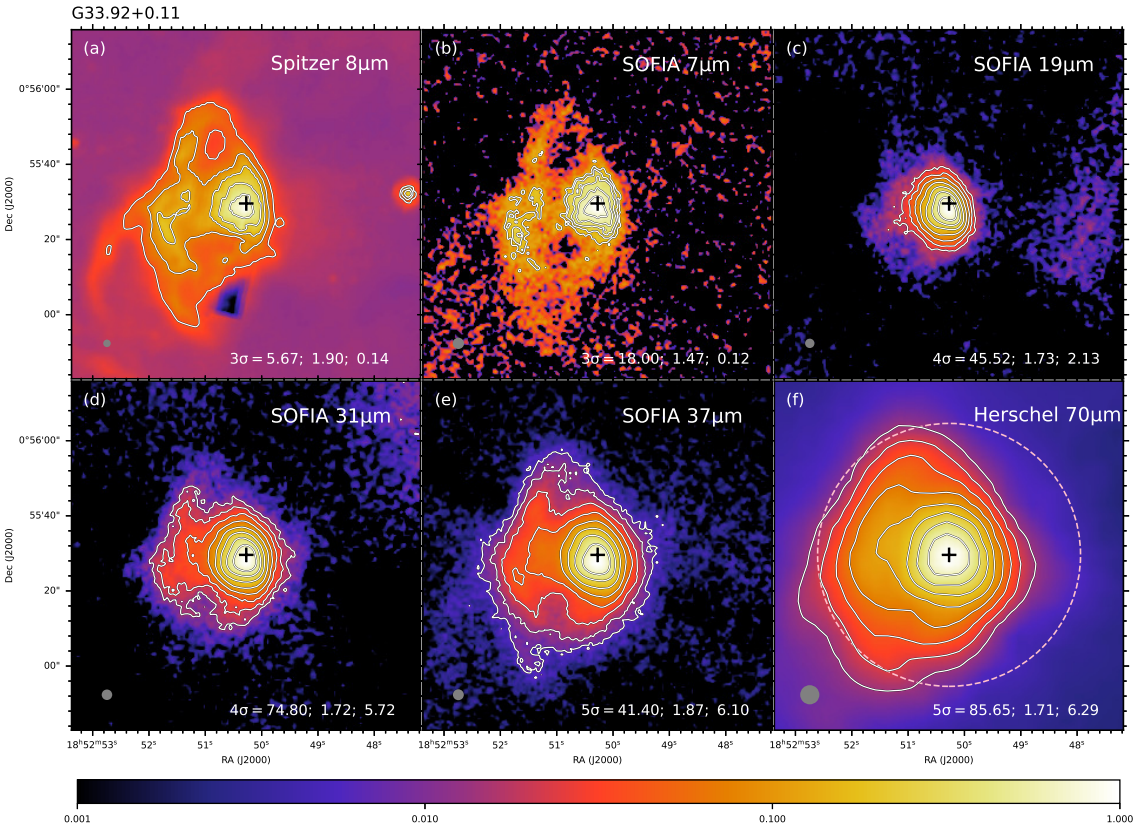

Fig. 7.2.— Multi-wavelength images of G339.88-1.26, following the format of Figure 7.1. The black cross in all panels denotes the peak position of the 2.7 mm, 2 cm, and 3.6 cm continuum emission from Watt et al. (1999) at R.A.(J2000) = $18^h52^m50\overset{s}{.}273$, Decl.(J2000) = $+00°55'29\overset{''}{.}594$.

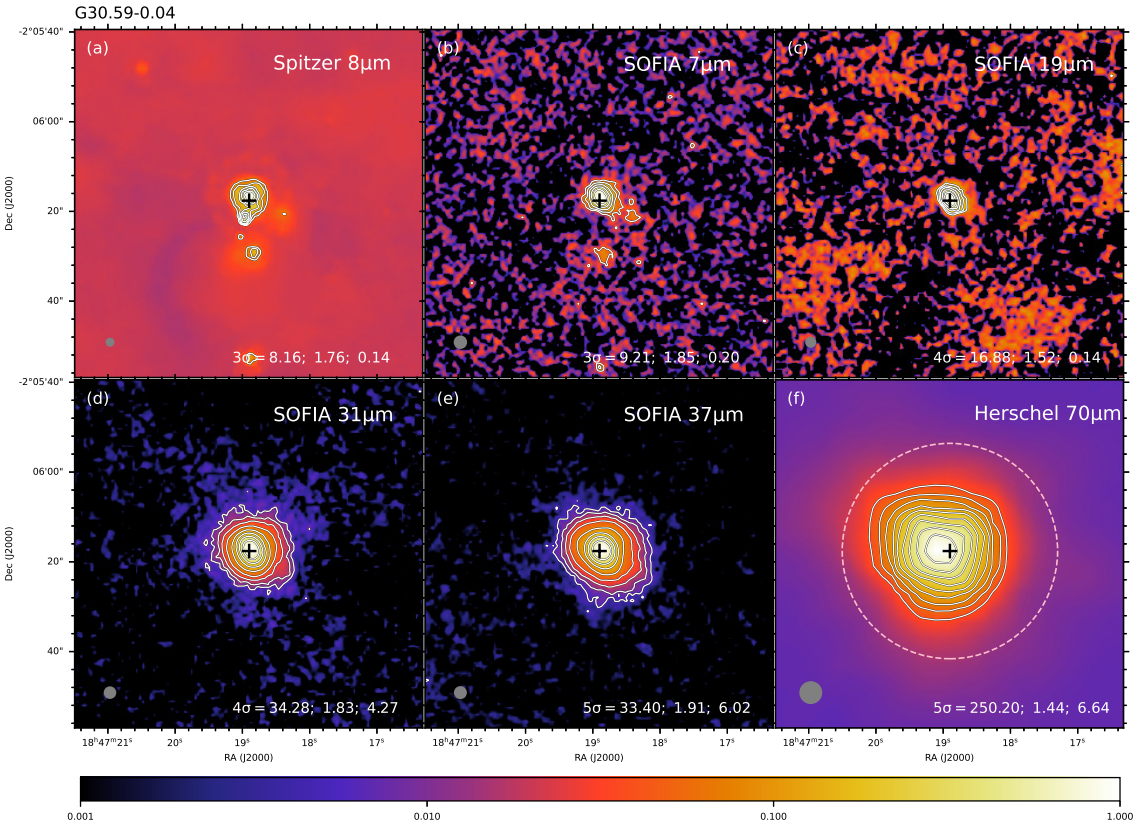

Fig. 7.3.— Multi-wavelength images of G339.88-1.26, following the format of Figure 7.1. The black cross in all panels denotes the peak position of the 6 cm continuum emission from Giveon et al. (2008) at R.A.(J2000) = $18^h47^m18\overset{s}{.}9$, Decl.(J2000) = $-02°06'17\overset{''}{.}6$.

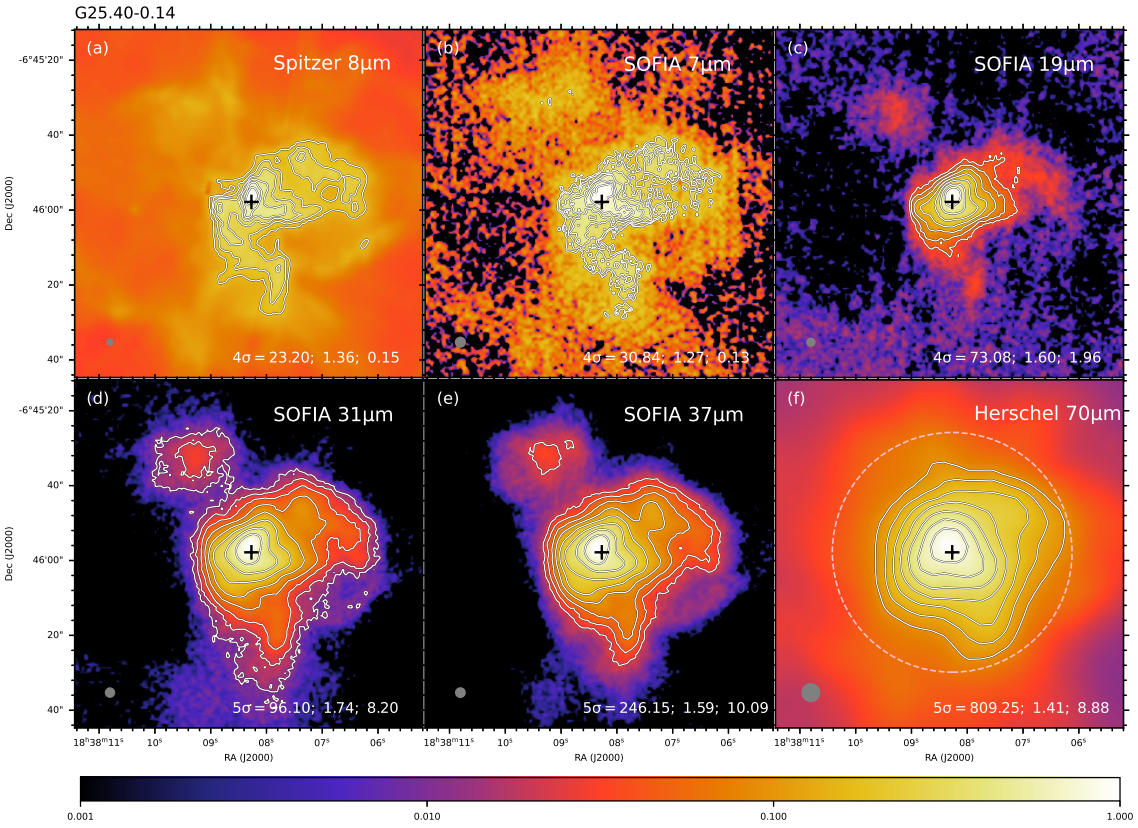

Fig. 7.4.— Multi-wavelength images of G339.88-1.26, following the format of Figure 7.1. The black cross in all panels denotes the peak position of the 6 cm continuum emission from Giveon et al. (2005) at R.A.(J2000) = $18^h38^m08\overset{s}{.}270$, Decl.(J2000) = $-06°45'57\overset{''}{.}82$.

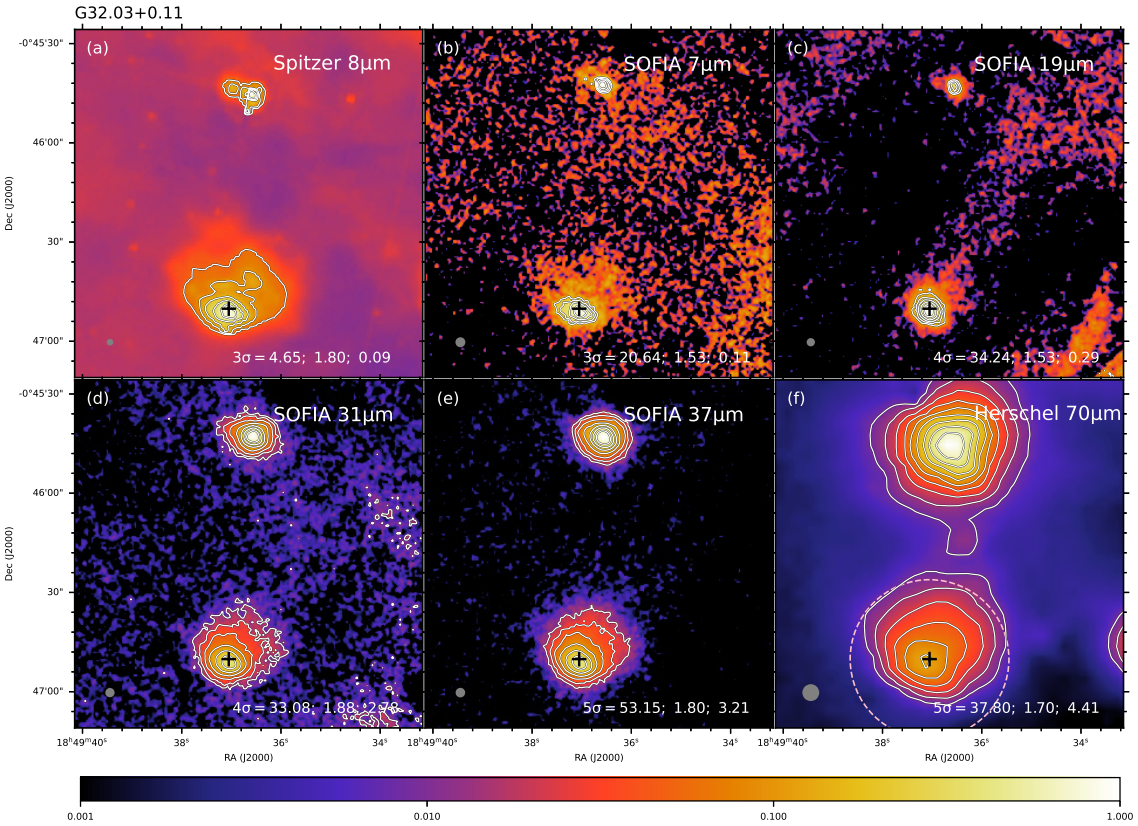

Fig. 7.5.— Multi-wavelength images of G339.88-1.26, following the format of Figure 7.1. The black cross in all panels denotes the peak position of the 6 cm continuum emission from White et al. (2005) at R.A.(J2000) = $18^h49^m37\overset{s}{.}052$, Decl.(J2000) = $-00°46'50\overset{''}{.}15$.

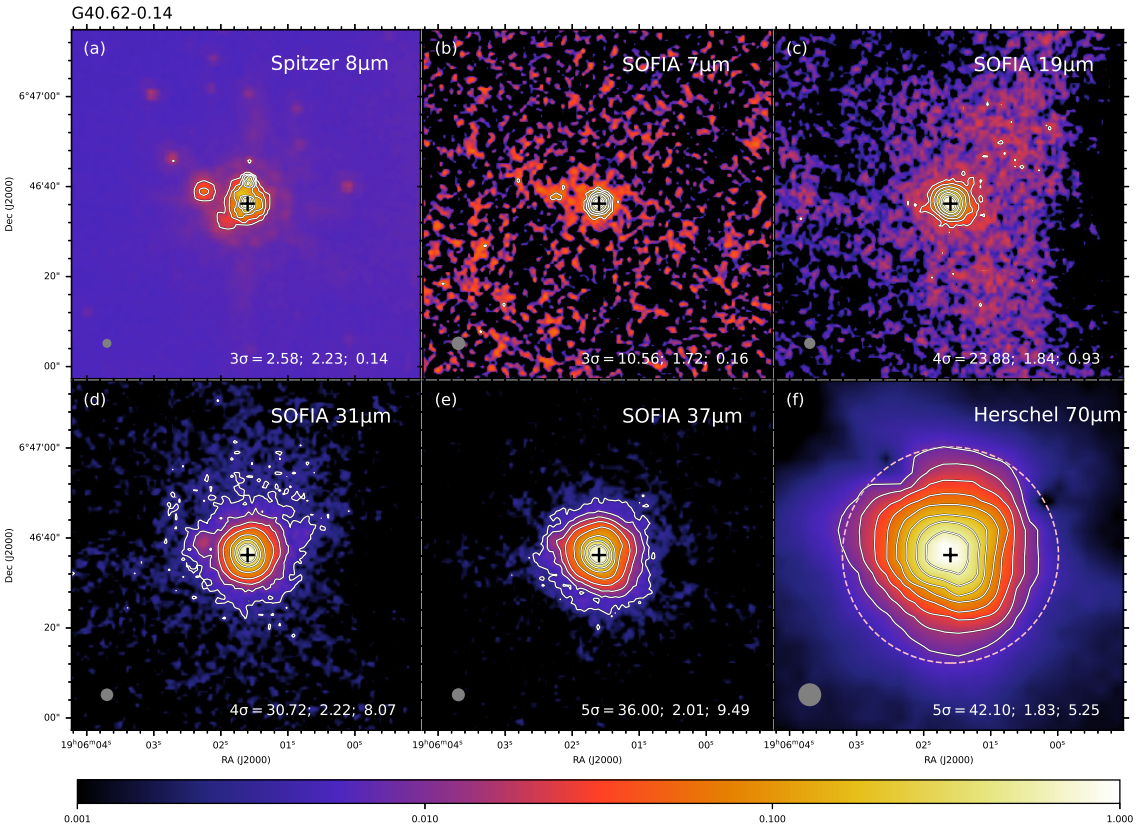

Fig. 7.6.— Multi-wavelength images of G339.88-1.26, following the format of Figure 7.1. The black cross in all panels denotes the peak position of the 1.3 cm and 6 cm continuum emission from Rosero et al. (2016) at R.A.(J2000) = $19^h06^m01\overset{s}{.}60$, Decl.(J2000) = $+06°46'36\overset{''}{.}2$.

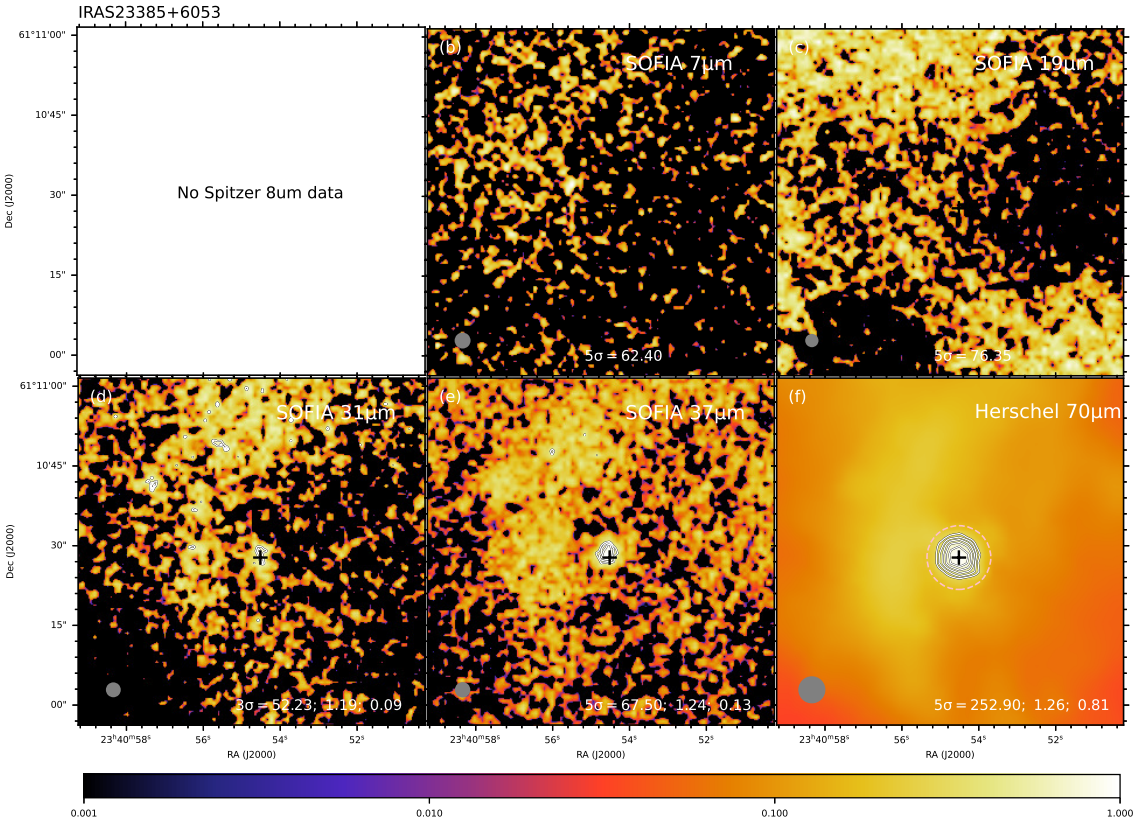

Fig. 7.7.— Multi-wavelength images of G339.88-1.26, following the format of Figure 7.1. The black cross in all panels denotes the position of the 3.4 mm source Mol 160 from Molinari et al. (2002) at R.A.(J2000) = $23^h40^m54\overset{s}{.}5171$, Decl.(J2000) = $+61°10'27\overset{''}{.}768$.

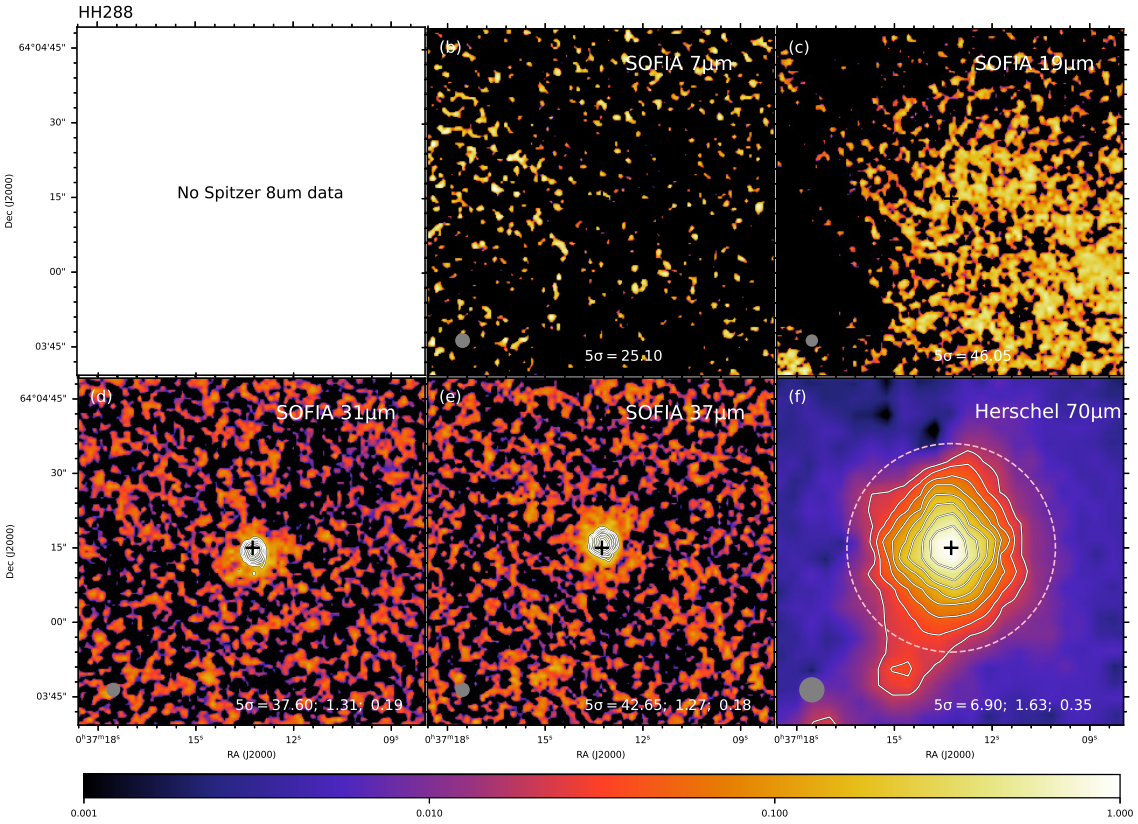

Fig. 7.8.— Multi-wavelength images of G339.88-1.26, following the format of Figure 7.1. The black cross in all panels denotes the position of the 3.5 cm source 2a from Franco-Hernández & Rodríguez (2003) at R.A.(J2000) = $0^h37^m13\overset{s}{.}258$, Decl.(J2000) = $+64°04'15\overset{''}{.}02$.

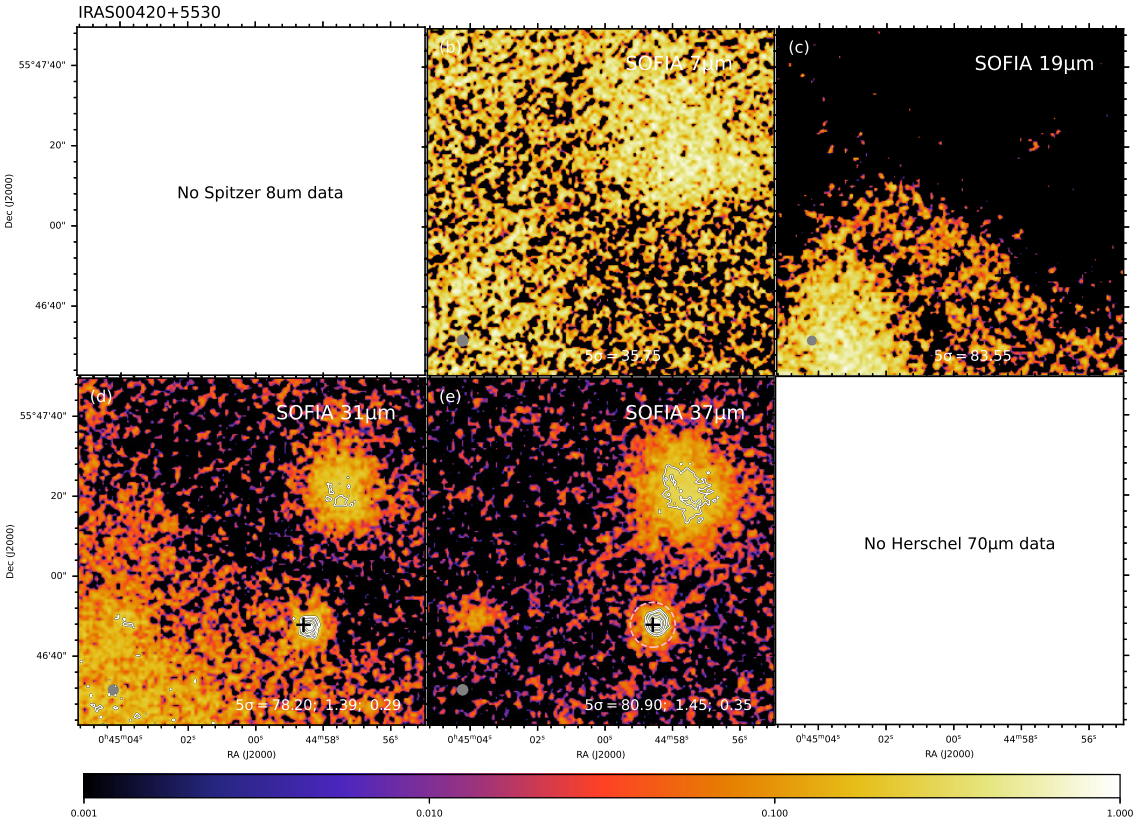

Fig. 7.9.— Multi-wavelength images of G339.88-1.26, following the format of Figure 7.1. The black cross in all panels denotes the position of the 3.6 cm source VLA3 from Molinari et al. (2002) at R.A.(J2000) = $0^h44^m58^s.5842$, Decl.(J2000) = $+55°46'45''.675$.

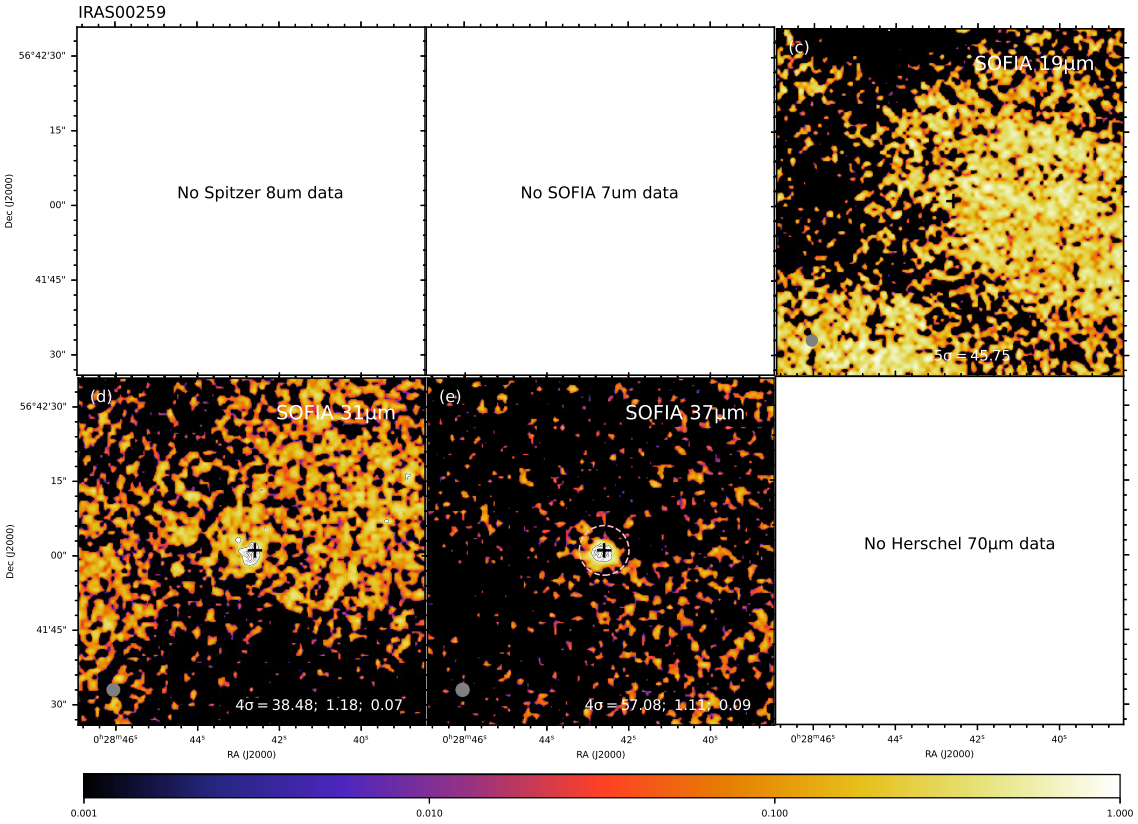

Fig. 7.10.— Multi-wavelength images of G339.88-1.26, following the format of Figure 7.1. The black cross in all panels denotes the position of the 1.3 mm and 3.3 mm source CB3-1 from Fuente et al. (2007) at R.A.(J2000) = $0^h28^m42\overset{s}{.}60$, Decl.(J2000) = $+56°42'01\overset{''}{.}11$.

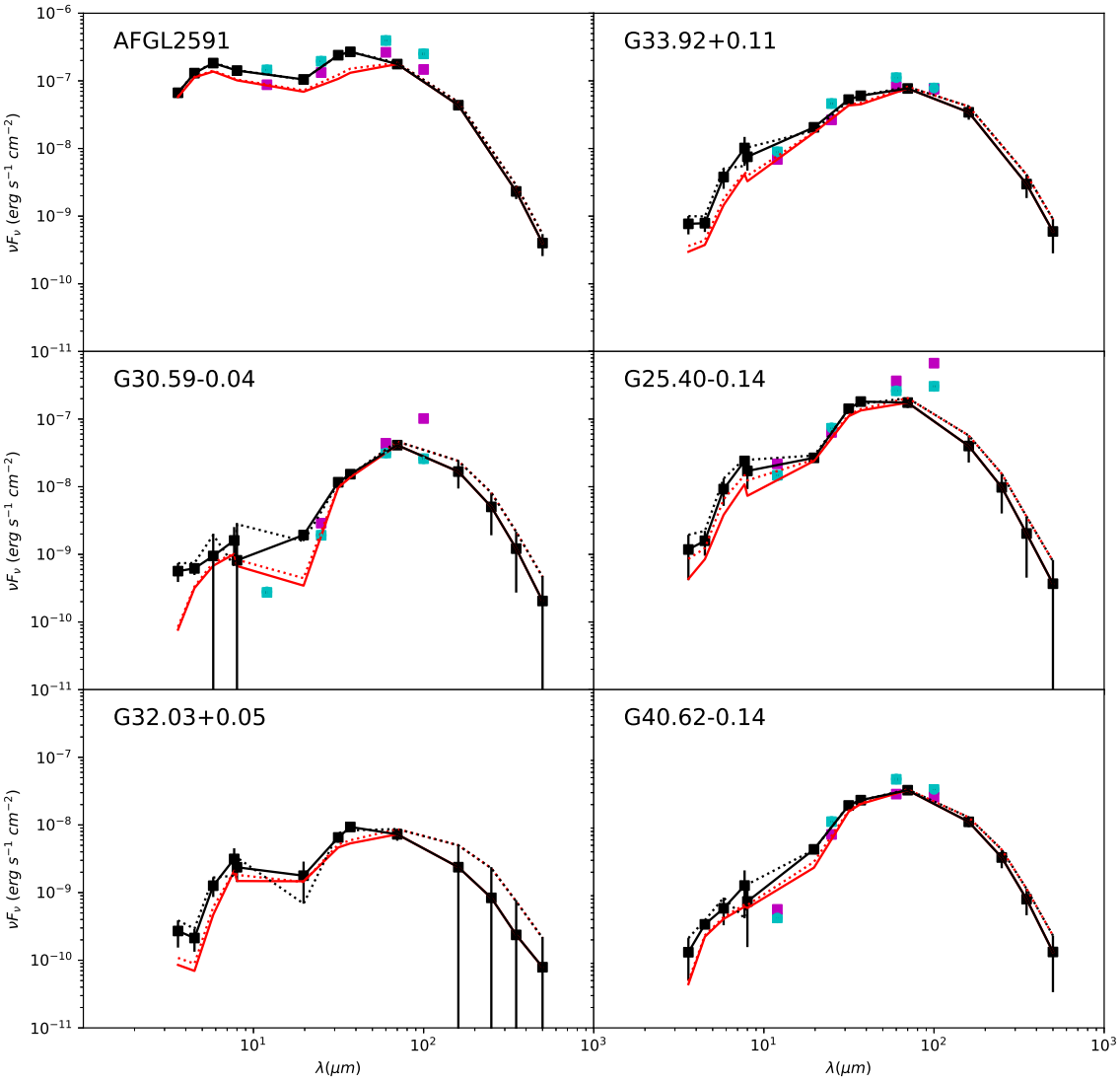

Fig. 7.11.— SEDs of the 10 presented sources. Total fluxes with no background subtraction applied are shown by dotted lines. The fixed aperture case is black dotted; the variable aperture (at < 70 μm) case is red dotted. The background subtracted SEDs are shown by solid lines: black for fixed aperture (the fiducial case); red for variable aperture. Black solid squares indicate the actual measured values that sample the fiducial SED. The cyan squares denote flux densities of *IRAS* data derived with 2D gaussian fitting with fixed major axis, minor axis and position angle. The magenta squares denote flux densities of *IRAS* data derived with 2D gaussian fitting with free parameters.

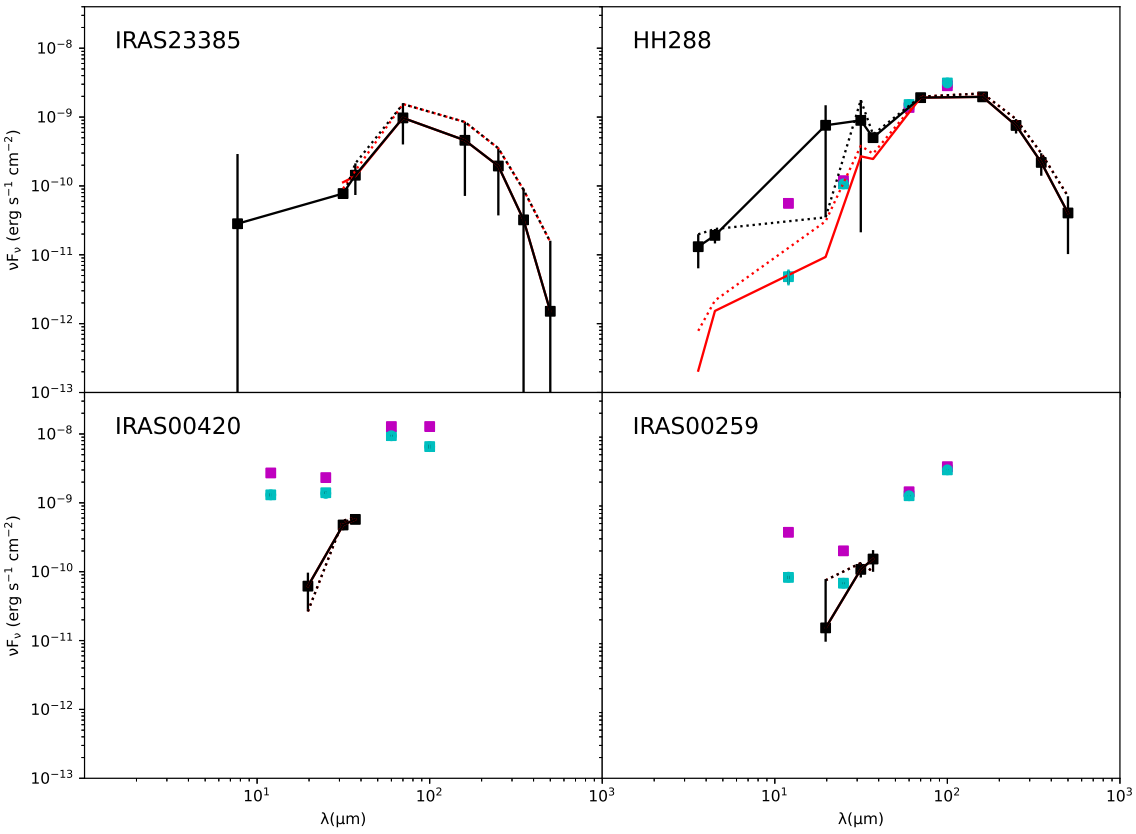

Fig. 7.11.— (cont.)

Table 7.1. Parameters of the Best Five Fitted Models

Source	χ^2	$M_{\rm c}$ ($M_\odot$)	$\Sigma_{\rm cl}$ (g cm^{-2})	$R_{\rm core}$ (pc) ($''$)	m_* ($M_\odot$)	$\theta_{\rm view}$ (°)	A_V (mag)	$M_{\rm env}$ ($M_\odot$)	$\theta_{w,{\rm esc}}$ (deg)	$\dot{M}_{\rm disk}$ ($M_\odot$/yr)	$L_{\rm bol,iso}$ ($L_\odot$)	$L_{\rm bol}$ ($L_\odot$)
AFGL2591	2.71	480	0.3	0.287 (18)	32.0	13	72.7	406	22	3.9e-04	1.3e+06	2.0e+05
d = 3.3 kpc	3.35	160	3.2	0.052 (3)	24.0	29	47.5	115	23	1.4e-03	2.6e+05	3.0e+05
R_{ap} = 27 $''$	3.50	480	0.3	0.287 (18)	48.0	29	84.8	352	30	4.5e-04	1.2e+06	4.1e+05
= 0.44 pc	3.73	200	3.2	0.059 (4)	32.0	29	84.8	140	25	1.7e-03	5.1e+05	4.6e+05
	3.84	240	3.2	0.064 (4)	48.0	34	100.0	138	33	2.1e-03	1.1e+06	7.5e+05
G33.92+0.11	3.94	320	3.2	0.074 (2)	24.0	22	52.5	277	15	1.8e-03	3.3e+05	3.1e+05
d = 7.1 kpc	4.38	240	3.2	0.064 (2)	24.0	29	37.4	194	18	1.6e-03	2.6e+05	3.1e+05
R_{ap} = 35 $''$	4.61	240	3.2	0.064 (2)	32.0	29	87.9	175	23	1.9e-03	4.5e+05	5.0e+05
= 1.20 pc	5.12	200	3.2	0.059 (2)	24.0	29	44.4	156	20	1.5e-03	2.6e+05	3.1e+05
	5.44	400	3.2	0.083 (2)	24.0	22	27.3	362	13	1.9e-03	3.0e+05	3.0e+05
G30.59-0.04	0.93	400	3.2	0.083 (1)	24.0	22	88.9	362	13	1.9e-03	3.0e+05	3.0e+05
d = 11.8 kpc	1.11	480	3.2	0.091 (2)	24.0	22	69.7	441	12	2.0e-03	2.9e+05	2.9e+05
R_{ap} = 24 $''$	1.19	480	1.0	0.161 (3)	32.0	22	98.0	414	19	9.3e-04	3.7e+05	3.0e+05
= 1.37 pc	1.23	320	3.2	0.074 (1)	24.0	29	85.9	277	15	1.8e-03	2.7e+05	3.1e+05
	1.28	480	1.0	0.161 (3)	24.0	22	22.2	433	15	8.2e-04	1.9e+05	2.1e+05
G25.40-0.14	0.51	480	1.0	0.161 (6)	64.0	48	0.0	325	32	1.2e-03	2.8e+05	8.4e+05
d = 5.7 kpc	0.79	480	1.0	0.161 (6)	48.0	34	16.2	367	25	1.1e-03	3.0e+05	5.4e+05
R_{ap} = 32 $''$	1.05	400	3.2	0.083 (3)	24.0	22	11.1	362	13	1.9e-03	3.0e+05	3.0e+05
= 0.88 pc	1.11	320	3.2	0.074 (3)	24.0	34	0.0	277	15	1.8e-03	2.5e+05	3.1e+05
	1.15	480	1.0	0.161 (6)	96.0	62	1.0	238	43	1.3e-03	2.5e+05	1.6e+06
G32.03+0.05	0.11	400	0.1	0.465 (17)	96.0	89	100.0	46	76	8.3e-05	3.5e+04	1.2e+06
d = 5.5 kpc	0.11	160	0.1	0.294 (11)	24.0	86	43.4	87	45	8.5e-05	1.9e+04	7.8e+04
R_{ap} = 24 $''$	0.17	40	3.2	0.026 (1)	16.0	55	67.7	10	44	6.8e-04	2.4e+04	1.1e+05
= 0.64 pc	0.18	160	0.1	0.294 (11)	16.0	80	11.1	116	32	8.1e-05	1.4e+04	3.3e+04
	0.19	240	0.1	0.360 (14)	12.0	68	0.0	211	19	8.5e-05	1.4e+04	2.0e+04
G40.62-0.14	0.25	400	0.1	0.465 (44)	8.0	34	22.2	386	10	8.1e-05	9.5e+03	1.0e+04
d = 2.2 kpc	0.26	320	0.1	0.416 (39)	8.0	65	7.1	307	11	7.7e-05	7.7e+03	8.8e+03
R_{ap} = 24 $''$	0.31	480	0.1	0.510 (48)	8.0	29	17.2	463	9	8.5e-05	9.3e+03	9.7e+03
= 0.26 pc	0.34	240	0.1	0.360 (34)	8.0	44	32.3	226	13	7.1e-05	9.1e+03	1.1e+04
	0.78	160	0.1	0.294 (28)	12.0	58	63.6	130	25	7.4e-05	1.1e+04	1.9e+04
IRAS23385	0.08	20	3.2	0.019 (1)	4.0	65	4.0	12	34	3.1e-04	8.0e+02	3.3e+03
d = 4.9 kpc	0.09	30	1.0	0.040 (2)	4.0	39	71.7	22	28	1.5e-04	9.7e+02	2.0e+03
R_{ap} = 6 $''$	0.09	60	0.3	0.101 (4)	4.0	83	91.9	51	19	8.2e-05	9.6e+02	1.4e+03
= 0.14 pc	0.09	100	0.3	0.131 (6)	4.0	89	38.4	91	14	9.5e-05	8.8e+02	1.1e+03
	0.10	100	0.3	0.131 (6)	2.0	22	5.1	96	9	6.8e-05	7.6e+02	8.3e+02
HH288	1.53	400	0.1	0.465 (48)	2.0	39	100.0	391	4	4.1e-05	5.5e+02	5.5e+02
d = 2.0 kpc	1.61	320	0.1	0.416 (43)	4.0	62	100.0	308	7	5.5e-05	5.1e+02	5.4e+02
R_{ap} = 21 $''$	1.67	480	0.1	0.510 (53)	2.0	39	100.0	477	4	4.3e-05	5.8e+02	5.7e+02
= 0.20 pc	1.92	240	0.1	0.360 (37)	2.0	55	100.0	233	6	3.6e-05	5.0e+02	5.2e+02
	2.74	200	0.1	0.329 (34)	4.0	89	100.0	194	10	4.8e-05	5.7e+02	6.7e+02
IRAS00420	0.24	60	0.1	0.180 (17)	2.0	44	40.4	55	15	2.5e-05	3.0e+02	3.5e+02
d = 2.2 kpc	0.24	80	0.1	0.208 (20)	2.0	22	54.5	75	12	2.7e-05	3.5e+02	3.5e+02
R_{ap} = 6 $''$	0.28	50	0.1	0.165 (16)	2.0	86	3.0	46	16	2.4e-05	2.2e+02	3.1e+02
= 0.06 pc	0.32	100	0.1	0.233 (22)	2.0	22	58.6	97	11	2.9e-05	3.8e+02	3.8e+02
	0.33	200	0.1	0.329 (31)	2.0	22	25.3	194	7	3.5e-05	3.6e+02	3.5e+02
IRAS00259	0.00	30	0.1	0.127 (11)	0.5	55	1.0	29	10	1.1e-05	8.0e+01	9.0e+01
d = 2.4 kpc	0.00	40	0.1	0.147 (13)	0.5	34	1.0	39	8	1.1e-05	8.5e+01	8.8e+01
R_{ap} = 5 $''$	0.00	20	0.1	0.104 (9)	1.0	51	56.6	17	20	1.3e-05	1.0e+02	1.5e+02
= 0.06 pc	0.01	50	0.1	0.165 (14)	0.5	22	0.0	49	7	1.2e-05	8.7e+01	8.7e+01
	0.01	20	0.1	0.104 (9)	2.0	83	39.4	15	30	1.7e-05	8.7e+01	1.9e+02

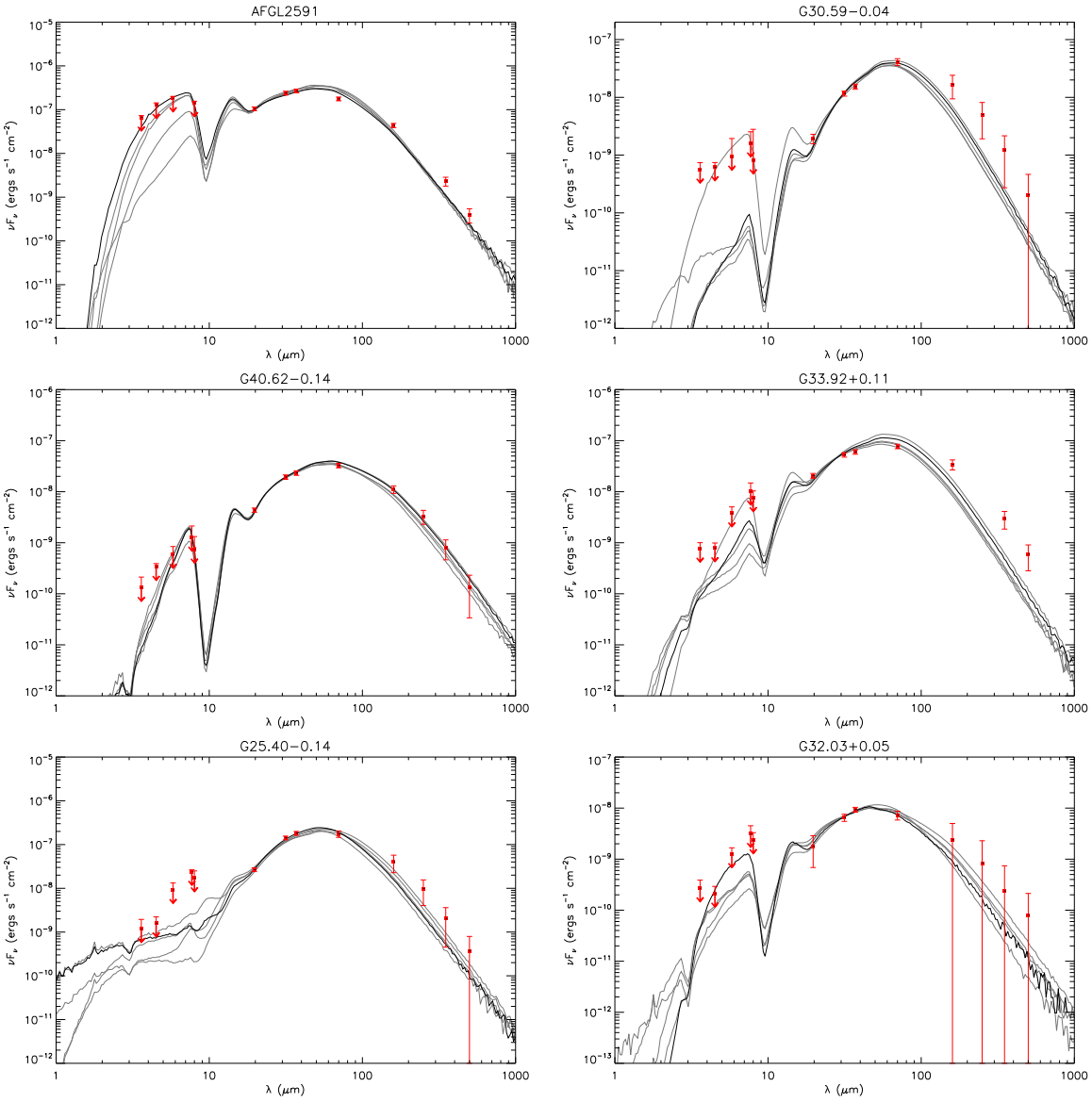

Fig. 7.12.— Protostar model fitting to the fixed aperture, background-subtracted SED data using the ZT model grid. For each source, the best fit model is shown with a solid black line and the next four best models are shown with solid gray lines. The resulting model parameter results are listed in Table 7.1.

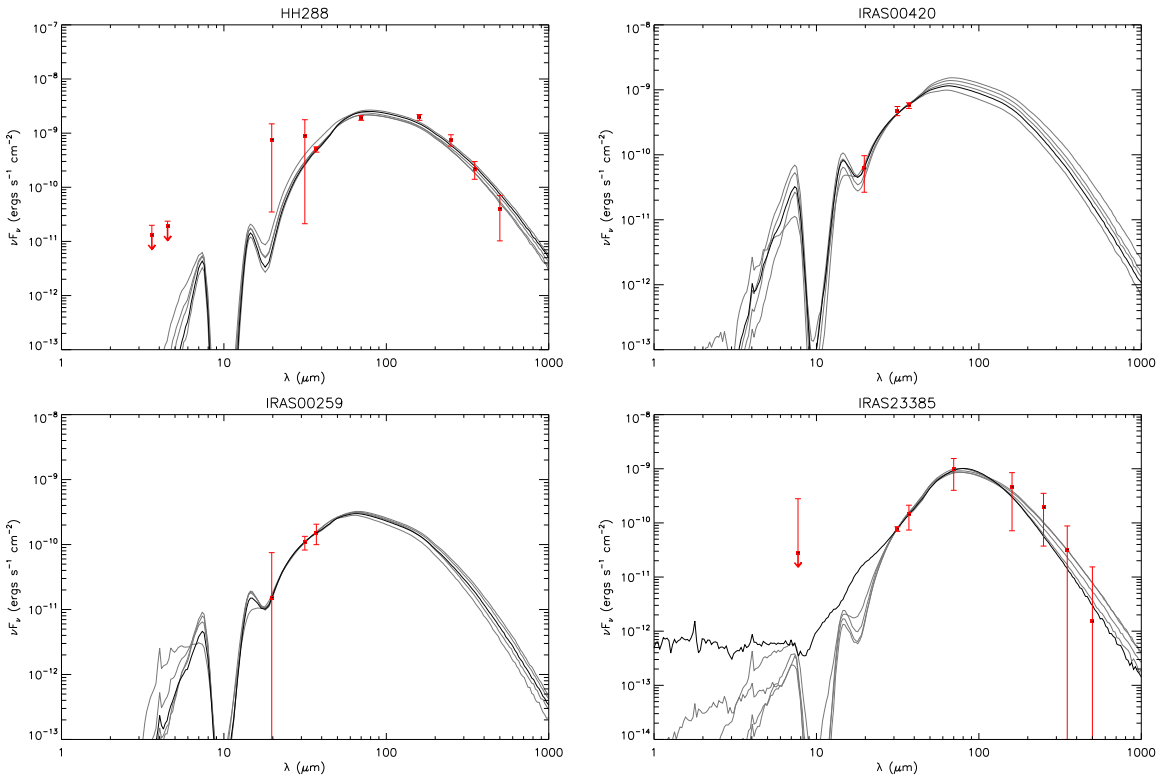

Fig. 7.12.— (cont.)

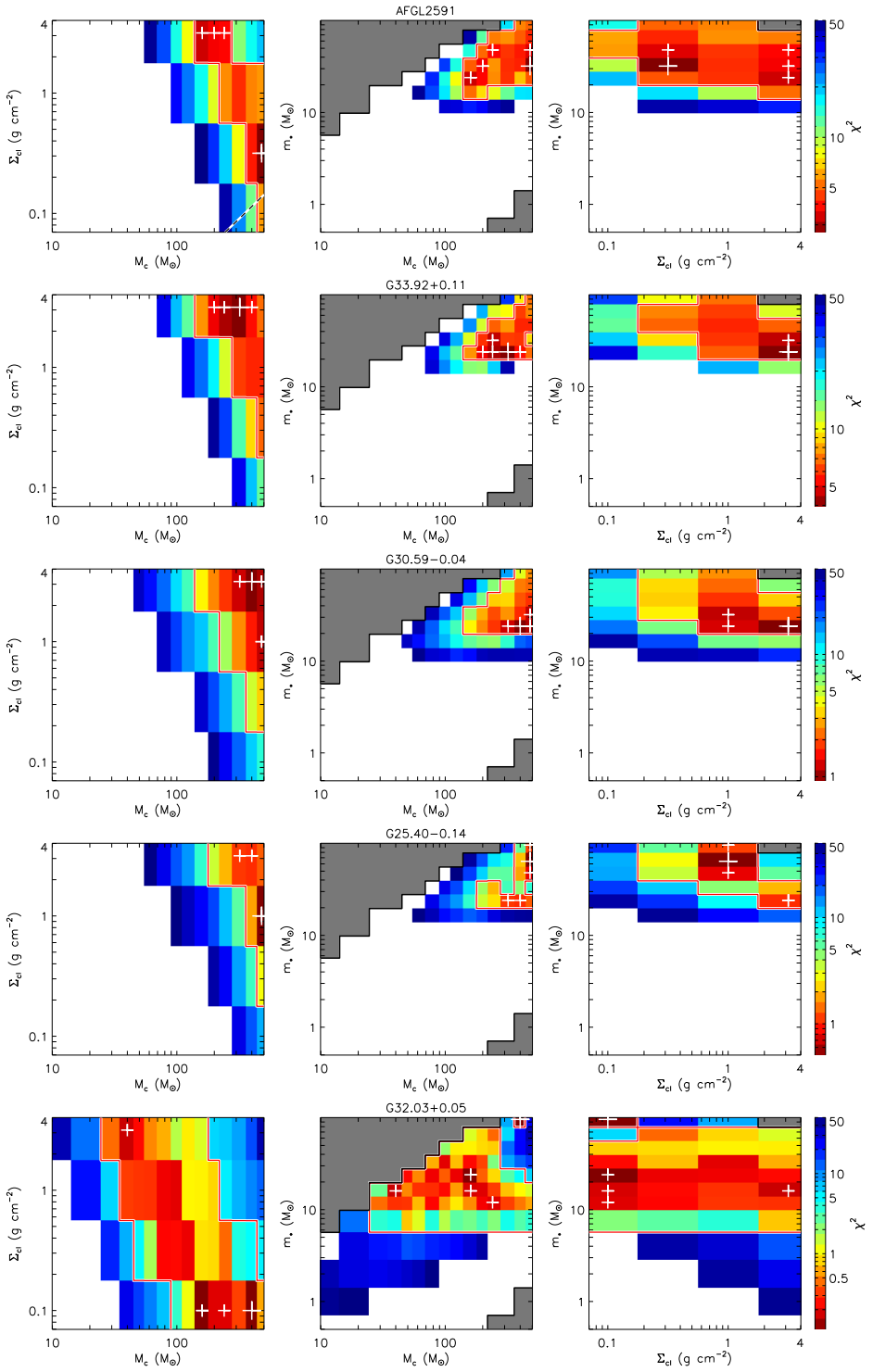

Fig. 7.13.— Diagrams of χ^2 distribution in $\Sigma_{\rm cl}$ - M_c space, m_* - $M_{\rm c}$ space and m_* - $\Sigma_{\rm cl}$ space. The white crosses mark the locations of the five best models, and the large cross is the best model. The grey regions are not covered by the model grid, and the white regions are where the χ^2 is larger than 50. The red contours are at the level of $\chi^2 = \chi^2_{min} + 5$. The dashed line denotes when $R_c = R_{\rm ap}$.

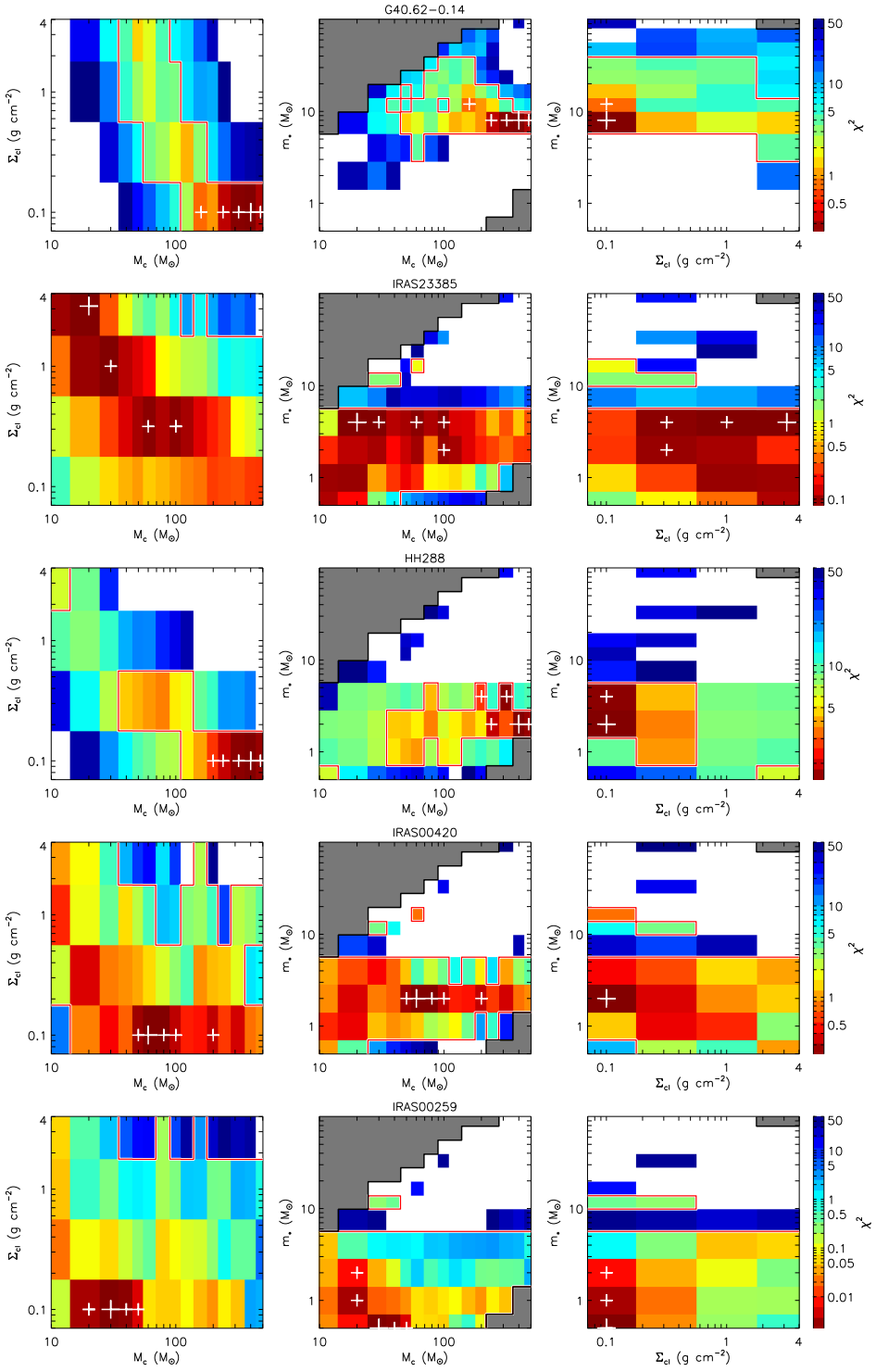
G40.62−0.14
IRAS23385
HH288
IRAS00420
IRAS00259
Σcl (g cm−2)
M⋆ (M⊙)
Mc (M⊙)
χ2

Fig. 7.13.— (cont.)

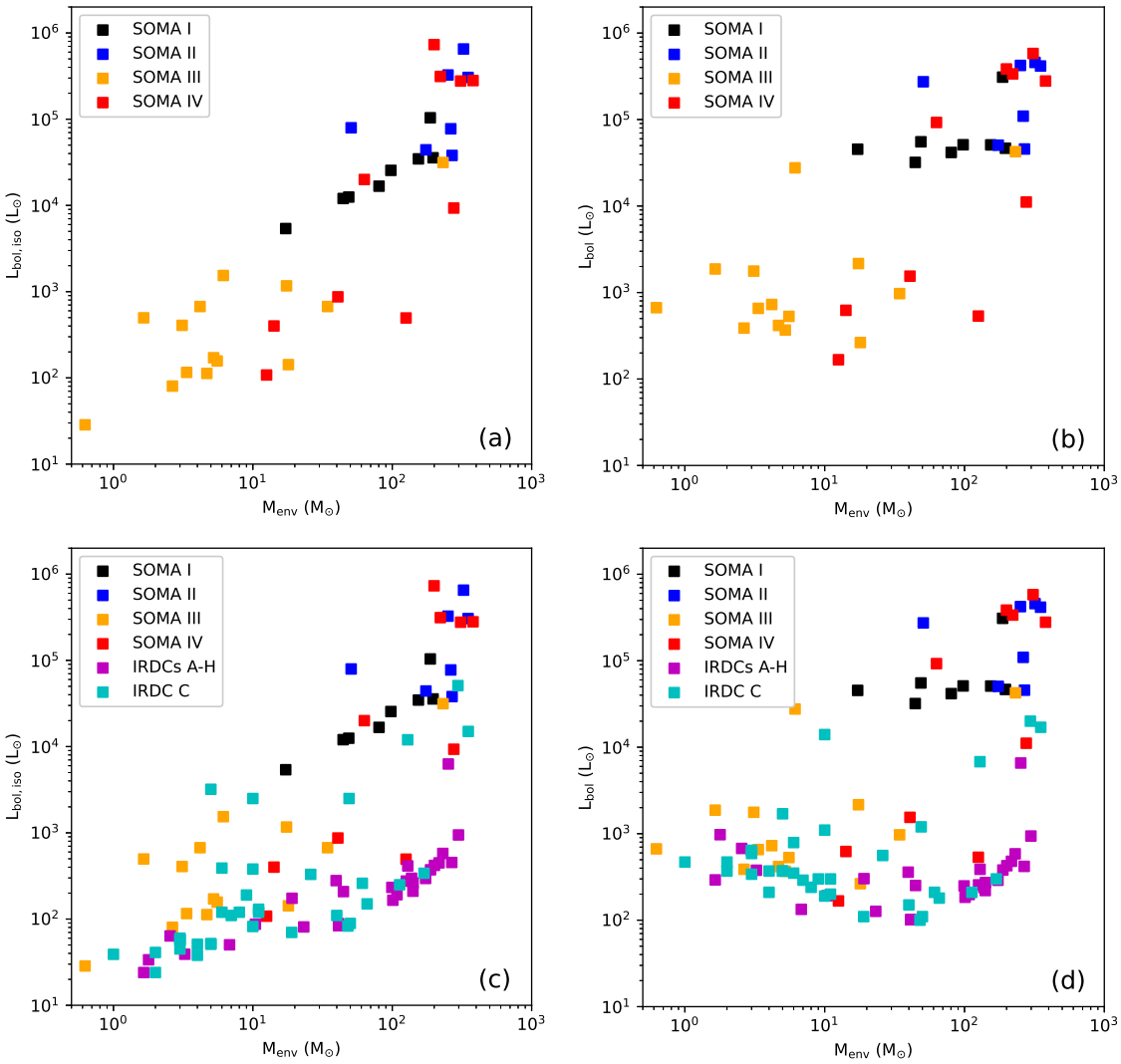

Fig. 7.14.— (a) Average (geometric mean) isotropic bolometric luminosity versus envelope mass returned by the average of the best five or fewer models with $R_c \lesssim 2R_{\rm ap}$ and $\chi^2 < \chi^2_{\rm min} + 5$ for each SOMA source from Papers I, II,III and IV (this work), as labelled. (b) Same as (a), but now with true bolometric luminosities plotted versus envelope mass. (c) Same as (a), but now also including IRDC sources. (d) Same as (c), but now also including IRDC sources.

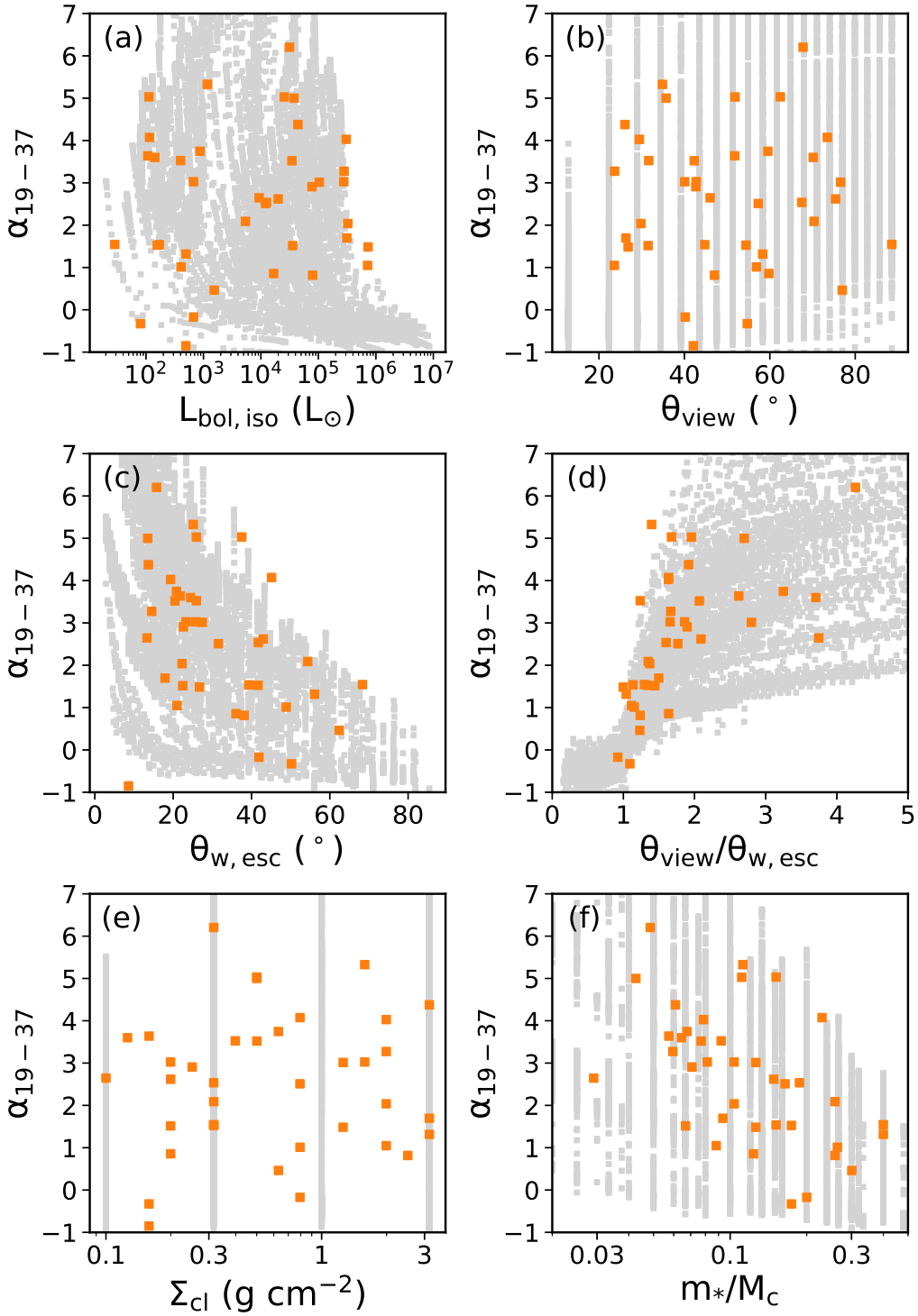

Fig. 7.15.— Spectral index, α_{19-37} between 19 μm and 37 μm (see text) versus: the geometric mean isotropic luminosity $L_{\rm bol,iso}$ (a: top left); the arithmetic mean inclination of viewing angle $\theta_{\rm view}$ (b: top right); the arithmetic mean opening angle $\theta_{w,\rm esc}$ (c: middle left); arithmetic mean $\theta_{\rm view}/\theta_{w,\rm esc}$ (d: middle right); the geometric mean clump surface density $\Sigma_{\rm cl}$ (e: bottom left); and geometric mean $m_*/M_{\rm c}$ (f: bottom right) returned by the best five or fewer models with $R_c \lesssim 2R_{\rm ap}$ and $\chi^2 < \chi^2_{\rm min} + 5$. The grey squares represents the ZT18 protostar models. Note that the spectral index of the models are calculated without foreground extinction and thus could be different from observations.

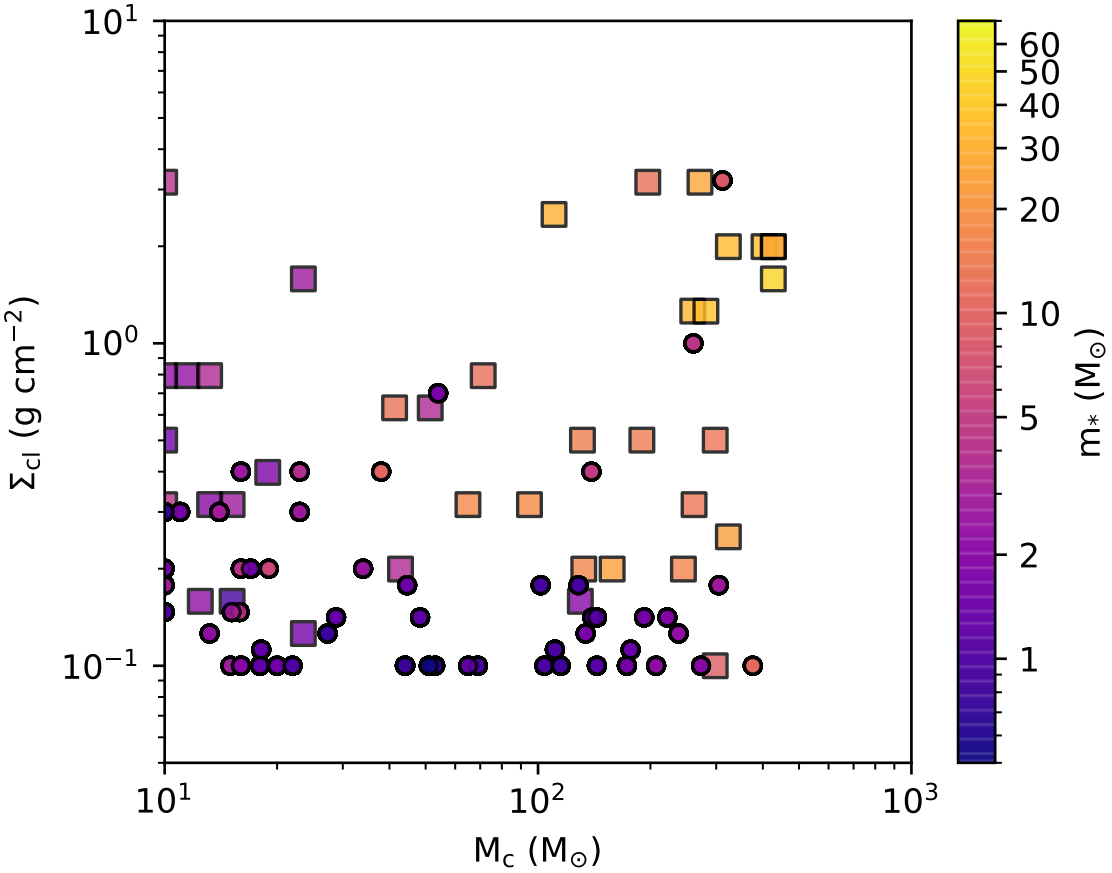

Fig. 7.16.— Average clump mass surface density, $\Sigma_{\rm cl}$, versus average initial core mass, M_c, of the SOMA sources (squares) and IRDC sources (circles, Liu et al. 2018; Moser et al. 2020; Liu et al. 2020b), based on ZT model fits: the average is made for the best five or fewer models with $R_c \lesssim 2R_{\rm ap}$ and $\chi^2 < \chi^2_{\rm min} + 5$.

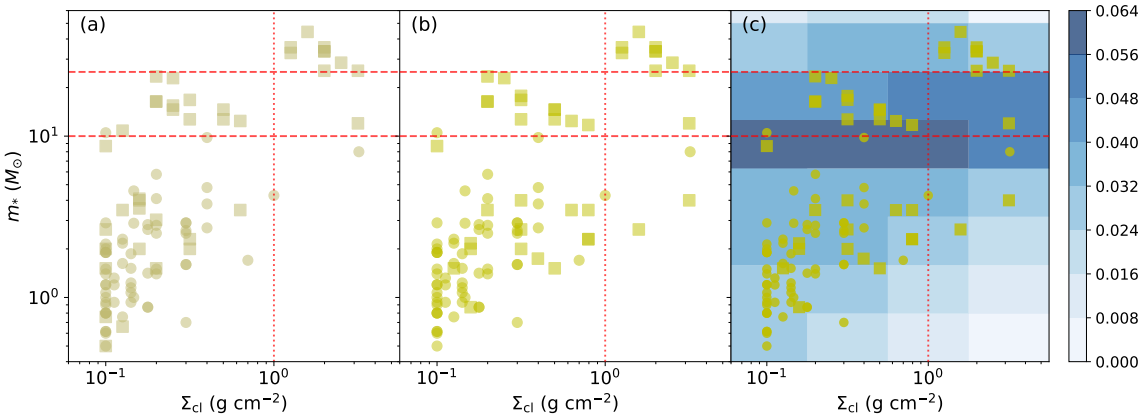

Fig. 7.17.— *a) Left:* Average protostellar mass, m_*, versus average clump mass surface density, $\Sigma_{\rm cl}$, of SOMA sources (squares) and IRDC sources (circles, Liu et al. 2018; Moser et al. 2020; Liu et al. 2020b), based on ZT model fits: the average is made for the best five selected models. The red dotted and dashed lines indicate fiducial threshold values of m_* (10 and 25 $M_\odot$) and $\Sigma_{\rm cl}$ (1 g cm^{-2}, see text). *b) Middle:* Same as (a), but with the average made for best five or fewer models with $R_c \lesssim 2R_{\rm ap}$ and $\chi^2 < \chi^2_{\rm min} + 5$. *c) Right:* Same as (b), but now also showing the distribution of models in the ZT model grid (shading indicates the density of models).

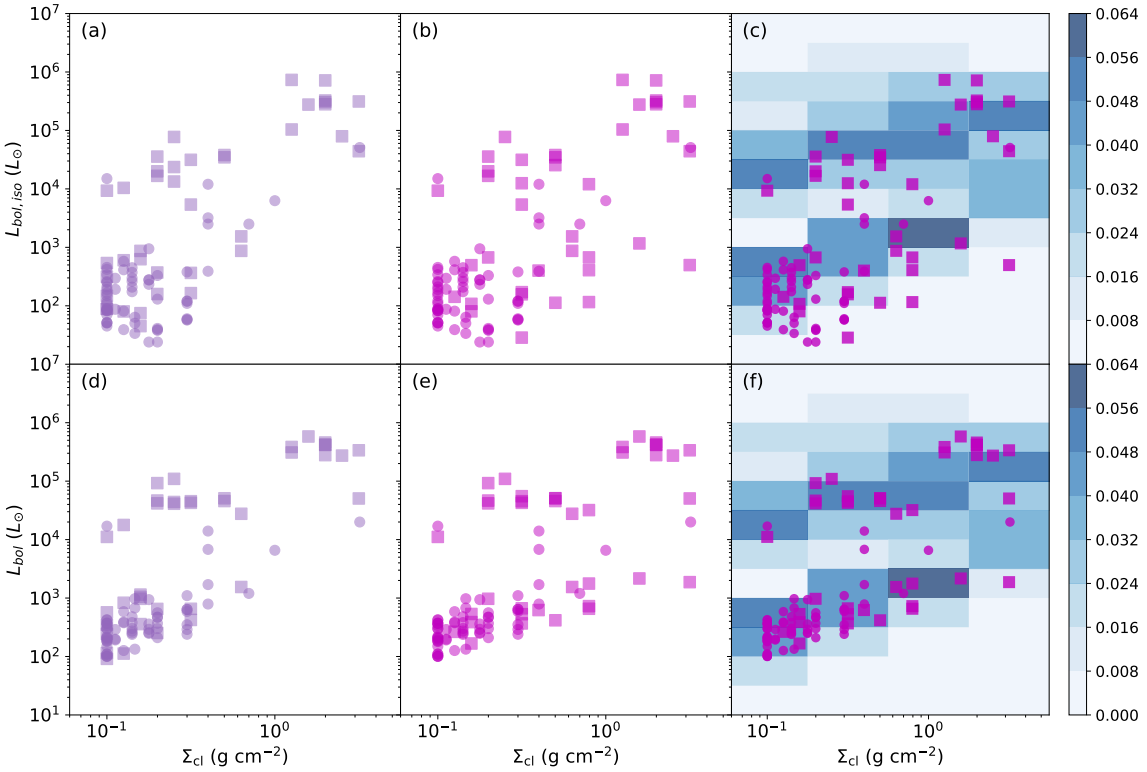

Fig. 7.18.— *a) Top Left:* Average protostellar isotropic bolometric luminosity, $L_{\rm bol,iso}$, versus average clump mass surface density, $\Sigma_{\rm cl}$, of SOMA sources (squares) and IRDC sources (circles, Liu et al. 2018; Moser et al. 2020; Liu et al. 2020b), based on ZT model fits: the average is made for the best five selected models. *b) Top Middle:* Same as (a), but with the average made for best five or fewer models with $R_c \lesssim 2R_{\rm ap}$ and $\chi^2 < \chi^2_{\rm min} + 5$. *c) Top Right:* Same as (b), but now also showing the distribution of models in the ZT model grid (shading indicates the density of models). *d) Bottom Left:* Same as (a), but now for intrinsic bolometric luminosity, $L_{\rm bol}$. *e) Bottom Middle:* Same as (b), but now for intrinsic bolometric luminosity, $L_{\rm bol}$. *f) Bottom Right:* Same as (c), but now for intrinsic bolometric luminosity, $L_{\rm bol}$.

References

Adams, F. C. 2010, ARA&A, 48, 47

Aguirre, J. E., Ginsburg, A. G., Dunham, M. K., et al. 2011, ApJS, 192, 4. doi:10.1088/0067-0049/192/1/4

Alves, J., Lombardi, M., & Lada, C. J. 2007, A&A, 462, L17

André, P., Men'shchikov, A., Bontemps, S., et al. 2010, A&A, 518, L102

Andre, P., Ward-Thompson, D., & Barsony, M. 1993, ApJ, 406, 122

Andre, P., Ward-Thompson, D., & Barsony, M. 2000, Protostars and Planets IV, 59

Anglada, G., Rodríguez, L. F., & Carrasco-Gonzalez, C. 2015, Advancing Astrophysics with the Square Kilometre Array (AASKA14), 121.

Anglada, G., Rodríguez, L. F., & Carrasco-González, C. 2018, Astronomy and Astrophysics Review, 26, 3.

Anglada, G. 1996, Radio Emission from the Stars and the Sun, 3.

Anthony-Twarog, B. J. 1982, AJ, 87, 1213

Arce, H. G., Shepherd, D., Gueth, F., et al. 2007, Protostars and Planets V, 245.

Arce, H. G., & Goodman, A. A. 2001, ApJ, 551, L171.

Argon, A. L., Reid, M. J., & Menten, K. M. 2000, The Astrophysical Journal Supplement Series, 129, 159.

Arquilla, R., & Goldsmith, P. F. 1984, ApJ, 279, 664

Ayala, S., Noriega-Crespo, A., Garnavich, P. M., et al. 2000, AJ, 120, 909

Bally, J. & Zinnecker, H. 2005, AJ, 129, 2281. doi:10.1086/429098

Bally, J., Ginsburg, A., Arce, H., et al. 2017, ApJ, 837, 60.

Bally, J. 1982, ApJ, 261, 558

Barentine, J. C., & Lacy, J. H. 2012, ApJ, 757, 111

Bastian, N., Covey, K. R., & Meyer, M. R. 2010, ARA&A, 48, 339

Beichman, C. A. 1979, Ph.D. Thesis

Beltrán, M. T., Girart, J. M., Estalella, R., et al. 2002, ApJ, 573, 246

Beltrán, M. T., Girart, J. M., & Estalella, R. 2006, A&A, 457, 865

Beltrán, M. T., Estalella, R., Girart, J. M., et al. 2008, A&A, 481, 93

Beltrán, M. T., Massi, F., López, R., et al. 2009, A&A, 504, 97

Beltrán, M. T., Cesaroni, R., Moscadelli, L., et al. 2016, A&A, 593, A49.

Beltrán, M. T. 2015, Ap&SS, 355, 283

Beltrán, M. T. & de Wit, W. J. 2016, A&ARv, 24, 6

Beltrán, M. T. & de Wit, W. J. 2016, A&ARv, 24, 6

Beltrán, M. T., Cesaroni, R., Moscadelli, L. et al. 2016, A&A, 593, A49

Benjamin, R. A., Churchwell, E., Babler, B. L., et al. 2003, PASP, 115, 953. doi:10.1086/376696

Beuther, H. & Schilke, P. 2004, Science, 303, 1167.

Beuther, H., Schilke, P., Sridharan, T. K., et al. 2002, A&A, 383, 892

Beuther, H., Schilke, P., Menten, K. M., et al. 2002, Hot Star Workshop III: The Earliest Phases of Massive Star Birth, 341.

Beuther, H., Soler, J. D., Vlemmings, W., et al. 2018, A&A, 614, A64

Birks, J. R., Fuller, G. A., & Gibb, A. G. 2006, A&A, 458, 181

Blandford, R. D., Payne, D., G., 1982, MNRAS, 199, 883

Boley, P. A., Sobolev, A. M., Krushinsky, V. V., et al. 2009, MNRAS, 399, 778

Boley, P. A., Linz, H., van Boekel, R., et al. 2013, A&A, 558, A24.

Bonnell, I. A., Bate, M. R., & Zinnecker, H. 1998, MNRAS, 298, 93

Bonnell, I. A., Bate, M. R., & Zinnecker, H. 1998, MNRAS, 298, 93.

Bonnell, I. A., Bate, M. R., Clarke, C. J., & Pringle, J. E. 2001, MNRAS, 323, 785

Bonnell, I. A., Bate, M. R., Clarke, C. J., & Pringle, J. E. 2001, MNRAS, 323, 785.

Bontemps, S., Andre, P., Terebey, S., et al. 1996, A&A, 311, 858

Brogan, C. L., Hunter, T. R., Cyganowski, C. J., et al. 2018, ApJ, 866, 87.

Brown, A. T., Little, L. T., MacDonald, G. H., & Matheson, D. N. 1982, MNRAS, 201, 121

Burns, R. A., Imai, H., Handa, T., et al. 2015, MNRAS, 453, 3163

Butler, M. J., & Tan, J. C. 2009, ApJ, 696, 484

Butler, M. J., & Tan, J. C. 2012, ApJ, 754, 5

Cabrit, S., & Bertout, C. 1992, A&A, 261, 274

Carey, S. J., Noriega-Crespo, A., Mizuno, D. R., et al. 2009, PASP, 121, 76. doi:10.1086/596581

Caselli, P., & Ceccarelli, C. 2012, A&A Rev., 20, 56

Casement, L. S., & McLean, I. S. 1996, ApJ, 462, 797

Caswell, J. L., Vaile, R. A., Ellingsen, S. P., et al. 1995, MNRAS, 272, 96.

Caswell, J. L. 1997, MNRAS, 289, 203.

Caswell, J. L. 1998, MNRAS, 297, 215.

Caswell, J. L. 2004, MNRAS, 349, 99.

Cesaroni, R., Felli, M., Testi, L., Walmsley, C. M., & Olmi, L. 1997, A&A, 325, 725

Cesaroni, R., Felli, M., Jenness, T., et al. 1999, A&A, 345, 949

Cesaroni, R., Felli, M., & Walmsley, C. M. 1999, A&AS, 136, 333

Cesaroni, R., Neri, R., Olmi, L., et al. 2005, A&A, 434, 1039

Cesaroni, R., Sánchez-Monge, Á., Beltrán, M. T., et al. 2017, A&A, 602, A59.

Chen, X., Arce, H. G., Zhang, Q., et al. 2016, ApJ, 824, 72.

Cheng, Y., Tan, J. C., Liu, M., et al. 2018, ApJ, 853, 160

Choi, M., Kang, M., Lee, J.-E., et al. 2017, The Astrophysical Journal Supplement Series, 232, 24.

Choudhury, R., Mookerjea, B., & Bhatt, H. C. 2010, ApJ, 717, 1067

Churchwell, E., Walmsley, C. M., & Cesaroni, R. 1990, Astronomy and Astrophysics Supplement Series, 83, 119.

Churchwell, E., Povich, M. S., Allen, D., et al. 2006, ApJ, 649, 759. doi:10.1086/507015

Churchwell, E. 2002, ARA&A, 40, 27. doi:10.1146/annurev.astro.40.060401.093845

Claussen, M. J., Wilking, B. A., Benson, P. J., et al. 1996, The Astrophysical Journal Supplement Series, 106, 111.

Codella, C., Bachiller, R., & Reipurth, B. 1999, A&A, 343, 585.

Codella, C., Bachiller, R., Nisini, B., et al. 2001, A&A, 376, 271

Codella, C., Cabrit, S., Gueth, F., et al. 2007, A&A, 462, L53.

Cosentino, G., Jiménez-Serra, I., Henshaw, J. D., et al. 2018, MNRAS, 474, 3760

Cosentino, G., Jiménez-Serra, I., Henshaw, J. D., et al. 2020, MNRAS, doi:10.1093/mnras/staa2942

Crimier, N., Ceccarelli, C., Alonso-Albi, T., et al. 2010, A&A, 516, A102

Csengeri, T., Leurini, S., Wyrowski, F., et al. 2016, A&A, 586, A149.

Cunningham, N. J., Moeckel, N., & Bally, J. 2009, ApJ, 692, 943

Cunningham, N. J., Moeckel, N., & Bally, J. 2009, ApJ, 692, 943.

Curiel, S., Canto, J., & Rodriguez, L. F. 1987, Revista Mexicana de Astronomia y Astrofisica, vol. 14, 14, 595.

Cyganowski, C. J., Whitney, B. A., Holden, E., et al. 2008, AJ, 136, 2391

Cyganowski, C. J., Brogan, C. L., Hunter, T. R., et al. 2009, ApJ, 702, 1615.

Cyganowski, C. J., Brogan, C. L., Hunter, T. R., et al. 2011, ApJ, 743, 56.

Davies, B., Hoare, M. G., Lumsden, S. L., et al. 2011, MNRAS, 416, 972

De Buizer, J. M., & Vacca, W. D. 2010, AJ, 140, 196

De Buizer, J. M. & Fisher, R. S. 2004, High Resolution Infrared Spectroscopy in Astronomy, eds. H.U. Kaufl, R. Siebenmorgen and A. Moorwood (Springer-Verlag: ESO Astrophysics Symposia), 84

De Buizer, J. M., Piña, R. K., & Telesco, C. M. 2000, The Astrophysical Journal Supplement Series, 130, 437.

De Buizer, J. M., Walsh, A. J., Piña, R. K., et al. 2002, ApJ, 564, 327.

De Buizer, J. M., Osorio, M., & Calvet, N. 2005, ApJ, 635, 452.

De Buizer, J. M., Radomski, J. T., Telesco, C. M., & Piña, R. K. 2005, ApJS, 156, 179

De Buizer, J. M., Liu, M., Tan, J. C., et al. 2017, ApJ, 843, 33

De Buizer, J. M., Liu, M., Tan, J. C., et al. 2017, ApJ, 843, 33.

De Buizer, J. M., & Vacca, W. D. 2010, AJ, 140, 196.

De Buizer, J. M. 2003, MNRAS, 341, 277

De Buizer, J. M. 2006, ApJ, 642, L57

De Buizer, J. M. 2007, ApJ, 654, L147

de Wit, W. J., Testi, L., Palla, F., et al. 2005, A&A, 437, 247. doi:10.1051/0004-6361:20042489

de Wit, W. J., Hoare, M. G., Fujiyoshi, T., et al. 2009, A&A, 494, 157

Deharveng, L., Zavagno, A., Cruz-Gonzalez, I., et al. 1997, A&A, 317, 459

Deharveng, L., Zavagno, A., Anderson, L. D., et al. 2012, A&A, 546, A74

Dent, W. R. F., Little, L. T., Kaifu, N., Ohishi, M., & Suzuki, S. 1985a, A&A, 146, 375

Dent, W. R. F., Little, L. T., Sato, S., Ohishi, M., & Yamashita, T. 1985b, MNRAS, 217, 217

Dent, W. R. F., Sandell, G., Duncan, W. D., & Robson, E. I. 1989, MNRAS, 238, 1497

Dewangan, L. K., & Anandarao, B. G. 2011, MNRAS, 414, 1526

Dewangan, L. K., & Ojha, D. K. 2017, ApJ, 849, 65

Dewangan, L. K., Ojha, D. K., Luna, A., et al. 2016, ApJ, 819, 66

Draine B. T. 2011, Physics of the Interstellar and Intergalactic Medium (Princeton: Princeton Univ. Press)

Draine, B. T. 2011, Physics of the Interstellar and Intergalactic Medium by Bruce T. Draine. Princeton University Press.

Duarte-Cabral, A., Bontemps, S., Motte, F., et al. 2014, A&A, 570, A1

Eislöffel, J. 2000, A&A, 354, 236

Ellingsen, S. P., Norris, R. P., & McCulloch, P. M. 1996, MNRAS, 279, 101.

Ellingsen, S. P., Shabala, S. S., & Kurtz, S. E. 2005, MNRAS, 357, 1003.

Evans, N. J., & Blair, G. N. 1981, ApJ, 246, 394

Fazio, G. G., Hora, J. L., Allen, L. E., et al. 2004, ApJS, 154, 10

Federrath, C., Schrön, M., Banerjee, R., et al. 2014, ApJ, 790, 128.

Fedriani, R., Caratti o Garatti, A., Purser, S. J. D., et al. 2019, Nature Communications, 10, 3630

Felli, M., Palagi, F., & Tofani, G. 1992, A&A, 255, 293

Felli, M., Testi, L., Valdettaro, R., et al. 1997, A&A, 320, 594

Felli, M., Massi, F., Navarrini, A., et al. 2004, A&A, 420, 553

Felli, M., Massi, F., Robberto, M., et al. 2006, A&A, 453, 911

Fich, M., & Blitz, L. 1984, ApJ, 279, 125

Fish, V. L., Reid, M. J., Wilner, D. J., et al. 2003, ApJ, 587, 701.

Fontani, F., Cesaroni, R., Testi, L., et al. 2004, A&A, 424, 179

Forster, J. R., & Caswell, J. L. 1989, A&A, 213, 339

Frank, A., Ray, T. P., Cabrit, S., et al. 2014, Protostars and Planets VI, 451.

Fuente, A., Rizzo, J. R., Caselli, P., et al. 2005, A&A, 433, 535

Fuente, A., Castro-Carrizo, A., Alonso-Albi, T., et al. 2009, A&A, 507, 1475

Fujisawa, K., Sugiyama, K., Motogi, K., et al. 2014, PASJ, 66, 31

Fujisawa, K., Takase, G., Kimura, S., et al. 2014, PASJ, 66, 78

Gao, J., Jiang, B. W., & Li, A. 2009, ApJ, 707, 89.

Garay, G., Ramirez, S., Rodriguez, L. F., Curiel, S., & Torrelles, J. M. 1996, ApJ, 459, 193

Gibb, A. G., Hoare, M. G., Little, L. T., & Wright, M. C. H. 2003, MNRAS, 339, 1011

Gibb, A. G., Davis, C. J., & Moore, T. J. T. 2007, MNRAS, 382, 1213.

Ginsburg, A., Darling, J., Battersby, C., et al. 2011, ApJ, 736, 149.

Ginsburg, A., Bally, J., & Williams, J. P. 2011, MNRAS, 418, 2121

Ginsburg, A., Glenn, J., Rosolowsky, E., et al. 2013, ApJS, 208, 14. doi:10.1088/0067-0049/208/2/14

Ginsburg, A., Glenn, J., Rosolowsky, E., et al. 2013, The Astrophysical Journal Supplement Series, 208, 14

Goddi, C., Ginsburg, A., Maud, L., et al. 2018, arXiv e-prints , arXiv:1805.05364.

Goetz, J. A., Pipher, J. L., Forrest, W. J., et al. 1998, ApJ, 504, 359

Goldsmith, P. F., & Langer, W. D. 1999, ApJ, 517, 209.

Gómez, J. F., Torrelles, J. M., Estalella, R., et al. 1992, ApJ, 397, 492

Gómez, J. F., Sargent, A. I., Torrelles, J. M., et al. 1999, ApJ, 514, 287

González, R. F., & Cantó, J. 2002, ApJ, 580, 459.

Goodman, A. A., Benson, P. J., Fuller, G. A., Myers, P. C., 1993, ApJ, 406, 528

Griffin, M. J., Abergel, A., Abreu, A., et al. 2010, A&A, 518, L3

Gueth, F., Schilke, P., & McCaughrean, M. J. 2001, A&A, 375, 1018

Guilloteau, S., Bachiller, R., Fuente, A., et al. 1992, A&A, 265, L49.

Gusdorf, A., Anderl, S., Lefloch, B., et al. 2017, A&A, 602, A8

Guzmán, A. E., Garay, G., & Brooks, K. J. 2010, ApJ, 725, 734.

Guzmán, A. E., Garay, G., Brooks, K. J., et al. 2011, ApJ, 736, 150.

Guzmán, A. E., Garay, G., Rodríguez, L. F., et al. 2014, ApJ, 796, 117.

Harju, J., Lehtinen, K., Booth, R. S., et al. 1998, Astronomy and Astrophysics Supplement Series, 132, 211.

Hatchell, J., Fuller, G. A., & Richer, J. S. 2007, A&A, 472, 187

Heaton, B. D., & Little, L. T. 1988, A&A, 195, 193

Hernández-Hernández, V., Zapata, L., Kurtz, S., & Garay, G. 2014, ApJ, 786, 38

Herter, T. L., Vacca, W. D., Adams, J. D., et al. 2013, PASP, 125, 1393

Hillenbrand, L. A., Meyer, M. R., Strom, S. E., et al. 1995, AJ, 109, 280. doi:10.1086/117272

Hirota, T., Ando, K., Bushimata, T., et al. 2008, PASJ, 60, 961

Hirota, T., Machida, M. N., Matsushita, Y., et al. 2017, Nature Astronomy, 1, 146.

Hoare, M. G., Roche, P. F., & Glencross, W. M. 1991, MNRAS, 251, 584.

Hoare, M. G., Kurtz, S. E., Lizano, S., et al. 2007, Protostars and Planets V, 181

Hoare, M. G., Purcell, C. R., Churchwell, E. B., et al. 2012, PASP, 124, 939

Hofner, P., Cesaroni, R., Olmi, L., et al. 2007, A&A, 465, 197

Hosokawa, T., Omukai, K., 2009, ApJ, 691, 823

Hosokawa, T., Yorke, H. W., Omukai, K., 2010, ApJ, 721, 478

Hughes, V. A., & Wouterloot, J. G. A. 1984, ApJ, 276, 204

Hunter, T. R., Phillips, T. G., & Menten, K. M. 1997, ApJ, 478, 283.

Israel, F. P., & Felli, M. 1978, A&A, 63, 325

Jiménez-Serra, I., Caselli, P., Tan, J. C., et al. 2010, MNRAS, 406, 187.

Johnston, K. G., Keto, E., Robitaille, T. P., & Wood, K. 2011, MNRAS, 415, 2953

Jones, T. J., Woodward, C. E., & Kelley, M. S. 2004, AJ, 128, 2448

Könyves, V., André, P., Men'shchikov, A., et al. 2015, A&A, 584, A91

Königl, A., Pudritz, R. E., 2000, in Protostars and Planets IV, ed. V. Mannings (Tucson: University of Arizona Press), 759

Konigl, A., & Pudritz, R. E. 2000, Protostars and Planets IV, 759.

Kauffmann, J., Pillai, T., Shetty, R., et al. 2010, ApJ, 716, 433

Keto, E., & Zhang, Q. 2010, MNRAS, 406, 102

Kirk, H. & Myers, P. C. 2012, ApJ, 745, 131. doi:10.1088/0004-637X/745/2/131

Klein, R., Posselt, B., Schreyer, K., et al. 2005, ApJS, 161, 361

Kong, S., Tan, J. C., Caselli, P., et al. 2017, ApJ, 834, 193

Kong, S., Arce, H. G., Maureira, M. J., et al. 2019, ApJ, 874, 104

Krassner, J., Pipher, J. L., Sharpless, S., et al. 1982, A&A, 109, 223

Kratter, K. M., Matzner, C. D., Krumholz, M. R., 2008, ApJ, 681, 375

Krishnan, V., Ellingsen, S. P., Reid, M. J., et al. 2015, ApJ, 805, 129.

Krishnan, V., Ellingsen, S. P., Reid, M. J., et al. 2017, MNRAS, 465, 1095.

Krumholz, M. R., & McKee, C. F. 2008, Nature, 451, 1082

Krumholz, M. R., & McKee, C. F. 2008, Nature, 451, 1082

Kumar Dewangan, L., & Anandarao, B. G. 2010, MNRAS, 402, 2583

Kurtz, S., Churchwell, E., & Wood, D. O. S. 1994, ApJS, 91, 659

Kurtz, S., Churchwell, E., & Wood, D. O. S. 1994, The Astrophysical Journal Supplement Series, 91, 659.

Kurtz, S. E., Watson, A. M., Hofner, P., et al. 1999, ApJ, 514, 232.

Kurtz, S., Hofner, P., & Álvarez, C. V. 2004, ApJS, 155, 149

Lada, C. J. & Lada, E. A. 2003, ARA&A, 41, 57. doi:10.1146/annurev.astro.41.011802.094844

López-Calderón, C., Bronfman, L., Nyman, L.-Å., et al. 2016, A&A, 595, A88.

López-Sepulcre, A., Walmsley, C. M., Cesaroni, R., et al. 2011, A&A, 526, L2.

Lada, C. J., & Fich, M. 1996, ApJ, 459, 638.

Lawrence, A., Warren, S. J., Almaini, O., et al. 2007, MNRAS, 379, 1599.

Lee, C.-F., Mundy, L. G., Reipurth, B., et al. 2000, ApJ, 542, 925.

Lee, C.-F., Hasegawa, T. I., Hirano, N., et al. 2010, ApJ, 713, 731.

Lee, H.-T., Liao, W.-T., Froebrich, D., et al. 2013, ApJS, 208, 23

Lee, C.-F., Hirano, N., Zhang, Q., et al. 2015, ApJ, 805, 186.

Lee, C.-F., & Sahai, R. 2004, ApJ, 606, 483.

Lefloch, B., Eisloeffel, J., & Lazareff, B. 1996, A&A, 313, L17

Lefloch, B., Cernicharo, J., Pacheco, S., et al. 2011, A&A, 527, L3

Lefloch, B., Gusdorf, A., Codella, C., et al. 2015, A&A, 581, A4

Leurini, S., Codella, C., López-Sepulcre, A., et al. 2014, A&A, 570, A49.

Li, J., Wang, J., Gu, Q., Zhang, Z.-Y., Zheng, X., 2012, ApJ, 745, 47

Li, S., Wang, J., Fang, M., et al. 2019, ApJ, 878, 29. doi:10.3847/1538-4357/ab1e4c

Li, S., Zhang, Q., Pillai, T., et al. 2019, ApJ, 886, 130. doi:10.3847/1538-4357/ab464e

Li, S., Sanhueza, P., Zhang, Q., et al. 2020, arXiv:2009.05506

Lim, B., Chun, M.-Y., Sung, H., et al. 2013, AJ, 145, 46. doi:10.1088/0004-6256/145/2/46

Lim, W., Tan, J. C., Kainulainen, J., Ma, B., & Butler, M. J. 2016, ApJ, 829, L19

Little, L. T., Kelly, M. L., & Murphy, B. T. 1998, MNRAS, 294, 105

Liu, T., Wu, Y.-F., & Wang, K. 2010, Research in Astronomy and Astrophysics, 10, 67

Liu, M., Tan, J. C., Cheng, Y., et al. 2018, ApJ, 862, 105

Liu, M., Tan, J. C., De Buizer, J. M., et al. 2019, ApJ, 874, 16

Liu, M., Tan, J. C., De Buizer, J. M., et al. 2020, arXiv:2006.06424, accepted by ApJ.

Liu, M., Tan, J. C., Marvil, J., et al. 2020, arXiv:2010.11294, submitted to ApJ.

Ma, B., Tan, J. C., & Barnes, P. J. 2013, ApJ, 779, 79.

Martins, F., Hillier, D. J., Paumard, T., et al. 2008, A&A, 478, 219. doi:10.1051/0004-6361:20078469

Matsushita, Y., Machida, M. N., Sakurai, Y., et al. 2017, MNRAS, 470, 1026.

Matthews, H. I. 1979, A&A, 75, 345

Matzner, C. D., & McKee, C. F. 1999, Star Formation 1999, 353

Matzner, C. D., McKee, C. F., 2000, ApJ, 545, 364

Maud, L. T., Moore, T. J. T., Lumsden, S. L., et al. 2015, MNRAS, 453, 645.

McCutcheon, W. H., Dewdney, P. E., Purton, C. R., et al. 1991, AJ, 101, 1435

McKee, C. F., & Tan, J. C. 2003, ApJ, 585, 850

McKee, C. F., & Tan, J. C. 2003, ApJ, 585, 850

McKee, C. F., & Tan, J. C. 2003, ApJ, 585, 850

McKee, C. F., & Tan, J. C. 2003, ApJ, 585, 850.

McLaughlin, D. E., Pudritz, R. E., 1996, ApJ, 469, 194

McLaughlin, D. E., Pudritz, R. E., 1997, ApJ, 476, 750

McLaughlin, D. E., & Pudritz, R. E. 1996, ApJ, 469, 194.

McMullin, J. P., Waters, B., Schiebel, D., et al. 2007, Astronomical Data Analysis Software and Systems XVI, 376, 127

Meakin, C. A., Hines, D. C., & Thompson, R. I. 2005, ApJ, 634, 1146

Mehringer, D. M. 1994, The Astrophysical Journal Supplement Series, 91, 713.

Men'shchikov, A., André, P., Didelon, P., et al. 2012, A&A, 542, A81.

Minniti, D., Lucas, P. W., Emerson, J. P., et al. 2010, , 15, 433.

Mitchell, G. F., & Hasegawa, T. I. 1991, ApJ, 371, L33

Molinari, S., Brand, J., Cesaroni, R., et al. 1996, A&A, 308, 573

Molinari, S., Testi, L., Rodríguez, L. F., et al. 2002, ApJ, 570, 758

Molinari, S., Pezzuto, S., Cesaroni, R., et al. 2008, A&A, 481, 345

Molinari, S., Pezzuto, S., Cesaroni, R., et al. 2008, A&A, 481, 345.

Molinari, S., Schisano, E., Elia, D., et al. 2016, A&A, 591, A149. doi:10.1051/0004-6361/201526380

Montes, V. A., Hofner, P., Oskinova, L. M., et al. 2018, arXiv e-prints , arXiv:1806.06293.

Mookerjea, B., & Ghosh, S. K. 1999, Journal of Astrophysics and Astronomy, 20, 1.

Moro-Martín, A., Noriega-Crespo, A., Molinari, S., et al. 2001, ApJ, 555, 146

Moscadelli, L., Reid, M. J., Menten, K. M., et al. 2009, ApJ, 693, 406

Moscadelli, L., Cesaroni, R., Rioja, M. J., Dodson, R., & Reid, M. J. 2011, A&A, 526, A66

Moscadelli, L., Sánchez-Monge, Á., Goddi, C., et al. 2016, A&A, 585, A71. doi:10.1051/0004-6361/201526238

Moser, E., Liu, M., Tan, J. C., et al. 2019, arXiv e-prints, arXiv:1907.12560, accepted to ApJ.

Moser, E., Liu, M., Tan, J. C., et al. 2020, ApJ, 897, 136.

Motte, F., Bontemps, S., Schilke, P., et al. 2007, A&A, 476, 1243.

Motte, F., Bontemps, S., & Louvet, F. 2018, ARA&A, 56, 41. doi:10.1146/annurev-astro-091916-055235

Motte, F., Nony, T., Louvet, F., et al. 2018, Nature Astronomy, 50

Mottram, J. C., Hoare, M. G., Lumsden, S. L., et al. 2010, A&A, 510, A89.

Mottram, J. C., Hoare, M. G., Urquhart, J. S., et al. 2011, A&A, 525, A149.

Murphy, T., Cohen, M., Ekers, R. D., et al. 2010, MNRAS, 405, 1560.

Narayanan, G., & Walker, C. K. 1996, ApJ, 466, 844

Neri, R., Fuente, A., Ceccarelli, C., et al. 2007, A&A, 468, L33

Neugebauer, G., Habing, H. J., van Duinen, R., et al. 1984, ApJ, 278, L1

Newman, M. E. J. 2005, Contemporary Physics, 46, 323

Nisini, B., Massi, F., Vitali, F., et al. 2001, A&A, 376, 553

Norris, R. P., Whiteoak, J. B., Caswell, J. L., et al. 1993, ApJ, 412, 222.

Offner, S. S. R., Clark, P. C., Hennebelle, P., et al. 2014, Protostars and Planets VI, 53

Offner, S. S. R., & Arce, H. G. 2014, ApJ, 784, 61.

Offner, S. S. R., & Chaban, J. 2017, ApJ, 847, 104.

Ohashi, S., Sanhueza, P., Chen, H.-R. V., et al. 2016, ApJ, 833, 209

Ortega, M. E., Paron, S., Cichowolski, S., Rubio, M., & Dubner, G. 2012, A&A, 546, A96

Ospina-Zamudio, J., Lefloch, B., Ceccarelli, C., et al. 2018, A&A, 618, A145

Ossenkopf V. & Henning T. 1994, A&A, 291, 943

Ossenkopf, V., & Henning, T. 1994, A&A, 291, 943

Ossenkopf, V., & Henning, T. 1994, A&A, 291, 943.

Palau, A., Sánchez-Monge, Á., Busquet, G., et al. 2010, A&A, 510, A5

Palau, A., Fuente, A., Girart, J. M., et al. 2013, ApJ, 762, 120

Palau, A., Fuente, A., Girart, J. M., et al., 2013, ApJ, 762, 120

Palla, F., & Stahler, S. W. 1993, ApJ, 418, 414

Palla, F., Cesaroni, R., Brand, J., et al. 1993, A&A, 280, 599

Palla, F., Cesaroni, R., Brand, J., et al. 1993, A&A, 280, 599.

Pang, X., Grebel, E. K., Allison, R. J., et al. 2013, ApJ, 764, 73. doi:10.1088/0004-637X/764/1/73

Paron, S., Fariña, C., & Ortega, M. E. 2013, A&A, 559, L2

Patel, N. A., Greenhill, L. J., Herrnstein, J., et al. 2000, ApJ, 538, 268

Phillips, C. J., Norris, R. P., Ellingsen, S. P., et al. 1998, MNRAS, 300, 1131.

Pilbratt, G. L., Riedinger, J. R., Passvogel, T., et al. 2010, A&A, 518, L1

Pillai, T., Wyrowski, F., Carey, S. J., & Menten, K. M. 2006, A&A, 450, 569

Plambeck, R. L., Wright, M. C. H., Friedel, D. N., et al. 2009, ApJ, 704, L25.

Plunkett, A. L., Arce, H. G., Mardones, D., et al. 2015, Nature, 527, 70.

Poglitsch, A., Waelkens, C., Geis, N., et al. 2010, A&A, 518, L2

Principe, D. A., Cieza, L., Hales, A., et al. 2018, MNRAS, 473, 879.

Purser, S. J. D., Lumsden, S. L., Hoare, M. G., et al. 2016, MNRAS, 460, 1039.

Qin, S.-L., Wang, J.-J., Zhao, G., Miller, M., & Zhao, J.-H. 2008, A&A, 484, 361

Qiu, K., Zhang, Q., Megeath, S. T., et al. 2008, ApJ, 685, 1005. doi:10.1086/591044

Qiu, K., Zhang, Q., Menten, K. M., Liu, H. B., & Tang, Y.-W. 2013, ApJ, 779, 182

Qiu, K., & Zhang, Q. 2009, ApJ, 702, L66.

Ragan, S. E., Bergin, E. A., & Gutermuth, R. A. 2009, ApJ, 698, 324

Rathborne, J. M., Jackson, J. M., & Simon, R. 2006, ApJ, 641, 389

Rathborne, J. M., Garay, G., Jackson, J. M., et al. 2011, ApJ, 741, 120. doi:10.1088/0004-637X/741/2/120

Ray, T. P., Poetzel, R., Solf, J., & Mundt, R. 1990, ApJ, 357, L45

Reid, M. J., Menten, K. M., Zheng, X. W., et al. 2009, ApJ, 700, 137-148

Reipurth, B., Raga, A. C., & Heathcote, S. 1992, ApJ, 392, 145.

Ressler, M. E., & Shure, M. 1991, AJ, 102, 1398

Ressler, M. E., Werner, M. W., Van Cleve, J., & Chou, H. A. 1994, Experimental Astronomy, 3, 277

Retes-Romero, R., Mayya, Y. D., Luna, A., et al. 2020, ApJ, 897, 53

Robitaille, T. P., Whitney, B. A., Indebetouw, R., et al. 2006, ApJS, 167, 256

Robitaille, T. P., Whitney, B. A., Indebetouw, R., et al. 2007, The Astrophysical Journal Supplement Series, 169, 328.

Rodríguez, L. F., Moran, J. M., Franco-Hernández, R., et al. 2008, AJ, 135, 2370. doi:10.1088/0004-6256/135/6/2370

Rodriguez, L. F., Ho, P. T. P., & Moran, J. M. 1980, ApJ, 240, L149

Rohde, P. F., Walch, S., Seifried, D., et al. 2019, MNRAS, 483, 2563.

Rosen, A. L., Offner, S. S. R., Sadavoy, S. I., et al. 2020, Space Sci. Rev., 216, 62. doi:10.1007/s11214-020-00688-5

Rosero, V., Hofner, P., Claussen, M., et al. 2016, The Astrophysical Journal Supplement Series, 227, 25.

Rosero, V., Tanaka, K. E. I., Tan, J. C., et al. 2019, ApJ, 873, 20.

Rosero, V., Hofner, P., Kurtz, S., et al. 2019, ApJ, 880, 99. doi:10.3847/1538-4357/ab2595

Rosolowsky, E. W., Pineda, J. E., Kauffmann, J., et al. 2008, ApJ, 679, 1338.

Rygl, K. L. J., Brunthaler, A., Reid, M. J., et al. 2010, A&A, 511, A2

Sánchez-Monge, Á., Palau, A., Estalella, R., et al. 2008, A&A, 485, 497

Sánchez-Monge, Á., Palau, A., Estalella, R., et al. 2010, ApJ, 721, L107

Sánchez-Monge, Á., Cesaroni, R., Beltrán, M. T., et al. 2013, A&A, 552, L10

Sánchez-Monge, Á., Beltrán, M. T., Cesaroni, R., et al. 2013, A&A, 550, A21.

Sánchez-Monge, Á., López-Sepulcre, A., Cesaroni, R., et al. 2013, A&A, 557, A94.

Sánchez-Monge, Á., Beltrán, M. T., Cesaroni, R., et al. 2014, A&A, 569, A11

Saito, H., Saito, M., Sunada, K., et al. 2007, ApJ, 659, 459

Sakai, T., Sakai, N., Hirota, T., et al. 2010, ApJ, 714, 1658.

Salpeter, E. E. 1955, ApJ, 121, 161

Sandell, G., Goss, W. M., & Wright, M. 2005, ApJ, 621, 839

Sanhueza, P., Jackson, J. M., Foster, J. B., et al. 2012, ApJ, 756, 60.

Sanhueza, P., Jackson, J. M., Foster, J. B., et al. 2013, ApJ, 773, 123. doi:10.1088/0004-637X/773/2/123

Sanhueza, P., Contreras, Y., Wu, B., et al. 2019, ApJ, 886, 102. doi:10.3847/1538-4357/ab45e9

Sanna, A., Moscadelli, L., Goddi, C., et al. 2018, A&A, 619, A107.

Saraceno, P., Ceccarelli, C., Clegg, P., et al. 1996, A&A, 315, L293

Sargent, A. I. 1977, ApJ, 218, 736

Schilke, P., Walmsley, C. M., Pineau des Forets, G., et al. 1997, A&A, 321, 293.

Schuller, F., Menten, K. M., Contreras, Y., et al. 2009, A&A, 504, 415. doi:10.1051/0004-6361/200811568

Serabyn, E., Guesten, R., & Mundy, L. 1993, ApJ, 404, 247

Seth, A. C., Greenhill, L. J., & Holder, B. P. 2002, ApJ, 581, 325

Shakura, N. I., Sunyaev, R. A., 1973, A&A, 24, 337

Shepherd, D. S., & Churchwell, E. 1996, ApJ, 457, 267

Shepherd, D. S., & Watson, A. M. 2002, ApJ, 566, 966

Shimoikura, T., Dobashi, K., Matsumoto, T., et al. 2016, ApJ, 832, 205

Shu, F. H., Najita, J. R., Shang, H., et al. 2000, Protostars and Planets IV, 789.

Shu, F. H., 1977, ApJ, 214, 488

Shure, M. A., Toomey, D. W., Rayner, J. T., Onaka, P. M., & Denault, A. J. 1994, Proc. SPIE, 2198, 614

Skrutskie, M. F., Cutri, R. M., Stiening, R., et al. 2006, AJ, 131, 1163

Smith, H. A., & Beck, S. C. 1994, ApJ, 420, 643

Smith, R. J., Longmore, S., & Bonnell, I. 2009, MNRAS, 400, 1775. doi:10.1111/j.1365-2966.2009.15621.x

Snell, R. L., & Bally, J. 1986, ApJ, 303, 683

Sokolov, V., Wang, K., Pineda, J. E., et al. 2017, A&A, 606, A133

Staff, J. E., Tanaka, K. E. I., & Tan, J. C. 2019, ApJ, 882, 123

Stojimirović, I., Snell, R. L., & Narayanan, G. 2008, ApJ, 679, 557

Stone, J. M., & Norman, M. L. 1993, ApJ, 413, 210.

Su, Y.-N., Liu, S.-Y., Chen, H.-R., Zhang, Q., & Cesaroni, R. 2007, ApJ, 671, 571

Sugitani, K., Fukui, Y., Mizuni, A., et al. 1989, ApJ, 342, L87

Sugitani, K., Matsuo, H., Nakano, M., et al. 2000, AJ, 119, 323

Takahashi, S., Saigo, K., Ho, P. T. P., et al. 2012, ApJ, 752, 10

Tan, J. C., Kong, S., Butler, M. J. et al. 2013, ApJ, 779, 96

Tan, J. C., Beltrán, M. T., Caselli, P., et al. 2014, Protostars and Planets VI, 149

Tan, J. C., Kong, S., Zhang, Y., et al. 2016, ApJ, 821, L3.

Tanaka, K. E. I., Tan, J. C., & Zhang, Y. 2017, ApJ, 835, 32

Tofani, G., Felli, M., Taylor, G. B., et al. 1995, A&AS, 112, 299

Torrelles, J. M., Gomez, J. F., Anglada, G., et al. 1992, ApJ, 392, 616

Torrelles, J. M., Verdes-Montenegro, L., Ho, P. T. P., Rodriguez, L. F., & Canto, J. 1993, ApJ, 410, 202

Torrelles, J. M., Gómez, J. F., Rodríguez, L. F., et al. 1998, ApJ, 505, 756

Towner, A. P. M., Brogan, C. L., Hunter, T. R., et al. 2017, The Astrophysical Journal Supplement Series, 230, 22.

Towner, A. P. M., Brogan, C. L., Hunter, T. R., et al. 2019, ApJ, 875, 135. doi:10.3847/1538-4357/ab1140

Trinidad, M. A., Rodríguez, T., & Rodríguez, L. F. 2009, ApJ, 706, 244

Ulrich, R. K., ApJ, 210, 377

Urquhart, J. S., Moore, T. J. T., Csengeri, T., et al. 2014, MNRAS, 443, 1555.

Urquhart, J. S., König, C., Giannetti, A., et al. 2018, MNRAS, 473, 1059

Vázquez-Semadeni, E., Gómez, G. C., Jappsen, A.-K., et al. 2009, ApJ, 707, 1023. doi:10.1088/0004-637X/707/2/1023

Vázquez-Semadeni, E., González-Samaniego, A., & Colín, P. 2017, MNRAS, 467, 1313. doi:10.1093/mnras/stw3229

Valdettaro, R., Palla, F., Brand, J., et al. 2005, A&A, 443, 535

van Kempen, T. A., Longmore, S. N., Johnstone, D., et al. 2012, ApJ, 751, 137

Velusamy, T., Langer, W. D., Kumar, M. S. N., et al. 2011, ApJ, 741, 60

Vig, S., Ghosh, S. K., Kulkarni, V. K., et al. 2006, ApJ, 637, 400.

Walsh, A. J., Burton, M. G., Hyland, A. R., et al. 1998, MNRAS, 301, 640.

Walsh, A. J., Burton, M. G., Hyland, A. R., & Robinson, G. 1999, MNRAS, 309, 905

Walsh, A. J., Burton, M. G., Hyland, A. R., et al. 1999, MNRAS, 309, 905.

Walsh, A. J., Bertoldi, F., Burton, M. G., & Nikola, T. 2001, MNRAS, 326, 36

Walsh, A. J., Bertoldi, F., Burton, M. G., et al. 2001, MNRAS, 326, 36.

Walsh, A. J., Chapman, J. F., Burton, M. G., et al. 2007, MNRAS, 380, 1703.

Walsh, A. J., & Burton, M. G. 2006, MNRAS, 365, 321.

Wang, Y., Zhang, Q., Rathborne, J. M., et al. 2006, ApJ, 651, L125.

Wang, P., Li, Z.-Y., Abel, T., & Nakamura, F. 2010, ApJ, 709, 27

Wang, P., Li, Z.-Y., Abel, T., & Nakamura, F. 2010, ApJ, 709, 27.

Watson, C., Araya, E., Sewilo, M., et al. 2003, ApJ, 587, 714.

Weintraub, D. A., & Kastner, J. H. 1996, ApJ, 458, 670

Werner, M. W., Becklin, E. E., Gatley, I., et al. 1979, MNRAS, 188, 463

White, R. L., Becker, R. H., & Helfand, D. J. 2005, AJ, 130, 586

Whitney, B. A., Wood, K., Bjorkman, J. E., Wolff, M. J., 2003, ApJ, 591, 1049

Whitney, B. A., Robitaille, T. P., Bjorkman, J. E., Dong, R., Wolff, M. J., Wood, K., Honor, J., 2013, ApJS, 207, 30

Wilking, B. A., Mundy, L. G., Blackwell, J. H., et al. 1989, ApJ, 345, 257

Wilking, B., Mundy, L., McMullin, J., et al. 1993, AJ, 106, 250

Williams, J. P., de Geus, E. J., & Blitz, L. 1994, ApJ, 428, 693

Wilner, D. J., Ho, P. T. P., & Zhang, Q. 1996, ApJ, 462, 339

Wood, D. O. S., & Churchwell, E. 1989, ApJS, 69, 831

Wouterloot, J. G. A., & Walmsley, C. M. 1986, A&A, 168, 237

Wu, Y., Wei, Y., Zhao, M., et al. 2004, A&A, 426, 503

Wu, Y., Zhang, Q., Chen, H., et al. 2005, AJ, 129, 330

Wu, Y. W., Sato, M., Reid, M. J., et al. 2014, A&A, 566, A17

Wynn-Williams, C. G., Becklin, E. E., & Neugebauer, G. 1974, ApJ, 187, 473

Wynn-Williams, C. G., Becklin, E. E., Beichman, C. A., Capps, R., & Shakeshaft, J. R. 1981, ApJ, 246, 801

Young, E. T., Herter, T. L., Güsten, R., et al. 2012, Proc. SPIE, 8444, 844410

Zapata, L. A., Rodríguez, L. F., & Kurtz, S. E. 2001, , 37, 83

Zapata, L. A., Ho, P. T. P., Rodríguez, L. F., et al. 2007, A&A, 471, L59

Zapata, L. A., Fernandez-Lopez, M., Curiel, S., Patel, N., & Rodriguez, L. F. 2013, arXiv:1305.4084

Zavagno, A., Lagage, P. O., & Cabrit, S. 1999, A&A, 344, 499

Zhang, Y., & Tan, J. C. 2011, ApJ, 733, 55

Zhang, Y., & Tan, J. C. 2015, ApJ, 802, L15

Zhang, Q., Hunter, T. R., Sridharan, T. K., & Cesaroni, R. 1999, ApJ, 527, L117

Zhang, B., Zheng, X. W., Reid, M. J., et al. 2009, ApJ, 693, 419

Zhang, Y., Tan, J. C., & McKee, C. F. 2013, ApJ, 766, 86

Zhang, Y., Tan, J. C., De Buizer, J. M., et al. 2013b, ApJ, 767, 58

Zhang, C.-P., Wang, J.-J., Xu, J.-L., et al. 2014, ApJ, 784, 107.

Zhang, Y., Tan, J. C., & Hosokawa, T. 2014, ApJ, 788, 166

Zhang, Q., Wang, K., Lu, X., & Jiménez-Serra, I. 2015, ApJ, 804, 141

Zhang, Y., Tan, J. C., Sakai, N., et al. 2019, ApJ, 873, 73. doi:10.3847/1538-4357/ab0553

Zhang, Y., & Tan, J. C. 2018, ApJ, 853, 18

Zinnecker, H. & Yorke, H. W. 2007, ARA&A, 45, 481. doi:10.1146/annurev.astro.44.051905.092549